F. P. Bakker

Trench Siltation near the ETM of a Well-mixed Estuary

Master Thesis Report

Trench Siltation near the ETM of a Well-mixed Estuary

Master Thesis Report

By

F. P. Bakker

Thesis committee:	Prof. Dr. Ir. S. G. J. Aarninkhof,	TU Delft, Chairman
	Prof. Dr. Ir. Z. B. Wang,	TU Delft, Deltares
	Dr. C. Chassagne,	TU Delft
	Ir. A. Hendriks,	Boskalis

Version	1.0
Date	27th of February 2020

TU Delft Boskalis

Preface

This report marks the final step in obtaining the title of Master of Science in Civil Engineering, the degree achieved by successfully fulfilling the master program of Hydraulic Engineering at the Delft University of Technology. I would like to thank a number of people for their help and support during the research.

First of all, I would like to acknowledge the members of my committee, *Stefan Aarninkhof*, who helped me focusing on the broader and practical picture of the research, *Zheng Bing Wang*, who caused me a lot of headaches when digging into the detailed fundamental estuarine processes and mechanisms, *Claire Chassagne*, who let me sharpen the technical formulations and thereby helped me in zooming out of the details, and *Antoon Hendriks*, who helped me a lot with the direction, practical (engineering) problems and formalities during the thesis.

A special thanks to *Antoon Hendriks*, and *Boskalis*, and *Hydronamic* in particular, for giving me the opportunity to perform the research at such a wonderful company. I could not have obtained the same personally satisfactory results without the resources provided by Boskalis. Furthermore, as I met and cooperated with a lot of new colleagues and students during my thesis, they created a pleasurable working environment.

Additionally, I would like to thank *Thijs van Kessel*, *Jebbe van der Werf*, and *Deltares* for their help in the implementation of the detailed numerical model. Without them, this vital and extensive part of the thesis would have cost me even more time, then it already did now.

Finally, I would like to give special thanks to my family and friends for their support and distraction. In particular, I would like to thank my parents, Nanouk and Arjan, and my brother, Mees for their everlasting support, motivation and patience during the thesis. Without them, I could not have finished my graduation and studies in such a personally satisfactory way.

Floor Bakker,
Gouda, February, 2020

Summary

To exploit its socio-economic functions, engineering measures are regularly applied in estuaries. Estuaries are, however, known to be very complex systems. Stemming from this complexity is the generation of a so-called estuarine turbidity maximum (ETM), which poses great siltation problems to the engineering measures.

An engineering measure, which is looked upon in this thesis, is a trench accommodating for the construction of a submerged tunnel. Despite the complexity of estuaries, trench siltation rates are predicted in practice by simple empirical formulas. However, a lot of uncertainty is associated with the predicted trench siltation rates, as such engineering tools do not capture the complex estuarine mechanisms. These mechanisms are found to dominate the sediment supply to the trench and the subsequent trapping of sediment in the trench.

Therefore, in this thesis, it is investigated to which degree of certainty trench siltation rates in estuaries can be predicted, based on a process-oriented and engineering-oriented viewpoint. This is researched according to the implementation of a detailed process-based numerical model, which is considered to be highly accurate. For this purpose, the following case study is adopted: a trench near the ETM of the well-mixed Scheldt Estuary, at Oosterweel, Belgium.

The uncertainty of the numerical model is estimated based on a sensitivity analysis, which maps the epistemic uncertainty, and a scenario analysis, which approximates the intrinsic uncertainty. For verification purposes, modelling results are compared with the state-of-the-art theory on trench siltation mechanisms, and estuarine sediment transport and trapping mechanisms. These are thoroughly analyzed in this thesis based on an extensive literature study. Additionally, a link to practice is made by comparison of the degree of certainty and practicality of the numerical model with the engineering tools.

The numerical model predicted mainly sand to be deposited in the more exposed areas of the trench and mainly (fluid) mud in the more sheltered areas. Furthermore, it was found that the model predicts considerable variation in sedimentation over a tidal cycle with generally less sedimentation during flood. It could be estimated, based on the parameter uncertainty, that the epistemic uncertainty of the numerical model equals approximately 1.5 times the predicted siltation volumes. A similar uncertainty due to intrinsic uncertainty was estimated, as the trench siltation rates showed a strong dependency on the governing environmental conditions regarding tide, river and storms at sea. In total, this led to a quantifiable uncertainty in the order of 2.5 times the expected siltation volumes.

Regardless of this uncertainty, great confidence is put in the performance of the numerical model, as in accordance with existing literature of the study area and theory on well-mixed estuary, important mechanisms in the supply of sediment to the trench were found to be: *salinity-induced circulation, tidal rectification, Stokes' drift* and *river discharge*. Additionally, the governing sediment trapping mechanisms of the trench, found by the model, are in line with state-of-the-art literature. In contrast, yet unidentified by literature, the longitudinal salinity gradient over the estuary also seem to dominantly influence the trapping efficiency of the trench, in particular during flood in which it induces a strong decrease in sediment trapping.

In comparison, it is believed that engineering tools, applied for trenches in estuaries, are prone to very high epistemic uncertainty caused by model inadequacy. This is because stand-alone application of the engineering tool on the problem gave a significant over-estimation of the siltation volumes, as predicted by the numerical model. Furthermore, the engineering tool was found to behave differently within a tidal cycle, and on changing environmental conditions. Above epistemic uncertainties due to model inadequacy could, however, not be quantifiably supported.

In conclusion, the degree of certainty of the trench siltation rates is believed to be improved significantly using a detailed numerical model instead of engineering tools. However, a huge drawback of the application of detailed numerical models, is the complexity and the impracticality of the numerical model. Therefore, this thesis opts for the development/use of a more sophisticated semi-empirical tool for engineering measures in estuaries. Though, more research is recommended on trenches in both similar and different type of estuaries in order to generalize and confirm the findings of this thesis.

Content

List of Figures

List of Tables

1 Introduction

1.1 Background

Estuaries are semi-enclosed coastal water bodies which have a free connection to the ocean or sea and within which salty water is diluted by freshwater, originating from terrestrial sources (Cameron & Pritchard, 1963). Hence, they are subject to both marine influences (tides, waves and saline water) and fluvial influences (freshwater discharge). Estuaries are considered to be efficient traps for both fluvial and marine sediments and are, therefore, characterized by high concentrations of suspended particulate matter (SPM) (Meade, 1969). Moreover, estuaries are known to be very complex, dynamic, and adaptive systems. Their elements are interconnected and adjust to changing circumstances, stemming from both natural and anthropogenic causes. It makes the behavior of an estuary generally non-linear, non-deterministic, and erratic (Van Buuren & Gerrits, 2008). Due to spatio-temporal gradients in environmental conditions (e.g. in hydrodynamics, salinity, nutrient-rich suspended sediment concentrations (SSC), etc.), estuaries are highly productive ecological systems. As a consequence, they provide great socio-economically benefits for humanity (e.g. recreation, fishing, agriculture, shipping, etc.) (McLusky & Elliott, 2004). To exploit these functions, often anthropogenic engineering measures are applied in the system.

An example of a local engineering measure, which is looked upon in this thesis, is the construction of a **trench** to accommodate for the construction of an immersed tunnel. As an open trench is prone to **siltation** (sedimentation of fine sediments (e.g. mud (clay, silt) and sand)), the main challenge in the construction of a trench is to keep the design depth of the trench and to remove fluid mud (highly-concentrated suspension of mud) from the bed. The danger of this fluid mud is twofold:

- tunnel elements may not be able to reach the bed during submersion, as fluid mud increases the density of the water;
- the fluid mud under the submerged element may weaken the later to be constructed sand key, which may eventually result in subsidence of the tunnel

Posing a serious threat to the construction of a trench in an estuary is the formation of a so-called **estuarine turbidity maximum (ETM)**, which stems from the complexity of an estuary. This is a zone of high SPM concentrations in which the turbidity may be 5-100 times greater than that at the seaward limit or at the river upstream. ETMs are induced by resuspension of a bottom pool of mud. This bottom pool of mud is locally formed through convergent SPM transport (Becherer, 2013a; Burchard, Schuttelaars, & Ralston, 2018). Underlying mechanisms of this convergent transport are known as **sediment transport and trapping mechanisms**. These individual mechanisms act asymmetrically over a tidal cycle, resulting in a residual exchange flow, and hence, residual SPM transport throughout the estuary. The interconnectivity of the mechanisms leads to zero residual transport at a distinct location in the estuary, at which sediment is trapped and an ETM may be formed. Consequently, high sediment transport fluxes are found near an ETM, which are also affected by the same transport mechanisms, as they influence the local hydrodynamics

The sediment transport and trapping mechanisms have been studied by many researchers, starting with the work of Pritchard (1952, 1954, 1956), and Postma & Kalle (1955). They focused on the drivers of the classical estuarine circulation: the longitudinal residual flow pattern in an estuary induced by the density gradient along the estuary, which is created by the difference in density of seawater and river water. More recently, other mechanisms have also been investigated in their role of sediment transport and trapping in estuaries. Examination of ETMs show that these local circulation mechanisms induce similar SPM transport and trapping as the classical longitudinal mechanisms. Furthermore, **micro-scale**

mechanisms on particle level, such as flocculation of cohesive particles, were found to be important mechanisms in the trapping of SPM (Burchard et al., 2018; Winterwerp, 1999).

The governing sediment transport and trapping mechanisms differ, however, among estuaries. This is mainly dependent on the characteristics in time-varying forcing due to: tides, wind, waves, river. Therefore, in order to generalize findings, estuaries are being classified. The most cited classification is based on the relative importance of **mixing** due to tidal currents and the **degree of stratification (baroclinicity)** due to river discharge, which are both forcing terms of the classical gravitational circulation (Hansen & Rattray, 1965). Another characteristic of estuaries, which is considered important in the effectiveness of the (local) mechanisms, and on which estuaries are widely classified on, is **geomorphology** (Valle-Levinson, 2010). Based on the above, there is significant spatio-temporal variation in the location and intensity of the ETM (Burchard et al., 2018).

1.2 Problem Description

As stated earlier, the complexity of an estuary forms a huge constraint in the design, functioning, construction and maintenance of a trench. In particular, siltation (sedimentation of fine sediments) is considered an enormous challenge due to the high suspended sediment concentrations (SSC) near an ETM. As trench siltation involves two main elements, namely (Deltares, 2011):

- the sediment carried by the water towards the trench: if no sediment will be supplied to the trench, there will be no sedimentation.
- the trapping efficiency of the trench: if the supplied sediment cannot deposit in the trench, there will be no sedimentation.

it is believed that a lot depends on the described spatio-temporal variation and interconnectivity of the macro-scale and micro-scale estuarine sediment transport and trapping mechanisms.

In practice, however, simple **engineering tools** are used to predict siltation rates for trench siltation. In such tools, empirical formulations are imposed, which estimate the difference in sediment transport between the ambient area and the trench, and the efficiency of the trench in trapping the excess sediment. Engineering tools do not capture the complex estuarine mechanisms, and are, therefore, believed to result in very uncertain siltation rates.

An additional problem is the state-of-the-art knowledge of the sediment transport and trapping mechanisms in estuaries. There is a lack of knowledge on which mechanisms are dominant, as this differs among estuaries, and among locations within an estuary. Furthermore, according to the author's knowledge, no research has been performed to date on the interaction between the estuarine mechanisms and local engineering measures. For example, the effect of a longitudinal salinity gradient on the trapping efficiency of trenches is yet not looked into.

1.3 Research objective

The objective of this research is to **improve the estimation of the trench siltation rates in estuaries** through implementation of a detailed numerical model, which is deemed to identify:

- the (degree of uncertainty around the predicted) siltation rates and sedimentation distribution over the trench,
- the governing estuarine sediment transport and trapping mechanisms,
- potential interaction between the sediment transport and trapping mechanisms and the trench,
- the variability of the distinct sediment transport and trapping mechanisms under different environmental conditions.

To narrow down the scope, this research will mainly focus near the location of the ETM of a **well-mixed** estuary. Such an estuary is classified as a macrotidal system with relatively small river runoff, leading to intensified mixing and, accordingly, a low degree of baroclinicity. As a consequence, a (nearly) vertically uniform salinity profile can be found, and a gradual longitudinal salinity gradient. Furthermore, the ETM may be tens of kilometers wide, as there is no clear location of zero residual sediment transport, as for instance for a stratified (salt wedge) estuary.

To reach this objective, the following research question is formulated:

*To which **degree of certainty** can **siltation rates of trenches** near the **estuarine turbidity maximum** of a **well-mixed estuary** be predicted, using a detailed numerical model, which identifies and captures the **normative sediment transport and trapping mechanisms**, their **variability over time**, and their **interaction with the trench**, based on a **process-oriented** and **engineering-oriented viewpoint**?*

For practicality, a case study is adopted to answer this research question. This case study is illustrated in the next section.

Figure 1 – Overview of the Oosterweel-connection project in which the submerged tunnel under the Scheldt, named the Scheldt Tunnel (2), is one of the five parts (RoTS).

1.4 Application: case study submerged Scheldt Tunnel at Oosterweel

Underlying this research is a submerged tunnel construction project in Antwerp, a large city in Belgium with 850,000 inhabitants. Due to its strategic location along the Scheldt Estuary, Antwerp has developed a port, which, at the moment of publication, is the second largest port of Europe (Port of Antwerp, 2018). Also having an airport, Antwerp is an important logistic and economic node in Europe. The necessity of good mobility is, therefore, considered very important. However, the accessibility of Antwerp and its port is becoming very poor due to increasing traffic, leading to economic loss and a decrease in quality of life for the inhabitants (Oosterweel-verbinding, 2018).

To improve the mobility of Antwerp, the Flemish Government has established Masterplan Antwerp in 2020. The goal of this plan is mainly to improve traffic flows in and around Antwerp.

One of the plans is to realize the Oosterweel-connection, which is presented in Figure 1. The Oosterweel-connection will complete the ring-road of Antwerp, by providing a second highway link across the Scheldt Estuary. This is believed to reduce the traffic intensity elsewhere on the ring-road. The project will consist of 5 parts, of which one is a 1.8 km long tunnel under the Scheldt Estuary; the Scheldt Tunnel. The tunnel is designed as an immersed tunnel, consisting of prefabricated reinforced concrete tunnel caissons, which will be placed in a dredged trench (Oosterweel-verbinding, 2018).

As for this trench, initially a simple hydrodynamic and sediment transport model was set up in order to predict its siltation rates. However, given the complex conditions at the planned location of the immersed tunnel, it is believed that a simple model study might result in very uncertain siltation rates. This complexity is due to the fact that the SSC is very high, as there is an ETM located in this particular stretch of the Scheldt Estuary (Van Kessel, Vanlede, & Bruens, 2006). This is visualized in Figure 2.

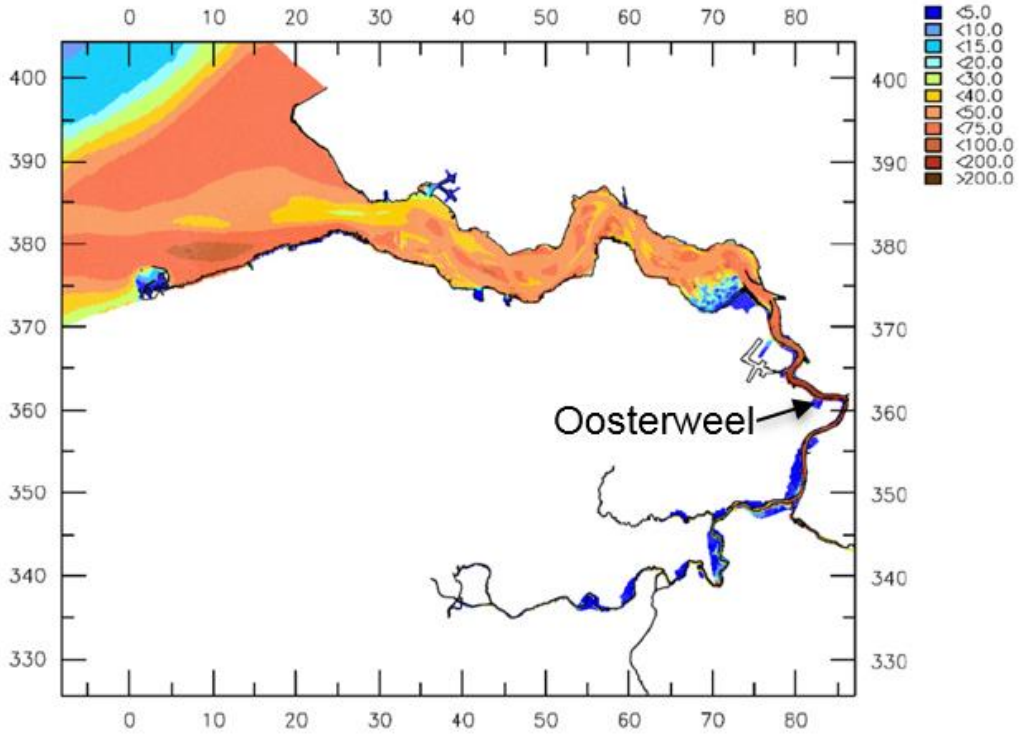

Figure 2 – Computed fortnightly averaged SPM surface concentrations in the Western Scheldt Estuary. An ETM is observed near the city of Antwerp (After: Van Kessel et al., 2011)

The results of the simple model were, therefore, advised to be interpreted as an indication rather than a certainty. The presence of the ETM is expected to result in high trench siltation rates, which poses a huge risk to the construction and maintenance of the trench. As the working method of excavation and maintenance of the trench highly depends on the siltation rates, it is worthwhile to develop an alternative model with the intention to be able to predict the siltation rates with higher accuracy.

Trench design

The design of the trench is visualized in Figure 3. It is curved and obliquely aligned with the estuary. The trench has a maximum designed depth of 27.5 m TAW at the location of the estuarine channel, which has a depth of about 15 m TAW. TAW is the national levelling system of Belgium (Tweede Algemene Waterpassing). A total of 8 tunnel elements are planned to be submerged. The designed across-trench directed slopes of the trench have a gradient of 1:4-1:7. The design lifetime of the trench is approximately 3-4 months, as the caissons are preferably submerged during neap tide. For other details of the design of the trench and Scheldt tunnel, one is referred to Lantis Antwerp.

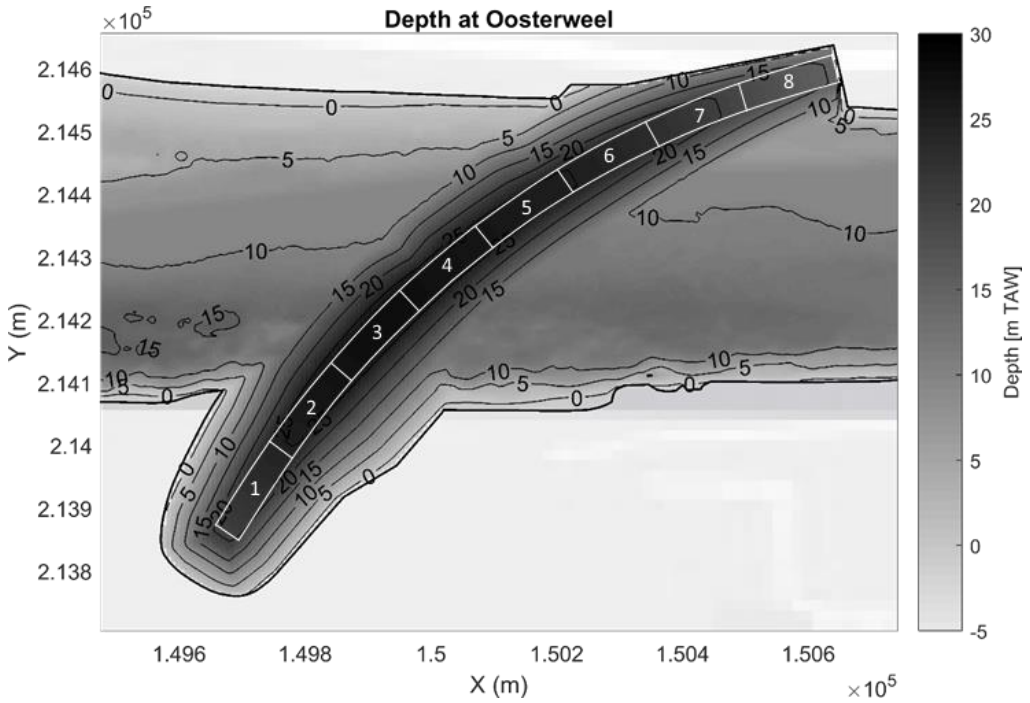

Figure 3 – Design of the trench of the Scheldt Tunnel at Oosterweel

1.5 Research approach

The general approach of this research is visualized in Figure 4. The main element of this approach is the implementation of a detailed numerical model which captures the area of the ETM of the Scheldt Estuary. The purpose of this model is to accurately estimate the trench siltation rates and sedimentation distribution over the trench. Through a fine mesh of the detailed numerical model the macro-scale (especially horizontal and lateral) and micro-scale mechanisms are aimed to be modelled accurately. The basis of this model lies in the combination of a:

- Literature study
  Through an extensive literature study, it is aspired to create a theoretical framework in which the estuarine processes and sediment transport and trapping mechanisms are identified, described and quantified. Moreover, the framework tends to capture the theory on the trapping efficiency mechanisms of trenches. This gives the required information which processes to model and to specify the study area description (see next bullet point). A summative scheme is constructed, giving a complete overview of the mechanisms, their dependencies and their interactions. Later in the research, modelling results can be analyzed thoroughly based on this framework and verified extensively through comparison with theory.
- Study area description
  An study area analysis is performed on the Scheldt Estuary, and for the location of the ETM in specific. The goal is to identify the dynamics of the system and its underlying mechanisms. This is believed to be vital in understanding the behavior of the estuary and eventually in the verification of the numerical modelling results in the remainder of the research. Additionally, it may give information on the mechanisms which are not able to be captured by the numerical model.
- Large-scale numerical model
  Since it is also of great importance to capture the large scale estuarine dynamics in the detailed model, an existing validated three-dimensional large-scale numerical model of the entire Scheldt Estuary is analyzed. This model is called NEVLA3D/LTV Slib and is implemented by Deltares and Flemish Hydraulics, commissioned by Rijkswaterstaat. The most recent model run (year 2014) of the model is used, which

shows remarkably good results in the hydro- and morphodynamics of the system, and in particular in the prediction of the ETM. Therefore, it is investigated which processes are taken into account. Furthermore, the result of the run are applied on the boundaries of the detailed numerical model.

The detailed numerical model is calibrated and validated with the help of measurement data from stations and transects, and siltation rates of sluice basins. As the trench has not been constructed yet, it is assumed that a validated detailed numerical for the situation without the trench could also be used as a valid model for the situation including the trench.

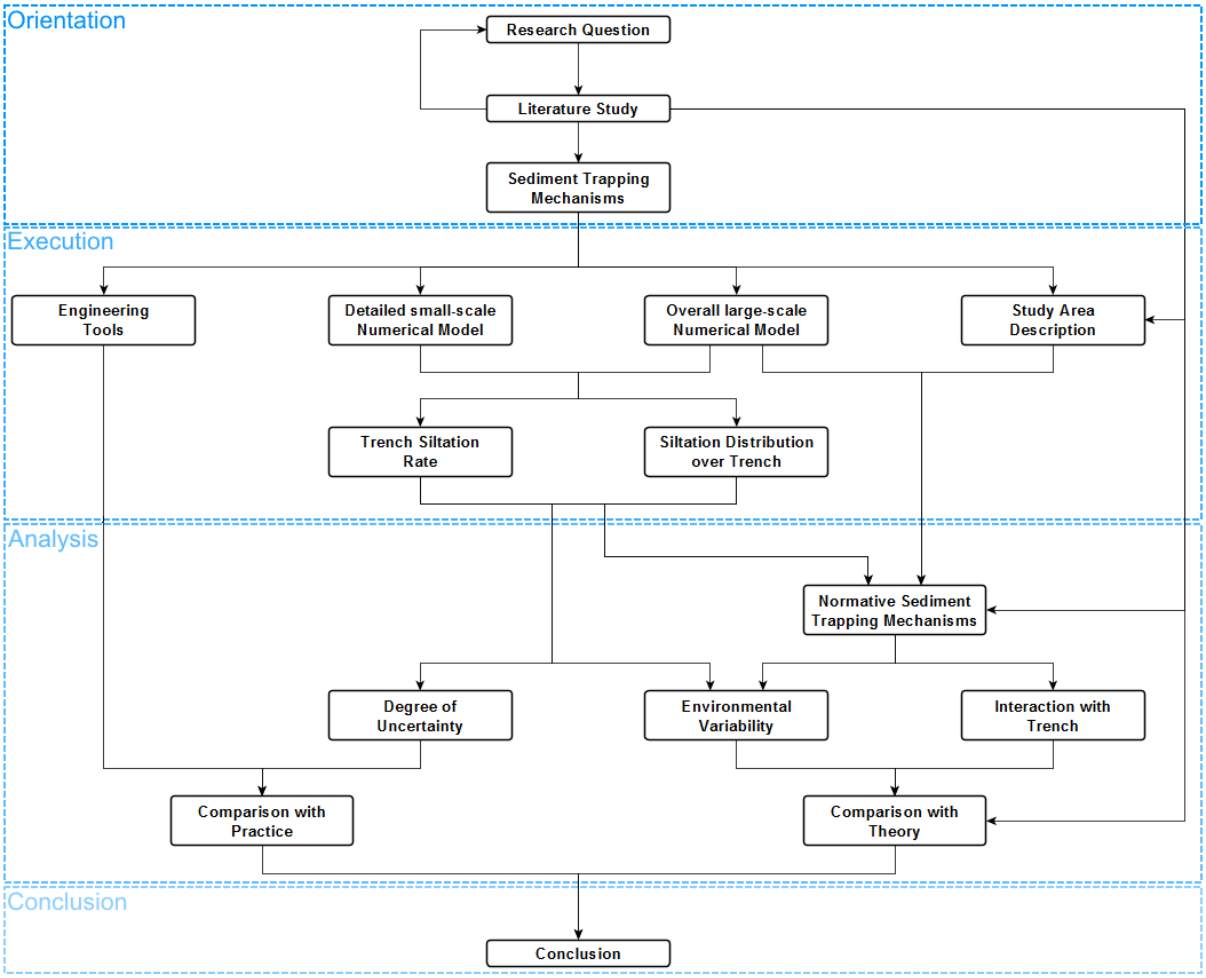

Figure 4 – Conceptual approach of the research

Analysis

The identification of the governing sediment transport and trapping mechanisms, their variability in nature, and their possible interaction with the trench, are researched through a thorough analysis of the modelling results, using the theoretical framework and the results of the study area description. It is aimed through comparison with state-of-the-art theory to verify the modelling results.

The degree of uncertainty of the detailed model is investigated through both a scenario analysis on the variability of the environmental components (intrinsic uncertainty), as well as a sensitivity analysis on to the author's and experts', and literature's believed to be most determining parameters for trench siltation (epistemic uncertainty).

A probabilistic assessment will result in the estimation of the total degree of uncertainty around the trench siltation rates. Comparison with the uncertainty of an engineering tool reveals the practicality of the detailed model.

Eventually, it is believed that above steps will result in a conclusion to which degree of uncertainty trench siltation rates can be modelled using a complex 3D model near the ETM of an well-mixed estuary.

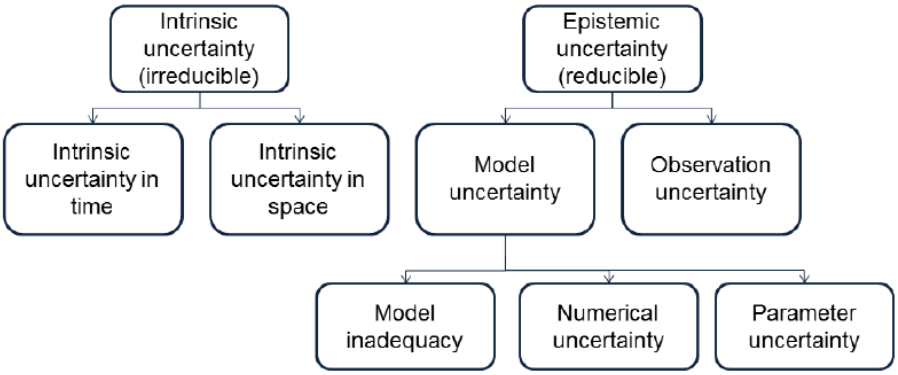

Figure 5 – Types of uncertainty in sediment transport and trapping modelling throughout an estuary (after: A.Kroon (2020).

1.6 Reader

This report starts with a theoretical framework of the general estuarine macro- and micro-scale sediment transport and trapping mechanisms in Chapter 2, including trapping efficiency mechanisms of trenches. This is followed by a system analysis of the Scheldt Estuary in Chapter 3. Chapter 4 gives a description of the numerical models which are used/implemented in this thesis. Subsequently, Chapter 5 goes briefly into the validation of the detailed numerical model. Chapter 6 introduces the various model simulation scenarios, after which Chapter 7 gives the results of these simulations. These modelling results are thoroughly discussed in Chapter 8. This research ends with a conclusion in Chapter 9 and recommendations for improvements on this research and further research in Chapter 10.

2 Theoretical Framework

This chapter focuses on the identification of possible physical processes and mechanisms in the transport and trapping of sediment in a trench in an estuary. As there is a general lack of knowledge on the governing processes and mechanisms, the purpose is to create a complete overview of possible governing mechanisms. The theoretical framework is, therefore, a vital part in this research, as it:

- determines the modelling approach,
- specifies the study area description,
- details the post-processing of the modelling results;
- verifies the modelling results based on state-of-the-art theory.

First, the mechanisms determining the trapping efficiency of trenches are discussed. Subsequently, possible underlying estuarine sediment transport and trapping mechanisms governing the transport of sediment to the trench are described. The theoretical framework will conclude with a summative overview of the found mechanisms in a flow chart, in which all identified mechanisms are arranged on their characteristics. Also, their dependencies and interactions with each other are visualized. This scheme is opted to be applicable for other general types of estuaries.

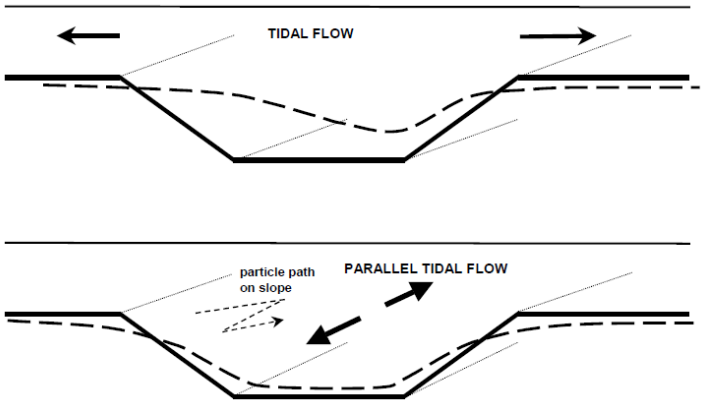

Figure 6 – Channel deposition and erosion (Van Rijn, 2017)

2.1 Trapping Efficiency of the Trench

The trapping efficiency of trenches is primarily determined by the influence of the trench on the local hydro- and morphodynamics, as the current velocity and SSC profiles gradually adapt over the trench to reach an equilibrium with the new depth. The trapping efficiency of trenches is found to be dependent on (Van Rijn, 2017):

- the alignment of the trench with respect to the direction of the approaching currents
- the dimensions of the trench (width and depth)
- the local current

Jensen, Madsen, & Fredsøe (1999a, 1999b) found that trench siltation is mainly dependent on the angle of incidence of the current with respect to the normal axis of the trench. However, trench dimensions and local currents may significantly alter the magnitude of the siltation by intensifying the hydro- and morphodynamical patterns.

In the below, the influence of the relative alignment of the trench with respect to the approaching currents on the governing hydro- and morphodynamics is discussed in detail. Subsequently, the influence of the trench dimensions and the local currents on these pattern are clarified.

2.1.1 Alignment of trench

In estuaries, three different flow patterns over the trench may occur, which are depicted in Figure 6. These are: (Van Rijn, 2017):

- Tidal flow parallel to the normal trench axis
- Tidal flow perpendicular to the normal trench axis
- Tidal flow oblique to the normal trench axis

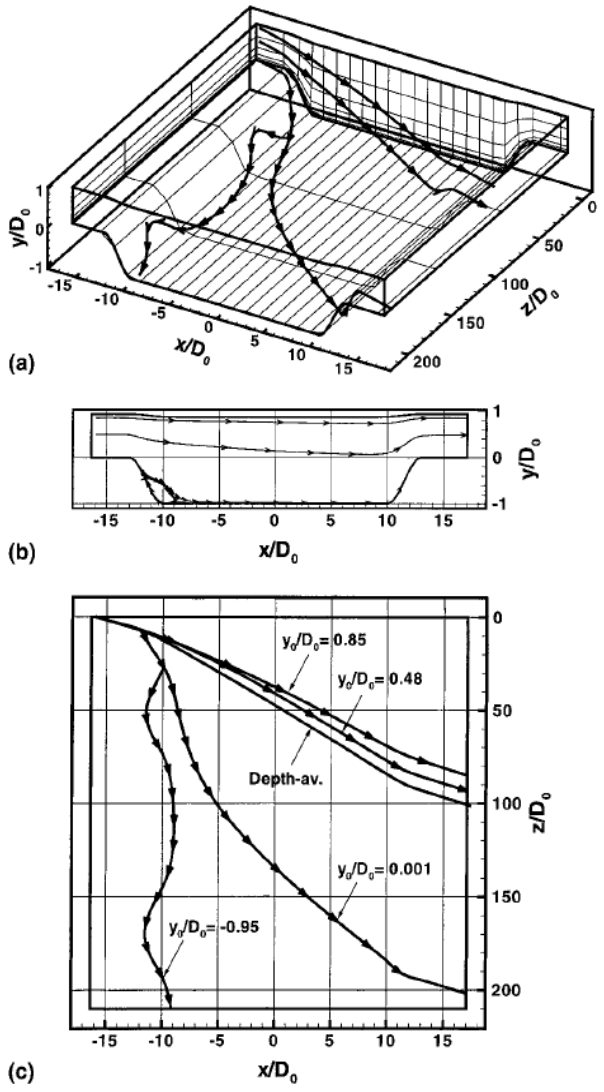

Figure 7 – Streamlines for obliquely approaching current over an trench/channel; a) 3D visualization of refracted streamlines; b) streamline projection on (x,y)-plane; c) streamline projection on (x,z)-plane (Jensen et al., 1999a).

Hydrodynamics

If the trench is parallel to the current, the trench will attract the current due to the increased depth of the trench, which reduces bottom friction. Current velocities may, therefore, increase with respect to the ambient current. Furthermore, slightly upstream of the trench, flow contraction is found to occur over a short distance, yielding a local increase and subsequent decrease in flow velocity. On the contrary, a perpendicularly approaching current decreases in magnitude due to an sudden increase of the depth. Additionally, flow separation may occur with a subsequent return current. This is dependent on the steepness of the slopes of the trench: flow separation tend to occur for slopes which are 1:5 and steeper (Van Rijn, 2017).

Oblique flow

For currents oblique to a trench, the above described flow patterns for both parallel and perpendicular flow will occur simultaneously. The smaller the angle of obliquity, the more the flow is attracted by the trench. Additionally, currents are deflected through a refraction-type pattern in the channel, especially when currents velocities are small (Van Rijn, 2017). This mechanism causes the smaller near-bed velocities to be more refracted than the greater velocities in the water column. Consequently, a secondary motion develops (see Figure 7). Furthermore, a corkscrew-type secondary current at the upstream slope may develop for obliquely aligned trenches, as can be observed in Figure 7. This is caused by flow separation and refracted parallel flow simultaneously (Jensen et al., 1999a).

Morphodynamics

Suspended load

The suspended sediment transport within a trench is highly dependent on the altered hydrodynamics. It is mainly determined by the degree of turbulence and bed shear stress, which may differ considerably over the trench. This is dependent on (Jensen et al., 1999b):

1. the degree of flow separation on the upstream slope of the trench,

2. the increase/decrease in elevation of sediment particles relative to the bed level,
3. the variation in along-trench flow direction over vertical,
4. settling velocity of the particles,
5. the acceleration of the along-trench velocity component over the trench,
6. the magnitude of the along-trench velocity component over the trench,
7. the acceleration of the across-trench velocity component over the trench;
8. the magnitude of the across-trench velocity component over the trench.

In general, trench siltation due to SPM increases with obliquity of the trench: the more the trench is perpendicular aligned to the current, the more sedimentation. Transport of SPM in cross-trench direction increases over the upstream slope (see Figure 8). This is caused by an increase in turbulent kinetic energy, generated by (1) ,(2), and (3), which brings particles higher above the be. Subsequently, these particles are advected by an increase in (6). Although the turbulent kinetic energy increases, the along-trench SPM transport decreases due to an decrease in (8). This reduction in along-trench transport is, however, less than the increase in cross-trench transport of suspended sediment, which implies that the upstream slope experiences erosion. Furthermore, sediment may be trapped, depending on (1), which becomes more efficient at greater approach angles (Jensen et al., 1999b).

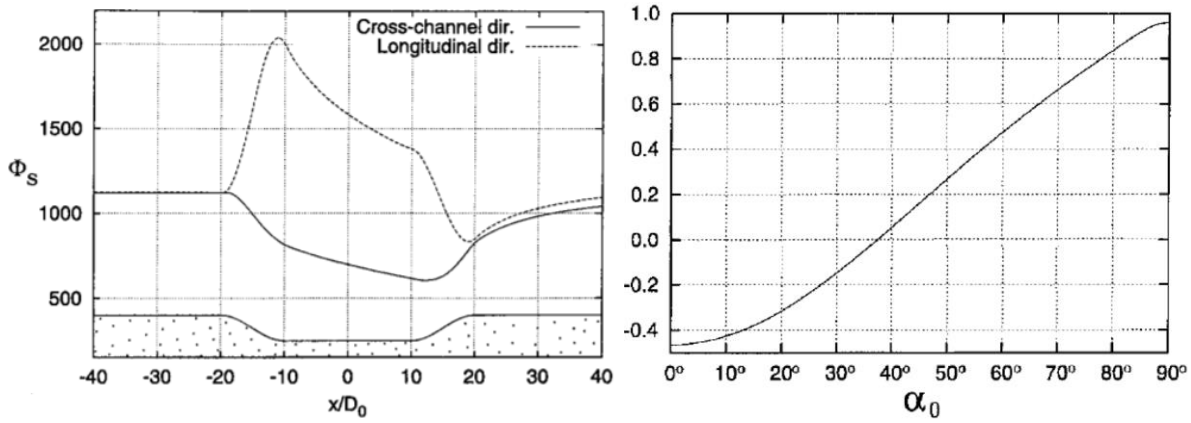

Figure 8 – Left: Across and along-trench components of suspended sediment transport across a channel/trench. Right: Erosion (negative)/Deposition (positive) of sediment in a trench/channel as a function of inlet angle (Jensen et al., 1999b).

Over the channel both the along- and cross-trench SPM transport decrease as turbulence diminishes due to a decrease in (5) and (7), and are advected less due to a decrease in (6) and (8). Accordingly, the SPM concentration profile adapts gradually over the trench through settling sediment particles, which is dependent on (4) (Jensen et al., 1999b).

For the downstream slope, mechanism (2) and (3) are now reversed. This causes the across-trench SPM transport to decrease initially. Nevertheless, turbulent kinetic energy increases at this slope (and beyond) due to an increase in (7). Also (8) increases, which leads to an increasing along- and cross-channel sediment transport. These will eventually equal the initial transport fluxes (Jensen et al., 1999b).

Bedload transport

Jensen et al. (1999b) found that an approach angle of 45°, the sedimentation rate of a trench due to bedload transport is minimal and will not differ much with obliquity of the trench. This is because of counteracting mechanisms:

- the supply of sand increases with increasing obliquity (also holds for SPM).
- the strength of the flow separation increases with increasing obliquity.
- the sediment transport capacity across the trench becomes more uniform with decreasing obliquity due to the prolonged exposure time of the sediment in the trench (Jensen et al., 1999b).

Depending on the ratio between the SPM load and bedload, the trench may backfill differently.

2.1.2 Trench dimensions

The dimensions of the trench regarding the width and depth may significantly modify the in the above described hydro- and morphodynamical patterns for differently aligned trenches with respect to the governing currents.

In general, a deeper trench magnifies the described patterns (Jensen et al., 1999b). Difference in width, however, may alter the described situation. For wider perpendicular trenches, the flow and SSC can reach equilibrium at which no erosion or sedimentation takes place. Furthermore, wider oblique trenches tend to deflect more cross-trench current to the along-trench direction, leading to more turbulence and less siltation. The influence of the width decreases with increasing obliquity (Jensen et al., 1999b).

2.1.3 Local current

Above considerations are based on an uniform and steady flow. These conditions are hardly found in nature. Therefore, local unsteady flow can alter above described sedimentation patterns significantly. Trench siltation is dependent on the strength of the local current and the distribution of the local current over the cross-section, and consequently, on the ambient bathymetry (Van Rijn, 2017). This highlights the influence of the various estuarine sediment transport and trapping mechanisms.

2.2 Sediment Supply to Trench

Gross sediment transport fluxes are determining the supply of sediment to the trench, whereas gradients in gross sediment transport in space and variation of the fluxes over time determine the sedimentation distribution over the trench.

In an estuary, large gross transport fluxes can be found for both suspended sediment and bed load sediment. Gross estuarine sediment transport is primarily a result of the tidal and river flow, and is affected by the complex sediment transport mechanisms and trapping mechanisms, which also determine the sediment availability. Due to large availability of fines, large gross transport fluxes are present in the area of the ETM, leading possibly to extreme siltation rates.

In this thesis, sediment transport and trapping mechanisms are subdivided in:

- **macro-scale mechanisms**, which determine the horizontal transport of sediment in suspension and affect bedload transport;
- **micro-scale mechanisms** are classified as mechanisms which regulate the vertical transport of fine sediment in suspension.

There may be strong interaction between above mechanisms on various spatial scales. In the remainder of this section, macro-scale and micro-scale sediment transport and trapping mechanisms are discussed separately.

2.2.1 Macro-scale mechanisms

Macro-scale mechanisms in an estuary can be subdivided based on:

1. Underlying processes:
   Macro-scale mechanisms can either be classified as (Van Maren, Van Kessel, Cronin, & Sittoni, 2015):
   - Barotropic mechanisms
     Mechanisms in which gradients in water density can be disregarded.
   - Baroclinic mechanisms
     Mechanisms in which a gradient in water density plays a dominant role, such as gradients induced by differences in salinity, temperature, and SSC (Becherer, 2013a).

2. Direction of work:
   Macro-scale mechanisms can also be categorized in (Becherer, 2013a):
   - Direct drivers
     Mechanisms which act in the same direction during the entire tidal cycle, thereby creating asymmetry.
   - Indirect drivers
     These are mechanisms which are able to break otherwise symmetric quantities, while changing direction throughout the tidal cycle.
3. Orientation
   Although the sediment transport mechanisms create a complex three-dimensional pattern, individual mechanisms can be separated in three different directions of vorticity (circulation), ω, as can be seen in Figure 9:
   - Longitudinal
   - Horizontal
   - Lateral

   Note that within the estuary, mechanisms within differently orientated planes may interact with each other (Becherer, 2013a).

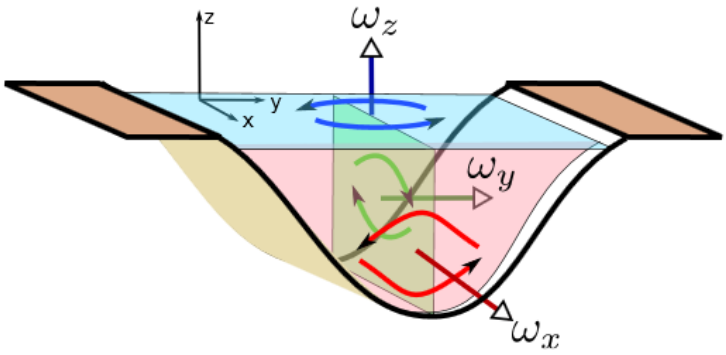

Figure 9 – Three circulation or vorticity components in a tidal channel aligned with x, in which ω_x resembles lateral circulation, ω_y longitudinal circulation, and ω_z horizontal circulation (Becherer, 2013).

In the below, examples of mechanisms are given, which are typically found in well-mixed estuaries. Other possible mechanisms which may play a role in estuaries in general are listed in Appendix A.

Barotropic mechanisms
Barotropic mechanisms are defined as interactions between fine sediment and the motion of water in which density variations are considered to be unimportant. Well-known barotropic processes, occurring in well-mixed estuaries: are tides, wind, river discharge, and short-crested waves (Allen, Salomon, Bassoullet, Du Penhoat, & De Grandpre, 1980; Burchard et al., 2018; Friedrichs, Armbrust, & De Swart, 1998; Uncles, 2002). Apart from river discharge, barotropic mechanisms are considered to act indirectly.

In the below, three major tidal barotropic processes are discussed: tidal rectification, Stokes' drift and lag effects. Other important barotropic sediment transport and trapping mechanisms are clarified in Appendix A, which, as well, gives a more elaborate explanation of the mechanisms in the below.

Tidal rectification
Tidal rectification is the generation of tidal residual currents (Tee, 1976), oriented in either the longitudinal, horizontal or lateral plane:

1. *Longitudinal circulation*
   Peak-velocity asymmetry is given as the difference in magnitude between the average peak flood and consecutive average peak ebb tidal velocity. The mechanism may result in a net sediment transport in the direction of the maximum tidal velocities, in

particular for medium and coarse sediments, so-called flood- or ebb-dominant transport (Dronkers, 1986).

Peak-velocity asymmetries are generated through deformation of the tidal wave, as it propagates. It is explained by the difference in wave celerity between the flood and ebb tidal wave (Dronkers, 1986). Furthermore, the same asymmetries are generated through the interaction of the tidal wave with itself (Sassi & Hoitink, 2013). Peak-velocity asymmetry is dependent on the estuarine hypsometry (Li & O'Donnell, 1997). Furthermore, the tidal asymmetry may also be influenced by externally generated tidal asymmetry in the adjacent sea (Uncles, 2002). Furthermore, tidal asymmetry may be time-dependent, since the tidal wave may be varying over time (e.g. spring-neap cycle) (Toublanc, Brenon, Coulombier, & Le Moine, 2015; Wang, Jeuken, & De Vriend, 1999).

2. *Horizontal circulation*
   Geomorphology of the estuary may result in horizontal residual current eddies. This is a consequence of nonlinear advection (Zimmerman, 1981). Examples are horizontal circulation due to headlands/structures, shoals, and channel curvature: meandering tidal channels tend to produce horizontal residual circulation, as nonlinear advection causes flow to shoot out the bends. Consequently, residual eddies develop which are directed in ebb-direction at the seaward part of the outer bend, and in flood direction at the seaward part of the inner bend, and the other way around for the landward part of the bend (Li, Chen, Guadagnoli, & Georgiou, 2008).

3. *Lateral circulation*
   In bends, secondary lateral circulation occurs due to the interplay between centrifugal forces, and a subsequent balancing pressure gradient. A pattern arises, which is directed to the outer bend near the surface and to the inner bend near the bed. Since the centrifugal forces are directed to the outer bend during both flood and ebb, a lateral residual current emerges over a full tidal cycle (Nidzieko, Hench, & Monismith, 2009).

Stokes' Drift

Another important barotropic sediment trapping and transport mechanism is called Stokes' drift. This is the mass flux associated with tidal propagation of a (partly) progressive tidal wave, resulting in net inflow of water. (Guo, Van der Wegen, Roelvink, & He, 2014; Li & O'Donnell, 1997; Wang et al., 1999). This inflowing flux is compensated by an opposing outgoing flow, which is generated by a pressure gradient due to a longitudinal water level set-up. The interaction between the Stokes' return flow and tides can cause a net seaward-directed residual longitudinal sediment transport (Li & O'Donnell, 1997; Wang et al., 1999). Stokes' drift may also develop horizontal residual circulation, as it is dependent on the depth (Li and O'Donnell, 1997).

Lag Effects

Another set of well-known barotropic mechanisms composes of lag effects of fine sediment. This is caused by the transport of fines, which is not in equilibrium with the current velocity, as the relaxation timescales of erosion and sedimentation are of the same order as the tidal period. This is in contrast to medium to coarse sediments. In the remainder of this subsection, two important lag effects are discussed, which act in the longitudinal direction: acceleration/deceleration asymmetry and settling lag (Gatto, Van Prooijen, & Wang, 2017; Wang et al., 1999):

1. *Acceleration (asymmetry)*
   Asymmetry in acceleration and deceleration of a tidal wave, also known as slack water asymmetry, is caused by asymmetry in the tide: the rate at which the velocity changes between both consecutive slack waters may differ between flood and ebb tide. The larger the acceleration/ deceleration, the larger the difference between the actual suspended sediment concentration and the equilibrium concentration (Wang et al., 1999).

2. Settling Lag

Settling lag is the delayed particle deposition after the onset of settling. As the settling to the bed takes time, particles are carried with the slackening tidal currents to deposit at a location further upstream (downstream) during flood (ebb) tide (Gatto et al., 2017; Postma, 1961; Van Straaten & Kuenen, 1958). This is presented in Figure 10a. Averaged over a tidal cycle this does not lead to a net transport of suspended particles. Nevertheless, coexisting sub-mechanisms may interact with settling lag to generate a net transport of suspended sediment. These sub-mechanisms are: velocity damping, bed-level variation and water-depth variation. Due to velocity damping in landward direction, the re-entrainment of particles during ebb tide is caused by a water parcel whose velocity amplitude is smaller than the water parcel that transported the particle in landward direction. This results in a net landward-directed transport of particles, as presented in Figure 10b (Gatto et al., 2017; Pritchard & Hogg, 2003). A landward decrease in bed-level may also lead to net transport of suspended sediment, as settling lag effects reduce in landward direction. Consequently, the pick-up of the particle at the onset of ebb is caused by approximately the same water parcel that transported the particle landward. This can be seen in Figure 10c (Gatto et al., 2017; Van Straaten & Kuenen, 1958). Furthermore, if there is a (partly) progressive tidal wave, the deposition threshold is attained at a lower water depth during ebb than during flood. Again, this leads to net landward displacement of the particles, as depicted by Figure 10d (Gatto et al., 2017).

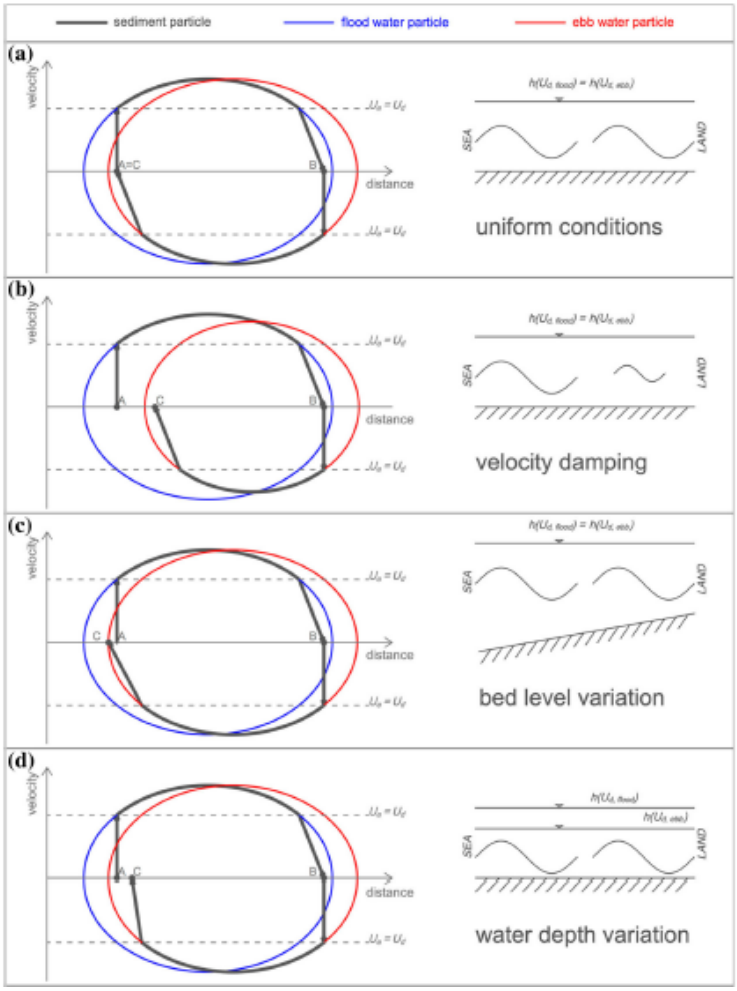

Figure 10 – Settling lag mechanisms. Redrawn and extended after Pritchard and Hogg (2003). The x-axis represents the streamwise distance from the inlet, the y-axes the velocity of the sediment (water) particle. The dotted lines are the threshold velocities for erosion and deposition. A different sub-mechanism is illustrated in each panel (Gatto et al., 2017).

Lag effects also have a temporal character, which is caused by time-varying sediment characteristics due the micro-scale sediment trapping mechanisms, such as flocculation (see micro-scale mechanisms) (Gatto et al., 2017).

Baroclinic mechanisms

Baroclinic mechanisms are the assembly of interactions between fine sediment and hydrodynamic processes, which are driven and/or affected by density differences. Density differences in an estuary are primarily induced by the transition between fresh water discharge

and the salty sea water. Major baroclinic processes are: gravitational circulation (direct mechanism) and internal mixing asymmetries (indirect mechanisms) (Burchard et al., 2018).

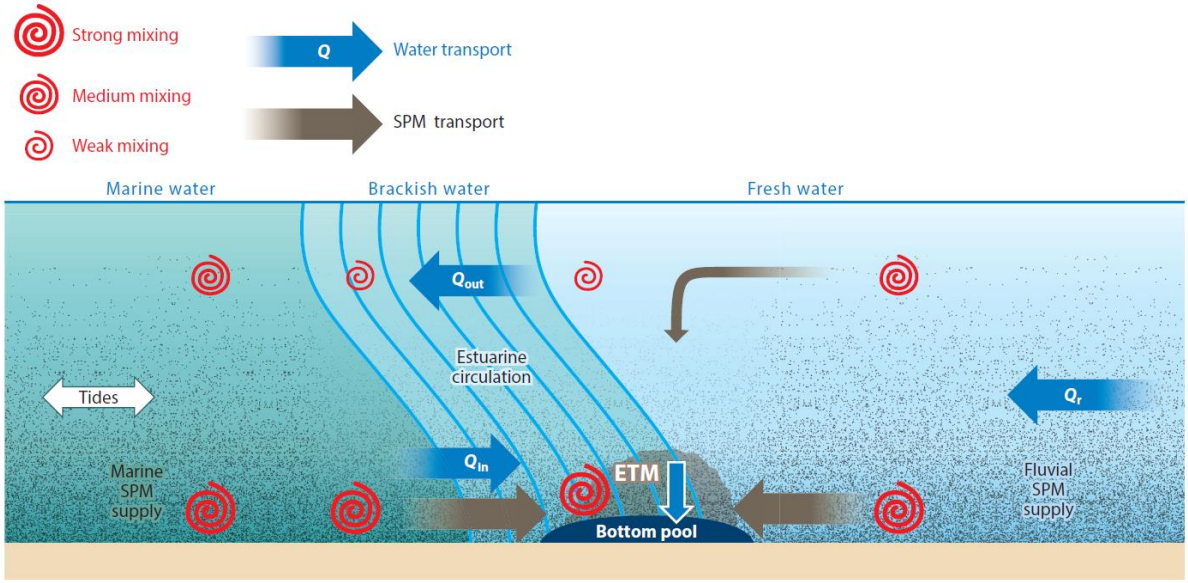

Figure 11 – Estuarine gravitational circulation due to which sediment transport fluxes convergence that lead to the creation of a mud pool of both marine and fluvial sediments, and consequently to the formation of an ETM due to resuspension of the pool during tidal flow (Burchard et al., 2018)

Gravitational Circulation

Gravitational (or: classical estuarine) circulation is caused by the longitudinal baroclinic pressure gradient, which is generated by the difference in salinity between the sea and the estuarine/fluvial water. The pressure gradient results in a characteristic exchange flow with up-estuarine flow near the bottom and down-estuarine flow near the surface. This is visualized in Figure 11. Mixing counteracts the circulation (Becherer, 2013a; Geyer & MacCready, 2014; Hansen & Rattray, 1965; Jay & Musiak, 1994; MacCready & Geyer, 2010; Pritchard, 1956; Simpson, Brown, Matthews, & Allen, 1990; Stacey, Burau, & Monismith, 2001; Stacey, Monismith, & Burau, 1999).

Mixing asymmetry

Longitudinal mixing asymmetries can yield residual estuarine exchange flow, as they initiate different current velocity and SSC profiles between ebb and flood tide respectively (Jay & Musiak, 1994). It is expressed in vorticity. Mixing asymmetries are considered as an indirect mechanism, as they are dependent on the tidal current velocities. Tidal mixing asymmetries can be subdivided in external mixing and internal mixing asymmetries (Becherer, 2013a). Furthermore, longitudinal mixing asymmetries may be induced by asymmetries caused by vorticity in another plane of orientation. This is due to momentum rectification, which is the redistribution of along-channel momentum caused by the transformation of horizontal vorticity in longitudinal vorticity through lateral circulation (Becherer, 2013a; Burchard, Hetland, Schulz, & Schuttelaars, 2011; Huijts, De Swart, Schramkowski, & Schuttelaars, 2011; Lacy, Stacey, Burau, & Monismith, 2003; Lerczak & Geyer, 2004; Scully, Geyer, & Lerczak, 2009).

1. *Internal mixing: tidal straining*
   Internal mixing asymmetries are mechanisms associated with time-varying vertical stratification and its inhibiting effect on the vertical momentum flux. An asymmetric degree of baroclinicity over the tidal cycle leads to a mixing asymmetry, and hence, residual longitudinal circulation. The most prominent internal mixing asymmetry is tidal straining, or strain-induced periodic stratification (SIPS) (Simpson et al., 1990; Stacey et al., 1999).

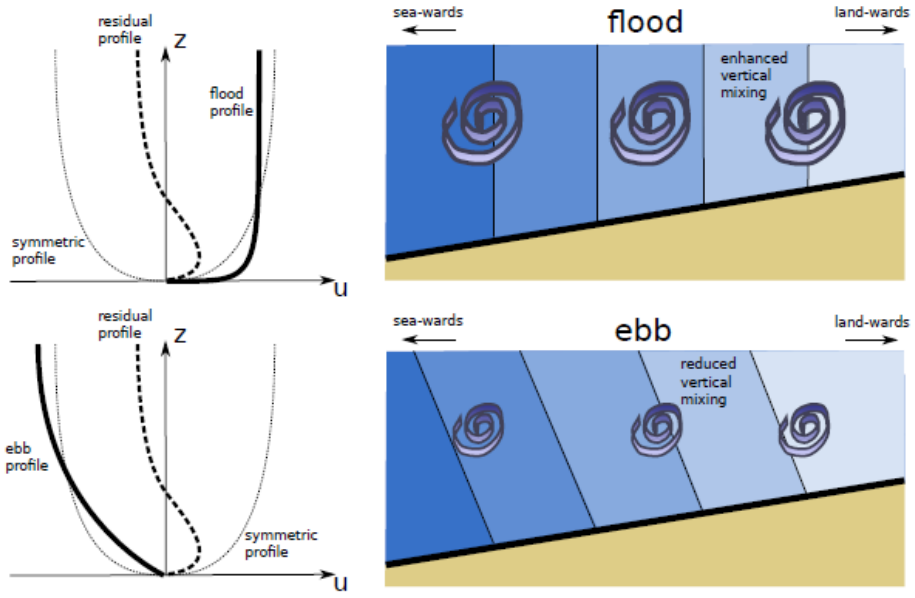

Figure 12 – Sketch of tidal straining mechanism, which induces asymmetrical generation of turbulence throughout the brackish stretch of the estuary, resulting in a residual current velocity profile.

As during flood tide more saline water is advected with the maximum currents, there is unstable stratification, and hence, intensified mixing. This corresponds to a positive contribution to longitudinal vorticity and, hence, a more homogenous current velocity profile. In contrast, during ebb tide, less saline water is advected on top of the saltier water. Therefore, there is some re-stratification during ebb tide: straining of the isohalines. This damps the turbulence, which is a negative contribution to the longitudinal vorticity. Consequently, a more sheared along-channel velocity profile persists. This results in a similar residual current velocity profile, as classical gravitational circulation, which can be observed in Figure 12 (Becherer, 2013a; Jay & Musiak, 1994; Simpson et al., 1990).

2. *External mixing*
   External tidal mixing is caused by barotropic mechanisms, which may lead to tidally asymmetrical generation of turbulence, such as tidal rectification. Most important is the longitudinally-oriented peak-velocity asymmetry. Other differently-oriented mechanisms may also induce longitudinal vorticity through momentum rectification, such as lateral circulation due to bend flow. However, since the same mechanism occurs during flood and ebb tide, these differently-oriented vorticities may not contribute to longitudinal circulation (see Figure 13). Nevertheless, the interaction of external mixing due to horizontal and lateral viscosity with a lateral buoyancy gradient may lead to asymmetric generation of turbulence over a tidal cycle: see internal mixing due to lateral circulation in the below (Becherer, 2013a; Buijsman & Ridderinkhof, 2008).

3. *Internal mixing asymmetry: lateral circulation*
   Residual longitudinal circulation may also be caused by mixing asymmetries through momentum rectification of lateral vorticity in combination with a horizontal salinity gradient, created by horizontal vorticity (Wong, 1994). This is due to the internal tendency of re-stratification, which leads to lateral circulation over the tidal cycle. Depending on the relative orientation of the lateral circulation and the horizontal circulation, mixing may be intensified or dampened: surface water advected to the maximum (minimum) tidal currents near the surface (bed) increases (decreases) longitudinal vorticity. Three mechanisms may induce a horizontal salinity gradient caused by differential advection, as can be seen in Figure 13 (Becherer, 2013a; Geyer & MacCready, 2014):

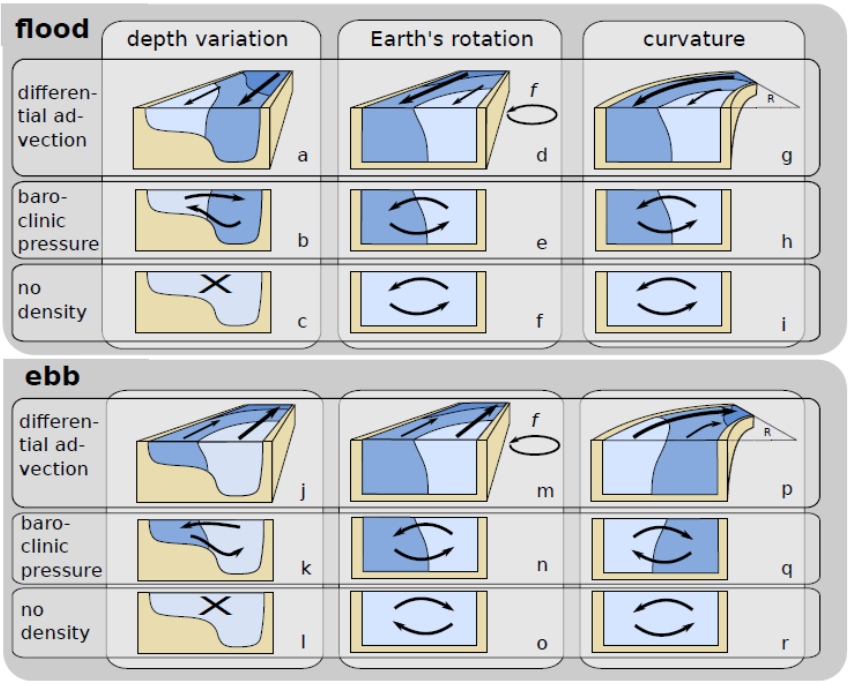

Figure 13 – Different drivers of lateral circulation induced by lateral depth variations, Coriolis forcing and curvature forcing and their interaction with a baroclinic pressure gradient during flood and ebb respectively (Becherer, 2013a).

- Coriolis deflection
  Maximum tidal currents are asymmetrically advected towards opposing banks over the tide, advecting more (less) saline water to one (other) bank, leading to symmetric lateral circulation.
- Centrifugal deflection:
  Maximum tidal currents are symmetrically advected towards the outer bend, advecting more (less) saline water to the outer bend during flood (ebb) tide, leading to asymmetric lateral circulation.
- Depth differences
  Maximum tidal currents are symmetrically advected towards the deeper parts, advecting more (less) saline water to the deeper parts during flood (ebb) tide, leading to asymmetric lateral circulation.

Internal mixing asymmetries only occur if the degree of baroclinicity is low, such as in well-mixed estuaries (Chant, 2002; Chant & Wilson, 1997; Kim & Voulgaris, 2008; Lacy & Monismith, 2001).

2.2.2 Micro-scale mechanisms

Another group of sediment trapping mechanisms is formed by micro-scale mechanisms. These mechanisms, which dominate the vertical sediment transport within the water column, tend to influence the supply to and pick up of SPM from to the bed, and hence the local availability of sediment.

In general, fine sediment is distributed in layers in the vertical (see Figure 14): there is a dilute suspension in the water column according to a balance between turbulence and gravity of the sediment particles. Furthermore, a high-concentration fluid mud layer may be formed on the bed which consolidates over time to form a muddy bed layer. Non-cohesive SPM is distributed likewise, although this may not form a fluid mud layer. An overview of important micro-scale mechanisms is given in Figure 14. These mechanisms (settling, *flocculation and break-up, deposition, resuspension (erosion, entrainment), consolidation, diffusion, advection*) are discussed in the remainder of this subsection.

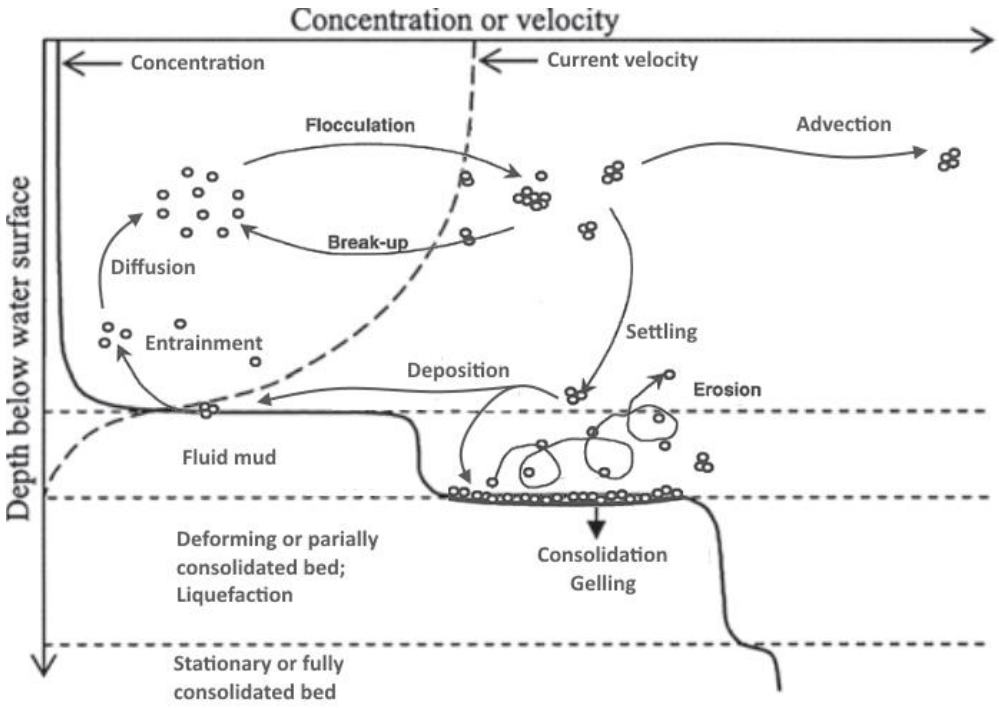

Figure 14 – Overview of micro-scale mechanisms for SPM in water column and in bed for cohesive sediment (after: (Van Rijn et al., 1993))

Settling

Settling is the downward motion of SPM under the influence of gravity. If the SSC is sufficiently low, non-cohesive SPM can settle freely with velocities proportional to their size and density (Van Rijn et al., 1993). Hindered settling effects may come into play during high SSC (Amy, Talling, Edmonds, Sumner, & Lesueur, 2006; Pierre Le Hir, Cayocca, & Waeles, 2011; Lockett & Al-Habbobby, 1974; Manning, Baugh, Spearman, & Whitehouse, 2010; Winterwerp, 1999). Moreover, non-cohesive and cohesive SPM may interact with each other during setting (Manning et al., 2010; Mitchener & Torfs, 1996; Van Ledden, Van Kesteren, & Winterwerp, 2004).

Flocculation and break-up

Furthermore, settling of cohesive SPM may be affected by flocculation (floc formation), which is counteracted by break-up of flocs. For cohesive sediments, in specific, the settling velocities are modified by the formation of flocs, depending on their size and relative density (Winterwerp, 1999). Flocculation is dependent on the collision frequency of particles and the break-up forces. Therefore, it is dependent on suspended concentration and turbulence (Pierre Le Hir et al., 2011; Shi, 2010; Van Leussen, 2011). Two types of flocs may be formed, inducing a bi-model floc distribution (Van Leussen, 2011):

- Microflocs
  Microflocs are small and dens flocs, which are particularly formed at low sediment concentrations. They are characterized by strong bonds, such that the flocs are preserved during high turbulence and may eventually deposit, as they resist the disruptive near-bed shear stresses.
- Macroflocs
  These flocs are formed by microflocs at high concentration and cannot resist turbulence or bed shear. Consequently, macroflocs are broken down in the water column or resuspended quickly once deposited.

Flocculation may be enhanced by salinity and biological polymeric substances (Tolhurst, Gust, & Paterson, 2002).

Deposition

Near-bed SPM may be deposited if the bed-shear stress is sufficient low. Deposition fluxes of different sediment classes are proportional to the product of their respective bottom concentration and settling velocities (Le Hir, Cayocca, & Waeles, 2011). Four ranges can be distinguished, which are based on the SSC (McAnally, 2007; Van Rijn, 2005):

- Free settling range (concentrations smaller than ~0.3 g/l)
- Flocculation settling range (concentrations from ~0.3 to ~10 g/l)
- Hindered settling range (concentrations larger than ~10 g/l)
- Negligible settling range

Depending on the settling stage and the magnitude of the (critical) bed shear stresses, there may either be full deposition, hindered/partial deposition of flocs, deposition as fluid mud, or no deposition. Furthermore, deposition of SPM may be affected by sand-mud interactions (Van Rijn et al., 1993).

Fluid mud

Fluid mud is a viscoplastic high-concentration suspension of fine sediment particles in which settling is substantially hindered by the close proximity of sediment particles and flocs, but which has not yet formed an interconnected matrix of bonds strong enough to eliminate the potential for mobility. It is a transitional phase between the hindered settling and (primary) consolidation phase. Fluid mud is formed by abundant local and supplied mud, and generally important at the location of the ETM, as well as its transport (e.g. shear flow, entrainment) (Azhikodan & Yokoyama, 2018; Becker et al., 2013; Mcanally et al., 2007b; Parsons et al., 2005; Torfs, Mitchener, Huysentruyt, & Toorman, 1996; L. C. Van Rijn, 2016; Yuanyang, Roelvink, Weihua, Dingman, & Fengfeng, 2014).

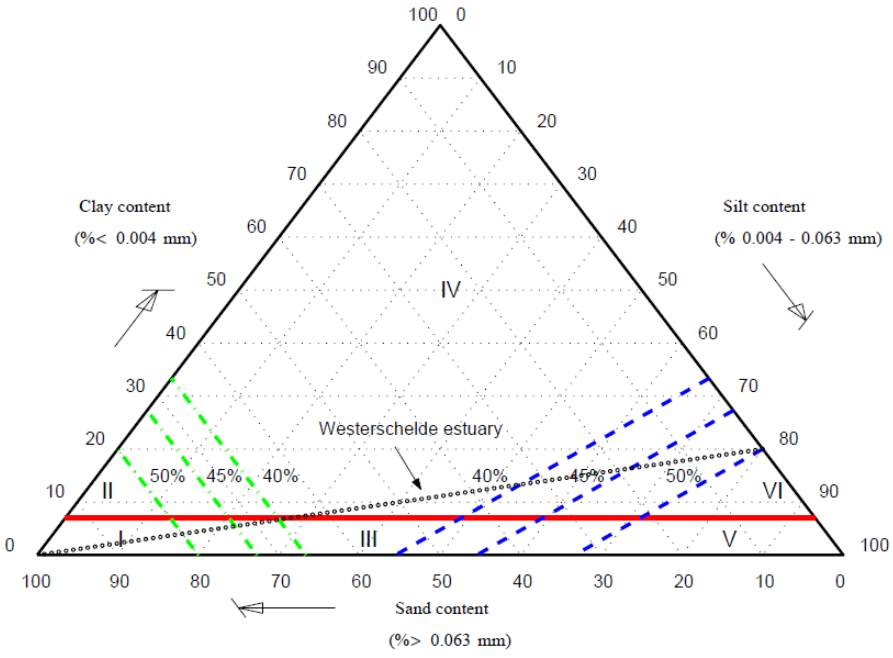

Figure 15 – Sand-silt-clay triangle with transitions for cohesion (red line) and network structure (Areas I-VI), as separated by the critical volume fractions of sand (green dot-dashed lines) and silt (blue dot-dashed lines) (Van Ledden et al., 2004).

Consolidation

Consolidation is a process of floc compaction under the influence of gravity forces. Pore water is expulsed from the fluid mud, which results in a gain in strength of the bed material. Three distinct consolidation stages can be distinguished (Torfs et al., 1996; L. C. Van Rijn, 2016):

- Hindered settling phase (hours-days):
- Primary consolidation phase (weeks-months): density of ~100-200 kg/m^3
- Secondary consolidation phase (Terzaghi-type consolidation; months-years): ~1,000-1,200 kg/m^3

Consolidated bed

The structure of a consolidated bed depends on the deposition rates of sand and mud. Various bed types may form, which can be classified according to their network structure (see Figure 15) (Flemming, 2000; Pejrup, 1988; Van Ledden et al., 2004):

- Non-cohesive sand-dominated (I): sand volume fraction of 40-50%
- Cohesive sand-dominated (II): sand volume fraction of 40-50%
- Non-cohesive mixed (III)
- Cohesive clay-dominated (IV)
- Non-cohesive silt-dominated (V): silt volume fraction of 40-50%
- Cohesive silt-dominated (VI): silt volume fraction of 40-50%

Advection

The transport of SPM in the dilute suspension layer is caused by advection due to tidal currents. Transport may occur in three modes (Van Rijn, 2016):

- Non-saturated mud transport in conditions with mud percentages in the bed < 30% (supply-limited conditions)
- Saturated mud transport in conditions with percentages if mud in the bed >70% (bed-dominated conditions) (Bagnold, 1962; Xu, 1999; Winterwerp, 2001, 2006, 2011; Van Rijn, 2007, 2015).
- Over-saturated mud transport in conditions with a large input of mud from upstream in combination with hindered settling effects resulting in hyper concentrations (supply-dominated conditions).

Diffusion

The mechanism of upward movement of SPM is called diffusion and is caused by the net effect of turbulence, as turbulence advects suspended particles both upwards and downwards in the water column.

Resuspension

Erosion of bed material is dependent on the bed shear stress and bed shear strength, which is a function of the mud content. Sandy beds with certain critical mud content, may either show non-cohesive (Alvarez-Hernandez, 1990), or cohesive behavior (Jacobs, Le, Van Kesteren, & Cann, 2011; Kuti & Yen, 1976; Murray, 1976):

1. *Non-cohesive (granular) behavior*
   Erosion and mobilization of non-cohesive beds is described by the deviation with respect to a specific equilibrium situation in which supply of sediment equals erosion. This equilibrium transport is fully dependent on the flow conditions, if sediment is abundant. (Van Rijn, Nieuwjaar, Van der Kaay, Nap, & Van Kampen, 1993).

2. *Cohesive behavior*
   For cohesive beds there is no equilibrium. Instead, resuspension of cohesive beds is dependent on flow condition and bed properties (Winterwerp, Kesteren, Van Prooijen, & Jacobs, 2012). There are four resuspension modes for cohesive sediments:

   1. Entrainment
   2. Erosion of individual flocs,
   3. Erosion of surface layers (drained failure);
   4. Erosion of lumps of mass (undrained failure)

The transition between cohesive and non-cohesive behavior is also depending on the grain size of the sand (Jacobs et al., 2011; Pierre Le Hir, Cann, Waeles, Jestin, & Bassoullet, 2008; Pierre Le Hir et al., 2011; Panagiotopoulos, Voulgaris, & Collins, 1997; Van Ledden et al., 2004).

2.3 Summary

Trench siltation in an estuary is dependent on the **gross sediment transport fluxes** and **trapping efficiency** of the trench. The sedimentation distribution over the trench is dependent on the distribution in gross sediment transport over the cross-section and the difference in gross sediment transport over the tidal cycle.

The gross sediment transport fluxes are dependent on the **interconnectivity** of **sediment transport and trapping mechanisms**, which affects the **local hydrodynamics** and determine the **sediment availability** by inducing **net sediment transport fluxes** over the estuary. At the location of zero residual sediment transport, fine sediment is trapped in a mud reach. As this mud reach is cyclically resuspended by the tidal flow, an **estuarine turbidity maximum** (ETM) is induced within the estuary, at which high suspended sediment concentrations are present. Consequently, high gross sediment transport fluxes can be found near the ETM, which may lead to high trench siltation rates.

Sediment trapping and transport mechanisms can be subdivided in:

- **Macro-scale mechanisms**
  These mechanisms are responsible for the general sediment transport and trapping patterns in the estuary. These mechanisms can either be caused by **barotropic** (density gradients unimportant) and **baroclinic** (density gradients important) mechanisms. Furthermore, the three-dimensional mechanisms can be partitioned in **working direction** (*direct or indirect*) and in three **planes of orientation**: longitudinal, horizontal, and lateral. Important large-scale mechanisms are: *lag effects, tidal rectification, Stokes' drift, mixing asymmetries,* and *gravitational circulation*.
- **Micro-scale mechanisms**
  These mechanisms dominate the sediment transport within the vertical. They may act within the water column (*settling, advection, diffusion*), near the bed (*deposition, resuspension*), in the bed (*consolidation*) or on particle scale (*flocculation, break-up*), thereby altering the supply and pick-up of sediment to/from the bed, and consequently, the trapping of sediment.

The **trapping efficiency** of the trench is mainly determined by the **alignment** of the trench with the **local governing currents** and to a lesser extent to the **dimensions** of the trench: depth with respect to the ambient depth of the domain, and width.

All identified sediment transport and trapping mechanisms in the theoretical framework are summarized in Figure 16, which concludes this chapter. The scheme takes is build up according to the same subdivision, described in this study. Details on the individual mechanisms can be found in Appendix A. Although the scheme is opted to be applicable for a wide range of estuaries, in the remainder of this thesis, this scheme is used as background to find which mechanisms are governing for trench siltation near the ETM of a **well-mixed** estuary.

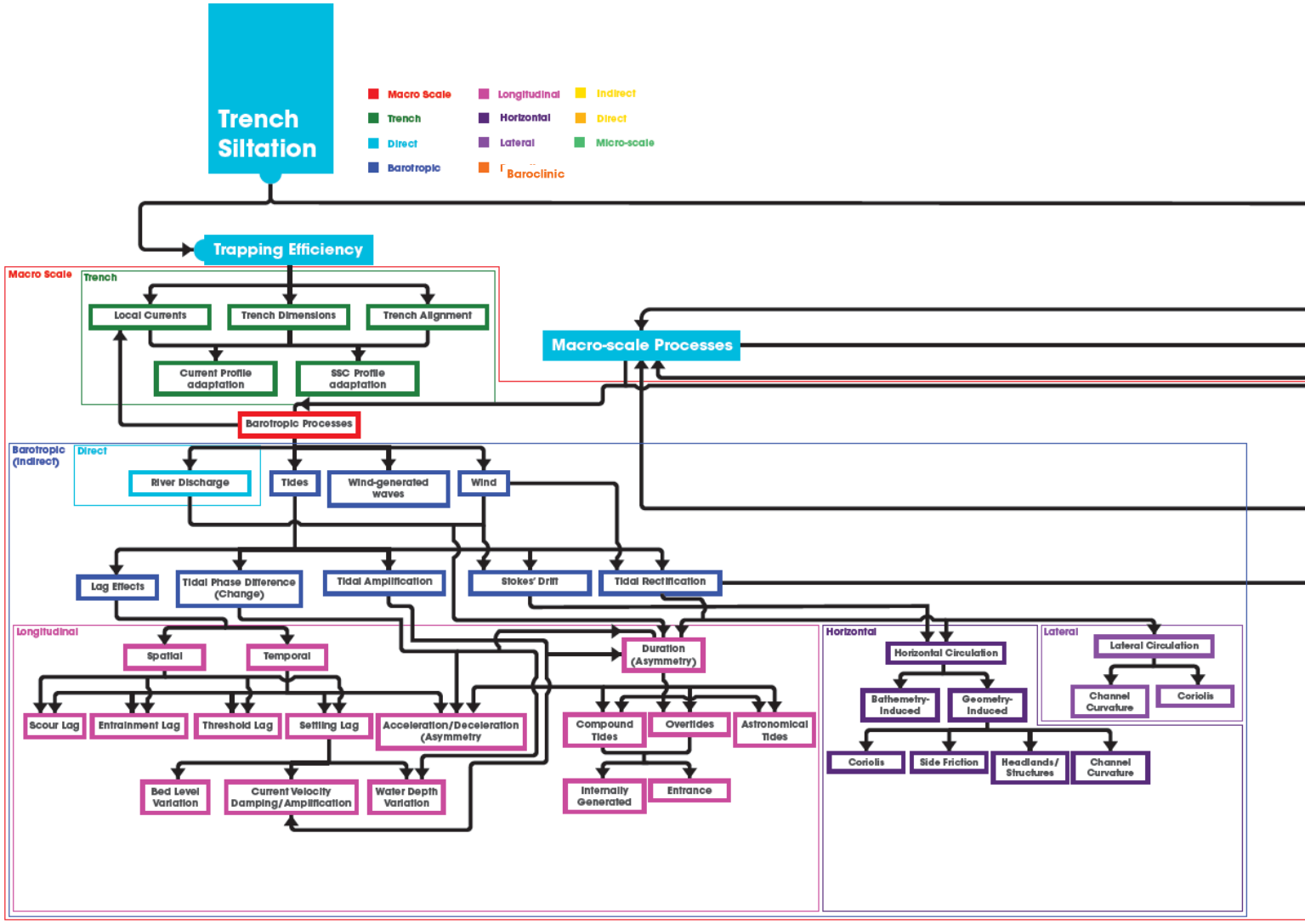

Figure 16 – Flow chart in which all found sediment transport and trapping mechanisms are listed, including their dependencies and interactions, which may determine trench siltation in a general estuary

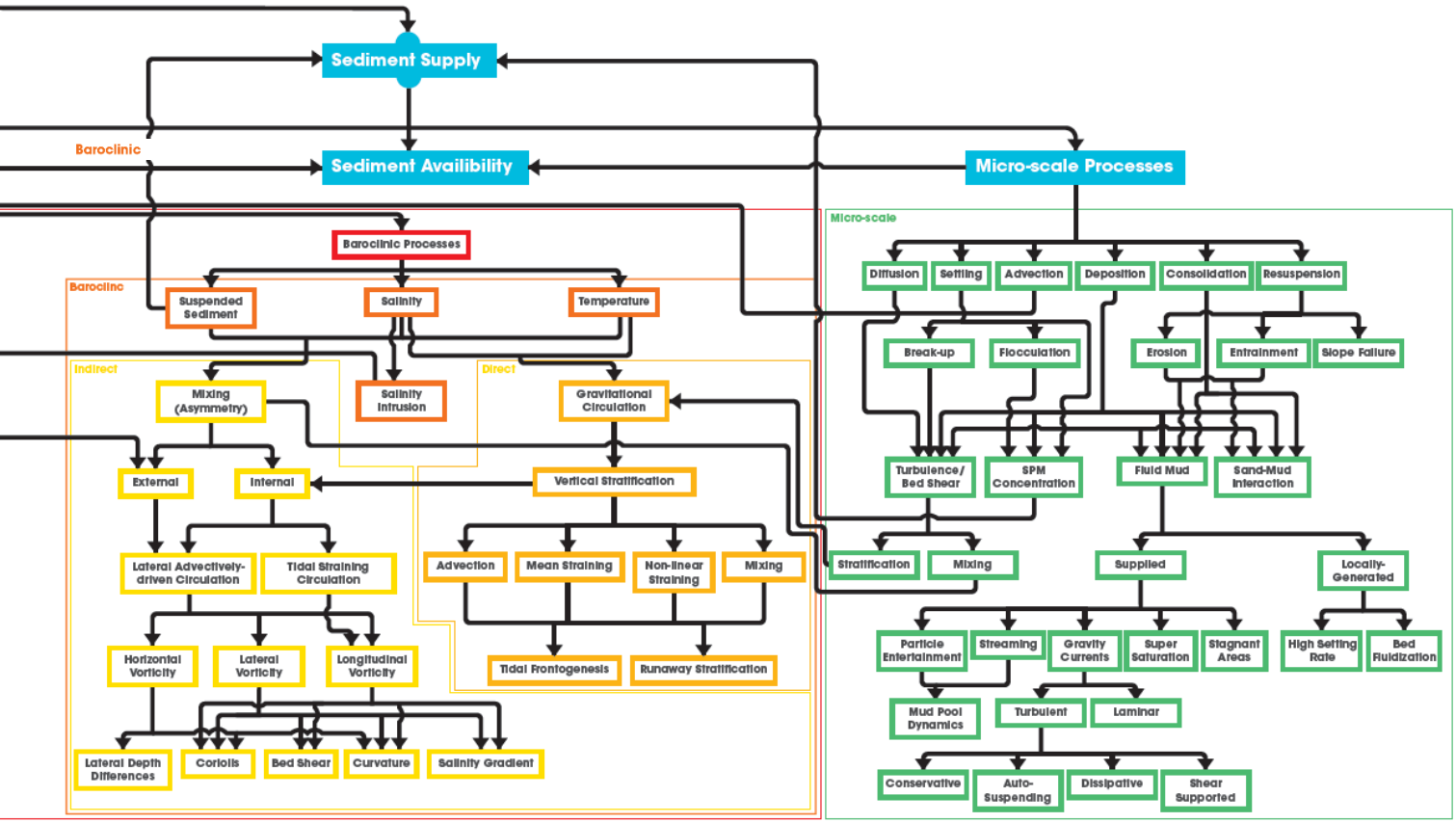
Sediment Supply
Baroclinic
Sediment Availibility
Micro-scale Processes
Baroclinic Processes
Baroclinic
Suspended Sediment
Salinity
Temperature
Indirect
Direct
Mixing (Asymmetry)
Salinity Intrusion
Gravitational Circulation
External
Internal
Vertical Stratification
Lateral Advectively-driven Circulation
Tidal Straining Circulation
Advection
Mean Straining
Non-linear Straining
Mixing
Horizontal Vorticity
Lateral Vorticity
Longitudinal Vorticity
Tidal Frontogenesis
Runaway Stratification
Lateral Depth Differences
Coriolis
Bed Shear
Curvature
Salinity Gradient
Micro-scale
Diffusion
Settling
Advection
Deposition
Consolidation
Resuspension
Break-up
Flocculation
Erosion
Entrainment
Slope Failure
Turbulence / Bed Shear
SPM Concentration
Fluid Mud
Sand-Mud Interaction
Stratification
Mixing
Supplied
Locally-Generated
Particle Entertainment
Streaming
Gravity Currents
Super Saturation
Stagnant Areas
High Setting Rate
Bed Fluidization
Mud Pool Dynamics
Turbulent
Laminar
Conservative
Auto-suspending
Dissipative
Shear Supported

3 Study Area Description

This chapter will summarize the characteristics of the Scheldt Estuary in general, and in detail for the area of interest at the location of the trench, as both systems are highly interconnected. The purpose of this study area description, which was guided by the theoretical framework in Chapter 2, is to become familiar with the system in order to:

- obtain the characteristics of the system to be implemented/captured in the detailed numerical model,
- verify the modelling results of the detailed numerical model,
- identify possible governing sediment trapping mechanisms which cannot be captured by the detailed numerical model;
- discover the applicability of the findings of this thesis.

A more detailed study area description of the entire Scheldt Estuary can be found in Appendix B.

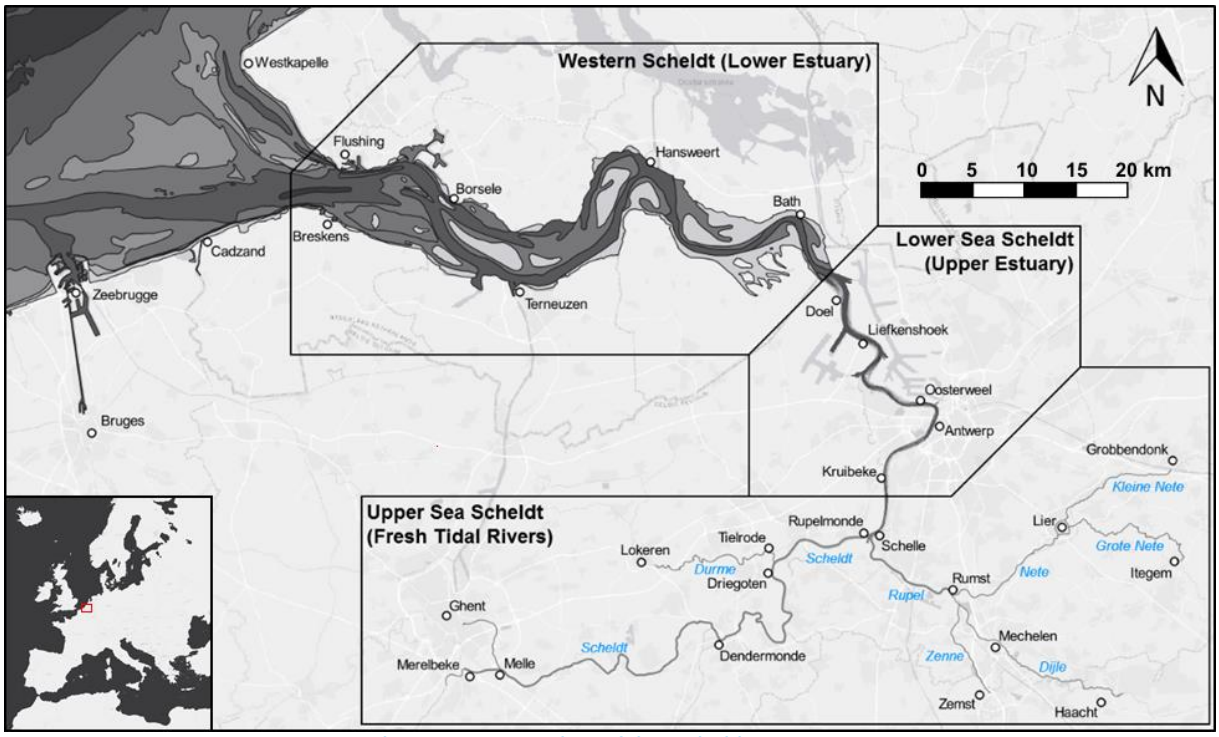

Figure 17 – Overview of the Scheldt Estuary.

3.1 Scheldt Estuary

The Scheldt Estuary is a tide dominated water body on a coastal plain through which the Scheldt River and its tributaries discharge water into the North Sea. It extents up to the tidal limits of the Scheldt river and its tributaries. The tidal limit of the Scheldt river is located at 156 km from the river mouth up in Ghent, at which the tidal wave is blocked by a sluice.

3.1.1 Geomorphology

The estuary has a funnel-shaped geometry; its width reduces from about 6000 m between Flushing and Breskens to less than 100 m near Ghent (Bolle, Wang, Amos, & De Ronde, 2010; Wang, Jeuken, Gerritsen, De Vriend, & Kornman, 2002). It can be subdivided into the following geomorphological parts (see Figure 17); from downstream to upstream (Baeyens, Eck, Lambert, Wollast, & Goeyens, 1998):

1. Lower estuary (Western Scheldt):
   The Western Scheldt runs from mouth between Flushing and Breskens to the Belgian-Dutch border. It is characterized by a braided network of a separate flood and ebb channel (Winterwerp et al., 2001). In front of the Western Scheldt lies a large ebb tidal delta, known as the Vlakte van de Raan.
2. Upper estuary (Sea Scheldt):
   The braiding network of the lower estuary stops at the Belgian-Dutch border, at which the estuary becomes a one channel system: the upper estuary. The so-called Sea Scheldt can be divided in two parts (Maris et al., 2014):
   - Lower Sea Scheldt
     This brackish water body has one meandering tidal channel with relatively small mudflats and salt marches (Maris et al., 2014; P. Meire et al., 2005).
   - Upper Sea Scheldt and tidal-dependent tributaries:
     The Upper Sea Scheldt is characterized by a long tidal-dependent freshwater zone, which is composed of the Scheldt River up to Ghent, and the tidal-dependent parts of its tributaries: Nete, Dijle, Zenne, Durme, Leie, and Dender.

The Scheldt Estuary becomes shallower in landward direction: from width-averagely 14.25 m TAW at the mouth, to only 3 m TAW near Ghent. Furthermore, intertidal flat area increases up to the Lower Sea Scheldt, after which it reduces in landward direction (Plancke, Vereecken, Vanlede, Verwaest, & Mostaert, 2014).

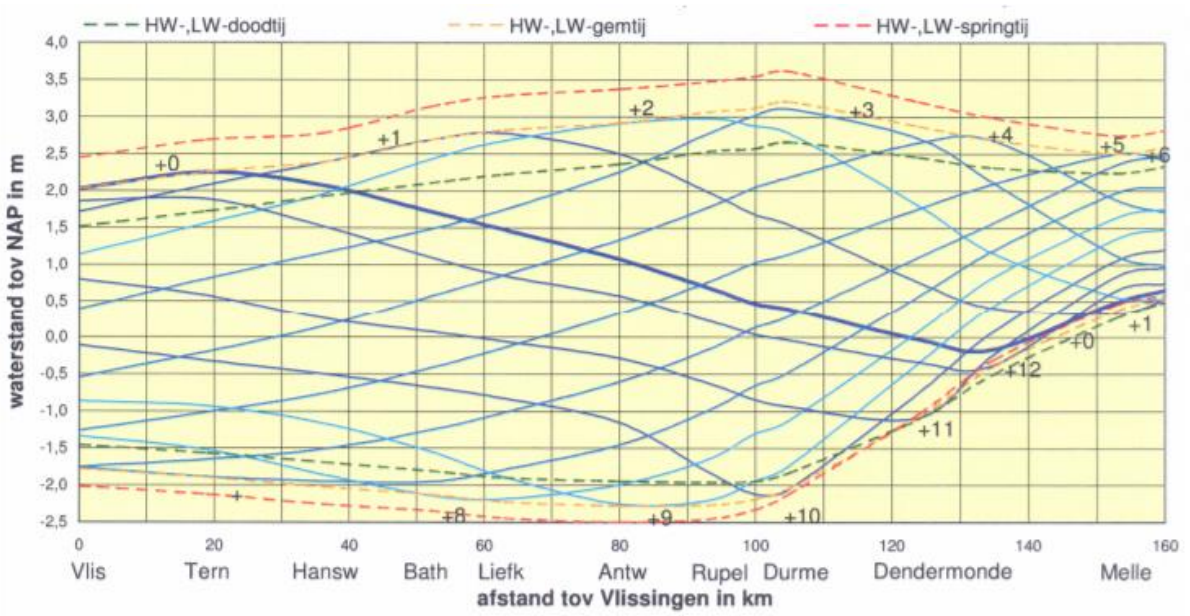

Figure 18 – Water surface profiles in the Scheldt Estuary for each hour after HW in Flushing (Pieters, 2002).

3.1.2 Tide

The Scheldt Estuary predominantly has a semidiurnal macrotidal regime, as it is excited at its mouth by a very regular (slightly distorted sinusoidal) tide, which is present in the North Sea. The amplitude of the tidal discharge at the estuary mouth has an annual average of 50,000 m^3/s (Verlaan, 1998; Wang et al., 2002). The estuary has a strong spring-neap cycle.

The vertical tide is initially amplified by a combination of funneling, reflection, and shoaling of the tidal wave, caused by the shallow funnel-shaped geometry of the estuary. Upstream of Schelle, the tidal amplitude decreases rapidly due to increased frictional damping (Van Rijn, 2011; Winterwerp, 2013). Furthermore, the tidal wave is steepening in the estuary.

The horizontal tide runs ahead of the vertical tide by approximately 1-2 hours. This makes the tidal wave partially progressive, partially standing. This is common in long, funnel-shaped

estuaries. At the landward limit of the estuary a fully standing wave is observed, as the wave is reflected by a sluice (Van Rijn, 2011).

Typical tidal peak-velocities of 1.0-1.5 m/s are found in the estuary. As a consequence, the tidal excursion length is approximately 10 to 20 km (Van Rijn, 2011), depending on the governing tide and river discharge.

Asymmetry
In general, the asymmetry in the horizontal tide shows different behavior compared to the asymmetry in the vertical tide. The flood dominant vertical tide at the estuary mouth decreases in flood dominance up to Bath, after which it shows increasingly flood dominance in landward direction. The asymmetry of the horizontal tide is, cross-sectionally averaged, however, rather weak, with no clear dominancy. This is believed to be caused by the hypsometry of the estuary (Wang et al., 1999). Residual tidal currents are dominated by Stokes' drift, and horizontal Eulerian currents: ebb channels generally show strong ebb dominance and flood channels strong flood dominance (Bolle, 2006; L. C. Van Rijn, 2011b).

3.1.3 River discharge

The annual average river discharge of the Scheldt amounts 104 m^3/s. However, since the Scheldt River is typically a rainfed river, it shows strong seasonality: the average discharge may vary from 60 m^3/s during dry summers, to 180 m^3/s during wet winters. The maximum instantaneous discharge may reach 600 m^3/s. The fresh water supply is, therefore, small compared to the tidal discharge, contributing to only about 0.5% of the tidal volume (Baeyens et al., 1998).

3.1.4 Wind

The dominant wind in the Scheldt Estuary are the westerly winds, coming from the southwest. These winds have an average wind speed of 5 to 10 m/s, while during storms the wind speed may reach 20-25 m/s. The wind climate is subject to seasonality. There are stronger and more frequently occurring westerly storms present during winter than during summer. Also, easterly storms occur in winter, which may have a wind speed of 15-20 m/s (B. W. F. Van Rijn, 2012).

Due to wind set-up, water levels at Flushing can raise another 3.0 - 4.5 m NAP during a severe westerly storm (Kuijper & Lescinksi, 2013). Wind has not been reported to influence the hydrodynamics in estuary directly.

3.1.5 Waves

Waves are limited to the western part of the estuary (< 40 km). Further upstream from the mouth, the influence of waves is negligible due to dissipation, sheltering and small fetch lengths (Chen, Wartel, Van Eck, & Van Maldegem, 2005; Van Kessel, Vanlede, & de Kok, 2011).

The wave climate is characterized by a combination of short-crested waves propagating from the North Sea into the Western Scheldt, and locally generated waves. To a lesser degree, also, swell waves, which are generated in the northern part of the North Sea, may be present at the mouth of the estuary (B. W. F. Van Rijn, 2012).

The yearly-averaged significant wave height at the estuary mouth is 0.8 m, with peaks of 2-3 m during severe storms. The peak period of the waves ranges from 2 to 10 s. The highest waves are generated during north-westerly winds due to a longer fetch (Sistermans & Nieuwenhuis, 2004; Van der Werf et al., 2015).

3.1.6 Salinity

The salt limit in the Scheldt Estuary is located on average between Kruibeke and Rupelmonde (see Figure 19) , which is primarily determined by the magnitude of the river discharge: during high river discharge, seawater only penetrates to about Antwerp (~80 km from mouth), whereas during low discharge it penetrates upstream of Rupelmonde (>100 km). Salt intrusion

retreats quickly during river floods. However, the salinity is not able to recover from this instantaneously; there is a strong lag of approximately 5 days. At the mouth, salinity is nearly constant with a magnitude of 32 g/l. Over a tidal cycle, there is an additional shift in salinity of approximately 10 km. (Baeyens et al., 1998; Chen, Wartel, Van Eck, et al., 2005; Fettweis & Sas, 1997; P. Meire et al., 2005; Van Kessel et al., 2011).

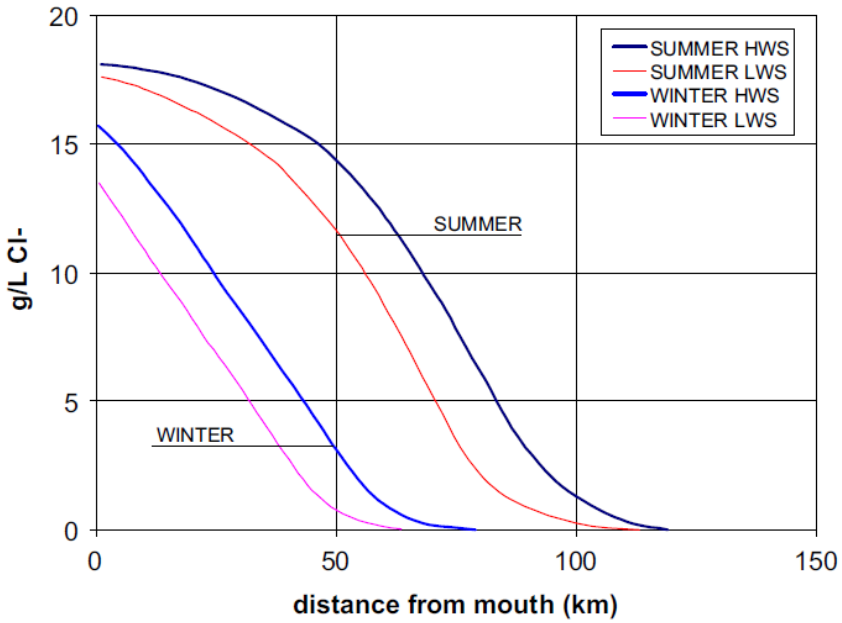

Figure 19 – Longitudinal salinity distribution in the Scheldt estuary for a high and a low discharge situation (after Claessens (1988) and Verlaan (1998)).

Over the vertical, the salinity is nearly uniform, given the average difference of only 1‰. (Fettweis & Sas, 1997; Van Kessel et al., 2011). Furthermore, horizontal salinity gradients are reported in the Scheldt Estuary (Winterwerp, Wang, Van der Kaaij, Verelst, & Bijlsma, 2006).

3.1.7 Residual current

In general, the residual current velocity in the lower estuary is directed towards to the sea at the surface, while it is directed in landward direction at the bottom. This is due to salinity-induced circulation. In the upper estuary, the residual currents in the bottom layer are also directed seaward due to the greater influence of the river run-off. Also, the return current due to Stokes' drift is considered to be important in the seaward directed residual current. The area of zero net residual bottom flow is located approximately at 70 km distance from the mouth, shifting up- and downstream, depending on the conditions. Locally, horizontal tidal rectification influences the direction of the residual currents (Baeyens et al., 1998; Chen, Wartel, Van Eck, et al., 2005).

3.1.8 Sediment

Both sand and mud are present in the Scheldt Estuary. Sediment is generally transported as suspended load (fine sand and mud), although there is some sand transported as bedload (~10-20% of suspended load) as well (Van der Werf & Brière, 2014).

Bed Composition

The median grain size and bed composition in the Scheldt Estuary are strongly varying in space. In general, the bed composition consists of fine to medium grained sand with a grain size of 170 µm (+/- 61 µm). The bed layer has an average mud content of about 16.4% (+/- 29.9%) (Van Eck, 1999).

In Table 1, it can be seen that the bed material first becomes finer in landward direction, after which it coarsens again (Kuijper, Van der Kaaij, & De Goede, 2006; Van den Neucker et al., 2007; Van Eck, 1999). Related to this distribution, an increasing mud content is observed in

landward direction along the estuary from its mouth, which sharply increases towards Antwerp (>50%), and decreases again in landward direction in the Upper Sea Scheldt (Van Ledden, 2003).

Table 1 – General sediment characteristics throughout the Sea Scheldt for distinct areas over the cross-section.

Location		Median grain size diameter [µm]			Mud content [%]		
		Channels	Shoals	Margins	Channels	Shoals	Margins
Western Scheldt	Mouth	300	-	-	-	-	-
	Inner	150	50-150	<125	~0.10	~0.35	~0.5
Lower Sea Scheldt	Mesohaline	93±10	84±10	-	0.42	0.57	-
	Oligohaline	169±26	93±6	-	0.15	0.23	-
Upper Sea Scheldt		230±28	84±6	-	0.14	0.35	-

The bed sediment characteristics, however, differ greatly within the cross-section. In general, the grain size diameter of the bed material is found to be larger in the channels than on the shoals and estuarine margins (Van Eck, 1999). In contrast, the percentage of mud is generally much larger alongside the estuarine margins, and at the intertidal and subtidal areas, (McLaren, 1994). In the Sea Scheldt, a similar distribution over the cross-section can be found (Van den Neucker et al., 2007).

The composition of the mud consist of approximately 35% lutum (clay minerals, organic matter and carbonates) and 65% silt (quartz) (Braat, Van Kessel, Leuven, & Kleinhans, 2017; Wartel, 1977). It can be physically classified as silty-clay and sandy-clay (Wartel & van Eck, 2000). The organic fraction is found to be approximately 8.5-25% of the dry weight. The typical settling velocity of the individual particles is estimated to be 0.1-0.4 mm/s. Furthermore, the mud has a critical erosion velocity of approximately 0.56 m/s (Chen, Wartel, Van Eck, et al., 2005).

Transport

The local fining of sediment is explained by the longitudinal residual currents in the estuary, which induce zero residual sediment transport in the mesohaline part (Bath-Antwerp) of the estuary. Consequently, fine sand and mud are trapped in this area: residual transport of sediment in the lower estuary is landward directed, while it is seaward directed in the upper estuary (Cleveringa, 2013; Cleveringa & Dam, 2013; Haecon, 2006; Vandenbruwaene et al., 2017). Due to this convergent transport, there exists a sharp transition zone in the type of mud: fluvial mud dominates the upper estuary, while marine mud dominates the lower estuary (Chen, Wartel, Van Eck, et al., 2005; Jacobs, 2011; Ten Brinke, 1994; Terwindt, 1967; Verlaan, 2000; Wartel & van Eck, 2000). Therefore, most (~80%) of the fluvial mud is retained by the Scheldt Estuary.

The fluvial supply is strongly correlated with actual river discharge: ~90% of the mud is discharged during the ~10% highest run-off events (Van Kessel, Vanlede, & Bruens, 2006; Van Kessel et al., 2011). The mud transport in the Scheldt Estuary is often divided in two fractions: a permanently suspended fraction (wash load) and a tidally-fluctuating fraction, which is alternately deposited and resuspended during a tidal cycle (Van Kessel et al., 2006).

Flocculation may contribute to the trapping of mud in the mesohaline part of the estuary, due to intensified deposition, although studies differ (Chen, Wartel, & Temmerman, 2005; Van Kessel et al., 2011; Wollast, 1988). In the Scheldt Estuary, the floc size is dependent on the current velocity, turbulent intensity, organic content and the SSC, rather than salinity (Chen, Wartel, Van Eck, et al., 2005; Temmerman, Govers, Wartel, & Meire, 2003; Van Kessel et al., 2011). Floc sizes are found to vary within a tidal cycle (Manning et al., 2007).

Estuarine turbidity maximums

The SSC varies significantly throughout the estuary. In the lower estuary, the distribution of SPM over both the horizontal and vertical is rather uniform, while there is a lot of variation in the middle and upper estuary (Chen, Wartel, Van Eck, et al., 2005; Van Kessel et al., 2011;

Verlaan, 1998). Usually three ETMs are observed, which may be present depending on the prevailing conditions (Chen, Wartel, Van Eck, et al., 2005):

- A marine-dominated ETM is observed in the mouth of the estuary between Flushing and Zeebrugge and reaches more than a few hundred mg/l. It is caused during storms by a combination of wave and tidal energy, which resuspends marine mud from the shoals. This entrained mud is advected throughout the estuary (Chen, Wartel, Van Eck, et al., 2005).
- A river-dominated ETM is located near Ghent and is present during high river discharges. SSC may be up to 300 mg/l.

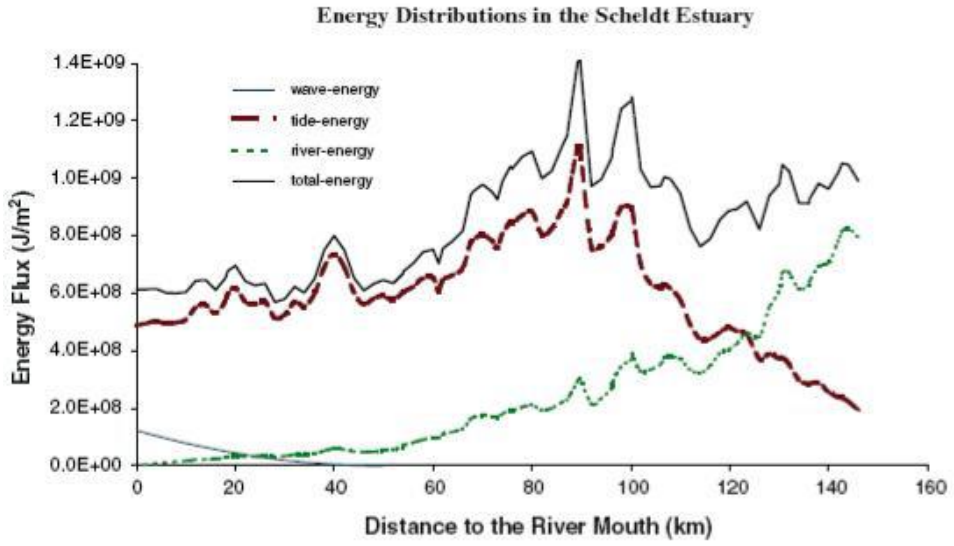

Figure 20 – Energy distributions in the Scheldt Estuary (Chen et al., 2005).

- The most prominent ETM is situated in the entire Lower Sea Scheldt (58-100 km) with maximum near-bed SSC of several hundreds of milligrams to grams per liters near Antwerp. It's presence can be explained by two factors (Van Kessel et al., 2011):
  - a large availability of mud in the area, caused by the convergence of mud
  - strong resuspension due to maximal total energy in the area (see Figure 20) caused by tide- and river-energy

  The ETM show variation on several time scales (Chen, Wartel, Van Eck, et al., 2005; Van Kessel et al., 2011):

  1. Flood-ebb tide (asymmetry, hysteresis, turbulence, sediment availability):
     The ETM is more prominent (factor 2-10) during maximum flood and ebb velocities, and nearly absent during the slack waters. Additionally there is higher-order variation in SSC over a flood or ebb period. This is explained by differences in turbulence, peak-velocities, floc size, varying sediment supply, and the inhomogeneous composition and distribution of the fine sediments in the bed (Fettweis & Sas, 1997; Manning et al., 2007).
  2. Spring-neap tide:
     The SSC in the ETM may be 2-3 times greater during spring tide than during neap tide due to greater tidal current velocity magnitudes. This makes that the spring cycle is characterized by erosion and the neap cycle by deposition of fine material. At the bed the difference in concentration is smaller during a spring-neap cycle than higher up in the water column (Fettweis & Sas, 1997).
  3. Seasonal variations:
     The ETM is highly dependent on the seasonality with higher concentrations in the winter than in summer by at least a factor 2. This is predominantly caused by an increase in fresh water discharge of the river, and to a lesser extent by

an increase biological activity in the spring and summer. Furthermore, storm surges and storm waves increase the marine sediment supply at the mouth of the estuary (Fettweis & Sas, 1997).
Moreover, the location of the maximum SSC in the ETM may shift between 50 km from the mouth (at the Verdronken Land of Saeftinghe), during high river discharge, and 110 km from the mouth (at Rupelmonde), at low river discharge. At the location of 50 km from the mouth, there is less energy, such that mud is able to permanently deposit (Van Kessel et al., 2011).

4. Decades (climate change, anthropogenic intervention)

3.2 Location of the ETM: Oosterweel

Oosterweel is located in the Lower Sea Scheldt. At this location, the ETM, on average, shows maximum SSC.

3.2.1 Geomorphology

The bathymetry at the location of the ETM in the Scheldt Estuary is characterized by a single tidal channel with a minimum depth of approximately 14 m to accommodate for shipping to the Port of Antwerp. The area has a typical transitional bathymetry from an estuarine (e.g. flood/ebb chute formation) to a riverine system (e.g. deeper outer bends, bar formation). Furthermore, there is a meandering pattern of rapidly following opposing bends. The width is converging from approximately 900 m at Liefkenshoek, to 500 m at Oosterweel, to 400 m at Kruibeke. There is few intertidal area. A lot of deep harbor (Deurganckdok) and sluice basins have been constructed along this particular stretch of the Lower Sea Scheldt. The sluices, such as the Boudewijnsluis, Kallosluis and Royersluis, give access to the tideless harbor basins of the Port of Antwerp.

3.2.2 Tide

Vertical Tide

Measurements of the tidal water level in 2014 at Antwerp show that there is a rather stepwise flood period and a gradual ebb period present near the ETM (see Figure 21). It can be seen that the vertical tide is flood dominant. There is, furthermore, a strong spring-neap cycle.

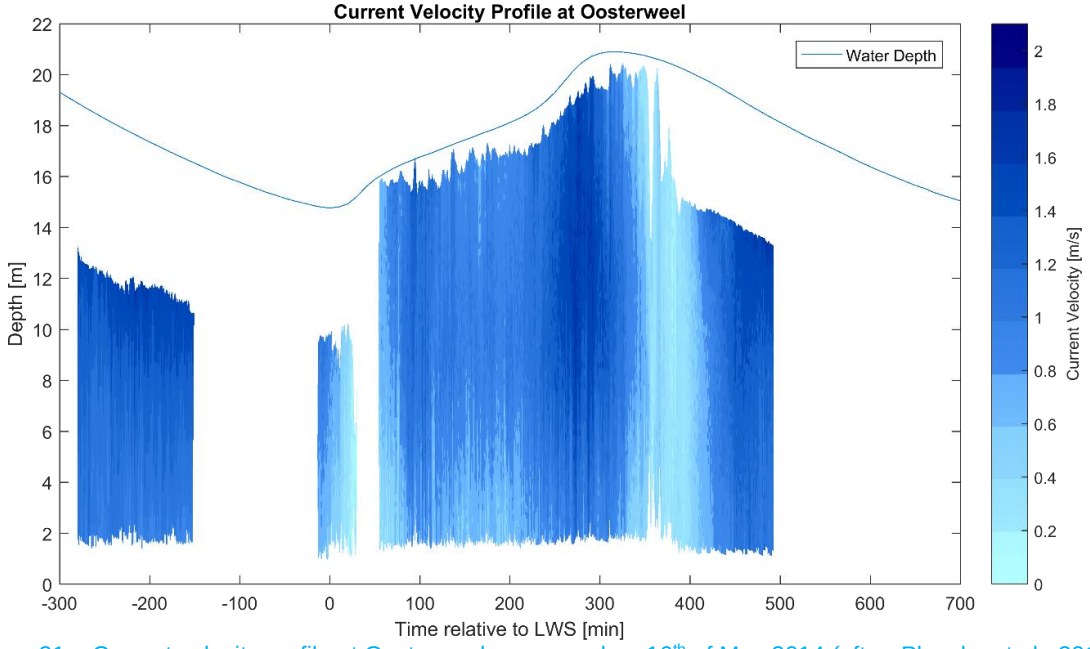

Figure 21 – Current velocity profile at Oosterweel, measured on 16th of May 2014 (after: Plancke et al., 2014).

Horizontal Tide

The yearly-averaged maximum current velocity at Oosterweel is approximately 1.50 m/s during flood with slightly lower velocities during ebb of around 1.25 m/s. These maxima may

vary 0.30-0.75 m/s during the spring-neap cycle. The flood current velocity shows two distinct peaks, which corresponds with the step-wise water level signal. During spring these distinct peaks are more pronounced than during neap tide. Furthermore, it can be observed that the ebbing current velocity has a more gradual profile, with a maximum close to the water surface, while during flood, the profile is more uniform, with a maximum located somewhat beneath the water surface (Plancke et al., 2014).

Asymmetry
Although the vertical tide shows a strong flood dominancy, the horizontal tide is rather neutral. Within the cross-section, asymmetry in tidal currents may be strong and opposing due to horizontal Eulerian residual circulation. Moreover, there is strong residual transverse circulation found, in particular in the bends (Winterwerp et al., 2006).

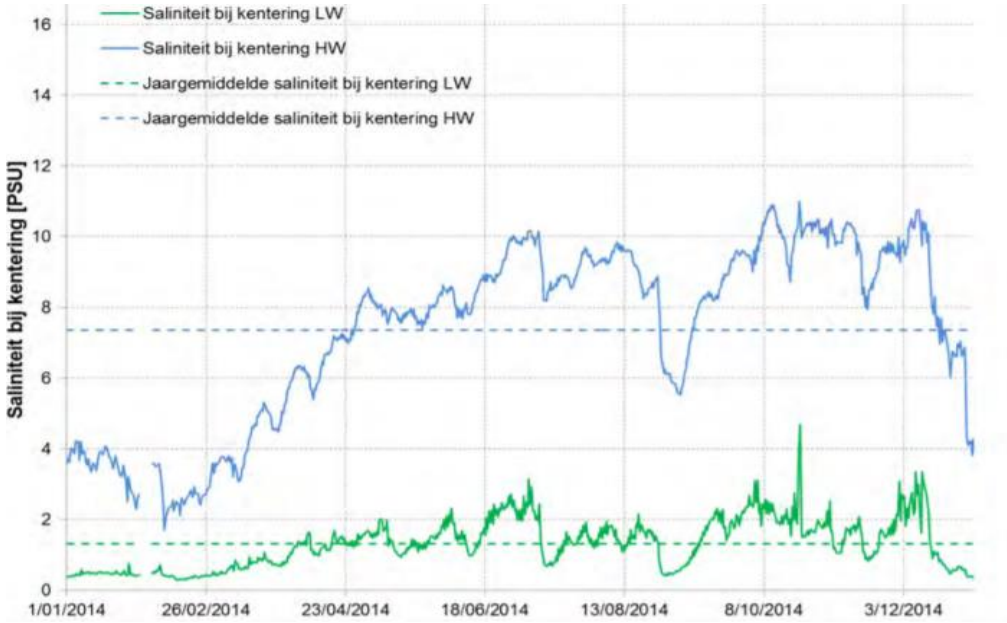

Figure 22 – Salinity measurements at Oosterweel for year 2014 (Vanlierde et al., 2014)

3.2.3 Salinity

Salinity at Oosterweel (see Figure 22) shows a great dependency on seasonality and period within the tidal cycle. The salinity decreases in winter due to increased river discharge, pushing the saline water seawards, after which it steadily recovers in spring. Also, the spring-neap cycles can be resolved, but to a lesser extent. Furthermore, it can be seen that the difference in salinity between HWS and LWS increases in summer. The above corresponds with the salinity distribution over the estuary throughout the year (recall Figure 19) (Vanlierde et al., 2014). In the vertical, the salinity profile is fairly uniform over the vertical. Furthermore, strong transversal salinity gradients are found due to differential advection of salt within the transverse direction (Winterwerp et al., 2006).

3.2.4 Sediment

Composition
The bed load composition at Oosterweel consists of widely-graded fine sand with a median grain size diameter of 139 µm. Other characteristic grain size diameters are summarized in Table 2.

Table 2 – Characteristic grain size diameters of bottom samples at Oosterweel [in µm] (Plancke et al., 2014)

D10	D35	D50	D65	D90
16	106	139	178	327

The characteristic mud contents in the area of the ETM, based on samples, are listed in Table 3. It indicates that there is strong segregation of sediments within the cross-section.

Table 3 – Bed composition for each distinct ecotope (Vandenbruwaene et al., 2017)

Area	Mud Content [%]
Subtidal	~60
Intertidal	~54
Shallow Subtidal	~17
Subtidal	~20
Deep Subtidal	~18
Anthropogenic Subtidal	~86

Most mud is deposited in the calm areas, such as the sluice basins (anthropogenic subtidal area), shoals (margins) and inner bends. The bed in the calm areas can be classified as sandy-clay or silty-clay, while the channels contain clayey-sand. Furthermore, certain areas consist of non-erodible material, such as stiff, consolidated clay lumps, gravel and shells, and vegetation. This in particular holds in the outer bends of the Lower Sea Scheldt, at which non-erodible Boom clay is exposed. Furthermore, shoals, such as the Plaat van Boomke, may consist of hard surface layers (Mathys, 2013).

The grain size diameters of the suspended load, based on samples of suspended matter, are summarized in Table 4. The suspended load consists of mud (mainly clayey silt) and some fine sand. It was observed that the composition of the suspended matter did not change significantly over the tide.

Table 4 – Characteristic grain size diameters averaged over time of samples of suspended matter at Oosterweel [in µm] (Plancke et al., 2014)

D10	D35	D50	D65	D90
4	12	20	31	78

Research of Manning et al., (2007) on flocculation at the location of the ETM proved that both micro- macroflocs are present with a bi-modal distribution. Their respective average floc diameters are 150 µm and 500 µm. The microflocs tend to have an mean effective density of approximately 120 kg/m^3 and a mean settling velocity of roughly 0.9 mm/s, while macroflocs have less dense structures (~50 kg/m^3), but a faster settling velocity of approximately 3.9 mm/s.

Transport

The gross sediment transport fluxes may be up to 4000 m^3 per tide. The transport consist of mainly suspended load (Plancke et al., 2014). Due to horizontal tidal rectification, the fluxes show maxima at opposing sides within the cross-section. Furthermore, the fluxes are highly dependent on the location of the maximum SSC of the ETM: a more downstream (upstream) located maximum increases the flood-(ebb-)directed gross sediment transport flux (Fettweis & Sas, 1997). Due to the large gross transports, sheltered harbor and sluice basins are prone to a lot of sedimentation of mud (~1-2 cm/day) (Sas & Verhaegen, 1992)

Dynamics

Measurements of the suspended sediment concentration at Oosterweel, which are plotted in Figure 23, show that the concentration rapidly increases during both ebb and flood tide. Furthermore: maximum depth-averaged SSC generally coincide with the maximum depth-averaged flow velocities: two distinct peaks in SSC during flood, and a more gradual increase in SSC during ebb. Moreover, at neap tide the concentrations are lower than at spring tide. SSC between normal tide and spring tide do not seem to differ that much during begin-flood and begin-ebb tide. Resuspension of bottom sediments is, therefore, found to be highly important at the location of the ETM. However, the SSC does not always coincide with the maximum current velocity, but often lags behind due to lag effects (Chen, Wartel, Van Eck, et al., 2005; Van Kessel et al., 2011). Also some hysteresis can be observed due to differences in the current velocity and turbulence patterns, but also from local resuspension of inhomogeneous mud layers (Chen, Wartel, Van Eck, et al., 2005).

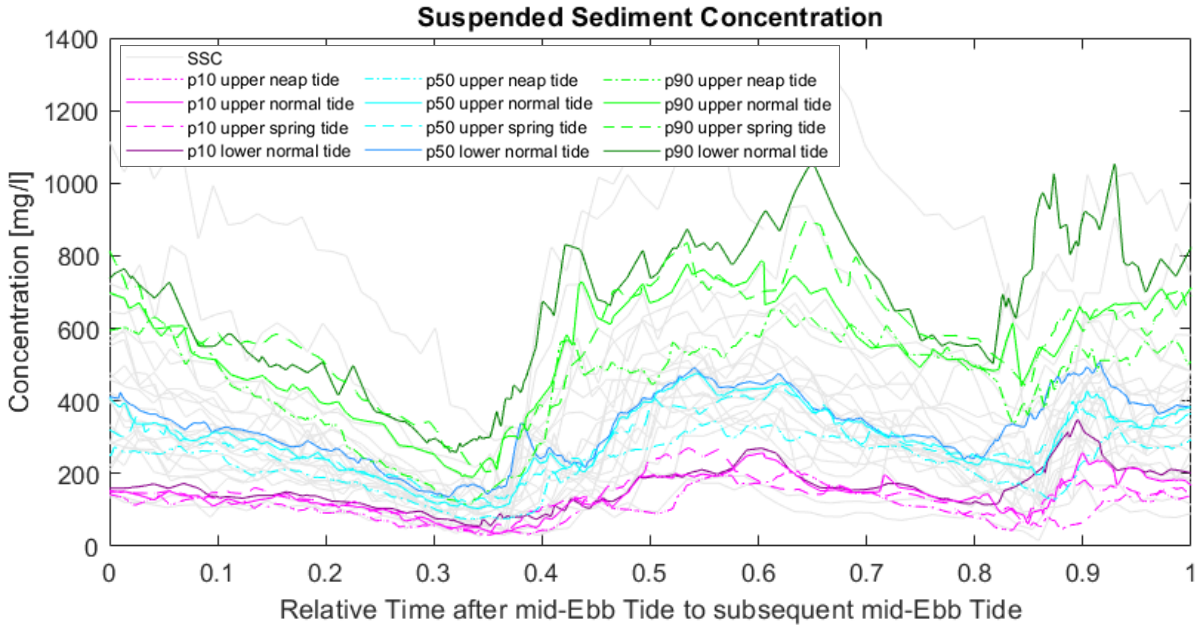

Figure 23 – Measured SSC at Oosterweel in year 2014. The 10th, 50th, and 90th percentile are calculated for the upper station (at 4.5m above bed) for neap, normal and spring tides. Furthermore, these percentiles are visualized for the lower station (at 1.0m above bed) for normal tide.

Additionally, it can be seen that the SSC is rather uniformly distributed in the vertical around mid-ebb and mid-flood tide, while during HWS and LWS and begin-ebb and begin-flood tide, SSC is greater at the bed. Especially during HWS this difference becomes more pronounced, whereas during LWS concentrations are generally lower.

Floc size measurements during neap tide reveal that the mean floc size at high water the SPM composes of 80% of macroflocs with an average settling rate of 2.3 mm/s. During maximum ebb tidal current, the floc size halves to less than 100 µm (60% microflocs). Consequently, the settling velocity drops by nearly an order of magnitude. Around LW slack tide, the flocs steadily grow from 200 µm with a settling velocity of 1.15 mm/s to around 250-375 µm with a mean fall velocity of 1.4 mm/s. During flood, the same behavior is found. However, microflocs are more abundant in this period as there are very dynamic conditions. As a consequence, during the slack waters, the total settling flux comprises ~97% of macroflocs, while during turbulent conditions microflocs are more abundant and dominated the settling flux. (Manning et al., 2007).

3.3 Summary

The Scheldt Estuary is a **semi-diurnal**, **macrotidal**, **tide-dominated** estuary. Its geomorphology is **long** and **funnel-shaped**. The meandering channel(s) decrease in depth in landward direction, especially in the uppermost part of the estuary. The lower estuary has a two channel system with increasing tidal flat area in landward direction. On the contrary, the upper estuary has a one channel system with decreasing tidal flat area in landward direction.

River discharge is relatively small. Therefore, salinity is vertically **uniform** over the estuary. This is typical for a **well-mixed** estuary, in which tidal mixing dominates. Furthermore, there is a very **gradual longitudinal salinity gradient** over the estuary, which distribution is highly dependent on the river discharge: it is pushed seaward during high river run-off. Moreover, the salinity distribution moves up and down with the tide. **Strong transverse salinity gradients** can be found at distinct location in the estuary due to **differential advection**. Wind and waves only affect the hydrodynamics of the lowermost part of the estuary.

The estuary is excited by a slightly distorted regular tide with a strong **spring-neap cycle**. Due to the geomorphology of the estuary, this wave becomes a **partially standing tidal wave**,

which is initially **amplified**. The **distorting** vertical tidal wave is increasingly becoming flood dominant. The horizontal tide, in contrast, is rather neutral. However, there is strong asymmetry in the horizontal tide within the cross-section due to **horizontal residual circulation**. Also strong **lateral residual circulation** is found (channel curvature, transverse salinity gradient).

Sediment (sand and mud) is mainly transported as **suspended load**. Due to a combination of **tidal pumping** and **salinity-induced circulation** (and **time-varying flocculation**), there is **convergence** of transport in the Lower Sea Scheldt. This leads to a wide **bottom pool of fine sediment**. As there is **maximum energy** in this stretch, due to tide and river discharge, there is strong resuspension of material and, hence, the formation of an **estuarine turbidity maximum (ETM)**. As a consequence, **large gross sediment transport fluxes** can be found at this area. They are, furthermore, opposing within the cross-section due to strong horizontal residual circulation.

The location and magnitude of the **maximum suspended sediment concentration (SSC)** in the ETM show very **dynamic** behavior in time. There is great **seasonality** and **spring-neap cycle**. Greater concentrations are found during spring tides, and in winter, during which there is more input of fines due to high river run-off and storms in the mouth. Additionally, there is a lot of variation over the **tidal cycle**: the ETM is nearly absent during slack water. SSC generally corresponds with the current velocity, although some **lag effects** and **hysteresis** is observed. The location of the maximum SSC shifts predominantly with river discharge.

4 Model Description

In this chapter, the numerical models are defined, which are used in this research to predict the hydro- and morphodynamics of the system and subsequently the trench siltation rates and sedimentation distribution over the trench. The choice and set-up of the numerical models is based on their included processes and characteristics, which were found to be governing in estuaries (Chapter 2) and/or in specific for the (area of the ETM in the) Scheldt Estuary (Chapter 3). Details on the models can be found in Appendix E.

Firstly, the already developed and validated NEVLA3D (*NEderlands-VLAams 3D*) model is discussed. It models the hydrodynamics of the entire Scheldt Estuary. The numerical model produces incredibly accurate results and is, therefore, extensively used in various research studies. As NEVLA3D does not model mud and sand transport, the hydrodynamic output is regularly used by water quality modules to model the mud dynamics in the estuary.

In this research, the already developed and validated LTV Slib (*Long Term Vision Mud*) model is used to model the large-scale mud dynamics of the Scheldt Estuary. This water quality module imports the modelled hydrodynamics of NEVLA3D. The model reproduces the mud dynamics very accurately.

Lastly, the detailed model around the ETM, which was set up in this research, is specified. This model, named SETMO (*Scheldt Estuary Turbidity Maximum Oosterweel model*), predicts the local hydrodynamics and sediment dynamics of both sand and mud in the area. The hydrodynamics of SETMO are driven by NEVLA3D, while the mud dynamics are regulated by LTV Slib.

4.1 NEVLA3D

NEVLA3D is set up in the module WAQUA (*WAter movement and water QUAlity modelling*) of the numerical model SIMONA (*SImulatie MOdellen NAtte waterstaat*) by Flanders Hydraulics and Deltares, which was commissioned by Rijkswaterstaat. It models the three-dimensional hydrodynamics of the entire Scheldt Estuary. In this research, the last updated version of the model is used, which was calibrated by Chu (2017) for year 2014. General characteristics are summarized in Appendix E.1. For further details on the model, the reader is referred to Maximova, Ides, De Mulder, & Mostaert (2009), Grasmeijer (2013), Chu (2017), and the user manual of SIMONA.

The grid of NEVLA3D is visualized in Figure 24. It consists of 1,137,000 grid cells with an average grid size of approximately 100 x 50 m. In the vertical, the model has six sigma layers. The time step used in the model is 7.5 s. NEVLA3D includes salinity in its calculations, but no sediment. Furthermore, an uniform wind field, based on measurements, is taken into account as extra physical process (Chu, 2017; Vanlede et al., 2015). Above characteristics lead to a computational time in the order of 2-3 months for a year of simulation.

The upstream hydrodynamic boundary conditions consists of daily measured discharges of rivers, and sluices and weirs, bordering the estuary. On the downstream end, harmonic water levels and currents with corrected tidal phases are imposed through two current velocity boundaries and a Riemann boundary. These time series are derived from ZUNO *(ZUidelijke NOorderzee model)*. Also, the measured salinity is nested from ZUNO with some corrections. Furthermore, wind velocities are imposed on the downstream boundary. These are nested from forecasted wind field data of HIRLAM *(High Resolution Limited Area Model)*, as is used in ZUNO (Chu, 2017).

4.2 LTV Slib

LTV Slib is a water quality model, which predicts the mud transport in the Scheldt Estuary. It is constructed in the Delwaq module of Delft3D. The model imports the grid and the hydrodynamics of NEVLA3D. This makes LTV Slib computational efficient (1-2 days of computational time for a year of simulation). Additionally, wave effects are taken into account based on a separate wave model in SWAN *(Simulating Waves Nearshore)*. Herein, observed wave spectra are imposed on the North Sea boundaries and the nested wind fields are taken into account, accompanied by an uniform wind speed and direction, measured at Flushing.

Figure 24 – Model domain of NEVLA3D and LTV Slib; The cells in the model domain of SETMO are indicated in red.

LTV Slib takes into account two separate mud fractions: a fluvial fraction and a marine fraction. Both fractions have more or less the same characteristics. The mud transport model calculates the erosion and deposition fluxes of fine sediment based on the bed shear stresses due to both currents and waves, and erosion parameters. Advection of mud in the water column is calculated with the hydrodynamics of NEVLA3D by imposed dispersion coefficients.

In the model, mud is deposited in two layers: a temporarily-varying buffer (fluff) layer and a thin well-mixed uniform bed layer with constant thickness. 10% of the mud is directly deposited in the bed, while 90% settles within the buffer layer. Mud is both eroded from the fluff layer and the bed layer. For details on this model, the reader is referred to Van Kessel & Vanlede (2010), Van Kessel et al., (2006, 2011), Van Kessel, Vanlede, Kuijper, & De Kok (2007), the Delwaq User Manual.

4.3 SETMO

SETMO is set up in the SED3D module of Delft3D. It attempts to predict the three-dimensional hydrodynamics and sediment dynamics of both sand and mud with high accuracy around the location of the ETM in order to estimate the siltation rate and sedimentation distribution over the trench of the Scheldt Tunnel at Oosterweel. Consequently, SETMO is aimed to capture the sediment transport and trapping mechanisms and trench hydrodynamics in detail. This

could not be achieved by using the existing NEVLA3D model, since its numerical grid is considered to be too coarse. Therefore, SETMO is designed as a local updated refinement of NEVLA3D with inclusion of mixed sediment.

The detailed numerical model is calibrated and validated with measurement data and verified by literature. An overview of the model is given in Appendix E.3. The characteristics of SETMO are briefly discussed in the remainder of this section.

4.3.1 Domain

Grid

The local updated grid of SETMO is visualized in Figure 25. The grid of SETMO consist of 38,498 horizontal grid cells. The grid lines follow the bathymetry and geometry of the Scheldt as accurate as possible. The area of interest is covered by horizontal grid cells of approximately 5 x 5 m, such that there will be at least 10 horizontal grid cells present on the slopes of the trench. This is to accurately capture the trench hydrodynamics. The grid size increases exponentially to the boundaries. Here, the grid cells are approximately 100 x 55 m and 100 x 40 m at the downstream and upstream boundary respectively, at which they precisely overlap with the grid of the NEVLA model. The purpose of this is hidden in the derivation and implementation of the boundary conditions, as is further explained in section 4.3.4.

The exponential distribution of the grid size creates a linear and gradual grid refinement towards the area of interest, thereby improving the numerical accuracy. Furthermore, within the cross-section, more refinement is given to the channel than the shoals. Reason for this is that higher accuracy is desired for the fastest flowing water, which is likely to transport the most sediment.

In the vertical, SETMO consists of 20 layers. The distribution of the layers refines near the bed and surface to be able to model the shear stresses and turbulence with sufficient accuracy. This improves the estimation of the pick-up and deposition fluxes of the fine sediment.

Bathymetry

The bathymetry is generated by triangular interpolation of the samples of bathymetric soundings of the Lower Sea Scheldt and ground height data of the Flemish Digital Terrain Model. Data of 2014 is used, as is used in NEVLA3D. This is believed to model the hydrodynamics more smoothly. Near the trench the bathymetric data is replaced by more recent data of 2017 in order to obtain a more accurate representation of the area of interest. The different datasets fit each other adequately.

Since the depth values are given to the vertices of the grid cells only, interpolation may sometimes ‘miss’ the crest of the dikes. Therefore, the depth values behind the dike crest were set to the dike height, such that water cannot artificially overtop the dike. The minimum of the four depth values on the vertices is used in the calculation.

4.3.2 Time Frame

A time step of 1.2 seconds is chosen. This is based on numerical consistency reasons, as is explained in further detail in Appendix D.4. In general, a period of 2 tidal cycles is chosen as simulation time, whereas 12 tidal cycles were found to be required to spin-up the bed composition, and to a lesser extent the spin up of the hydrodynamics, salinity, and SSC.

4.3.3 Included Processes

SETMO takes into account salinity and sediment. Details regarding the algorithm of salinity can be found in Appendix D.

Figure 25 – Model domain of the SETMO model within the NEVLA3D model domain of the Lower Sea Scheldt; there is a close up of the model domain at the trench

4.3.4 Initial and Boundary Conditions

Initial Conditions

The initial conditions of SETMO consist of water levels and salinity. For numerical consistency reasons, the (spin-up) calculation is started with an uniform high water, equal to the water level on the upstream boundary condition. The initial values for salinity are derived by linear interpolation between the salinity values of both boundary conditions, as the salinity over the estuary is diminishing fairly linear in landward direction (as discussed in subsection 3.1.6). Hence, the initial salinity profile is close to the expected dynamic steady state solution. For the suspended sediment an initial concentration of 0.3 g/l is imposed for the mud fraction, while no initial concentration is given for the sand fraction. This is in line with what is typically found in the area at the time of HW.

Boundary Conditions

Hydrodynamics

Both at the upstream and downstream boundary, discharges per grid cell are imposed. Although preference was given to an interplay between a water level boundary and a discharge/flow velocity boundary, or two Riemann boundary conditions, to both fix the horizontal and vertical water motion, this proved either to be infeasible or led to poorer results (e.g. the generation of an artificial reflective wave during flood tide).

Constituents

At both boundaries salinity and SSC mud fraction are imposed on the up- and downstream boundary. For the sand fraction, which is generally transported in equilibrium, an equilibrium concentration is used through a Neumann condition.

The boundary conditions for both the hydrodynamics and the constituents are based on modelled data from the model run of NEVLA3D and LTV Slib for year 2014. The derivation of the time series is cumbersome, as the output files of these models had a frequency of once in 30 minutes. Furthermore, the vertical grid of NEVLA3D is different than that of SETMO. Therefore, over the depth, the boundary conditions are obtained with higher order interpolation. Corrections are applied to the obtained time series, based on the comparison of layer-integrated and depth-integrated discharges and mass fluxes of the imposed constituents between the models. In time, cubic spline interpolation is applied to create a smooth signal, since the vertically interpolated 30-minute interval time series would lead to artificial shock waves. Details on the applied boundary conditions can be found in Appendix E.4.

4.3.5 Physical Parameters

SETMO takes into account the same physical parameters as NEVLA3D, preferably leading to the same dynamics. In line with NEVLA3D, the model resolves saline water with its corresponding physical parameters. The bottom roughness is given as an uniform Manning coefficient, which equals the value for the particular stretch in NEVLA3D. The depth-dependent Manning roughness is calculated to spatially- and temporally-varying Chézy roughness. Furthermore, the model takes into account turbulence through the diffusivity and viscosity principle, according to the well-known k-ε turbulence model. Details regarding the physics of the numerical model can be found in Appendix D.

4.3.6 Sediment and Morphology

Sediment

Two co-existing and interacting fractions of inorganic matter are included in SETMO: a cohesive mud fraction (IM1) and a non-cohesive sand fraction (IM2). This is in line with the reported literature for the area in ETM. The cohesive fraction is transported in suspension. The material, which is composed of both fluvial and marine mud, has the same characteristics as the two separate mud fractions in LTV Slib model. The magnitudes of the pick-up and sedimentation fluxes are calculated with the Parteniades-Krone formula. Dispersion of fine sediments over the vertical and the advection throughout the estuary is dependent on the online modelled hydrodynamics.

Although an additional flocculation module was opted to be implemented in SETMO by the researcher, as this is one of the identified processes/mechanisms found in the literature study and study area description, it was decided not to apply it. Reason was that the implementation and calibration of SETMO was very cumbersome: an additional flocculation module, such as the Manning model, would, based on expert knowledge, lead to a very long calibration period, which was not feasible in the given time of this thesis.

In contrast, the non-cohesive fraction, which is considered to be fine sand with a median diameter of 150 µm, is transported both in suspension and as bed load. The underlying formula, which calculates both fluxes, is known as Van Rijn (1993). Details on both transport formulae are given in Appendix D.

Morphology

In SETMO, a layered bed stratigraphy with temporarily varying bed layer composition is implemented with inclusion of a time-dependent fluff layer. This is schematized in Figure 26. Furthermore, there is interaction between the mud and the sand fraction in the bed. There is no morphological bed level update in SETMO, as the simulation period is limited. In contrast, the bed composition is updated. Additionally, no morphological factor is applied. The concepts of the fluff layer, sand-mud interaction and the layered bed stratigraphy are clarified separately in the below.

Fluff Layer

Fluff is superficial bed strata, comprised of fine sediment flocs, which are deposited on the bed during slack water. Due to its low shear strength, the sediment is generally easily eroded

during the subsequent flood or ebb tide. The fluff layer consolidates over time to a less erodible bed layer. It is prominently present in estuaries, predominantly at the location of the ETM. Therefore, the implementation of a fluff layer in the numerical model is vital for accurately reproducing the fine sediment dynamics (Mathew & Winterwerp, 2017).

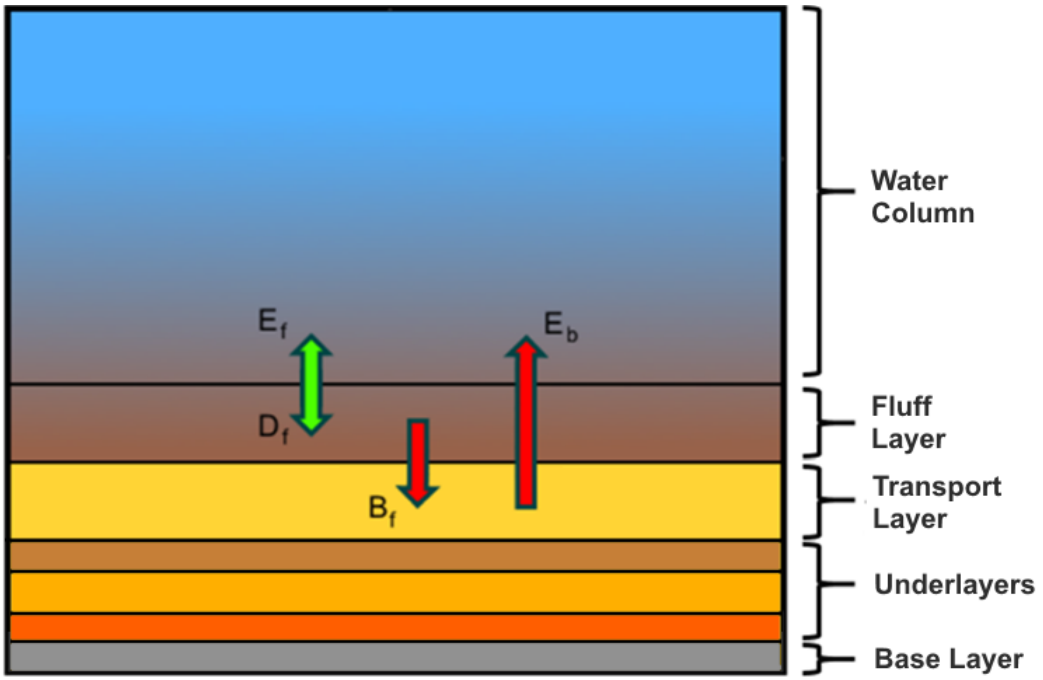

Figure 26 – Schematized overview of the morphological physics in the SETMO model

It works as follows: settling mud is first deposited in the distinct fluff layer (D_f), which does not contribute to the bed composition. Once in the fluff layer, mud is buried in the bed layer according to a mass-dependent flux (B_f): the more mass in the fluff layer the greater the burial flux. This burial flux is bounded by a defined maximum.

During flood and ebb tide, mud in the fluff layer is resuspended due to the bed shear stresses. A resuspension flux is calculated based on the mass in the fluff layer (E_f). Again, the flux is limited by a maximum flux. Also mud from the bed layer is eroded (E_b). This flux is calculated according to its own similar mass-dependent erosion flux.

Sand-mud interaction
SETMO takes into account separate cohesive and non-cohesive regimes in its domain. This distinction is made according to a critical mud content in the bed. Based on promising numerical modelling results of Van Ledden (2003), the critical mud content is set to 30%.

In the non-cohesive regime, mud is proportionally eroded with sand. Furthermore, the critical shear stress of sand increases with increasing mud content. In the cohesive regime, the erosion fluxes of sand and mud are proportional to their respective fractions. The erosion flux in this regime is calculated by interpolation between the erosion flux in the non-cohesive regime and fully cohesive regime, in which erosion is calculated according to Partheniades-Krone.

Layered bed stratigraphy
In SETMO, a layered bed stratigraphy is applied, which is treated in a mixed Lagrangian-Eulerian frame. Multiple distinct layers are applied:

- Active transport layer
  This erodible top layer is prone to sedimentation and erosion fluxes. It has a constant thickness of only 5 cm. The transport layer can, therefore, be considered as a Lagrangian layer which moves up (down) during deposition (erosion). This greatly

reduces the spin-up time of the bed composition. Moreover, the availability of mud is limited in order to prevent excessive resuspension. If there is erosion of the transport layer, it will be replenished with sediment of the upper underlayer.

- Underlayers
  A number of 5 erodible underlayers is applied below the active transport layer. These underlayers have maximum thickness and a constant composition. They are treated in a Eulerian framework. The uppermost underlayer will reduce in thickness during erosion. During deposition, underlayers are created until the defined number is reached. If this number is exceeded, the bottom underlayer is merged with the base layer. The number of layer is chosen such that there is sufficient resolution in the deposition of mud in the bed, which is then not being lost to the deeper layers.
- Base layer
  The base layer is the bottommost layer of erodible sediment without a maximum defined thickness. It grows in size if there is excess sedimentation. If the active transport layer reaches the base layer, the base layer is being eroded. If the amount of sediment is less than the required for the thickness of the transport layer, erosion fluxes are reduced until all erodible sediment has been eroded.
- Non-erodible layer
  This layer of sediment cannot be eroded. This layer is exposed at the non-erodible areas.

4.3.7 Numerical Parameters

Convergent numerical schemes are used, which are both consistent and stable without producing too much artificial numerical effects. The discretization and schematization of the problem works solid and efficient. Details can be found in Appendix D.

4.4 Summary

In this study, a **numerical model** was implemented, which is aimed to accurately estimate **the trench siltation rate** and **sedimentation distribution** over the trench of the Scheldt Tunnel at Oosterweel. This model, named **SETMO** (*Scheldt Estuary Turbidity Maximum Oosterweel model*), is designed to capture the **three-dimensional hydrodynamics** and **sediment transport and trapping mechanisms** in the area of the ETM and trench

SETMO is a locally **updated** and **refined** model of the existing, large-scale **NEVLA3D** model. This overall numerical model predicts the hydrodynamics throughout the whole Scheldt Estuary. As NEVLA3D has a coarse grid, refinement and update of the model was necessary in order to reach above aim with sufficient accuracy.

In SETMO the following processes are modelled: **salinity** and **sediment** (**sand** and **mud**). The dynamics of sand and mud in both the water column and the bed are taken into account. It takes into account **fluid mud** and **sand-mud interaction** through a **layered bed stratigraphy**. Although there is no morphological update, account is taken of **sedimentation and erosion fluxes** and the **bed composition** is **updated**. The sediment characteristics are in line with reported values.

The model is driven at its open boundaries by **modelled discharges** and **mud concentrations per cell**, which were derived based on **time-** and **depth-interpolation**. These data originate from the output of NEVLA3D and **LTV Slib** respectively. The latter numerical model imports the modelled hydrodynamics of NEVLA3D and predicts the estuarine mud dynamics. For the sand dynamics, equilibrium concentrations are imposed on the boundaries.

SETMO simulates a period of two consecutive tidal waves due to high computational time. Discretization in space and time, schematizations and initial conditions are chosen such that there is numerical consistency in the model.

5 Model Validation

This chapter focuses on the validation of SETMO, which was described in detail in Chapter 4. It explains the methodology used in the calibration of the numerical model. Furthermore, there is a section dedicated to the available data within the model domain. Eventually, this chapter presents the validation results of the final calibrated SETMO.

5.1 Methodology

The validation of SETMO is based on the comparison of the following modelled quantities:

- water levels,
- current velocity magnitude,
- current velocity direction,
- salinity;
- suspended sediment concentration,

with measurement data at various locations within the model domain of SETMO for (a distinct period of time in) year 2014. In order to evaluate the modelling results, two statistical biases are calculated: the mean error (ME) and the unbiased root-mean-square error (uRMSE). The ME can be calculated according to difference between the average simulated (x) and the average measured values (y):

$$ME = \frac{1}{n}\sum_{i=1}^{n}(x_i - y_i) = \bar{x} - \bar{y}$$

A positive (negative) ME implies an overestimation (under-estimation) of the regarded quantity by the model. The uRMSE is a measure to quantify the dispersion error of the simulated quantity. It can be calculated through (Zhang, Zhang, Zhou, Shao, & Gao, 2017):

$$uRMSE = sign(\sigma_x - \sigma_y)\sqrt{\frac{1}{n}\sum_{i=1}^{n}(x_i - y_i)^2 - ME^2}$$

in which the standard deviations of the modelled and measured quantity are calculated by:

$$\sigma_x = \sqrt{\frac{1}{n}\sum_{i=1}^{n}(x_i - \bar{x})^2}\,, \qquad \sigma_y = \sqrt{\frac{1}{n}\sum_{i=1}^{n}(y_i - \bar{y})^2}$$

A positive (negative) uRMSE suggests more (less) variation of the regarded quantity in the model compared to the measurements.

5.2 Available Data

Above mentioned quantities are monitored in the Sea Scheldt by the WL (Waterbouwkundig Laboratorium) based on a monitoring campaign, known as MONEOS (MONitoring Effecten Ontwikkeling-Schets). As known by the researcher, two monitoring programs were carried out in 2014 in the area of the ETM:

- ‘continuous’ point measurements throughout the year at various fixed locations, at which water levels, currents, SSC, salinity, and/or river discharge may be measured;

– 13h vertical profile measurements around mid-ebb tide along various transects along which currents, discharges, suspended sediment concentrations and fluxes are measured and bed samples are taken.

The locations of the stations and transects are depicted in Figure 27. Conveniently, a measurement transect and a measurement station are situated close to the location of the trench. This gave the opportunity to calibrate parameters in such a manner that the modelling results are accurately describing the measured quantities in the area of the trench. Transect Oosterweel was measured on the 16th and 17th of May 2014 between 05:30 and 06:00 hours respectively. Consequently, this was chosen as the validation period.

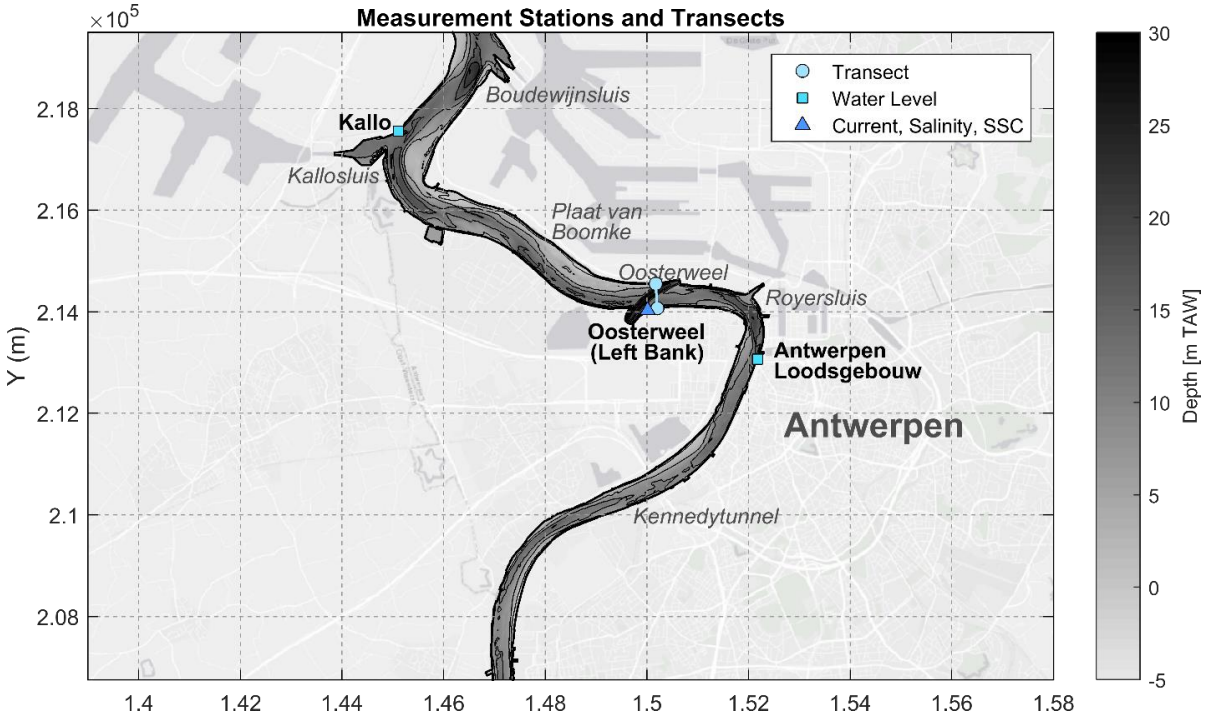

Figure 27 – Measurement locations and transects in the stretch of the Lower Sea Scheldt within the model domain and their monitored quantities

The validation of the numerical model is mainly based on the data of the measurement stations, as it became clear that the 13h transects measurements were ill-defined and of poor quality. Furthermore, during the calibration of the model, more emphasis was given to current velocity and suspended sediment concentration, since these quantities are generally considered most important for (suspended) sediment transport.

Moreover, it was decided to compare the results of SETMO with the modelling results of the overall numerical models. Since the boundary conditions of SETMO are derived from modelling results of the NEVLA3D and LTV Slib model, which knowingly have errors with respect to the measurement data, background errors are introduced to SETMO. Unfortunately, these errors cannot be resolved by calibration.

5.3 Results

In this section, the results of the model are presented for the water level, current velocity, salinity and suspended sediment concentration near the trench at Oosterweel. For the background errors of the overall numerical models, the reader is referred to the report of Chu (2017).

5.3.1 Water Level

Figure 28 compares the measured water level at station Antwerp Loodsgebouw. It can be seen that SETMO significantly overestimates the water level, especially during LWS. Furthermore, it shows less variation over a tidal cycle.

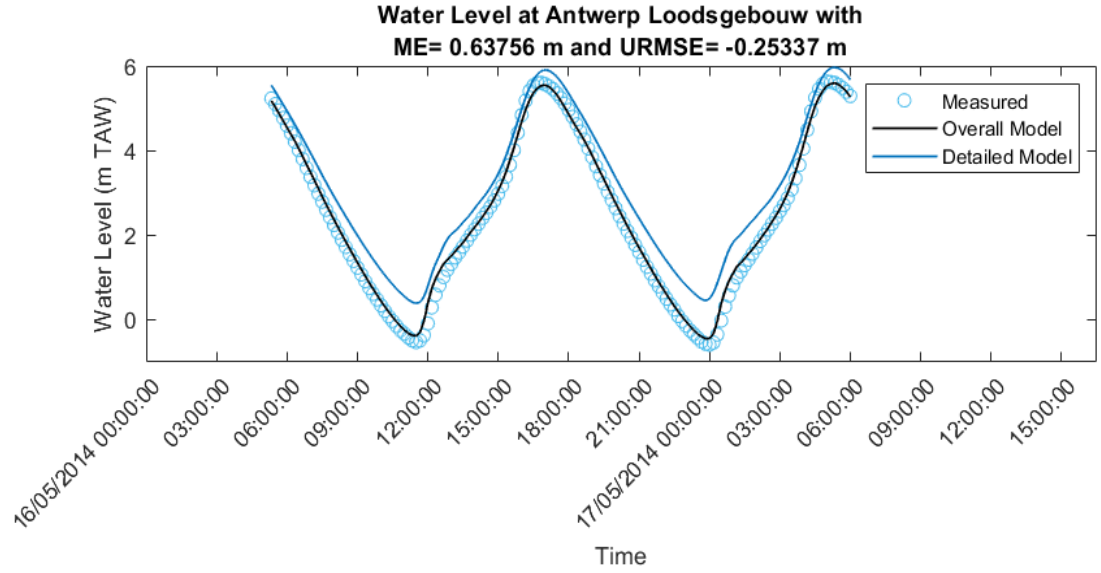

Figure 28 – Comparison of the measured and overall and detailed modelled water level at station Antwerp Loodsgebouw.

These errors are believed primarily to be caused by the internally more refined grid of SETMO with respect to the grid of NEVLA3D. As a consequence, more detail is given to the numerical bathymetry within the SETMO modelling domain. This led to the fact that SETMO has a greater wet volume and a generally greater along-channel cross-sectional area compared to NEVLA3D. Accordingly, it modifies the vertical water motion imposed at the boundaries. Fruitless efforts were made to artificially adapt the bathymetry/change the roughness coefficients to reduce this effect.

Additionally, small additional background errors are introduced in SETMO as the vertical water motion is not fixed in the model at one or both of the boundaries. It was chosen only to apply horizontal water motion at the boundaries, as this proved to lead to the better reproduction of current velocities in the domain. Implementation of Riemann boundaries, fixing both the horizontal and vertical motion of the water, would probably have led to better modelling results regarding the water levels in the domain. However, implementation of these boundaries was futile.

5.3.2 Current Velocity

The reproduction of the current velocity by SETMO is more promising, as can be seen in Figure 29. Although SETMO greatly underestimates the magnitude of the current velocity during ebb tide, it accurately captures the quantity during flood tide. Given that in NEVLA3D the current velocity is significantly overestimated during flood tide and slightly underestimated during ebb tide, the overall smaller predicted current velocities in SETMO are again believed to be caused by the increase in wet cross-sectional area in SETMO compared to NEVLA3D.

Comparison between the results of the upper and lower sensor reveals that the biased and unbiased errors in current velocity magnitude and direction slightly decrease towards the bottom.

5.3.3 Salinity

Salinity is heavily underestimated by both SETMO and NEVLA3D during the calibration period, as can be seen in Figure 30. Furthermore, the modelled salinity shows less variation compared

to the measured salinity. The applied boundary conditions can largely be accounted for this underestimation. Moreover, salinity is slightly more underestimated at the lower sensor. This error persists over the full tidal cycle, meaning that slightly less stratification is captured in SETMO.

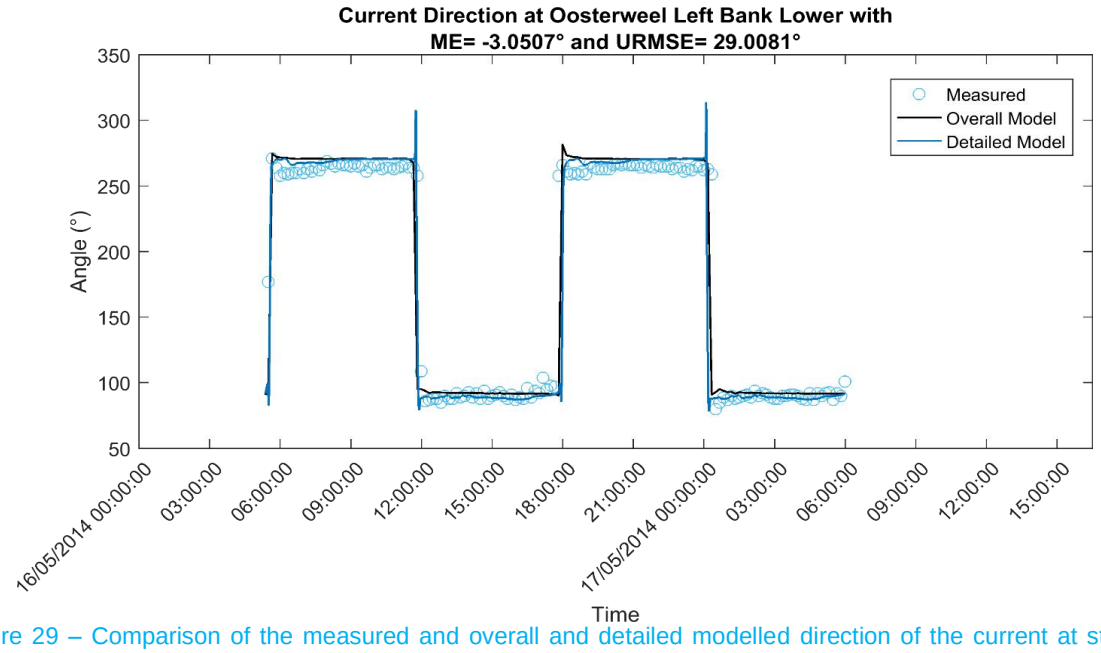

Figure 29 – Comparison of the measured and overall and detailed modelled direction of the current at station Oosterweel Left Bank Lower (at 1.0 m above bed).

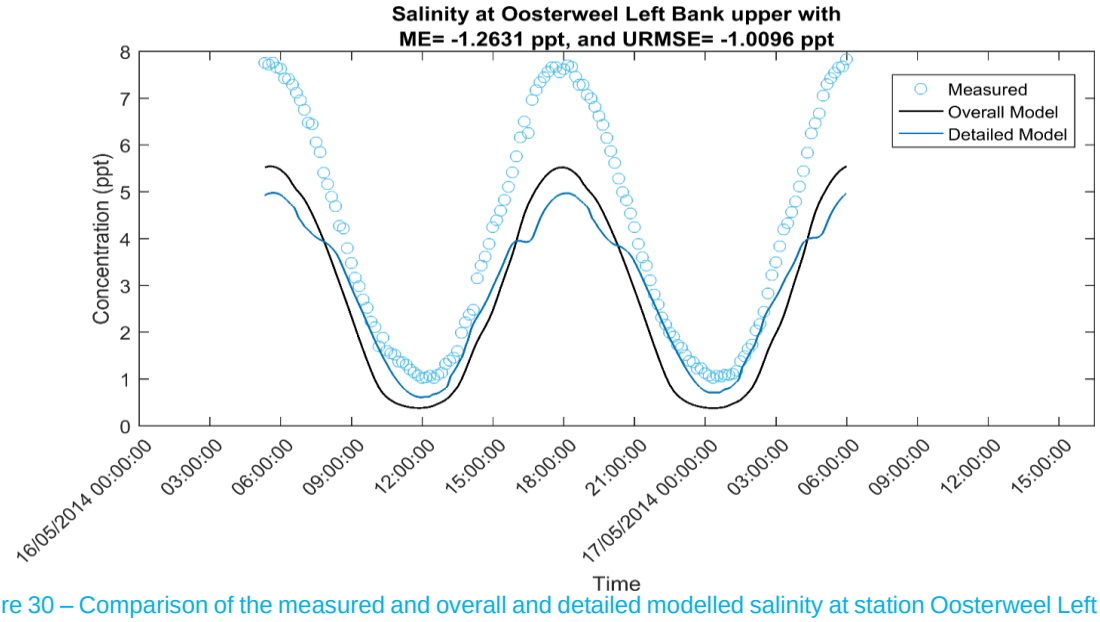

Figure 30 – Comparison of the measured and overall and detailed modelled salinity at station Oosterweel Left Bank Upper (at 4.5 m above bed).

Regarding the behavior of the salinity, SETMO accurately models the salinity around LWS, while the signal shows increasing errors around HWS. During the latter period, an unexplained higher order oscillation can be observed, which is not captured by the measurements, neither in the results of NEVLA3D. Efforts during calibration of the numerical model to remove this oscillation proved futile.

5.3.4 Suspended Sediment Concentration

Analyzing the modelled and measured SSC in Figure 31, it can be observed that SETMO overestimates the measured sediment concentrations at the upper sensor. Furthermore, there

is less variation of the modelled SSC over the tidal cycle compared to the measurements, particularly during LWS.

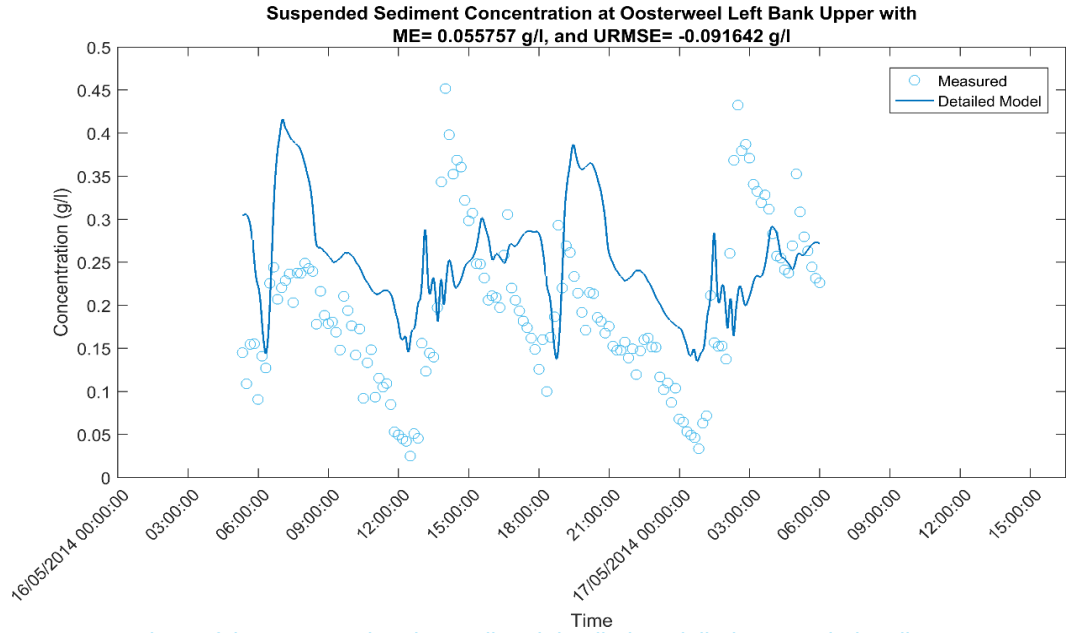

Figure 31 – Comparison of the measured and overall and detailed modelled suspended sediment concentration at station Oosterweel Left Bank Upper (at 4.5 m above bed).

Based on theory on vertical SSC profiles and SSC transport (Yu, Flemming, & Gao, 2011), the above observations indicate that the applied fall velocity in the model is either too high (amplitude is attenuated too strong in water column) or too low (lag effects are too much present around LWS). This may hint on the fact that there is an interplay between multiple mud (clay and silt) fractions in the system and/or a time-varying fall velocity. Unfortunately, no extra fractions and/or additional flocculation model could be taken into account in the model as computation times would increase severely. Therefore, care should be taken in the interpretation of the modelling results of SETMO.

Unfortunately, no errors could be calculated with respect to the model results of LTV Slib, as observation stations applied to both models were later found to differ. Visual comparison revealed an at least comparable quality of the SSC. This is believed to be caused by the great dependency of the SSC in SETMO on the boundary conditions, which contain the modelled SSC of LTV Slib.

5.4 Summary

SETMO has been **calibrated** based on comparison of the following modelled **quantities** with respect to the measurements:

- Water levels
- Salinity
- Current velocities and directions
- Suspended sediment concentrations

These quantities are measured **'continuously'** throughout the year at a certain depth at permanent **measurement stations**. Furthermore, the latter two quantities are measured throughout the water column along a transect during a yearly **13h measurement campaign**. For the transect within the model domain, this campaign was held on the 16th and 17th of May 2014 between 05:30 and 06:00 hours. This period was, therefore, adopted as the **validation period**.

The calibration results were evaluated based on the combination of a **biased** and an **unbiased root-mean squared error estimator**. The former identifies the **under- or overestimation** of a measured quantity by the model, the latter determines the **difference in numerical dispersion** of the modelled quantity with respect to the measurements.

Results of the **validation** reveal that above quantities are modelled with **sufficient accuracy** in the model, although **improvements** are possible. Errors regarding water levels and current velocities are believed to be introduced by **differently discretized geomorphology** between SETMO and NEVLA3D; the latter of which the hydrodynamics are imposed on the boundaries of SETMO. Errors regarding salinity are thought of to be caused by **errors** in the modelled salinity in NEVLA3D, set on the **boundaries**. This difference may introduce fundamentally different physical behavior in the model. Errors in the SSC are believed to be induced by the **imposal** of only one **single mud fraction** with a constant fall velocity, as there seems to be an interplay between multiple fractions with different settling velocities.

6 Model Simulations

In this chapter, the general modelling approach and the set-up of the individual model simulation scenarios of the detailed numerical model, SETMO, (see Chapter 4) are explained. These are constructed accordingly to:

1. predict the trench siltation rate and its distribution over the trench
2. identify the total degree of uncertainty around the predicted trench siltation rate.
3. discover the governing large-scale and small-scale mechanisms for trench siltation,
4. investigate the interaction of the trench with the normative mechanisms;
5. check the link between trench siltation and environmental conditions.

A powerful approach, also adopted in this research, is to develop a base case, which takes into account the best calibrated input parameters and modelling settings. This run typically simulates a period during which average conditions prevail. The output of the base case serves as a comparison tool for all subsequent simulations to which variation is given. These simulations can be distinguished based on differences in:

- Model parameters
  Simulations in which the magnitude of one individual parameter is changed to be able to identify the degree of epistemic uncertainty of the prediction of the trench siltation rate (see subsection 6.1.1).
- Model settings
  Simulations in which fundamental changes are applied to the set-up of the model (i.e. exclusion of salinity) with the purpose to discover the governing large-scale and small-scale mechanisms for trench siltation (see subsection 6.1.2).
- Bathymetry
  Runs in which the trench is excluded from the bathymetry in order to investigate the interaction between the trench and the normative mechanisms (see subsection 6.1.3).
- Simulation period
  Runs with different simulation periods to create scenarios in which different environmental conditions are governing. These simulations serve to estimate the intrinsic uncertainty of the area (see section 6.2).

The above is summarized in Table 5. Due to constraints in time, it was decided not to investigate cross-relations between the environmental components, but to limit this research to variation of the individual components. Consequently, environmental variability runs were set-up in which one of the components has an extreme, while the other components show more or less average behavior.

Table 5 – Overview of the general modelling approach

Run Type	Spin Up	Variation	Purpose	Code	Section
Base	Base Case (simBC14a)	None	Base Case	simBC14a	6.1
		Model settings	Identification mechanisms	simBC14b#	6.1.1
		Bathymetry	Influence trench	simBC14c	6.1.2
		Model parameters	Epistemic uncertainty (sensitivity analysis)	simBC14d#	6.1.3
Scenario	Scenario (simSC14a#)	Simulation period	Environmental variability; Intrinsic uncertainty	simSC14a#	6.2

in the code symbolizes the number of the calculation as will be indicated for each run in the remainder of this chapter

Furthermore, again due to time constraints, it was decided only to construct additional simulations with different model settings for the base case scenario, although it is known from literature that different mechanisms may be dominant under different environmental conditions. It is, therefore, assumed that direct comparison between the modelling results of the scenario runs and the base case run is sufficient to identify these differences. The same holds for the influence of the trench on the governing mechanisms in the base case scenario. Lastly, for simplicity, it is assumed that the uncertainty around the prediction of the trench siltation rates is independent of the prevailing environmental conditions. Consequently, the sensitivity analysis was only applied on the base case.

In the remainder of this chapter, the distinct runs are specified according to the described approach in the above (summarized in Table 5). In general, the runs comprise of a long spin-up time of 5 days in which the hydrodynamics, salinity, suspended sediment, fluff layer and bed composition are preferably reaching a dynamical equilibrium state for the situation without the trench. After 5 days, the computation is halted. Its output serves as a starting point for the subsequent run(s) in which model settings are changed (i.e. the implementation of the trench). These runs consist of a spin-up time of 2 days, to account for smoothing of the hydrodynamics from the starting condition and the buildup of the fluff layer, and a final simulation period of 1 day.

Table 6 – Characteristics of the base case and the scenario runs

Name	**Base**		**High River Discharge**		**Low River Discharge**	
Code	simBC14a		simSC14a1		simSC14a2	
Conditions	Tide	Tide	Tide	Normal	Tide	Normal
	River	Medium	River	Low	River	Medium
	Wind	Wind	Wind	Calm	Wind	Calm
Spin Up Period	Start	13-09-2014 06:30:00	Start	17-01-2014 04:30:00	Start	17-06-2014 06:30:00
	End	18-09-2014 10:30:00	End	22-01-2014 07:00:00	End	22-06-2014 11:30:00
Simulation Period	Start	20-09-2014 20:30:00	Start	24-01-2014 16:00:00	Start	24-06-2014 21:00:00
	End	21-09-2014 21:30:00	End	25-01-2014 16:00:00	End	25-06-2014 22:00:00
Bathymetry	Trench included		Trench included		Trench included	
Model settings	As listed in Appendix D.3		As listed in Appendix D.3		As listed in Appendix D.3	
Parameters	As listed in Appendix D.3		As listed in Appendix D.3		As listed in Appendix D.3	
Name	**Spring Tide**		**Neap Tide**		**Stormy Weather**	
Code	simSC14a3		simSC14a4		simSC14a5	
Conditions	Tide	Normal	Tide	Normal	Tide	Normal
	River	High	River	Low	River	Medium
	Wind	Calm	Wind	Calm	Wind	Calm
Spin Up Period	Start	04-08-2014 20:00:00	Start	10-09-2014 04:30:00	Start	04-05-2014 14:30:00
	End	09-08-2014 02:00:00	End	15-09-2014 07:30:00	End	09-05-2014 22:00:00
Simulation Period	Start	20-08-2014 11:00:00	Start	17-09-2014 16:30:00	Start	11-05-2014 08:00:00
	End	12-08-2014 11:30:00	End	18-09-2014 18:00:00	End	12-05-2014 09:00:00
Bathymetry	Trench included		Trench included		Trench included	
Model settings	As listed in Appendix D.3		As listed in Appendix D.3		As listed in Appendix D.3	
Parameter	As listed in Appendix D.3		As listed in Appendix D.3		As listed in Appendix D.3	

6.1 Base runs

The base case run simulates a scenario in which the conditions, regarding the tide, discharge and wind, are simultaneously close to average. This condition was found to be governing on

21th of September 2014. The characteristics of the base case simulation, which are listed in Table 6, are also used in the runs to investigate the normative mechanisms, the influence of the trench and the epistemic uncertainty around the trench siltation rate.

6.1.1 Epistemic uncertainty

The degree of epistemic uncertainty of the predicted trench siltation rates is explored through a (probabilistic) sensitivity analysis. The focus in this analysis lies on the most important parameters for sediment transport and deposition, which are found according to literature, expert knowledge, and researcher's insights. Table 7 gives an overview of the constructed sensitivity runs. These can be divided into parameters which regulate:

- the erosion flux (*erosion parameter, critical bed shear stress, critical mud content, sand-mud coefficient*)
- the deposition flux (*fall velocity, burial flux*)
- turbulence (*eddy viscosity/diffusivity*)
- sediment characteristics (*fall velocity, grain size distribution, critical mud content*)

Ranges, consisting of a minimum and maximum value, are given to the parameters. These boundary values are determined using a certain percentage of the base case value in such a manner that realistic ranges are constructed for each governing parameter. Also, the uncertainty regarding the applied sediment transport formula is investigated. Details on the method of the probabilistic sensitivity analysis can be found in Appendix F.

Table 7 – Overview of the sensitivity runs of the base case simulation

Code	simBC14d1	simBC14d2	simBC14d3	simBC14d4	simBC14d5	simBC14d6
Parameter	Erosion Parameter Fluff Layer	Erosion Parameter Bed Layer	Fall Velocity	Critical Bed Shear Stress Fluff Layer	Eddy Viscosity/ Diffusivity	Critical Bed Shear Stress Bed Layer
Min	2.2*10^-4 $m^{-2}s^{-1}$	5.0*10^-4 $m^{-2}s^{-1}$	1.0 mm s^{-1}	0.10 N m^{-1}	0.35 / 0.50 m^2s^{-1}	0.25 N m^{-1}
Base Case	4.3*10^-4 $m^{-2}s^{-1}$	1.0*10^-3 $m^{-2}s^{-1}$	2.0 mm s^{-1}	0.20 N m^{-1}	0.70 / 1.0 m^2s^{-1}	0.50 N m^{-1}
Max	8.6*10^-4 $m^{-2}s^{-1}$	2.0*10^-3 $m^{-2}s^{-1}$	3.0 mm s^{-1}	0.40 N m^{-1}	1.4 / 2.0 m^2s^{-1}	1.0 N m^{-1}
Code	**simBC14d7**	**simBC14d8**	**simBC14d9**	**simBC14d10**	**simBC14d11**	
Parameter	Burial Flux	Grain Size Distribution Sand	Sand-Mud Coefficient	Critical Mud Content	Sediment Transport Formula	
Min	2.5*10^-6 $m^{-2}s^{-1}$	100/200 µm	2.0	0.20	Van Rijn (2007)	
Base Case	5.0*10^-6 $m^{-2}s^{-1}$	150/300 µm	3.0	0.30	Van Rijn (1994)	
Max	1.0*10^-5 $m^{-2}s^{-1}$	200/400 µm	4.0	0.40		

6.1.2 Normative Mechanisms

Five additional model simulations of the base case are ran to fully identify the normative sediment trapping mechanisms. In these simulations, fundamental changes in the model settings are applied to exclude certain processes and, hence, certain sediment trapping and transport mechanisms. This makes it easier to identify certain mechanisms and their relative importance with respect to the other mechanisms. The additional simulations are summarized in Table 8.

Table 8 – Changes in the set-up of the base case for the purpose of identification of normative trapping mechanisms

Code	simBC14b1	simBC14b2	simBC14b3	simBC14b4	simBC14b5
Model setting	No salinity	No Coriolis	No sediment density	No fluid mud	No sand-mud interaction

6.1.3 Trench Interaction

The base case was also appointed to investigate a possible interaction of the trench with the trapping mechanisms. For this purpose, the bathymetry of the trench is not implemented in the simulation. Comparison with the modelling results of the base case is believed to point out to which extent the trench influences the normative trapping mechanisms.

6.2 Scenario runs

In this research, five different simulation periods have been chosen, based on an analysis of the governing conditions. This analysis concentrated on the relative influence of the tide, river discharge and wind at sea throughout year 2014. This is in line with the literature on the Scheldt Estuary (Van Kessel et al., 2011), which stated that suspended sediment concentrations in the Scheldt Estuary are primarily dependent on these conditions. The purpose is to check the variation of the trench siltation rates on the environmental conditions in order to estimate the degree of intrinsic uncertainty. Each scenario focuses on a condition in which one individual environmental component experiences an extreme (both minima and maxima), while the other components show average behavior. The details of the distinct scenario runs are listed in Table 6, along the base case run. The method of the scenario analysis corresponds with the method of the sensitivity analysis (see Appendix F).

6.3 Summary

In this research, the modelling approach of a **base case** is adopted in which average conditions dominate and **best-calibrated input parameters** and **model settings** are used. Subsequently, **additional simulations** are constructed within the simulation period of the base case, in which:

1. model parameters are differed:
   to identify the degree of epistemic uncertainty around the predicted trench siltation rate,
2. the trench is not included (different bathymetry):
   to investigate the interaction of the trench with the normative mechanisms;
3. model settings are changed:
   to discover the governing macro- and micro-scale mechanisms for trench siltation.

Furthermore, **different model scenarios** with distinct simulation periods are adopted in which different environmental conditions prevail. This is in order to estimate the degree of intrinsic uncertainty of the trench siltation rates.

7 Results: trench siltation

In this chapter, the results of the simulations of the detailed numerical model, SETMO (Chapter 4), as described in Chapter 6, are presented. Firstly, the trench siltation rates and sedimentation distributions over the trench will be presented in detail for the base case. Subsequently, the results of the probabilistic sensitivity analysis on the governing parameters and physical processes, consisting of the uncertainty ranges around the trench siltation rates, will be presented. Additionally, the chapter will give similar results of the probabilistic scenario analysis on the varying environmental conditions.

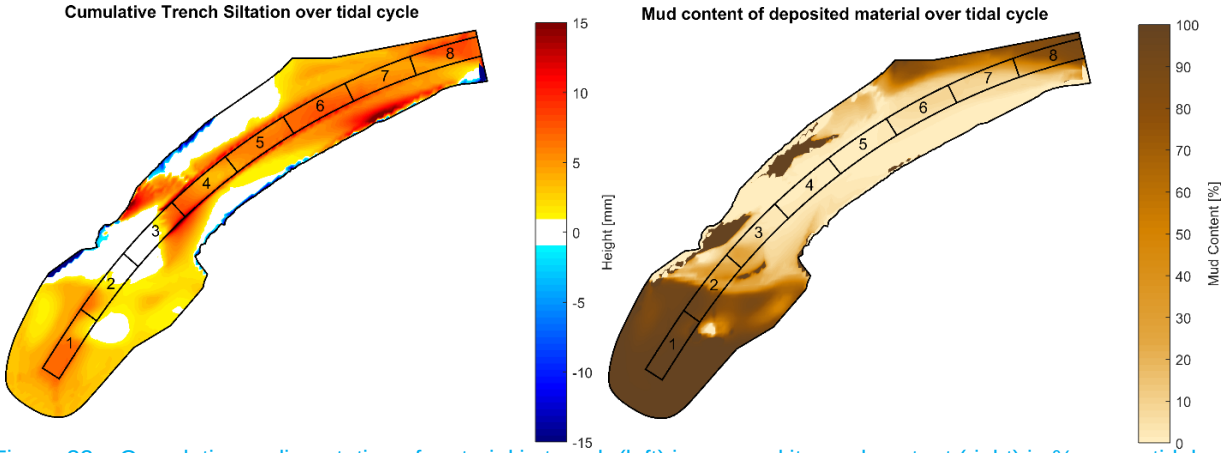

Figure 32 – Cumulative sedimentation of material in trench (left) in mm and its mud content (right) in % over a tidal cycle for the base case.

7.1 Base Case

It can be seen in Figure 32, that SETMO predicts net deposition of both mud and sand in the trench over a full tidal cycle. Simultaneously, the model resolves erosion at the edges of the slopes of the trench. Also, the generation of a fluid mud layer on top of the bed is resolved.

The net average siltation volume rates over the tide (and ebb and flood tide respectively) of both mud and sand are visualized in Figure 33 for the locations of the separate tunnel elements. A total siltation volume of 300.2 m^3/tide at the locations of the tunnel elements is found, of which 67.0% is mud and 32.1% is sand. Furthermore, each tide 133.4 m^3 of fluid mud is build up on the bed of the trench.

One can observe that SETMO predicts most sediment to be deposited in the bed at the location of tunnel elements 4, 5, 6, and 8, while the least sedimentation is estimated to occur at the location of tunnel elements 2 and 3. Most fluid mud is generated in the sheltered areas. Furthermore, it expects considerable variation over the tidal wave. In general, more sedimentation is found during ebb tide than during flood tide. In the remainder of this subsection, the above results are presented in more detail for both mud and sand separately.

7.1.1 Deposition of (fluid) mud

It can be seen from Figure 32 and Figure 33 that SETMO predicts mainly mud to be deposited in the more sheltered areas of the trench. This mud originates from fluid mud, which is present in the fluff layer.

Fluid mud

Figure 34 reveals that SETMO predicts the fluff layer to be primarily built up in the exposed areas during ebb tide, while this fluff layer is again resuspended in its entire during flood tide. In contrast, the sheltered areas show a more or less continuous generation of fluid mud over the tidal cycle. Furthermore, Figure 35 shows that the model estimates most buildup in the

more exposed areas to occur around the slack waters, while there is total depletion of the fluff layer during mid-flood and -ebb tide. Closer to the sheltered areas, there is more or less continuous buildup of fluid mud; exceptions being during late-flood and mid-ebb tide, which correspond with peak-tidal flow.

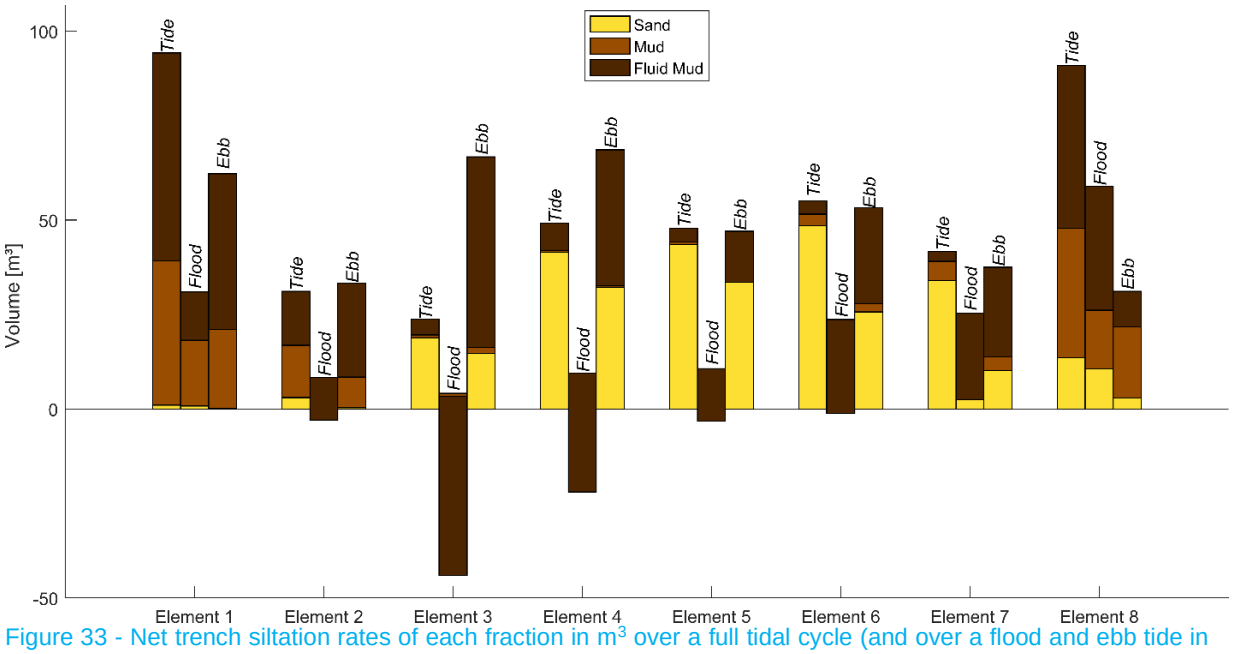

Figure 33 - Net trench siltation rates of each fraction in m^3 over a full tidal cycle (and over a flood and ebb tide in specific), averaged over the location of each separate tunnel element and summed up over the full tunnel alignment.

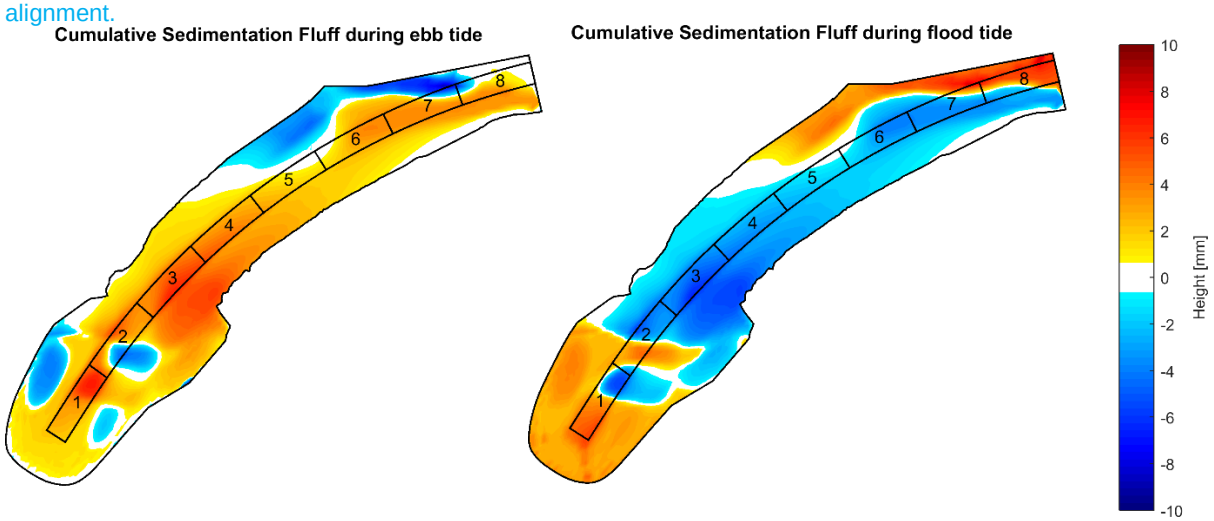

Figure 34 – Cumulative deposition of suspended matter in the fluff layer in mm for the base case during ebb tide (left) and flood tide (right) respectively.

Consolidated mud in bed

The cumulative deposition of mud in the bed layer over the tide is presented in Figure 36 at the location of each separate tunnel element. Obviously, it is closely related to the deposition of mud in the fluff layer. According to SETMO, there is continuous deposition of mud in the bed layer in the sheltered areas, since at those locations, there is a permanent fluff layer present. Although the siltation rate is found to differ slightly over the tide due to variation of the thickness of the fluid mud. In the more exposed areas, a subsequent erosion and deposition of mud during flood and ebb tide respectively is modelled by SETMO, which is similar to the simulated development of the fluff layer over the tide.

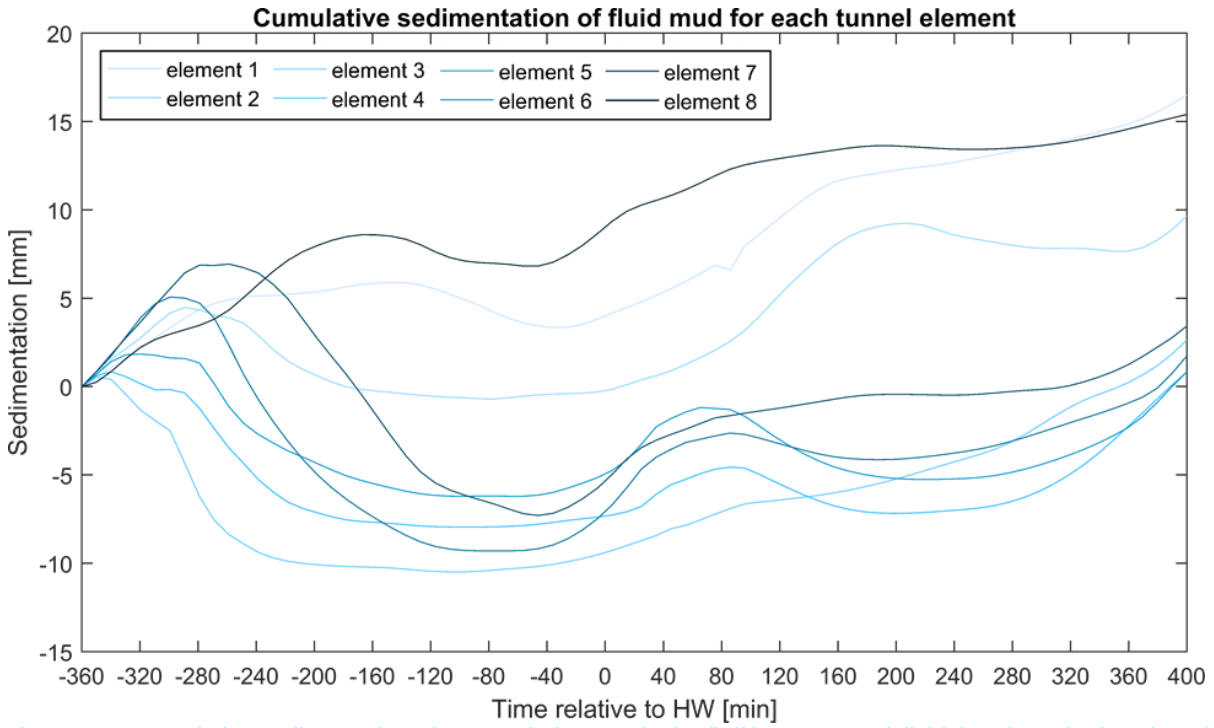

Figure 35 – Cumulative sedimentation of suspended matter in the fluff layer over a full tidal cycle at the location of each tunnel element in mm for the base case simulation.

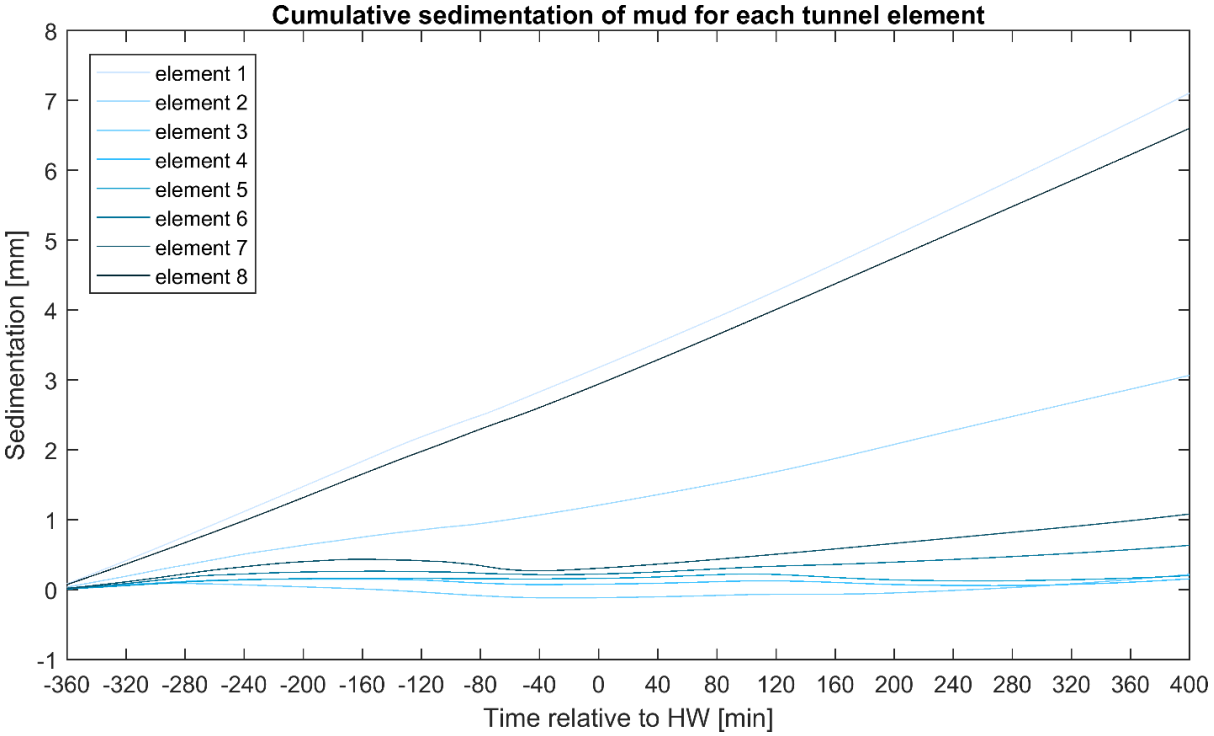

Figure 36 – Cumulative sedimentation of mud in the bed layer over a full tidal cycle at the location of each tunnel element in mm for the base case simulation.

7.1.2 Deposition of sand

Sand is found to be deposited in the more exposed areas of the trench, as can be seen in and Figure 33. One may observe that SETMO predicts two distinct peaks of deposited sand: one is located near the southern bank at the downstream slope of the trench, and the other one at the northern bank at the upstream slope. In between the peaks, sand is estimated to be mainly deposited at the location of the tunnel elements, rather than on the slopes. Moreover, during

flood (ebb) tide SETMO models some significant erosion of sand on the upstream (downstream) slope.

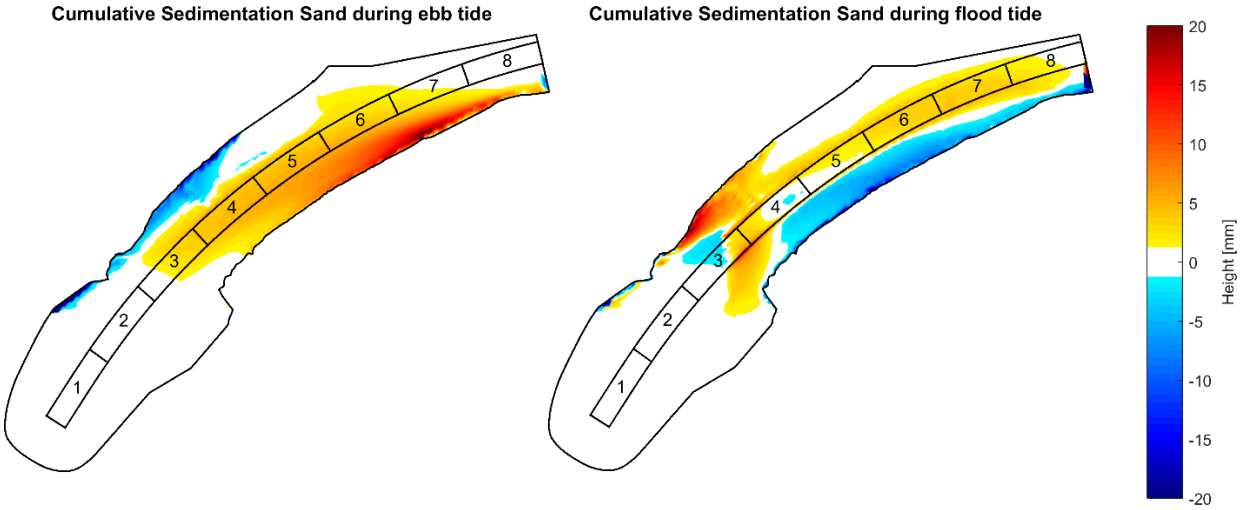

Figure 37 – Cumulative sedimentation of sand in mm for the base case during ebb tide (left) and flood tide (right) respectively.

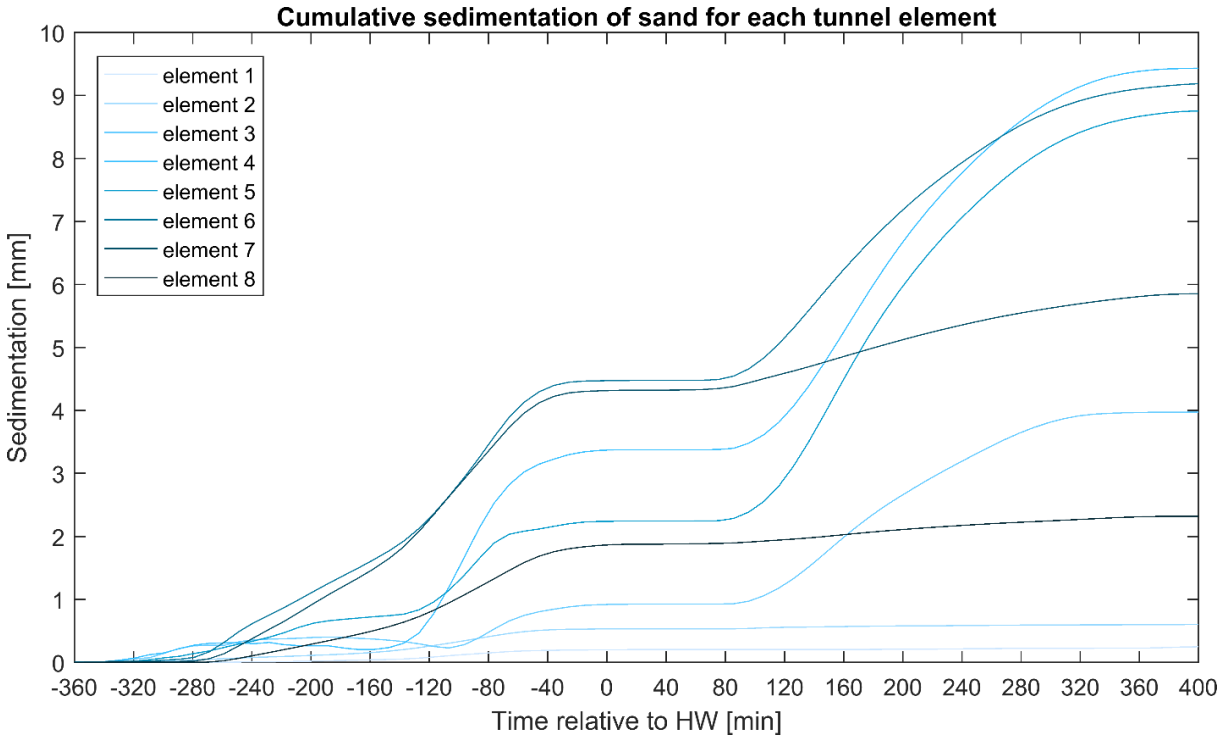

Figure 38 – Cumulative sedimentation of sand over a full tidal cycle at the location of each tunnel element in mm for the base case simulation.

A closer look at the evolution of the deposition of sand in Figure 38 at the locations of the separate tunnel elements, reveals that SETMO simulates a rather step-wise deposition of sand: mainly deposition during mid-flood and mid-ebb tide without any sedimentation during both slack waters. Most sand is found to be deposited during (late-)flood tide at the location of the tunnel elements in the northern area of the trench and in the southern sheltered area, while more sedimentation is expected during (early-)ebb tide for the elements at the southern part of the exposed area. Moreover, there is some erosion of sand at this area at peak-flood flow during late-flood tide.

7.2 Sensitivity analysis

In this section, the results of the sensitivity analysis on the most influential parameters and physical processes regarding trench siltation are presented. The sensitivity analysis on the most influential parameters results in the (partial) quantification of the epistemic uncertainty of the numerical model. The sensitivity of the model on the physical processes gives an indication which sediment trapping and transport mechanisms are likely to dominate trench siltation in the estuary.

7.2.1 Numerical model parameters (epistemic uncertainty)

The sensitivity analysis on the most influential parameters for trench siltation reveals that SETMO is highly sensitive to its input parameters, which impose great epistemic uncertainty to the predicted siltation volumes. This can be seen in Table 9. The table presents the influence of the tested parameters on the trench siltation volumes of each sediment fraction (sand, mud, and fluid mud) on the location of each separate tunnel element. Also, the average dependency of the siltation volumes on the parameters over the entire trench is presented in the last column.

Table 9 – Dependency matrix between the most influential parameters and the trench siltation volumes of each sediment fraction on the distinct locations of the tunnel elements and the average over trench. Green colors indicate a positive relation between the siltation volume and the magnitude of the parameter, while red colors indicate a negative relation between the two. The stronger the shade of the color, the stronger this relationship. Yellow colors indicate no or a weak relation.

Par.	1			2			3			4			5			6			7			8			Mean		
	S	M	F	S	M	F	S	M	F	S	M	F	S	M	F	S	M	F	S	M	F	S	M	F	S	M	F
BF																											
PC																											
EPF																											
BT																											
FV																											
CBSF																											
CBSB																											
EPB																											
EVD																											
GSD																											
STF																											

BF (Burial Flux), PC (critical mud content bed), EPF (Erosion Parameter mud in Fluff layer), BT (sand-mud coefficient), FV (Fall Velocity), CBSF (Critical Bed Shear mud in Fluff layer), CBSB (Critical Bed Shear mud in Bed layer), EPB (Erosion Parameter of mud in Bed layer), EVD (Eddy Viscosity/Diffusivity), GSD (Grain-Size Distribution), STF (Sediment Transport Formula); S (Sand), M (Mud), F (Fluid mud)

From the dependency matrix, it can be seen that, in general, the most influential parameters for trench siltation are: *the burial flux*, *the critical bed shear stress of mud in the bed layer*, *the eddy viscosity/diffusivity*, and *the grain-size distribution*. Also, the critical bed shear stress of mud in the fluff layer, fall velocity, and the erosion parameter of both the fluff and bed layer can be considered to be important. The uncertainty in the critical mud content and sand-mud coefficient can be neglected. In the below, the results are discussed for each described parameter class.

Erosion flux

The critical bed shear stress of mud in the bed layer shows a strong negative correlation on the siltation volumes of all sediment fractions. Apparently, an increase in shear strength of mud in the bed layer reduces the supply of both sand and mud to the trench. This is because both fractions are entrained proportionally due to the sand-mud interaction in the model. The reverse is found by SETMO for the critical bed shear stress of the fluff layer and the erosion parameter of mud in the bed layer, meaning that more sediment is supplied to the trench, when the critical bed shear stress is lowered. Although, the influence of the erosion parameter of the fluff layer is marginal, it shows a negative dependency for elements 2-4 and a rather positive dependency for elements 1 and 5-8. Understandably, an increase in erosion

parameter of the mud in the fluff layers leads to more sediment supply to the trench, but will also result in a more rapid entrainment of the fluff layer within the trench, in particular for the most turbulent areas during flood tide.

Deposition flux
The deposition flux is primarily dependent on the applied burial flux. SETMO shows a negative dependency to the trench siltation volume of fluid mud, and a positive dependency to the siltation of mud. Obviously, an increase in burial flux, rearranges more deposited mud from the fluff layer to the bed layer. Furthermore, indicated by the darker shade of the red color, there will be less supply of sediment to the trench in general. Evidently, this is caused by the fact that mud in the ambient bed is more difficult to entrain than mud in the fluff layer. The influence of the fall velocity of mud on the siltation volumes is limited, although there seems to be a weak negative dependency in the southern area of the trench. Possibly, an increase in fall velocity decreases the advection of fines to the sheltered areas.

Turbulence
The dependency matrix shows that an increase in eddy viscosity/diffusivity, in general, decreases the siltation of (fluid) mud and increases the siltation of sand in the trench. Apparently, SETMO supplies more sediment to the trench for increased turbulence, but simultaneously less sediment is able to deposit in the trench. Furthermore, the dependency seems to be specific on the location within the trench. Evidently, an increase of the eddy viscosity/diffusivity results in a stronger supply of sediment to the more sheltered areas, while in the exposed areas there is a stronger prohibiting effect on the deposition of sediment in the trench.

Sediment characteristics
The characteristics of the sediment also play a dominant role in the prediction of the siltation volumes of the trench. It can be seen that an increase in the grain size distribution lead to less siltation volumes in the trench. Obviously, coarser sand particles reduce the supply of sediment to the trench, thereby influencing the supply of mud to the trench as well.

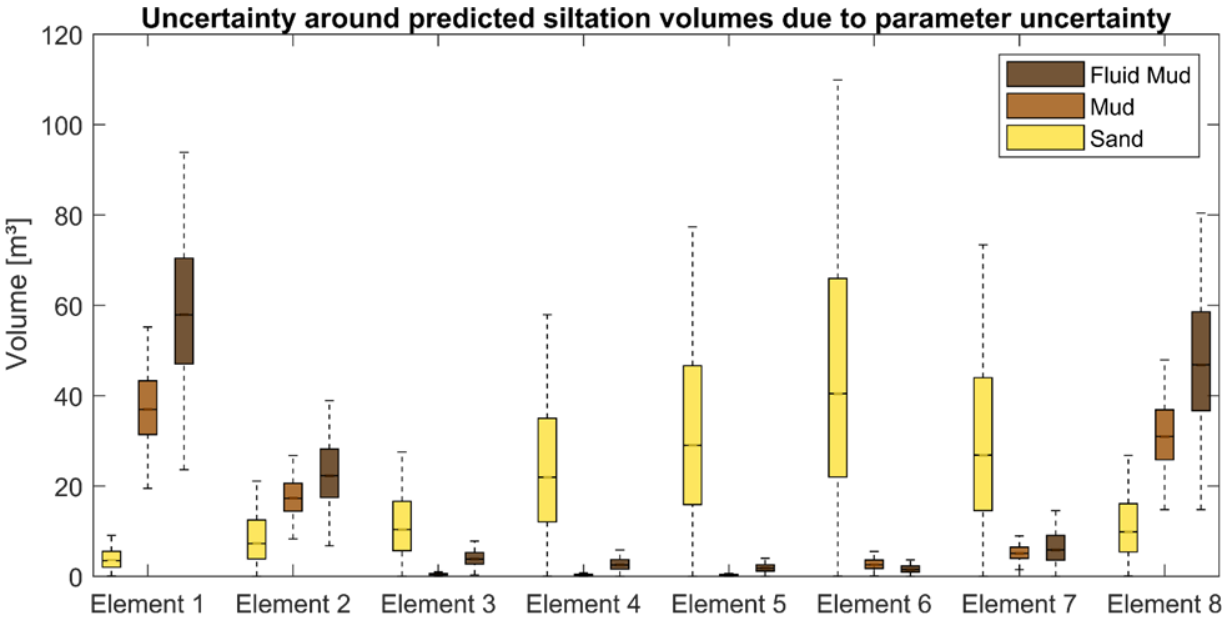

Figure 39 – Estimation of the epistemic uncertainty of the predicted siltation volumes of the base case simulation.

Epistemic uncertainty
Based on above parameter uncertainties, including the seemingly great influence in the choice of the sediment transport formula, the total quantifiable epistemic uncertainty can be estimated through a Monte Carlo simulation (see Appendix F). This leads to expected value with a certain confidence range for the siltation volumes at each location of the tunnel elements. The results of the simulation are visualized in Figure 39.

Comparison with the base case results in Figure 33 reveals that there is a lot uncertainty in the siltation volumes over the trench. The greatest epistemic uncertainty lies in the prediction of the siltation volumes of sand in the exposed areas, and in the predicted siltation volumes of (fluid) mud in the sheltered areas. For sand the 50% confidence interval may be bounded by up to a factor 1.75 of the expected siltation volume, while for (fluid) mud this may be up to a factor 1.25. On average, this means a factor 1.5.

It can be noticed that the simulated trench siltation volumes of the base case lie close to the expected siltation volumes. Hence, the best-guessed, validated input parameters do not result in a great over- or underestimation of the siltation rates.

7.2.2 Physical processes

Table 10 presents the dependency of the predicted trench siltation volumes on the applied physical processes. It can be noticed that the application of salinity and fluid mud in the model are most influential to the siltation of the trench. Furthermore, trench siltation volumes are locally affected by the inclusion of the interaction between sand and mud. In contrast, the Coriolis effect and the effect of sediment concentration on the density of water have a minor effect.

Table 10 – Dependency matrix between the applied physical processes and the trench siltation volumes of each sediment fraction on the distinct locations of the tunnel elements and the average over trench. A red color indicates a negative effect (decrease) on the siltation rates due to the inclusion of the physical process, while a yellow color indicates no or a weak effect and a green color depicts a positive effect (increase). The darker the shade of the color, the stronger the dependency.

Par.	1			2			3			4			5			6			7			8			Mean		
	S	M	F	S	M	F	S	M	F	S	M	F	S	M	F	S	M	F	S	M	F	S	M	F	S	M	F
Sal.																											
Cor.																											
SD																											
FM																											
SM																											

Sal. (Salinity), Cor. (Coriolis), SD (Sediment Density), FM (Fluid Mud), SM (Sand-Mud interaction); S (Sand), M (Mud), F (Fluid mud)

Salinity

In general, inclusion of salinity in the numerical model seems to lead to less trench siltation compared with the base case. In particular, this is caused by less siltation of sediment in the sheltered areas. In contrast, salinity causes more deposition of sand at the northern bank. Moreover, SETMO predicts salinity not to have an effect on the siltation volumes in the most exposed areas, except for sand at the location of tunnel element 4, which increases by inclusion of salinity.

Fluid mud

Obviously, application of a fluff layer in the model results overall in a shift in siltation of mud from the bed layer to the fluff layer. This particularly holds at the more exposed areas of the trench, whereas more sedimentation of both (fluid) mud can be expected in the sheltered areas. Apparently, fluid mud formation is important in SETMO in the transport of mud to the sheltered areas of the trench. Additionally, less sand will be deposited at the location of tunnel element 1 if fluid mud is accounted for.

Sand-mud interaction

Although not having a significant net effect on the average siltation volume over the trench, inclusion of sand-mud interactions in SETMO causes somewhat more mud to be deposited in the exposed area, while simultaneously less mud will be deposited in the sheltered areas of the trench. Furthermore, less sand is expected to be deposited in the exposed areas of the trench, while an increase is observed at the location of tunnel element 2.

7.3 Scenario analysis (intrinsic uncertainty)

In this section, the results of the numerical model simulations, in which different governing environmental conditions (scenarios) are imposed, are presented. These results consist of the trench siltation volumes of the different sediment fractions on the location of the distinct tunnel elements. Comparison with the predicted volumes by the base case run is made, resulting in the estimation of the intrinsic uncertainty of the siltation volumes of the trench.

Table 11 – Dependency matrix between the different dominating environmental conditions and the trench siltation volumes of each sediment fraction on the distinct locations of the tunnel elements and the average over trench. The green colors indicate an increase in trench siltation due to the condition. A darker shade indicates a stronger increase.

Par.	1			2			3			4			5			6			7			8			Mean		
	S	M	F	S	M	F	S	M	F	S	M	F	S	M	F	S	M	F	S	M	F	S	M	F	S	M	F
LD																											
HD																											
NT																											
ST																											
SW																											

LD (Low river Discharge), HD (High river Discharge), NT (Neap Tide), ST (Spring Tide), SW (Stormy Weather at sea); S (Sand), M (Mud), F (Fluid mud)

The influence of the individual environmental conditions on the siltation volumes is depicted in a dependency matrix (see Table 11). It can be seen that the trench siltation volumes of especially (fluid) mud are strongly dependent on the governing environmental conditions. Siltation volumes of mud tend to increase significantly during high river run-off, neap tide and stormy weather at sea. Sand is not or weakly affected by the individual environmental conditions, increasing somewhat during high river run-off and spring tide. Based on the difference in response during a neap compared with a spring tide, seemingly, both the supply and deposition of mud are dominated by the different conditions. Furthermore, some variability between the tunnel elements is found by SETMO: there is a generally stronger response in the lesser exposed areas.

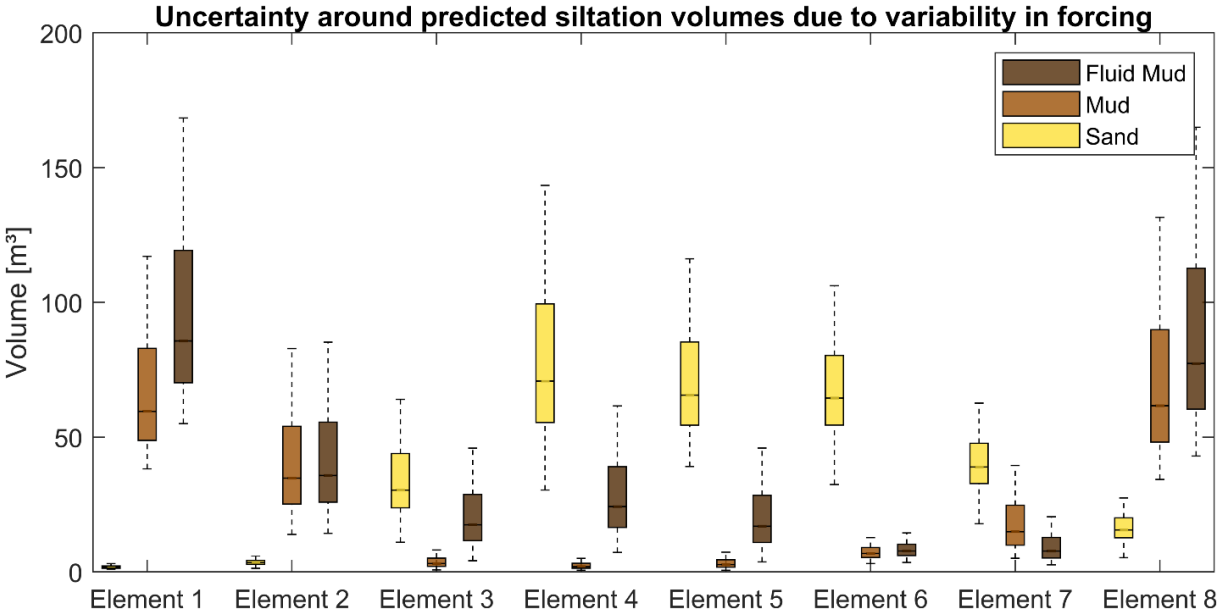

Figure 40 – Estimation of the intrinsic uncertainty of the predicted siltation volumes of the base case simulation.

Intrinsic uncertainty

The variation in the different environmental components leads to intrinsic uncertainty in the predicted siltation volumes of the base case run. This degree of uncertainty can be estimated based on a same Monte Carlo simulation, used for the epistemic uncertiainty (see Appendix F). The results are visualized in Figure 40.

By comparison with the base case results (see Figure 33), one can notice that there is a lot of intrinsic uncertainty in the predicted trench siltation volumes. Furthermore, it can be observed that the base case siltation volumes are significantly underestimating the expected siltation problem, as they fall regularly outside the 50% confidence interval.

The 75th percentile of the estimated siltation volumes may be a factor 2.5 of the estimated siltation volumes of the base case run. This holds more or less for all sediment fractions in SETMO. With respect to the epistemic uncertainty, the intrinsic uncertainty of the governing environmental conditions in the area pose similar uncertainty to the siltation problem, as the confidence intervals are bounded by approximately 1.5 times the expected siltation volumes.

Table 12 – Degree of uncertainty of the trench siltation volumes at the locations of the separate tunnel elements, expressed by the estimated bounds in total siltation volumes and factorized volumes with respect to the median, both for the 50% and 90% confidence intervals.

Tunnel Element	5th percentile		25th percentile		median	75th percentile		95th percentile	
	Total Volume [m³]/tide	Factor of median	Total Volume [m³]/tide	Factor of median	Total Volume [m³]/tide	Total Volume [m³]/tide	Factor of median	Total Volume [m³]/tide	Factor of median
1	38.03	0.58	51.43	0.78	65.59	88.21	1.34	143.29	2.18
2	27.91	0.50	40.98	0.73	55.94	81.71	1.46	162.86	2.91
3	7.72	0.35	15.09	0.69	21.88	31.87	1.46	57.82	2.64
4	12.20	0.30	26.25	0.64	41.04	62.82	1.53	117.68	2.87
5	14.27	0.30	30.57	0.64	47.69	71.74	1.50	126.00	2.64
6	16.79	0.28	35.56	0.59	59.83	95.50	1.60	170.04	2.84
7	13.23	0.27	29.02	0.60	48.15	75.10	1.56	131.36	2.73
8	35.36	0.52	51.31	0.75	68.36	94.61	1.38	159.80	2.34
Total	**165.51**	**0.41**	**280.21**	**0.69**	**408.48**	**601.56**	**1.47**	**1068.85**	**2.62**

Total degree of uncertainty

Combining the degree of intrinsic and epistemic uncertainty and summing up the siltation volumes of mud and sand, the total degree of uncertainty around the trench siltation volumes both bed sediment can be determined. The results are summarized in Table 12 and visualized in Figure 41. Herein, also the uncertainty around the buildup rate of the fluff layer is visualized.

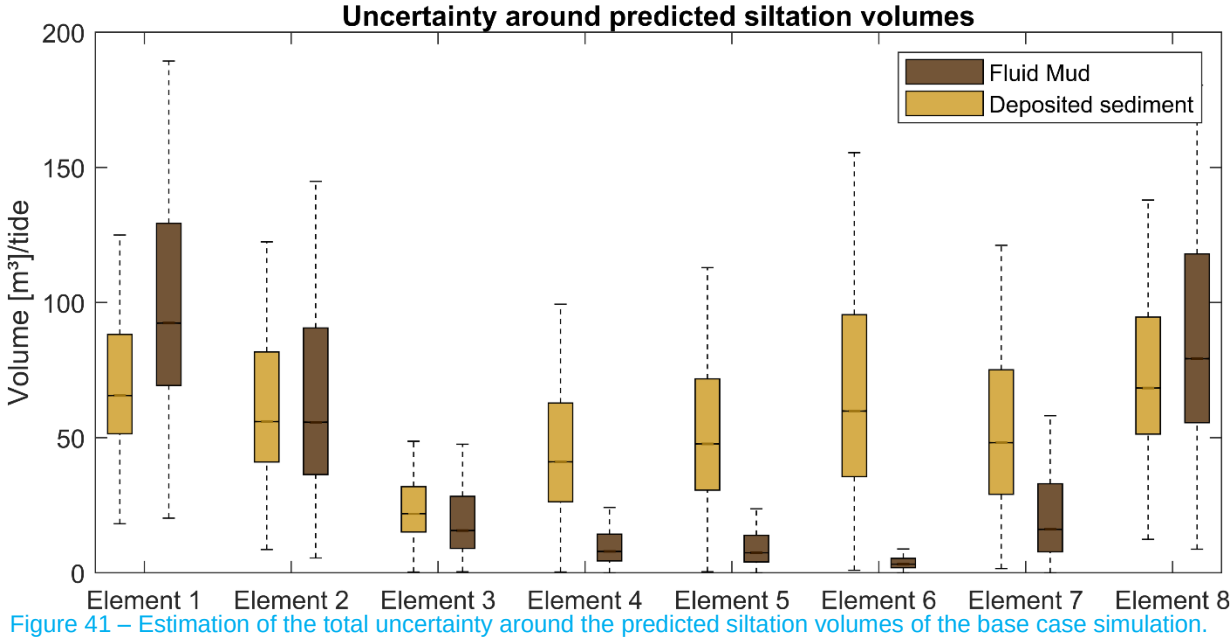

Figure 41 – Estimation of the total uncertainty around the predicted siltation volumes of the base case simulation.

The total degree of uncertainty of the total trench siltation volume, expressed as the 50 % (90%) confidence interval, is bounded by a factor of approximately 1.5 (2.5) of the expected trench siltation volume. The expected trench siltation volume is underestimated by the base

case by a factor 1.4. The highest degree of certainty is associated with the siltation volumes at the locations of trench elements 1 and 8, while the highest degree of uncertainty is coupled with the location of tunnel elements 2, 4 and 6.

7.4 Summary

SETMO predicts the **siltation** of **sand**, **mud** and **fluid mud** in the trench with a total **siltation volume** of **300.2 m^3/tide** at the locations of the tunnel elements **67.9%** of the deposited material in the bed is mud and **32.1%** is sand. **Maximum siltation rates** are estimated to be found in the more **sheltered areas** of the trench at the northern and southern bank. These can reach ~**6.5 mm/tide**. In general, sand is deposited in the more **exposed areas** of the trench, while mud is deposited in the more sheltered areas of the trench. Furthermore, more (fluid) mud is deposited during **ebb tide**, while most of this mud is eroded during **flood tide**. For sand, there is both sedimentation during ebb and flood tide, although this is according to different **patterns**.

A sensitivity analysis on the parameters in the model resulted in the finding that the **burial flux**, the **critical bed shear stress of mud in the bed layer**, the **eddy viscosity/ diffusivity**, and the **grain-size distribution**, are most influential to the predicted siltation volumes by SETMO. **Epistemic uncertainty** due to the **uncertainty** in the **magnitudes** of the **parameters** is estimated to cause a range in the predicted siltation volumes in the order of **1.5**.

Furthermore, a similar sensitivity analysis on the **physical processes** in SETMO revealed that inclusion of **salinity** and **fluid mud** tend to have the most effect on the predicted siltation rates. Salinity is found to **reduce** the siltation rates, especially that of mud in the sheltered areas, while inclusion of fluid mud causes a **shift in distribution of mud** from the bed layer to the fluff layer and a subsequent **increase** of the siltation volumes of mud in the sheltered areas of the trench.

Additionally, **variability in environmental conditions** is significantly increasing the siltation volumes over the trench. SETMO found that in particular **river floods**, **neap tides** and **storms at sea** are events that cause a lot of deposition of material in the trench. Also, **draughts** and **spring tides** are increasing the siltation volumes. The **intrinsic uncertainty** due to the variation in environmental components is estimated to be **similar** in magnitude as for the epistemic uncertainty. However, it was found that the base case lead to a severe underestimation (factor 2.5) of the expected **trench siltation volumes** based on the intrinsic uncertainty.

The above uncertainties resulted in the **total degree of uncertainty** around the siltation volumes of approximately **1.5** and **2.5** times the expected siltation volumes, for the **50%** and **90% confidence intervals** respectively. A **total underestimation** of a **factor 1.4** of the expected siltation volumes by the base case was found.

8 Discussion

This chapter discusses the results of the detailed numerical model, SETMO (Chapter 4), as presented in the Chapter 7. Firstly, the discussion focuses on the identification of the normative mechanisms for the trench siltation rates, and compares the results with literature. Subsequently, the link of the results with the practice is explored by comparison with the results of an engineering tool. This chapter continues by discussing the potential sources of error in the research. Lastly, the applicability of the findings of this thesis is made explicit. More results of the analysis, applied on the base case run, can be found in Appendix G.

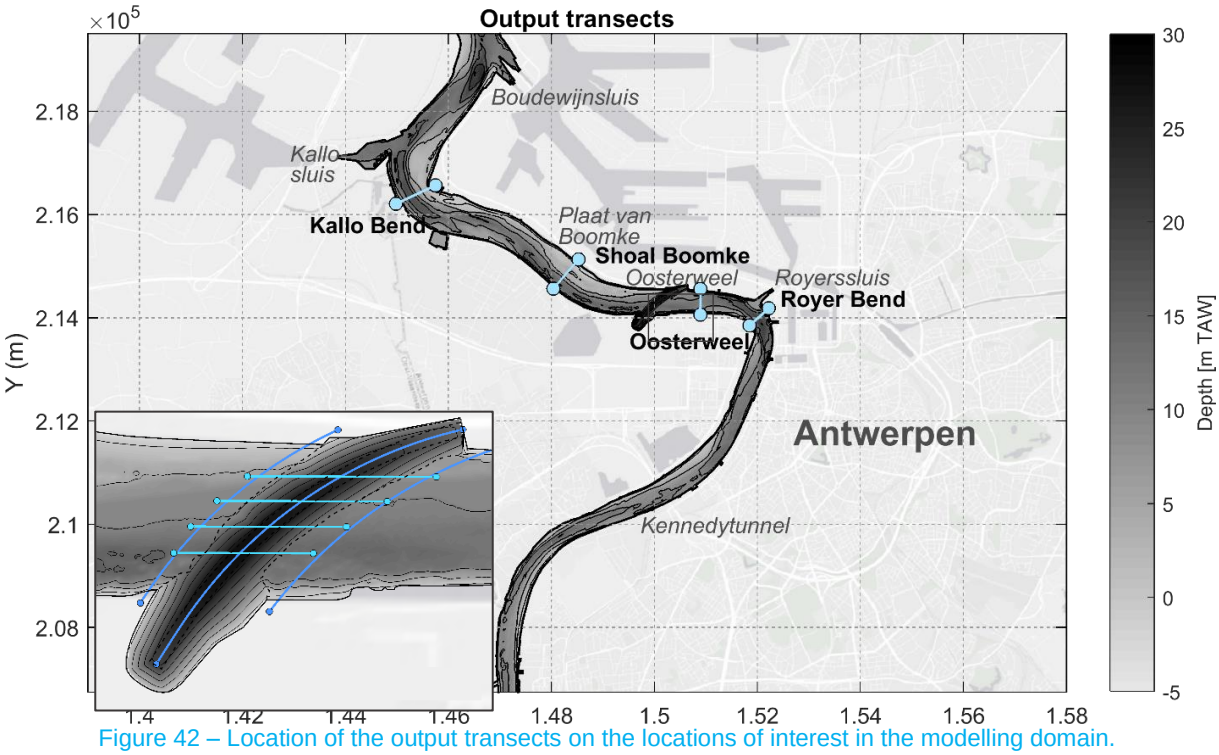

Figure 42 – Location of the output transects on the locations of interest in the modelling domain.

8.1 Normative mechanisms

In order to identify the theoretical significance, a thorough analysis is performed on the modelling results. This analysis focuses on the identification of the normative sediment trapping mechanisms and the trapping efficiency of the trench, underlying the predicted siltation rates. Through comparison of the identified mechanisms with literature on the Scheldt Estuary and on state-of-the-art theory, it is opted to verify the modelling results. Similar as in the theoretical framework, distinction is made within the analysis between the scale and plane of orientation of the mechanism. Therefore, the following results are analyzed:

- Horizontal acting trapping mechanisms are looked into by examining depth-averaged quantities over the domain (see depth in Figure 42)
- Longitudinal acting mechanisms are researched through width-averaged quantities along the thalweg.
- Lateral acting mechanisms are explored by capturing quantities across transects at distinct locations of interests (see Figure 42):
  - Two bends: *Transect Kallo and Transect Royer*
  - Shoal: *Transect Boomke*
  - Straight section: *Transect Oosterweel*

- Along trench: *Transect seaward (West), along the axis,* and *landward (East) of the trench*
- Across trench: *Transects aligned at 30, 35, 40,* and *45 degrees with the governing currents*

In the remainder of this section, the results of the analysis are separately discussed for the supply of sediment to the trench and the trapping efficiency of the trench.

8.1.1 Sediment supply

Supply of sediment to the trench in SETMO is found to be predominantly caused by the gross sediment transport fluxes. These are dominated by the tidal motion in the estuary (see Figure 43), as SSC is resuspended and advected with the currents.

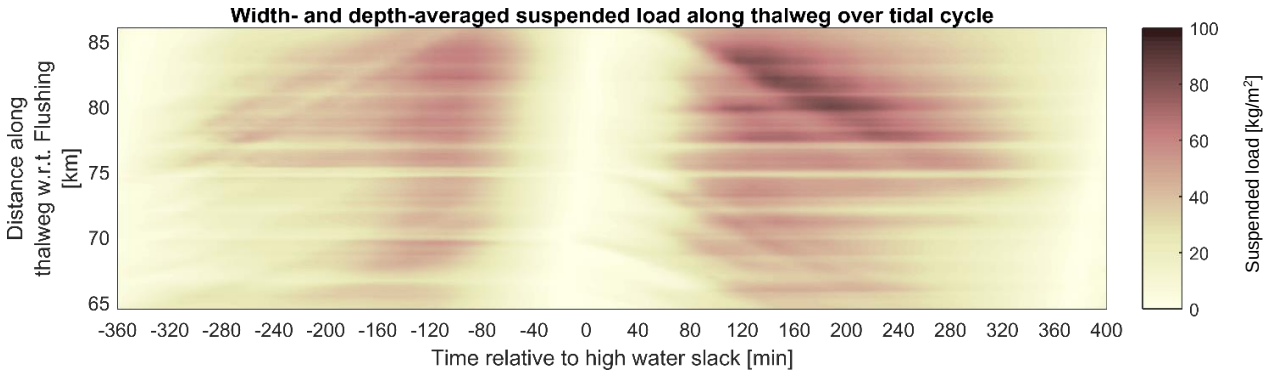

Figure 43 – Width- and depth-averaged longitudinal suspended sediment load over time along the thalweg. The trench is located at 75 km from Flushing. A clear drop in transport can be seen.

The maximum gross sediment transport rates of sand correspond with the maximum tidal currents, while for mud other three-dimensional mechanisms seem to come in play. Furthermore, the fluxes are affected by the local availability of mud in the area, which is induced by the net sediment transport fluxes over the estuary.

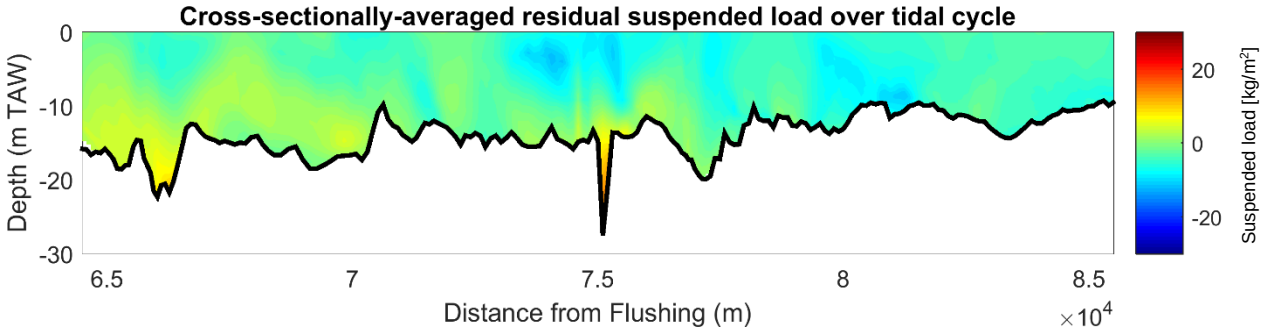

Figure 44 – Cross-sectionally-integrated residual suspended sediment transport along the domain. Positive fluxes are directed landward (to the right in the figure), negative fluxes are directed seaward (to the left in the figure)

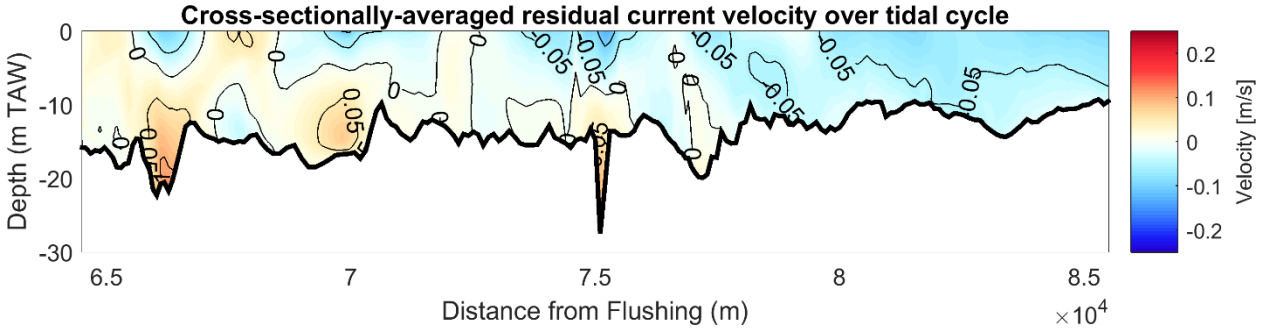

Figure 45 – Cross-sectionally-averaged residual current velocity along the domain. Residual currents, depicted in red, are directed landward (to the right in this figure). Ebb directed currents (to the left in this figure) are depicted in blue.

Macro-scale mechanisms

SETMO found both tide- and river-induced barotropic and salinity-induced baroclinic mechanisms to dominate the supply of sediment to the trench: on the one hand by supplying mud to the area through net sediment transport fluxes, and on the other hand by affecting the hydrodynamics in the area.

Longitudinal plane

Figure 44 presents the cross-sectionally-integrated residual suspended sediment transport throughout the domain. It can be seen that downstream of the trench (which is located at approximately 75 km from the mouth at Flushing) net suspended sediment transport is directed landward near the bed, and seaward at the surface, while upstream of the trench, transport is generally directed seaward. This near-bottom convergent net transport traps fines in the area, leading to high gross sediment transport fluxes. The net transport of fines is in close agreement with the residual current velocity pattern along the thalweg (see Figure 45). This pattern is in line with literature on the Scheldt Estuary (Chen, Wartel, Van Eck, et al., 2005), as was discussed in Chapter 3. The following longitudinally acting sediment transport and trapping mechanisms, which are governing for this pattern, seem to be captured by SETMO:

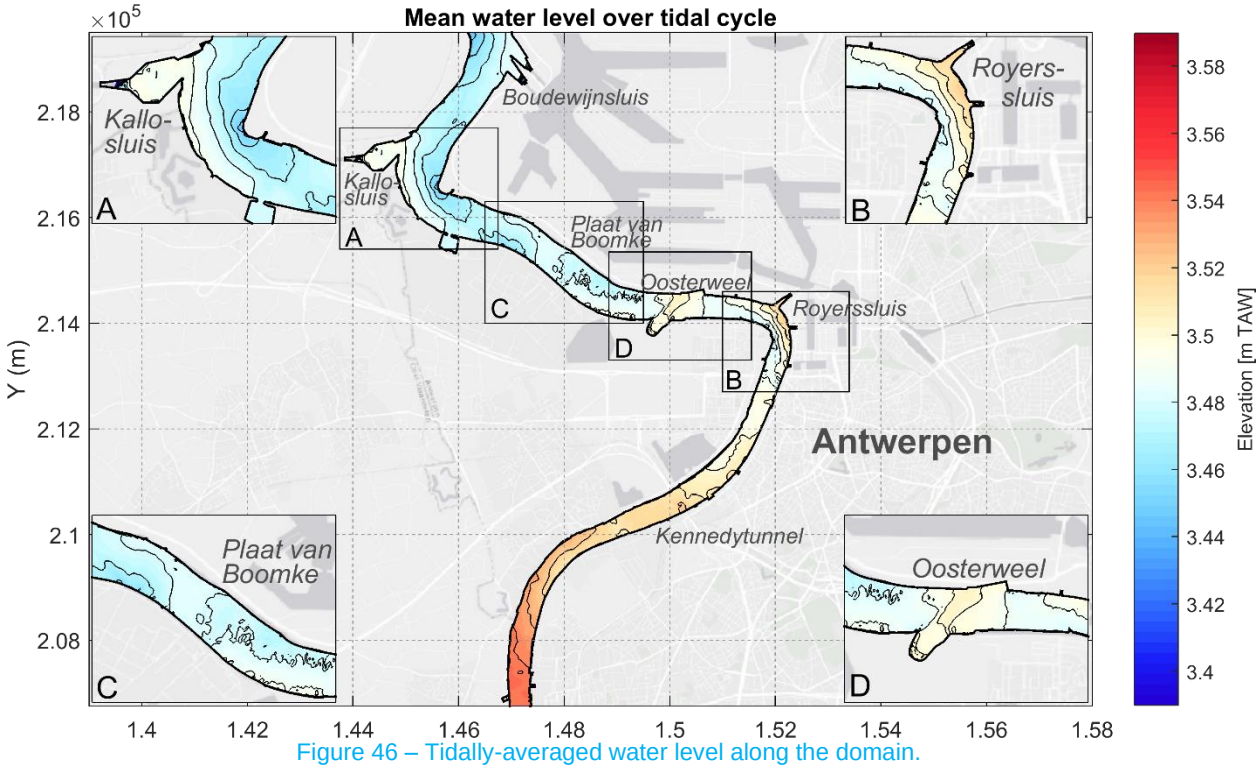

Figure 46 – Tidally-averaged water level along the domain.

1. *River discharge*
   It can be calculated based on analytical expressions, which are listed in Appendix A, that river discharge is becoming increasingly important in landward direction in the seaward transport of sediment. This is caused by the funnel-shaped geometry of the estuary. The tidally-averaged river discharge can be estimated to be 0.01 m/s at the downstream end of the domain, increasing to nearly 0.03 m/s at the landward end of the domain. The more pronounced becoming influence of the river discharge on the net seaward transport of fines is in line with the theory on the Scheldt Estuary (Chen, Wartel, Van Eck, et al., 2005).

2. *Stokes' drift*
   SETMO predicts a water level set-up over its domain, which can be seen in Figure 46. This set-up is well known to compensate for Stokes' drift, which is also found in literature to occur in the area (Chen, Wartel, Van Eck, et al., 2005; Van der Werf &

Brière, 2014; Van Kessel et al., 2011; L. C. Van Rijn, 2011b). It can be estimated, using the formula in Appendix A for Stokes' drift, that the seaward-directed return current is estimated to reach 0.03 m/s.

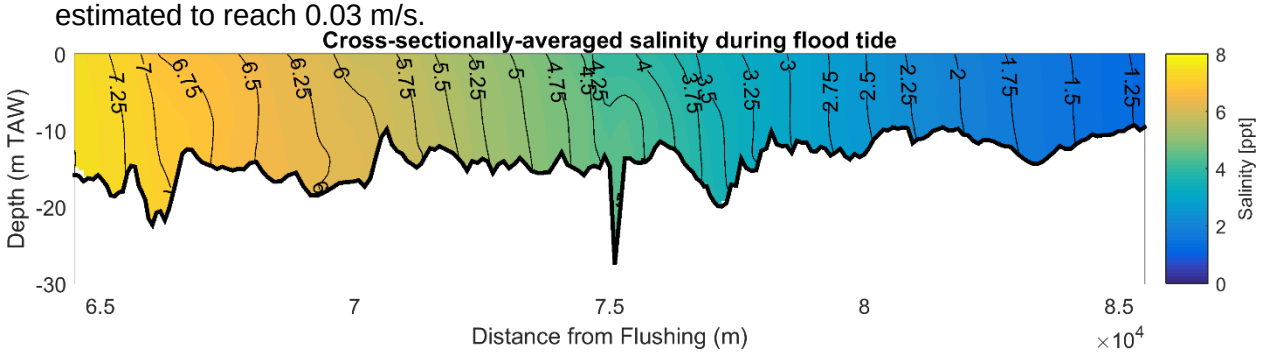

Figure 47 – Mean width-averaged salinity during flood tide

3. *Salinity-induced circulation*
The landward-directed residual current is caused by circulation due to the longitudinal salinity gradient over the estuary (see Figure 47). Post-processing of the modelling results reveals that this circulation can be assigned primarily to two mechanisms:

   - Gravitational circulation
   - Mixing asymmetry

   Applying the results of SETMO to the analytical expression for gravitational circulation, one can estimate a residual current to be developed in the order of only 0.005 m/s, which is an order of magnitude smaller compared to the residual current due to river discharge and return current of Stokes' drift. Still, gravitational circulation is influential in the deeper parts, in which it may reach 0.01 m/s. However, this mechanism is not able to compensate for Stokes' drift and river discharge alone. This forms a discrepancy with literature on the study area (Chen, Wartel, & Temmerman, 2005; Van Kessel et al., 2011), which assigns all landward-directed residual current to gravitational circulation.

   However, according to state-of-the-art theory on well-mixed estuaries (Becherer, 2013b; Burchard et al., 2011), baroclinic mixing asymmetries are dominant in inducing this circulation. SETMO seems to agree on this, although this could not be quantified with analytical expressions. The mixing asymmetries in the numerical model are likely to be induced by:

   - Tidal straining
   - Horizontal density differences, due to differential advection (*bends and depth-differences*), as can be seen in Figure 48.

   This finding can be qualitatively supported by examination of the longitudinal and lateral Simpson numbers, which scales the tendency of stratification by mixing due to tidal currents. The numbers can calculated to be on average approximately 0.15 and 0.45 respectively. Since both numbers are below unity, mixing is dominant over stratification. However, the magnitudes are high enough to induce straining circulation (Becherer, 2013b; Burchard et al., 2011). Furthermore, based on the relative magnitudes, horizontal density differences are likely the dominating term in the mixing asymmetries caused. Visual proof of tidal straining has, however, not been found within the modelling results.

4. *Horizontal circulation*
Horizontal geometry-induced circulation is also found by SETMO to be influential in the residual current velocity pattern. More details on horizontal circulation can be found

in the dedicated subsection in the below. SETMO predicts a pattern of ebbing and flooding currents, which are rhythmically pushed to the deeper parts of the domain. This causes a pattern of landward- and seaward-directed residual bottom currents to develop. This can be seen in the left (landward) part of Figure 45, which is also captured to a lesser extent with the run without salinity.
Although this pattern of horizontal circulation is in agreement with literature on the Scheldt Estuary (Winterwerp et al., 2001), it is not yet identified as a mechanism to induce the found longitudinal circulation. Consequently, its magnitude cannot analytically quantified. Therefore, this mechanism is only given as a hypothesis in creating some additional longitudinal residual circulation.

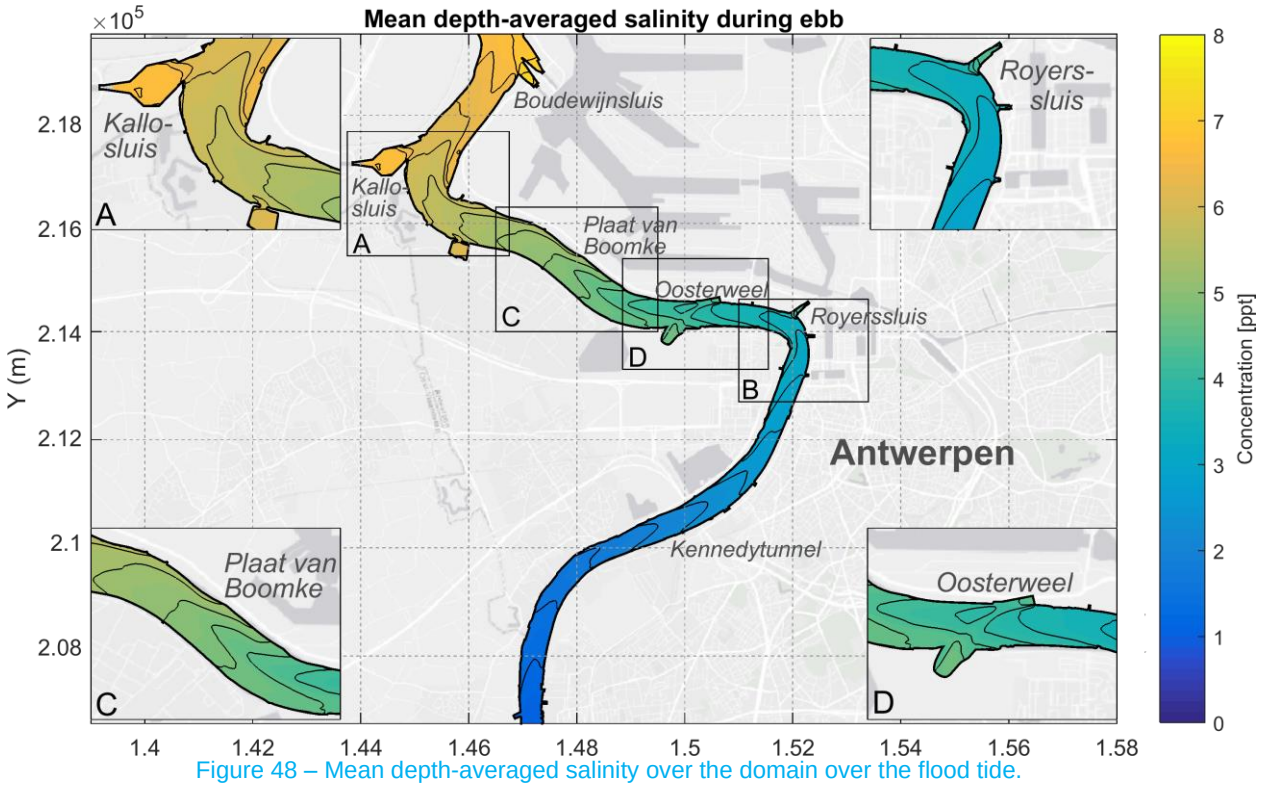

Figure 48 – Mean depth-averaged salinity over the domain over the flood tide.

Horizontal plane

The net depth-averaged suspended sediment transport fluxes in the horizontal plane, visualized in Figure 49, are closely related to the residual depth-averaged currents. Although these horizontal circulation patterns do not directly increase the availability of fines in the area, they give an indication of having a significant influence on the gross sediment transport fluxes, and induce horizontal salinity gradients, which may lead to sediment trapping through lateral circulation. The mechanisms dominating horizontal circulation are:

1. *Geometry-induced circulation due to channel curvature*
   SETMO predicts oppositely directed residual currents on the down- and upstream side of a bend. Due to the sequence of opposite bends, a rhythmic pattern of circulation cells is modelled. Estimation of the magnitude of the circulation current due to the mechanism, based on analytical expressions in Appendix A, gives a residual current velocity of approximately 0.2 m/s. This more or less corresponds with the modelling results of SETMO. As mentioned, the mechanism is in close agreement with the literature of the study area (Winterwerp et al., 2001).
2. *Geometry-induced horizontal circulation due to a promontory*
   It can be seen that there is a promontory located on the opposite bank of the Kallosluis, which creates a residual eddy on opposite sides of the promontory. It can be calculated using the expressions in Appendix A, that such a promontory would result in a residual current of approximately 0.1 m/s in addition to the residual current due to geometry-

induced horizontal circulation due to bend flow. This is captured in SETMO, although it is not explicitly mentioned in site specific literature.

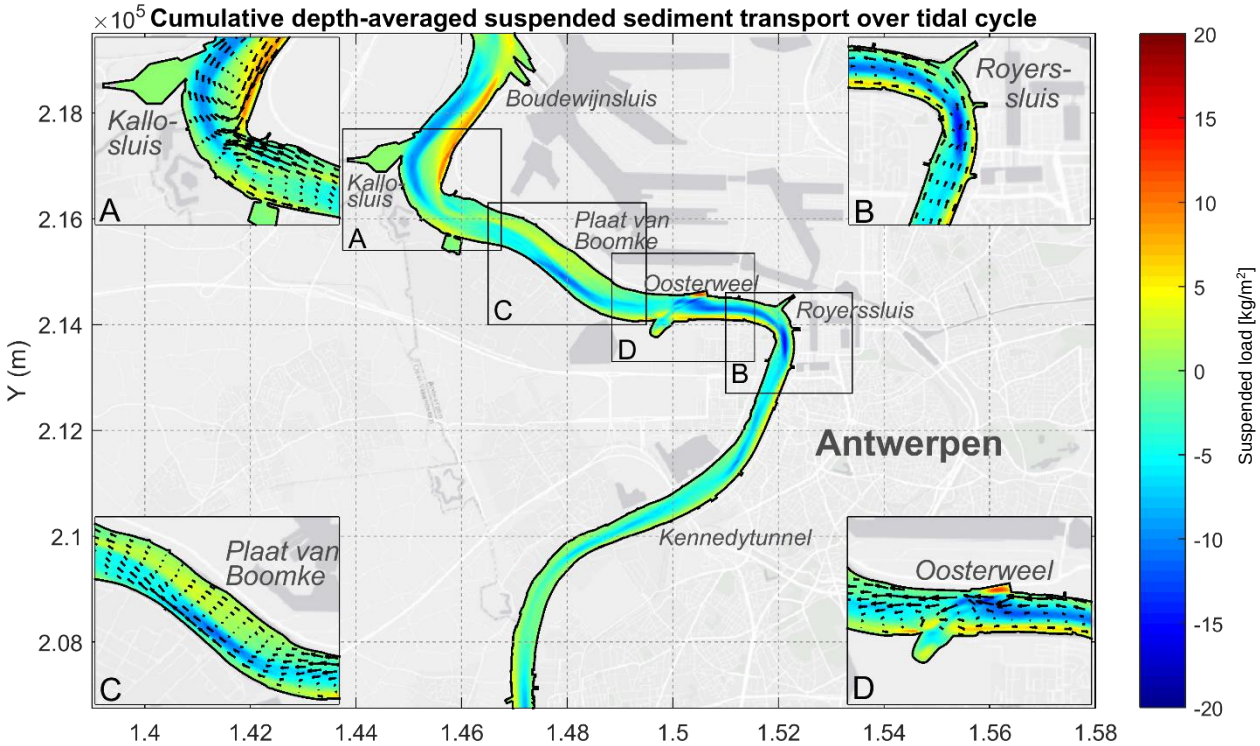

Figure 49 – Residual depth-averaged suspended sediment transport along the domain. Negative values indicate ebb-directed transport (to the bottom part of the figure), while positive transports indicate flood-directed transports (to the upper part of this figure).

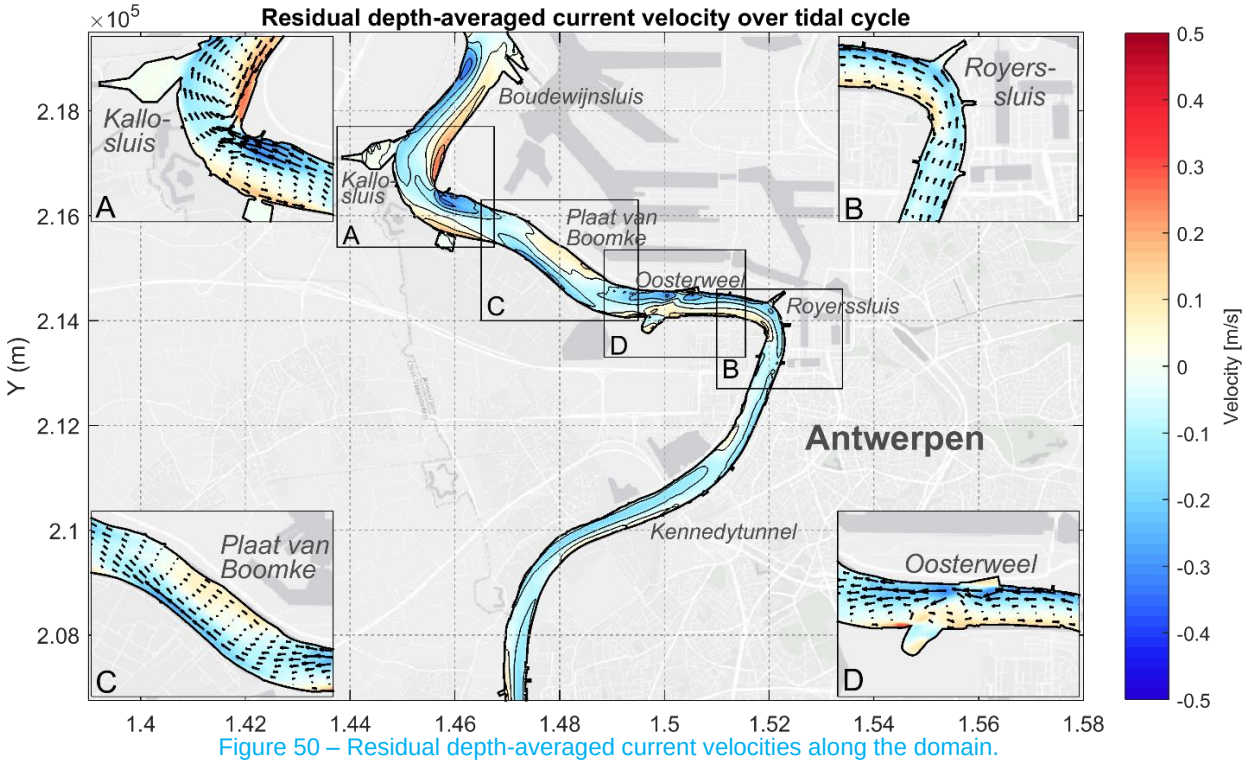

Figure 50 – Residual depth-averaged current velocities along the domain.

3. *Bathymetry-induced horizontal circulation due to Stokes' drift*
   As explained to be dominating in the longitudinal plane, Stokes' drift also intensifies horizontal circulation. This is because the mechanism is more efficient in shallow waters, while its return current is dominating in the deeper sections. Analytical

expressions estimate an additional residual current of approximately 0.1 m/s due to the shoal at the Plaat van Boomke. SETMO seems to replicate this effect, as horizontal circulation is increased at this location. Again, this mechanisms is not mentioned in literature on the Scheldt Estuary.

Lateral plane

Within the transverse direction, SETMO is estimating some lateral circulation, which is found to significantly influence the gross sediment transport patterns. This can be seen from the longitudinal directed net SPM transport across the bend at the Royerssluis (see Figure 51), and in downstream direction of this bend: lateral circulation seems to alter the depth-integrated net sediment transport patterns by reducing upstream-directed SPM transport to the southern bank, and decreasing downstream-directed SPM transport to the northern bank (see Figure 49). Furthermore, lateral circulation is believed to cause an internal mixing asymmetry, and hence sediment trapping. The following mechanisms were identified:

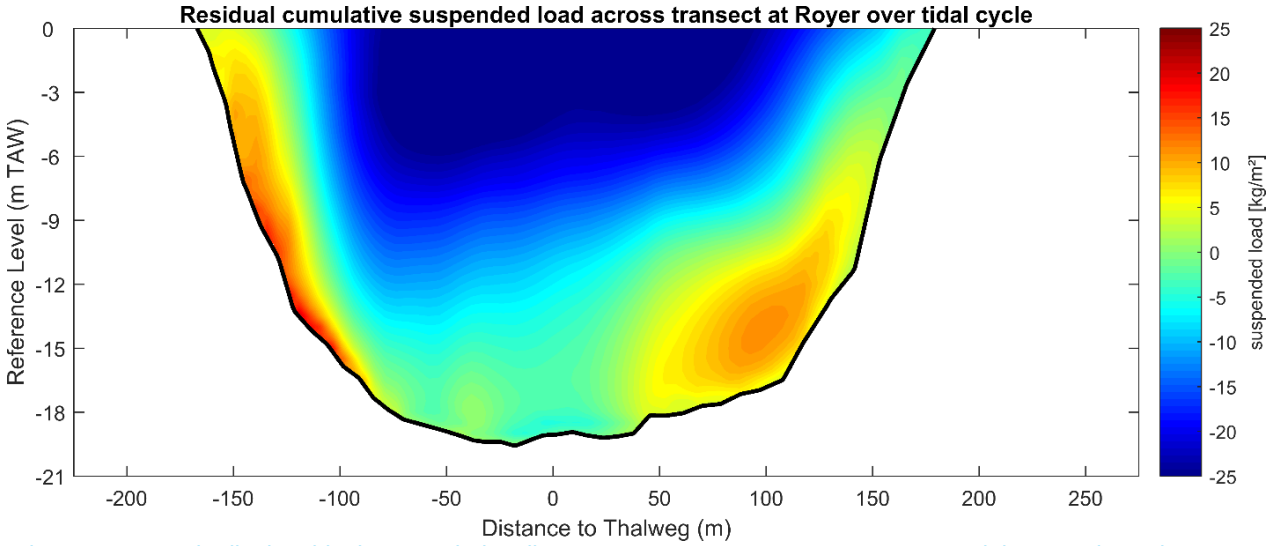

Figure 51 – Longitudinal residual suspended sediment transport across transect at Royerssluis. Negative values indicate ebb-directed transport (into this paper), while positive transports indicate flood-directed transports (out of this paper).

1. *Curvature-induced secondary flow*
   It can be calculated, based on the analytical expressions in Appendix A, that circulation is mainly due to channel curvature (~0.1 m/s). This corresponds with the modelling results, which can be seen in Figure 52. Due to this circulation, which is, in line with classical theory, directed to the outer bend at the water surface, and to the inner bend at the bottom, SSCs are found greatest in the inner bend during ebb tide, which are advected in seaward direction. This causes the gross sediment transport flux during ebb to be greater near the southern bank, while greatest ebbing currents are found to the northern bank.

   A more complex lateral curvature-induced circulation pattern is predicted during flood tide by SETMO. As the maximum flooding currents are estimated to be located below the water surface (due to salinity-induced longitudinal circulation), the inner bend directed near bottom lateral current tends to be reduced. Research in the area has identified a similar pattern during food tide (Winterwerp et al., 2006).

2. *Lateral circulation due to a horizontal salinity gradient*
   This circulation is deemed to be an order of magnitude smaller than curvature-induced secondary flow (~0.01-0.05 m/s). Therefore, it does not seem to affect the gross sediment transport fluxes. However, as was explained in the above in the subsection on normative mechanisms in the longitudinal plane, the horizontal salinity gradient

causes a lateral circulation which is strong enough to induce an internal mixing asymmetry, causing longitudinal straining circulation.

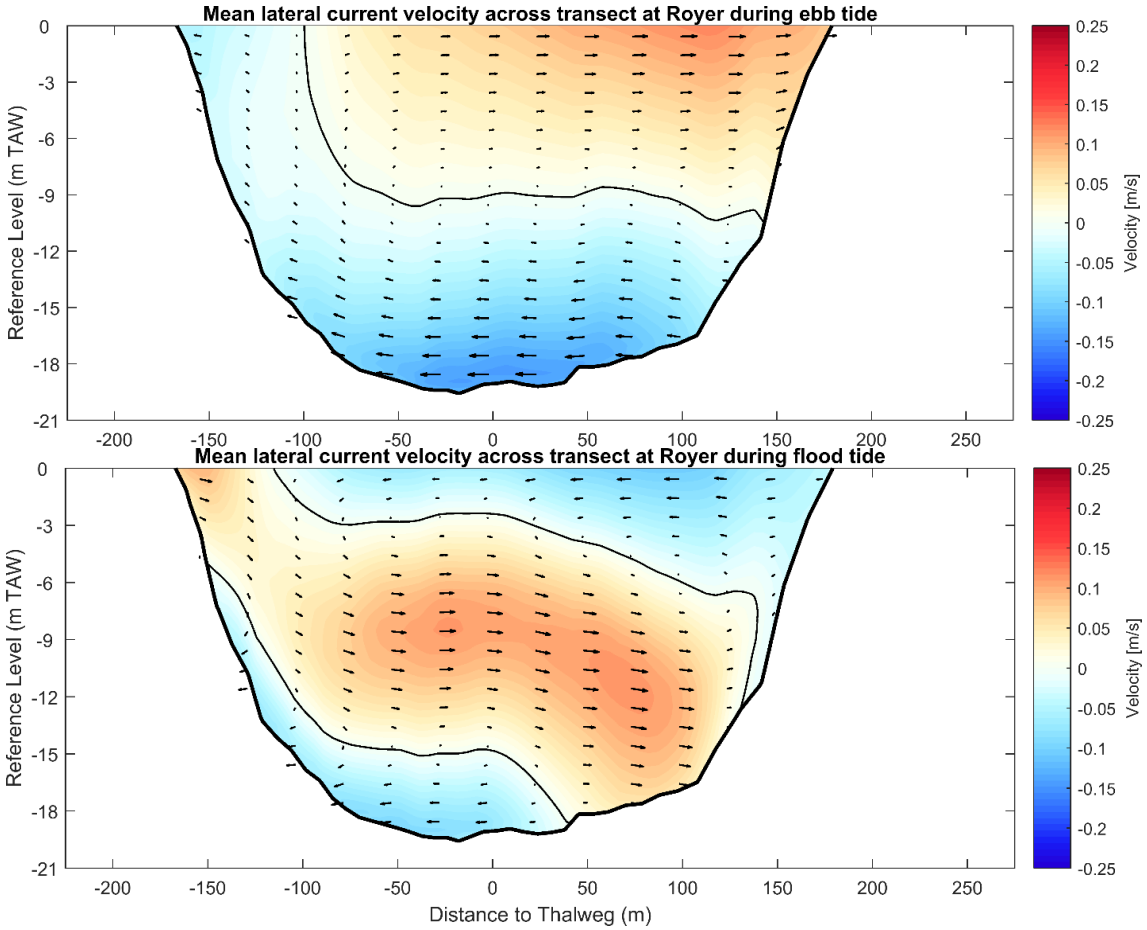

Figure 52 – Lateral current velocity across transect at Royerssluis during ebb (upper) flood tide (lower). The vectors are scaled along wise the color bar.

Micro-scale mechanisms

It was found, based on the study area description (Chapter 3) that (tidally-varying) flocculation is rather important in the trapping of mud (Chen, Wartel, Van Eck, et al., 2005; Manning et al., 2007). Although tidally-varying floc size was not implemented in the model, it signifies the importance flocculation in the area, as high fall velocities had to be applied during the calibration phase. Such high fall velocities indirectly account for the flocculation effects. Furthermore, the calibration phase revealed that the implementation of a fluff layer is vital in the modelling of the mud dynamics near the ETM. This is in line with literature of the study area (Baeyens et al., 1998), which identifies strong temporal deposition and resuspension of fluid mud in estuaries. The same holds for sand-mud interactions in the bed, as the modelling results are found to be highly dependent on the critical bed shear stress of mud in the bed layer. Lastly, it was found that the eddy viscosity/diffusivity has a great influence on the siltation volumes, due to its effect on advection and diffusion of SPM in the water column.

Resulting sediment supply to trench

Due to the identified sediment transport and trapping mechanisms, sand, of which 90% in suspension, and mud are supplied to the trench by the tidal currents. The gross sediment transport fluxes of suspended sediment are large due to the large availability of mud in the area. It can be seen in Figure 53 that the flood tidal gross sediment transport of both suspended (c) and bedload (e) more or less coincides with the maximum tidal currents (a), whereas this is not the case during ebb tide (b,d,f). The greater flux to the southern bank is believed to be caused by lateral circulation due to channel curvature in the bend at Royerssluis. This mechanism causes SSC to increase in the inner bend, which is subsequently advected with the ebbing currents. The general current pattern of maximum

flooding (ebbing) currents near the deeper (shallower) southern (northern) bank is forced by geometry-induced horizontal circulation due to channel curvature.

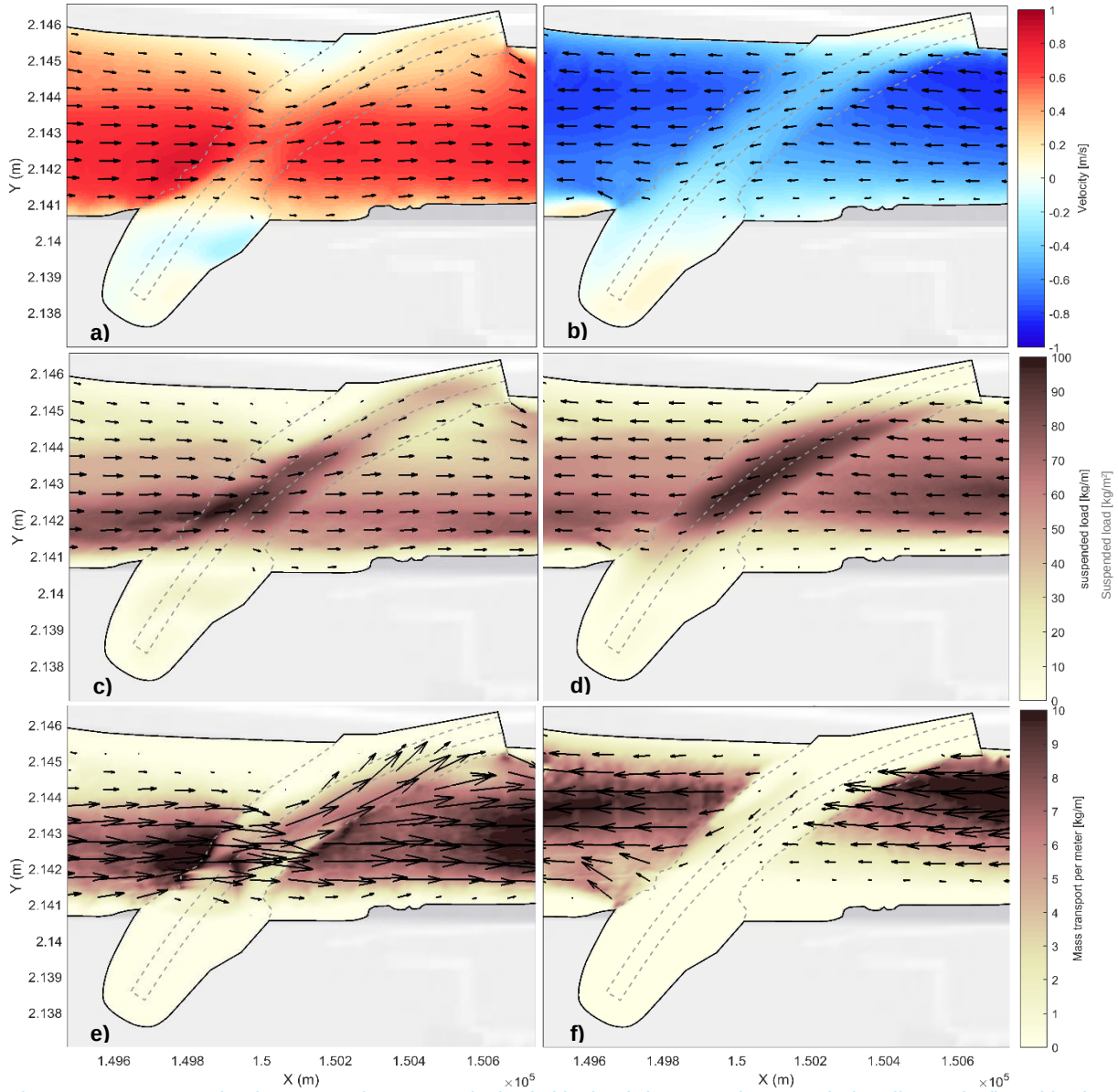

Figure 53 – Average depth-averaged current velocity (a,b), depth-integrated suspended sediment (c,d) and bed load transport (e,f) in the area near the location of the trench, for flood (left) and ebb (right) tide. The vectors indicate the relative magnitude and direction of the current/flux, along wise the color bar.

8.1.2 Trapping efficiency

The trapping efficiency of the trench in SETMO is found to be regulated by mechanisms reported in literature (Jensen et al., 1999a, 1999b; L. C. Van Rijn, 2017). However, also, a new dominant mechanism may have been found, which is not yet captured in the theory on trench siltation.

Development of current velocity

As can be seen in Figure 53, the magnitudes of the tidal current velocity are predicted to increase due to concentration of streamlines on the approach to the trench, after which they reduce significantly over the trench. Furthermore, due to the obliquely aligned trench, flood (ebb) tidal currents are deflected to the northern (southern) bank. Moreover, the slower moving tidal currents are deflected to a greater extent than the fastest moving currents. Additionally, a horizontal residual eddy develops over the southern sheltered area during both flood and

ebb tide (although in opposite direction), which is in line with the theory (Jensen et al., 1999a). This eddy supplies fines to these areas.

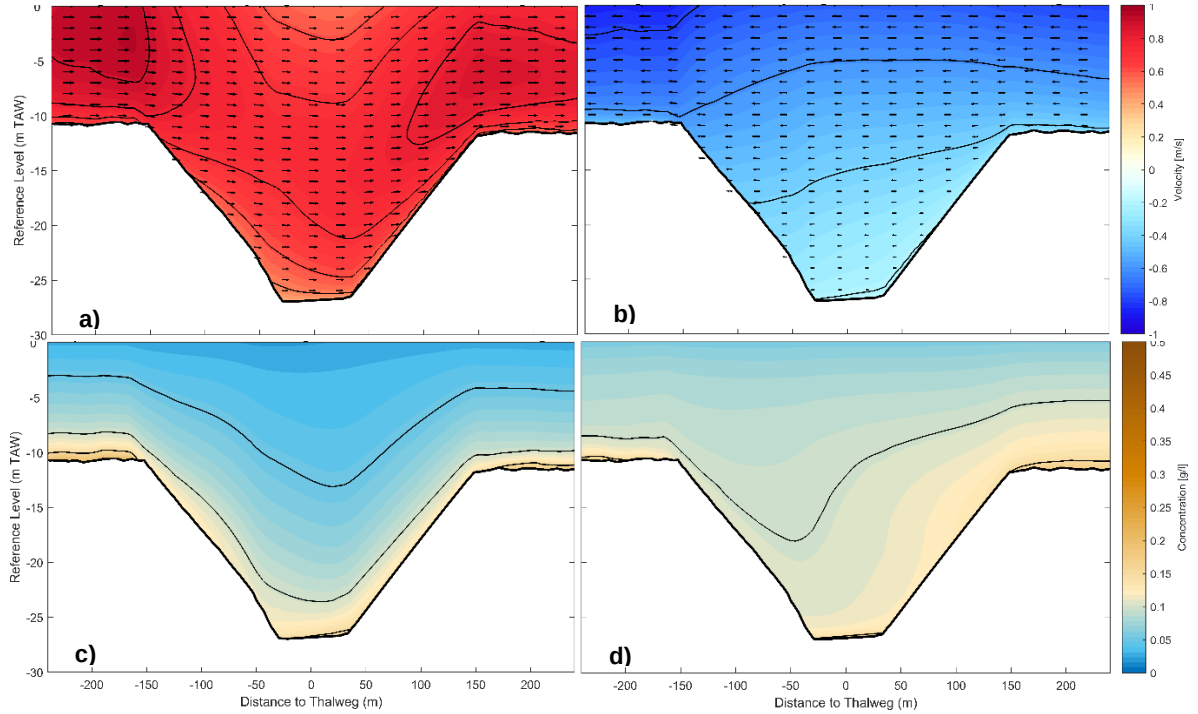

Figure 54 – Current velocity (a,b) and suspended sediment concentration (c,d) across the trench for flood (left) and ebb tide (right) of a transect which intersects the along-trench direction at an angle of 35 degrees. The vectors are scaled along wise the color bar.

Another trapping efficiency mechanism found by SETMO, which is in line with the literature (Jensen et al., 1999a), is the gradual modification of the current velocity profile over the trench (see Figure 54). In general, the current profiles are becoming more uniform by increased turbulent mixing over the trench. The adapting current velocity profiles crash into the second encountered slope, increasing the bed shear stress on that slope.

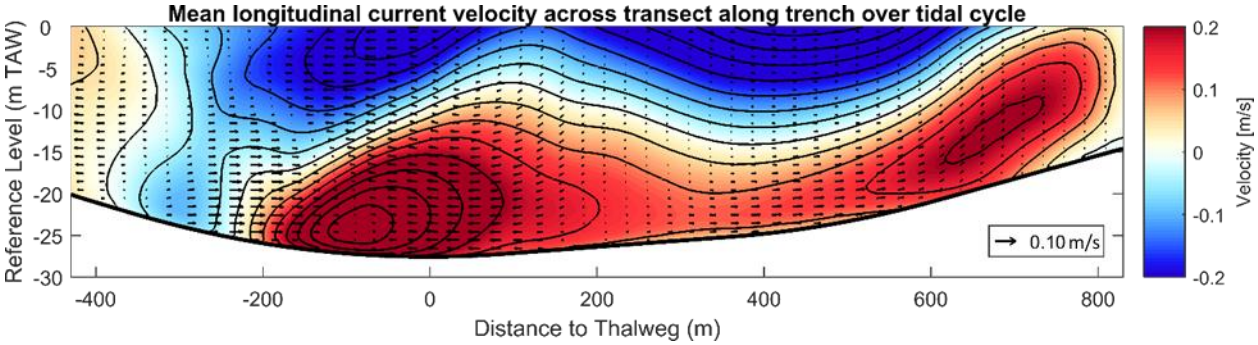

Figure 55 – Mean across-trench velocity over a tidal cycle along the normal trench axis. Negative velocities are directed in flood direction(out of the paper), while negative velocities are directed to the ebbing(right side of the figure) in the trench. Mean along-trench velocity over a tidal cycle is indicated with vectors.

Influence of salinity

In agreement with theory on estuaries, but not mentioned specifically in theory on trenches, SETMO seems to predict a higher degree of baroclinicity to occur at the location of the trench. This can be explained by the locally decreased magnitudes of the tidal currents and the sudden increase in depth. As a consequence, there is an increase in salinity-induced (gravitational) circulation: maximum flood tidal currents are directed to the bottom, in contrast, maximum ebbing currents stick at the water surface (see Figure 54 and Figure 55). Based on analytical expressions in Appendix A, the magnitude of the circulation can be estimated to reach 0.1 m/s, which more or less corresponds with the modelling results of SETMO. Due to

the strong flood tidal currents near the bed, previously deposited material is likely re-entrained in the water column during flood tide, which corresponds with the predicted erosion of fluid mud during flood tide.

Furthermore, SETMO estimates a strong horizontal salinity gradient to develop (see Figure 48), with higher (smaller) salinity in the sheltered areas during ebb (flood) tide, compared with the exposed areas. The gradient in salinity causes a strong lateral circulation current to develop, which has a comparable magnitude with the lateral currents due to current deflection.

Distribution of sediment in trench

The sedimentation distribution in the trench, estimated by SETMO, can be fully explained by the identified trapping efficiency mechanisms, which are typically found for trenches in general (Jensen et al., 1999b).

Due to the described current velocity patterns in Figure 53 and Figure 54, the across-trench transport of sand significantly decreases over the first encountered slope and deepest parts (locations of the tunnel elements) of the exposed area of the trench. This results in significant deposition of sand, which is generally able to withstand the posed bed shear stresses by the (deflected) tidal currents. However, due to the stronger bed shear stresses during flood tide, more sand is able to be deposited during ebb tide. Sand is only marginally deposited in the sheltered areas, as the lateral currents directed to these areas are too small.

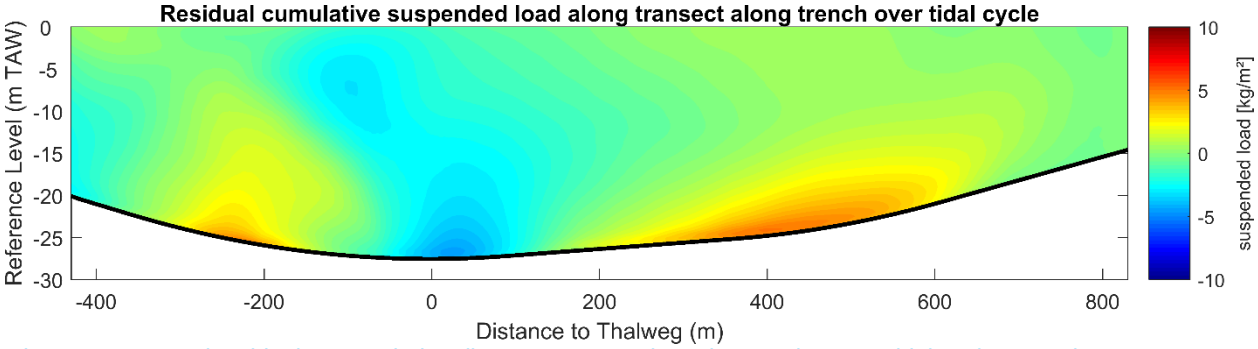

Figure 56 – Lateral residual suspended sediment transport along the trench over a tidal cycle. Negative transport is directed to the south (left side of the figure), while positive transport is directed to the north (right side of the figure) in the trench.

In contrast, the along-trench transport of mud increases significantly over the trench in along-trench direction, while the transport in across-trench direction drops as the SSC profile breaks down (Figure 54). Therefore, mud is only marginally deposited at the exposed area, in particular during ebb tide. Furthermore, as bed shear stresses are too high during flood tide. Due to the deflection of the lower magnitude flooding currents in the trench, most (fluid) mud is deposited in the northern sheltered area during flood tide. Similarly, at the southern sheltered area there is more siltation of (fluid) mud during ebb tide, although the salinity-induced lateral circulation counters the near-bottom transport of mud to this area. This pattern can be seen in Figure 56.

8.1.3 Environmental variability

It is found that the siltation rates are highly dependent on the governing environmental conditions. An increase of the siltation rates especially occurs during high river discharge, neap tide and stormy weather, but also during low river discharge and spring tide. In this subsection, the causes for such behavior is investigated, and subsequently related to the theory.

It can be found, based on the modelling results of SETMO, that during high discharge events an increase in both landward and seaward supply of sediment to the trench is predicted, which is in according with the governing literature. This is mainly due to the increased sediment

supply by the river (see Figure 57c) and not by decreased bed shear stresses, although some decrease is found in the southern sheltered area, which is believed to be caused by a decrease in horizontal salinity gradient (see Figure 57a). Sediment supply also increases during high river discharge due to the landward shift in maximum SSC within the area of the ETM, which increases the landward sediment supply significantly (close to the southern bank).

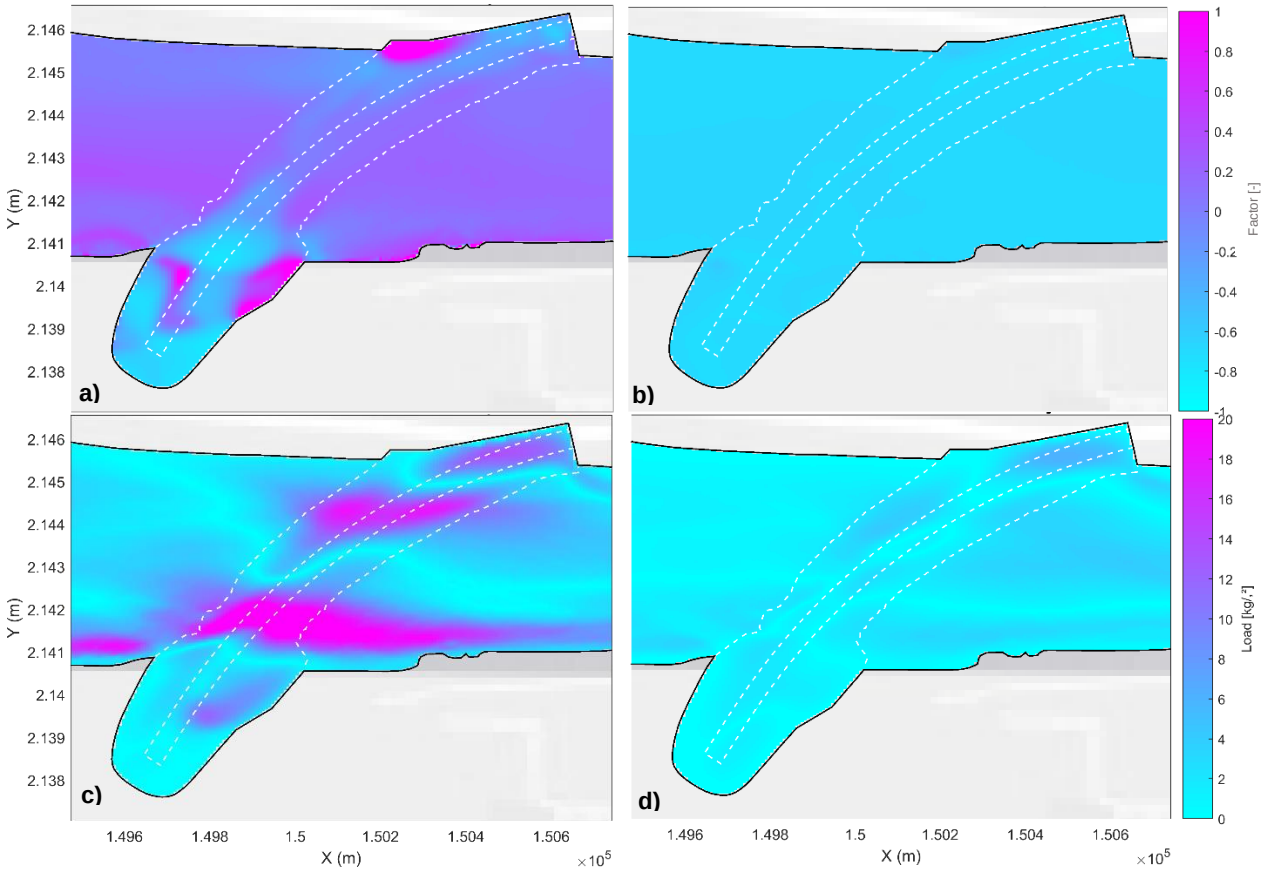

Figure 57 – Differences in factorized bed shear stress (a,b) and magnitude in sediment supply (c,d) for the case with high river discharge (left) and neap tide (right) with respect to the base case.

Furthermore, results reveal that during neap tides, supply of sediment is not affected/decreases (see Figure 57d). However, the trapping efficiency of the trench significantly increases due to the reduced bed shear stresses (see Figure 57b). Consequently, the siltation volumes are increasing. This is in line with theory. Likewise, during spring tide, during which the sediment supply significantly increases, sediment is more prohibited to deposit in the trench due to the turbulent conditions.

During stormy weather there is increasing sediment supply from the landward direction. This is in close agreement with literature. However, the increase of sedimentation during low discharge is found to be counterintuitive. SETMO predicts an increase in sediment supply from upstream, which is likely due to the upstream location of the ETM.

8.1.4 Interaction with trench

It can be seen in Figure 58 that SETMO estimates that most influence of the trench on the hydrodynamics is very local, although marginal differences can be seen far up- and downstream. On the approach to the trench, residual currents are amplified in the case with the trench, while within the trench itself, these currents are dampened.

Furthermore, the trench seems to interact with the longitudinal salinity gradient. This can be seen in Figure 48. Since SETMO predicts the flooding currents to be pushed downward at the location of the trench, they seem to advect more saline near-bottom in the upstream direction

near the trench. Hence, an increased degree of baroclinicity is found in this area. This process is known as tidal frontogenesis, and is not resolved by SETMO during ebb tide, as maximum tidal ebbing currents are located more at the surface. Moreover, it is hypothesis that there is increased sediment supply to the upstream region near the trench, since turbulence is dampened by the increased degree of baroclinicity, as can be seen in Figure 54 based on the increased SSC during ebb tide. Sufficient prove is, however, lacking, and, hence, the interaction needs more research.

8.2 Comparison with engineering tools

In this section, a comparison is made between the practicality and degree of certainty of the numerical model with those of the simple engineering tools. An example of such a tool is the so-called SED-PIT tool. This is an one-dimensional empirical model, which estimates the siltation volume in a highly schematization trench by estimation of the difference in depth-integrated sediment transport with the ambient area, and the efficiency of the trench in trapping the excess sediment (see Appendix C for more details).

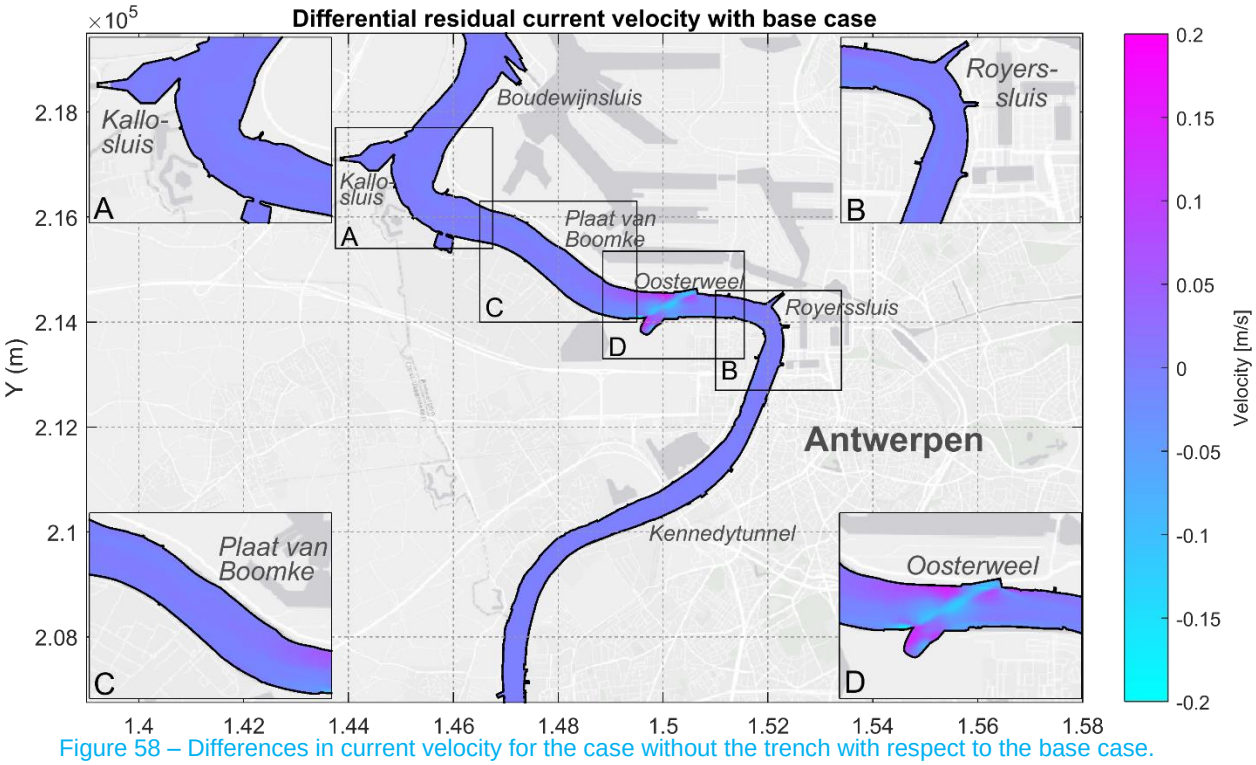

Figure 58 – Differences in current velocity for the case without the trench with respect to the base case.

Stand-alone application of SED-PIT at the location of tunnel element 4, in which the input settings and modelling results of SETMO were applied, gave a significant over-estimation: a factor 3.5 of the predicted siltation volumes by the numerical model. This is greater than expected, as it is known that SED-PIT overestimates these numerically estimated siltation rates by approximately a factor 1.5, when applied on trenches at 40 degrees with the governing currents. The over-estimation is primarily caused during flood tide, during which the siltation volume are overestimated by a factor 10 (!), while during ebb the expected factor 1.5 is found.

Applying the same uncertainty analysis on SED-PIT as on the numerical model, a similar degree of epistemic uncertainty due to parameter uncertainty can be estimated. The most influential parameters of SED-PIT are found to be the sediment density, fall velocity, the grain-size distribution of the sand, and some calibration factors (Van Rijn and sand transport factor). The latter finding is important, as it indicates that a lot depends on tuning of the model to the estimated siltation volumes of SETMO.

Furthermore, the degree of intrinsic uncertainty also shows the same order of magnitude compared with the numerical model. However, SED-PIT behaved differently on changing environmental conditions compared with the numerical model. While the numerical model predicts the deposition of sand at the location of tunnel element 4 to increase significantly during high river run-off and spring tides, SED-PIT estimates the sedimentation to also increase significantly during low river run-off. Additionally, it also finds significantly less sedimentation during neap tides and stormy weather, compared with the model.

Although the total quantifiable degree of uncertainty of SED-PIT does not seem to be substantially higher than that of SETMO, it is believed, based on the significantly different behavior of SED-PIT, that a lot of epistemic uncertainty in SED-PIT is associated with model inadequacy. This is, however, not quantifiable. First of all, SED-PIT does not take into account various trapping efficiency mechanisms, as it highly simplifies the (adaptation of) current velocity and SSC patterns around the trench. The tool assumes fully developed logarithmic velocity profiles, thereby significantly under-estimating the bed shear stresses and turbulence in the trench. This is in particular leading to overestimation of the trench siltation rates in estuaries, as the longitudinal salinity gradient seems to be a dominant term in the trapping efficiency by pushing the flooding currents to the bottom of the trench.

Additionally, SED-PIT does not take into account the sediment trapping and transport mechanisms. Therefore, applied for a trench in an estuary, in which complex dynamics play a huge role in the sediment supply pattern to the trench, it is fully dependent regarding current velocities and suspended sediment concentrations on a numerical model or detailed measurements. Moreover, the complex geometry of the trench is not captured by SED-PIT, such that along-trench sediment transport is not accounted for. This is in particular important for transport of mud to the more sheltered areas.

8.3 Sources of error

Possible errors in this research are listed in the below.

Endogenous complexity
The estimation of the degree of intrinsic uncertainty is based on a scenario analysis on the influence of the individual environmental components. This method, however, neglects the uncertainty caused by interconnectivity of the components, and hence, simplifies the endogenous complexity of the estuary. This is believed to have significantly distorted the estimation of the intrinsic uncertainty of SETMO. Furthermore, this same endogenous complexity made the identification of the individual sediment trapping and transport mechanisms quite cumbersome. Moreover, the individual mechanisms are susceptible to variations due to this non-linear interconnectivity. This may have led to misinterpretation of the results in which processes and mechanisms may have been overlooked or falsely identified.

Transient periods
Another drawback of the applied scenario analysis is the fact that the estuary is constantly in a transient phase to a new dynamic equilibrium. This is because the environmental conditions are constantly changing over time (spring-neap cycle, low- and high river runoff and storm periods), which cause a rapid response and subsequent slow recovery of the estuary. As a consequence, the estuary is constantly off its time averaged equilibrium, which may have significantly altered the results of the scenario analysis, and hence, the quantification of the intrinsic uncertainty.

A strong example is the location of the maximum SSC of the ETM. A period of high river discharge (e.g. in winter) shifts the salinity and ETM in seaward direction. The estuary is known to recover very slowly from this. As the location of the ETM is determining to a great extent the magnitudes of the gross sediment transport fluxes in the area, a modelling scenario of a high river discharge in winter may lead to different results than a high river discharge in summer.

Model inaccuracy
In this thesis, it became clear that the numerical model may produce some anomalies with respect to the measurements. There are some concerns regarding the modelling results of, in particular, current velocities, salinity, and water levels. This may have led to distorted results, and possible falsely identified governing mechanisms. More concerning is the assumption of hydrostacity in SETMO. Although the slopes are not believed to be steep enough to cause flow separation, they are steep enough to cause non-hydrostatic effects on the hydrodynamics. As such effects are not captured by Delft3D, the flow around the trench may be inaccurate, causing discrepancies regarding the actual trapping efficiency. Additionally, the model does not take into account the frequent dredging activities in the area and ship waves. Both may lead to intensified SSC in the area, causing more sedimentation in the more sheltered areas of the trench.

Other model uncertainties
The comparison of the model uncertainty between SETMO and SED-PIT is quite peculiar, as some types of model uncertainties have been omitted in this study, as they could not be quantified. For example, model inadequacy is likely to dominate the uncertainty of SED-PIT.

8.4 Applicability of this thesis

Reflecting on the introduction and theoretical framework of this thesis, it has become clear that dominant mechanisms in the transport and trapping of sediment differ among estuaries. Therefore, in order to generalize the findings of this thesis, the Scheldt Estuary, and in particular the Lower Sea Scheldt, needs to be classified and compared with other types of estuaries.

8.4.1 Classification of an estuary

Numerous authors have classified estuaries based through parameterizations of the estuarine forcing terms of the degree of salinity-induced baroclinicity: tidal mixing and freshwater flow (Hansen & Rattray, 1965; MacCready & Geyer, 2010; Valle-Levinson, 2010). The degree stems from the vertical salinity structure, which is one of the most prominent characteristic of an estuary determining the importance of the baroclinic mechanisms and influence on their barotropic counterpart. In this thesis, the nondimensionalized parameter space of Geyer & Maccready (2014) is used, which scales the above mentioned forcing terms, taking into account the time dependent estuarine dynamics. These dynamics are found to be of high importance, in particular in partly- and well-mixed estuarine systems.

The parameter space (see Figure 59) is constructed on the one axis by the freshwater Froude number, which nondimensionalizes the freshwater flow (Geyer & Maccready, 2014):

$$Fr_f = \frac{U_R}{\sqrt{\beta g s_{ocean} H}}$$

This is the net velocity due to river flow scaled by the maximum possible frontal propagation speed of the salinity. On the other axis, a mixing parameter is imposed, which quantifies the effectiveness of tidal mixing in a stratified estuary (Geyer & Maccready, 2014):

$$M = \sqrt{\frac{C_D U_T^2}{\omega N_0 H^2}}$$

in which N_0 is the buoyancy frequency, defined as:

$$N_0 = \sqrt{\frac{\beta g s_{ocean}}{H}}$$

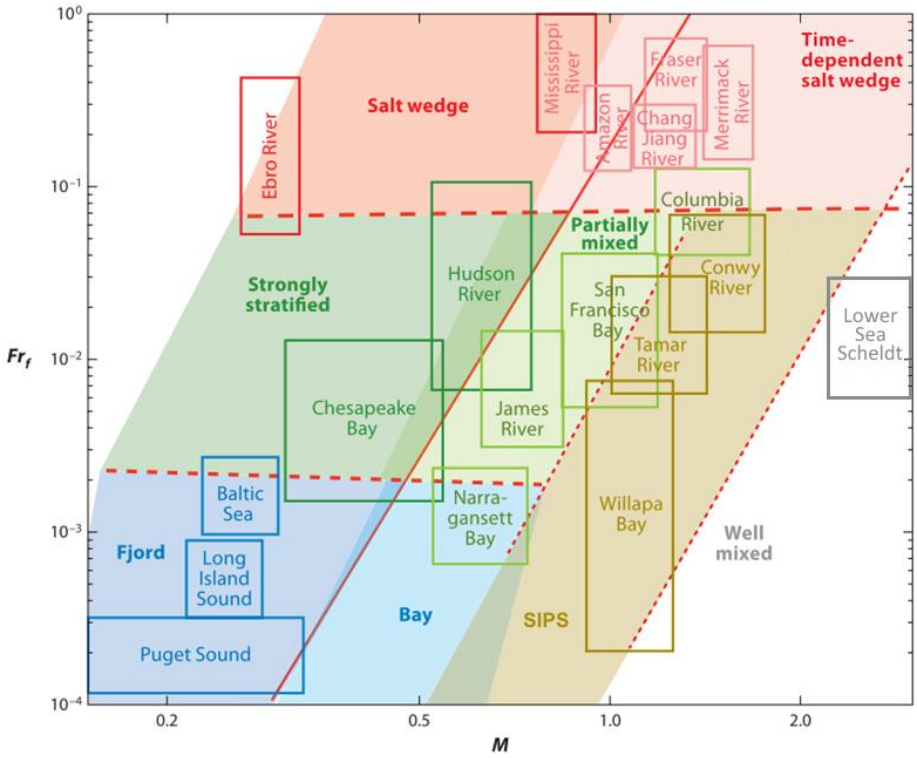

Figure 59 – Estuarine parameter space, based on the freshwater Froude number and mixing number. the different regimes are indicated in distinct colors. The solid red diagonal line indicates the value for critical mixing in which the tidal boundary layer is able to reach the water surface. This line separates temporally stratified estuaries from the permanently stratified estuaries. Estuaries are depicted in the space as squares, since they are prone to variations in tidal and freshwater velocities (e.g. spring-neap cycles, river floods, etc.) (Geyer & MacCready, 2014).

It can be calculated, based on the characteristics of the system that the parameter range of the Lower Sea Scheldt falls inside the well-mixed estuarine regime, although the right conditions may shift the regime to a nearly well-mixed SIPS estuary (Simpson et al., 1990). Baroclinic mechanisms in estuaries, falling in the same (nearly) well-mixed regime, will likely have the same importance and influence on their barotropic counterpart. Governing mechanisms in the supply and trapping of sediment to/in the trench are then believed to show similarities. Nevertheless, as research to reference trenches is lacking to the researchers' knowledge, this claim should be taken with great care. Furthermore, one should keep in mind that other characteristics of estuaries, and trenches in specific, may come into play. Some are discussed in the below.

Other characteristics

Barotropic mechanisms may be governing in the supply of sediment to the trench. This especially holds for well-mixed estuaries, meaning that estuarine geomorphology, sediment characteristics, and barotropic forcing terms (e.g. wind, waves, tides, river discharges) should also be carefully mapped before any comparison can be made with findings in this thesis (Valle-Levinson, 2010). The Lower Sea Scheldt, for example, is find to be classified as a tide-dominated, macro-tidal, funnel-shaped, long, meandering and sheltered coastal plain estuary. Furthermore, other terms of baroclinicity may come into play, such high SSC (e.g. in hyper-turbid estuaries) and gradients in temperature (differential heating and rain-fall) (Becherer, 2013a; Becker, Maushake, & Winter, 2018). For the Lower Sea Scheldt, which is non-hyper turbid and where temperature gradients can be neglected, above mechanisms do not play a role.

In specific for trenches, the alignment with respect to the governing currents (*parallel, oblique, perpendicular*), and geometry (*width, relative depth*) may significantly change the governing trapping efficiency mechanisms (Jensen et al., 1999a, 1999b; L. C. Van Rijn, 2017). This is believed to hold in particular for trenches in (well-mixed) estuaries, as it is hypothesized that

the stronger degree of baroclinicity in the trench with respect to the ambient area reduces the trapping efficiency significantly. As this strengthened stratification was primarily caused by a drop in current velocity and increase in depth, trench geometry and alignment may be of great importance.

8.4.2 Identification of governing mechanisms

The findings of this thesis have proven that application of the schematic overview of the different general sediment transport and trapping mechanisms is rather successful in the identification of the governing mechanisms underlying the trench siltation, at least for the Lower Sea Scheldt Estuary. This scheme and its underlying theory can be generally applied to any type of estuary and is a strong and clear assessment tool for clarifying and tackling the problem.

9 Conclusion

In this thesis, in which it was aimed to improve the degree of certainty in the estimation of siltation rates for trenches in complex estuaries with respect to the high uncertainty associated with simple engineering tools, it can be concluded that implementation of a detailed three-dimensional numerical model is able to achieve a degree of certainty of approximately a factor 2.5 of the expected siltation volumes. The magnitude of this factor is primarily caused by a combination of epistemic parameter uncertainty and intrinsic uncertainty, rather than epistemic uncertainty caused by model inadequacy. This latter statement, which, however, could not be supported quantitively, can be substantiated qualitatively.

Evidence of the significant adequacy of the detailed numerical model is found in the captured complex estuarine processes and mechanisms. The most influential processes were found to be: *geomorphology, tide, river discharge, salinity*, and *fluid mud*. This is in line with literature on the Scheldt Estuary and also in agreement by state-of-the-art theory on well-mixed estuaries. Based on this, it was discovered that the following mechanisms are dominant in the transport and trapping of sediment, as is visualized in colors in the schematic overview in Appendix H:

- geometry-induced residual currents due to channel curvature,
- Stokes' drift,
- lateral circulation due to bend flow,
- various micro-scale mechanisms (*resuspension, diffusion/advection, etc.*);
- salinity-induced longitudinal circulation (*gravitational circulation, and internal mixing asymmetries*).

Again, this is in line with literature and theory. Moreover, it was found that the local trapping efficiency mechanisms, imposed by the trench in the model, corresponded with the mechanisms listed in theory. Examples are: *current adaptation (attraction, acceleration, deflection),* and *horizontal* and *lateral circulation currents*.

Besides mechanisms mentioned in theory, in this thesis, the longitudinal salinity gradient was also found to be a dominant mechanism in the trapping efficiency of the trench. The longitudinal salinity gradient, accompanied by a decrease in current velocity at the location of the trench, is believed to cause a local increase in baroclinicity, leading to amplified near-bed flooding currents (increased salinity-induced longitudinal circulation), and subsequent increased bottom shear during flood tide. This is believed to reduce the trapping of sediment during flood significantly. Furthermore, tidal frontogenesis (advection of the degree of baroclinicity) may seem to be generated by the trench due to the above mechanism.

Although the same probabilistic uncertainty analysis applied on the engineering tool (SED-PIT) resulted in similar quantifiable epistemic and intrinsic uncertainties around the expected siltation rates as were found for the numerical model, stand-alone implementation proved that engineering tools are likely prone to high epistemic uncertainty due to model inadequacy. This inadequacy is believed to be caused by not accounting for the physical processes, complex trench geometry (both affecting the trapping efficiency), and estuarine sediment transport and trapping mechanisms (affecting the sediment supply). As a consequence, SED-PIT gave a significant over-estimation of the siltation volumes during flood tide, and behaved differently on changing environmental conditions. It can, therefore, be concluded that SED-PIT is seemingly not suitable for application in an estuary.

A huge drawback of the implementation of a three-dimensional numerical model, however, is the complexity and the practicality. Additionally, due to its complexity, there are some serious concerns of the applied numerical model about the physical behavior of the model regarding

the hydrodynamics at the location of the trench due to possible non-hydrostatic effects, and some validation errors regarding salinity, water level, and current velocity. This may have caused discrepancies with the theory, which likely distorted the results of this thesis. This need more research.

In practice, therefore, this thesis opts for the development/use of more sophisticated semi-empirical models to predict the trench siltation rates in estuaries. These models are required to account for the governing estuarine processes and mechanisms involved regarding sediment supply to the trench and local trapping efficiency of the trench. As these mechanisms likely differ between estuaries and trench geometries, more research is needed for the development of such a model.

10 Recommendations

Recommendations for further research, which may be necessary for:

- the applicability range of SED-PIT.
- future application of detailed numerical models to predict siltation rates for local engineering measures in an estuary with higher accuracy
- the development of a more sophisticated (semi-)empirical engineering tool for the prediction of trench siltation rates in estuaries;
- research to sediment transport and trapping mechanisms in estuaries in general,

are given by:

1. *More research to siltation problems in similar type of estuaries*
   According to the researcher's knowledge, no reference studies have been performed on trench siltation in estuaries. Verification of the found estuarine processes and mechanisms is, therefore, required to generalize the findings in this thesis for other well-mixed estuaries, as possible model discrepancies may have distorted the (analysis of the) modelling results. As an example, the occurrence of the seemingly great influence of the longitudinal salinity gradient on the trapping efficiency of the trench, and the consequent finding of the existence of tidal frontogenesis, needs to be verified.

2. *More research to the Scheldt Estuary*
   The necessity of more research to the area of the ETM/trench in the Scheldt Estuary is:
   - To exclude the fact that the simplifications which have been applied in this study (e.g. no flocculation model, no inclusion of dredging activities and ship waves, application of a hydrostatic numerical model, etc.), have led to significantly distorted modelling results. This also includes more proper calibration of the detailed numerical model, and a longer modelling period (full spring-neap cycle).
   - For this purpose, it is advised to perform more measurements in the area regarding sediment transport fluxes, 3D current velocity profiles, longitudinal and horizontal salinity gradients.
   - To verify the predicted trench siltation rates and sedimentation distributions over the trench to check whether the modelling approach has been sufficient accurate.
   - To improve the method of the estimation of the total degree of uncertainty, as the probabilistic method used in this thesis was quite simple (no interconnectivity of environmental conditions, assumption of independent model parameters, etc.) and based on only a few runs, given the complex interconnectivity of the environmental components, and the transient state of the estuary.
   - To improve the practicality of the numerical model by decreasing its runtime and complexity through a more sophisticated numerical sensitivity analysis (e.g. less grid cells/sigma layers, turbulence models, etc.).

3. *More (similar) research to siltation problems in different type of estuaries*
   As stated in the discussion, the applicability range of this thesis falls within the category of well-mixed estuaries. Further research to trench siltation problems in other type of estuaries should be performed in order to discover the applicability of the findings of this thesis in other estuaries.

References

2019 Facts & Figures. (2019). Port of Antwerp. Retrieved from https://www.portofantwerp.com/sites/portofantwerp/files/Facts_en_Figures_2019.pdf

Allen, G., Salomon, J. C., Bassoullet, P., Du Penhoat, Y., & De Grandpre, C. (1980). Effects of tides on mixing and suspended sediment transport in macrotidal estuaries. *Sedimentary Geology*, *26*, 69–90.

Alvarez-Hernandez, E. M. (1990). *The influence of cohesion on sediment movement in channels of circular cross-section*. Department of Civil Engineering University of Newcastle Upon Tyne.

Amy, L. A., Talling, P. J., Edmonds, V. O., Sumner, E. J., & Lesueur, A. (2006). An experimental investigation of sand – mud suspension settling behaviour: implications for bimodal mud contents of submarine flow deposits. *Sedimentology*, *53*, 1411–1434. https://doi.org/10.1111/j.1365-3091.2006.00815.x

Azhikodan, G., & Yokoyama, K. (2018). Estuarine , Coastal and Shelf Science Sediment transport and fl uid mud layer formation in the macro-tidal Chikugo river estuary during a fortnightly tidal cycle. *Estuarine, Coastal and Shelf Science*, *202*, 232–245. https://doi.org/10.1016/j.ecss.2018.01.002

Baeyens, W. F. J., Eck, B. Van, Lambert, C., Wollast, R., & Goeyens, L. (1998). General description of the Scheldt estuary. *Hydrobiologia*, (366), 1–14.

Becherer, J. (2013a). *Estuarine Circulation in well-mixed tidal inlets*. Mathematical Science Faculty Rostock University.

Becherer, J. (2013b). *Estuarine Circulation in well-mixed tidal inlets*. Rostock Universityh.

Becker, M., Maushake, C., & Winter, C. (2018). Observations of mud-induced periodic stratification in a hyperturbid estuary. https://doi.org/10.1029/2018GL077966

Becker, M., Schrottke, K., Bartholomä, A., Ernstsen, V., Winter, C., & Hebbeln, D. (2013). Formation and entrainment of fluid mud layers in troughs of subtidal dunes in an estuarine turbidity zone. *Journal of Geophysical Research: Oceans*, *118*, 2175–2187. https://doi.org/10.1002/jgrc.20153

Bolle, A. (2006). Sediment Exchange between the Dutch Coast and the Tidal Basin Western Scheldt, (December).

Bolle, A., Wang, Z. B., Amos, C., & De Ronde, J. (2010). The influence of changes in tidal asymmetry on residual sediment transport in the Western Scheldt. *Continental Shelf Research*, *30*(8), 871–882. https://doi.org/10.1016/j.csr.2010.03.001

Boon, J. D., & Byrne, R. J. (1981). On basin hypsometry and the morphodynamic response of coastal inlet systems. *Marine Geology*, *40*, 27–48.

Bowers, D. G., & Al-Barakati, A. (1997). Tidal Rectification on Drying Estuarine Sandbanks. *Estuaries*, *20*(3), 559–568.

Braat, L., Van Kessel, T., Leuven, J. R. F. W., & Kleinhans, M. G. (2017). Effects of mud supply on large-scale estuary morphology and development over centuries to millennia. *Earth Surface Dynamics*, *5*, 617–652. https://doi.org/10.5194/esurf-5-617-2017

Buijsman, M. C., & Ridderinkhof, H. (2008). Variability of secondary currents in a weakly stratified tidal inlet with low curvature. *Continental Shelf Research*, *28*, 1711–1723.

https://doi.org/10.1016/j.csr.2008.04.001

Burchard, H., Hetland, R. D., Schulz, E., & Schuttelaars, H. M. (2011). Drivers of Residual Estuarine Circulation in Tidally Energetic Estuaries: Straight and Irrotational Channels with Parabolic Cross Section. *Journal of Physical Oceanography*, *41*, 548–570. https://doi.org/10.1175/2010JPO4453.1

Burchard, H., & Hofmeister, R. (2008). A dynamic equation for the potential energy anomaly for analysing mixing and stratification in estuaries and coastal seas. *Estuarine, Coastal and Shelf Science*, *77*, 679–687. https://doi.org/10.1016/j.ecss.2007.10.025

Burchard, H., Schuttelaars, H. M., & Ralston, D. K. (2018). Sediment Trapping in Estuaries. *Annual Review of Marine Science*, *14*, 1–25.

Cameron, W. M., & Pritchard, D. W. (1963). *Estuaries*. *The Sea* (Hill, M.N., Vol. II). New York: John Wiley and Sons.

Chant, R. J. (2002). Secondary circulation in a region of flow curvature: Relationship with tidal forcing and river discharge. *Journal of Geophysical Research*, *107*(C9), 3131–3142. https://doi.org/10.1029/2001JC001082

Chant, R. J., & Wilson, R. E. (1997). Secondary circulation in a highly stratified estuary. *Journal of Geophysical Research*, *102*(C10), 23,207-23,215.

Chen, M. S., Wartel, S., & Temmerman, S. (2005). Seasonal variation of floc characteristics on tidal flats , the Scheldt estuary. *Hydrobiologia*, (540), 181–195. https://doi.org/10.1007/s10750-004-7143-6

Chen, M. S., Wartel, S., Van Eck, B., & Van Maldegem, D. (2005). Suspended matter in the Scheldt estuary. *Hydrobiologia*, *540*(1–3), 79–104. https://doi.org/10.1007/s10750-004-7122-y

Cheng, P., & Valle-Levinson, A. (2009). Influence of Lateral Advection on Residual Currents in Microtidal Estuaries. *Journal of Physical Oceanography*, *39*, 3177–3190. https://doi.org/10.1175/2009JPO4252.1

Cheng, P., Wang, A., & Jia, J. (2017). Analytical study of lateral-circulation-induced exchange flow in tidally dominated well-mixed estuaries. *Continental Shelf Research*, *140*, 1–10. https://doi.org/10.1016/j.csr.2017.03.013

Chernetsky, A. (2012). *Trapping of sediment in tidal estuaries*. TU Delft.

Chu, K. (2017). *Update the NEVLA3D model to the year 2014*.

Claessens, J. (1988). HET HYDRAULISCH REGIME VAN DE SCHELDE. *Water*, *43*, 163–169.

Cleveringa, J. (2013). *Grootschalige sedimentbalans Westerschelde. version 2.0. Project LTV Veiligheid en Toegankelijkheid: LTV V&T-rapport G_2*.

Cleveringa, J., & Dam, G. (2013). *De rol van slib in de Westerschelde. Basisrapport grootschalige ontwikkeling G-3. Instandhouding vaarpassen Schelde Milieuvergunningen terugstorten baggerspecie LTV – Veiligheid en Toegankelijkheid*.

Coen, I. (2008). *De eeuwige Schelde? Ontstaan en ontwikkeling van de Schelde*. Borgerhout, Belgium: Waterbouwkundig Laboratorium.

Csanady, G. T. (1973). Wind induced barotropic motions in long lakes. *Journal of Physical Oceanography*, *3*, 429–438.

Csanady, G. T. (1980). Longshore pressure gradients caused by offshore wind. *Journal of*

Geophysical Research, *85*(C2), 1076–1084.

Deltares. (2011). Sedimentation in channels and ports.

Dijkstra, Y. M., Schuttelaars, H. M., & Schramkowski, G. P. (2019). Can the Scheldt River Estuary become hyperturbid?: A model analysis of suspended sediment concentrations and transport in response to channel deepening. *Ocean Dynamics*, *69*, 809–827. https://doi.org/10.1007/s10236-019-01277-z

Dronkers, J. (1986). TIDAL ASYMMETRY AND ESTUARINE MORPHOLOGY, *20*, 117–131.

Dyer, K. R. (1995). Sediment transport processes in estuaries. In G. M. E. Perillo (Ed.), *Geomorphology and Sedimentology of Estuaries. Developments in Sedimentology 53*. Elsevier Science B.V.

Fettweis, M., & Sas, M. (1997). Langdurige meting van slibconcentratie, saliniteit en temperatuur te prosperpolder (beneden zeeschelde), (92), 15–26.

Flemming, B. W. (2000). A revised textural classification of gravel-free muddy sediments on the basis of ternary diagrams. *Continental Shelf Research*, *20*, 1125–1137.

Friedrichs, C., Armbrust, B. D., & De Swart, H. E. (1998). Hydrodynamics and equilibrium sediment dynamics of shallow, funnel-shaped tidal estuaries. In *Physics of Estuaries and Coastal Seas, Dronkers & Scheffers (eds)* (pp. 315–327). Rotterdam: Balkema.

Friedrichs, C., & Aubrey, D. G. (1988). Non-linear Tidal Distortion in Shallow Estuaries: a Synthesis. *Estuarine, Coastal and Shelf Science*, *27*, 521–545.

Garel, E., Pinto, L., Santos, A., & Ferreira, O. (2009). Tidal and River Discharge Forcing upon Water and Sediment Circulation at a Rock-Bound Estuary (Guadiana Estuary, Portugal). *Estuarine, Coastal and Shelf Science*, *84*, 269–281. https://doi.org/10.1016/j.ecss.2009.07.002

Gatto, V. M., Van Prooijen, B. C., & Wang, Z. B. (2017). Net sediment transport in tidal basins: quantifying the tidal barotropic mechanisms in a unified framework. *OceanDynamics*, *67*, 1385–1406. https://doi.org/10.1007/s10236-017-1099-3

Geyer, W. R. (1993). Three-dimensional tidal flow around headlands. *Journal of Geophysical Research*, *98*(C1), 955–966.

Geyer, W. R., & Maccready, P. (2014). The Estuarine Circulation, (August 2013), 175–197. https://doi.org/10.1146/annurev-fluid-010313-141302

Geyer, W. R., & MacCready, P. (2014). The Estuarine Circulation. *Annual Review of Fluid Mechanics*, *46*, 175–197.

Godin, G. (1984). The tide in rivers. *International Hydrographic Review*, *61*(2), 159–170.

Grasmeijer, B. (2013). *Actualisatierapport Delft3D Schelde-estuarium. LTV – Veiligheid en Toegankelijkheid: Instandhouding vaarpassen Schelde Milieuvergunningen terugstorten baggerspecie. Achtergrondrapport A-27.*

Green, M. O. (2011). Very small waves and associated sediment resuspension on an estuarine intertidal flat. *Estuarine, Coastal and Shelf Science*, *93*, 449–459. https://doi.org/10.1016/j.ecss.2011.05.021

Green, M. O., Black, K. P., & Amos, C. L. (1997). Control of estuarine sediment dynamics by interactions between currents and waves at several scales. *Marine Geology*, *144*, 97–116.

Guo, L., Van der Wegen, M., Roelvink, J. A., & He, G. (2014). The role of river flow and tidal

asymmetry on 1-D estuarine morphodynamics. *Journal of Geophysical Research: Earth Surface*, *119*, 2315–2334. https://doi.org/10.1002/2014JF003110

Haecon. (2006). *Actualisatie van de zandbalans van de Zee-en Westerschelde*.

Hansen, D. V., & Rattray, M. J. (1965). Gravitational Circulation in Straits and Estuaries. *Journal of Marine Research*, *23*(2), 104–122.

Hir, P. Le, Roberts, W., Cazaillet, O., Christie, M., Bassoullet, P., & Bacher, C. (2000). Characterization of intertidal flat hydrodynamics. *Continental Shelf Research*, *20*, 1433–1459.

Huijts, K. M. H., De Swart, H. E., Schramkowski, G. P., & Schuttelaars, H. M. (2011). Transverse structure of tidal and residual flow and sediment concentration in estuaries. *Ocean Dynamics*, *61*, 1067–1091. https://doi.org/10.1007/s10236-011-0414-7

Hunt, S., Bryan, K. R., & Mullarney, J. C. (2015). Geomorphology The influence of wind and waves on the existence of stable intertidal morphology in meso-tidal estuaries. *Geomorphology*, *228*, 158–174. https://doi.org/10.1016/j.geomorph.2014.09.001

Jacobs, W. (2011). *Sand-mud erosion from a soil mechanical perspective*. Delft University of Technology. Retrieved from https://repository.tudelft.nl/islandora/object/uuid%3A6d908f04-14fd-47f3-b292-af4b99a8fb11?collection=research

Jacobs, W., Le, P., Van Kesteren, W. G. M., & Cann, P. (2011). Erosion threshold of sand – mud mixtures. *Continental Shelf Research*, *31*, S14–S25. https://doi.org/10.1016/j.csr.2010.05.012

Jay, D. A., & Musiak, J. D. (1994). PDXScholar Particle Trapping in Estuarine Tidal Flows. *Journal of Geophysical Research*, *99*(C10), 20,445-20,461.

Jensen, J. H., Madsen, E. ., & Fredsøe, J. (1999a). Oblique Flow over Dredged Channels I: Flow Description. *Journal of Hydraulic Engineering*, (125), 1181–1189.

Jensen, J. H., Madsen, E. ., & Fredsøe, J. (1999b). Oblique Flow over Dredged Channels II: Sediment Transport and Morphology. *Journal of Hydraulic Engineering*, (125), 1190–1198.

Kamphuis, B. J. W., & Hall, K. R. (1983). Cohesive material erosion by unidirectional current. *Journal of Hydraulic Engineering*, *109*, 49–61.

Kim, Y. H., & Voulgaris, G. (2008). Lateral circulation and suspended sediment transport in a curved estuarine channel: Winyah Bay , SC , USA. *Journal of Geophysical Research*, *113*(C09006). https://doi.org/10.1029/2007JC004509

Kjerfve, B., & Proehl, J. A. (1979). Velocity variability in a cross-section of a well-mixed estuary. *Journal of Marine Research*, *37*(3).

Kuijper, K., & Lescinksi, J. (2013). *Data analyses water levels ebb and flood volumes and bathymetries Western Scheldt*.

Kuijper, K., Van der Kaaij, T., & De Goede, E. (2006). *LTV-O&M actieplan voor morfologisch onderzoek modelinstrumentarium. Rapport Z3950*.

Kuti, E. O., & Yen, C.-L. (1976). Scouring of cohesive soils. *Journal of Hydraulic Research*, *14*(3), 195–206. https://doi.org/10.1080/00221687609499667

Lacy, J. R., & Monismith, S. G. (2001). Secondary currents in a curved, stratified, estuarine channel. *Journal of Geophysical Research*, *106*(C12), 31283–31302.

Lacy, J. R., Stacey, M. T., Burau, J. R., & Monismith, S. G. (2003). Interaction of lateral baroclinic forcing and turbulence in an estuary. *Journal of Geophysical Research*, *108*(C3), 3089. https://doi.org/10.1029/2002JC001392

Le Hir, P., Cann, P., Waeles, B., Jestin, H., & Bassoullet, P. (2008). Erodibility of natural sediments: experiments on sand / mud mixtures from laboratory and field erosion tests. In *Sediment and Ecohydraulics: INTERCOH 2005* (pp. 137–153).

Le Hir, P., Cayocca, F., & Waeles, B. (2011). Dynamics of sand and mud mixtures: A multiprocess-based modelling strategy. *Continental Shelf Research*, *31*(10 SUPPL.). https://doi.org/10.1016/j.csr.2010.12.009

Lerczak, J. A., & Geyer, W. R. (2004). Modeling the Lateral Circulation in Straight , Stratified Estuaries *. *Journal of Physical Oceanography*, *34*, 1410–1428.

Li, C., Chen, C., Guadagnoli, D., & Georgiou, I. Y. (2008). Geometry-induced residual eddies in estuaries with curved channels : Observations and modeling studies. *Journal of Geophysical Research*, *113*(C01005), 1–14. https://doi.org/10.1029/2006JC004031

Li, C., & O'Donnell, J. (1997). Tidally driven residual circulation in shallow estuaries with lateral depth variation. *Journal of Geophysical Research*, *102*(C13), 27,915-27,929. https://doi.org/10.1029/97JC02330

Li, C., & O'Donnell, J. (2005). The Effect of Channel Length on the Residual Circulation in Tidally Dominated Channels. *Journal of Physical Oceanography*, *35*, 1826–1840.

Lockett, M. J., & Al-Habbobby, H. M. (1974). Relative Particle Velocities in Two-Species Settling. *Powder Technology*, *10*, 67–71.

MacCready, P. (1999). Estuarine Adjustment to Changes in River Flow and Tidal Mixing. *Journal of Physical Oceanography*, *29*, 708–726.

MacCready, P., & Geyer, W. R. (2010). Advances in Estuarine Physics Advances in Estuarine Physics. *Annual Review of Marine Science*, *2*, 35–58. https://doi.org/10.1146/annurev-marine-120308-081015

Manning, A. J., Baugh, J. V, Spearman, J. R., & Whitehouse, R. J. S. (2010). Flocculation settling characteristics of mud: sand mixtures. *Ocean Dynamics*, *60*, 237–253. https://doi.org/10.1007/s10236-009-0251-0

Manning, A. J., Martens, C., De Mulder, T., Vanlede, J., Winterwerp, J. C., Ganderton, P., & Graham, G. W. (2007). Mud Floc Observations in the Turbidity Maximum Zone of the Scheldt Estuary During Neap Tides. *Journal of Coastal Research*, (SI 50 (Proceedings of the 9th International Coastal Symposium)), 832–836.

Maris, T., Bruens, A., Van Duren, L., Vroom, J., Holzhauer, H., De Jonge, M., … Meire, P. (2014). *Evaluatiemethodiek Schelde-estuarium, update 2014. Deltares rapportnummer 1209394.*

Maris, T., & Meire, P. (2017). *Onderzoek naar de gevolgen van het Sigmaplan, baggeractiviteiten en havenuitbreiding in de Zeeschelde op het milieu. Geïntegreerd eindverslag van het onderzoek verricht in 2016. ECOBE 017-R206*.

Mathew, R., & Winterwerp, J. C. (2017). Surficial sediment erodibility from time-series measurements of suspended sediment concentrations: development and validation. *Ocean Dynamics*, *67*(6), 691–712. https://doi.org/10.1007/s10236-017-1055-2

Mathieu, P., Deleersnijder, E., Cushman-Roisin, B., Beckers, J.-M., & Bolding, K. (2002). The role of topography in small well-mixed bays , with application to the lagoon of Mururoa. *Continental Shelf Research*, *22*, 1379–1395.

Mathys, M. (2013). *Harde lagen Beneden-Zeeschelde. Achtergrondrapport A-29*.

Maximova, T., Ides, S., De Mulder, T., & Mostaert, F. (2009). *TV O&M thema veiligheid: deelproject 1. Verbetering hydrodynamisch NEVLA model ten behoeve van scenario-analyse. versie 2.0. WL Rapporten, 756_05*.

Mcanally, W. H., Asce, F., Friedrichs, C., Hamilton, D., Hayter, E., Shrestha, P., … Teeter, A. (2007a). Management of Fluid Mud in Estuaries, Bays, and Lakes . I : Present State of Understanding on Character and Behavior. *Journal of Hydraulic Engineering*, 9–22. https://doi.org/10.1061/(ASCE)0733-9429(2007)133

Mcanally, W. H., Asce, F., Friedrichs, C., Hamilton, D., Hayter, E., Shrestha, P., … Teeter, A. (2007b). Management of Fluid Mud in Estuaries , Bays , and Lakes . I : Present State of Management of Fluid Mud in Estuaries , Bays , and Lakes . I : Present State of Understanding on Character and Behavior, *9429*(January). https://doi.org/10.1061/(ASCE)0733-9429(2007)133

McCave, I. N. (1984). Erosion, transport and deposition of fine-grained marine sediments.

McLaren, P. (1994). *Sediment Transport in the Western Scheldt between Baarland and Rupelmonde*. Cambridge, UK.

McLusky, D. S., & Elliott, M. (2004). *The Estuarine Ecosystem: ecology, threats and management.* Oxford, UK: Oxford University Press. https://doi.org/10.1093/acprof

Meade, R. H. (1969). Landward transport of bottom sediments in estuaries of the Atlantic Coastal Plain. *J. Sediment. Petrol.*, (39), 222–234.

Meire, D., Kolokythas, G. K., & Plancke, Y. (2017). Wave measurements along an estuary with heavy ship traffic. *Hydraulic Measurements and Experimental Methods 2017 Conference (HMEM 2017)*. Retrieved from http://www.vliz.be/nl/open-marien-archief?module=ref&refid=288532%0Ahttp://documentatiecentrum.watlab.be/owa/imis.php?module=ref&refid=288532

Meire, P., Ysebaert, T., Damme, S. Van, Bergh, E. Van Den, Maris, T., & Struyf, E. (2005). The Scheldt estuary : a description of a changing ecosystem. *Hydrobiologia*, (540), 1–11. https://doi.org/10.1007/s10750-005-0896-8

Methta, A. J., & McAnally, W. H. (2008). Fine-Grained Sediment Transport. In *Sedimentation Engineering* (pp. 253–306).

Mitchener, H., & Torfs, H. (1996). Erosion of mud / sand mixtures. *Coastal Engineering*, *29*, 1–25.

Murray, Wi. A. (1976). *Erodibility of Coarse Sand / Clayey Silt Mixtures*.

Nichols, M. M. (1992). Effects of fine sediment resuspension in estuaries. In *Estuarine Cohesive Sediment Dynamics* (Vol. 14).

Nidzieko, N. J., Hench, J. L., & Monismith, S. G. (2009). Lateral Circulation in Well-Mixed and Stratified Estuarine Flows with Curvature. *Journal of Physical Oceanography*, *29*, 831–851. https://doi.org/10.1175/2008JPO4017.1

Panagiotopoulos, I., Voulgaris, G., & Collins, M. B. (1997). The influence of clay on the threshold of movement of fine sandy beds. *Coastal Engineering*, *32*, 19–43.

Parchure, B. T. M., & Mehta, A. J. (1985). Erosion of Soft Cohesive Sediment Deposits. *Journal of Hydraulic Engineering*, 1308–1326.

Park, M.-J., & Wang, D.-P. (2000). Tidal Vorticity Around a Coastal Promontory. *Journal of Oceanography*, *56*, 261–273.

Parsons, J. D., Friedrichs, C., Traykovski, P. A., Mohrig, D., Imran, J., Syvitski, J. P. M., … Hole, W. (2005). The mechanics of marine sediment gravity flows.

Paterson, D. M. (1989). Short-term changes in the erodibility of intertidal cohesive sediments related to the migratory behavior of epipelic diatoms. *Limnol. Oceanography*, *34*(1), 223–234.

Paterson, D. M. (2001). Microphytobenthos in Constrasting Coastal Ecosystems: Biology and Dynamics. In K. Reise (Ed.), *Ecological Studies, Vol.151* (Ecological). Berlin Heidelberg: Springer-Verlag. https://doi.org/10.1007/978-3-642-56557-1

Pejrup, M. (1988). The Triangular Diagram Used for Classification of Estuarine Sediments: A New Approach. In P. L. De Boer el al. (Ed.), *Tide-Influenced Sedimentary Environments and Facies* (pp. 289–300). D. Reidel Publishing Company. https://doi.org/10.1007/978-94-015-7762-5

Pieters, T. (2002). *The tide in the Western Scheldt Estuary (in Dutch). Document BGW-0102*.

Plancke, Y., Vereecken, H., Vanlede, J., Verwaest, T., & Mostaert, F. (2014). *Integraal plan Boven-Zeeschelde: Deelrapport 3 – Factual data-rapport sediment transport metingen in de Zeeschelde in 2014. Versie 4.0. WL Rapporten, 13_131.*

Postma, H. (1961). Transport and accumulation of suspended matter in the Dutch Wadden Sea. *Journal of Sea Research*, *1*(1/2), 148–190.

Postma, H., & Kalle, K. (1955). Die Enstehung von Trübungszonen im Unterlauf der Flüsse speziell im Hinblick at die Verhiiltnisse in der Unterelbe. *Dtsch. Hydrogr. Z.*, (8), 137–144.

Pritchard, D. W. (1952). Salinity distribution and circulation in the Chesapeake Bay estuarine system. *Journal of Marine Research*, (11), 106–173.

Pritchard, D. W. (1954). A study of the salt balance in a coastal plain estuary. *Journal of Marine Research*, (13), 133–144.

Pritchard, D. W. (1956). The dynamic structure of a coastal plain estuary. *J. Mar. Res.*, *15*(4), 33–42.

Pritchard, D. W., & Hogg, A. J. (2003). Cross-shore sediment transport and the equilibrium morphology of mudflats under tidal currents. *Journal of Geophysical Research*, *108*(C10), 3313–3328. https://doi.org/10.1029/2002JC001570

Ralston, D. K., Geyer, W. R., & Warner, J. C. (2012). Bathymetric controls on sediment transport in the Hudson River estuary: Lateral asymmetry and frontal trapping. *Journal of Geophysical Research*, *117*(C10013), 1–21. https://doi.org/10.1029/2012JC008124

Sanford, L. P. (2008). Modeling a dynamically varying mixed sediment bed with erosion, deposition, bioturbation, consolidation, and armoring. *Computers & Geosciences*, *34*, 1263–1283. https://doi.org/10.1016/j.cageo.2008.02.011

Sas, M., & Verhaegen, K. (1992). *Aanslibbing in de toegangsgeul tot de Kallosluis. PR1735*. Borgerhout, Belgium.

Sassi, M. G., & Hoitink, A. J. F. (2013). River flow controls on tides and tide-mean water level profiles in a tidal freshwater river. *Journal of Geophysical Research: Oceans*, *118*, 4139–4151. https://doi.org/10.1002/jgrc.20297

Scully, M. E., & Geyer, W. R. (2012). The Role of Advection, Straining, and Mixing on the Tidal Variability of Estuarine Stratification. *Journal of Physical Oceanography*, *42*, 855–868. https://doi.org/10.1175/JPO-D-10-05010.1

Scully, M. E., Geyer, W. R., & Lerczak, J. A. (2009). The Influence of Lateral Advection on the

Residual Estuarine Circulation: A Numerical Modeling Study of the Hudson River Estuary. *Journal of Physical Oceanography*, *39*, 107–124. https://doi.org/10.1175/2008JPO3952.1

Shi, J. Z. (2010). Geomorphology Tidal resuspension and transport processes of fi ne sediment within the river plume in the partially-mixed Changjiang River estuary , China : A personal perspective. *Geomorphology*, *121*(3–4), 133–151. https://doi.org/10.1016/j.geomorph.2010.04.021

Simpson, J. H., Brown, J., Matthews, J., & Allen, G. (1990). Tidal Straining, Density Currents, and Stirring in the Control of Estuarine Stratification. *Estuaries*, *13*(2), 125–132. https://doi.org/10.2307/1351581

Sistermans, P., & Nieuwenhuis, O. (2004). *WESTERN SCHELDT ESTUARY (THE NETHERLANDS)*.

Smolders, S., Plancke, Y., Bi, Q., Vanlede, J., & Kolokythas, G. (2019). A Sand Transport Model for the Scheldt Estuary : The 3D Scaldis Sand Model. *Conference Paper*.

Sosio, R., & Crosta, G. B. (2009). Rheology of concentrated granular suspensions and possible implications for debris flow modeling. *Water Resources Research*, *45*(3). https://doi.org/10.1029/2008WR006920

Speer, P. E., Aubrey, D. G., & Friedrichs, C. (1991). Nonlinear Hydrodynamics of shallow tidal inlet/bay systems. In *Nonlinear tidal interactions in shallow water* (pp. 321–339).

Stacey, M. T., Burau, J. R., & Monismith, S. G. (2001). Creation of residual flows in a partially stratified estuary. *Journal of Geophysical Research*, *106*(C8), 17,013-17,037.

Stacey, M. T., Monismith, S. G., & Burau, J. R. (1999). Observations of Turbulence in a Partially Stratified Estuary. *Journal of Physical Oceanography*, *29*, 1950–1970.

Svasek Hydraulics. (2013). *ZNSH, versterking en Onderhoud Kustdeel RSP17.00-RSP28.32*. Rotterdam.

Tee, K. T. (1976). Tide-induced residual current, a 2-D non-linear numerical tidal model. *Journal of Marine Research*, (34), 603–628.

Temmerman, S., Govers, G., Wartel, S., & Meire, P. (2003). Spatial and temporal factors controlling short-term sedimentation in a salt and freshwater tidal marsh, scheldt estuary, Belgium, SW Netherlands. *Earth Surface Processes and Landforms*, *28*, 739–755. https://doi.org/10.1002/esp.495

Ten Brinke, W. B. M. (1994). *De menging van marien en fluviatiel slib in het estuarine van de Schelde*.

Terwindt, J. H. J. (1967). Mud transport in the Dutch delta area and along the adjacent coastline. *Journal of Sea Research*, *3*(4), 505–531.

Tolhurst, T. J., Gust, G., & Paterson, D. M. (2002). The influence of an extracellular polymeric substance (EPS) on cohesive sediment stability. In J. C. Winterwerp & C. Kranenburg (Eds.), *Fine Sediment Dynamics in the Marine Environment* (pp. 409–425). Elsevier Science B.V.

Torfs, H., Mitchener, H., Huysentruyt, H., & Toorman, E. A. (1996). Settling and consolidation of mud / sand mixtures. *Coastal Engineering*, *29*, 27–45.

Toublanc, F., Brenon, I., Coulombier, T., & Le Moine, O. (2015). Fortnightly tidal asymmetry inversions and perspectives on sediment dynamics in a macrotidal estuary (Charente,. *Continental Shelf Research*, *94*, 42–54.

Uncles, R. J. (2002). Estuarine Physical Processes Research: Some Recent Studies and Progress. *Estuarine, Coastal and Shelf Science*, *55*, 829–856. https://doi.org/10.1006/ecss.2002.1032

Valle-Levinson, A. (2010). *Definition and classification of estuaries*. *Contemporary Issues in Estuarine Physics*. New York: Cambridge Univeristy Press.

Valle-Levinson, A. (2011). Large Estuaries (Effects of Rotation). In *Treatise on Estuarine and Coastal Science* (Vol. 2, pp. 123–140). Elsevier Inc. https://doi.org/10.1016/B978-0-12-374711-2.00208-4

Valle-levinson, A., & Li, C. (2000). Convergence of lateral flow along a coastal plain estuary. *Journal of Geophysical Research*, *105*(C7), 17,045-17,061.

Van Buuren, A., & Gerrits, L. (2008). Understanding and managing a complex estuary: the process towards more congruence between the physical system characteristics and the management system of the Westerschelde (Netherlands). *Hydrology and Earth System Sciences Discussions*, *5*. https://doi.org/10.5194/hessd-5-1371-2008

Van de Kreeke, J., & Robaczweska, K. (1993). Tide-induced residual transport of coarse sediment; application to the ems estuary. *Netherlands Journal of Sea Research*, *31*(3), 209–220.

Van den Neucker, T., Verbessem, I., De Belder, W., De Regge, N., Soors, J., & Van Den Bergh, E. (2007). *Overzicht analyseresultaten van de sedimentkarakteristieken langs de Zeeschelde en haar zijrivieren (1999 tot september 2005). INBO.IR.2007.30*.

Van der Werf, J., & Brière, C. (2014). *The influence morphology on tide and sand transport in the Scheldt Estuary. Report I/RA/11387/13.082/GVH*.

Van der Werf, J., Van Oyen, T., De Maerschalck, B., Nnafie, A., Van Rooijen, A., Taal, M., … Van der Wegen, M. (2015). MODELING THE MORPHODYNAMICS OF THE MOUTH OF THE SCHELDT ESTUARY. *E-Proceedings of the 36th IAHR World Congress, 28 June – 3 July, 2015, The Hague, the Netherlands*, 80–86.

Van Eck, B. (1999). *de Scheldeatlas: een beeld van een estuarium*. Zierikzee: LnO.

Van Kessel, T. (1997). *Generation And Transport Of Subaqueous Fluid Mud Layers*. TU Delft.

van Kessel, T., Spruyt-de Boer, A., van der Werf, J., Sittoni, L., van Prooijen, B., & Winterwerp, H. (2012). Bed module for sand-mud mixtures. *Report in Framework of BwN Project NTW 1.3 Mud Dynamics (Nr 1200327-000-ZKS-0013)*, 129.

Van Kessel, T., & Vanlede, J. (2010). *Impact of harbour basins on mud dynamics Scheldt estuary in the framework of LTV*.

Van Kessel, T., Vanlede, J., & Bruens, A. (2006). Development of a mud transport model for the Scheldt estuary in the framework of LTV: phases 1 and 2, (August).

Van Kessel, T., Vanlede, J., & de Kok, J. (2011). Development of a mud transport model for the Scheldt estuary. *Continental Shelf Research*, *31*(10 SUPPL.), S165–S181. https://doi.org/10.1016/j.csr.2010.12.006

Van Kessel, T., Vanlede, J., Kuijper, K., & de Kok, J. (2007). *Further development and first application of a mud transport model for the Scheldt estuary. LTV Framework. Phase 2. Raport: Z4375*.

Van Ledden, M. (2003). *Sand-mud segregation in estuaries and tidal basins*. Delft University of Technology.

Van Ledden, M., Van Kesteren, W. G. M., & Winterwerp, J. C. (2004). A conceptual framework

for the erosion behaviour of sand – mud mixtures. *Continental Shelf Research*, *24*, 1–11. https://doi.org/10.1016/j.csr.2003.09.002

Van Leussen, W. (2011). Macroflocs, fine-grained sediment transports, and their longitudinal variations in the Ems Estuary. *Ocean Dynamics*, *61*, 387–401. https://doi.org/10.1007/s10236-011-0384-9

Van Prooijen, B. C., & Winterwerp, J. C. (2010). A stochastic formulation for erosion of cohesive sediments. *Journal of Geophysical Research*, *115*(C01005). https://doi.org/10.1029/2008JC005189

Van Rijn, B. W. F. (2012). *INFLUENCE OF WAVE CLIMATE SCHEMATISATION ON THE SIMULATED MORPHOLOGICAL DEVELOPMENT OF THE WESTERN SCHELDT ENTRANCE*. Delft University of Technology.

Van Rijn, L. C. (2011a). Analytical and numerical analysis of tides and salinities in estuaries; part I: tidal wave propagation in convergent estuaries. *Ocean Dynamics*, (61), 1719–1741. https://doi.org/10.1007/s10236-011-0453-0

Van Rijn, L. C. (2011b). *Tidal Phenomena in the Scheldt Estuary , part 2. Document: 1204410-000-ZKS-0001*.

Van Rijn, L. C. (2016). *Fluid mud formation*.

Van Rijn, L. C. (2017). *Basics of Channel Deposition/Siltation*. Retrieved from http://www.albayan.ae

Van Rijn, L. C., Nieuwjaar, M. W. C., Van der Kaay, T., Nap, E., & Van Kampen, A. (1993). Transport of fine sands by currents and waves. *Journal of Waterway, Port, Coastal, and Ocean Engineering*, *119*(2), 123–143.

Van Straaten, L. M. J. U., & Kuenen, H. (1958). Tidal action as a cause of clay accumulation. *Journal of Sedimentary Petrology*, *28*(4), 406–413.

Vandenbruwaene, W., Levy, Y., Plancke, Y., Vanlede, J., Verwaest, T., & Mostaert, F. (2017). *Integraal plan Boven- Zeeschelde: Deelrapport 8 – Sedimentbalans Zeeschelde, Rupel en Durme. Versie 4.0. WL Rapporten, 13_131_8.*

Vanlede, J., Delecluyse, K., Primo, B., Verheyen, B., Leyssen, G., Plancke, Y., … Mostaert, F. (2015). *Verbetering randvoorwaardenmodel: Deelrapport 7: Afregeling van het 3D Scheldemodel. Version 2.1. WL Rapporten, 00_018.*

Vanlierde, E., Ferket, B., Michielsen, S., Vereycken, K., Levy, Y., Plancke, Y., … Mostaert, F. (2014). *MONEOS - jaarboek monitoring WL 2014: Factual data rapportage van monitoring hydrodynamiek en fysische parameters zoals gemeten door WL in het Zeescheldebekken in 2014. Versie 4.0. WL Rapporten, 12_070.*

Verlaan, P. A. J. (1998). *Mixing of marine and fluvial particles in the Scheldt estuary*. Technische Universiteit Delft.

Verlaan, P. A. J. (2000). Marine vs fluvial bottom mud in the Scheldt Estuary. *Estuarine, Coastal and Shelf Science*, *50*, 627–638. https://doi.org/10.1006/ecss.1999.0599

Wang, Z. B., Jeuken, M. C. J. L., & De Vriend, H. J. (1999). *Tidal asymmetry and residual transport in estuaries. A literature study and applications to the Western Scheldt*.

Wang, Z. B., Jeuken, M. C. J. L., Gerritsen, H., De Vriend, H. J., & Kornman, B. A. (2002). Morphology and asymmetry of the vertical tide in the Westerschelde estuary. *Conti*, *22*, 2599–2609.

Wartel, S. (1977). Composition, transport and origin of sediments in the Scheldt estuary.

Geologie En Mijnbouw, *56*, 219–233.

Wartel, S., & van Eck, G. T. M. (2000). *Slibhuishouding van het Schelde Estuarium. C-14046*.

Winant, C. D. (2007). Three-Dimensional Tidal Flow in an Elongated, Rotating Basin. *Journal of Physical Oceanography*, *37*, 2345–2362. https://doi.org/10.1175/JPO3122.1

Winterwerp, J. C. (1999). *On the dynamics of high-concentrated mud suspensions*. TU Delft. Retrieved from http://www.narcis.nl/publication/RecordID/oai:tudelft.nl:uuid:0b503064-91ad-48de-8174-761c315f8132

Winterwerp, J. C. (2013). *On the response of tidal rivers to deepening and narrowing*.

Winterwerp, J. C., Van Kesteren, W. G. M., Van Prooijen, B. C., & Jacobs, W. (2012). A conceptual framework for shear flow – induced erosion of soft cohesive sediment beds. *Journal of Geophysical Research*, *117*(C10020). https://doi.org/10.1029/2012JC008072

Winterwerp, J. C., Wang, Z. B., Stive, M. J. F., Arends, A., Jeuken, M. C. J. L., Kuijper, C., & Thoolen, P. M. C. (2001). A new morphological schematization of the Western Scheldt Estuary, The Netherlands. *2nd IAHR Symposium on River Coastal and Estuarine Morphodynamics, Obihiro, Japan*, 525–533.

Winterwerp, J. C., Wang, Z. B., Van der Kaaij, T., Verelst, K., & Bijlsma, A. (2006). Flow velocity profiles in the Lower Scheldt estuary Flow velocity profiles in the Lower Scheldt estuary. *Ocean Dynamics*, (56), 284–294. https://doi.org/10.1007/s10236-006-0063-4

Wollast, R. (1988). *The Scheldt Estuary*. (W. Salomons, B. L. Bayne, E. K. Duursma, & U. Fornster, Eds.), *Pollution of the North Sea*. Berlin, Heidelberg, New York: Springer-Verlag.

Wong, K. (1994). On the nature of transverse variability in a coastal plain estuary. *Journal of Geophysical Research*, *99*(C7), 14,209-14,222.

Young, R. N., & Southard, J. B. (1978). Erosion of fine-grained marine sediments: Sea-floor and laboratory experiments. *Geological Society of American Bulletin*, *89*, 663–672.

Yu, Q., Flemming, B. W., & Gao, S. (2011). Tide-induced vertical suspended sediment concentration profiles : phase lag and amplitude attenuation, 403–410. https://doi.org/10.1007/s10236-010-0335-x

Yu, Q., Wang, Y., Gao, J., Gao, S., & Flemming, B. W. (2014). Turbidity maximum formation in a well-mixed macrotidal estuary: The role of tidal pumping. *Journal of Geophysical Research: Oceans*, *119*, 7705–7724. https://doi.org/10.1002/2014JC010228.Received

Yuanyang, W., Roelvink, D., Weihua, L., Dingman, Q., & Fengfeng, G. (2014). Geomorphology Observation and modeling of the storm-induced fl uid mud dynamics in a muddy-estuarine navigational channel. *Geomorphology*, *217*, 23–36. https://doi.org/10.1016/j.geomorph.2014.03.050

Zhang, X., Zhang, T., Zhou, P., Shao, Y., & Gao, S. (2017). Validation analysis of SMAP and AMSR2 soil moisture products over the United States using ground-based measurements. *Remote Sensing*, *9*(104), 1–26. https://doi.org/10.3390/rs9020104

Zimmerman, J. T. F. (1978). Dispersion by tide-induced residual current vortices. In J. C. J. Nihoul (Ed.), *Hydrodynamics of Estuaries and Fjords* (pp. 207–216). Elsevier Scientific Publising Company.

Zimmerman, J. T. F. (1981). Dynamics, diffusion and geomorphological significance of tidal residual eddies. *Nature*, *290*, 549–555.

F. P. Bakker

Trench Siltation near the ETM of a Well-mixed Estuary

Master Thesis Report - Appendices

Trench Siltation near the ETM of a Well-mixed Estuary

Master Thesis Report - Appendices

By

F. P. Bakker

Thesis committee:	Prof. Dr. Ir. S. G. J. Aarninkhof,	TU Delft, Chairman
	Prof. Dr. Ir. Z. B. Wang,	TU Delft, Deltares
	Dr. C. Chassagne,	TU Delft
	Ir. A. Hendriks,	Boskalis

Version	1.0
Date	27th of February 2020

TU Delft Boskalis

Content

Appendix A. Sediment transport and trapping mechanisms

In this appendix, the estuarine sediment transport and trapping mechanisms, which are captured in the schematic overview (see Figure 16), concluding the theoretical framework (see Chapter 2), are discussed in detail. The schematic is believed to give an overview of all state-of-the-art identified processes and mechanism which may play a role in the sediment supply within an estuary.

A.1 Macro-scale mechanisms

Macro-scale mechanisms in an estuary can be subdivided in barotropic and baroclinic processes. The barotropic processes are the assembly of interactions between fine sediment particles and the hydrodynamics of constant water density, whereas turbidity caused by baroclinic processes is related to the interaction between the fresh water discharge and the asymmetrically incoming tidal wave of salty sea water (Van Maren, Van Kessel, Cronin, & Sittoni, 2015). Both processes and their related mechanisms are treated separately in the below.

A.1.1 Barotropic processes

Barotropic processes are defined as interactions between fine sediment and the (tidal) motion of water in which density variations are unimportant. Well-known barotropic mechanisms are velocity asymmetry, such as peak-velocity asymmetry, residual currents (Stokes' drift, river discharge, circulation currents), lag effects (settling, scour, etc.), and resuspension by short-crested waves (Allen et al., 1980; Burchard et al., 2018; Friedrichs et al., 1998; Uncles, 2002).

Barotropic processes are important in inducing residual currents, and subsequent sediment trapping, and in affecting the gross sediment transport fluxes. They move the ETM up- and downstream with the tide. Increasing flood currents over a mud reach increase the turbidity in landward direction, while increasing ebb currents increase the turbidity again in seaward direction. This oscillation is not symmetrical, given that the upstream migration is mostly more pronounced than the downstream one. In addition, the two SSC peaks around both high water slack tide (for locations upstream of the ETM) and low water slack tide (for locations downstream of the ETM) slack tide are not identical: upstream of the ETM the peaks are higher and narrower than downstream of the ETM, and the troughs between the two upstream peaks being less pronounced than between the downstream ones. This is a consequence of the funnel-shaped geometry of an estuary (Friedrichs et al., 1998; Yu et al., 2014). Furthermore, high river discharges may push the ETM and its muddy bed reach downstream, reducing the magnitude of the ETM due to a larger cross-section, given a converging estuary (Friedrichs et al., 1998; Uncles, 2002).

Tidal amplification

Suspended sediment concentrations are dependent on the magnitude of the tidal current, which is related to the propagation of the tidal wave. An important feature of a tidal wave is its range, which may show variations over the estuary. The tidal range is affected by four processes (Van Rijn, 2011):

- Inertia related to acceleration and deceleration effects

- Rate of convergence of the planform of the estuary in landward direction
- Damping due to bottom friction
- Partial reflection at the landward end and sides of the estuary

Friedrichs & Aubrey (1988) found that especially the latter three processes are dominant for tidal range amplification/damping throughout an estuary, although inertia may be important at the landward end of the estuary (tidal wave reflection) and for tidal waves with strong asymmetry, as will be discussed in the next subsection. Also river discharge (through convective acceleration which slows down the incoming tidal wave and amplifies the reflected wave) and tidal flats adjacent to the main channel (loss of momentum of both the rising and falling tide) contribute to this nonlinearity. If in an estuary the effect of the rate of convergence is stronger than the damping of the tidal wave, the tidal range is amplified, while for the reverse, the tidal amplitude is dampened.

Following the derivation of Van Rijn (2011), which considers the horizontal energy balance for wave propagation, taking into account the friction, caused by bed shear stress, and the flux of transferred energy to the fluid of rest in front of the wave, a dimensionless parameter can be derived which gives the first order estimate (for only one tidal component) of tidal amplification or damping for a converging estuary:

$$\alpha_H = \frac{3\pi(\beta+\gamma)C^2 H h \cos(\varphi)}{16\bar{u}^2}$$

If this parameter exceeds unity, the tidal wave is amplified. The tidal wave is damped if the parameter is below unity.

Based on analytical solutions of simplified equations of continuity and momentum (linearized friction, horizontal bottom slope, and exponentially converging estuary, no convective acceleration), another dimensionless parameter can be constructed (Van Rijn, 2011):

$$\alpha_H = \frac{\beta}{2\mu}, \qquad \beta = \frac{1}{L_b}$$

$$\mu = (2)^{-0.5} k_0 \left[-1 + \left(\frac{0.5\beta}{k_0}\right)^2 + \left\{ \left(-1 + \left(\frac{0.5\beta}{k_0}\right)^2 \right)^2 + \left(\frac{m}{\omega}\right)^2 \right\}^{0.5} \right]^{0.5}$$

where m is the linearized Lorentz damping parameter:

$$m = \frac{8g|\bar{u}|}{3\pi C^2 R} \cong \frac{8g|\bar{u}|}{3\pi C^2 h_0}$$

For strongly converging estuaries, a propagative tidal wave shows the behavior of a (partially) standing wave, since it is constantly partially reflected by the sides of the estuary due to its steadily converging width and the landward end. However, the reflected wave is generally not strong since it moves in opposite direction (divergent estuary) and hence quickly damps out. Furthermore, the wave propagation velocity may be greater than predicted by the classical wave theory (Van Rijn, 2011).

Stokes' Drift

One of the mechanisms is called Stokes' drift. This is the mass flux associated with tidal propagation of an (at least partly) progressive tidal wave. It is dependent on the tidal water level and velocity amplitude, their relative phase shift, and the water depth. For a (partly) progressive wave the phase shift between the elevation and velocity is smaller than 90 degrees, resulting in net inflow of water. In most estuaries Stokes' drift is stronger at the mouth of an estuary, since the tidal wave is generally more propagative at this location. More landward the tidal wave might be reflected to locally become a more standing wave.

Furthermore, the tidal amplitude/velocity is generally greater at the inlet (Guo, Van der Wegen, Roelvink, & He, 2014; Li & O'Donnell, 1997; Wang et al., 1999).

The first order magnitude of Stokes' drift is dependent on the phase coupling between the horizontal and the vertical tide and their individual amplitudes. Hence, the longitudinal residual current due to Stokes' drift can be estimated through:

$$u_{r,S} = \frac{H\hat{u}cos(\varphi)}{4h}$$

The mass flux is compensated by an opposing outgoing flow, which is generated by a pressure gradient due to water set-up, shown by an increasing residual mean elevation landward. This gradient is approximately uniform (laterally independent) across the channel and, for most estuaries, stronger at the inlet. Therefore, there is generally a stronger seaward return flow at the mouth. The interaction between the Stokes' return flow and tides can cause a net seaward residual sediment transport (Li & O'Donnell, 1997; Wang et al., 1999). The residual current caused by this term can be estimated by:

$$u_{r,p} = -\frac{3\pi C^2 h}{8u}\frac{\partial \zeta}{\partial x} \approx -\frac{3\pi C^2 h}{8u}\frac{\Delta \zeta}{\Delta x}$$

Another, mostly less important, horizontal residual current mechanism is non-linear advection in the longitudinal direction. The residual current can be calculated according to (Li & O'Donnell, 1997):

$$u_{r,a} = -\frac{3\pi C^2 h}{8gu}\left(u\frac{\delta u}{\delta x} + v\frac{\delta u}{\delta y}\right) \approx -\frac{3\pi C^2 h}{8gu}\left(u\frac{\delta u}{\delta x}\right)$$

Longitudinal circulation: peak-velocity (duration) asymmetry

Peak-velocity asymmetry is given as the difference in magnitude between the average peak flood and consecutive average peak ebb tidal velocity. Since sediment transport is proportional to the bed shear stress (the square of the current velocity), peak-velocity asymmetry might result in a net sediment transport in the direction of the maximum tidal velocities. This may lead to import or export of medium and coarse sediments, known as flood-dominance and ebb-dominance respectively. Also, the equilibrium suspended sediment concentration is dependent on the bed shear stresses. Peak-velocity asymmetry, therefore, may create asymmetry in the equilibrium concentration and a possible subsequent net transport of fine sediments throughout the estuary.

Peak-velocity asymmetries are generated through so-called overtides and compound tides of the pure astronomical tide. This astronomical tide is solely generated by attraction forces of the earth, moon and sun, consisting of semi-diurnal components, such as M2 and S2. These semi-diurnal tidal waves are not necessarily the same height, since there is daily inequality generated by the declinations of the moon and sun. Furthermore, there are diurnal components, such as K1 and O1, which are a consequence of the interaction between the attraction forces and the continents. Since, these (semi-)diurnal components typically slightly differ in frequency, a fortnightly cycle may be generated, known as a spring-neap cycle.

In shallow areas, however, such as seas and estuaries, there is deformation of the tidal wave, as it propagates. This is explained by the difference in wave celerity between the flood and ebb tidal wave, as the tidal wave celerity is proportional to the water depth. It results in an slowly increasing asymmetry of the tidal wave from the estuary mouth. Also contributing to the strength of the deformation of the tidal wave are the length of the estuary and amount of induced (non-linear) friction. For a propagative wave in a prismatic channel, the ebb tide experiences more friction than flood tide, since the water depth is lower during ebb tide (Dronkers, 1986).

Whether the high or low water propagates faster through the estuary depends on the basin hypsometry and relative tidal amplitude. Relative shallow estuaries with small intertidal flats (concave profiles) tend to be flood-dominant, while estuaries with relatively more intertidal flats and deep channels (convex profiles) tend to be ebb-dominant (Boon & Byrne, 1981; C. Friedrichs & Aubrey, 1988; Speer, Aubrey, & Friedrichs, 1991).

Given a schematized trapezoidal cross-section, Speer and Aubrey (1985) derived the following equation which identifies the transition between flood and ebb dominance of the vertical tide, using the simplified one dimensional mass and momentum equations:

$$\frac{V_s}{V_c} = \frac{2\frac{H}{h} + \frac{8}{3}\frac{\left(\frac{H}{h}\right)^2}{1-\frac{H}{h}}}{\frac{3}{4} + \frac{1}{4}\frac{H}{h}}$$

For the horizontal tide the transition is described by:

$$\frac{V_s}{V_c} = \frac{2\frac{H}{h} + \frac{8}{3}\frac{\left(\frac{H}{h}\right)^2}{1-\frac{H}{h}}}{\frac{3}{4} + \frac{1}{4}\frac{H}{h}} \cdot \frac{1+\frac{H}{h}}{1-\frac{H}{h}}$$

In order to get a first insight in the importance of peak-velocity asymmetry in the estuary, the latter equation can be made dimensionless through:

$$\alpha_{u,asym} = V_c V_s^{-1} \frac{2\frac{H}{h} + \frac{8}{3}\frac{\left(\frac{H}{h}\right)^2}{1-\frac{H}{h}}}{\frac{3}{4} + \frac{1}{4}\frac{H}{h}} \cdot \frac{1+\frac{H}{h}}{1-\frac{H}{h}}$$

If this parameter exceeds unity, the horizontal tide shows flood dominancy. Ebb dominance is present if the parameter is below unity. There is no asymmetry in the peak-velocities if the parameter equals unity.

Furthermore, Li & O'Donnell (1997) showed that the relative length of the estuary with respect to the wave length, the degree of convergence of the width of the estuary and the ratio of the tidal period and the decay time scale due to friction may influence tidal asymmetry.

Both the horizontal as the vertical tide may display asymmetry (Wang et al., 1999):

- Horizontal tide:
  The average peak flood current may be greater than the average peak ebb current (or vice versa), leading to flood-dominance (or ebb-dominance). This is called skewness of the horizontal tide.
- Vertical tide:
  The rising period and falling period of the tide are not equal. This is known as saw-tooth asymmetry of the vertical tide.

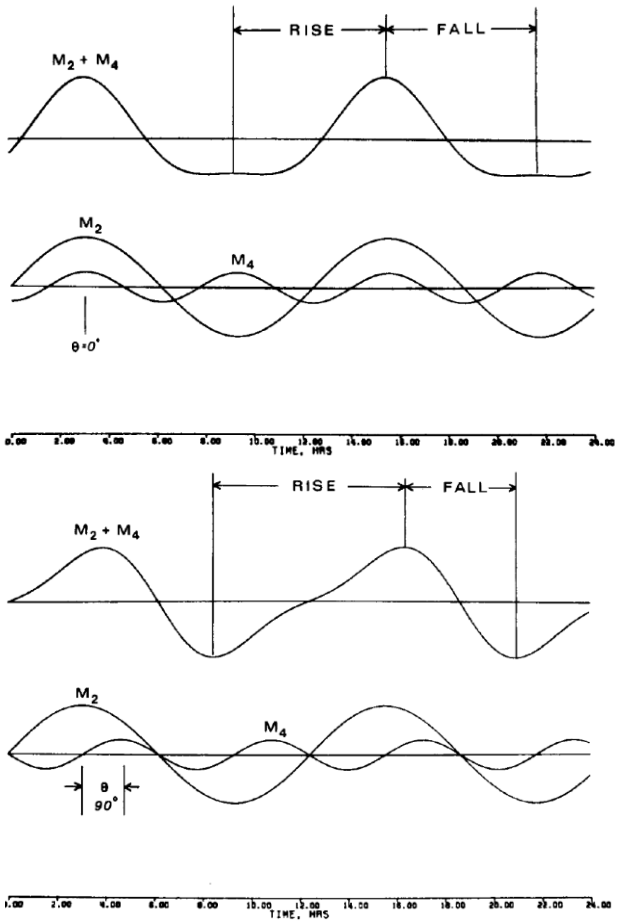

Figure 60 – Tidal Asymmetry. Left: acceleration asymmetry of the vertical tide; Right: Peak-velocity asymmetry of the vertical tide (Boon & Byrne, 1981)

There is a link between the horizontal and vertical tide. An asymmetric vertical tide will lead to asymmetry in the horizontal tide. It is however a non-linear relationship, since it is dependent on the geometry of the estuary, namely the storage width and cross-sectional area (friction), and phase shift between both tides. This might result in a different amplitude ratio and relative phase shift between tidal constituents in the horizontal tide with respect to the vertical tide. Therefore, the strength of the asymmetry of both tides might differ. The asymmetry may become more pronounced upstream the estuary (Wang et al., 1999).

Mathematically, tidal distortion and asymmetry can be described by the inclusion of higher harmonics, which contain tidal periods that do not originate from astronomical forcing, but form integer fractions of the periods of the basic astronomical constituents. Two important sources for non-linearity in the tidal propagation are bottom friction and continuity and advective acceleration, generating M3 and M6, and M4 and M8 tides for a M2 tide respectively (see Figure 60). These higher harmonics are called overtides or shallow-water tides. Depending on their relative phase shift, interactions of tidal constituents with its generated overtides may create asymmetrical current velocity signals around the horizontal axis, hence tidally-averaged net transport terms (Speer et al., 1991).

For example, Van de Kreeke and Robaczewska (1993) found that interaction of the M2 and M4 tide results in net transport of medium to coarse sediment, depending on their phase shift. Flood dominant systems were found for a phase shift between -90 to 90 degrees between these constituents, while there was ebb dominancy for a phase shift between 90 to 270 degrees. Interaction of the M2 and M6 tides was found not to result in a net transport, while the phase shift between the M4 tide and the M6 tide relative to the phase of the M2 tide also contributes to a net transport (Van de Kreeke & Robaczweska, 1993). For the vertical tide a

phase shift between M2 and M4 of 0 to 180 degrees results in flood dominancy, while a phase shift between 180 and 360 degrees results in ebb dominancy (Speer et al., 1991).

Furthermore, compound tides are generated through the interaction of tidal constituents with other constituents. Especially the interaction between M2 and N2 and S2, respectively resulting in compounds constituents MN4 and MS4, can reach significant amplitudes. Complex interactions between the semi-diurnal parent tides and forced quarter-diurnal constituents, such as M2, N2 and MN4 ($\phi_{M2} + \phi_{N2} - \phi_{MN4}$) and M2, S2 and MS4 ($\phi_{M2} + \phi_{S2} - \phi_{MS4}$) arise. These reinforce the tidal asymmetry imparted by the M2 and M4 constituents ($2\phi_{M2} - \phi_{M4}$), having approximately the same phase shift. The interactions include linear ones between different tidal constituents, such as between the M2-O1-K1 tides, as well. Likewise, these are also able to generate tidal residual sediment transport (Sassi & Hoitink, 2013). It is however known that compound tides, resulting in asymmetry, can be represented by the phase difference between the M2 and the M4 constituents only (Speer et al., 1991; Wang et al., 1999).

The tidal asymmetry can also be reinforced by externally generated tidal asymmetry in the adjacent sea, which makes tidal asymmetry more effective (Uncles, 2002). Furthermore, tidal asymmetry is time-dependent, since tidal constituents interact with each other at periods larger than a tidal cycle (e.g. spring-neap cycle). Varying tidal wave heights, hence varying storage and friction, can alter the tidal asymmetry. This is depending on the hypsometry of the estuary (Toublanc et al., 2015; Wang et al., 1999).

Tidal asymmetry could also differ transversally. Intertidal flats, for example, only experience part of the tidal wave, namely at high water. Depending on the progressivity of the tidal wave (the amount the high slack water lags the flood currents), and also depending on the tidal asymmetry or residual currents of the estuary, (more) flood dominancy occurs on those flats. Therefore, typically faster and longer lasting flood tidal currents are found on the flats with respect to the tidal channel. This is called tidal rectification. Tidal rectification is stronger near the mouth of an estuary, where the tidal wave is generally more propagative (Bowers & Al-Barakati, 1997).

River Flow

Rivers enhance river-supplied sediment seaward (Garel, Pinto, Santos, & Ferreira, 2009). Rivers therefore tend to enhance ebb dominance. This river-induced asymmetry is dependent on the strength of both river discharge and tide. It is found that river-induced asymmetry cannot be neglected if the ratio between the tidal mean discharge and the mean river discharge is greater than 20. This can be translated to the following dimensionless factor (Sassi & Hoitink, 2013):

$$\alpha_r = \frac{u_t}{20u_r}$$

If this factor is greater than one, tidal discharge dominates river discharge, while if the ratio is below one, river discharge dominates. The threshold value of 20 may differ per estuary (Sassi & Hoitink, 2013). This is because river also tend to damp the incoming tidal wave through enhancement of tidal friction by the river discharge, thereby removing tidal wave reflection at the landward end (Godin, 1984; Sassi & Hoitink, 2013). The importance of this mechanism can be estimated through the dimensionless ratio of the contributions to the subtidal friction of both river-tide interaction and river discharge (Buschman et al., 2009):

$$\alpha_{rt} = \frac{S_{rt}}{S_r} = \frac{3bu_r u_t^2}{2(au_r + bu_r^3)}$$

Again, if this parameter exceeds unity, river discharge is important in the damping of the tidal wave, while if this parameter is below unity, river discharge can be considered unimportant in the damping of the tidal wave. A stronger river discharge does not necessarily result in ebb-

dominancy of the system through an increased seaward sediment transport, since the net transport of sediment is also dependent on the hypsometry of the estuary, degree of flood tidal asymmetry and sediment availability. The river-induced asymmetry can be a dominant mechanism when the residual currents are small compared to the tidal currents (Guo et al., 2014).

Wind

Residual circulation in an estuary may also be created by wind stress. Landward wind tends to induce down wind currents on the shallower parts of the estuary, which cause a water level set-up. The resulting surface-slope induces a pressure gradient, which generates an up-wind current in the deeper channels of the estuary. This is because wind tends to induce larger currents in shallower areas in the estuary and deeper waters have larger inertia (respond slower to forcing). The described pattern reverses for seaward directed wind. Furthermore, the enhancement of seaward-directed residual currents over the subtidal channel during landward directed wind is greater than the enhancement of landward-directed residual currents for seaward directed wind. This is explained by the fact that the return current due to set-up is less effective for seaward directed wind, since water is escaping through the inlet (Csanady, 1973, 1980; Hunt, Bryan, & Mullarney, 2015; Mathieu, Deleersnijder, Cushman-Roisin, Beckers, & Bolding, 2002). Assuming an infinite long channel with idealized bathymetry, the maximum and minimum residual currents due to wind can be estimate through:

$$u_{r,w} = \frac{\sigma h \rho_{air} C_D U_{10}^2}{v}\left(\frac{3}{4}\sigma\frac{h}{h_*} - \frac{3}{2}\frac{h}{h_*} + 1\right)$$

in which:

$$h_* = \frac{\int_0^b h^3 dy}{\int_0^b h^2 dy}$$

Horizontal Residual Currents

Tides may generate residual currents through (Tee, 1976):

- nonlinear bottom friction,
- the non-linear terms in the continuity equation;
- the nonlinear advective terms in the momentum equation (inertia)

In an estuary, the various mechanisms can be identified, which are described separately in the below.

Bathymetry-Induced Residual Currents

Based on observations of various estuaries it was found that in different parts of an estuary there are residual currents which may be directed in opposite direction within a cross-section due to depth differences (Kjerfve & Proehl, 1979; Zimmerman, 1981). In principle, these bathymetry-induced residual currents are caused by two mechanisms: Stokes' drift and its counterbalancing residual pressure gradient. Stokes' drift is inversely proportional to the water depth due to stronger non-linearity in shallower water.

The importance of Stokes' drift as horizontal residual circulation mechanism can be estimated by averaging the second-order shallow water equations, as derived by Li and O'Donnell (1997) through Fourier decomposition. The following term arises:

$$u_{r,S} = 2\frac{\overline{\zeta u}}{h}$$

If we consider a short channel, where the wave is close to a standing wave, this term can be approximated to the first order as:

$$u_{r,S} = 2\frac{\overline{\zeta u \sin(\omega t)\cos(\omega t - \varphi)}}{h}$$

where phase shift, φ, is a function of the depth. The phase shift between the vertical and horizontal tide is 90 degrees on average, but decreases with increasing depth within the cross-section. Hence, for short channels, the residual Stokes' drift is directed landward in the channel, and seaward at the shoals (Li & O'Donnell, 2005).

On the contrary, for long channels with a (partly) propagative tidal wave, the residual velocity term for Stokes' drift can be approximated to the first order as:

$$u_{r,S} = 2\frac{\overline{\zeta u \sin(\omega t)\sin(\omega t - \varphi)}}{h}$$

Generally, close to the mouth, the tidal wave is more propagative than landward. Hence, there is landward residual flow on the shoals and seaward residual flow in the channel at the mouth, while the reverse occur close to the landward end, where the tidal wave is more a standing wave (Li & O'Donnell, 2005). This is depicted in Figure 61.

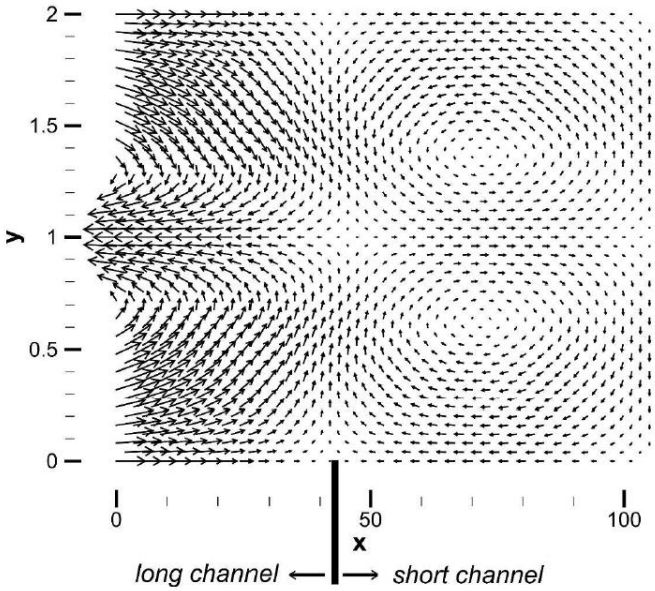

Figure 61 – Bathymetry-induced residual flow depending on the channel length (Li & O'Donnell, 2005)

Furthermore, tidal propagation over shoals may generate residual currents due to residual eddies. Shoals increase the hydraulic roughness, thereby decreasing the tidal velocity over it. This results in vorticity, which first order, averaged over the tide, does not result in a residual current eddy, as the longitudinal gradient reverses during a tidal cycle. However, nonlinear advection results, given the situation in Figure 62, in an clockwise and counter-clockwise residual current eddy over the shoal during flood and ebb respectively. Eddy formation is balanced by mainly topographic and frictional vorticity. Centrifugal accelerations may enhance eddy formation by causing an water level depression, which is greatest at the tip of the shoal. This induces an acceleration when fluid particles move toward the shoal and a deceleration when fluid particles move away from the shoal. Maximum velocity is therefore near the tip of the shoal. Coriolis may enhance or counteract the residual current eddy vortices, depending on the direction of the flow (Park & Wang, 2000; Zimmerman, 1978, 1981).

This non-linear (differential) advection effect, as described by Zimmerman (1981) (explained in the following subsection about geometry-induced residual currents), also contributes to the tide-induced residual current, but is believed to be small compared to the two mechanisms (Li & O'Donnell, 1997; Wang et al., 1999). Non-linear advection effect by variation in lateral bathymetry can be approximated to the first order by (Li & O'Donnell, 1997):

$$u_{r,a} = -\frac{3\pi C^2 h}{8gu}\left(u\frac{\delta u}{\delta x} + v\frac{\delta u}{\delta y}\right) \approx -\frac{3\pi C^2 h}{8gu}\left(v\frac{\delta u}{\delta y}\right)$$

Geometry-Induced

Also headlands and hydraulic structures, such as groynes, can result in residual current eddies. Again, this is a consequence of a net generated vorticity by nonlinear (vorticity) advection. These vorticities are counter-acted by topographic vorticity and in a smaller amount by frictional vorticity. Nonlinear advection is caused by the subsequent acceleration and deceleration of the tidal flow, which may lead to inertia dominated flow. A friction boundary layer develops, diminishing the current velocity towards the side. For a situation as schematized in Figure 62, net vorticity is produced with a maximum near the headland/structure. This results in a downstream net flux of clockwise vorticity out of the upper reach into the lower reach, which is equivalent to the situation during flood. The situation induces a vortex pair of opposite sign at both ends of the headland/structure, creating a residual eddy/current averaged over the tidal wave. Coriolis and centrifugal acceleration may enhance the residual current eddy vortices, while Coriolis, if working in opposite direction, may also counteract these vortices (Park & Wang, 2000; Zimmerman, 1978, 1981).

Curved tidal channels also tend to produce residual currents across the channel through opposing currents, forming residual eddies near the curvature of the channel. Counter-clockwise flows develop on the west side of the bend and clockwise flows on the east side of a southward bend for a tidal wave propagating eastward. These are largely generated by nonlinear advection momentum and in a smaller amount by the pressure gradient and nonlinear wave propagation (Li et al., 2008).

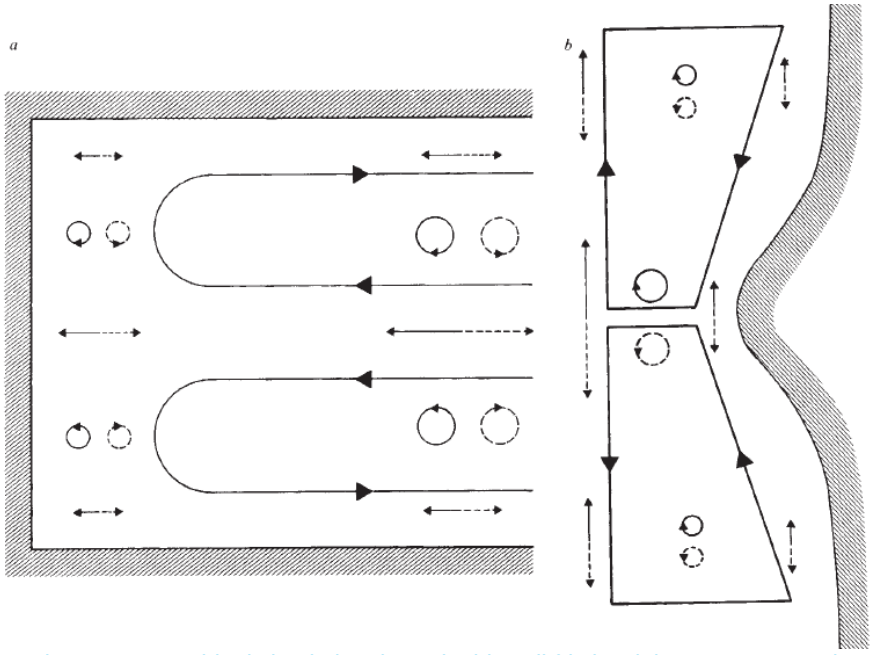

Figure 62 – Residual circulation through sidewall friction (Zimmerman, 1981)

Increased friction near closed sides of the estuary due to side friction result in lower tidal velocities at the sides with respect to the main channel(s) of the estuary. For a tidal wave propagating westward (see Figure 62), flood will lead to clockwise vortices at the northern side and counter-clockwise vortices at the southern side. On the contrary, ebb will induce counter-clockwise eddies at the northern side and clockwise vortices at the southern side. For a damped tidal wave, the velocity amplitude is decreasing in landward direction. Hence, more counter-clockwise eddies are leaving the basin at the north side of the estuary during ebb. This is equivalent to the generation of more clockwise current eddies. During flood, more clockwise vortices are entering the estuary. Similarly, at the southern side of the basin more counter-clockwise vortices are generated. Consequently, side friction generally results in a

residual ebb current on the north and south side of the estuary and a residual flood current in the estuary (Zimmerman, 1981).

Lateral Residual Currents

In bends or around headlands and shoals, curved streamlines occur, which pose a secondary residual circulation perpendicular to the main flow direction. Water particles in a curved streamline are prone to outward centrifugal forces, which strengthen with increasing current velocity and decreasing radii of curvature. The force is higher at the water surface, considering a logarithmic current velocity profile. A lateral water level gradient will depth-averagely balance the force through a pressure gradient, which has a uniform profile over depth. Due to the different depth-distribution of the forces, a circulation current pattern arises, which is directed to the outer bend at the surface and to the inner bend at the bed. Since the centrifugal forces are directed to the outer bend during both flood and ebb, a lateral residual current emerges through a tidal cycle (Nidzieko et al., 2009). Using the linear approximation of Kalkwijk and Booij (1984) the magnitude of the curvature-induced secondary flow can be estimated by:

$$v_{r,R} = 3\frac{|\bar{u}|h}{\kappa^2 R}m_b$$

in which:

$$m_b \approx \frac{m_1}{2} - \alpha m_1, \qquad m_1 = 3$$

with friction parameter α defined as:

$$\alpha = \frac{\sqrt{\frac{\tau_s}{\rho}}}{\bar{u}\kappa} = \frac{\sqrt{\frac{g}{C^2}u|u|}}{\bar{u}\kappa}$$

Coriolis induced circulation currents show the same behavior as curvature-induced circulation currents. However, in contrast to the centrifugal force, Coriolis is dependent on the propagation direction of the current. Hence, during flood, Coriolis is in opposite direction than during ebb. Coriolis may strengthen the curvature-induced circulation current, when directed in the same direction as the centrifugal forces, and weaken bend flow, when directed in the opposite direction. The relevance of lateral flows caused by the Earth's rotation can be determined by considering the ratio between the dynamical depth and the total water depth. If the total water depth is 4 times the dynamical depth, lateral circulation due to Coriolis is noticeable (Valle-Levinson, 2011). Hence, the following dimensionless parameter can be constructed:

$$\alpha_{r,Cor} = \frac{H}{4d} = \frac{H}{4\sqrt{\left(\frac{2v_z}{f}\right)}}$$

If this parameter exceeds unity, Coriolis may be important. Secondary flow due to Coriolis can be linearly approximated by (Kalkwijk & Booij, 1986):

$$u_{n,C} = \frac{3fh}{2\kappa^2}m_c$$

with:

$$m_c = \frac{m_1}{2} - \alpha m_1, \qquad m_1 = 3$$

Lag Effects

Another well-known barotropic process is the mechanism of fine sediments being prone to lag effects. This is because the relaxation timescales of erosion and sedimentation for which the suspended concentration approaches the equilibrium concentration are of the same order as

the tidal period. Therefore, suspended sediment concentration and subsequent transport is generally not in equilibrium with the current velocity. This is in contrast to medium to coarse sediments. In the remainder of this section, the different identified lag effect mechanisms are discussed (Wang et al., 1999). If the timescale of reaching the equilibrium concentration is in the same order as the tidal period, than lag effects are important for the sediment dynamics in the estuary. The following dimensionless parameter can be constructed:

$$\alpha_{lag} = \frac{10T_{eq}}{T}$$

If this parameter exceeds unity, lag effects for the suspended sediment may be present in the estuary. The equilibrium timescale is dependent on the considered mechanism. Important lag effect mechanisms are: acceleration/deceleration asymmetry, settling lag, threshold lag, scour lag and entrainment lag. These will separately be discussed in the below.

Acceleration/deceleration asymmetry

Asymmetry in the acceleration and deceleration, also (falsely) known as slack water asymmetry, is caused by asymmetry in the horizontal and vertical tide (see Figure 60) (Gatto et al., 2017; Wang et al., 1999):

- Horizontal tide:
  The velocity signal may be saw-tooth asymmetric around the vertical, which means that the rate at which the velocity changes between both consecutive slack waters is different for ebb and flood.
- Vertical tide:
  The high (low) water slack may be longer than the low (high) water slack duration due to skewness of the vertical tide. The longer the period of slack water, the more time suspended particles have to settle. Net transport of suspended sediment is therefore generally in the direction of the longest lasting slack water.

The larger the acceleration/deceleration, the larger the difference between the actual suspended sediment concentration and the equilibrium (Wang et al., 1999).

Although the asymmetry is present during whole the acceleration and deceleration period, this difference in concentration stems from the asymmetry in the slack water period. For example, if the slack water period at high water (HWS) lasts longer than at low water (LWS), strong sedimentation occurs after flood. Hence, averaged over the tidal cycle, fine sediment is transported landward. However, also the depth during HWS and LWS is important, since fine sediment needs time to settle. The effect of net landward transport in the example can be counterbalanced if during LWS the averaged depth is smaller than during HWS. Therefore, an indicative parameter to estimate whether acceleration/deceleration asymmetry can be found in the ratio between both slack water periods, scaled with relaxation timescale for sedimentation, T_{Se}, as will be discussed in the next subsection:

$$\alpha_{swa} = \frac{\frac{T_{2,slack}}{T_{Se}}}{\frac{T_{1,slack}}{T_{Se}}} = \frac{\frac{T_{2,slack}}{\overline{h_2}/w_s}}{\frac{T_{1,slack}}{\overline{h_1}/w_s}}$$

If this parameter is below one, acceleration asymmetry will tend to transport fine sediment in seaward direction, while if the parameter exceeds one, fine sediment will be transported in landward direction. There will be no worth mentioning net fine sediment transport direction if the parameter is close to one.

Settling Lag

Settling lag is the delayed particle deposition after the onset of settling. At the end of flood, the current gradually decreases in velocity and the suspended sediment load can no longer be retained in the water column: the local fluid velocity has fallen below the threshold for

deposition. This causes particles to drop out of the suspension to settle on the bed. However, this process takes some time, resulting in depositing particles to be carried landward with the slackening current. Therefore, particles settle at a location where, if the flow reverses at the onset of ebb, the water parcel that formerly carried the sediment particle is not strong enough to resuspend the particle. Consequently, the particle is picked up from the bed by a water parcel, originating from further upstream. Averaged over a tidal cycle, this does not lead to a net transport of suspended particles. This is presented in Figure 10a (Gatto et al., 2017; Postma, 1961; Van Straaten & Kuenen, 1958).

Settling lag both has a spatial and a local or temporal character. The advection of a single particle (in a Lagrangian Framework) can be classified as the spatial component of settling lag. Coexisting sub-mechanisms interacting with settling lag to possibly generate a net transport of suspended sediment are: velocity damping, bed-level variation and water-depth variation.

If hydrodynamic conditions are uniform in an estuary, the trajectory of the water parcel during flood mirrors the trajectory during ebb such that the settling lag does not lead to a net displacement of the particle. However, if there is damping of the velocity amplitude throughout the basin towards the landward end, the re-entrainment of particles during ebb tide is caused by a water parcel whose velocity amplitude is smaller than the water parcel that transported the particle landward. Repetition of this process over a sequence of tidal cycles results in a net landward transport of particles. This is presented in Figure 10b (Gatto et al., 2017; Pritchard & Hogg, 2003).

Bed-level variation throughout an estuary may also lead to net transport of suspended sediment. For example, if the water depth towards the mouth is greater than the water depth towards the landward end, settling lag effects reduce landward. This is because depositing particles have to settle less distance to the bed. Consequently, the pick-up of the particle at the onset of ebb is caused by approximately the same water parcel that transported the particle landward. Since lag effects are more effective closer to the mouth due to generally greater depths, the particle is re-entrained at the onset of flood by a water parcel located further seaward. This generally causes net seaward transport of suspended sediments, as can be seen in Figure 10c. The effect of bed-level variation is, however, twofold. If the mouth has a sufficient large depth, the particle will not settle at all at the estuary mouth and is transported by the same water parcel, promoting net landward displacement (Gatto et al., 2017; Van Straaten & Kuenen, 1958).

Furthermore, since the tidal wave is never a purely standing wave, the deposition threshold is attained at a lower water depth during ebb than during flood. This makes that the particle has to cover less vertical distance to settle during ebb, and hence settling earlier. Consequently the particle is resuspended by a water parcel, located more landward, enhancing landward transport, as depicted by Figure 10d (Gatto et al., 2017).

The deposition of material also has a time-dependent (local) component, governed by the many micro-scale processes, such as flocculation (see micro-scale mechanisms), which have a certain adaptation time (Gatto et al., 2017). In an Eulerian framework, both the spatial as the temporal characters have to be taken into account.

The typical time scale for sedimentation, representing settling lag, can be determined through:

$$T_{sed} = \frac{h}{w_s} = \frac{d + \zeta}{w_s}$$

Threshold Lag

Threshold lag or final settling lag, as was originally identified by Van Straaten and Kuenen (1958), is the mechanism of particles becoming trapped at a landward location. At this location the tidal currents are too weak to be able to resuspend the deposited material. This

mechanism becomes present when an erosion threshold is adopted. Since settling lag and its coexisting mechanisms are likely to enhance landward residual suspended sediment transport, where the velocity amplitude generally decreases, the time of re-entrainment at ebb tide will be progressively delayed each tidal cycle until the local flow velocity is not strong enough to lift the particle anymore. Exceedance of the erosion threshold is then only possible through waves, stronger spring tidal cycles and/or scour (Gatto et al., 2017; Van Straaten & Kuenen, 1958).

Scour Lag

Another lag effect is scour lag. Scour lag consists of the time taken by particles to be re-entrained at approximately the moment of flow reversal. The threshold for erosion is generally greater than the threshold for deposition due to the cohesive behavior of deposited fine sediment particles (as will be discussed in the section about process-oriented mechanisms) and the lower current velocities at near the bed. Consequently, considering a damped tidal wave in an estuary, a water parcel from a location even further landward is required to resuspend the particle (see Figure 10e). The smaller the particles, the greater the difference between the thresholds for erosion and deposition (Gatto et al., 2017; Van Straaten & Kuenen, 1958).

By assuming a perfect sinusoidal M2 signal for the tidal current velocity, the following simplified time scale for scour lag can be derived:

$$\mathrm{T_{scour}} = \frac{1}{\omega} abs\left[\sin^{-1}\left(\frac{\mathrm{U_e}}{\hat{u}}\right) - \sin^{-1}\left(\frac{\mathrm{U_d}}{\hat{u}}\right)\right]$$

Entrainment Lag

Entrainment lag is the time delay for particles to cross the bed-load layer and be lifted up in the water column after entrainment. This temporal entrainment is called re-dispersion. During this time the near-bed layer flow will dominate the movement of the particles. Depending on the coexisting mechanisms it may enhance or weaken landward directed transport. Entrainment lag can be equally important as settling lag. It has a time scale of approximately:

$$T_{mix} = \frac{h^2}{\varepsilon} = \frac{10h}{u^*} = \frac{10h}{\sqrt{\frac{c_f u|u|}{\rho}}}$$

Only for (very) small particles, the settling lag will dominate over entrainment lag (Dyer, 1995; Gatto et al., 2017; Nichols, 1992).

Small amplitude waves

In shallow waters, small locally generated waves may exert a bed shear stress, which may be in the same order as the bed shear stress generated by the tidal current (Le Hir et al., 2000). Wind waves are important in sediment transport processes due to stirring/mobilization of fines by orbital velocities. They keeps fine sediment in suspension. Waves, therefore, prevent deposition of sediment, which has a comparable effect as reducing the slack water period. Furthermore, small period waves have the potential to influence the sediment transport regime of intertidal areas (Green, Black, & Amos, 1997; Green, 2011). Moreover, wave-induced resuspension and subsequent transport through the estuary may contribute to the magnitude of the ETM or generate a separate ETM in the mouth of the estuary. Orbital velocities increase with amplitude and wave length, but decrease exponentially with increasing depth (Hunt et al., 2015).

The relative magnitude of the bed shear stresses due to tidal currents in the deeper intertidal areas and wave stirring in the shallower intertidal areas result either in import or export of fine sediment onto or from the flats. If the bed shear stress on the shallow intertidal flats due to waves is greater than on the deeper intertidal flats due to the tidal current, there will be

sediment export. For the reverse situation, however, there will be import of fine sediment. This mechanism is explained by a gradient in suspended sediment concentration which leads to advection of fine material. For a tide-only situation, the shallow intertidal flats generally show flood dominancy. Advection of sediment onto the flats is then likely to dominate, since shear stress is smaller than compared with the channel (Hunt et al., 2015).

There exist a non-linear feedback between wave-enhanced bed shear stress, wind circulation, estuary morphology and the resultant tidal asymmetry. As waves are not likely to change the tidal asymmetry due to their oscillatory nature, they may generate only small net transport of fine sediment. Their role is generally to stir up sediment and to keep these particles in suspension. However, depending on the profile of the subtidal and intertidal areas (concave or convex), wave can lead to net transport. For example, large fetch lengths are available at high water, resulting in higher waves. However, larger depths during high water cause attenuation of wave orbital velocities. Concave estuaries, being generally flood dominant, tend to have large fetches with relatively small water depth during mid tides, but relative deep waters during high tide. This results import of fines on the intertidal areas and landward transport by wind driven circulation or tidal asymmetry, whereas convex estuaries, which are mostly ebb dominant, tend to have large fetches with shallow depths at high tide, leading to export of fines from the flats and subsequent seaward transport of fines (Hunt et al., 2015).

A.1.2 Baroclinic Processes

Baroclinic processes are the assembly of interactions between fine sediment on the one hand and the hydrodynamic processes between the fresh water discharge and the salt sea water, due to a density gradient. These processes may lead to the formation of an ETM near the salt intrusion limit of an estuary. Major baroclinic processes are gravitational circulation, tidal straining and lateral straining (Burchard et al., 2018). These will be discussed separately in the remainder of this section. Density gradients can also emerge due to differences in SSC and temperature.

Gravitational Circulation

Gravitational Circulation is caused by a baroclinic pressure gradient, which is realized by a difference in salinity and/or temperature between the sea and the estuarine/fluvial water. The pressure gradient results in an characteristic exchange flow with up-estuarine flow near the bottom and down-estuarine flow near the surface. This is visualized in Figure 11. The drivers of gravitational circulation are an alongshore buoyancy gradient, stratification and mixing (Becherer, 2013a; Geyer & MacCready, 2014; Hansen & Rattray, 1965; Jay & Musiak, 1994; MacCready & Geyer, 2010; Pritchard, 1956; Simpson et al., 1990; Stacey et al., 2001, 1999).

The residual current due to gravitational circulation can be estimated using (Burchard, 2010):

$$u_E = \frac{g\beta s_0 h}{48K_M}\frac{\partial S}{\partial x} = \frac{U}{48}S_i$$

Alongshore buoyancy gradient

The salinity gradient will vary over time, owing to the variations in the river outflow and tidally induced salt transport processes. Increased river flow pushes the salt intrusion seaward and increases the salinity gradient (MacCready, 1999; Simpson et al., 1990).

Stratification

A measure of stratification is the potential energy anomaly, which was introduced by Simpson (1981). It is defined as the amount of mechanical energy required to instantaneously homogenize the water column with a given density stratification, which is formulated as:

$$\Phi = \frac{g}{D}\int_{-H}^{\eta}(\bar{\rho}-\rho)zdz = -\frac{1}{D}\int_{-H}^{\eta}gz\bar{\rho}dz$$

Burchard and Hofmeister (2008) derived a time-dependent dynamic equation for the potential energy by combining the equation above and the dynamic equation for potential density. This led to the following equation:

$$\delta_t \Phi = \underbrace{-\boldsymbol{\nabla}_h(\overline{\boldsymbol{u}}\Phi)}_{(A)} + \underbrace{\frac{g}{D}\boldsymbol{\nabla}_h(\bar{\rho})\int_{-H}^{\eta} z\overline{\boldsymbol{u}}dz}_{(B)} - \underbrace{\frac{g}{D}\int_{-H}^{\eta}\left(\eta - \frac{D}{2} - z\right)\widetilde{\boldsymbol{u}}\boldsymbol{\nabla}_h(\tilde{\rho})dz}_{(C)}$$
$$\underbrace{-\frac{g}{D}\int_{-H}^{\eta}\left(\eta - \frac{D}{2} - z\right)\widetilde{w}\partial_z\tilde{\rho}dz}_{(D)} +$$
$$\underbrace{+\frac{\rho_0}{D}\int_{-H}^{\eta} P_b dz}_{(E)} \underbrace{-\frac{\rho_0}{2}\left(P_b^s + P_b^b\right)}_{(F)} + \underbrace{\frac{g}{D}\int_{-H}^{\eta}\left(\eta - \frac{D}{2} - z\right)Q dz}_{(G)}$$
$$\underbrace{+\frac{g}{D}\int_{-H}^{\eta}\left(\eta - \frac{D}{2} - z\right)\boldsymbol{\nabla}_h(K_h\boldsymbol{\nabla}_h(\rho))dz}_{(H)}$$

Herein, the vertical buoyancy flux, P_b, is given as:

$$P_b = \langle w'b' \rangle = \frac{g}{\rho_0}K_v\partial_z\rho$$

The different terms of the dynamic equation for potential energy anomaly have the following meaning (Becherer, 2013a; Burchard & Hofmeister, 2008):

A. Advection of potential energy anomaly:
   Potential energy anomaly advection is caused by the depth-averaged horizontal velocity in both the longitudinal and lateral direction. For a divergence-free velocity field ($\boldsymbol{\nabla}_h\overline{\boldsymbol{u}} = 0$) this term cancels.
B. Depth-mean straining:
   This term describes the vertical mean horizontal density gradient strained by the deviation from the depth-mean velocity vector, both in along and across-channel direction. Along-channel straining, or classical tidal straining, de-stratifies the water column during flood and stratifies it during ebb. Across-channel or lateral straining may be more important due to suppression of turbulent momentum flux, which yields a positive feedback loop: stronger lateral circulation leads to more vertical stratification, which leads to stronger lateral circulation and so forth (Dyer, 1995; Geyer, 1993).
C. Non-mean straining term:
   Non-mean-straining is the straining of the deviation from the vertical mean horizontal density gradient. Hence, this term is dependent on the longitudinal and lateral gradient of the deviation of the buoyancy from its vertical mean.
D. Vertical advection:
   There is advection of potential energy anomaly through the water column due to deviation of the vertical velocity from the linear vertical velocity. Largest potential energy anomaly occurs when the isopycnal (the boundary layer between fresh and salt water) is located at mid-depth.
E. Vertical mixing terms:
   The vertical mixing terms are proportional to the depth-mean of the turbulent buoyancy flux, depending on the turbulent eddy diffusivity and stratification. Contributing to the vertical mixing is lateral circulation, as will be discussed in a separate subsection in the below.
F. Surface and bottom buoyancy fluxes
G. Inner sinks or sources of potential density
H. Divergence of horizontal turbulent transport

Mixing Asymmetry
Mixing asymmetries can yield residual estuarine exchange flow through a difference in vertical momentum flux between ebb and flood (Jay & Musiak, 1994). Tidal mixing asymmetries can be subdivided in external and internal asymmetries (Becherer, 2013a).

External
External tidal mixing asymmetries are processes which cause a tidal asymmetrical generation of turbulence. Examples are peak velocity asymmetry, as discussed in the barotropic processes. The interaction of these processes with the baroclinic processes may be non-linear (Becherer, 2013a).

Internal
Internal mixing asymmetries are processes associated with vertical stratification and its inhibiting effect on the vertical momentum flux. Asymmetric vertical stratification limit the turbulent mixing length scale, thereby repressing the vertical momentum flux. The most prominent internal mixing asymmetry is tidal straining or strain-induced periodic stratification (SIPS), as is depicted in Figure 11 (Simpson et al., 1990; Stacey et al., 1999).

Tidal straining causes stratification to be dependent on the tidal velocity and the phase of the tide. The rate of destratification increases during the flood tide (unstable stratification) and decreases during ebb tide (re-stratification). This is due to intensified mixing during flood, since saltier flood currents collide with the fresher water, present in the estuary. In contrast, during ebb tide, fresher seaward moving water overtops the saltier water. Estuaries may therefore experience tidal variation in stratification. SIPS is subject to strong asymmetry of the magnitude of the eddy viscosity. This yields an asymmetry in the vertical profile of the along-channel tidal currents. The enhanced vertical stratification during ebb suppresses vertical flux of momentum, which lead to a more layered current velocity profile, whereas during flood, stratification is weak which allows for a strong vertical momentum exchange and consequently a more uniform current velocity profile. For weakly stratified estuaries, tidal straining is dominant over gravitational circulation, while for highly stratified estuaries, gravitational circulation is dominant (Becherer, 2013a; Jay & Musiak, 1994; Simpson et al., 1990).

The level of stratification is also dependent on the spring-neap cycle. During neap tides, stratification can be stable, while during spring tides the tidal energy increases, causing the estuary to be well-mixed. This process is known as runaway stratification. During neap tides the potential energy input due to straining by the mean gravitational circulation exceeds the buoyancy flux due to tidal mixing. This further isolates boundary layer mixing from the overlying water column. However, there exists a time lag for re-stratification. Re-stratification is more rapid if there is lateral straining. Also frontogenesis leads to more rapid re-stratification. It is caused by along-channel variation of stratification at the end of the ebb tide due to increase in width and depth in the down-estuary direction and/or varying conditions, such as an increase in fresh water discharge. This favors the intensification of the near-bottom salinity gradient. During the subsequent flood tide the stratification propagates upstream the . This is tidal frontogenesis. (Becherer, 2013a; Geyer & MacCready, 2014; Ralston, Geyer, & Warner, 2012) (Geyer, Ralston, 2015).

Lateral Circulation
Lateral processes are other important drivers for estuarine circulation. Lateral structure of the estuarine circulation results mainly from lateral variations in the baroclinicity and stress distribution (Wong, 1994). Lateral variability causes the estuarine circulation to become more effective due to the tendency to stratify the water column. This reduces the influence of vertical mixing, since the exchange flows are laterally segregated. Lateral circulation has three ways through which it can generate longitudinal circulation (Becherer, 2013a; Geyer & MacCready, 2014):

- Coriolis deflection
- Centrifugal deflection

- Momentum rectification

Coriolis and centrifugal deflection are barotropic processes, in which lateral vorticity is transformed in longitudinal vorticity. These processes were already discussed along the other barotropic processes in the destined section in the above.

Momentum Rectification
Momentum rectification is the redistribution of along-channel momentum caused by the transformation of horizontal vorticity in longitudinal vorticity through lateral circulation. The relative orientation of the horizontal and lateral vorticity components determines whether there is an increase or decrease of longitudinal vorticity. If the vorticities have the same orientation, they tend to decrease the longitudinal vorticity. This corresponds to a positive contribution to estuarine circulation and, hence, a more homogenous current velocity profile. However, if the horizontal and lateral vorticities have opposing orientations, there is a negative contribution to estuarine circulation. This gives a more sheared along-channel velocity profile. The direction of the different vorticities may change during a tidal cycle, resulting in asymmetrical mixing and hence residual circulation. Momentum rectification may create more residual exchange flow than classical gravitational circulation. The main drivers for momentum rectification are lateral depth differences, Coriolis and curved flow in bends (see Figure 13) (Becherer, 2013a; Burchard et al., 2011; Huijts et al., 2011; Lacy et al., 2003; Lerczak & Geyer, 2004; Scully et al., 2009).

Lateral depth differences
Nunes and Simpson (1985) identified that lateral depth differences may create lateral density gradients, which are able to drive lateral circulation. Deeper sections of the cross-section tend to have less bottom friction and, hence, faster tidal currents than shallower sections. As a consequence, a greater net contribution of baroclinicity is advected through the deeper sections. During flood, this causes a situation where the density in the channels is larger than on the shoals. A reversed situation arises during ebb (Becherer, 2013a; Valle-levinson & Li, 2000). A lateral density gradient emerges, which drives a two counter-rotating cell structure. Surface water is carried towards the center of the channel during flood tide. The reverse occurs during ebb tide. Depending on the tidal characteristics, the situation during ebb may not fully develop but only diminish the evolved lateral density gradient, which evolved during flood (or the reverse: the lateral density gradient during flood does not (fully) develop). This leads to an asymmetric differential advection. In general, ebb have to overcome a greater density gradient than flood. Hence, lateral circulation tends to be much stronger during flood than ebb tides. The advection of low-momentum fluid from the sides to the main channel results in the slowing down of the near-surface current during flood tide, stimulating stratification, especially for narrow weakly stratified estuaries. This effect diminishes for both well-mixed as highly stratified estuaries and with increasing width (Burchard et al., 2011; Lerczak & Geyer, 2004). Weaker lateral circulation during ebb causes the shoals to be more ebb dominant, while the channel becomes more flood dominant (Becherer, 2013a; Buijsman & Ridderinkhof, 2008; Cheng, Wang, & Jia, 2017; Lerczak & Geyer, 2004).

Curvature
Vertically sheared along-channel momentum is deflected to the outer bend due to centrifugal deflection. A barotropic pressure gradient balances the centrifugal forces depth-averagely. However, since the centrifugal forces increase with velocity and the pressure gradient is uniform over the depth, this leads to a lateral exchange flow with surface water flowing to the outer bend and a near-bed flow towards the inner bend (Becherer, 2013a; Buijsman & Ridderinkhof, 2008).

Curvature-induced secondary flow may generate a density gradient and interact with this gradient, depending on the level of stratification. In strongly stratified estuaries, vertical stratification is known to reduce lateral circulation due to the associated tilting of the denser bottom water, which builds up a baroclinic pressure gradient, compensating for the curvature-

induced lateral circulation (Chant, 2002; Chant & Wilson, 1997; Kim & Voulgaris, 2008; Lacy & Monismith, 2001). In weakly stratified estuaries, however, vertical stratification has the tendency to increase lateral circulation through damping of vertical mixing of momentum (Buijsman & Ridderinkhof, 2008; Geyer, 1993). Secondary circulation in such systems can also generate vertical stratification due to straining of lateral density gradients, which may lead to a positive feedback loop between lateral circulation and vertical stratification (Becherer, 2013a; Cheng & Valle-Levinson, 2009; Lacy et al., 2003; Nidzieko et al., 2009; Scully & Geyer, 2012).

Coriolis

For wide estuaries, Coriolis deflection drives a one-cell lateral circulation in the transverse section through the vertical shear of the along-estuary flow. Water is set-up at one side of the basin due to stronger Coriolis deflection of faster propagating water, which is counterbalanced by a water pressure force. Coriolis may also be counteracted by a lateral salinity gradient, generated through lateral advection (Becherer, 2013a; Cheng & Valle-Levinson, 2009; Cheng et al., 2017; Winant, 2007).

Combination of the processes described above give rise to an asymmetric and complex two-cell structure of lateral and vertical velocities. Differing topography and bathymetry, resulting in different contributions and sums of Coriolis, pressure gradient, and advection, induce along-estuary varying strengths of estuarine circulation (Eulerian flow), velocity and salinity (Cheng et al., 2017). Frontogenesis may then come into play to stratify the rest of the estuary.

The interplay between (lateral) circulation currents and stratification can be investigated using the vorticity balance of lateral and along-channel circulation respectively:

$$\partial_t[\omega_x] = \underbrace{\partial_y\langle b\rangle_z}_{\substack{Baroclinic\\ Pressure\\ Gradient}} + \underbrace{f[\omega_y]}_{Coriolis} - \underbrace{\frac{2}{R}\langle u\rangle_z[\omega_y]}_{Bend\ Flow} - \underbrace{\frac{8}{D^2}\langle v'w'\rangle|_{\frac{1}{2}(\eta-H)}}_{Internal\ Friction} + \underbrace{\frac{4}{D^2}\langle v'w'\rangle|_{-H}}_{Bottom\ Friction}$$

$$\partial_t[\omega_y] = \underbrace{-\partial_x\langle b\rangle_z}_{\substack{Baroclinic\\ Pressure\\ Gradient}} - \underbrace{f[\omega_x]}_{Coriolis} + \underbrace{\frac{1}{R}\langle u\rangle_z[\omega_x]}_{Bend\ Flow} + \underbrace{\partial_y\langle u\rangle_z[\omega_x]}_{\substack{Lateral\\ Momentum\\ Redistribution}} + \underbrace{\frac{8}{D^2}\langle u'w'\rangle|_{\frac{1}{2}(\eta-H)}}_{Internal\ Friction} - \underbrace{\frac{4}{D^2}\langle u'w'\rangle|_{-H}}_{Bottom\ Friction}$$

in which the three-dimensional vorticity is simplified as:

$$\omega_x = \partial_y w - \partial_z v \approx -\partial_z v$$

$$\omega_y = \partial_z u - \partial_x w \approx +\partial_z u$$

$$\omega_z = \partial_x v - \partial_y u \approx -\partial_y u$$

Hence, the along-channel gradient of streamwise and lateral velocity and the lateral gradient of vertical velocity are neglected. Furthermore, the baroclinic pressure gradient is assumed to be constant over the vertical and no surface momentum fluxes are taken into account.

The vorticity balances can be simplified even further by, first of all, parameterization of the internal friction terms, applying a down-gradient approach for the turbulent momentum fluxes:

$$\langle u'w'\rangle = -\nu_t\partial_z u \approx -\nu_t[\omega_y], \qquad \langle v'w'\rangle = -\nu_t\partial_z v \approx \nu_t[\omega_x]$$

Secondly, the bottom friction terms can be calculated using the friction velocity:

$$\langle u'w'\rangle = u_*^2\sin(\alpha), \qquad \langle v'w'\rangle = u_*^2\cos(\alpha)$$

Lastly, assuming well-mixed conditions, the across-channel vorticity scales approximately with the vertical shear of the law of the wall:

$$[\omega_y] \approx \partial_z u|_{\frac{1}{2}(\eta-H)} \approx \frac{u_*}{\kappa(z-H)}\Big|_{\frac{1}{2}(\eta-H)} = \frac{2u_*}{\kappa D} = \frac{2C_D u|u|}{\kappa D}$$

These simplifications result in the following vorticity balance:

$$\partial_t[\omega_x] = \frac{b_1 - b_2}{y_1 - y_2} + \frac{2fC_D|u|u}{\kappa D} - \frac{4C_D u^2|u|}{\kappa DR} + \frac{8}{D^2} v_t^i[\omega_x] - \frac{4}{D^2} u_*^2 \sin(\alpha_{u_{bl}})$$

$$\partial_t[\omega_y] = -\frac{b_1 - b_2}{x_1 - x_2} - f[\omega_x] + \frac{1}{R}\langle u\rangle_z[\omega_x] + [\omega_z][\omega_x] - \frac{16C_D|u|u}{\kappa D^3} v_t^i + \frac{4}{D^2} C_D^2 u^4 \cos(\alpha_{u_{bl}})$$

Sediment-induced stratification

High sediment concentrations at the location of the ETM may develop a turbidity current, which may produce an additional sediment transport through vertical sediment-induced stratification (Chernetsky, 2012). It is controlled by a balance of hindered settling and entrainment of (fluid) mud, caused by tidal currents, which inhibit consolidation of the settled material (Winterwerp, 2002; Wolanksi et al., 1988). SSC in the fluid mud layer is therefore below the gelling concentration, such that it remains mobile, while its thickness may reach a significant fraction of the water depth (Kirby and Parker, 1983). This is further explained in the section about process-based mechanisms. A two-layer structure may develop, causing sediment-induced stratification. This stratification may be asymmetric over a tidal cycle due to asymmetry in entrainment and flocculation.

For example, the following situation may arise. During flood tide, the fluid mud layer is entrained into the upper layer with larger flocs higher up in the water column. These flocs are transported upstream as well as the fluid mud layer itself due to upstream advection. At the onset of high water slack tide, the flood current decreases and the fines settle rapidly to form a dense and stable concentration profile with larger flocs near the bed, re-stratifying the water column. During ebb, the vertical mixing is damped due to the vertical sediment-induced stratification. Since flow acceleration during ebb is then much more confined to the upper water column, small velocities will be near the bottom, which cause the fluid mud layer to be decoupled from the water. Entrainment during ebb is therefore limited to the mud layer surface only. There is slightly ebb-directed advection of the fluid mud due to the sediment-induced pressure gradient (Talke et al., 2009). At LWS, the fluid mud settles and consolidates even further, when it is again entrained during flood (Becker et al., 2018; Winterwerp et al., 2011, 2017). However, depending on the characteristics of the estuary, a different situation may arise.

Sediment-induced stratification may result in a net flood transport of fine sediment if the concentration is high enough (above saturation concentration) (Winterwerp et al., 2011). The stratification asymmetry may also alter the hydrodynamics to more ebb-dominancy due to increasing ebbing currents, causing a net down-estuary displacement of the fluid mud layer (Becker et al., 2018). Furthermore, the diffusivity of the fluid mud tends to spread the ETM zone (Chernetsky, 2012).

A.2 Micro-scale mechanisms

In combination with macro-scale mechanisms, there are micro-scale sedimentary mechanisms, such as flocculation, re-suspension, deposition, erosion, turbulence damping, hindered settling, drag reduction, which have a direct effect on the sediment supply to a trench. These processes tend to influence the formation of the ETM, since they impact settling and entrainment rates and settling velocities. Locally, the micro-scale processes are likely to be influenced by the construction of the trench.

Deposition

Mud, consisting of non-cohesive silt and fine sand, and cohesive clay particles (<63 µm), and organic calcareous materials, is generally transported in suspension. These sediments particles may be deposited if the bed-shear stress is sufficient low. Deposition fluxes of different sediment classes are proportional to the product of the respective bottom concentration and settling velocities (Le Hir, Cayocca, & Waeles, 2011).

Deposition processes are dependent on the suspended sediment concentration. Four ranges can be distinguished, as can be seen in Figure 63 (McAnally, 2007; Van Rijn, 2005):

- Negligible settling range
- Hindered settling range: concentrations larger than ~10 kg/m^3:
  Deposition is in the form of fluid mud of sediment flocs which are partially supported by the escaping fluid and partially supported by inter-floc contacts. This is known as the hindered settling effect. Fluid mud will be discussed separately in the below.
- Flocculation settling range: concentrations from ~0.3 to ~10 kg/m^3:
  Flocculation governs the deposition process. Two types of flocs are formed:
  - Flocs with strong bonds (microflocs):
    These flocs can resist the disruptive near-bed shear stresses and will be able to reach the bottom and form strong bonds with deposited flocs.
  - Flocs with weak bonds (macroflocs):
    These flocs do not have sufficiently strong bonds and will be broken down before reaching the bed. This results in quick resuspension due to the weak bonds with the deposited material. The weak flocs are deposited on top of the strong bonds.

  Depending on the bed-shear stress, one of the following deposition processes can be distinguished for the flocculation settling range:
  1. Full deposition
  2. Hindered or partial deposition
  3. No deposition
- Free settling range: concentrations smaller than ~0.3 kg/m^3 :
  Flocculation plays a minor role due to the low SPM concentration, such that the following processes can be distinguished, which are dependent on the bed-shear stress:
  1. Full deposition
  2. No deposition

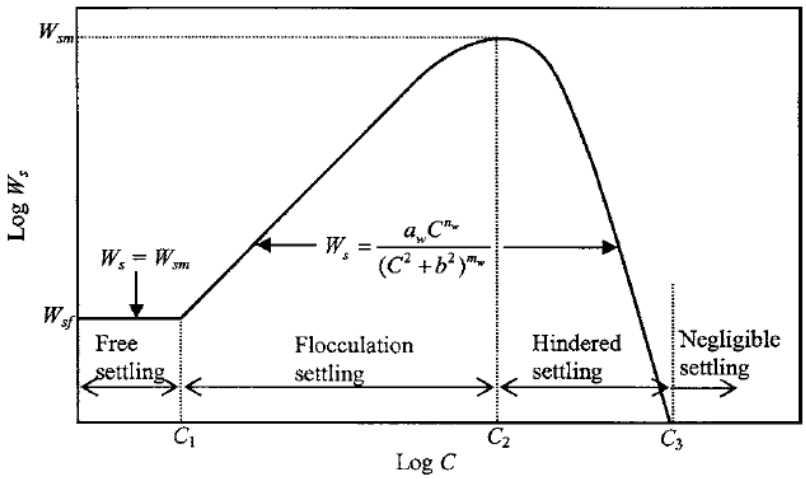

Figure 63 – Schematic of average suspension settling velocity dependence on concentration (Metha, 1991)

Sand-mud interaction

When the initial mixture density is low, sand particles and dense flocs can be deposited through the soft mud and form a dense sand/mud layer on the bottom, while freshly deposited

sparse mud particles will mix on top with the soft mud. Segregation of sand particles through the mud particles depends on the sand content, input rate and mud concentration. It generally occurs at low mud concentrations and high sand contents. For slow sediment input rates the sand is held in the matrix of the consolidating mud, while at high input rates, the matrix structure of the soft mud is not strong enough to hold the sand particles. Furthermore, segregation is dependent on the mineralogical and chemical composition and organic content of the mud and biological processes within the mud. On the contrary, if the mud bed is consolidated, a new layer of deposited sandy material may form (Torfs et al., 1996). If the concentration is sufficient high (flocculation stage), sand and mud may interact in forming flocs, resulting in a mixed sediment layer.

Consolidation

Consolidation is a process of floc compaction under the influence of gravity forces with a simultaneous expulsion of pore water and a subsequent gain in strength of the bed material. Sediments are moved downwards, while pore water is expelled in upward direction. Three distinct consolidation stages can be distinguished (Van Rijn et al., 2018)

- Hindered settling phase (initial hours-days):
  Settling particles are hindered by the return flow of water displaced by the moving particles. The flocs are grouped in an open structure with large pore volume. The weakest bonds are broken down first. Dry density concentrations are approximately 10-150 kg/m^3.
  After a few days, there is a transitional fluid mud phase in which particles/flocs make contact with each other. This results in a gel/slurry-type structure. The effective settling velocity decreases significantly. At the onset of this phase, mixtures reach the so-called gel point concentration (~100-200 kg/m^3).
- Primary consolidation phase (weeks-months):
  The pore volume is reduced, since pore water is expelled trough thinly formed vertical drains. This is accompanied by large strains. The dry bulk density is approximately 300-400 kg/m^3 at the start of the primary consolidation phase and may reach 600-700 kg/m^3 in the end.
- Secondary consolidation phase (Terzaghi-type consolidation; months-years):
  Pore volume is further reduced, while flocs are broken down further to form a firm soil. It is characterized by small strains and dry bulk densities in the range of 1,000-1,200 kg/m^3.

Consolidation is affected by the initial thickness of the layer, its density (depending on clay:silt:sand ratio), concentration and its permeability (Van Rijn, 2005). The thicker the clay layer, the longer it takes for consolidation to end. This occurs when the maximum concentration of a well-sorted sediment or mixed sediment is reached or when the vertical load gradient vanishes (Le Hir et al., 2011). The dry density increases with depth as the self-weight of the soil

The structure of a bed depends on the sediment concentration, settling and consolidation rate, sand content and mud properties. A network structure of sand particles is found for a sand volume fraction of 40-50%, while a network of silt is found when the silt volume fraction relative to the pore volume is about 40-50%. Otherwise, a network structure of clay particles is formed. Various bed types may form, which can be classified according to their network structure (see Figure 15) (Van Ledden et al., 2004):

- Non-cohesive sand-dominated (I)
- Cohesive sand-dominated (II)
- Non-cohesive mixed (III)
- Cohesive clay-dominated (IV)
- Non-cohesive silt-dominated (V)
- Cohesive silt-dominated (VI)

Ratios between clay and silt in practice are fairly constant, which indicates that bed properties are a function of the sand content only (dotted line in
Figure 15) (Flemming, 2000; Pejrup, 1988; Van Ledden et al., 2004).

Sand-mud interaction

Increasing sand content appears to increase the gel point density, at which a soil forms a matrix, and the end density. Before this point is reached, larger sand particles and compact flocs can settle at the bed. The passage of sand through the mud also increases the consolidation rate by leaving drainage paths through the mud at high initial concentrations. Furthermore, densification of the mud layer may occur due to dragging of fine silts through the mud bed by the depositing sand particles. The degree of consolidation, consolidation rate and densification is however limited to a maximum sand content (~30%), since if too much drainage paths are created the mud becomes more open structured (Torfs et al., 1996).

Sorting processes due to tidal current resuspension of a sand and mud mixture may lead to dynamic bed armoring in which the resuspended sand particles protect the surficial mud layer from resuspension. This is because sand particles stay close to the bed layer and deposit fast (Le Hir et al., 2011).

A muddy deposit will form a new layer on sandy sediment when the spaces of the voids between the particles in the sand layer are filled (Le Hir et al., 2011; Sanford, 2008). Bioturbation might introduce additional mixing between the sediment layers.

Fluid Mud Dynamics

Fluid mud is a viscoplastic high-concentration suspension of fine sediment particles in which settling is substantially hindered by the close proximity of sediment particles and flocs, but which has not yet formed an interconnected matrix of bonds (above gelling concentration) strong enough to eliminate the potential for mobility (McAnally et al., 2007). Before the stage of hindered settling and fluid mud formation, aggregation of the primary fine sediment particles into flocs occurs. During the fluid mud stage, fluid mud consolidates to from a bed layer through dewatering, leading to sinking of the bed surface. Consolidation can take hours to years and continues after dewatering ends as internal rearrangements of particles may occur as secondary consolidation (McAnally et al., 2007).

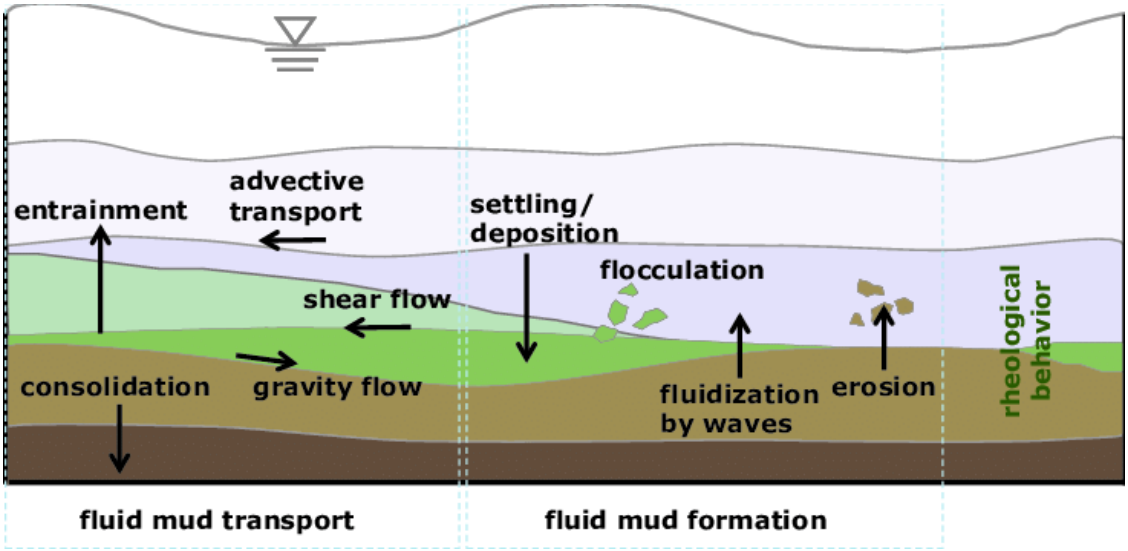

Figure 64 – Significant physical processes governing fluid mud dynamics. Left: transport processes of mud suspensions. Right: processes for the formation of fluid mud (Wehr and Malcherek, 2012)

A three layer fluid mud system can be distinguished, as can be seen in Figure 14 (Van Rijn, 2016):

- Dilute mud suspension: c = 0-10 kg/m^3
  Flocculation is dominant in this layer. The flocs and particles are prone to the hydrodynamic conditions. If the dilute mud suspension layer is more turbulent than the fluid mud suspension layer, mud will be entrained and mixed with the flocs and particles (Van Rijn, 2016).
- Fluid mud suspension layer: c = 10-300 kg/m^3
  This layer is bounded by the hyperpycnal and the lutocline and may be 0.1-3m thick. The flocs and particles in the fluid mud layer are hindered from settling due to escaping fluid. The fluid mud layer can be subdivided in (Van Rijn, 2016):
  - a turbulent upper layer: c = 10-100 kg/m^3
    If the turbulent layer is more turbulent than the dilute suspension layer (i.e. during accelerating spring tide), mud from the lower laminar viscous layer tends to be mixed into the turbulent layer as well as water from the upper dilute suspension layer. This creates a low concentration upper fluid mud layer but with a high lutocline. During neap tide, the turbulent upper layer is generally less turbulent than the dilute suspension layer and a thin concentrated fluid mud layer will emerge (Van Rijn, 2016).
  - a laminar viscous lower layer: c = 100-300 kg/m^3
    This layer is built up during neap tides with low turbulence and breaks down during spring tides with high turbulence (Van Rijn, 2016).
- Consolidated mud layer: c = 200-300 kg/m^3
  An internal framework which supports flocs and particles (Van Rijn, 2016).

The behavior of fluid mud is strongly dependent on the material composition, such as the percentage of clay particles and organic materials and coarse sediments (Van Rijn, 2016). It also depends on the thixotropy (stress history). A sufficient long period of high strain rates or stresses decreases the fluid mud viscosity and yield strength (McAnally et al., 2007).

Fluid mud in a dredged trench can form under various conditions (Van Rijn, 2016):

- Locally-generated (mobile) fluid mud:
  Erosion and settling of mud suspensions during respectively accelerating and decelerating tidal flow. For high SPM concentrations, collision processes of suspended particles lead to aggregation and floc formation, thereby enhancing settling rates to ultimately result in mud deposition. The strength and thickness of the mud deposition is dependent on the consolidation/setting time and the sediment supply. The retention period of fresh mud deposits is dependent on the duration of slack water, the erosive capacity of the next tide and the rate of sediment consolidation (Becker et al., 2013; Van Rijn, 2016). Two types of locally-generated fluid mud exist:
  - At slack water a temporary layer of fluid mud may be formed from the sediment particles raining out from high concentrations. If the settling rate is greater than the dewatering rate, fluid mud will be formed (Kirby and Parker, 1977; Ross and Mehta, 1988). This may be due to convergent horizontal advection of sediment-laden flow or raining out of suspended particle from the water column during decelerating slackening currents.
    During spring tides this layer will be resuspended as a whole. However, during neap tide the formed fluid mud layer will not completely be re-entrained. Instead, the thickness of this layer will increase during neap tides and a small layer of fluid mud may consolidate (Van Rijn, 2016).
  - Furthermore, fluid mud can be generated by the fluidization of cohesive beds by upward moving pore fluid caused by small amplitude waves. These waves exert a drag force on the sediment aggregates, which may exceed a minimum value, causing the destruction of the soil matrix by excess pore pressure build-

up. Depending on the thickness of the muddy bottom and the degree of consolidation, fluidization proceeds from the hard bottom up (thin un-consolidated mud) or from the top down (consolidated thick mud) (McAnally et al., 2007).

- Supplied mobile fluid mud:
  Elsewhere generated fluid mud may be advected up and down the estuary within shear flows generated by the tidal current. This can be through (Van Rijn, 2016):
  - Entrainment of high density suspension:
    Supply of mobile fluid mud by entrainment is caused by turbulent energy resulting from eddy generation in the boundary layer. The fluid mud, located around the ETM, is washed away during higher tidal energy. The layer is dispersed and deposited more landward during flood and more seaward during ebb. Hence, it moves with the tide (Yuanyang et al., 2014).
  - Supersaturation of suspensions:
    Suspensions may become supersaturated due to the smaller bed-shear stresses and velocities, which causes the turbulence to decline and SPM to settle rapidly, ultimately forming a fluid mud layer (Van Rijn, 2016). The suppression of turbulence decreases the carrying capacity of the water even further, resulting in a positive feedback for settling of fine sediments; the SPM concentration profile collapses. This occurs at the so-called saturation concentration. Subsaturated and supersaturated conditions are separated by the critical flux Richardson number. In the hyperconcentration regime, the subsaturated conditions are re-established (see Figure 65). Turbidity currents are a manifestation of this regime. (Winterwerp, 2006).
  - Settling of high-concentration mud suspensions as stagnant fluid mud:
    In low-flow or stagnant areas, thick fluid mud layers can be formed if the settling rate of the supplied suspended particles is larger than the dewatering rate of the bed surface.
  - Fluid mud streaming by waves and/or current shear:
    Waves fluidize the top layers and move it as a near-bottom fluid mud layer in the same direction as wave propagation (McAnally et al., 2007). The undrained failure is caused by pressure gradients on the bed surface, resulting in liquefaction through positive pore pressure and subsequently shear stresses inside the layer that exceed the yield strength. A transition from elastic to viscous behavior (shear-thinning behavior through floc break-up) may then be observed, which makes transport of the fresh fluid mud is possible (Van Kessel, 1997).
    This transport is dependent on the rheology of the fluid mud, which is rather complex as the viscosity and yield strength are functions of shear rate and shear rate history (thixotropy). Rheology has two independent times-scales: one for structural changes within the particle aggregates responding to changes in shear rate (dynamic structure), and another for changes in the interaction between the aggregates (static structure). Compared to the dynamic structure of the fluid mud, the build-up of the static structure takes more time and is broken up at very low shear rates by gel-formation. The dynamic structure is build-up quickly by the growth or change of shape of particle aggregates without all aggregates being interconnected. This is dependent on the cohesivity and subsequent effective viscosity of the mud at certain sediment concentrations (Van Kessel, 1997). Important parameters for the rheology of the (fluid) mud are the solid volume concentration, the grain-size distribution and the ion concentration (Sosio & Crosta, 2009).

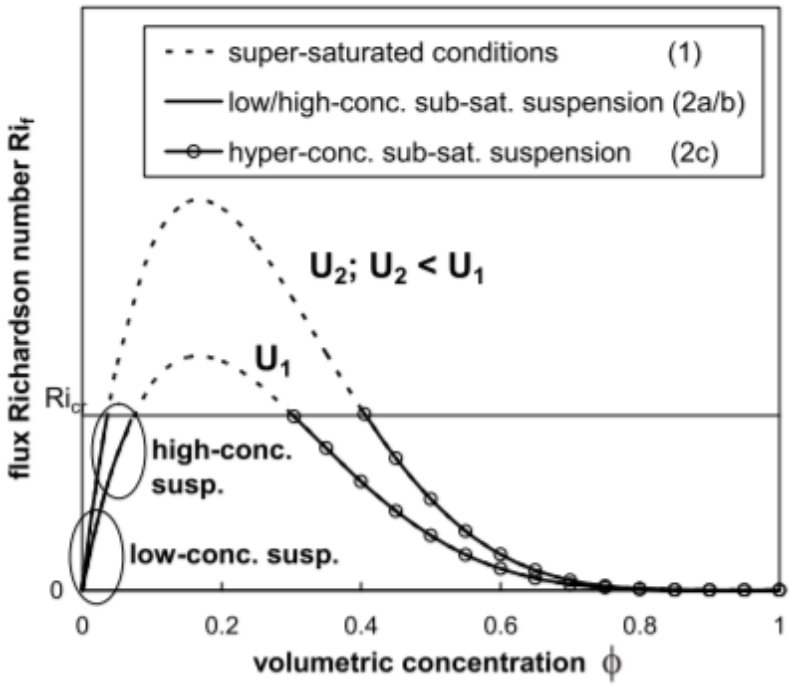

Figure 65 – Stability diagram for sediment-laden flow (Winterwerp, 2006)

(Undrained) yield strength is almost linearly correlated with the effective stresses (both in horizontal and vertical direction), depth, the permeability of the mud, time-scale of loading and the pore pressure. Also the cohesion is important at low effective stress levels. This cohesion may increase by ageing. The effective stress state depends on the effective stress history (thixotropy), which may be greater than would follow from the actual state of effective stress (Van Kessel, 1997).

- Gravity Currents:
  Additionally, fluid mud can be transported downslope as a gravity flow of a sediment-fluid mixture. Three types of this mechanism can be distinguished (McAnally et al., 2007; Van Rijn, 2016):
  - Turbulent turbidity gravity flows supported in suspension by the turbulence generated by their own downslope movement (Yuanyang et al., 2014):
    A critical slope determines the difference between laminar and turbulent gravity flow. If the slope is too gentle, the flow remains laminar and cannot generate sufficient internal shear to overcome its inherently stable density anomaly in order to generate turbulence. This current will slow down with time and stop eventually. The critical slope depends on the concentration of the fluid mud and hence viscosity (McAnally et al., 2007). Three regimes of turbulent turbidity currents may occur (Parsons et al., 2005):
    - Conservative current:
      This turbidity current does not interact with its boundaries, and their speed and depth-averaged and depth-integrated concentrations remain constant as they propagate downslope. This is however not likely to occur in nature (McAnally et al., 2007).
    - Auto-suspending current:
      Auto-suspending turbidity currents produce enough bed stress to increase their sediment load by bed erosion such that density and speed increase with run-out distance (Parker et al., 1986; Scully et al., 2002; Wright et al., 2001).
    - Dissipative current:
      This currents slows down as they lose sediment upward via interfacial mixing.

Many turbidity currents have aspects of both auto-suspension and dissipation (McAnally et al., 2007).

- Turbulent gravity-flow supported by the shear associated with ambient currents and waves:
  An ambient current and/or waves increases the frictional resistance to the turbulent current and slows the fluid mud gravity current; however, it simultaneously allows the fluid mud suspension to persist by keeping it in suspension (McAnally et al., 2007).

The fluid mud current may experience inertia (McAnally et al., 2007)

Both SPM availability and local (residual) flow regime are of critical importance for the trapping probability of sediment and the occurrence of fluid mud. In addition, other sedimentary processes such as flocculation and hindered settling are likely beneficial for the formation and maintenance of fluid mud. However, there is poor theoretical understanding of complex interaction between currents, sediment and other forces near the bed in the channel.

Hysteretic effects between the shear stress and SSC during spring tidal cycles, as well as asymmetrical neap-spring-neap tidal cycles, may influence the near-bed sediment dynamics and induce the formation of fluid mud. For example, during flood tide, both fine particles and flocs erode and subsequently settle and slightly consolidate during high water slack. This causes the SSC during ebb to be generated by fine particles only, which is smaller in magnitude than during flood. A temporal fluid mud layer may be generated, which, through consolidation, may result in net sedimentation each semilunar tidal cycle. There may also be a time lag between maximum SSC and peak tidal amplitude due to the cohesiveness of fine particles (consolidation). This leads to the formation of fluid mud during intermediate-to-neap tides (Azhikodan and Yokoyama, 2018).

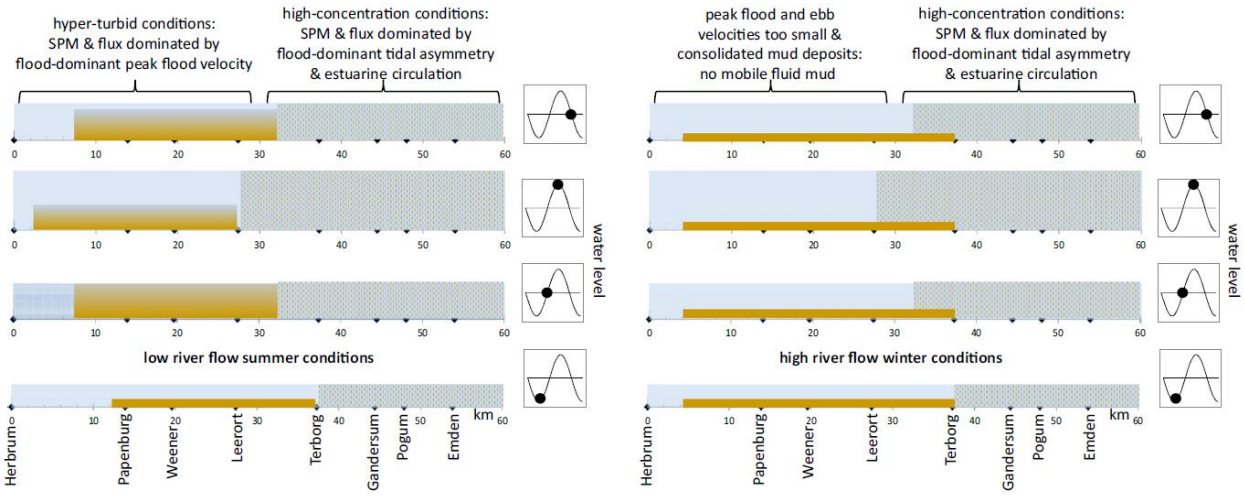

Figure 66 – SPM dynamics over a tidal cycle during low (left) and high (right) river flow.

Mud Pool Dynamics

Around the ETM a fluid mud pool may exist. This pool is entrained rapidly into the water column during flood and transported up-estuary. The mixing is governed by the entrainment of SPM-poor water into the turbulent turbid layer. At high water slack (HWS) the suspended sediments settle, whereafter the mud pool is transported downstream with the ebb tide. At low water slack (LWS) the suspended sediment settles again, and the cycle is repeated. SPM concentrations may fluctuate with a period of about 10 and 180 s through the generation of internal Kelvin-Helmholtz instabilities or Holmboe waves. These may have a length of 10m and a height of about 1m, propagating with a speed between 0.5 and 1.7 m/s. Furthermore, ebb currents may not be as effective in entraining mud as flood currents. This is because of the more uniform current velocity profile during flood due to tidal asymmetry and straining (Winterwerp et al., 2017).

For well-mixed, hyper-turbid estuaries, if the river discharge increases, the SPM profiles collapse (see Figure 66). This is because the river discharge decreases the flood velocity. The mud layer will therefore not be entrained. As a consequence, after onset of normal river discharges, the critical peak velocity for SPM profile recovery will be greater than the critical velocity for collapse due to consolidation of the mud and/or armoring due to sand from the river. For relatively higher river discharges, the fluid mud pool may be washed out of the estuary (Winterwerp et al., 2017).

Mud Transport
The transport of mud can occur in three modes (Van Rijn, 2016):

- Non-saturated mud transport in conditions with mud percentages in the bed < 30% (supply-limited conditions)
- Saturated mud transport in conditions with percentages if mud in the bed >70% (bed-dominated conditions) (Bagnold, 1962; Xu, 1999; Winterwerp, 2001, 2006, 2011; Van Rijn, 2007, 2015). The saturation concentration is proportional to the local velocity to the power 3 and inversely proportional to the settling velocity and water depth.
- Over-saturated mud transport in conditions with a large input of mud from upstream in combination with hindered settling effects resulting in hyper concentrations (supply-dominated conditions)

Saturated mud in relatively deep trenches with low river discharges and large salinity intrusion may lead to the formation of fluid mud (Winterwerp, 2011; Winterwerp and Wang, 2013; Van Maren et al., 2015b) (Van Rijn and Grasmeijer, 2018).

Erosion/Resuspension
Sandy and muddy sediments may be mixed or can be layered in the bed. This is dependent on history of forcing events. Generally, areas with high sand content and relatively high time intervals between events tend to have a layered bed structure (Torfs et al., 1996). Furthermore, they may exhibit a horizontal gradient from gradients in currents or waves (Le Hir et al., 2011). Erosion characteristics for sand mud mixtures can differ drastically ranging from pure muddy to fully sandy beds. Resistance of a sandy sediment bed increases with mud content and tend to show cohesive behavior at a certain mud content (5-10%), at which mud particles bind the sand particles together (Kuti & Yen, 1976; Murray, 1976). Below this mass percentage, the bed can be considered cohesionless and fines may be washed out (Alvarez-Hernandez, 1990). Another distinction between cohesive and non-cohesive behavior is through the plasticity index (PI). A bed with a PI smaller than 2 show purely granular behavior, while for larger PI two types of erosion exist: floc (time dependent) and surface (time independent) erosion (Jacobs, Le Hir, Kesteren, & Cann, 2011).

The transition between cohesive and non-cohesive behavior is determined by the mud fraction, depending on the sand grain size: the coarser the sand, the higher the mud content before the sediment becomes cohesive. This is because the mud particles need to fill up the large voids between the coarse sand particles. According to results of erosion tests of Panagiotopoulos, Voulgaris, & Collins (1997), sediment behaves like pure sand below a critical mud fraction, whereas above this critical value the shear strength increases with mud fraction (Jacobs et al., 2011; Le Hir et al., 2011; Le Hir, Cann, Waeles, Jestin, & Bassoullet, 2008; Van Ledden et al., 2004).

Non-Cohesive (Granular) Behavior
Erosion and mobilization of non-cohesive beds is described by the deviation with respect to a specific equilibrium situation in which supply of sediment equals erosion. This equilibrium transport is fully dependent on the flow conditions, assuming an uniform and stationary situation with abundant sediment. Particle size, solid density and particle shape are the dominant parameters in erosion of non-cohesive sediments (Van Rijn, Nieuwjaar, Van der Kaay, Nap, & Van Kampen, 1993). Increasing silt content results in higher erosion thresholds, while very fine particles are washed out from the bed first.

Cohesive Beds

For cohesive beds there exist no such as an equilibrium. Instead, erosion of cohesive beds is dependent on flow condition and bed properties (Winterwerp, Kesteren, Van Prooijen, & Jacobs, 2012). There are four erosion modes for cohesive sediments:

1. Entrainment:
   Fluid mud is entrained by turbulent flow.
2. Floc Erosion:
   Disruption of individual flocs from the surface of the bed by flow-induced peak bed shear stresses.
3. Surface Erosion:
   Drained failure due to exceedance of the mean erosion threshold by the mean bed shear stresses. Herein, the cohesive strength of the sediment bed is important. Increasing water content (decreasing packing density) reduces the surface erosion threshold. For cohesive granular beds the erosion threshold increases with clay content.
4. Mass Erosion:
   Undrained process during which lumps of material are eroded due to external fluid stresses. For cohesive granular beds, the undrained cohesion decreases with increasing clay content (increasing volume concentration of clay, hence looser packing) (Jacobs et al., 2011; Van Prooijen & Winterwerp, 2010).

The critical mud content is dependent on the grain size and porosity of the sand. Below a certain mud concentration (30%), the critical shear stress is dependent on the grain size of the sand. At higher mud contents, the bed behaves as mud, since sand particles are trapped within the mud matrix. Conversely, some sand content in a muddy bed may also slightly increase the erosion resistance due to changes in the micro-structure of the mud (McCave, 1984).

Furthermore, the critical shear stress of cohesive beds increases with depth because of consolidation (decrease in water content), physical-chemical changes due to overburden and the variation of particle size with depth (Parchure & Mehta, 1985). Biological activity can also affect erosion behavior (resistance increases with increasing organic content) (Paterson, 1989; Young & Southard, 1978).

Kamphuis & Hall (1983) found that particle size of eroded particles decreases with increasing sand content. The transport mode for mixtures is size dependent. At low shear stresses the finer fraction seems to be washed out and at higher shear stresses the larger grain size material is eroded (Methta & McAnally, 2008).

Increasing mud content will smoothen the bed and induce less bed shear stress. However, large-scale roughness may also increase with increasing mud content, since irregular surface topography is retained and given that surface erosion is irregular over a flat muddy bed (Mitchener & Torfs, 1996).

Settling and Flocculation

For non-cohesive sediments, if the concentration is low, particles can settle separately with settling velocities proportional to their size (laminar region or turbulent region (drag correction)) and density (Van Rijn et al., 1993). For increasing concentration, the movement of grains downwards causes an equal volume of interstitial fluid to be displaced upwards. This return current may carry small particles upward, causing segregation. At very high concentrations, this segregation is suppressed by particle interlocking, hydrodynamic processes and high rates of bed aggradation. This state continues until the maximum packing concentration is reached (Amy et al., 2006; Lockett & Al-Habbobby, 1974; Manning et al., 2010).

For cohesive sediments, the settling velocities are modified by the formation of microflocs and subsequent macroflocs due to electrostatic molecular forces between the particles. This may be enhanced by biological polymeric substances (Tolhurst et al., 2002). Macroflocs are formed by microflocs at high concentration and low turbulence. They are weaker than microflocs, which are formed at higher turbulence levels. Smaller but denser flocs will be formed at higher sediment concentrations (Van Leussen, 2011). The settling velocity of flocs is a function of their size and relative density (Winterwerp, 1999). If turbidity levels increase, cohesive particles experience hindered settling effects (Manning et al., 2010; Methta & McAnally, 2008) and highly concentrated benthic suspension (fluid mud) may be formed at the gelling concentration (Torfs et al., 1996) (Spearman & Manning, 2017).

The mud and sand in estuaries may either be deposited as alternating layers or as mixtures. The former occurs for low concentrations, when there is little bonding and flocculating interactions between the cohesive and non-cohesive sediment fractions. Hence, two independent suspensions co-exist with each their own fall velocity, forming two well-sorted layers (Manning et al., 2010; Van Ledden et al., 2004).

Flocculation

Mud particles themselves and particles in co-existing sand and mud suspensions may interact with each other when settling by gluing to each other to form larger particles. This process is called flocculation (Mitchener & Torfs, 1996). Microflocs settle faster during higher sand content due to bindings between the two, while macroflocs tend to fall slightly slower for higher sand contents. The ratio micro- to macroflocs is dependent on the shear stress (turbulent mixing), SSC and the sand content. Higher shear stress increases the microflocs, where macroflocs are falling apart. Flocs namely prefer to interact with turbulent eddies of a similar size (Kolmogorov microscale). More microflocs are formed at higher sand content (less cohesive suspension), while the reverse is true for macroflocs. The greater the sand content the higher the mass settling flux (Manning et al., 2010).

Fine cohesive particles are likely to flocculate. Flocculation is dependent on the suspended concentration, turbulence (Le Hir et al., 2011; Van Leussen, 2011) and flow acceleration/deceleration (larger Reynold stresses during decelerating flow and higher bed shear during accelerating flow); the latter affecting the turbulence and bottom shear stress and therefore concentration profiles by enhancing the collision frequency, but also the breaking-up of flocs (Shi, 2010). Therefore, floc sizes are greater during neap tide, at slack water and at the surface during a tidal cycle, since there is less turbulence at that phase and location respectively. Hence, macroflocs can form, while for high turbulent flows microflocs will be present (bimodal size distribution). Depending on the effective density of the macroflocs, these will settle slower/faster, causing high/low SSC at the surface and, hence, low/high settling rates. High sediment concentrations (Le Hir et al., 2011), as well as stratification (and SIPS), tend to create turbulence damping. Due to this damping, vertical mixing and hence turbulence is reduced. This leads to a higher falling velocity of particles, but also less turbulence for flocculation (Lacy et al., 2003).

In addition to physical processes, biological activity may affect the settling properties of the suspended matter and enhance mixing of bed sediment particles prior to resuspension (Paterson, 2001; Tolhurst et al., 2002).

Hindered Settling

Hindered settling is the process by which the settling of sediment particles becomes impeded due to the proximity of other sediment particles (Le Hir et al., 2011; Winterwerp, 1999). This occurs at high SPM concentrations. It is a separate settling regime, as discussed in the above.

Slope instability

There are three basic mechanisms for slope instability (Van Rijn, 2005):

1. Slope collapse for steep slopes

For very steep slopes (1:2 or 1:3)

2. Liquefaction and successive mass slide
   Occurs for loosely packed sandy layers due to decrease in grain stress (slope effect)
3. Breaching and retrogressive gradual erosion
   Fine sandy material under local initial steep slope (greater than angle of repose), producing a quasi-steady turbidity current of sediment

Appendix B. Scheldt Estuary

The Scheldt Estuary is a tide dominated water body on a coastal plain through which the Scheldt River and its tributaries discharge water into the North Sea. The river is a typical meandering lowland-river with a total length of 355 km, in which it falls 100 m. The Scheldt River runs from the source in Saint Quentin in North-France, through Belgium, to the mouth at Flushing in The Netherlands. The total catchment area is estimated to be 21,836 km^2 (Baeyens et al., 1998; P. Meire et al., 2005).

B.1 Geomorphology

The estuary extents up to the salt limit, which on average is located between Kruibeke and Rupelmonde. The estuary has a funnel-shaped geometry; its width reduces from about 6000 m between Flushing and Breskens to less than 300 m near Kruibeke, and 100 m near Ghent (Bolle et al., 2010; Wang et al., 2002).

The Scheldt Estuary can be subdivided into the following geomorphological parts (see Figure 17); from downstream to upstream (Baeyens et al., 1998):

- Lower estuary (Western Scheldt):
  The Western Scheldt runs from mouth between Flushing and Breskens to the border between Belgium and The Netherlands. It is characterized by a braided network of a separate flood and an ebb channel. The area can be subdivided into seven estuarine macro-cells, each consisting of a separate flood and ebb channel, intertidal area and interconnecting channels (Winterwerp et al., 2001). The braiding network stops at the Belgian-Dutch border, at which the estuary becomes a one channel system. In front of the Western Scheldt lies a large ebb tidal delta, known as the Vlakte van de Raan.
- Upper estuary (Sea Scheldt):
  The Sea Scheldt can be divided in two parts (Maris et al., 2014):
  - Lower Sea Scheldt
    The brackish water body between the Belgian-Dutch border and Rupelmonde is called the Lower Sea Scheldt. This part of the estuary is typically characterized as transition between an estuarine and riverine geomorphology. The Lower Sea Scheldt has one meandering tidal channel with relatively small mudflats and salt marches (Maris et al., 2014; P. Meire et al., 2005).
  - Upper Sea Scheldt and tidal-dependent tributaries:
    The Upper Sea Scheldt is characterized by a long tidal-dependent freshwater zone, which is composed of the Scheldt River between Rupelmonde and the tidal limit at Ghent, and its tidal-dependent tributaries: Rupel, Nete (Kleine en Grote Nete), Zenne, Dender, Leie, and Dijle. In the tributaries the tidal limits are present around Grobendonk (Kleine Nete), Itegem (Grote Nete), Zemst (Zenne), Haacht (Dijle), Dendermonde (Dender) and Merelbeke (Leie). It has a typical riverine bathymetry.

  The Sea Scheldt can be divided in 11 cells with equal salinity and/or residence times of fresh water (Maris et al., 2014).

The Scheldt Estuary becomes shallower in landward direction. Furthermore, intertidal flat area increases up to the Lower Sea Scheldt, after which it reduces in landward direction (Plancke et al., 2014).

B.2 Evolution of the Scheldt Estuary

The Scheldt estuary, in particular its mouth, has undergone a lot of changes in its geomorphology. During the Last Glacial Period, the Scheldt River primarily debouched through the Flemish Valley into the North Sea at the present Dogger Bank, accompanied by the Thames River, Rhine River and Meuse River. The planform of the Lower Sea Scheldt was more or less fixed due to the formation of Boom, which consist of stiff, plastic clay with high erosive strength (Coen, 2008).

After the Last Glacial Period, this situation changed due to sea level rise and the formation of sand ridges along the present Flemish coast. These ridges created protected salt water basins in which both marine and fluvial clay could form marches. This led to the situation where the Scheldt River discharged its water through the mouth of the Rhine and Meuse Rivers. Over time, the influence of the North Sea increased in the area, which caused a breach in the coast and the subsequent formation of a network tidal creeks, which form the present Eastern Scheldt. This sea arm eventually connected to the Scheldt River. South of the Eastern Scheldt, another sea arm was created by a sequence of storms, nowadays known as the Western Scheldt (Coen, 2008).

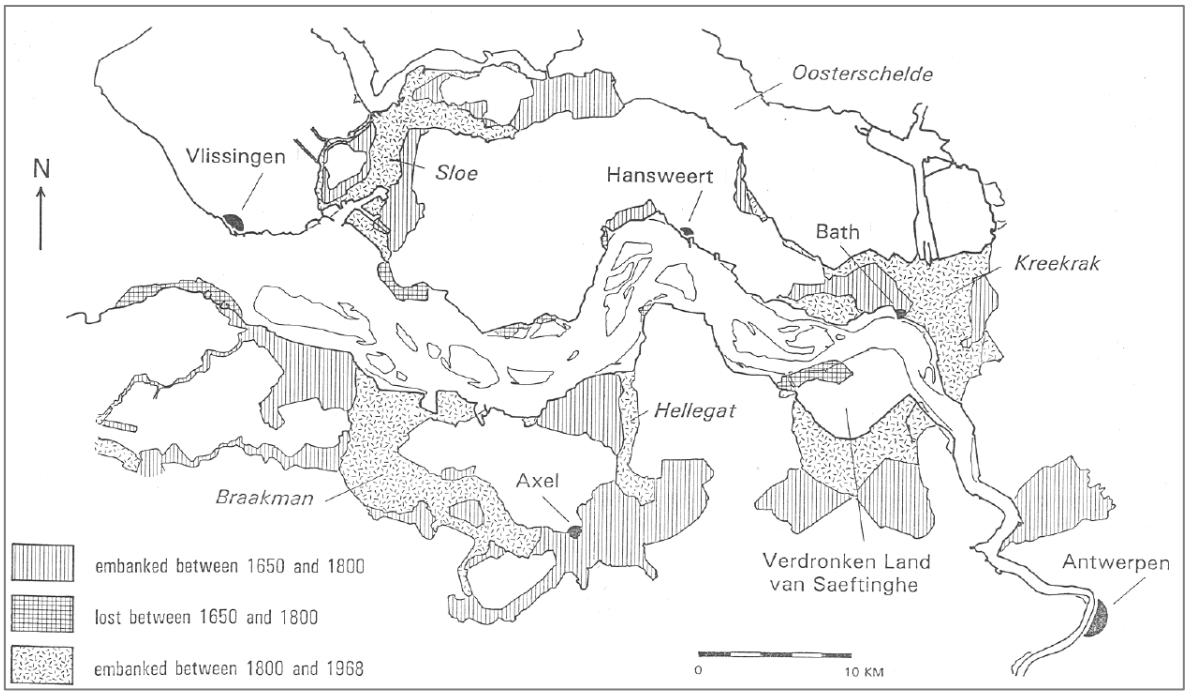

Figure 67 – Development of the Scheldt Estuary (Van der Spek, 1994)

Since the early middle ages some tidal marshes were reclaimed by embankments to create agricultural lands. Between 1000 and 1500 the estuary increased rapidly in size because of natural processes (storms, floods, subsidence and sea level rise). This eventually led to the connection of the Western Scheldt and the Scheldt River. As a consequence of the new hydraulic regime, a salt march developed between the Eastern and Western Scheldt (Winterwerp et al., 2006).

Reclamation of tidal marches in and along the Scheldt basin continued during the late 17th century and 18th century, as can be seen in Figure 67. After some losses of impoldered areas due to storms and erosion, land reclamations were continued during the 19th and 20th century for industrial and urban development. This permanently separated the Eastern Scheldt from the Western Scheldt, which led to the current situation: the debouching of the Scheldt River into the North Sea solely through the Western Scheldt (Coen, 1988). Later, the estuary was trained and diked, which were regularly strengthened, heightened and widened in outward direction. These developments led to a loss of intertidal area (Meire, 2005).

The last decades, the channels of the estuary have been dredged and trained to guarantee larger ships to have safe access to the Port of Antwerp. Most dredging has taken place in the Western Scheldt and most downstream part of the Lower Sea Scheldt at the bars where ebb and flood channels merge. The dredged material has mainly be relocated within the estuary. Sea level rise, sea bottom subsidence and, recently, the 18.6 year tidal cycle, contribute to the present evolution of the geomorphology of the estuary (Meire, 2005).

B.3 Bathymetry

The Scheldt Estuary changes from a sea environment to a riverine environment. Hereby, the width-averaged depth decreases from 15 m at Flushing to only 3 m near Ghent. The bathymetric features are discussed in this subsection for each distinctive part of the Scheldt Estuary separately.

Western Scheldt
The Western Scheldt has a typical estuarine geomorphology, characterized by a two-channel system. There is a distinct ebb channel and flood channel in the Western Scheldt, separated by shallow sub- and intertidal areas. At some location the channels merge and separate again. The Western Scheldt can therefore be characterized by multiple macro-cells, each having a separate flood and ebb channel, inter- and subtidal area and interconnecting (tertiary, marginal) channels.

The course of the ebb and flood channel in the Western Scheldt show little dynamic behavior as they are more or less bounded by the embanked geometry. Although in history the dominancy between the ebb and flood channels changed frequently over time, nowadays the ebb channel is dominant over the flood channel throughout most the Western Scheldt. An exception is at the Platen van Ossenisse, where due to a bend cut off the flood channel is dominant. Reason for this static behavior is the regular deepening of the dominant channel for navigation from the North Sea to the Port of Antwerp in combination with dumping of dredged material in the secondary and tertiary channels (Swinkels et al., 2009).

Most interconnecting channels in the Western Scheldt have been developed between the ebb and flood channels due to difference in tidal propagation between the ebb and flood channels, centrifugal forces in bends and the Coriolis force. They can either be classified as bar connecting or shoal connecting channels, depending on their location (at bar or shoal area). They used to show very dynamic behavior. However, due to frequent dumping activities, most interconnecting channels tend to diminish in size and become more fixed over time (Swinkels et al., 2009).

Table 13 – Bathymetric features of the Western Scheldt (Kuijper and Lescinski, 2013).

Parameter		Flushing-Terneuzen	Terneuzen-Hansweert	Hansweert-Bath
Depth [m LAT]	Width-averaged	14.25	12.20	11.40
	Main Channel	20.30	18.00	15.20
	Secondary Channel	13.50	11.30	9.50
	Intertidal flats	2.10	2.00	1.90
Area [m^2]	Channel	$9.18\ 10^7$	$5.94\ 10^7$	$3.7\ 10^7$
	Intertidal flats	$2.68\ 10^7$	$2.38\ 10^7$	$1.73\ 10^7$
	Ratio	0.29	0.40	0.47
Water Volume [m^3]	Channel	$1.31\ 10^9$	$7.2\ 10^8$	$4.2\ 10^8$
	Intertidal flats	$5.2\ 10^7$	$5.0\ 10^7$	$3.5\ 10^7$
	Ratio	0.04	0.07	0.09

In Table 13 the bathymetric features of the Western Scheldt are listed. Over the last decades, both the water volume in the channels and the channel area have increased, especially between Hansweert and Bath. This is related to the deepening of the navigation channel and the evolution of the tidal characteristics in the Scheldt Estuary. Furthermore, the intertidal

areas have increased in height and their slopes have steepened. However, there is a slightly negative trend for the water volume above the intertidal flats and intertidal flat area (Kuijper et al., 2013).

Lower Sea Scheldt

The one channel system of the Western Scheldt at the Belgian-Dutch border continues throughout the Lower Sea Scheldt. The system is very static due to a combination of training measures and the narrow planform through the stiff and plastic Boom clay. The bathymetry of the Lower Sea Scheldt is typically characterized as transition between an estuarine geomorphology with a single channel and some intertidal flats, and a fluvial geomorphology, characterized by a meandering main channel with shallow parts in the inner bends, deep parts in the upper bends and transition bars in the straight sections. Some bathymetric features of the Lower Sea Scheldt are summarized in Table 14.

Table 14 – Bathymetric features of the Lower Sea Scheldt (Plancke et al, 2012).

Parameter		Bath-Liefkenshoek	Liefkenshoek-Antwerp	Antwerp-Schelle
Depth	Depth-averaged	9.30 m TAW	9.00 m TAW	6.00 m TAW
	Main channel	15.00 m TAW	15.00 m TAW	8.00 m TAW
Water Volume	Channel	1.64×10^8 m^3	8.4×10^7 m^3	3.9×10^7 m^3
	Intertidal flats	3.7×10^7 m^3	1.4×10^7 m^3	6.0×10^6 m^3
	Ratio	0.23	0.17	0.15

The Lower Sea Scheldt, in particular the most downstream part between Bath and Liefkenshoek, show more or less the same trend as the Western Scheldt. Over the last decades, the channel depths have increased. Again, this is due to the deepening of the channel to facilitate larger ships to the Port of Antwerp and changed tidal characteristics. Furthermore, the water volume above the intertidal flats has decreased between Bath and Liefkenshoek, while this volume has remained quasi-constant elsewhere in the Lower Sea Scheldt (Plancke et al, 2012).

Upper Sea Scheldt

In the Upper Sea Scheldt has a characteristic meandering riverine bathymetry as described for the Lower Sea Scheldt. The average depth decreases from 7.5 m LAT in Tielrode to 3 m LAT in Dendermonde, which remains more or less constant up to Ghent (Meyvis). The system shows static behavior.

In the past, the planform of the Scheldt river and its tributaries in the Upper Sea Scheldt have been normalized and rectified by engineering works. Most were completed before 1930. After 1970, the river bed has deepened by 1.5 - 2 m, probably as a response of the engineering works and/or sand mining activities further down-estuary or due to the geomorphological changes in the Western and Lower Sea Scheldt. This led to changes in the tidal propagation through the Scheldt Estuary (Winterwerp, 2013). Recently, large retention areas have been created from polder area to increase the discharge capacity of the Upper Sea Scheldt. These areas are overflowing in a controlled manner during river floods (Vandenbruwaene et al., 2017).

B.4 Tide

The Scheldt Estuary predominantly has a semidiurnal meso- to macrotidal regime in which the M_2 and S_2 constituents are the most prominent. The mean tidal prism is 2.2×10^9 m^3 at the estuary mouth at Flushing, reducing to only 0.2×10^9 m^3 at the Belgian-Dutch border and 0.1×10^9 m^3 at Antwerp. The tidal discharge at the estuary mouth has an annual average of 50,000 m^3/s for both mean ebb and flood tides (Verlaan, 1998; Wang et al., 2002).

Table 15 – Characteristics of the vertical tide throughout the Scheldt Estuary (Vanlierde et al., 2014)

		Flushing	Terneuzen	Hansweert	Bath	Liefkenshoek	Antwerp	Schelle	Dendermonde	Melle
Distance to Mouth [km]		2	21	36	52	63	78	91	122	151
Spring Tide	Range [m]	4.47	4.83	4.96	5.59	5.89	6.03	6.03	4.61	2.71
	HAT [m TAW]	5.43	5.77	6.06	6.36	6.53	6.78	6.85	6.77	6.41
	MHWS [m TAW]	4.82	5.06	5.14	5.52	5.72	5.79	5.85	5.68	5.30
	MLWS [m TAW]	0.35	0.23	0.18	-0.07	-0.17	-0.24	-0.18	1.07	2.59
	Mean Flood Period	5:53	5:38	5:56	5:42	5:24	5:05	5:13	4:42	4:14
	Mean Ebb Period	6:26	6:42	6:25	6:38	6:56	7:13	7:04	7:35	7:59
	HW time lag w.r.t. Antwerp [H:MM]	-1:40	-1:24	-0:37	-0:15	-0:13	0:00	0:47	1:52	3:31
	LW time lag w.r.t. Antwerp [H:MM]	-2:24	-1:54	-1:23	-0:48	-0:28	0:00	0:38	2:14	4:17
Mean Tide	Range [m]	3.84	4.16	4.44	4.94	5.19	5.37	5.45	4.33	2.65
	MHW [m TAW]	4.41	4.63	4.77	5.09	5.25	5.35	5.49	5.37	5.09
	MSL [m TAW]	2.49	2.55	2.55	2.62	2.66	2.67	2.77	3.21	3.76
	MLW [m TAW]	0.57	0.47	0.33	0.15	0.06	-0.02	0.04	1.04	2.44
	Mean Flood Period [H:MM]	5:58	5:50	6:02	5:53	5:41	5:28	5:29	4:53	4:24
	Mean Ebb Period [H:MM]	6:27	6:35	6:23	6:32	6:44	6:56	6:55	7:32	8:00
	HW time lag w.r.t. Antwerp [H:MM]	-1:45	-1:25	-0:45	-0:23	-0:17	0:00	0:39	1:40	3:19
	LW time lag w.r.t. Antwerp [H:MM]	-2:09	-1:44	-1:15	-0:44	-0:26	0:00	0:38	2:14	4:23
Neap Tide	Range [m]	3.01	3.28	3.64	3.97	4.25	4.54	4.68	3.97	2.62
	MHWN [m TAW]	3.84	4.06	4.23	4.46	4.60	4.82	4.98	4.95	4.81
	HLWN [m TAW]	0.83	0.78	0.59	0.49	0.35	0.28	0.30	0.98	2.19
	LAT [m TAW]	-0.23	-0.35	-0.42	-0.65	-0.62	-0.68	-0.61	0.67	1.74
	Mean Flood Period [H:MM]	6:11	6:08	6:17	6:15	6:09	5:59	5:53	5:13	4:45
	Mean Ebb Period [H:MM}	6:30	6:31	6:23	6:25	6:31	6:44	6:53	7:33	8:05
	HW time lag w.r.t. Antwerp [H:MM]	-1:40	-1:21	-0:51	-0:27	-0:19	0:00	0:31	1:30	3:06
	LW time lag w.r.t. Antwerp [H:MM]	-1:47	-1:27	-1:04	-0:38	-0:24	0:00	0:39	2:19	4:27

Throughout the estuary, the tidal wave is deforming, which is caused by steepening (shoaling), reflection, amplification and damping of the tidal wave. This both affects the vertical and horizontal tide. Furthermore, the tidal characteristics of the Scheldt Estuary have changed significantly in the recent past.

Vertical Tide

The estuary is excited at its mouth by a very regular (slightly distorted sinusoidal) water level signal, present in the North Sea. There is a strong spring-neap cycle present in the Scheldt Estuary, caused by the difference in frequency between the M_2 and S_2 constituents.

The tidal range changes significantly throughout the estuary, as can be seen in Figure 18 and Table 15. It can be noticed that initially the tidal wave is amplified from the mouth up to Schelle, as the tidal range increases. This is explained by a combination of funneling of the tidal wave, partial and abrupt reflections, both caused by the funnel-shaped geometry of the estuary, and shoaling of the tidal wave. According to Pieters (2002), 20 to 30% of the tidal range at Flushing is caused by reflection of the tidal wave. Upstream of Schelle, the tidal amplitude decreases rapidly due to diminishing depths, and hence, increased frictional damping (Van Rijn, 2011; Winterwerp, 2013).

Furthermore, based on the decreasing flood period in upstream direction, it can also be observed that the tidal wave is deforming: the wave front is steepening over time. Another phenomenon of the vertical tide in the Scheldt Estuary is the increase in mean sea level. This is believed to be caused by a combination of Stokes' Drift and the above explained distortion of the tidal wave (Van Rijn, 2011).

As a consequence of the presence of the spring-neap cycles in the estuary, posing variation in tidal range, the above mentioned phenomena are also prone to variation. For example, due to a decreased tidal range during neap tide, there is less distortion of the vertical tidal wave and hence, less increase in mean sea level, compared to during spring tide (Van Rijn, 2011).

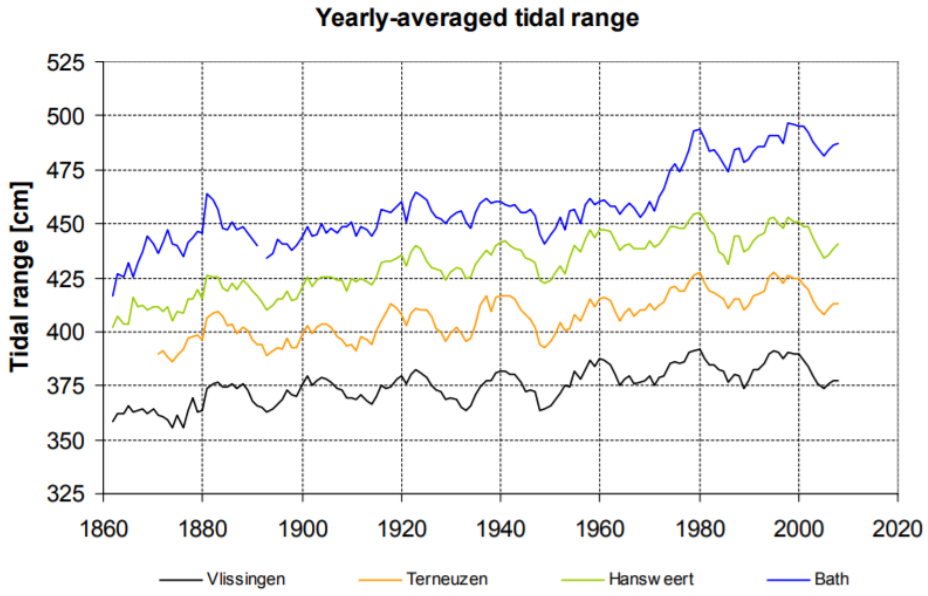

Figure 68 – Yearly-averaged tidal range in the Western Scheldt (Kuijper, 2013)

The vertical tide has changed dramatically during the 20th century, particularly the tidal range, which has increased with an average rate of 0.2 m/century at the mouth (Kuijper, 2013) to an average rate of about 1.1 m/century at Schelle (Plancke, 2013). This is visualized in Figure 68 and Figure 69. In particular the mean high waters have increased (0.3-0.4 m/century), while the low waters also increased, although, with lesser extent (~0.2 m/century). The propagation of the vertical tide throughout the estuary has changed due to this increase. Whereas in the past the tidal wave dampened in the Lower Sea Scheldt from Bath onwards, this nowadays occurs near Schelle. The last decades the tidal range stayed more or less the same (Kuijper, 2013) (Plancke, 2013).

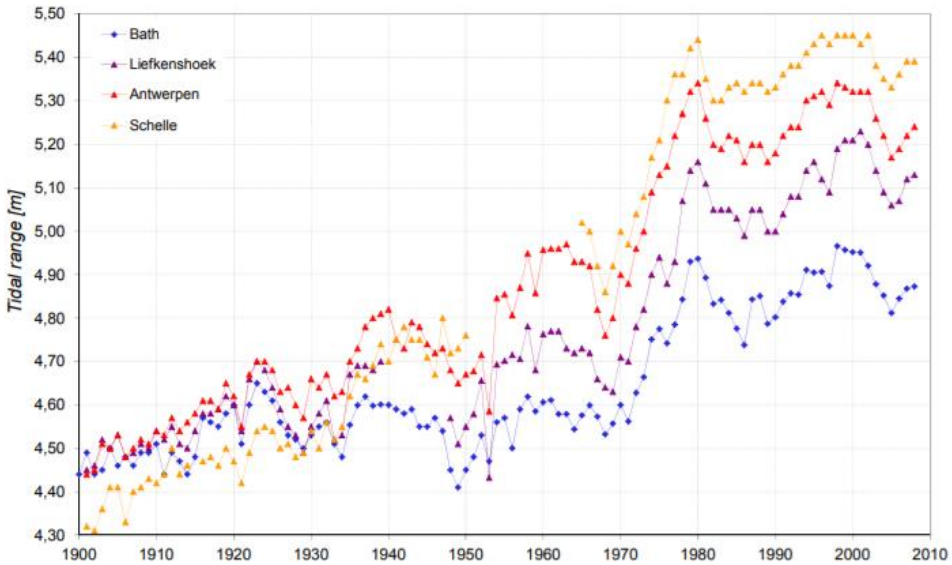

Figure 69 – Yearly-averaged tidal range at Bath, Liefkenshoek, Antwerp and Schelle (Plancke, 2013).

The increase in tidal range in the long term is explained by the land reclamations in the Scheldt Estuary, which increased the convergence of the estuary and decrease in water retention

areas and friction. This amplification has increased even further during the 70s and 80s, due to large scale deepening of the channels in the Western Scheldt and Lower Scheldt Estuary, which reduced the hydraulic roughness considerably. Additionally, the changes dredging and dumping strategy may have had contributed to the evolution of the tidal range in this section (Kuijper, 2013). The range in the Upper Sea Scheldt has also increased. This is mainly caused by the deepening of the system in 1960 as response to anthropogenic interference and in a lesser extent due to changes of the tidal range in the down-estuarine parts (Western Scheldt and Lower Sea Scheldt) (Winterwerp, 2013).

Constituents

The vertical tide can also be described by analyzing the Fourier components of the water level signals throughout the estuary. The results can be found in Table 16. It can be noticed that indeed the earlier mentioned M_2 and S_2 constituents are most prominent in the estuary. Other important astronomical constituents present in the estuary are (2'')N_2, K_2, L_2, λ_2, K_1 and O_1. The tidal components have interfered with each other in the North Sea, which resulted in additional compound tides at the mouth of the estuary. Most prominent of these is the M_4 tide, while also the 2''MS_6, MS_4, M_6 tides are present.

Inside the estuary, it can be seen that the amplitudes of most tidal constituents are increasing. This is, of course, due to the tidal phenomena which increase the tidal range throughout the estuary. Furthermore it can be observed that the compound tides become more pronounced due to continued non-linear interactions of the tidal components inside the estuary. The generation of the M_8 and 2''MN_6 tides are also a consequence of this.

Another important feature is the generation of a strong MU_2 and NU_2 tides in Antwerp. These are generated by the Fourier analysis to simplify the M_2 component of the water level signal. At Antwerp, this is believed to be necessary due to the narrow cross-section. Consequently, the tidal water level signal is highly distorted during run-off events in the Scheldt River.

Table 16 – Governing vertical tidal constituents through Scheldt Estuary

	Flushing		Terneuzen		Hansweert		Antwerp	
	Amplitude [m]	Phase [°]	Amplitude [m]	Phase [°]	Amplitude [m]	Phase [°]	Amplitude [m]	Phase [°]
M_2	1.730	30.6	1.830	40.3	1.956	54.1	2.318	225.5
S_2	0.478	87.6	0.492	100.2	0.514	116.0	0.559	173.3
N_2	0.266	7.2	0.278	19.1	0.293	33.2	0.358	48.3
M_4	0.135	54.6	0.119	78.4	0.104	117.0	0.131	71.0
K_2	0.132	86.1	0.136	97.8	0.144	113.1	0.119	318.7
O_1	0.105	176.3	0.106	183.4	0.108	191.2	0.079	3.2
2''MS_6	0.105	70.6	0.082	106.9	0.074	179.2	0.124	250.9
L_2	0.092	47.2	0.103	53.6	0.113	66.5	0.212	213.3
MS_4	0.073	116.4	0.073	133.7	0.055	175.6	0.077	14.7
K_1	0.062	355.8	0.066	3.9	0.065	14.0	0.064	30.2
M_6	0.057	19.1	0.076	78.7	0.102	137.4	0.145	317.0
λ_2	0.053	47.6	0.062	62.9	0.070	76.8	0.081	159.7
NU_2	-	-	-	-	-	-	0.138	93.6
MU_2	-	-	-	-	-	-	0.238	76.9
2''N_2	-	-	-	-	-	-	0.074	261.9
2''MN_6	`-	-	-	-	-	-	0.074	133.9
M_8	-	-	-	-	-	-	0.062	92.6

Asymmetry

The vertical tide in the Scheldt Estuary typically shows flood dominancy throughout the whole estuary. This can be noticed by the duration of the flood period, which is shorter than the ebb

period. The flood dominancy of the vertical tide is in particular strong in the mouth and in the upper estuary (where it increases rapidly), while it decreases somewhat near Hansweert and Bath (Plancke, 2013). According to Wang et al. (1999), the hypsometry of the estuary tend to reinforce the asymmetry in the vertical tide.

The asymmetry of the vertical tidal wave is temporarily varying; asymmetry is found to be stronger during spring tide than during neap tide. This is both due to increasing amplitude ratios M4/M2 and M6/M2, as non-linearities become more pronounced for a greater tidal range. Moreover, the relative phase differences between M2 and M4 and between the M2 and M6 constituents shows larger scatter during neap tide than during spring tide. This scatter is however random and not explained by the physical interaction between M4 and MS4, and M6 and MS6 respectively (Wang et al., 1999).

Table 17 – Relative amplitudes and phases between pronounced tidal constituents leading to asymmetry in vertical tide.

Relative phase	Flushing	Terneuzen	Hansweert	Antwerp
$2\varphi_{M2} - \varphi_{M4}$	6.61	2.21	-8.79	19.89
$\varphi_{M2} + \varphi_{S2} - \varphi_{MS4}$	1.80	6.80	-5.50	24.08
Relative amplitude	**Flushing**	**Terneuzen**	**Hansweert**	**Antwerp**
MS4/(M2+/-S2)	0.033-0.058	0.031-0.055	0.022-0.038	0.027-0.044
M4/M2	0.078	0.065	0.150	0.057
S2/M2	0.276	0.269	0.263	0.241

Based on analysis of the relative amplitudes and phases of semi-diurnal and quarter-diurnal components in Table 17, it can be seen that the asymmetry is relatively weak. This is because the relative amplitudes between the MS_4, M_2, and S_4 components, and between the M_2 and M_4 constituents are not large. Additionally, the relative phases between these constituents are close to zero.

As for the tidal range, the vertical asymmetry of the tide has altered over the last century. The amplitudes of the M2 and M4 tidal component have increased, whereas the M6 component has not. This resulted in an increased amplitude ratio M4/M2. The amplitude ratio M6/M2 stayed more or less constant, being larger in the eastern part of the Estuary. This caused the asymmetry of the vertical tide in the eastern part to be stronger. The phases of the M2 and M6 tidal components stayed more or less the same, while the phase of M4 component increased at Bath and decreased at Hansweert. This let the phase difference between M2 and M4 tidal component to decrease at Bath and to increase at Hansweert. The phase difference between M2 and M6 components increased gradually, except at Bath, where it decreased. Overall, this resulted in the tidal asymmetry becoming less flood dominant in the eastern part of the Western Scheldt, between Hansweert and Bath, while in the western part of the Western Scheldt the estuary became slightly more flood dominant. The vertical asymmetry in the central part of the Western Scheldt is changing from ebb dominant to almost neutral. The decrease in flood dominancy in the deeper channels, and increased flood dominancy in the shallower channels are related to the dredging and dumping of soil material in the channels respectively (Bolle et al., 2010) (Kuijper, 2013).

In the Lower Sea Scheldt, the vertical tidal wave has become more ebb dominant; the duration of the rising tide increased, combined by a consequent decrease of the duration of the falling tide. This is a direct consequence of the deepening of the area (Plancke et al., 2013). The flood dominancy in the Upper Sea Scheldt has not increased neither decreased after 1900, although the increase in tidal amplitude. This is related to development of the Western Scheldt at Bath becoming less flood dominant and the increase in depth of the Upper Sea Scheldt (Winterwerp, 2013).

Phase shift horizontal and vertical tide

The horizontal tide runs ahead of the vertical tide by about 1-3 hours in the estuary. This makes the tidal wave partially progressive, partially standing, although the estuary is classified

as long. In funnel-shaped estuaries, however, there is continuous reflection of the tidal wave due to the converging sides, which continuously partially reflect the wave. At the landward limit of the estuary a fully standing wave is observed, as the wave is reflected by a sluice. Due to the increased tidal range, the tidal wave has become more standing over the last decades (Van Rijn, 2011).

Horizontal Tide
In the Western Scheldt the maximum tidal velocity does not exceed 1-1.5 m/s, while at the mouth this is about 0.9 m/s. In the Sea Scheldt, the maximum tidal velocity is 1.5-1.7 m/s. As a consequence, the tidal excursion length is approximately 10 to 20 km (Van Rijn, 2011), depending on the governing tide and river discharge.

Asymmetry
Although closely related to the asymmetry of the vertical tide, the asymmetry of the horizontal tide is rather complex to analyze. This is because long-term current velocity measurements are lacking, since they are expensive. Additionally, since current velocity is a vector in which constituents may have different principal directions, asymmetry of the horizontal asymmetry can no longer be characterized by an amplitude ratio and relative phase difference. An example is the M_4 component, which, due to flow curvature, can be perpendicular to the mean current direction (Wang et al., 1999).

In general, the asymmetry in the horizontal tide shows different behavior compared to the asymmetry in the vertical tide, which shows increasingly flood dominance in landward direction. It is believed that the hypsometry of the estuary reduces the asymmetry in the horizontal tide (Wang et al., 1999). Consequently, the width-averaged asymmetry of the horizontal tide is small and differs over the estuary. The lower estuary is generally slightly flood dominant (Bolle et al., 2010), while the upper estuary is slightly ebb dominant (Smolders, Plancke, Bi, Vanlede, & Kolokythas, 2019). However, there is strong asymmetry, which acts oppositely within the cross-section: the ebb channels generally show strong ebb dominance and the flood channels strong flood dominance (Van Rijn, 2011). This is primarily caused by horizontal Eulerian residual currents (Bolle, 2006). Asymmetry of the horizontal tide changed over the estuary due to recent developments of the geometry. In general, this resulted in a less flood dominant system (Bolle et al., 2010).

Although no literature was found about the duration and the difference between HW and LW slack tide period, it becomes clear that the moment of slack water with respect to HW and LW is different throughout the Scheldt Estuary. The further upstream, the smaller the lag between the extreme water levels and the slack periods. At the estuary mouth this lag is approximately 1 hour, while at the ends of the estuary there is no time lag (Claessens, 1988).

Propagation velocity
The average propagation velocity of the vertical tide is approximately 10 m/s, but varies along the thalweg. Due to deepening of the tidal channels, the propagation velocity of the high waters has increased from 9 to 18 m/s between Flushing and Terneuzen, while it remained more or less constant in the rest of the Western Scheldt. The propagation velocity of the low waters has changed to a lesser extent, decreasing somewhat between Hansweert and Bath and increasing slightly between Flushing and Hansweert (Van Rijn, 2013).

In the Lower Sea Scheldt and more upstream, the tidal wave celerity of both the high and low waters have increased somewhat due to decreased damping of the tidal wave. However, Winterwerp (2013) shows that the tidal wave propagates slower in the upper reaches of the Upper Sea Scheldt, as the wave has become more damped at that location. This is believed to be caused by increased reflection of the tidal wave against the weir at Ghent.

B.5 River discharge

The annual average river discharge of the Scheldt amounts 104 m^3/s. However, since the Scheldt River is typically a rainfed river, its average discharge may vary from 60 m^3/s (with a

minimum monthly-average of 30 m^3/s) during dry summers, to 180 m^3/s during wet winters (with a maximum monthly-average of 400 m^3/s). The maximum instantaneous discharge may reach 600 m^3/s. The major contributors to the discharge are the Scheldt River and its tributaries, the Dender, the Durme, and Ruper (including Nete, Zenne, and Dijle), accounting for about 27%, 6%, 10%, 56% (17%, 12%, 27%) to the discharge. In the Western Scheldt fresh water is also supplied by the Ghent-Terneuzen Canal (15 m^3/s), the discharge-sluice of Zoommeer Lake near Bath (11 m^3/s) and some minor discharges from polders (20 m^3/s in total). The fresh water supply is small compared to the tidal discharge (Baeyens et al., 1998).

During a tidal cycle 5 x 10^6 m^3 of freshwater is discharged into the North Sea, which contributes to only about 0.5% of the tidal volume (Baeyens et al., 1998). The residence time of freshwater in the Scheldt Estuary is estimated at 2-3 months (Wollast and Peters, 1978). No significant changes in the fresh water discharge of the Scheldt Basin over the recent past are reported.

B.6 Wind

The dominant wind in the Scheldt Estuary are the westerly winds, coming the southwest. These winds have an average wind speed of 5 to 10 m/s, while during storms the wind speed may reach 20-25 m/s. The wind climate is subject to seasonality due to variation in the temperature of the land mass with respect to the sea temperature. There are stronger and more frequent westerly storms present during winter than during summer. Also easterly storms occur in winter, which may have a wind speed of 15-20 m/s. During the milder summer season, there is also a large contribution of wind coming from the north-west (B. W. F. Van Rijn, 2012). Due to wind set-up, water levels at Flushing can raise another 3.0 - 4.5 m NAP by a severe western storm. The amount of storm surges has increased the last decades (Kuijper & Lescinksi, 2013). Wind has not been reported to directly influence the hydrodynamics in the upper estuary.

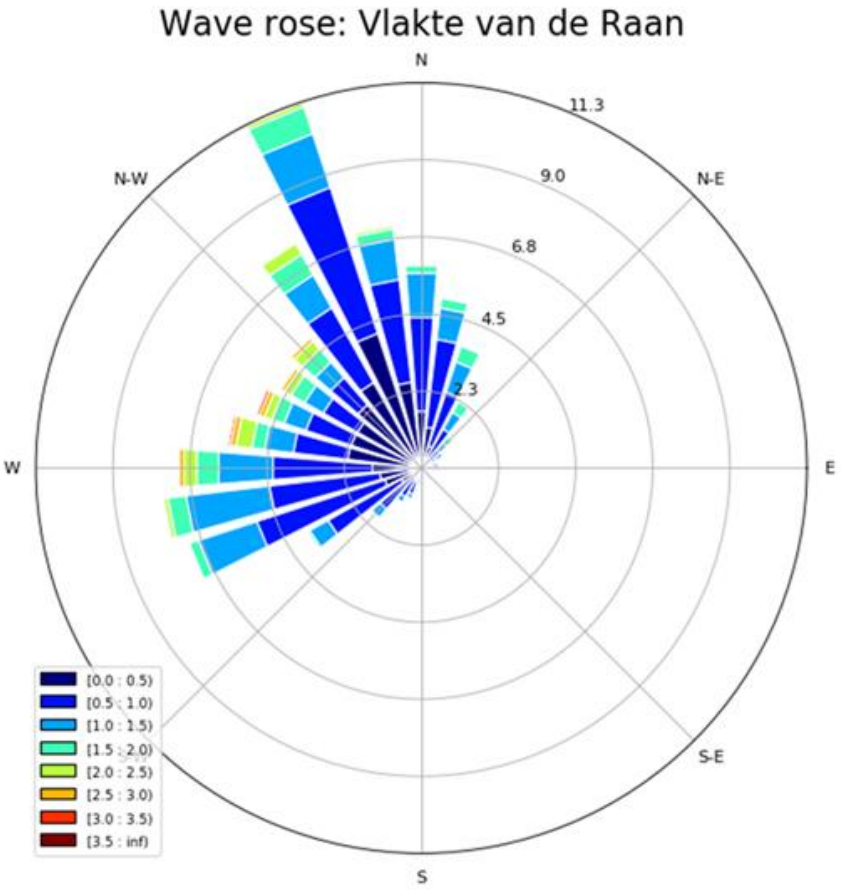

Figure 70 – Wave rose of measurement data of wave heights [in m] and directions at the Vlakte van de Raan in 2018.

B.7 Waves

The wave climate is characterized by both waves propagating from the North Sea into the Western Scheldt, and locally generated waves (see Figure 70). Hence, the wave speed and direction are to a large extent determined by the prevailing wind climate. Therefore, Scheldt Estuary has typically a storm wave climate with steep, short-crested and multi-directional waves. Also swell waves, which are generated in the northern part of the North Sea, are present at the mouth of the estuary (coming from the NNW) (B. W. F. Van Rijn, 2012).

The yearly-averaged significant wave height at the estuary mouth is 0.8 m, varying between 0.6 m averaged over the summer and up to 1.5 m in the winter with peaks of 2-3 m during severe storms. The peak period of the waves ranges from 2 to 10 s (Sistermans & Nieuwenhuis, 2004; Van der Werf et al., 2015). The highest waves are generated during north-westerly winds due to a longer fetch.

Waves only influence the western part of the estuary near the mouth between Flushing and Breskens. Further upstream from the mouth (> 40 km), the wave energy becomes negligible compared to tidal energy, as waves from the North Sea do not penetrate that far due to dissipation of shallow areas, such as on the shoals, tidal currents, and sheltering by the geometry of the estuary. It is believed that local wave generation by wind remains small because of limited fetch length (Chen, Wartel, Van Eck, et al., 2005; Van Kessel et al., 2011), not exceeding 0.2 m.

Due to the intense shipping by sea-going vessels in the lower part of the estuary, substantial primary and secondary ship waves are present in the estuary. According to research of Meire, Kolokythas, & Plancke (2017), most vessels create secondary ship waves in the range of 0.1-0.3m, while secondary ship waves of tankers, but especially cargo ships, may reach up to 1.0 m. The primary waves appear to be slightly smaller, having an amplitude of up to 0.8 m. The yearly-averaged traffic intensity in the lower part of the Scheldt is 3-4 ships per hour. One cargo ship passes each eight hours (Port of Antwerp, 2019).

B.8 Salinity

The salinity in the estuary smoothly varies from freshwater at Rupelmonde (0-5 g/l) to the nearly constant value of seawater at Flushing (32 g/l). The Scheldt Estuary can be divided into the following areas of equal salinity: mesohaline (Bath-Antwerp), oligohaline (Antwerp-Schelle) and fresh water regimes (Upper Sea Scheldt).

The length of the salt intrusion is primarily determined by the magnitude of the river discharge. During high river discharge, seawater only penetrates to about Antwerp (~70 km from mouth), whereas during low discharge it penetrates upstream of Rupelmonde (>92 km). In Figure 19 distinct salinity distributions are plotted per tidal phase for both winter (high river discharge) and summer (low river discharge) periods. The shift in salinity intrusion is over 40 km. Salt intrusion responds quickly to river floods. However, the salinity is not able to adapt instantaneous to decreasing river discharge; there is a strong lag of approximately 5 days before reaching equilibrium after an high run-off event. The shift of the salinity tip is to a lesser extent affected by the fortnightly spring-neap cycle (Baeyens et al., 1998; Chen, Wartel, Van Eck, et al., 2005; Fettweis & Sas, 1997; P. Meire et al., 2005).

Due to the minor contribution of river discharge to the tidal volume, the estuary is considered to be well-mixed. In the full mixing zone between Flushing and Rupelmonde the average vertical salinity difference over a tidal cycle is 1‰. The vertical distribution is however prone to variation. During spring tide, the vertical salinity gradient may reach 4‰, while during neap tide, this can be 2.8‰ (Fettweis & Sas, 1997). Apart from sluice and harbor basins, no strong lateral salinity gradients are reported in the estuary. Lateral salinity differences are found to be greater where a distinct separation between ebb and flood channels exists (Van Kessel et al., 2011).

B.9 Residual current

In general, the residual current velocity in the Scheldt estuary is directed towards to the sea close to the surface, while close to the bottom the residual current changes direction throughout the estuary. In the Western Scheldt, the bottom residual current is directed landward due to the salinity gradient over the estuary. Also the cross-sectionally averaged residual current is landward directed and amounts ~0.1 cm/s. In the Upper Sea Scheldt the residual currents in the bottom layer are directed seaward due to the influence of the river run-off. In this area, the cross-sectionally averaged residual current is also directed seaward. The area of zero net residual bottom flow is located in the Lower Sea Scheldt, at approximately 70 km distance from the mouth, shifting up- and downstream depending on the conditions (Baeyens et al., 1998; Chen, Wartel, Van Eck, et al., 2005).

Locally, the residual currents may have distinct patterns due to the influence of the geomorphology of the estuary (i.e. flood and ebb channel, inner and outer bend, sluice entrances, etc.) (Bolle et al., 2010; Chen, Wartel, Van Eck, et al., 2005; Winterwerp et al., 2001).

B.10 Sediment

Both sand and mud are present in the Scheldt Estuary. Sediment is generally transported as suspended load (fine sand and mud), although there is also some sand transported as bedload (~10-20% of suspended load) (Van der Werf & Brière, 2014). The gross sediment transport capacity is estimated to be 10 Mton/yr in the mouth of the estuary, which increases to 24 Mton/yr in the western part of the lower estuary. This decreases rather stepwise to only 2 Mton/yr in the upper reach of the Lower Sea Scheldt (Winterwerp et al., 2001). The Scheldt Estuary is a coupled system, in which the hydrodynamic and morphologic features interreact. As a consequence, there is sediment segregation throughout the estuary.

Bed composition
The median grain size and bed composition in the Scheldt Estuary is strongly varying in time and space. In general, the bed composition consists of fine to medium grained sand with a grain size of 170 µm (+/- 61 µm). The bed layer has an average mud content of about 16.4% (+/- 29.9%) (Van Eck, 1999).

From Table 1, it can be seen that cross-sectionally averaged the sandy material first becomes finer up-estuary, after which it coarsens again. This is explained by the presence of an ETM in the Lower Sea Scheldt. Consequently, in the up-estuarine section of the Western Scheldt, the grain size diameter in the channels is somewhat finer (90-120 µm) (Van Eck, 1999), while in the western part of the Western Scheldt this may increase to 300 µm (Kuijper et al., 2006). Furthermore, an increasing mud content is observed from the estuary mouth (<10%), which sharply increases towards Antwerp (>50%) (Van Ledden, 2003). In the Upper Sea Scheldt, the bed material coarsens again, as it forms a narrow passage within the Boom clay. Here the current velocity is large, and as a consequence fine sand and mud cannot deposit. At some places the Boom clay is exposed and eroded during high river run-off (Kuijper et al., 2006; Van den Neucker et al., 2007; Van Eck, 1999).

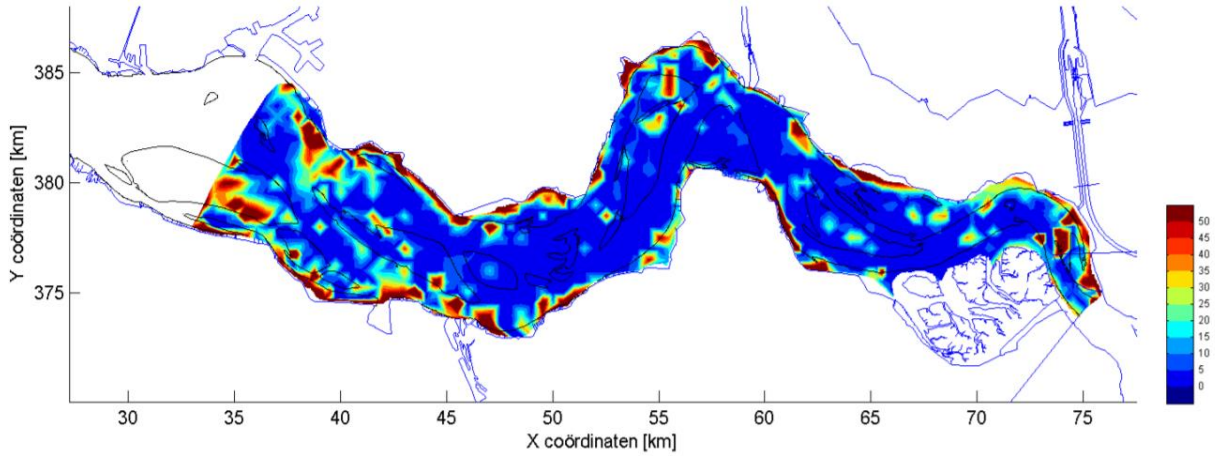

Figure 71 – Mud content in the Western Scheldt in [%] (McLaren, 1994)

However, the bed sediment characteristics differ greatly within the cross-section. In general, the grain size diameter of the bed material is found to be larger in the channels, than on the shoals and estuarine margins (Van Eck, 1999). Since in the Western Scheldt the mud content is inversely correlated with the characteristic values for the median diameter d_{50}, the percentage of mud is generally much larger alongside the estuarine margins, and at the intertidal and subtidal areas, (see Figure 71) (McLaren, 1994). In the Sea Scheldt a similar distribution over the cross-section can be found. This holds in particular for the Upper Sea Scheldt and oligohaline area of the Lower Sea Scheldt, while the difference in sediment characteristics between the sub- and intertidal areas in the mesohaline part of the Lower Sea Scheldt is marginal (Van den Neucker et al., 2007).

Sand transport

Western Scheldt (lower estuary)

In general, throughout the Western Scheldt there is import of sand, as can be seen in Figure 72. The greatest gross sand transport occurs in the flood and ebb channels, predominantly in suspension. Distinct areas may show different net sediment transport directions. For example, in the Western Scheldt flood channels and ebb channels show landward and seaward transport respectively.

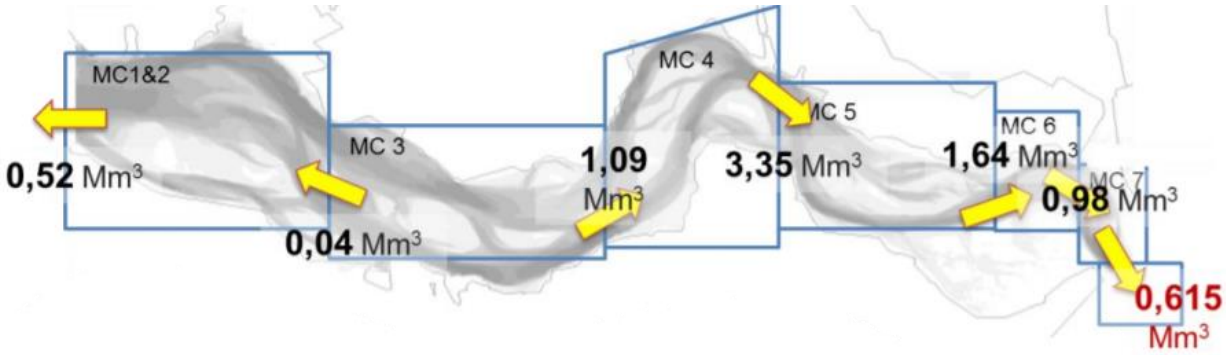

Figure 72 – Yearly net sand transport rates in the Western Scheldt for the period between 1994 and 2010 (Cleveringa & Dam, 2013)

A discrepancy in the general landward transport of sand in the estuary is the export of sand at the mouth to the ebb-tidal delta. This pattern has become present in the last decades and may be related to the fact that eastern part of the Western Scheldt and the Sea Scheldt have become broader and deeper. Consequently, more water has to enter the basin during a tidal cycle. As a reaction, channels at the mouth have to be broadened, which is possible by transporting sand to the mouth of the estuary (Taal, 2013). Furthermore, the export of sand is believed to be related to the changed dredging and dumping strategy from 1996 onwards, with more frequent dumping activities in the western part of the Western Scheldt (Cleveringa, 2013).

Despite the general import of sand in the estuary, the sand volumes of each macro-cell have not solely increased. The sand volumes in the western part of the Western Scheldt have steadily increased over time. At first, sand was mined in this area, which led to a decrease in sand volume, after which the sand volume more or less remained constant due to a decrease in the extraction of sand. Over the last decades, the sand volume has increased again, due to a further reduction in the extraction of sand and the dumping of sand from dredging works in the eastern part of the Western Scheldt. This eastern part is characterized by a continuous decrease in sand volume due to sand mining activities, a trend which has been strengthened over the last decades due to increased dredging volumes from the area (Cleveringa, 2013; Cleveringa & Dam, 2013; Haecon, 2006).

Sea Scheldt (upper estuary)
Also in the Lower Sea Scheldt the transport of sand is generally landward directed, as can be seen per cell of equal salinity in Figure 73. In the Upper Sea Scheldt, however, sand transport is directed down-estuary. Exceptions are the Durme and Gentbrugge-Melle, which form sand sinks. The incoming net sediment transport flux from the Western Scheldt corresponds with the magnitude, found by Cleveringa (2013).

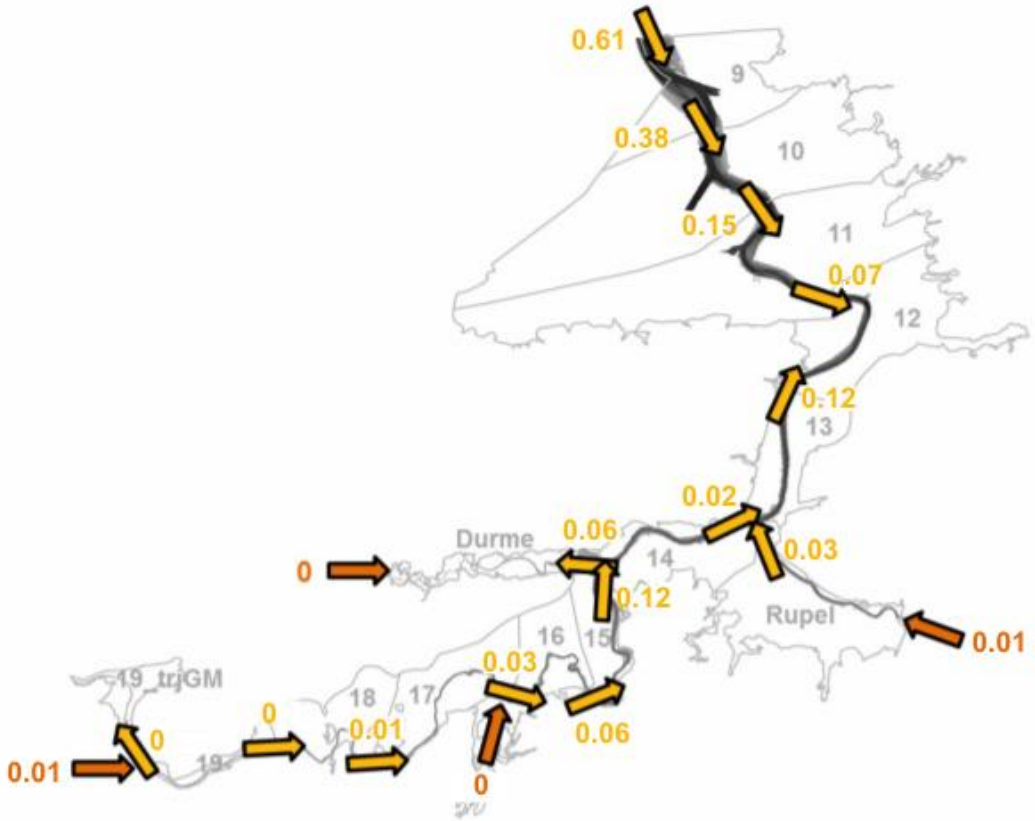

Figure 73 - Yearly net sand transport in Mm^3 in the Sea Scheldt in the period between 2001-2011 (Vandenbruwenaere, 2017).

The total sand volume has decreased somewhat in the Lower Sea Scheldt, while it remained more or less constant in the rest of the Sea Scheldt. This is mainly related to the sand mining activities, and to a lesser extent to the dredging and dumping activities in the area. The net effect of these interfering activities is the down-estuary movement of sand, mostly from cells 10 and 11 to cell 9. The volume of sand, which is mined in cell 9, is, however, greater than the volume of dumped sand in this cell. In cell 14 there is also loss of sand volume due to mining activities (Vandenbruwaene et al., 2017).

Mud

Both fluvial and marine mud exists in the Scheldt Estuary, which are transported in suspension. Marine mud originates from the English Channel and Flemish Banks and is imported through the estuary mouth, while fluvial mud originates from domestic, industrial and agricultural effluent and material eroded from muddy beds, and is discharged in the Scheldt Estuary through the Scheldt Basin (Van Kessel et al., 2011). Various studies to the origin and distribution of the mud (Chen, Wartel, Van Eck, et al., 2005; Jacobs, 2011; Ten Brinke, 1994; Terwindt, 1967; Verlaan, 2000; Wartel & van Eck, 2000) agree that, in general, marine mud dominates the Western Scheldt and fluvial mud dominates the Sea Scheldt. They found that there is a sharp transition between both fractions in the section between Liefkenshoek and the Verdronken Land of Saeftinghe (from 10% to 70% of marine bottom mud). The marine mud is transported somewhat further up-estuary. This is explained by the converging transport fluxes of both mud fractions at this location, as will be clarified in the subsection about mud dynamics in the below (Van Kessel, Vanlede, & Bruens, 2006).

Composition

The composition of the suspended matter is dominated by complex and cohesive organo-mineral aggregates, consisting of quartz, calcite, clay minerals (illite, montmorillonite, kaolinite and chlorite) and organic matter. In general, the mud consist of approximately 35% lutum (clay minerals, organic matter and carbonates) and 65% silt (quartz) (Braat et al., 2017; Wartel, 1977). It can be physically classified as silty-clay and sandy-clay, depending on the location in the estuary (Wartel & van Eck, 2000). The organic content of the mud supplied by the Scheldt River is high, but gradually decreases through the estuary due to degradation of the organic carbon load. The fraction is found to be approximately 8.5-25% of the dry weight (Chen et al., 2005). The typical settling velocity of the individual particles is estimated to be 0.1-0.4 mm/s. Furthermore, the mud has a critical erosion velocity of approximately 0.56 m/s (Chen, Wartel, Van Eck, et al., 2005).

Human activities have changed the suspended matter composition significantly through dumping of domestic waste with high organic content and industrial activities. The last decades, however, the organic content of the mud fraction has decreased from an average of about 18% ± 5% in 1996 to 10% ± 2% in 2001. This is explained by increased water treatment of domestic waste water. Consequently, the fine sand fraction has increased from 6.4% to 11.5% (Chen, Wartel, Van Eck, et al., 2005).

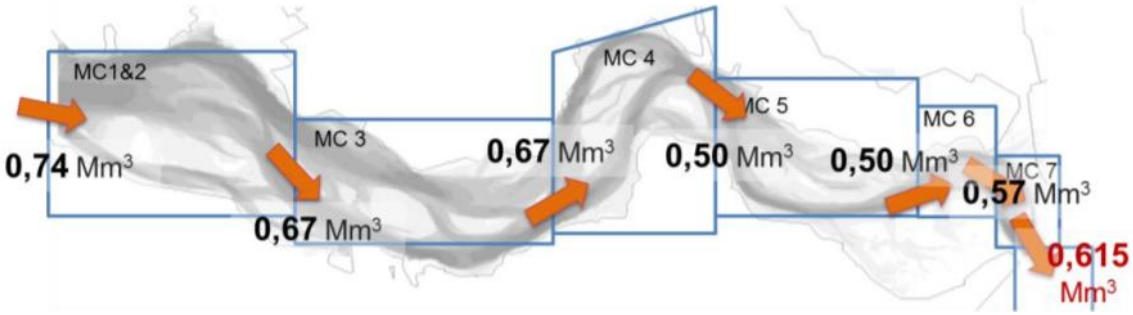

Figure 74 – Yearly net mud transport rates in the Western Scheldt for the period between 1994 and 2010 (Cleveringa & Dam, 2013)

In the Scheldt Estuary, the floc size is dependent on the current velocity, turbulent intensity, organic content and the suspended sediment concentration, rather than salinity (Chen, Wartel, & Temmerman, 2005). Large flocs (up to 120 µm) are observed in the upstream reaches of the Scheldt Estuary towards the limit of salinity intrusion (80-120 km from the mouth). However, the high energy level at the transition of the Western Scheldt and Sea Scheldt (40-80 km from the mouth) results in a local decrease in floc size (down to 30 µm). At the mouth of the estuary itself, flocs of around 60 µm are found. (Chen, Wartel, Van Eck, et al., 2005; Temmerman et al., 2003; Van Kessel et al., 2011). Flocs highly influence the deposition rates (Chen, Wartel, & Temmerman, 2005).

Transport

The mud transport in the Scheldt Estuary is often divided in two fractions: a permanently suspended fraction (washload) and a tidally-fluctuating fraction, which is alternately deposited and resuspended during a tidal cycle (Van Kessel et al., 2006).

As for sand, the transport of mud is directed up-estuary in the Western Scheldt, which can be seen in Figure 74. Due to this import of mud, there is a net increase in mud volume in the Western Scheldt in the order of hundreds of thousands of cubic meters (i.e. 420,000 m^3/year of sedimentation in the Middelgat). However, there is a decrease in mud volume in the eastern part of the Western Scheldt (macro-cells 6 and 7). It is believed that there is constant sedimentation in the channels and erosion of mud on the shoals. The flux of mud leaving the Western Scheldt at its landward end (0.615 Mm^3/year) consists both of the mud exported to the Lower Sea Scheldt and the sedimentation flux at the Verdronken Land of Saeftinghe (which is estimated to be 300,000-600,000 m^3) (Cleveringa & Dam, 2013).

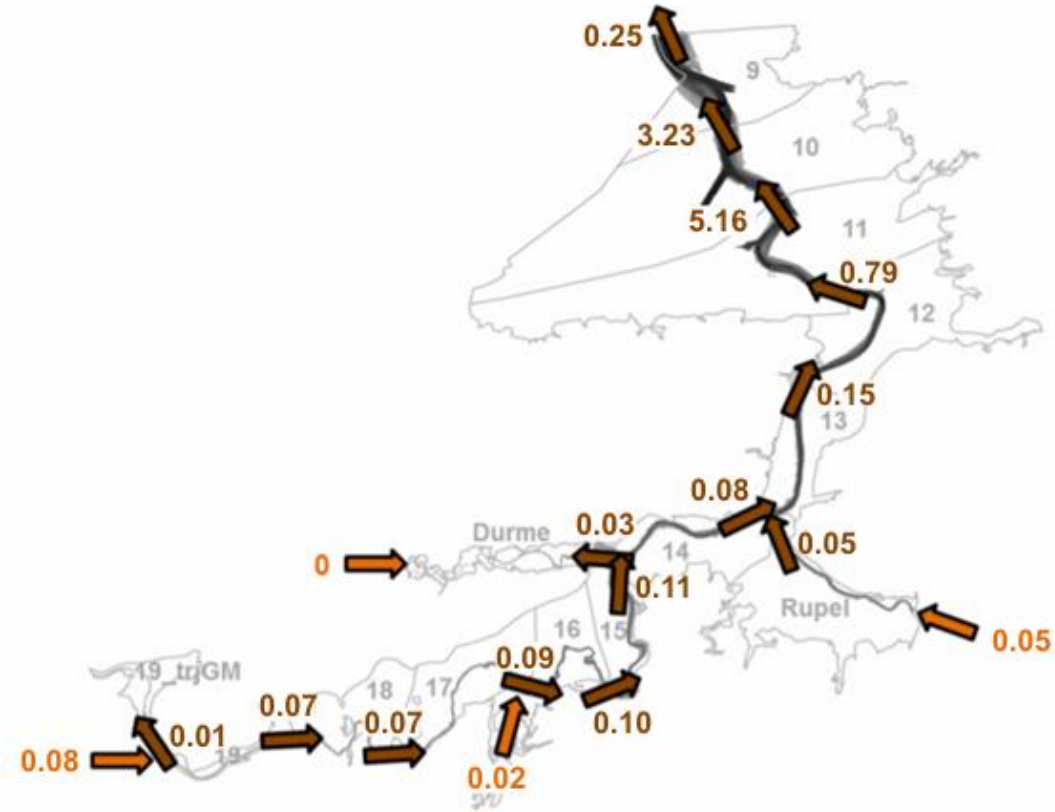

Figure 75 – Yearly net mud transport in Mm^3 in the Sea Scheldt in the period between 2001-2011 (Vandenbruwenaere, 2017).

The net mud transport in the Sea Scheldt is directed down-estuary. This is visualized in Figure 75. Due to a net downstream residual current, there is a net sediment flux towards the Western Scheldt, which indicates, considering the mud transport direction in the Western Scheldt, that close to the Verdronken Land of Saeftinghe there is convergence of mud transport. This confirms the large net increase in mud volume of mostly marine mud and the rather sharp transition of fluvial and marine mud in this area. Also the low-turbulent area at near the entrance of the Zandvliet-Berendrecht channel act as a trap for mud. Therefore, most (~80%) of the fluvial mud is retained. Furthermore, its supply is strongly correlated with actual river discharge: ~90% of the fluvial sediment is discharged during the ~10% highest run-off events (Van Kessel et al, 2006, 2011).

Similar for sand, the net transport of mud may be directed differently within a cross-section than the direction of the net transport between the cells (Chen, Wartel, Van Eck, et al., 2005).

In the 80's and 90's of the last century, the fluvial mud supply has decreased by the increased treatment of domestic waste water and the increased deposition upstream of Rupelmonde due to construction of a number of weirs and sluices (Van Kessel et al., 2011). Furthermore, the total volume of mud has decreased between the Belgian-Dutch border and Liefkenshoek, while it increased between Liefkenshoek and Kruibeke with an estimated rate of 50 Mm^3/decade. In the rest of the Sea Scheldt the mud volume was more or less constant. This is mainly due to the dredging and dumping activities in the Lower Sea Scheldt, which are an order of magnitude greater (!) than the natural mud transport rates. There is a large net flux of dredged mud from cells 9 and 10 to cells 11 and 12 (Vandenbruwaene et al., 2017).

Spatial dynamics
The SSC magnitude and distribution varies significantly over the estuary. In the lower estuary the distribution of suspended sediment over the both the horizontal and vertical is rather uniform, while there is a lot of variation in the middle and upper estuary (Chen, Wartel, Van Eck, et al., 2005; Van Kessel et al., 2011; Verlaan, 1998).

In the Western Scheldt, there is generally an uniform suspended sediment concentration which is below 50 mg/l, seldomly exceeding 100 mg/l. It does not significantly vary over time. Further upstream, in the middle part of the estuary, the uniform suspension layer has an average concentration of 100 ± 70 mg/l, while the bottom suspension layer has a concentration in the range of 150 mg/l to 2.5 g/l. The upper most part of the estuary has a uniform suspension layer with a mean concentration of 110 ± 65 mg/l, while the bottom suspension layer typically has a range of 100-1000 mg/l (Chen, Wartel, Van Eck, et al., 2005; Verlaan, 1998).

Locally, the suspended sediment concentration differs as well; in the Scheldt estuary usually three ETMs are observed, which may be present depending on the prevailing conditions (Chen, Wartel, Van Eck, et al., 2005):

- The first ETM is observed in the mouth of the estuary between Flushing and Zeebrugge and reaches more than a few hundred mg/l. It is caused by a combination of wave and tidal energy in the presence of marine mud on the flats. The ETM is, therefore, marine-dominated and generally present during storms (Chen et al., 2005).
- The second ETM is located near Ghent and is present when the freshwater discharge is high. It is therefore a river-dominated ETM. SPM concentrations may be up to 300 mg/l.
- A third ETM, which is the most prominent of the three ETMs, is situated in the Lower Sea Scheldt (from 58 extending up to 100 km w.r.t. Flushing). It's presence is explained, one the one hand, by the fact that there is maximal tidal and total energy (see Figure 20). On the other hand, there is a large availability of mud in the area, caused by the convergence of several large and small scale SPM trapping processes (Baeyens, 1998). As a consequence, there is huge local resuspension flux of fine material causing the ETM to develop. The near-bed SSC may reach several hundreds of milligrams per liter up to grams per liter, with maximum concentrations in vicinity of Antwerp (Chen et al., 2005).
  The location of maximum SSC shifts between 50 km from the mouth, at high river discharge, and 110 km from the mouth, at low river discharge. The sediment has a long residence time due to converging fluxes. Over a tidal cycle, the concentration of the ETM varies with a factor of 2-10, since the magnitude of the ETM depends on the magnitude of the tidal velocity. Consequently, the ETM is nearly absent during slack water. This hints that the suspended material is subject to deposition and resuspension within a tidal cycle.
  The location of the ETM determines whether the suspended sediment can be largely deposited. At the location at the Belgian-Dutch border and the Verdronken Land of Saeftinghe, where the ETM is present during high river run-off, there are sheltered basins present on which the mud can deposit and consolidate. On the opposite, near Antwerp, where the ETM is located under average conditions, these areas are lacking

and deposited mud is re-suspended again during the next tidal cycle. This clarifies the finding that the fraction of marine mud in the bottom shows such a sharp gradient (Van Kessel et al, 2011).

Temporal dynamics

The sediment concentrations in the Scheldt Estuary show variation on several time scales (Chen, Wartel, Van Eck, et al., 2005; Van Kessel et al., 2011):

1. Flood-ebb tide (asymmetry, hysteresis, turbulence, sediment availability):
   Suspended sediment concentrations are generally higher during maximum flood and ebb velocities, when mud is eroded, and low during both slack waters, when mud is deposited. This especially holds for the Lower Sea Scheldt, while in the Western Scheldt there is less variation over the tide. The variation in magnitude of SSC over the tidal cycle is greatly dependent on the local morphology (Chen, Wartel, Van Eck, et al., 2005). Furthermore this was found to be dependent on the location of the maximum SSC in the ETM (Fettweis & Sas, 1997).
   Higher-order variation in suspended sediment concentration over a flood or ebb phase is explained by differences in turbulence, peak-velocities, varying sediment supply, and the inhomogeneous composition and distribution of the fine sediments in the bottom. Three peaks in suspended sediment concentration can be observed. The first peak corresponds with the erosion of freshly-deposited mud, which has a low density and therefore low critical shear strength. The mud layers below this layer are stronger, and therefore more difficult to erode. A second peak can therefore been seen when the bed shear stress exceeds the critical erosion strength of the mud in the bed. The third peak corresponds with the maximum current velocity (Fettweis & Sas, 1997).
   Also, the floc size changes over a tidal cycle. Larger flocs are formed during high flood and ebb currents by increasing suspended sediment concentrations, up to a critical velocity when the flocs again decrease in size due to break-up. Furthermore, at slack waters the floc size is increasing, but to a lesser extent. Changes in floc size during a tidal cycle lead to temporarily varying deposition rates (Manning et al., 2007).
2. Spring-neap tide:
   The concentration is 2-3 times greater during spring tide than during neap tide due to greater tidal current velocity magnitudes. Furthermore, during spring tide the peak flood velocities are more asymmetric and show a double-peak, while during neap the profile is more smooth. The ebb velocity profile does not change that much during a spring neap-cycle. Therefore, there is more resuspension and transport of mud during spring tide. This makes that the spring cycle is characterized by erosion and the neap cycle by deposition of fine material. At the bottom the difference in concentration is smaller during a spring-neap cycle than higher up in the water column, which is caused by the stronger influence of local resuspension at the bottom and stronger influence of mud transport higher up in the water column (Fettweis & Sas, 1997).
3. Seasonal variations:
   The sediment concentration in the whole estuary is highly dependent on the seasonality with higher concentrations in the winter than in summer by at least a factor 2. This is explained by an increase in biological activity in the spring and summer due to annual temperature variation. Organisms reduce the fine sediment availability due to biostabilisation. Also, organic flocculation may reduce the sediment concentration, since larger flocs are much more difficult to be kept in suspension by the current. Moreover, due to the decreased land cover and the increased rainfall, more fluvial sediment is supplied to the estuary in the winter. Furthermore, storm surges and storm waves increase the marine sediment supply at the mouth of the estuary and may increase sediment concentration throughout the estuary due to increased

resuspension of fine material. These surges and storms are more frequent in the winter (Fettweis & Sas, 1997).

4. Decades (climate change, anthropogenic intervention)
   In the Lower Sea Estuary, the long-term suspended sediment concentration has gradually increased by several tens of milligrams per liter over the last decades (Maris & Meire, 2017; Vandenbruwaene et al., 2017), which may be related to development of the geomorphology of the estuary (Dijkstra, Schuttelaars, & Schramkowski, 2019).

Appendix C. Basics of the engineering tool: SED-PIT

C.1 Assumptions

SED-PIT is an empirical engineering tool in which the total siltation is calculated in a schematized rectangular trench with a certain angle with the ambient current. This is performed by calculation of the difference in bed and suspended load transport between the trench and the ambient surrounding area for a user-defined amount of time steps for a user-defined number of tidal waves. Three different sediment fractions are taken into account: clay, silt, and sand. The ambient transport fluxes are calculated based on imported depth-averaged current velocity magnitudes and directions, wave heights and periods, and suspended sediment concentrations. The transport fluxes within the trench are calculated based on empirically derived current velocities, which are derived from numerical solutions. Also, the current velocity due to waves is derived, which is done according to the linear wave theory. The transport formulations are based on measurements of physical modelling (L. C. Van Rijn, 2017; L. C. Van Rijn et al., 1993).

SED-PIT accounts for the following trapping efficiency mechanisms:

- Current deflection (dependent on the increase in depth)
- Increase in depth (stepwise)

Therefore, SED-PIT does not account for:

- Current velocity profile adaptation
- Suspended sediment profile adaptation
- Flow separation
- Current attraction

Especially the neglection of the latter mechanism causes the accuracy of SED-PIT to drop for flow approaching with a small angle of incidence with respect to the alignment of the trench (L. C. Van Rijn, 2017).

C.2 Input parameters

The following input parameters are required in the engineering tool:

ζ	[m]	Water level
H_s	[m]	Significant wave height
T_p	[s]	Peak wave period
u_0	[m/s]	Ambient current velocity
n_{tstep}	[-]	Number of time steps
n_{tides}	[-]	Number of tides with a period of 12 hours
C_{clay}	[kg/m^3]	Suspended sediment concentration of clay fraction
C_{silt}	[kg/m^3]	Suspended sediment concentration of silt fraction
α_0	[rad]	Angle of incidence of flow with respect to alignment of trench
L_1	[m]	Length of trench
B_0	[m]	Ambient stream width
B_1	[m]	Width of trench
d_0	[m]	Ambient depth
d_1	[m]	Depth of trench

d_{50}	[m]	Median grain size diameter
d_{90}	[m]	90th percentile grain size diameter
p_{mud}	[-]	Percentage of mud in bed
ρ_s	[kg/m^3]	Fluid density
ρ_w	[kg/m^3]	Water density
ν	[m^2/s]	Viscosity
$w_{s,clay}$	[m/s]	Fall velocity of clay fraction
$w_{s,silt}$	[m/s]	Fall velocity of silt fraction
$w_{s,sand}$	[m/s]	Fall velocity of sand fraction
r_1	[m]	Bed roughness of trench
c_{sand}	[-]	Calibration factor for sand transport
c_{vRijn}	[-]	Van Rijn coefficient

C.3 Equations

For each time step the thickness of the deposited material can be calculated according to:

$$\Delta H_{tot} = \frac{\Delta S_{tot,volume}}{L_1 B_1} \tag{C-1}$$

Summation of the thicknesses for each time steps give the total thickness of deposited material over the user-defined time frame, which is calculated in years as:

$$T = \frac{n_{tides} n_{tstep}}{365 \cdot 24} \tag{C-2}$$

The total deposited sediment volume in equation (C-1 depends on the total deposited mass, $\Delta S_{tot,volume}$, and the bulk density of the deposited material, ρ_{bulk}. These are calculated through:

$$\Delta S_{tot,volume} = \frac{\Delta S_{tot}}{\rho_{bulk}} \tag{C-3}$$

This total deposited mass, ΔS_{tot}, consist of the deposited mass of each fraction:

$$\Delta S_{tot} = \Delta S_{clay} + \Delta S_{silt} + \Delta S_{sand} \tag{C-4}$$

The bulk density is estimated according to:

$$\rho_{bulk} = \frac{\Delta S_{clay}}{\Delta S_{tot}}(0.415 + 0.43 \cdot 0.255\gamma) + \frac{\Delta S_{silt}}{\Delta S_{tot}}(1.12 + 0.43 \cdot 0.09\gamma) + \frac{\Delta S_{sand}}{\Delta S_{tot}}(1.55) \tag{C-5}$$

in which the consolidation rate is derived as:

$$\gamma = \left(\frac{T}{T-1}\right)\log(T) - 1 \tag{C-6}$$

The deposited sediment masses for each fraction, ΔS_i, are calculated through:

$$\Delta S_{clay} = e_{s,clay}\left(\frac{B_0}{L_{eff}} q_{s,0,clay} - q_{s,1,clay}\right) L_1 sin(\alpha_0)\left(\frac{n_{tides} \cdot 3600}{1000}\right) \tag{C-7}$$

$$\Delta S_{silt} = e_{s,silt}\left(\frac{B_0}{L_{eff}} q_{s,0,silt} - q_{s,1,silt}\right) L_1 sin(\alpha_0)\left(\frac{n_{tides} \cdot 3600}{1000}\right) \tag{C-8}$$

$$\begin{aligned}\Delta S_{sand} = {} & e_{s,sand}\left(\frac{B_0}{L_{eff}} q_{s,0,sand} - q_{s,1,sand}\right) L_1 sin(\alpha_0)\left(\frac{n_{tides} \cdot 3600}{1000}\right) + \\ & e_{s,sand}\left(\frac{B_0}{L_{eff}} q_{b,0,sand} - q_{b,1,sand}\right) L_1 sin(\alpha_0)\left(\frac{n_{tides} \cdot 3600}{1000}\right)\end{aligned} \tag{C-9}$$

These are dependent on the trapping efficiency for each fraction, $e_{s,i}$, the transport fluxes of suspended particulate matter for each fraction in- ($q_{s,0,i}$) and outside the trench ($q_{s,1,i}$), and bed load ($q_{b,0,sand}$ and $q_{b,1,sand}$) and an effective length for deposition, L_{eff}:

$$e_{s,clay} = 1 - \exp\left(-c_{vRijn}\left(\frac{w_{s,clay}}{\varepsilon u_{*,1}}\right)\left(1 + 2\left(\frac{w_{s,clay}}{\varepsilon u_{*,1}}\right)\right)\frac{L_{eff}H_0}{H_1^2}\right) \quad \text{(C-10)}$$

$$e_{s,silt} = 1 - \exp\left(-c_{vRijn}\left(\frac{w_{s,silt}}{u_{*,1}}\right)\left(1 + 2\left(\frac{w_{s,clay}}{u_{*,1}}\right)\right)\frac{L_{eff}H_0}{H_1^2}\right) \quad \text{(C-11)}$$

$$e_{s,sand} = 1 - \exp\left(-c_{vRijn}\left(\frac{w_{s,sand}}{u_{*,1}}\right)\left(1 + 2\left(\frac{w_{s,clay}}{u_{*,1}}\right)\right)\frac{L_{eff}H_0}{H_1^2}\right) \quad \text{(C-12)}$$

$$L_{eff} = \left(\frac{B_0}{sin(\alpha_1)}\right) \quad \text{(C-13)}$$

$$q_{s,1,mud} = \left(\frac{u_1}{u_0}\right)^3 q_{s,0,mud} \quad \text{(C-14)}$$

$$q_{s,1,silt} = \left(\frac{u_1}{u_0}\right)^3 q_{s,0,silt} \quad \text{(C-15)}$$

$$q_{s,1,sand} = \left(\frac{u_1}{u_0}\right)^3 q_{s,0,sand} \quad \text{(C-16)}$$

$$q_{b,1,sand} = \left(\frac{u_1}{u_0}\right)^3 q_{b,0,sand} \quad \text{(C-17)}$$

$$q_{s,0,clay} = u_0 C_{clay} H_0 \quad \text{(C-18)}$$

$$q_{s,0,silt} = u_0 C_{silt} H_0 \quad \text{(C-19)}$$

$$q_{s,0,sand} = 0.008\gamma_s c_{sand}\rho_s \cdot (1 - p_{mud}) u_0 H_0 M_e^{2.4}\left(\frac{d_{50}}{H_0}\right)^{1.2} \cdot D_*^{-0.6} \quad \text{if } u_e > u_{cr} \quad \text{(C-20)}$$

$$q_{b,0,sand} = 0.015\gamma_s c_{sand}\rho_s \cdot (1 - p_{mud}) u_0 H_0 M_e^{1.5}\left(\frac{d_{50}}{H_0}\right)^{1.2} \quad \text{if } u_e > u_{cr} \quad \text{(C-21)}$$

Herein, the critical velocity in the trench, u_*, the enhancement factor due to wave stirring, ε, the dimensionless particle size, D_*, the ambient water depth, H_0, the water depth at the trench, H_1, the flow angle in the trench with respect to the alignment of the trench, α_1, the current velocity within the trench, u_1, and the effective density, γ_s:

$$u_{*,1} = \frac{\sqrt{g}}{C_1 u_1} \quad \text{(C-22)}$$

$$\varepsilon = 1 + \frac{H_s}{H_1} \quad \text{(C-23)}$$

$$D_* = d_{50}\left[\frac{(s-1)g}{\nu^2}\right] \quad \text{(C-24)}$$

$$H_0 = d_0 + \zeta, \quad \text{(C-25)}$$

$$H_1 = d_1 + \zeta \quad \text{(C-26)}$$

$$\alpha_1 = \text{atan}\left(\left[\frac{H_0}{H_1}\right] tan(\alpha_0)\right) \quad \text{(C-27)}$$

$$u_1 = u_0\left(\frac{H_0}{H_1}\right)\left(\frac{\sin(\alpha_0)}{\sin(\alpha_1)}\right) \quad \text{(C-28)}$$

in which the relative density, s, and the Chézy roughness in the trench, C_1, is calculated respectively through:

$$s = \frac{\rho_s}{\rho_w} \tag{C-29}$$

$$C_1 = 18\log\left(\frac{12H_1}{r_1}\right) \tag{C-30}$$

It can be seen from equations (C-20 and (C-21 that the sediment transport of sand is dependent on a mobility parameter. This parameter is defined as:

$$M_e = \frac{u_e - u_{cr}}{\sqrt{(s-1)g d_{50}}} \tag{C-31}$$

This parameter is dependent on the effective current velocity, u_e, and critical current velocity of the sand, u_{cr}. The former is composed of the current velocity due to flow and waves:

$$u_e = u_0 + 0.4U_w \tag{C-32}$$

in which the current velocity due to waves, U_w, can be calculated according to the linear wave theory:

$$U_w = \frac{\pi H_s}{T_P \sinh(kH_0)} \tag{C-33}$$

in which the wave number can be calculated according to:

$$kH_0 = \left(\frac{4.02H_0}{{T_p}^2}\right)^{0.5}\left[1 + 0.166\left(\frac{4.02H_0}{{T_p}^2}\right) + 0.031\left(\frac{4.02H_0}{{T_p}^2}\right)^2\right] \tag{C-34}$$

The critical current velocity is calculated based on:

$$u_{cr} = \left(\frac{u}{u+U_w}\right)u_{cr,f} + \left(1 - \frac{u}{u+U_w}\right)u_{cr,w} \tag{C-35}$$

which is composed of the critical current velocities for flow, $u_{cr,f}$, and for waves, $u_{cr,w}$:

$$u_{cr,f} = 0.19{d_{50}}^{0.1}\log\left(\frac{12H_0}{3d_{90}}\right) \quad \text{for } 0.0001 < d_{50} < 0.0005\,m \tag{C-36}$$

$$u_{cr,f} = 8.5{d_{50}}^{0.6}\log\left(\frac{12H_0}{3d_{90}}\right) \quad \text{for } 0.0005 < d_{50} < 0.002m \tag{C-37}$$

$$u_{cr,w} = 0.24[(s-1)g]^{0.66}{d_{50}}^{0.33}{T_p}^{0.33} \quad \text{for } 0.0001 < d_{50} < 0.0005\,m \tag{C-38}$$

$$u_{cr,w} = 0.95[(s-1)g]^{0.57}{d_{50}}^{0.43}{T_p}^{0.14} \quad \text{for } 0.0005 < d_{50} < 0.002m \tag{C-39}$$

Appendix D. Basics of the numerical model: Delft3D

In this appendix, the modelling approach of the numerical model is explained in detail. First, based on well justified assumptions, it is clarified how the model schematizes the physics of the hydrodynamics and morphodynamics. Then, it is explained how these physical relations are solved in the numerical with the help of transformations and discretization in both time and space. More details can be found in the user manual of Delft3D and (van Kessel et al., 2012).

D.1 Assumptions

The numerical model uses the following assumptions:

- Incompressibility:
  Density does not depend on pressure. This makes that the pressure is solely dependent on salinity and temperature (ρ=ρ(s,T)). Furthermore, the rate of change of density of a fluid element is zero (Dρ/Dt = 0). Also, the velocity field is divergence-free.
- Scaling: horizontal scale is far greater than the vertical scale:
  The vertical acceleration is much smaller than the acceleration due to gravity. Therefore, vertical acceleration, Coriolis, stress components, and advection can be neglected. Under these assumptions the vertical pressure distribution is assumed to be hydrostatic.
- No precipitation and evaporation
- Boussinesq approximation:
  Density variations are generally small ($\Delta\rho \ll \rho$). Therefore, they have no important consequences for all terms in the momentum equations, except for the baroclinic forcing term. A constant background pressure, ρ_0, is adopted for the other pressure terms. Furthermore, it is assumed that the Reynolds stresses depend on the deformation rates of the mean flow only.
- Eddy viscosity concept: horizontal and vertical mixing
- No heat fluxes (T = constant)

D.2 Equations

The well-known Navier-Stokes equations underlie the description of the motion of water. The mass equation and momentum equations in a Cartesian coordinate system (x,y,z) for water are defined respectively as:

Mass Equation

$$\frac{\partial \rho}{\partial t} + u\frac{\partial \rho}{\partial x} + v\frac{\partial \rho}{\partial y} + w\frac{\partial \rho}{\partial z} = 0$$

Momentum Equation in u-direction

$$\frac{\partial \rho u}{\partial t} + \frac{\partial \rho u^2}{\partial x} + \frac{\partial \rho uv}{\partial y} + \frac{\partial \rho uw}{\partial z} + \frac{\partial p}{\partial x} - \frac{\partial \tau_{xx}}{\partial x} - \frac{\partial \tau_{xy}}{\partial y} - \frac{\partial \tau_{xz}}{\partial z} = \rho f_1$$

Momentum Equation in v-direction

$$\frac{\partial \rho v}{\partial t} + \frac{\partial \rho vu}{\partial x} + \frac{\partial \rho v^2}{\partial y} + \frac{\partial \rho vw}{\partial z} + \frac{\partial p}{\partial y} - \frac{\partial \tau_{yx}}{\partial x} - \frac{\partial \tau_{yy}}{\partial y} - \frac{\partial \tau_{yz}}{\partial z} = \rho f_2$$

Momentum Equation in w-direction

$$\frac{\partial \rho w}{\partial t}+\frac{\partial \rho w u}{\partial x}+\frac{\partial \rho w v}{\partial y}+\frac{\partial \rho w^2}{\partial z}+\frac{\partial p}{\partial z}-\frac{\partial \tau_{zx}}{\partial x}-\frac{\partial \tau_{zy}}{\partial y}-\frac{\partial \tau_{zz}}{\partial z}=\rho f_3$$

in which the stress tensors are defined, according to the Boussinesq eddy-viscosity approximation:

$$\tau_{ij}=\rho \nu_t\left(\frac{\partial u_i}{\partial x_j}+\frac{\partial u_j}{\partial x_i}\right)$$

given $(u_1,u_2,u_3)=(u,v,w)$ and $(x_1,x_2,x_3)=(x,y,z)$

Continuity Equation

The continuity equation is obtained by simplifying the mass conservation equation, using the assumption of incompressibility (ρ = constant):

$$\frac{\partial \rho}{\partial t}+u\frac{\partial \rho}{\partial x}+v\frac{\partial \rho}{\partial y}+w\frac{\partial \rho}{\partial z}=0 \;\rightarrow\; \frac{\partial u}{\partial x}+\frac{\partial v}{\partial y}+\frac{\partial w}{\partial z}=\nabla\cdot\vec{u}=0$$

Given the assumption that the horizontal scale is far greater than the vertical scale (w << u,v), the continuity equation for an incompressible fluid can be simplified by integrating it over the depth:

$$\int_{-d(x,y)}^{\zeta(x,y,t)}\left(\frac{\partial u}{\partial x}+\frac{\partial v}{\partial y}+\frac{\partial w}{\partial z}\right)dz=0 \;\rightarrow\; \int_{-d(x,y)}^{\zeta(x,y,t)}\left(\frac{\partial u}{\partial x}+\frac{\partial v}{\partial y}\right)dz+w(\zeta)-w(-d)=0$$

By taken into account the kinematic boundary conditions for a normal velocity to a moving surface and the normal velocity to the bottom respectively, as formulated below;

$$\frac{\partial \zeta}{\partial t}+u\frac{\partial \zeta}{\partial x}+v\frac{\partial \zeta}{\partial y}-w(\zeta)=0 \;\rightarrow w(\zeta)=\frac{\partial \zeta}{\partial t}+u\frac{\partial \zeta}{\partial x}+v\frac{\partial \zeta}{\partial y}$$

$$-u\frac{\partial d}{\partial x}-v\frac{\partial d}{\partial y}-w(-d)=0 \;\rightarrow\; w(-d)=-u\frac{\partial d}{\partial x}-v\frac{\partial d}{\partial y}$$

the depth-integrated continuity equation for incompressible fluids can be simplified by canceling terms to:

$$\frac{\partial \zeta}{\partial t}+\frac{\partial hU}{\partial x}+\frac{\partial hV}{\partial y}=0$$

Momentum equations

Using again the assumption of incompressible fluid (ρ = constant) and the scaling of the horizontal and vertical scales (w << u,v), the momentum equations can be simplified, using the same cartesian coordinate system, to:

u-direction

$$\frac{\partial u}{\partial t}+u\frac{\partial u}{\partial x}+v\frac{\partial u}{\partial y}+w\frac{\partial u}{\partial z}+\frac{\partial p}{\rho\partial x}-\frac{1}{\rho}\left(\frac{\partial \tau_{xx}}{\partial x}-\frac{\partial \tau_{xy}}{\partial y}-\frac{\partial \tau_{xz}}{\partial z}\right)=f_1$$

v-direction

$$\frac{\partial v}{\partial t}+u\frac{\partial v}{\partial x}+v\frac{\partial v}{\partial y}+w\frac{\partial v}{\partial z}+\frac{\partial p}{\rho\partial y}-\frac{1}{\rho}\left(\frac{\partial \tau_{yx}}{\partial x}-\frac{\partial \tau_{yy}}{\partial y}-\frac{\partial \tau_{yz}}{\partial z}\right)=f_2$$

w-direction

$$\frac{\partial p}{\rho \partial z} - \frac{\partial \tau_{zx}}{\partial x} - \frac{\partial \tau_{zy}}{\partial y} - \frac{\partial \tau_{zz}}{\partial z} = f_3$$

Forcing Terms

Herein, the force vector, f, takes into account both gravity and Coriolis. Hence, it can be written in simplified form as:

$$(f_1, f_2, f_3) = (fv, -fu, -g)$$

with: $f = 2\omega \sin(\varphi)$

Pressure Terms

By using the assumption of hydrostatic pressure, and the forcing terms the momentum equations can then be rewritten to:

$$\frac{\partial u}{\partial t} + u\frac{\partial u}{\partial x} + v\frac{\partial u}{\partial y} + w\frac{\partial u}{\partial z} + \frac{\partial p}{\rho_0 \partial x} - \frac{1}{\rho_0}\left(\frac{\partial \tau_{xx}}{\partial x} - \frac{\partial \tau_{xy}}{\partial y} - \frac{\partial \tau_{xz}}{\partial z}\right) = fv$$

$$\frac{\partial v}{\partial t} + u\frac{\partial v}{\partial x} + v\frac{\partial v}{\partial y} + w\frac{\partial v}{\partial z} + \frac{\partial p}{\rho_0 \partial y} - \frac{1}{\rho_0}\left(\frac{\partial \tau_{yx}}{\partial x} - \frac{\partial \tau_{yy}}{\partial y} - \frac{\partial \tau_{yz}}{\partial z}\right) = -fu$$

$$\frac{\partial p}{\partial z} = -\rho g$$

in which the density of the fluid, ρ, if not constant over the depth, is described by:

$$p = p_{atm} + g\int_z^\zeta \rho(t, x, y, z)dz$$

Using the Leibniz rule, this gives the following pressure terms for the x-direction, which is similar for the y-direction:

$$\frac{\partial p}{\partial x} = \frac{\partial p_{atm}}{\partial x} + \rho g\frac{\partial \zeta}{\partial x} + g\int_z^\zeta \frac{\partial \rho}{\partial x}dz$$

With the Boussinesq approximation (density differences are small), this leads to:

$$\frac{1}{\rho_0}\frac{\partial p}{\partial x} = \frac{1}{\rho_0}\frac{\partial p_{atm}}{\partial x} + g\frac{\partial \zeta}{\partial x} + \frac{g}{\rho_0}\int_z^\zeta \frac{\partial \rho}{\partial x}dz$$

Substituting this is the momentum equations gives:

$$\frac{\partial u}{\partial t} + u\frac{\partial u}{\partial x} + v\frac{\partial u}{\partial y} + w\frac{\partial u}{\partial z} + g\frac{\partial \zeta}{\partial x} - \frac{1}{\rho_0}\left(\frac{\partial \tau_{xx}}{\partial x} + \frac{\partial \tau_{xy}}{\partial y} + \frac{\partial \tau_{xz}}{\partial z}\right) = -\frac{1}{\rho_0}\frac{\delta p_{atm}}{\partial x} - \frac{g}{\rho_0}\int_z^\zeta \frac{\delta \rho}{\partial x}dz + fv$$

$$\frac{\partial v}{\partial t}+u\frac{\partial v}{\partial x}+v\frac{\partial v}{\partial y}+w\frac{\partial v}{\partial z}+g\frac{\partial \zeta}{\partial y}-\frac{1}{\rho_0}\left(\frac{\partial \tau_{yx}}{\partial x}+\frac{\partial \tau_{yy}}{\partial y}+\frac{\partial \tau_{yz}}{\partial z}\right)=-\frac{1}{\rho_0}\frac{\delta p_{atm}}{\partial y}-\frac{g}{\rho_0}\int_z^\zeta \frac{\delta \rho}{\partial y}dz-fu$$

By writing out the Reynolds-averaged turbulent stresses, by including the Boussinesq eddy-viscosity approximation, and by assuming that the vertical direction is smaller than the horizontal directions (z << x,y), the following set of momentum equations can be obtained, which are called the Reynolds-averaged 3D shallow water equations:

$$\frac{\partial u}{\partial t}+u\frac{\partial u}{\partial x}+v\frac{\partial u}{\partial y}+w\frac{\partial u}{\partial z}=\frac{\partial}{\partial x}\left(v_h\frac{\partial u}{\partial x}\right)+\frac{\partial}{\partial y}\left(v_h\frac{\partial u}{\partial y}\right)+\frac{\partial}{\partial z}\left(v_v\frac{\partial u}{\partial z}\right)-g\frac{\partial \zeta}{\partial x}-\frac{1}{\rho_0}\frac{\delta p_{atm}}{\partial x}+$$
$$-\frac{g}{\rho_0}\int_z^\zeta \frac{\delta \rho}{\partial x}dz+fv$$

$$\frac{\partial v}{\partial t}+u\frac{\partial v}{\partial x}+v\frac{\partial v}{\partial y}+w\frac{\partial v}{\partial z}=\frac{\partial}{\partial x}\left(v_h\frac{\partial v}{\partial x}\right)+\frac{\partial}{\partial y}\left(v_h\frac{\partial v}{\partial y}\right)+\frac{\partial}{\partial z}\left(v_v\frac{\partial v}{\partial z}\right)-g\frac{\partial \zeta}{\partial y}-\frac{1}{\rho_0}\frac{\delta p_{atm}}{\partial y}+$$
$$-\frac{g}{\rho_0}\int_z^\zeta \frac{\delta \rho}{\partial y}dz-fu$$

Herein, v_h and v_v, are the eddy viscosities in horizontal and vertical direction respectively.

Equation of State

The density in the baroclinic pressure gradient term is described by the equation of state which is a function of salinity, s, and temperature, t. For this model, the equation of Eckart is used, which reads:

$$\rho=\rho(s,T)=\frac{1{,}000P_0}{\lambda+\alpha_0 P_0}$$

with:

$$\lambda=1779.5+11.25t-0.0745t^2-(3.80+0.01t)s$$

$$\alpha_0=0.6980$$

$$P_0=5890+38t-0.375t^2+3s$$

These equations are only applicable for a range of: 0 < t < 40 °C and 0 < s < 40 ppt.

Transport Equation

Constituents, c, such as salinity, s, are described according to the convection-diffusion equation:

$$\frac{\partial c}{\partial t}+\frac{\partial uc}{\partial x}+\frac{\partial vc}{\partial y}+\frac{\partial wc}{\partial z}=\frac{\partial}{\partial x}\left(D_h\frac{\partial c}{\partial x}\right)+\frac{\partial}{\partial y}\left(D_h\frac{\partial c}{\partial y}\right)+\frac{\partial}{\partial z}\left(D_v\frac{\partial c}{\partial z}\right)$$

Furthermore, the diffusivity terms in the horizontal and vertical respectively, D_h and D_v, are formulated as:

$$D_h = \frac{v_h}{\sigma_c} = D_{SGS} + D_v + D_H^{back}, \qquad D_v = \frac{v_v}{\sigma_c} = \frac{v_{mol}}{\sigma_{mol}} + \max\left(D_{3D}, D_v^{back}\right)$$

The horizontal eddy diffusivity, D_h, is calculated by summation of the sub-grid scale eddy diffusivity, D_{SGS}, the background diffusivity, D_H^{back}, and the vertical eddy diffusivity, D_v. The three-dimensional eddy viscosity is determined by:

$$v_{3D} = v_v = c'_\mu L\sqrt{k} = c_\mu \frac{k^2}{\varepsilon}$$

given the coefficient, c_μ, , and the specific length scale of the turbulent eddies, L:

$$c_\mu = c_D c'_\mu, \qquad L = c_D \frac{k\sqrt{k}}{\varepsilon}$$

This eddy viscosity is calculated with the turbulence model, which is discussed in the next subsection.

Turbulence model

In this model, vertical mixing is described by the two equation or k-ε model. This is an empirical model, which determines the vertical turbulent eddy viscosity and diffusivity according to transport equations for both turbulent kinetic energy, k, and turbulent kinetic energy dissipation, ε. The mixing length then becomes a property of the flow. For this model, it is assumed that production, buoyancy, and dissipation are the dominating terms. Furthermore, as was assumed for the mass and momentum equations, the horizontal length scale is assumed to be far greater than the vertical one. The transport equations for k and ε are given by:

$$\frac{\partial k}{\partial t} + u\frac{\partial k}{\partial x} + v\frac{\partial k}{\partial y} + w\frac{\partial k}{\partial z} = \frac{\partial}{\partial z}\left(\frac{v_v}{\sigma_k}\frac{\partial k}{\partial z}\right) + v_v\left[\left(\frac{\partial u}{\partial z}\right)^2 + \left(\frac{\partial v}{\partial z}\right)^2\right] + \frac{v_v}{\sigma_p}\frac{g}{\rho_0}\frac{\partial p}{\partial z} - \varepsilon$$

$$\frac{\partial \varepsilon}{\partial t} + u\frac{\partial \varepsilon}{\partial x} + v\frac{\partial \varepsilon}{\partial y} + w\frac{\partial \varepsilon}{\partial z} = \frac{\partial}{\partial z}\left(\frac{v_v}{\sigma_\varepsilon}\frac{\partial \varepsilon}{\partial z}\right) + \frac{\varepsilon}{k}c_{\varepsilon_1}\left[v_v\left[\left(\frac{\partial u}{\partial z}\right)^2 + \left(\frac{\partial v}{\partial z}\right)^2\right] + (1 - c_{\varepsilon_3})\frac{v_v}{\sigma_p}\frac{g}{\rho_0}\frac{\partial p}{\partial z}\right] - c_{\varepsilon_2}\frac{\varepsilon^2}{k}$$

with: $c_\mu = 0.09, c_{\varepsilon_1} = 1.44, c_{\varepsilon_2} = 1.92, \sigma_k = 1.0, \sigma_\varepsilon = 1.3, \sigma_p = 0.5$

Boundary Conditions

Flow

To solve the Reynolds-averaged 3D shallow water equations, which are a parabolic set of partial differential equations, a set of initial and boundary conditions have to be specified to get a well-posed mathematical problem with an unique solution. This solution consists of a steady state solution and transient solution. The latter follows from the deviation between the initial conditions and steady state solution, which slowly dies out. The steady state solution is fully dependent on the boundary conditions.

For the continuity equation, it is considered that in the vertical the water surface and bed are impermeable. Hence, the vertical current velocity at the bed and at the surface equals zero:

$$w|_{z=-d} = 0, \qquad w|_{z=\zeta} = 0$$

For the momentum equations, however, there is shear stress at the bed and at the surface due to bed resistance and wind respectively. These boundary conditions are defined as:

$$v_V \frac{\partial u}{\partial z}\Big|_{z=-d} = \frac{\tau_{b,x}}{\rho_0}, \qquad v_V \frac{\partial v}{\partial z}\Big|_{z=-d} = \frac{\tau_{b,y}}{\rho_0}, \qquad \overrightarrow{\tau_b} = \rho_0 |\overrightarrow{u_*}| \overrightarrow{u_*} = \frac{\rho_0 g |\overrightarrow{u_b}|}{C_{3D}^2} \overrightarrow{u_b}$$

$$v_V \frac{\partial u}{\partial z}\Big|_{z=\zeta} = \frac{|\overrightarrow{\tau_w}|}{\rho_0} sin\varphi, \qquad v_V \frac{\partial v}{\partial z}\Big|_{z=\zeta} = \frac{|\overrightarrow{\tau_w}|}{\rho_0} cos\varphi, \qquad \overrightarrow{\tau_w} = \rho_{air} C_d |\overrightarrow{U_{10}}| \overrightarrow{U_{10}}$$

in which the three-dimensional Chézy coefficient is determined by:

$$C_{3D} = \frac{\sqrt{g}}{\kappa} \ln\left(1 + \frac{\Delta z_b}{2 z_0}\right)$$

Herein, bed roughness height, z_0, is calculated, using the two-dimensional Chézy coefficient:

$$z_0 = \frac{\zeta + d}{e^{1 + \frac{\kappa C_{2D}}{\sqrt{g}}} - e}$$

This two-dimensional Chézy coefficient is derived from the applied Manning roughness coefficient:

$$C_{2D} = \frac{(\zeta + d)^{\frac{1}{6}}}{n}$$

At the open boundaries of the model, the following boundary conditions can be applied:

1. *Discharge (upsteam)*
$$Q = F_Q(t)$$
2. *Velocity (downstream)*
$$U = F_U(t)$$
3. *Water Level (downstream)*
$$\zeta = F_\zeta(t)$$
4. *Riemann (downstream)*
$$U \pm \zeta \sqrt{\frac{g}{d}} = F_R(t)$$

At the closed boundaries, the current velocity equals zero. Furthermore, there is no shear stress (free slip condition).

Transport
The transport equation is of hyperbolic type. The following boundary conditions apply in the vertical, which indicate that there are no fluxes of substances through the bottom or water surface:

$$D_V \frac{\partial c}{\partial z}\Big|_{z=-d} = D_V \frac{\partial c}{\partial z}\Big|_{z=\zeta} = 0$$

Through the open boundaries, the concentration of the substance is set as a time series:

$$c_k = F_c(t)$$

Furthermore, there is no transport of substances through the closed boundaries and the concentration equals zero.

Turbulence
To solve the k-ε turbulence model, a local equilibrium of the production and dissipation of kinetic energy is assumed in the vertical at the surface and at the bed, which lead to the following Dirichlet boundary conditions:

$$k|_{z=-d} = \frac{u_{*b}^2}{\sqrt{c_\mu}}, \qquad \varepsilon|_{z=-d} = \frac{u_{*b}^3}{\kappa z_0}, \qquad u_{*b} = \sqrt{\frac{|\overrightarrow{\tau_b}|}{\rho_0}}$$

$$k|_{z=\zeta} = \frac{u_{*s}^2}{\sqrt{c_\mu}}, \qquad \varepsilon|_{z=\zeta} = \frac{u_{*s}^3}{\kappa \Delta z_\zeta}, \qquad u_{*s} = \sqrt{\frac{|\overrightarrow{\tau_w}|}{\rho_0}}$$

At the open boundaries, assuming a logarithmic current velocity profile is assumed, a linear distribution for the turbulent kinetic energy is applied, while this leads to a parabolic distribution for the turbulent kinetic energy dissipation:

$$k(z) = \frac{1}{\sqrt{c_\mu}}\left[u_{*b}^2\left(1 - \frac{z+d}{\zeta+d}\right) + u_{*s}^2\frac{z+d}{\zeta+d}\right]$$

$$\varepsilon(z) = \frac{u_{*b}^3}{\kappa(z+d)} + \frac{u_{*s}^3}{\kappa(\zeta - z)}$$

At the closed boundaries, there is no transport, production or dissipation of turbulent kinetic energy.

Sediment transport
Cohesive sediment
Erosion and deposition of mud is regulated by the Partheniades-Krone formulations. For the bed sediment this is:

$$E = \mathrm{p_{m,b}} \cdot \max\left\{M_b\left(\frac{\tau}{\tau_{cr,b,e}} - 1\right), 0\right\}$$
$$D = \max\left\{w_s c_b\left(1 - \frac{\tau}{\tau_{cr,d}}\right), 0\right\}$$

If a separate fluff layer is applied, the same fluxes are calculated through:

$$E = \mathrm{p_{m,f}} \cdot \max\left\{M_f\left(\tau - \tau_{cr,f,e}\right), 0\right\}$$

$$D = \max\left\{w_s c_b\left(1 - \frac{\tau}{\tau_{cr,d}}\right), 0\right\}$$

In which the erosion parameter of the fluff layer, M_f, is calculated as:

$$M_f = \min\left(M_{0,} m M_1\right)$$

The fall velocity, w_s, is dependent on the salinity:

$$w_s = \begin{cases} \frac{w_{s,max}}{2}\left(1-\cos\left(\frac{\pi S}{S_{max}}\right)\right)+\frac{w_{s,f}}{2}\left(1+\cos\left(\frac{\pi S}{S_{max}}\right)\right), & if\ S \le S_{max} \\ w_{s,max}, & if\ S > S_{max} \end{cases}$$

Dispersion of sediment throughout the water column is dependent on the mixing coefficient, calculated with the turbulence model. The advective transport of mud is calculated with the transport equation.

Non-cohesive sediment
Sand is transported in both suspension and bed load according to the Van Rijn (1993) formula. These fluxes are separated by a near-bed reference layer (kmz-layer), which is determined by the reference height of Van Rijn. The erosion and deposition of suspended sand can be calculated through:

$$E = a_2 c_a \left(\frac{\varepsilon_s}{\Delta z}\right)$$

$$D = \left(a_2\left(\frac{\varepsilon_s}{\Delta z}\right) + a_1 w_s\right) c_{kmz}$$

a_1 and a_2 are correction factors for the sediment concentration gradient, on which the erosion due diffusion is dependent on. These are calculated based on the derivative of a fitted Rouse profile, which is fitted based on SSC in the kmz-layer and at the reference concentration. This concentration is calculated by the transport formula as:

$$c_a = 0.015\rho_s \frac{D_{50}(T_a)^{1.5}}{a(D_*)^{0.3}}$$

in which:

$$D_* = D_{50}\left[\frac{(s-1)g}{\nu^2}\right]^{\frac{1}{3}}, \qquad T_a = \frac{(\mu_c\tau)-\tau_{cr}}{\tau_{cr}}$$

with:

$$\mu_c = \frac{f_c'}{f_c} = \frac{0.24\left[\log\left(\frac{12\mathrm{h}}{3\mathrm{D}_{90}}\right)\right]^{-2}}{0.24\left[\log\left(\frac{12\mathrm{h}}{\mathrm{k_s}}\right)\right]^{-2}}$$

Furthermore the mixing coefficient, originating from the turbulence model, is corrected based on:

$$\varepsilon_s = \beta_{eff} \cdot \varepsilon$$

in which:

$$\beta_{eff} = 1 + 2\left(\frac{w_s}{u_*}\right)^2$$

The fall velocity of the sandy sediment is calculated by:

$$w_s = \begin{cases} \dfrac{(s-1)gD_s^2}{18\nu}, & 65\mu m < D_s \leq 100\mu m \\ \dfrac{10}{\nu}\left(\sqrt{1+\dfrac{0.01(s-1)gD_s^3}{\nu^2}}-1\right), & 100\mu m < D_s \leq 1000\mu m \\ 1.1\sqrt{(s-1)gD_s}, & D_s > 1000\mu m \end{cases}$$

In contrast, the bed load transport is calculated according to:

$$|S_b| = 0.006\rho_s w_s D_{50} M^{0.5} M_e^{0.7},$$

in which:

$$M = \frac{v_{eff}^2}{(s-1)gD_{50}}$$

$$M_e = \frac{\left(v_{eff} - v_{cr}\right)^2}{(s-1)gD_{50}}$$

with v_{eff} is the velocity near the bed. The bedload transport rates in u- and v-direction are calculated by:

$$S_{b,u} = \frac{u_{b,u}}{|u_b|}S_b, \qquad S_{b,v} = \frac{u_{b,v}}{|u_b|}S_b$$

Furthermore, account is taken for the transport of bed particles on slopes due to gravity.

Morphology

Sand and mud are distributed in the bed according to their respective fractions. Interaction between the fractions is taken account for, and is dependent on the governing regime. In the non-cohesive regime ($p_m < p_{m,cr}$), in which mud is entrained proportional to the sand fraction, the critical bed shear stress and erosion fluxes are calculated as:

$$\tau_{e,cr} = \tau_{cr}(1+p_m)^{\beta}$$

$$S_i = \rho_i p_i E_i$$

In this regime, the erosion velocity for mud, E_m, equals the erosion velocity for sand, E_s. In the cohesive regime ($p_m > p_{m,cr}$), the erosion velocity for sand is calculated as:

$$E_s = \frac{1}{p_m}E_m$$

In which the erosion velocity for mud, E_m, is calculated according to interpolations of the erosion parameter, M, and critical bed shear stress of the fully mud regime (in which the erosion parameter is calculated with the Partheniades-Krone formula) and the non-cohesive regime:

$$M_c = M_{fm}\left(\frac{M_{nc}}{1-p_{m,cr}}\frac{1}{M_e}\right)^{\frac{1-p_m}{1-p_{m,cr}}}$$

$$\tau_{cr} = \left[\frac{\tau_{s,cr}(1-p_m)^{\beta} - \tau_{m,cr}}{1-p_{m,cr}}\right](1-p_m) + \tau_{m,cr}$$

D.3 Transformation

Horizontal coordinate system

The Reynolds-averaged 3D shallow water equations and its corresponding equations (transport, turbulence, state) cannot be used in the model, since the horizontal model domain is described by a system of orthogonal curvilinear co-ordinates of ξ- and η-coordinates. The advantage of such coordinate system is that it can follow the curved boundaries of the complex model area. The physical space is decomposed in directions perpendicular and parallel to the grid lines: instead of Δx and Δy, the curved face lengths $\sqrt{G\xi\xi}$, $\sqrt{G\eta\eta}$ are used.

Vertical coordinate system

The vertical domain is described by a σ coordinate system. The σ co-ordinate system is defined as:

$$\sigma = \frac{z-\zeta}{d+\zeta} = \frac{z-\zeta}{h}$$

where σ = -1 at the bottom and σ = 0 at the free surface. Layers are bounded by two σ-planes. The σ layers are defined by a percentage of the total water depth. Therefore, the number of layers is constant over the horizontal computational domain. The advantage of σ-layers is that these planes are not strictly horizontal, but instead follow the bottom topography and the free surface. This results in a smooth representation of the topography and the oscillatory free surface. The layer distribution can be chosen non-uniform to allow for more resolution in the zones of interest such as the bed area (boundary layer and sediment transport) and the free surface (wind and waves). For each layer a set of coupled conservation equations is solved.

Transformed Reynolds-Averaged 3D Shallow Water Equations

The transformation leads to the following Reynolds-averaged 3D shallow water equations and corresponding equations (transport, turbulence, state), which are solved in the model domain in Delft3D.

Continuity Equation

$$\frac{\partial\zeta}{\partial t} + \frac{1}{\sqrt{G_{\xi\xi}}\sqrt{G_{\eta\eta}}}\frac{\partial((d+\zeta)U\sqrt{G_{\eta\eta}})}{\partial\xi} + \frac{1}{\sqrt{G_{\xi\xi}}\sqrt{G_{\eta\eta}}}\frac{\partial((d+\zeta)V\sqrt{G_{\xi\xi}})}{\partial\eta} = (d+\zeta)Q$$

Momentum Equation in u-direction

$$\frac{\partial u}{\partial t} + \frac{u}{\sqrt{G_{\xi\xi}}}\frac{\partial u}{\partial\xi} + \frac{v}{\sqrt{G_{\eta\eta}}}\frac{\partial u}{\partial\eta} + \frac{w}{(d+\zeta)}\frac{\partial u}{\partial\sigma} - \frac{v^2}{\sqrt{G_{\xi\xi}}\sqrt{G_{\eta\eta}}}\frac{\partial\sqrt{G_{\eta\eta}}}{\partial\xi} + \frac{uv}{\sqrt{G_{\xi\xi}}\sqrt{G_{\eta\eta}}}\frac{\partial\sqrt{G_{\xi\xi}}}{\partial\eta} =$$

$$v_h\left(\frac{1}{\sqrt{G_{\xi\xi}}\sqrt{G_{\eta\eta}}}\frac{\partial^2 u}{d\xi^2} + \frac{1}{\sqrt{G_{\xi\xi}}\sqrt{G_{\eta\eta}}}\frac{\partial^2 u}{d\eta^2}\right) + \frac{1}{(d+\zeta)^2}\frac{\partial}{\partial\sigma}\left(v_v\frac{\partial u}{\partial\sigma}\right) - \frac{g}{\sqrt{G_{\xi\xi}}}\frac{\partial\zeta}{\partial\xi} +$$

$$-g\frac{d+\zeta}{\rho_0\sqrt{G_{\xi\xi}}}\int_{\sigma}^{0}\left(\frac{\partial\rho}{\partial\xi} + \frac{\partial\rho}{\partial\sigma}\frac{\partial\sigma}{\partial\xi}\right)d\sigma' - \frac{1}{\rho_0\sqrt{G_{\xi\xi}}}\frac{\partial P_{atm}}{\partial\xi} + fv + q_{in}(\hat{U}-u)$$

Momentum Equation in v-direction

$$\frac{\partial v}{\partial t}+\frac{u}{\sqrt{G_{\xi\xi}}}\frac{\partial v}{\partial \xi}+\frac{v}{\sqrt{G_{\eta\eta}}}\frac{\partial v}{\partial \eta}+\frac{w}{(d+\zeta)}\frac{\partial v}{\partial \sigma}-\frac{u^2}{\sqrt{G_{\xi\xi}}\sqrt{G_{\eta\eta}}}\frac{\partial \sqrt{G_{\xi\xi}}}{\partial \eta}+\frac{uv}{\sqrt{G_{\xi\xi}}\sqrt{G_{\eta\eta}}}\frac{\partial \sqrt{G_{\eta\eta}}}{\partial \xi}=$$

$$v_h\left(\frac{1}{\sqrt{G_{\xi\xi}}\sqrt{G_{\eta\eta}}}\frac{\partial^2 v}{d\xi^2}+\frac{1}{\sqrt{G_{\xi\xi}}\sqrt{G_{\eta\eta}}}\frac{\partial^2 v}{d\eta^2}\right)+\frac{1}{(d+\zeta)^2}\frac{\partial}{\partial \sigma}\left(v_v\frac{\partial v}{\partial \sigma}\right)-\frac{g}{\sqrt{G_{\eta\eta}}}\frac{\partial \zeta}{\partial \eta}+$$

$$-g\frac{d+\zeta}{\rho_0\sqrt{G_{\eta\eta}}}\int_{\sigma}^{0}\left(\frac{\partial \rho}{\partial \eta}+\frac{\partial \rho}{\partial \sigma}\frac{\partial \sigma}{\partial \eta}\right)d\sigma'-\frac{1}{\rho_0\sqrt{G_{\eta\eta}}}\frac{\partial P_{atm}}{\partial \eta}-fu+q_{in}(\hat{V}-v)$$

Transport Equation

$$\frac{\partial (d+\zeta)c}{\partial t}+\frac{1}{\sqrt{G_{\xi\xi}}\sqrt{G_{\eta\eta}}}\left\{\frac{\partial\left[\sqrt{G_{\eta\eta}}\,(d+\zeta)uc\right]}{\partial \xi}+\frac{\partial\left[\sqrt{G_{\xi\xi}}\,(d+\zeta)vc\right]}{\partial \eta}\right\}+\frac{\partial wc}{\partial \sigma}=$$

$$\frac{d+\zeta}{\sqrt{G_{\xi\xi}}\sqrt{G_{\eta\eta}}}\left\{\frac{\partial}{\partial \xi}\left(D_H\frac{\sqrt{G_{\eta\eta}}}{\sqrt{G_{\xi\xi}}}\frac{\partial c}{\partial \xi}\right)+\frac{\partial}{\partial \xi}\left(D_H\frac{\sqrt{G_{\xi\xi}}}{\sqrt{G_{\eta\eta}}}\frac{\partial c}{\partial \eta}\right)\right\}+\frac{1}{(d+\zeta)}\frac{\partial}{\partial \sigma}\left(D_v\frac{\partial c}{\partial \sigma}\right)+$$

$$-\lambda_d(d+\zeta)+(d+\zeta)(q_{in}c_{in}-q_{out}c)+Q_{tot}$$

Equation of State

$$\rho=\rho(s,T)$$

Turbulence Model

$$\frac{\partial k}{\partial t}+\frac{u}{\sqrt{G_{\xi\xi}}}\frac{\partial k}{\partial \xi}+\frac{v}{\sqrt{G_{\eta\eta}}}\frac{\partial k}{\partial \eta}+\frac{w}{(d+\zeta)}\frac{\partial k}{\partial \sigma}=\frac{1}{(d+\zeta)^2}\frac{\partial}{\partial \sigma}\left(D_k\frac{\partial k}{\partial \sigma}\right)+$$

$$+v_{3D}\frac{1}{(d+\zeta)^2}\left[\left(\frac{\partial u}{\partial \sigma}\right)^2+\left(\frac{\partial v}{\partial \sigma}\right)^2\right]+\frac{v_{3D}}{\rho\sigma_p}\frac{g}{(d+\zeta)}\frac{\partial \rho}{\partial \sigma}-\varepsilon$$

$$\frac{\partial \varepsilon}{\partial t}+\frac{u}{\sqrt{G_{\xi\xi}}}\frac{\partial \varepsilon}{\partial x}+\frac{v}{\sqrt{G_{\eta\eta}}}\frac{\partial \varepsilon}{\partial y}+\frac{w}{(d+\zeta)}\frac{\partial \varepsilon}{\partial z}=\frac{1}{(d+\zeta)^2}\frac{\partial}{\partial \sigma}\left(D_\varepsilon\frac{\partial \varepsilon}{\partial \sigma}\right)+$$

$$+c_{\varepsilon_1}\frac{\varepsilon}{k}\left\{v_{3D}\frac{1}{(d+\zeta)^2}\left[\left(\frac{\partial u}{\partial \sigma}\right)^2+\left(\frac{\partial v}{\partial \sigma}\right)^2\right]\right\}+c_{\varepsilon_1}\frac{\varepsilon}{k}(1-c_{\varepsilon_3})\left[\frac{v_{3D}}{\rho\sigma_p}\frac{g}{(d+\zeta)}\frac{\partial \rho}{\partial \sigma}\right]$$

$$-c_{\varepsilon_2}\frac{\varepsilon^2}{k}$$

Boundary Conditions

$$w|_{\sigma=-1}=0,\qquad \frac{v_V}{(d+\zeta)}\frac{\partial u}{\partial \sigma}\Big|_{\sigma=-1}=\frac{\tau_{b,x}}{\rho_0},\qquad \frac{v_V}{(d+\zeta)}\frac{\partial v}{\partial \sigma}\Big|_{\sigma=-1}=\frac{\tau_{b,y}}{\rho_0},$$

$$\frac{D_V}{(d+\zeta)}\frac{\partial c}{\partial \sigma}\Big|_{\sigma=-1}=0,\qquad k|_{\sigma=-1}=\frac{u_{*b}^2}{\sqrt{c_\mu}},\qquad \varepsilon|_{\sigma=-1}=\frac{u_{*b}^3}{\kappa z_0}$$

$$w|_{\sigma=0} = 0, \qquad \frac{v_V}{(d+\zeta)}\frac{\partial u}{\partial \sigma}\Big|_{\sigma=0} = \frac{|\overrightarrow{\tau_w}|}{\rho_0} sin\varphi, \qquad \frac{v_V}{(d+\zeta)}\frac{\partial v}{\partial \sigma}\Big|_{\sigma=0} = \frac{|\overrightarrow{\tau_w}|}{\rho_0} cos\varphi,$$

$$\frac{D_V}{(d+\zeta)}\frac{\partial c}{\partial \sigma}\Big|_{\sigma=0} = 0, \qquad k|_{\sigma=0} = \frac{u_{*s}^2}{\sqrt{c_\mu}}, \qquad \varepsilon|_{\sigma=0} = \frac{u_{*s}^3}{\kappa \Delta z_\zeta}$$

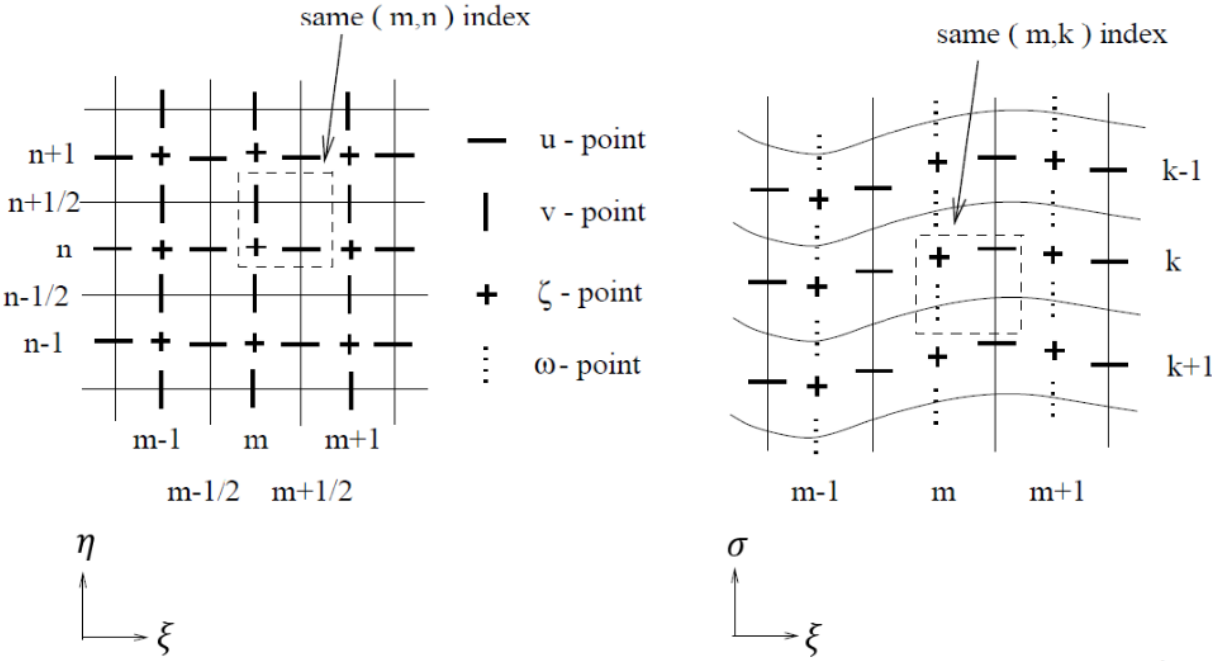

Figure 76 – Numbering of the computational grid: in the horizontal (left), in the vertical (left)

D.4 Numerical Aspects

Grid structure

In order to discretize the Reynold-averaged 3D shallow water equations, the primitive variables (water level (ζ) and current velocity (u,v,w)) are arranged in a so-called staggered grid. This particular arrangement is called the Arakawa C-grid in which the water level points are defined in the cell centers and the velocity components perpendicular to the grid cell faces, both in horizontal and vertical direction as is visualized in Figure 76. The horizontal directions are labelled with m and n, which run from 1,1 to Mmax, Nmax from one corner of the computational grid to another.

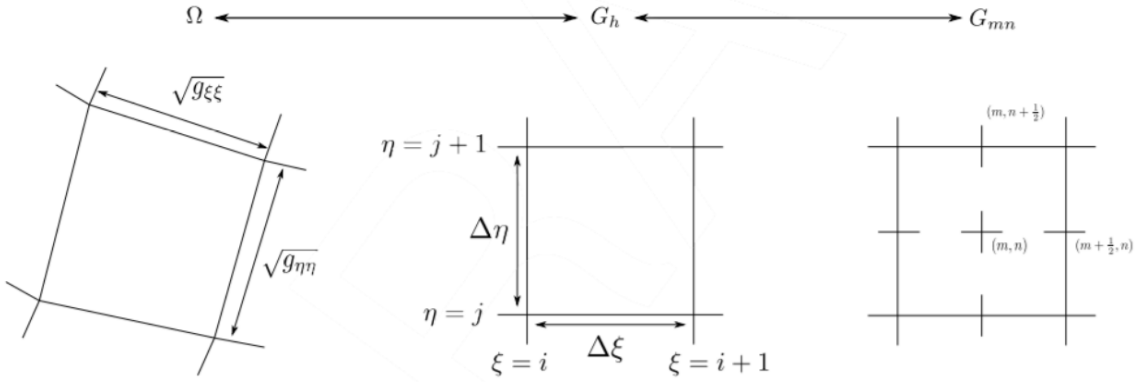

Figure 77 – Mapping of physical space to computational space

The constituents of the transport equation and turbulence model are set on the water level points. The mapping from orthogonal curvilinear coordinates in the horizontal direction to the

computational space is visualized in Figure 77. Depth values are defined in the grid cell vertices (see Figure 78).

The advantages of a staggered grid is that boundary conditions can be implemented in a simple manner. Furthermore with such grid arrangement it is possible to use a smaller number of discrete state variables to obtain the same accuracy. Moreover, a staggered grid prevents spatial oscillations in the water levels.

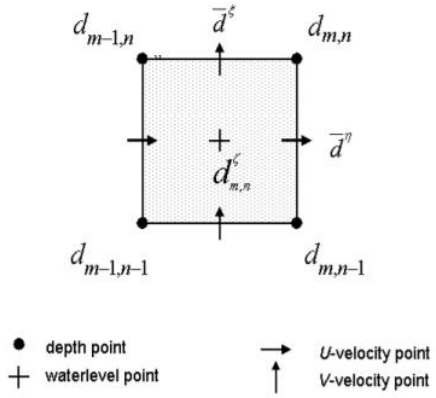

Figure 78 – Definition bottom depth on computational grid

Drying and flooding

The physical process of drying and flooding in the numerical model is represented by removing grid points from the flow domain if they become dry when the water levels drops and become flooded when the water level rises. A special algorithm is constructed which specifies when a grid cell (water level point) or cell boundary (velocity points) becomes dry or wet. A discontinuous movement of the closed boundaries is created in which the boundary can move only one grid cell per time step during flooding (explicit process). However, this does not lead to sharp gradients in the water level and/or oscillations in water levels and velocities as long as grid sizes and time step remain small and the bottom has smooth gradients. Furthermore, the computation is started at high water to allow for a smooth flooding behavior and non-negative water layers.

Artificial mixing

Grids transformed to σ-layers may give rise to numerical problems when integrating the baroclinic term and horizontal diffusion term in the vertical for a steep bottom slope to approximate the horizontal gradients. Since the very small horizontal density gradient is approximated with two large opposite terms according to the transformation to σ-layers, small truncation errors may lead to artificial flow. This is dependent on the grid cell size and the bottom gradient, which lead to the following hydrostatic consistency condition:

$$\left|\frac{\sigma}{(\zeta+d)}\frac{\delta(\zeta+d)}{\partial\xi}\right| < \left|\frac{\partial\sigma}{\delta\xi}\right|$$

Since the horizontal diffusion term is described by a second order derivative, even a more complex set of large opposite cross derivative terms is used to approximate the relative small horizontal gradient. For this, it is difficult to find a stable and positive discretization. This may lead to artificial mixing.

It is therefore assumed that the horizontal length scale is much larger than the water depth, such that the control volumes of the σ-grid can be redefined to rectangular volumes in z-coordinates, as is shown in Figure 79.

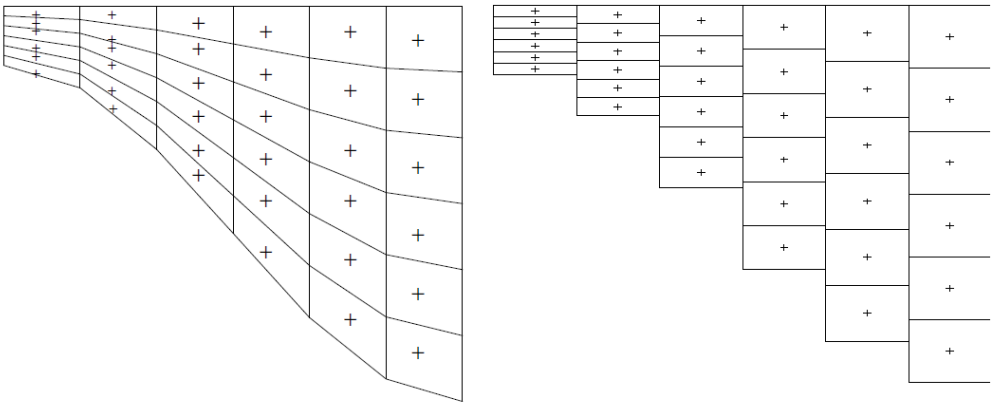

Figure 79 – Control volumes in 'normal' σ-grid (left) and rectangular control volumes in redefined σ-grid (right).

This 'anti-creep' correction gives a consistent, stable and monotonic approximation of both the horizontal pressure gradient and the horizontal diffusion term, even when the hydrostatic consistency condition is not fulfilled. The correction is based on the Finite Volume approach. Since the boxes in z-coordinates are not nicely connected to each other, interpolation is required to compute the fluxes at the interfaces (see Figure 80).

At the closed boundaries, the derivative is set to zero. The integration of the horizontal diffusion term is explicit and, hence, has a time step limitation, which is the following:

$$\Delta t \leq \frac{1}{D_H}\left(\frac{1}{\sqrt{G_{\xi\xi}}^2}+\frac{1}{\sqrt{G_{\eta\eta}}^2}\right)$$

The non-linear min/max limiters in the method prevent wiggles, but may sometimes underestimate the baroclinic pressure term, since the minimum of the two gradients is taken. This can be resolved by increasing the grid resolution and by applying the last two lines of the method, which may increase the baroclinic pressure term and simultaneously fulfils the min-max principle (the maximum and minimum of a variable being transported by diffusion do not increase or decrease).

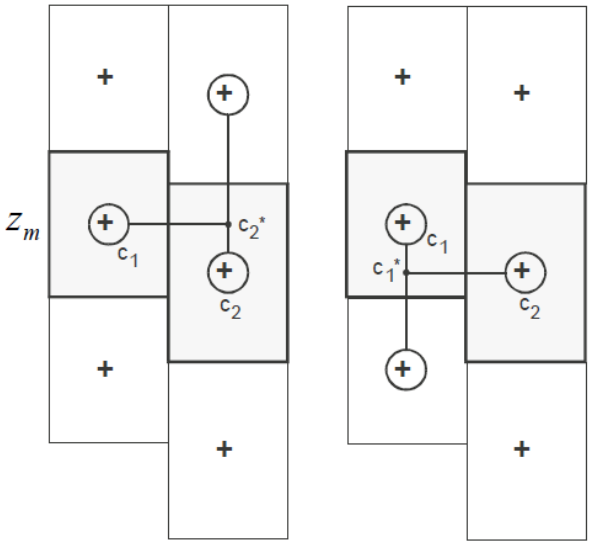

Figure 80 – Left and right approximation of a strict horizontal gradient

Time integration

Reynolds-Averaged 3D Shallow Water Equations

The time integration is according to the implicit finite difference approximation of the so-called Alternating Direction Implicit (ADI-)method splits one time step into two stages, each of a half time step. In the first step the terms in one direction, for instance in ξ, are taken implicitly, while the terms in the other direction, η, are taken explicitly. In the second step now the terms in η-direction are taken implicitly, while the terms in ξ-direction are taken explicitly. In both stages the horizontal terms of the model equations are solved in a consistent way, such that for each time step all terms are at least second order accuracy in space. In the vertical direction a fully implicitly time integration method is applied, which is first order accurate in time and leads to tri-diagonal systems of equations. Again this is solved with double sweep.

The advantage of the ADI-method is that it unconditionally stable, mass conserving, at least second order accurate, computationally efficient, since the integrated water levels and velocities are coupled along grid lines, leading to systems of equations with a small bandwidth (tri-diagonal system). A disadvantage is the ADI-effect, which is explained as follows. If grid lines do not smoothly follow the geometry and/or jumps in the bathymetry, a staircase or zig-zag alignment of grid cells with respect to the flow lines will emerge. Since, however, the ADI-method is splitting the spatial operator, surface waves and flow cannot travel through more than two bends of 90 degrees in one complete time step. This leads to inaccurate flow patterns. In the most critical situation, with waves and/or flow approach the grid cells under an angle of 45 degrees, the Courant number, to which wave propagation is related to, should be lower than $4\sqrt{2}$. The Courant number is defined as:

$$C = \frac{u_x \Delta t}{\sqrt{G_{\xi\xi}}} + \frac{u_y \Delta t}{\sqrt{G_{\eta\eta}}}$$

The non-linear terms in the mass and momentum equation require an iterative procedure. Furthermore, the simplified horizontal viscosity terms, resulting in Laplace operator along the grid lines, are integrated fully implicitly by using operator splitting. This is an unconditionally stable procedure. The full Reynolds stresses are used in the HLES-model for sub-grid viscosity. Herein, the stress tensors are integrated explicitly. Hence, the following stability condition applies:

$$\Delta t \leq \frac{1}{2\nu_H} \left(\frac{1}{\sqrt{G_{\xi\xi}}^2} + \frac{1}{\sqrt{G_{\eta\eta}}^2} \right)$$

Transport equation
The constituents, such as salinity, are located in the grid cell centers. In the transport equation, a the fully implicit ADI-method is used for the time integration in horizontal direction, while in the vertical direction a fully implicit scheme is used in the form of the central differences. This latter scheme is first order in team and leads to tridiagonal systems of equations, which can be solved by double sweep. The baroclinic term links the momentum equations with the transport equation. However, since the transport equation has slower temporal variations than the momentum equations, the baroclinic term is treated explicitly. The horizontal diffusion term are discretized in time by means of the Crank-Nicholson method, while the source terms are integrated explicitly and the sink terms implicitly in order to avoid negative concentrations and instabilities.

Turbulence model
The k-ε turbulence model is based on the eddy viscosity concept, which is always calculated on information of the previous half time step. The transport equations of the turbulent kinetic energy, k, and turbulent kinetic energy dissipation rate, ε, are solved in a non-conservative form.

Spatial integration

Reynolds-averaged 3D Shallow Water Equations

For the spatial integration of the advection terms, the cyclic method is used. The method integrates the advection terms implicitly with the second order BDF scheme in the stage of the ADI-method in the implicit stage, and explicitly using central differences in the explicit stage.

This introduces a leading phase error in the first step and a lagging phase error in the second step, which reduces the phase error by canceling terms. By using the BDF scheme and central differences, numerical diffusion is kept to a minimum. In both steps, the vertical advection terms are fully implicitly integrated by means of the second order central differences to prevent instabilities in shallow areas. The approximation of the vertical viscosity terms is also based on central differences. These terms are discretized as follows:

Transport Equation

The transport equation is spatially discretized with a mass conserving Finite Volume Approach in order to ensure that the total mass is conserved. The horizontal advection terms are discretized in space by means of the cyclic method. The upwind discretization is used in the stage in which both the horizontal advection and vertical viscosity term are integrated implicitly. This results in a diagonally dominant matrix with eleven diagonal, which can be solved by a Red Black Jacobi iterative scheme in the horizontal and with double sweep in the vertical. Near the open and closed boundaries the approximations for the fluxes are reduced to lower order.

Since the Cyclic method may be prone to non-physical oscillations on coarse grids near regions of steep gradients, a Forester filter is applied to remove negative values. First the horizontal Forester filter is used, followed by the vertical filter.

Turbulence Model

On the staggered grid, the turbulent quantities (k,ε) and vertical eddy viscosity, v_V, are positioned at the layer interfaces in the centers of the computational cells. This makes it possible to discretize the vertical gradients in the production and buoyancy term and to implement the boundary conditions at the bed and the free surface. First order upwind is used for the advection to provide positive solutions.

Appendix E. Numerical Model Characteristics

In this appendix, the detailed characteristics of the used (NEVLA3D, LTV Slib) and implemented (SETMO) numerical models are summarized. The characteristics consist of modelling input parameters and the general modelling approach. Note that NEVLA3D and SETMO are implemented in Delft3D, while LTV Slib is implemented in Delwaq, which may cause formulations for the same parameter to differ slightly.

E.1 NEVLA3D

Model Description			
Name	NEVLA3D *(NEderlands-VLAams)*		
Year	2009		
Study Area	Scheldt Estuary and all its tidal dependent tributaries *(Durme, Rupel, Nete, Dijle and Zenne)*		
Model Type	3D Hydrodynamic Model		
Software	SIMONA *(SImulatie MOdellen NAtte waterstaat)*		
Module	WAQUA (*WAter movement and water QUAlity modelling*)		
Coordinate Reference System	Nieuw Rijksdriehoekstelsel Amersfoort *(EPSG:7415)*		
Height Reference System	NAP *(Normaal Amsterdams Peil)*		
Runtime	~2.5 months		
Domain			
Grid Dimensions (M x N)	380 x 3001		
Average Grid Sizes	Δx	~100 m	
	Δy	~100 m	
Number of cells	1,137,000		
Layer Type	Sigma Layers		
Number of Layers	6		
Layer Distribution	Surface	10%	
		20%	
		30%	
		20%	
		15%	
	Bottom	5%	
Latitude	52.5°		
Bathymetry	Belgian Coastal Plain	Year	2004-2016
		Resolution	20 x 20 m
	Estuary Mouth	Year	2014
		Resolution	20 x 20 m
	Western Sea Scheldt	Year	2015
		Resolution	20 x 20 m
	Lower Sea Scheldt	Year	2014
		Resolution	5 x 5 m
	Upper Sea Scheldt	Year	2009
		Resolution	5 x 5 m
	Rupel, Nete, Zenne, Dijle	Year	2010
		Resolution	5 x 5 m

	Digital terrain model Sea Scheldt	Year	2007
		Resolution	1 x 1 m
	Cell center value	Mean	
Time Frame			
Simulation Period	Start	01-01-2014 00:00:00	
	End	31-12-2014 00:00:00	
Time Step	0.125 min *(7.5 s)*		
Spin-Up	2 days		
Processes			
Modeled constituents	Salinity		
Physical Processes	Wind *(Measured 10-min wind data at Hansweert)*		
Initial and Boundary Conditions			
Initial Conditions	Water Level	Linear interpolated water level measurements	
	Salinity	Linear interpolated salinity measurements *(0.3-33.1 ppt, 2.2 ppt near Antwerp)*	
Boundary Conditions	Upstream	Measured discharges *(Grobendonk (Kleine Nete), Itegem (Grote Nete), Eppegem (Zenne), Haacht (Dijle), Dendermonde (Dender) and Merelbeke (Bovenschelde and Leie), and Bath Canal and Gent-Terneuzen Canal)*	
	Downstream	Nested including corrections *(ZUNO (ZUidelijke NOorderzee) model)*: CRC *((Logarithmically profiled) Current (West), Riemann (North), (Logarithmically profiled) Current (East))*	
	Salinity	Nested salinity including corrections *(ZUNO)*	
	Wind	Nested HIRLAM *(High Resolution Limited Area Model)* 3-h wind fields *(ZUNO)*	
Physical Parameters			
Dynamic Water Viscosity	0.01 $kg.m^{-1}s^{-1}$		
Water Density	1023 $kg.m^{-3}$		
Air Density	1.205 $kg.m^{-3}$		
Gravity	9.813 $m.s^{-2}$		
Temperature	15 °C		
Bottom Roughness	Formula	Manning	
	Field	Spatial-varying Manning coefficient *(0.017-0.028 $m^{-1/3}s^{-1}$; 0.022-0.024 $m^{-1/3}s^{-1}$ near Antwerp)*	
	Relation for the calculation of Chézy	Velocity-ratio	
	Time interval to compute Chézy values from given friction-values	10 min	
	Slip condition	Free slip	
Viscosity	Horizontal	1 m^2s^{-1}	
	Vertical	k-ε turbulence model	
	Background (Vertical)	0 m^2s^{-1}	
	HLES	No	
Diffusivity	Horizontal	1 $m^2 s^{-1}$	
	Vertical	k-ε turbulence model	
	Background (Vertical)	0 m^2s^{-1}	
	Ozmidov length scale	None	

	HLES	No	
Wind	Height	10 m	
	Stress coefficient	0.0026	
Numerical Parameters			
Drying and Flooding	Threshold depth	0.005 m	
	Check method	Grid cell centers	
Depth at grid cell faces	Mean		
Continuity	Scheme	Central	
	Type of convergence	Water level	
	Convergence criterion	0.0005 m	
	Maximum number of iterations	16	
Momentum	Scheme	Central	
	Advection scheme	Time	ADI-method
		Space	Cyclic
	Maximum number of iterations	32	
Transport	Advection scheme	Central	
Forester filter	Both horizontal and vertical		
Correction for sigma-coordinates	Applied		

E.2 LTV Slib

Model Description		
Name	LTV Slib *(Long Term Vision Slib)*	
Study Area	Scheldt Estuary and all its tidal dependent tributaries *(Durme, Rupel, Nete, Dijle and Zenne)*	
Model Type	3D Water quality Model	
Software	Delft3D	
Module	Delwaq	
Coordinate Reference System	Belge Lambert 1972 *(EPSG:31370)*	
Height Reference System	TAW *(Tweede Algemene Waterpassing)*	
Runtime	~1.5 days	
Domain and hydrodynamics		
Imported from:	NEVLA3D	
Time Frame		
Simulation Period	Start	01-01-2014 00:00:00
	End	31-12-2014 00:00:00
Time Step	5 min	
Spin-Up	2 days	
Processes		
Modeled constituents	Mud	
Physical Processes	Wind *(Measured 10-min wind data at Vlissingen,Hansweert)*, Waves *(derived with SWAN)*	
Initial and Boundary Conditions		
Initial Conditions	SSC	Previous model simulation (2013)
Boundary Conditions	Upstream	Measured SSC based on remote sensing data
	Downstream	Constant SSC derived from sediment transport fluxes

		Wind nested from ZUNO
Physical parameters		
Dispersion first direction	1.0 m^2s^{-1}	
Dispersion second direction	1.0 m^2s^{-1}	
Vertical diffusion	5.0 10^{-6} m^2s^{-1}	
Gravity	9.81 ms^{-2}	
Kinematic viscosity	6.0 10^{-6} m^2s^{-1}	
Water density	1020 kgm^{-3}	
Manning roughness	0.024	
Additional vertical dispersion	Wave effects in estuary mouth (derived from SWAN)	
Numerical Parameters		
Transport	Integration method	Local flux-corrected transport (Zalezac)
	Maximum number of iterations	2
	Minimum depth	0.01 m
Sediment		
General	Specific density	2600 kg m^{-3}
	Bed shear stress Shields for resuspension pick up	1.0 N m^{-1}
	Porosity	0.4
	Medium grain size	300 µm
	Layers	2
	Critical suspended solid concentration for flocculation	1.0 10^{20} g m^{-3}
Marine mud *(IM1)*	Transport formula	Partheniades-Krone
	Free settling velocity	1.0 mm s^{-1}
	Percentage to bed layer	0.1
	Critical fluff shear stress for erosion	0.2 N m^{-1}
	Critical bed shear stress for erosion	0.5 N m^{-1}
	First order erosion parameter	2.3 10^{-5} m^{-2} s^{-1}
	Second order erosion parameter	3.5 10^{-7} m^{-2} s^{-1}
	Critical shear stress for deposition	1000 N m^{-1}
Fluvial mud *(IM2)*	Transport formula	Partheniades-Krone
	Free settling velocity	1.0 mm s^{-1}
	Percentage to bed layer	0.05

	Critical fluff shear stress for erosion	0.2 N m^{-1}
	Critical bed shear stress for erosion	0.5 N m^{-1}
	First order erosion parameter	2.3 10^{-5} m^{-2} s^{-1}
	Second order erosion parameter	3.5 10^{-7} m^{-2} s^{-1}
	Critical shear stress for deposition	1000 N m^{-1}
Initial bed composition	Spatially-varying layered bed layer with mud masses	
Buffer layer (S1)	Type	Percentage (α) to bed layer S2
	Burial parameter	5 10^{-6} s^{-1}
	Factor resuspension pick-up	3.5 10^{-6}
Bed layer (S2)	Type	Uniform bed layer
	Maximum number of layers	1
	Layer thickness	0.05 m

E.3 SETMO

Model Description		
Name	SETMO *(Scheldt Estuary Turbidity Maximum Oosterweel)*	
Study Area	ETM in Lower Sea Scheldt *(between Liefkenshoek and Kruibeke)*	
Model Type	3D Morphological Model	
Software	Delft3D	
Module	SED3D	
Coordinate Reference System	Belge Lambert 1972 *(EPSG:31370)*	
Height Reference System	TAW *(Tweede Algemene Waterpassing)*	
Runtime	~4.5 days	
Domain		
Grid Dimensions (M x N)	760 x 100	
Average Grid Size Model Domain	Δx	30 m
	Δy	15 m
Average Grid Size Area of Interest	Δx	5 m
	Δy	5 m
Average Grid Size Upstream Boundary	Δx	100 m
	Δy	40 m
Average Grid Size Downstream Boundary	Δx	100 m
	Δy	55 m
Number of cells	38,498	
Layer Type	Sigma Layers	
Number of Layers	20	

Layer Distribution	Surface	2% 2.6% 3.2% 4% 5% 6.2% 7.8% 9.7% 9.7% 9.7% 9.7% 7.6% 5.9% 4.6% 3.5% 2.7% 2.1% 1.7% 1.3%	
	Bottom	1%	
Latitude	51.2385°		
Bathymetry	Lower Sea Scheldt	Year	2014
		Resolution	5 x 5 m
	Oosterweel Trench	Year	2017
		Resolution	~ 1 x 1 m
	Digital Terrain Model	Year	2017
		Resolution	5 x 5 m
	Cell Center Value	Mor *(Min)*	
Processes			
Modeled constituents	Salinity, Sediment *(Sand, Mud)*		
Physical processes	Wind*		
Time Frame			
Simulation Period	Start	2014**	
	End	2014**	
Time Step	0.02 min *(1.2 s)*		
Spin-Up	6 days		
Initial and Boundary Conditions			
Initial Conditions	Water Level	High water	
	Salinity	Linear interpolated salinity from boundary conditions *(2.2 ppt near Antwerp)*	
	Sediment	Mud *(IM1)*	0.5 g/l
		Sand *(IM2)*	0.0 g/l
Boundary Conditions	Upstream	Nested discharge *(NEVLA)*	
	Downstream	Nested water levels *(NEVLA)*	
	Salinity	Nested salinity *(NEVLA)*	
	Sediment	Mud *(IM1)*	Nested suspended sediment concentrations *(NEVLA)*
		Sand *(IM2)*	Neumann condition
Physical Parameters			
Dynamic Water Viscosity	0.01 $kg.m^{-1}s^{-1}$		

Water Density	1023 kg.m^{-3}	
Air Density	1.205 kg.m^{-3}	
Gravity	9.813 m.s^{-2}	
Temperature	12 °C	
Bottom Roughness	Formula	Manning
	Field	*0.023 m$^{-1/3}$s^{-1}*
	Relation for the calculation of Chézy	Bed roughness height
	Slip condition	Free slip
Viscosity	Horizontal	1 m^{2}s^{-1}
	Vertical	k-ε turbulence model
	Background (Vertical)	0 m^{2}s^{-1}
	HLES	No
Diffusivity	Horizontal	1 m^2 s^{-1}
	Vertical	k-ε turbulence model
	Background (Vertical)	0 m^{2}s^{-1}
	Ozmidov length scale	None
	HLES	No
Wind	Field	Uniform wind field with time-varying direction and speed, based on time-series from measurements at station Hansweert
	Height	10 m
	Stress coefficient	0.0026
Sediment and Morphology		
General	Specific density	2650 kg m^{-3}
	Reference density for hindered settling	500 kg m^{-3}
Mud *(IM1)*	Transport formula	Partheniades-Krone
	Free settling velocity	2.0 mm s^{-1}
	Saline settling velocity	2.5 mm s^{-1}
	Dry bed density	500 kg m^{-3}
	Critical bed shear for sedimentation	1000 N m^{-1}
	Critical bed shear for erosion	0.5 N m^{-1}
	Erosion parameter bed	1 10^{-3} m^{-2} s^{-1}
	Critical fluff shear for erosion	0.05 N m^{-1}
	Erosion parameter fluff	2.6 10^{-4} s^{-1}
	Maximum erosion flux fluff	1 10^{-3} kg m^{-2} s^{-1}
Sand *(IM2)*	Transport Formula	Van Rijn (1993)

	Median diameter (D_{50})	150 µm**	
	90th-percentile diameter (D_{50})	300 µm**	
	Dry bed density	1600 kg m^{-3}	
Initial bed composition	Spatially-varying layered bed layer		
Morphological factor	1.0		
Morphological update	False		
Threshold sediment thickness for transport and erosion reduction	0.01 m		
Density effect sediment on fluid	True		
Fluff layer	Type	Burial to bed layer	
	Burial parameter	5 10^{-6} s^{-1}	
	Maximum burial flux	1 10^{-2} kg m^{-2} s^{-1}	
Bed layer	Type	Layered bed stratification of well-mixed layers	
	Maximum number of layers	5	
	Active transport layer thickness	0.05 m	
Numerical Parameters			
Drying and Flooding	Threshold depth	0.005 m	
	Check method	Both at grid cell centers and faces	
Depth at grid cell faces	Upwind		
Marginal depth	-999 m		
Smoothing time	60 min		
Continuity	Scheme		
	Type of convergence	Water level	
	Convergence criterion	0.0005 m	
	Maximum number of iterations	16	
Momentum	Scheme		
	Advection scheme	Time	ADI-method
		Space	Cyclic
	Maximum number of iterations	50	
Transport	Advection scheme	Central	
Forester filter	Both horizontal and vertical		
Correction for sigma-coordinates	Applied		

* optional
** simulation specific

Appendix F. Monte Carlo Simulation

In this appendix, the Monte Carlo simulation is briefly explained, which was used in the estimation of the total quantifiable degree of uncertainty around the predicted trench siltation rates. Furthermore, the application of this method on both the epistemic parameter and intrinsic uncertainty is clarified. For more information, one is referred to (Svasek Hydraulics, 2013).

F.1 General method

The Monte Carlo simulation is a probabilistic tool in which a distribution of a certain modelled quantity is constructed based on random sampling of independent distributions, which are derived from factorized model outcomes in which variation is given to most influential parameters, schematizations, processes, and/or simulations periods. This variation is caused by uncertainty involved in the independent variables. The derived distribution symbolized the total uncertainty of the modelled quantity. It works as follows:

1. A base case is constructed which resulted in a outcome for a given quantity based on the expected values of all variables.
2. The most influential variables are selected based on a sensitivity analysis or by literature/expert judgement.
3. For these independent variables, distribution types are assumed (e.g. deterministic, uniform, triangular, etc.). Distributions can also be based on measurement data of the variable.
4. Ranges are constructed for each variable, which must consist of a minimum and a maximum of the variable, which correspond to two percentiles (e.g. P0 and P100) for the factorized modelled quantity.
5. Depending on the given type of probability density function, one or two additional simulations with the numerical model are made for each variable range.
6. The given type distributions are constructed with factorized model outcomes of the selected quantity. In this thesis, three types of distributions were assumed (see Figure 81):
   - Uniform distribution:
     There is equal probability of a certain factor. The distribution is either constructed with one additional model simulation or two additional runs. The former results in an average range between the factorized results of the extra simulation and the base case, mapped around unity factor (see Figure 81a), while the latter results in a range constructed of the minimum and maximum factorized outcome (see Figure 81b).
   - Triangular distribution:
     This distribution simplifies a continuous distribution, and consists of three parameters: the zeroth percentile (P0), the expected value (E), and hundredth percentile (P100). The P0 and P100 factors can directly be calculated based on the model outcomes for the range of a certain quantity relative to the base case outcome (see Figure 81c). The expected value can be determined by calculation of the center of mass of the triangular distribution of the factors by assuming that the base case factor equals highest probability density. Hence, it is a function of the minimum, base case, and maximum factorized quantity.
   - Continuous distribution:

If the range of a variable has been measured, a distribution can be fitted using a General Extreme Value (GEV) distribution. The bounds of the range given to a certain variable correspond with a certain percentile of this fitted probability density function. Instead of the magnitude of the variables, the factors found by the modelling outcomes of a certain quantity can be implemented on the x-axis of the distribution (see Figure 81d). The scale of the x-axis can then be found by inter- and extrapolation between the factorized quantity In this thesis, this is performed linearly for simplicity, as depicted in the red striped line in the figure.

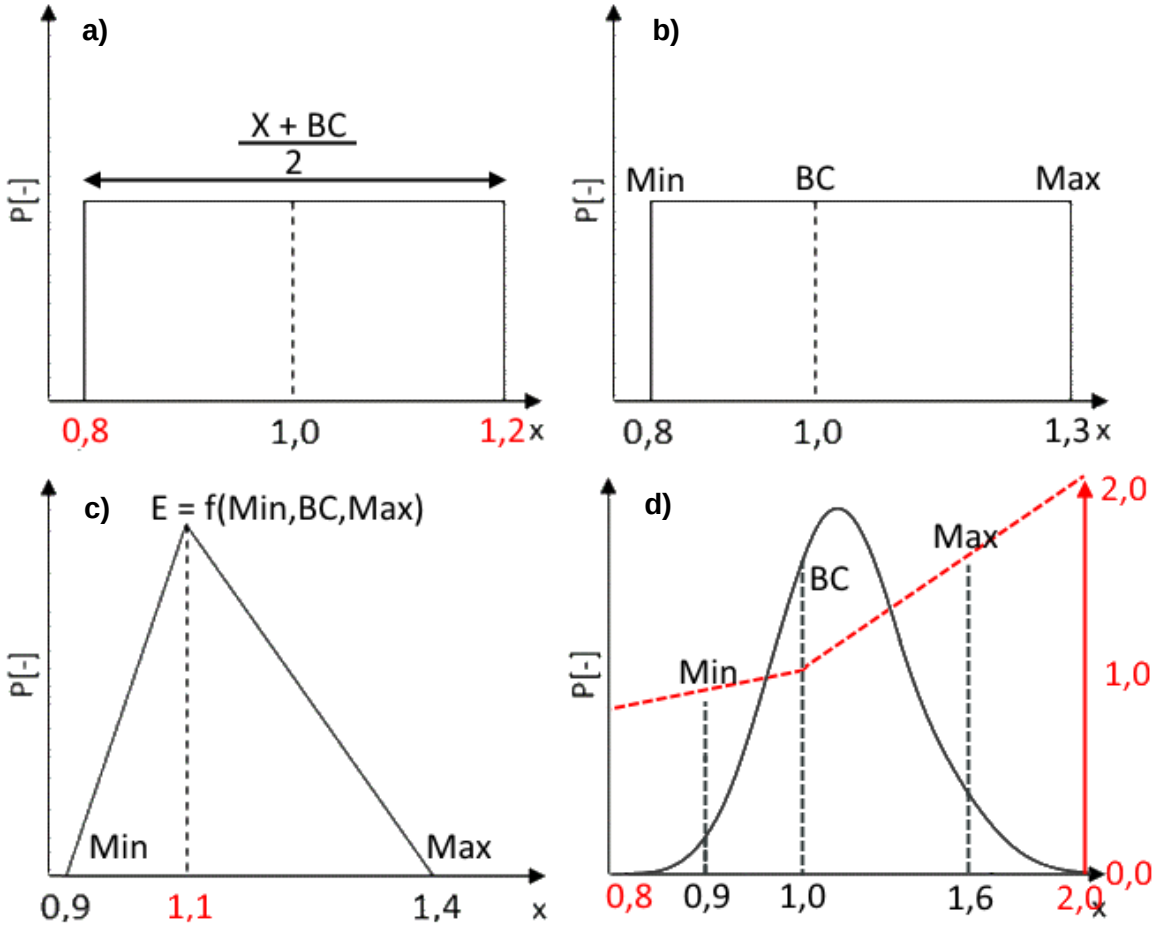

Figure 81 – Construction process of probability density functions of the factorized model outcome (X) for a chosen quantity for the separate variables: a) uniform with one additional run, b) uniform with two additional runs, c) triangular distribution with two additional runs; d) continuous distribution with linear interpolated (red striped line) factors. Red values are calculated factors, black values are factorized modelled outcomes, either a minimum (Min), base case (BC), or maximum (Max) value of the given range to the variable. E is the expected value, which is a function of the described values.

7. The estimated probability density functions of the factorized model outcomes for a certain quantity for each selected variable are sampled randomly by using a normalized uniform distribution. This results in an independent matrix of factorized model outcomes for the chosen quantity, which consist of n number of draws and m number of variables.
8. By calculation of the product of the factors for each single draw, an array can be constructed, in which the combined factors, resembling the uncertainty of the independent variables, are listed.
9. By fitting a GEV distribution to these factors, and by multiplying the factors with the base case outcome, the total uncertainty around the selected quantity can be quantified.

Some remarks of this method is the assumption of independence of the variables, which does not necessarily hold: especially for physical processes and their parameters involved. Furthermore, the assumption of a (triangular) distribution or the inter- and extrapolation of factors within a continuous distribution is a very crude simplification. However, the methods fits for the aim of this thesis, which is more about estimation of the total degree of uncertainty of the quantity 'trench siltation volume rate', rather than a perfect probabilistic description of the uncertainty.

F.2 Epistemic parameter uncertainty

In the sensitivity analysis, which was applied in this thesis to estimate the degree of epistemic uncertainty, ranges were given to the most influential parameters for trench siltation. Probability density functions (pdf) of factorized trench siltation rates for these parameters were derived by approximating the space of the model outcomes, given the applied range, by a triangular distribution. Also, variation was given to the sand transport formula schematization of Van Rijn (1993) by application of Van Rijn (2007). For this pdf, the use of the uniform distribution with a single additional model simulation was used, as model schematizations do not contain a probability of occurrence.

F.3 Intrinsic uncertainty

To estimate the degree of intrinsic uncertainty of the trench siltation rates, simulations were constructed with different simulation periods in which different environmental components dominated, which govern the sediment supply and trapping to and in the trench. The components were: tide, river discharge, and wind/waves. Ranges around the base case were constructed by modelling a period during neap and spring tide, low and high river discharge, and a storm at sea. Since water level, river discharge, and wind are measured quantities, distributions could be fitted. The magnitude of the quantity during the simulation period revealed the corresponding percentiles of the minimum, base case, and maximum value in the fitted distribution. These values were, subsequently, replaced with the factorized siltation rates between which interpolation was possible, and also extrapolation to the minimum and maximum of the pdf. For the tested simulations periods, this method resulted most of the time in positive factors on both sides of the base case factor of 1.0.

Appendix G. Additional output base case

In this appendix, all analyzed results of the base case are presented. Results of other model simulations are similar, although having different magnitudes, as is described in the discussion (see Chapter 8)

G.1 Domain

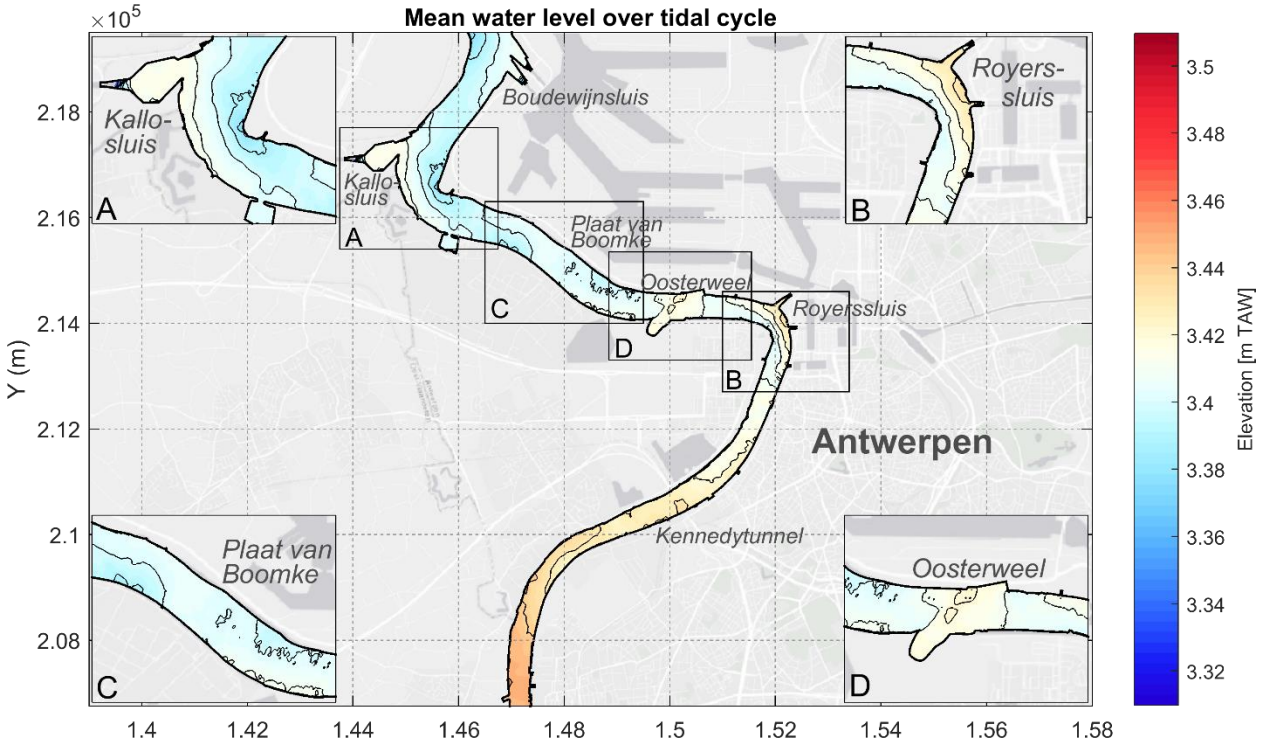

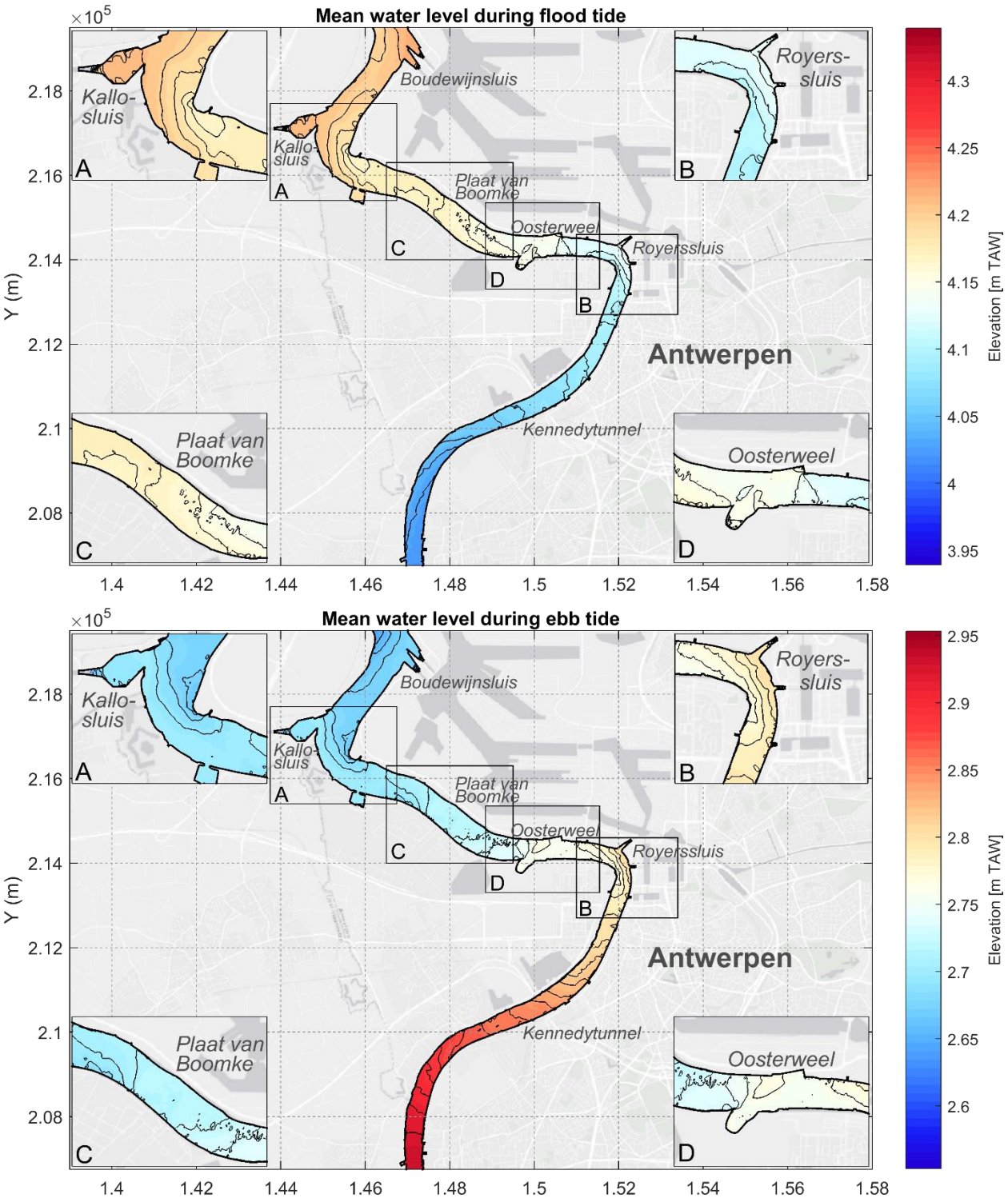
Mean water level during flood tide
Mean water level during ebb tide
×10^5
Y (m)
Elevation [m TAW]
Kallo-sluis
Boudewijnsluis
Royers-sluis
Plaat van Boomke
Oosterweel
Royerssluis
Kennedytunnel
Antwerpen
A
B
C
D

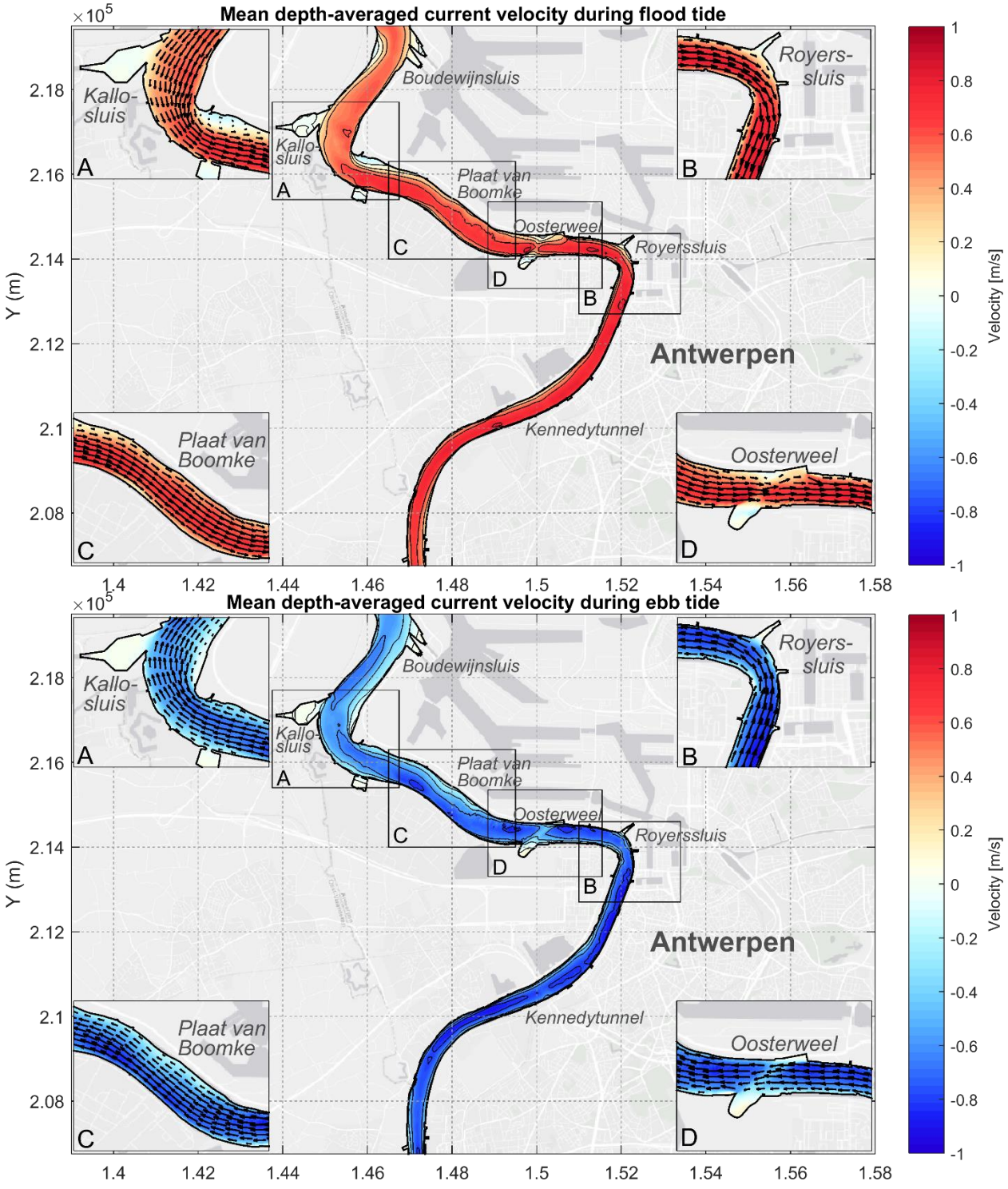
Mean depth-averaged current velocity during flood tide
Mean depth-averaged current velocity during ebb tide
×10^5
Y (m)
Velocity [m/s]
Kallo-sluis
Boudewijnsluis
Royers-sluis
Plaat van Boomke
Oosterweel
Royerssluis
Kennedytunnel
Antwerpen
A
B
C
D

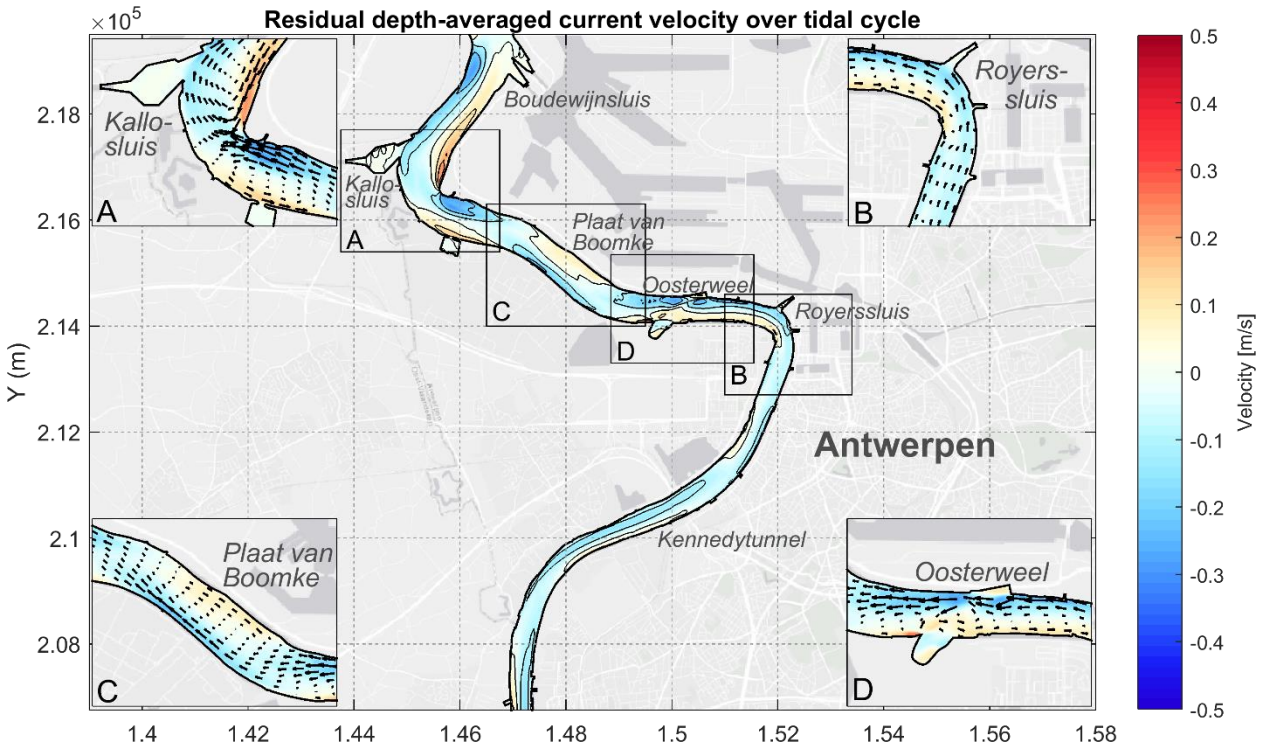
Residual depth-averaged current velocity over tidal cycle
×10^5
Y (m)
Velocity [m/s]
Kallo-sluis
Boudewijnsluis
Royers-sluis
Plaat van Boomke
Oosterweel
Royerssluis
Antwerpen
Kennedytunnel
A
B
C
D

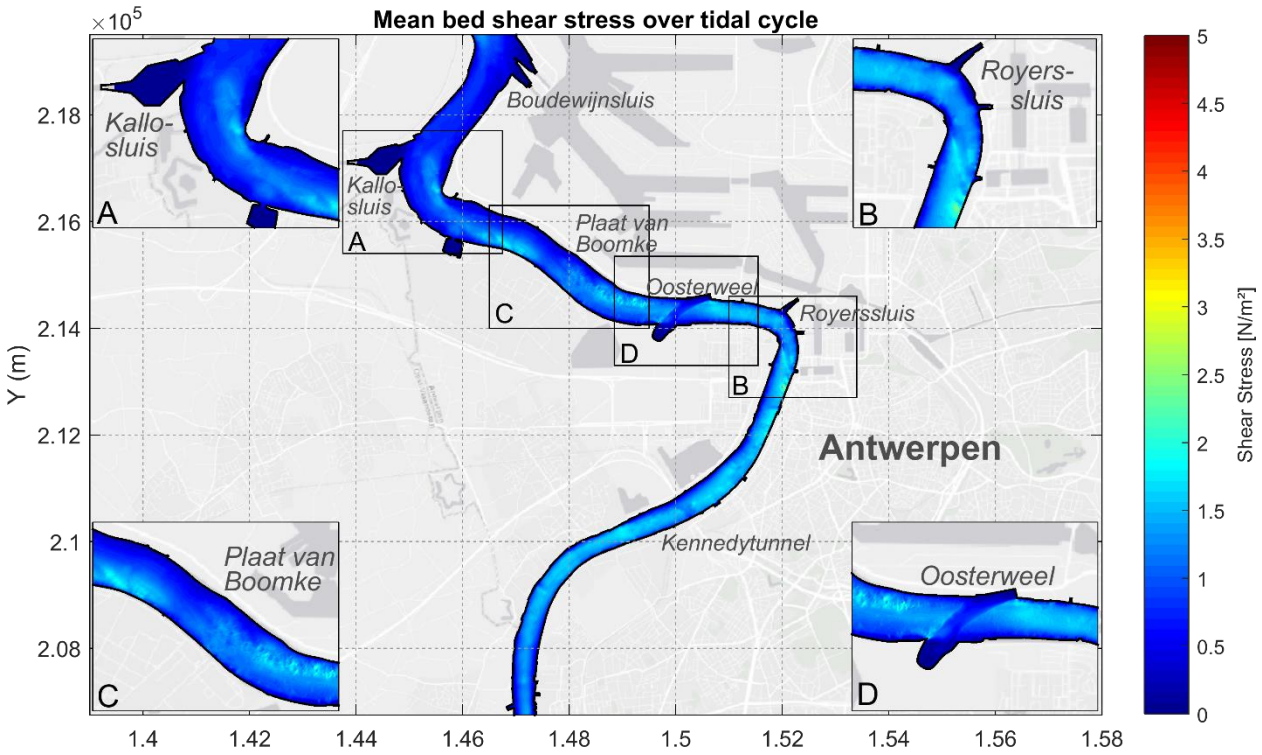
Mean bed shear stress over tidal cycle
×10^5
Y (m)
Shear Stress [N/m²]
Kallo-sluis
Boudewijnsluis
Royers-sluis
Plaat van Boomke
Oosterweel
Royerssluis
Antwerpen
Kennedytunnel
A
B
C
D

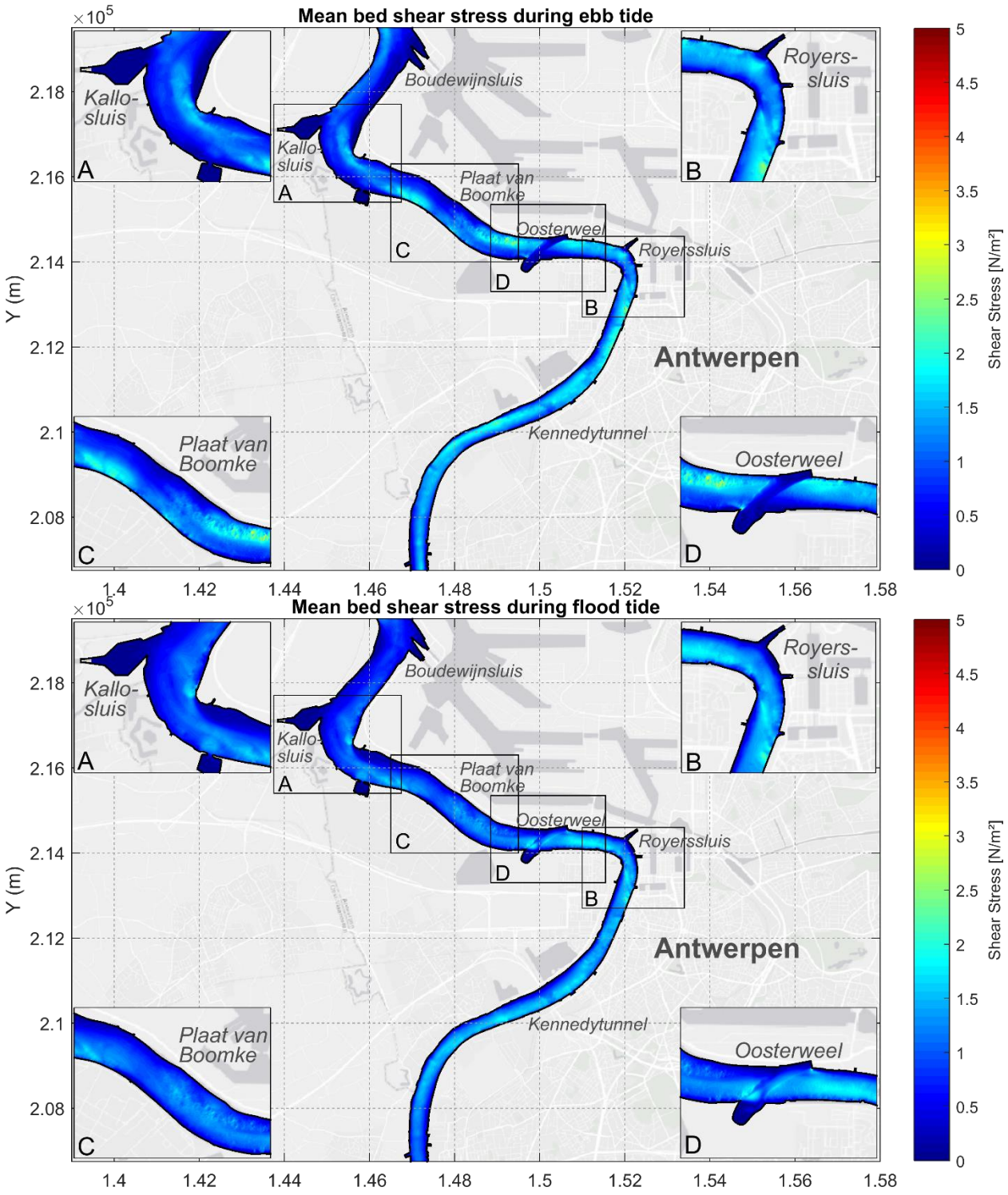
Mean bed shear stress during ebb tide
Mean bed shear stress during flood tide
×10^5
Y (m)
Shear Stress [N/m²]
Kallo-sluis
Boudewijnsluis
Royers-sluis
Plaat van Boomke
Oosterweel
Royerssluis
Kennedytunnel
Antwerpen
A
B
C
D

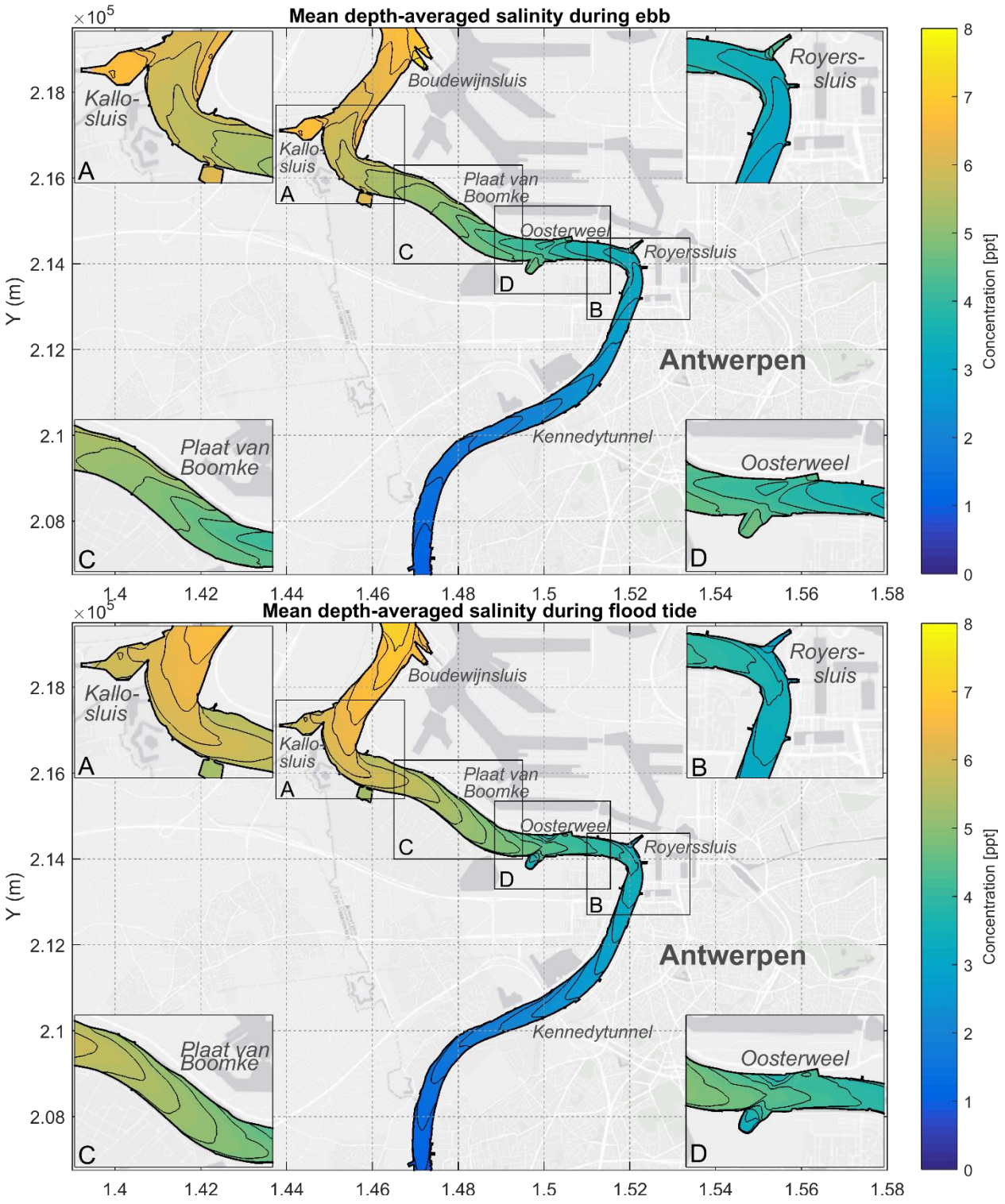
Mean depth-averaged salinity during ebb
Mean depth-averaged salinity during flood tide
×10^5
Y (m)
Concentration [ppt]
Kallo-sluis
Boudewijnsluis
Royers-sluis
Plaat van Boomke
Oosterweel
Royerssluis
Kennedytunnel
Antwerpen
A
B
C
D

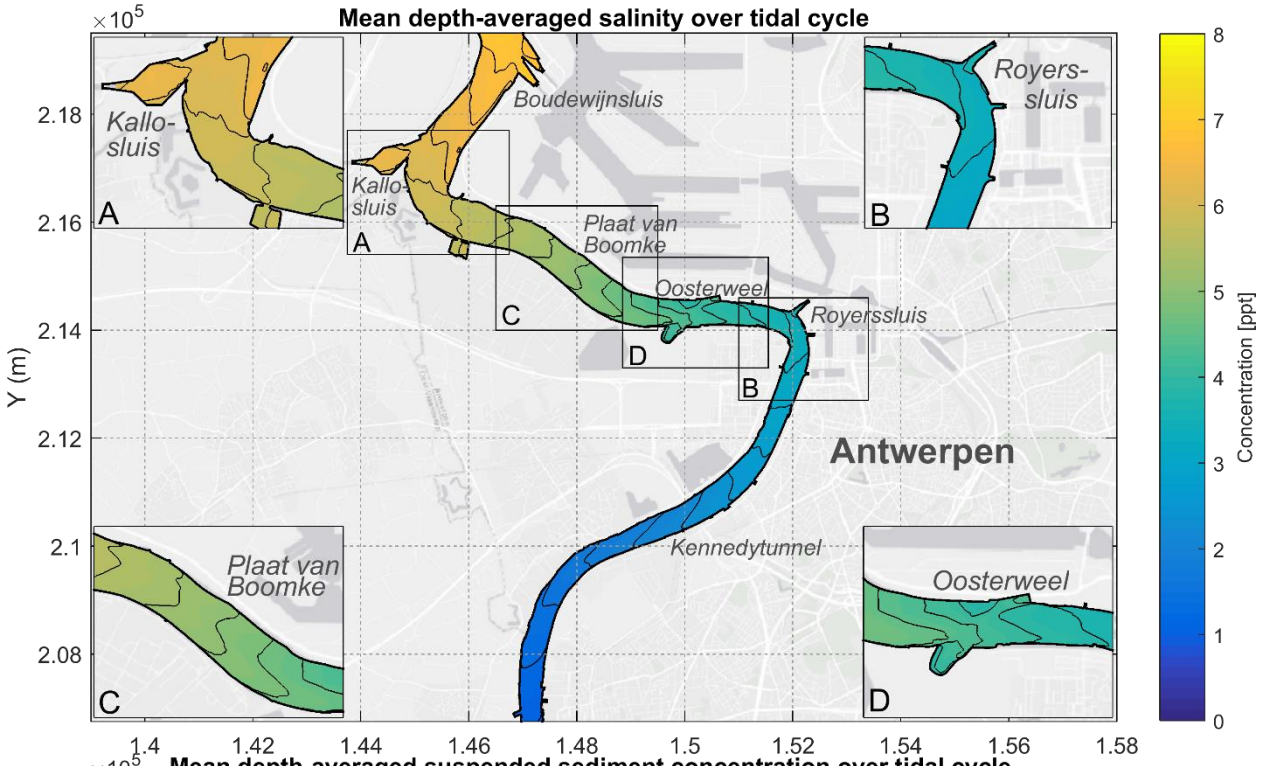
Mean depth-averaged salinity over tidal cycle
×10^5
Y (m)
Concentration [ppt]
Kallo-sluis
Boudewijnsluis
Royers-sluis
Plaat van Boomke
Oosterweel
Royerssluis
Kennedytunnel
Antwerpen
A
B
C
D

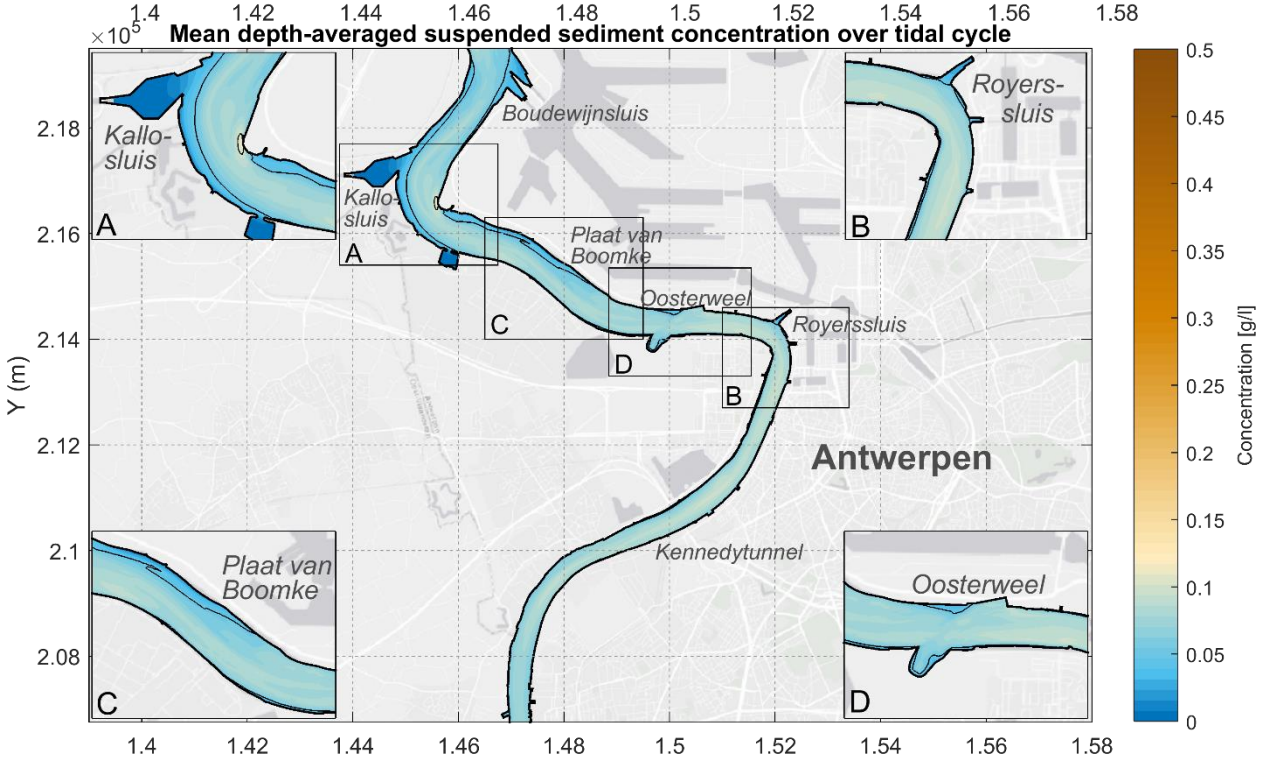
Mean depth-averaged suspended sediment concentration over tidal cycle
×10^5
Y (m)
Concentration [g/l]
Kallo-sluis
Boudewijnsluis
Royers-sluis
Plaat van Boomke
Oosterweel
Royerssluis
Kennedytunnel
Antwerpen
A
B
C
D

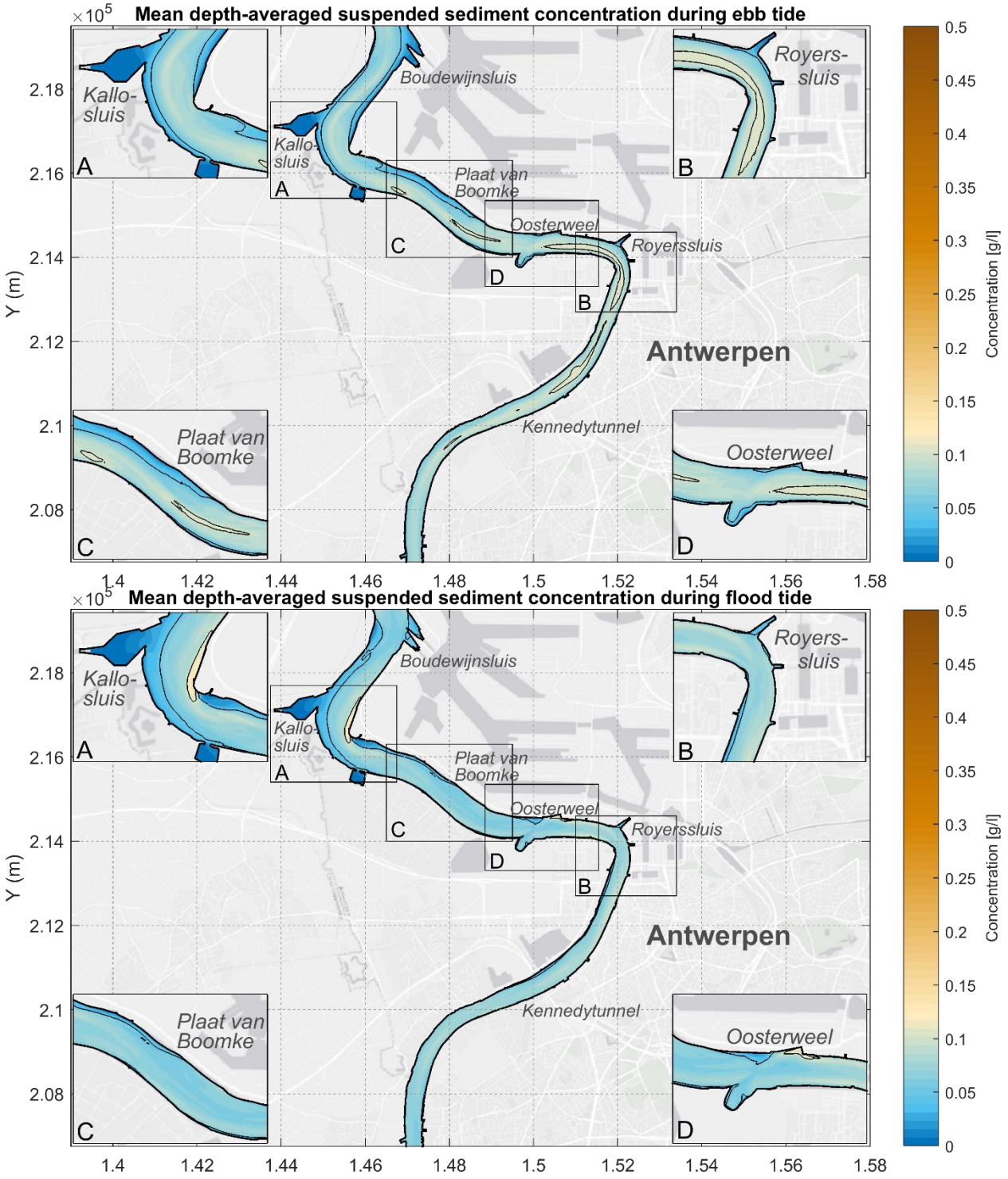
Mean depth-averaged suspended sediment concentration during ebb tide
Mean depth-averaged suspended sediment concentration during flood tide
×10^5
Y (m)
Concentration [g/l]
Kallo-sluis
Boudewijnsluis
Royers-sluis
Plaat van Boomke
Oosterweel
Royerssluis
Kennedytunnel
Antwerpen
A
B
C
D

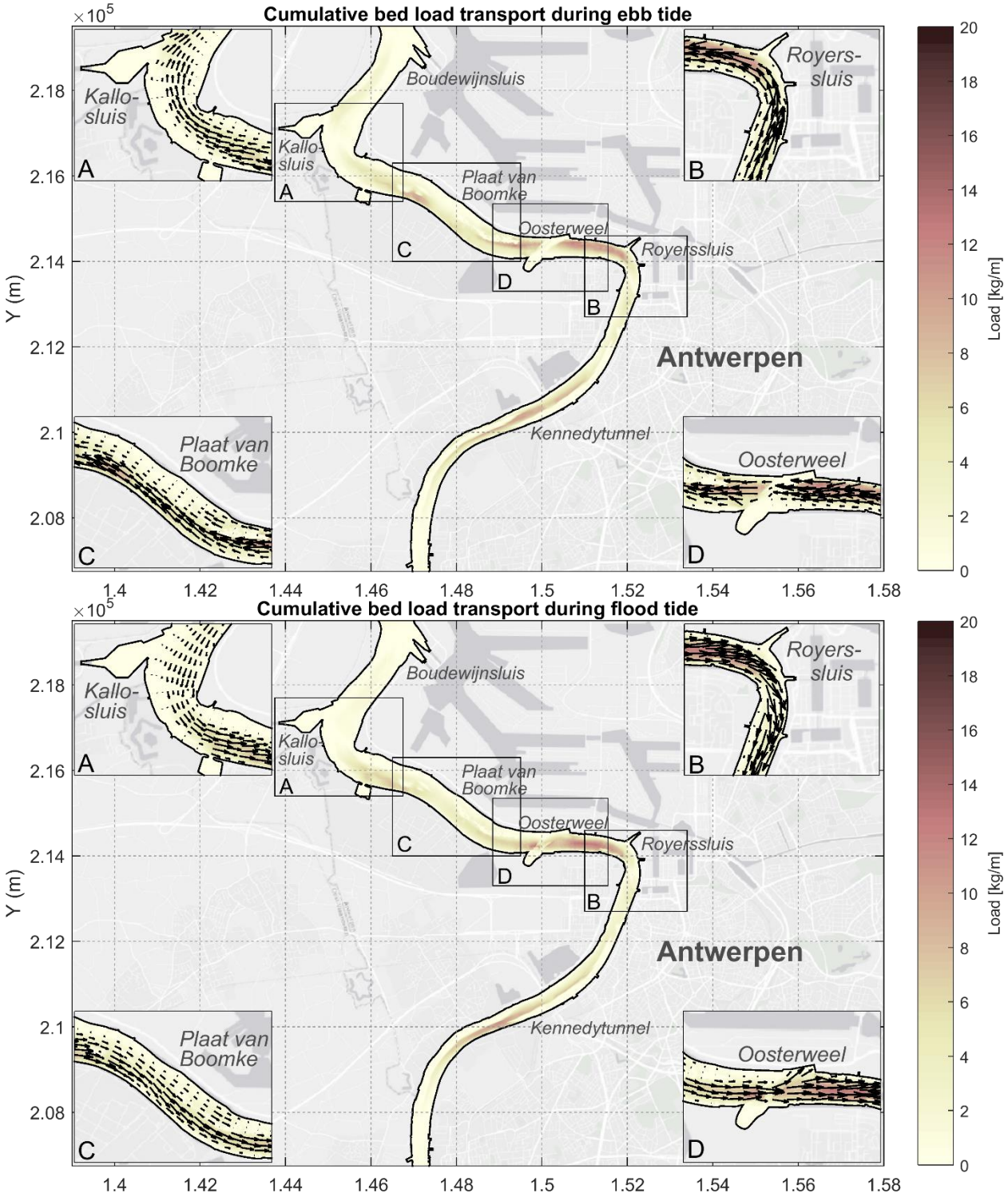
Cumulative bed load transport during ebb tide
Cumulative bed load transport during flood tide
×10^5
Y (m)
Load [kg/m]
Kallo-sluis
Boudewijnsluis
Royers-sluis
Plaat van Boomke
Oosterweel
Royerssluis
Kennedytunnel
Antwerpen
A
B
C
D

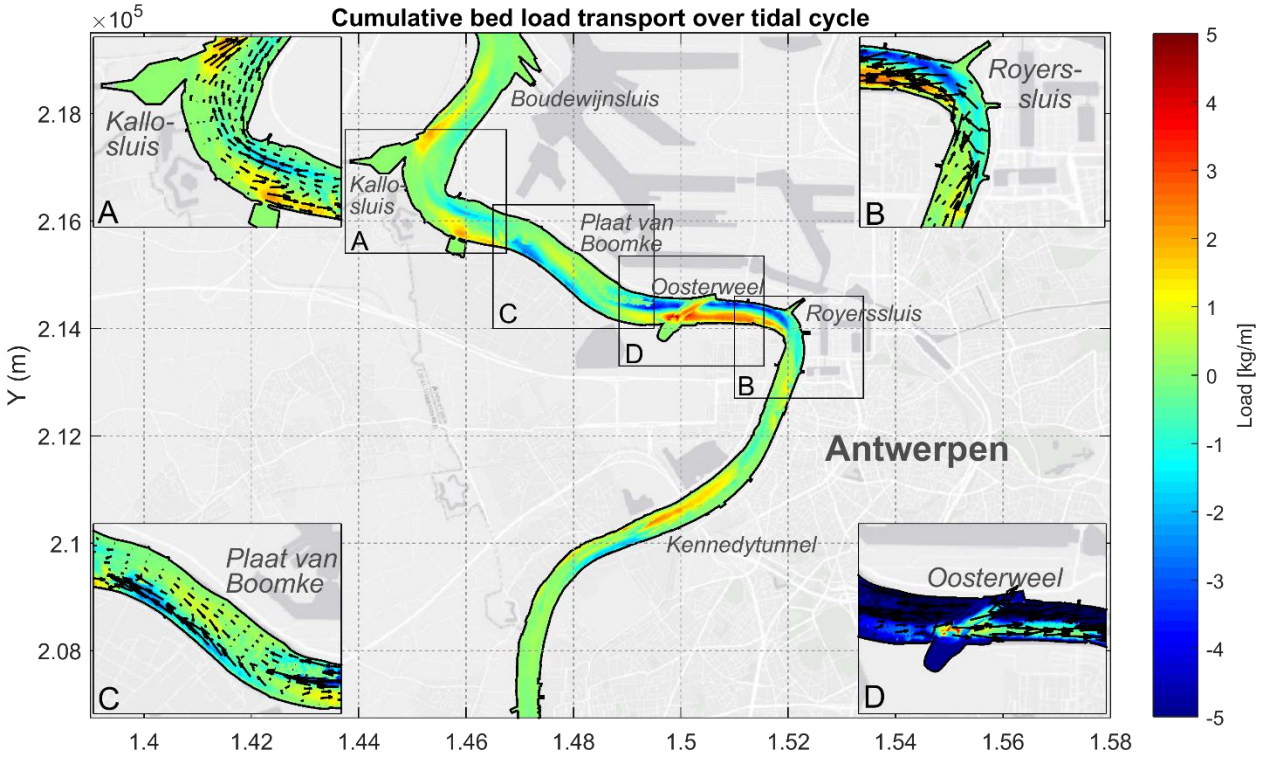
Cumulative bed load transport over tidal cycle
×10^5
Y (m)
Load [kg/m]
Kallo-sluis
Boudewijnsluis
Royers-sluis
Plaat van Boomke
Oosterweel
Royerssluis
Antwerpen
Kennedytunnel
A
B
C
D

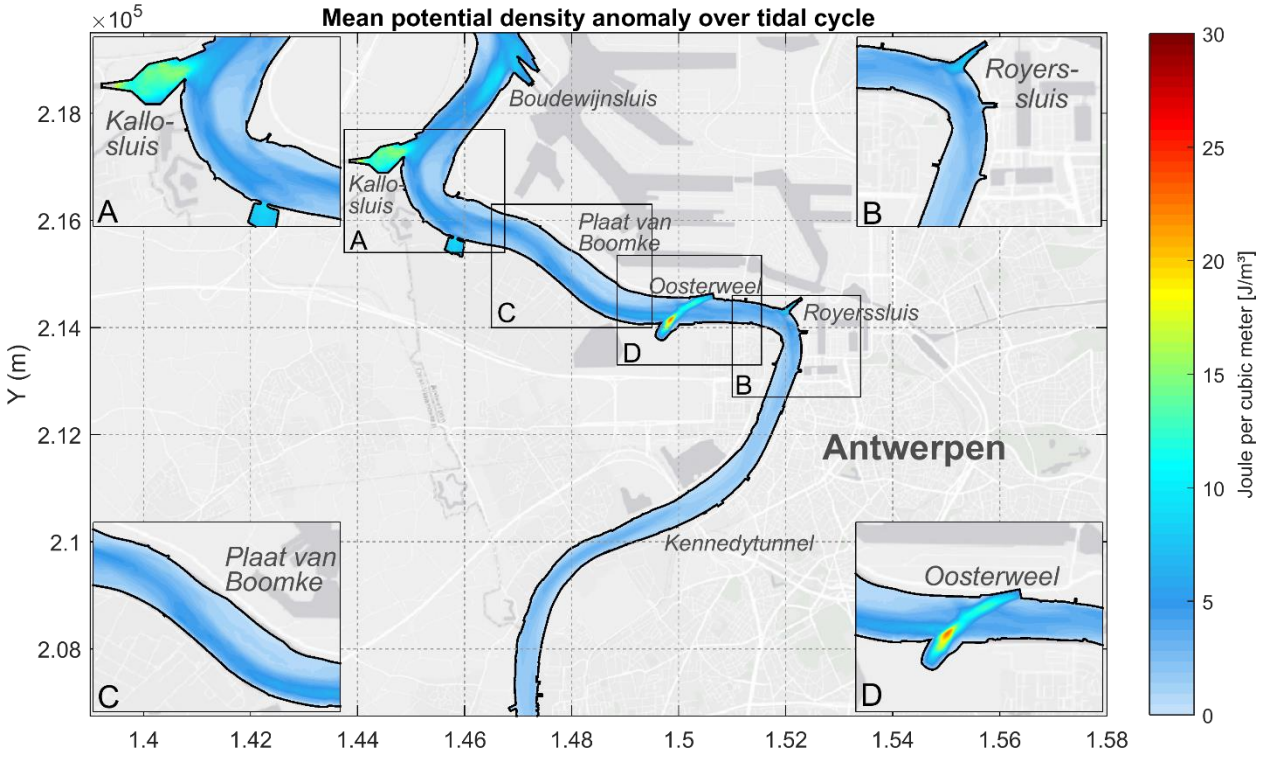
Mean potential density anomaly over tidal cycle
×10^5
Y (m)
Joule per cubic meter [J/m³]
Kallo-sluis
Boudewijnsluis
Royers-sluis
Plaat van Boomke
Oosterweel
Royerssluis
Antwerpen
Kennedytunnel
A
B
C
D

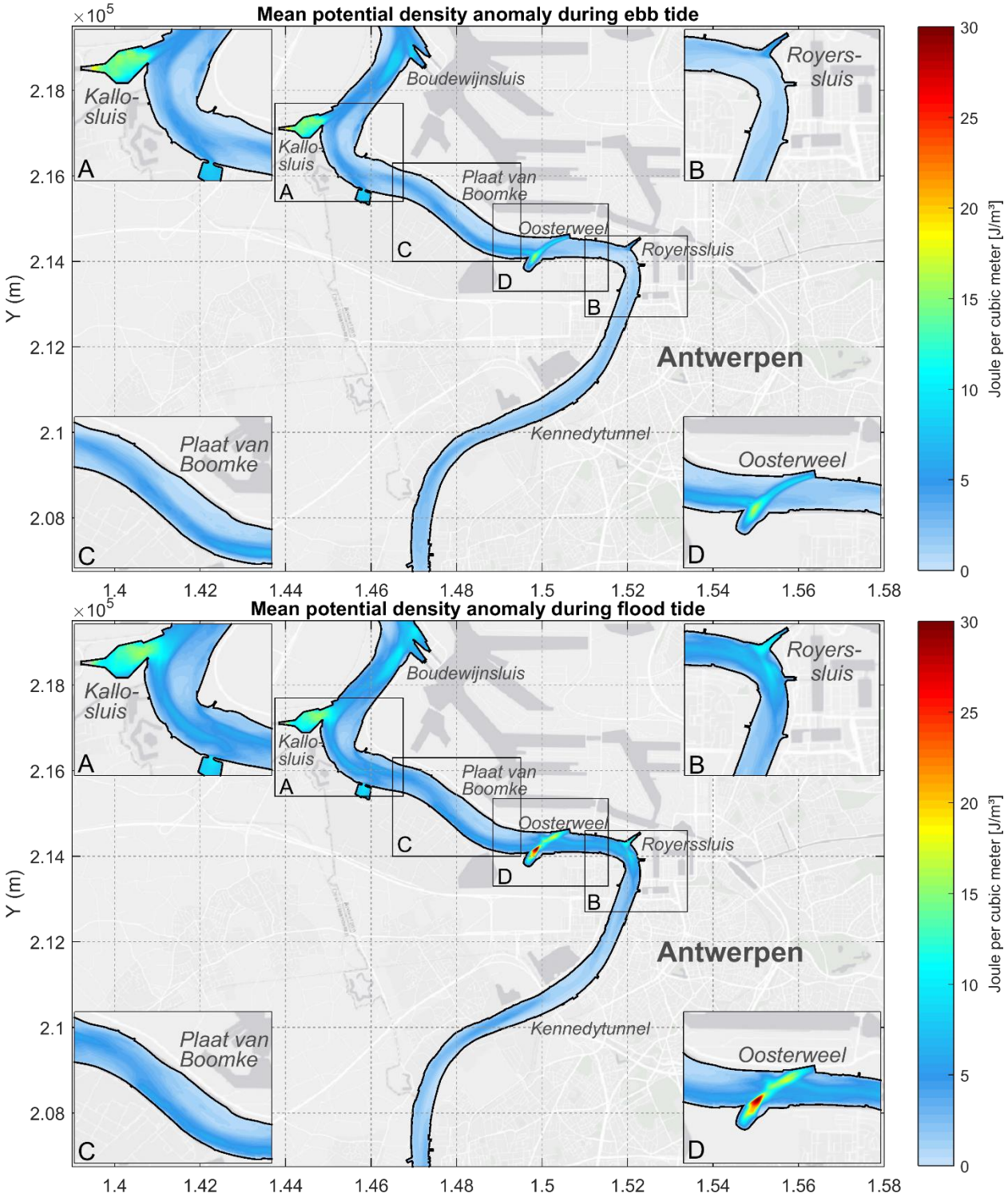
Mean potential density anomaly during ebb tide
Mean potential density anomaly during flood tide
×10^5
Y (m)
Joule per cubic meter [J/m³]
Kallo-sluis
Boudewijnsluis
Royers-sluis
Plaat van Boomke
Oosterweel
Royerssluis
Antwerpen
Kennedytunnel
A
B
C
D

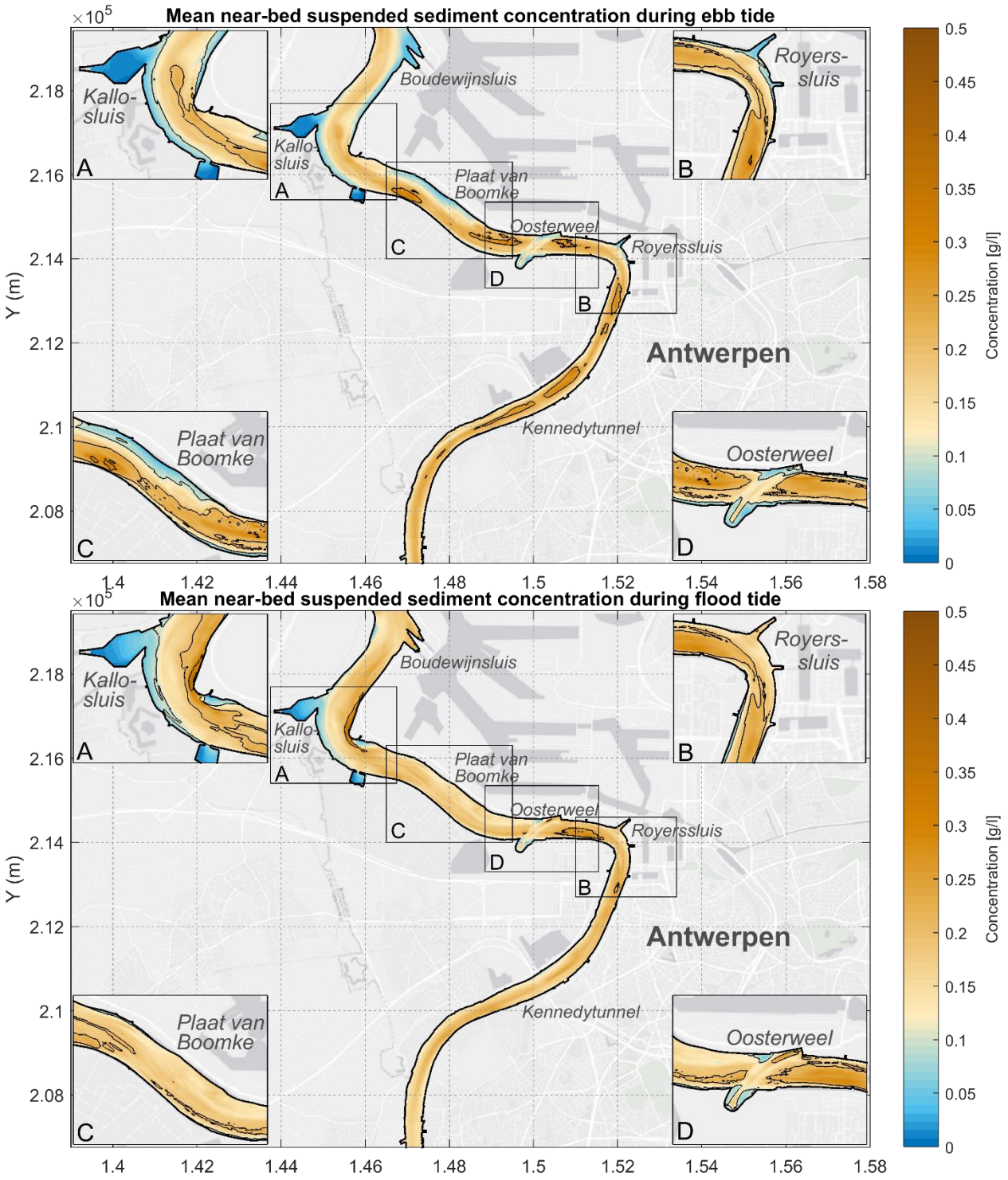
Mean near-bed suspended sediment concentration during ebb tide
Mean near-bed suspended sediment concentration during flood tide
×10^5
Y (m)
Concentration [g/l]
Kallo-sluis
Boudewijnsluis
Royers-sluis
Plaat van Boomke
Oosterweel
Royerssluis
Kennedytunnel
Antwerpen
A
B
C
D

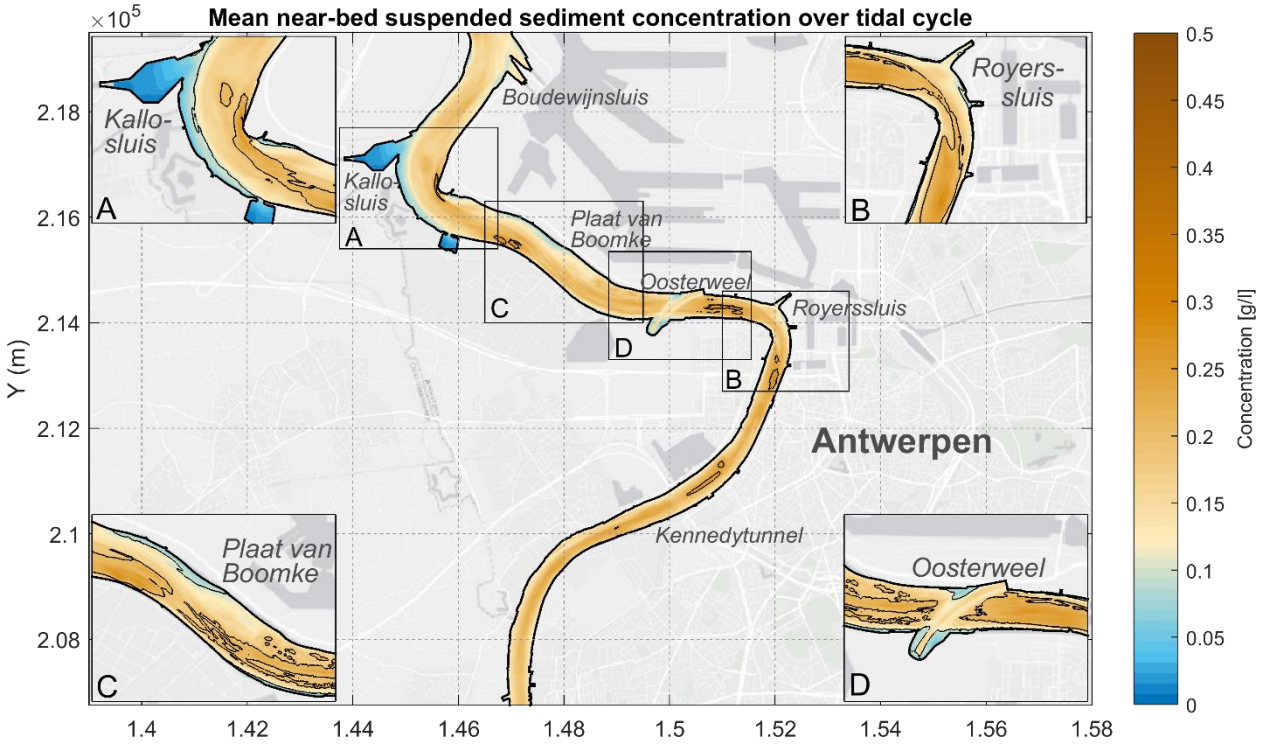
Mean near-bed suspended sediment concentration over tidal cycle
×10^5
Y (m)
Concentration [g/l]
Kallo-sluis
Boudewijnsluis
Royers-sluis
Plaat van Boomke
Oosterweel
Royerssluis
Kennedytunnel
Antwerpen
A
B
C
D

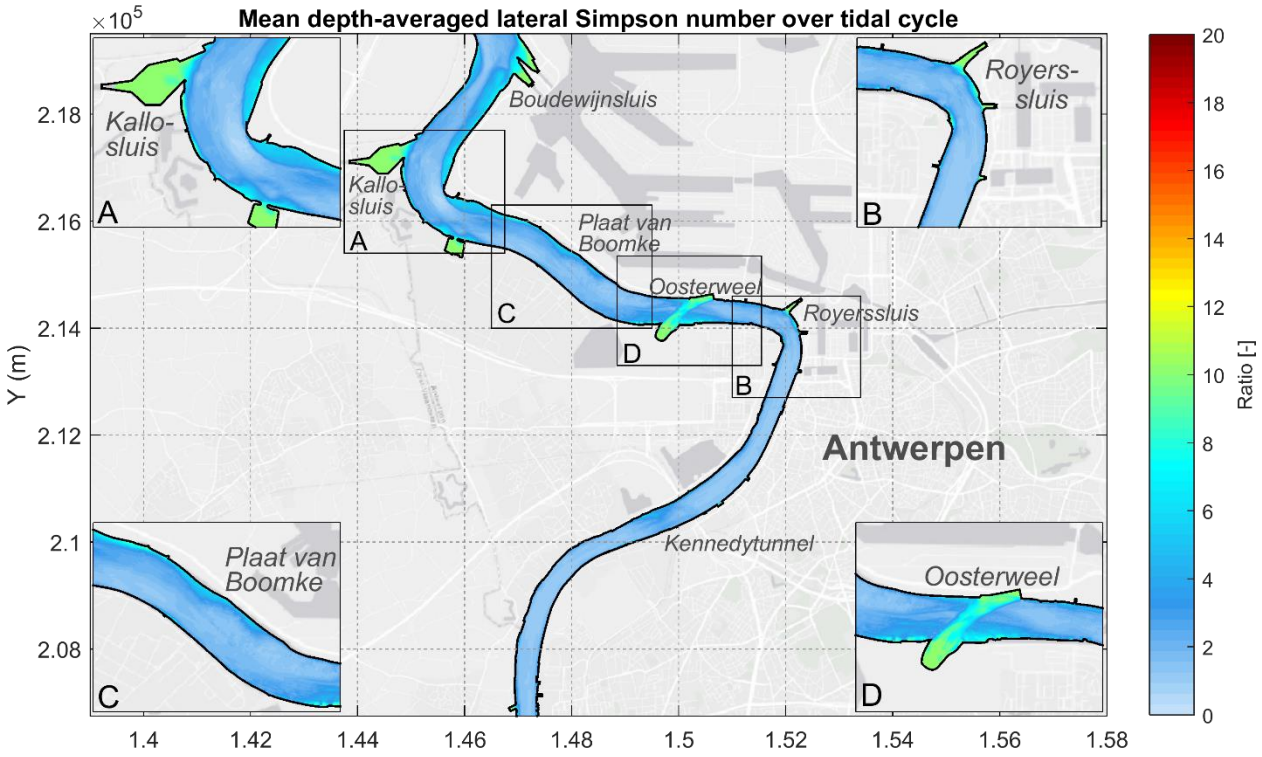
Mean depth-averaged lateral Simpson number over tidal cycle
×10^5
Y (m)
Ratio [-]
Kallo-sluis
Boudewijnsluis
Royers-sluis
Plaat van Boomke
Oosterweel
Royerssluis
Kennedytunnel
Antwerpen
A
B
C
D

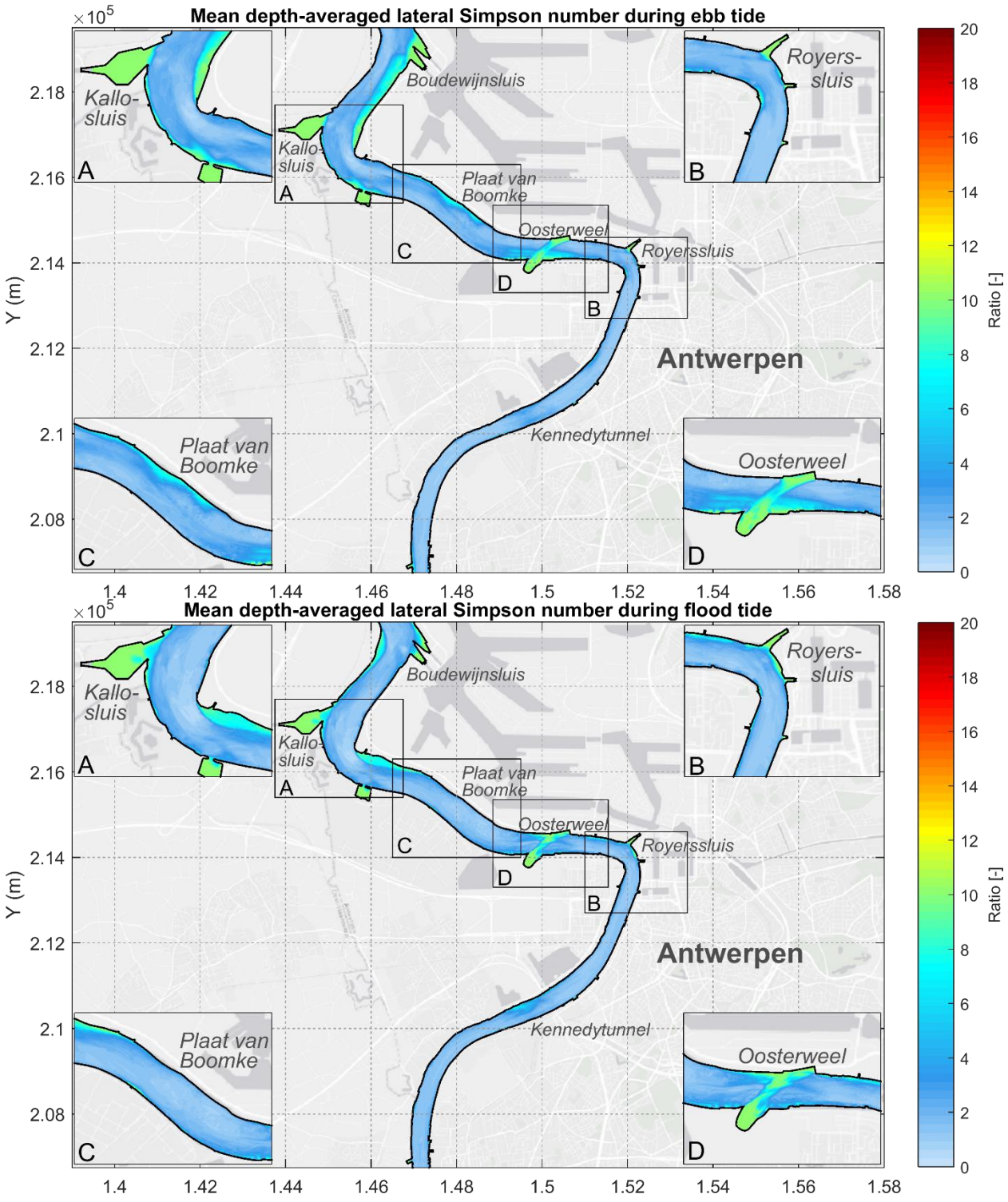
Mean depth-averaged lateral Simpson number during ebb tide
Mean depth-averaged lateral Simpson number during flood tide
×10^5
Y (m)
Ratio [-]
Kallo-sluis
Boudewijnsluis
Royers-sluis
Plaat van Boomke
Oosterweel
Royerssluis
Kennedytunnel
Antwerpen
A
B
C
D

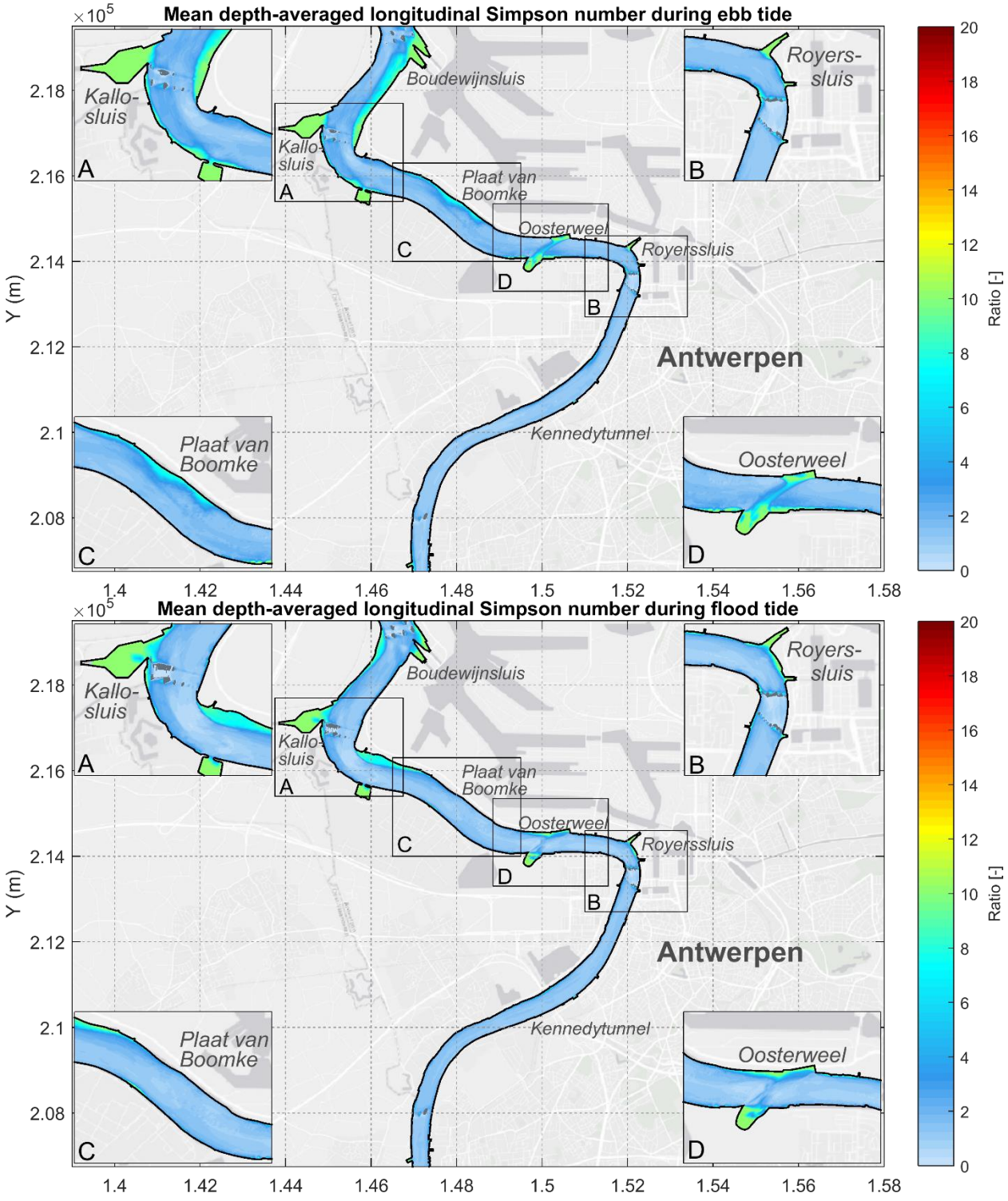
Mean depth-averaged longitudinal Simpson number during ebb tide
Mean depth-averaged longitudinal Simpson number during flood tide
×10^5
Y (m)
Ratio [-]
Kallo-sluis
Boudewijnsluis
Royers-sluis
Plaat van Boomke
Oosterweel
Royerssluis
Kennedytunnel
Antwerpen
A
B
C
D

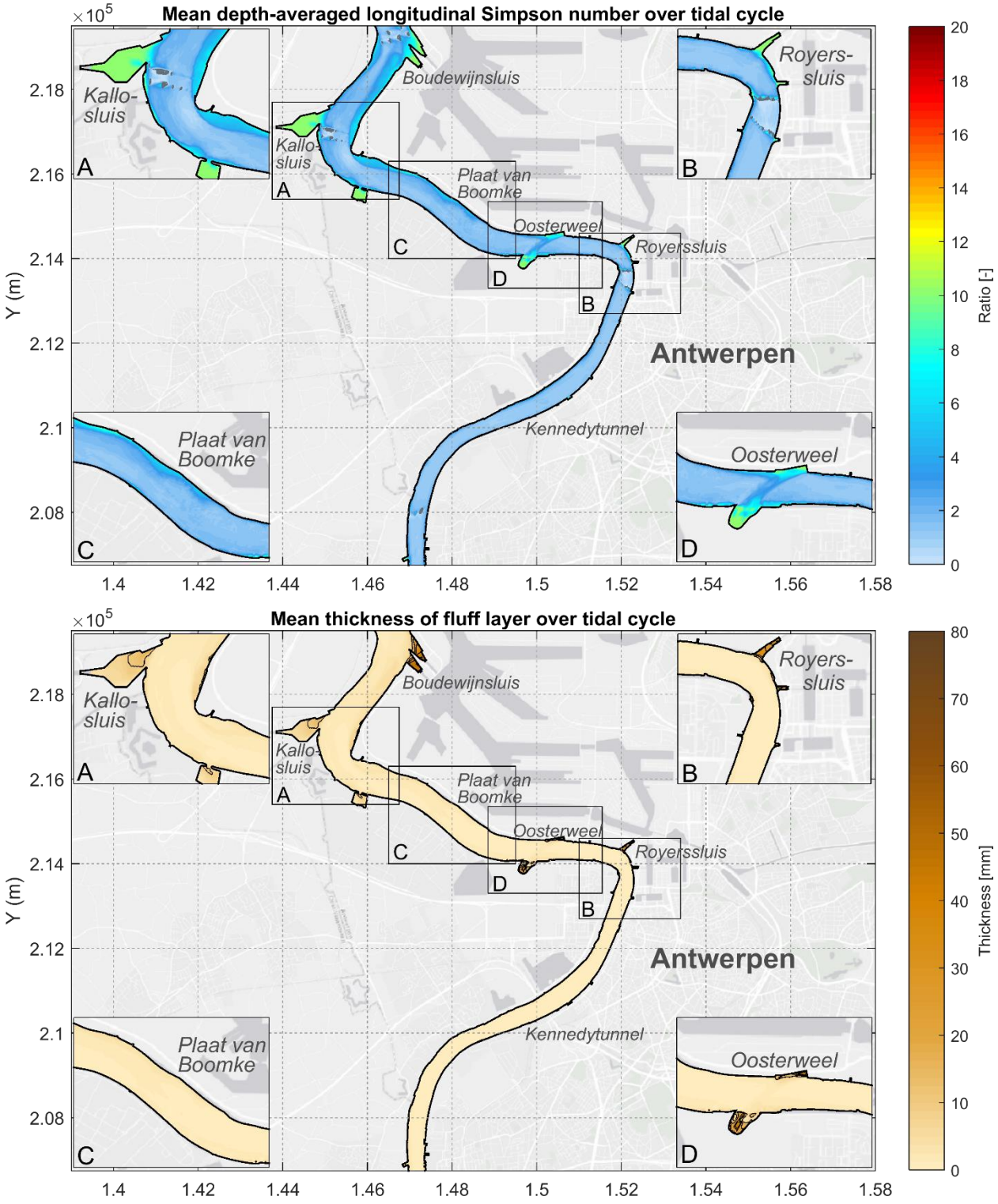
Mean depth-averaged longitudinal Simpson number over tidal cycle
×10^5
Y (m)
Ratio [-]
Kallo-sluis
Boudewijnsluis
Royers-sluis
Plaat van Boomke
Oosterweel
Royerssluis
Antwerpen
Kennedytunnel
A
B
C
D
Mean thickness of fluff layer over tidal cycle
Thickness [mm]

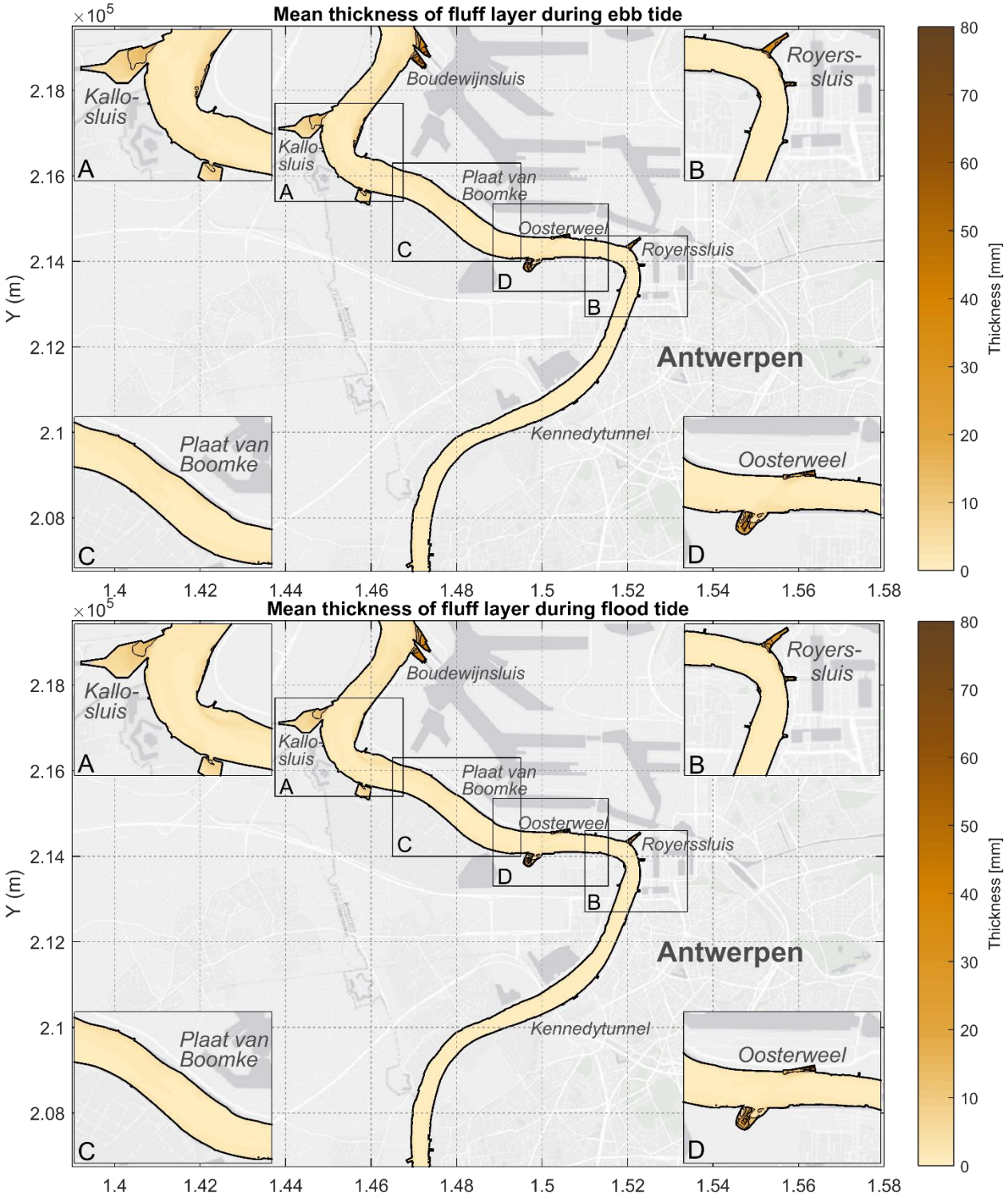
Mean thickness of fluff layer during ebb tide
Mean thickness of fluff layer during flood tide
×10^5
Y (m)
Thickness [mm]
Kallo-sluis
Boudewijnsluis
Royers-sluis
Plaat van Boomke
Oosterweel
Royerssluis
Kennedytunnel
Antwerpen
A
B
C
D

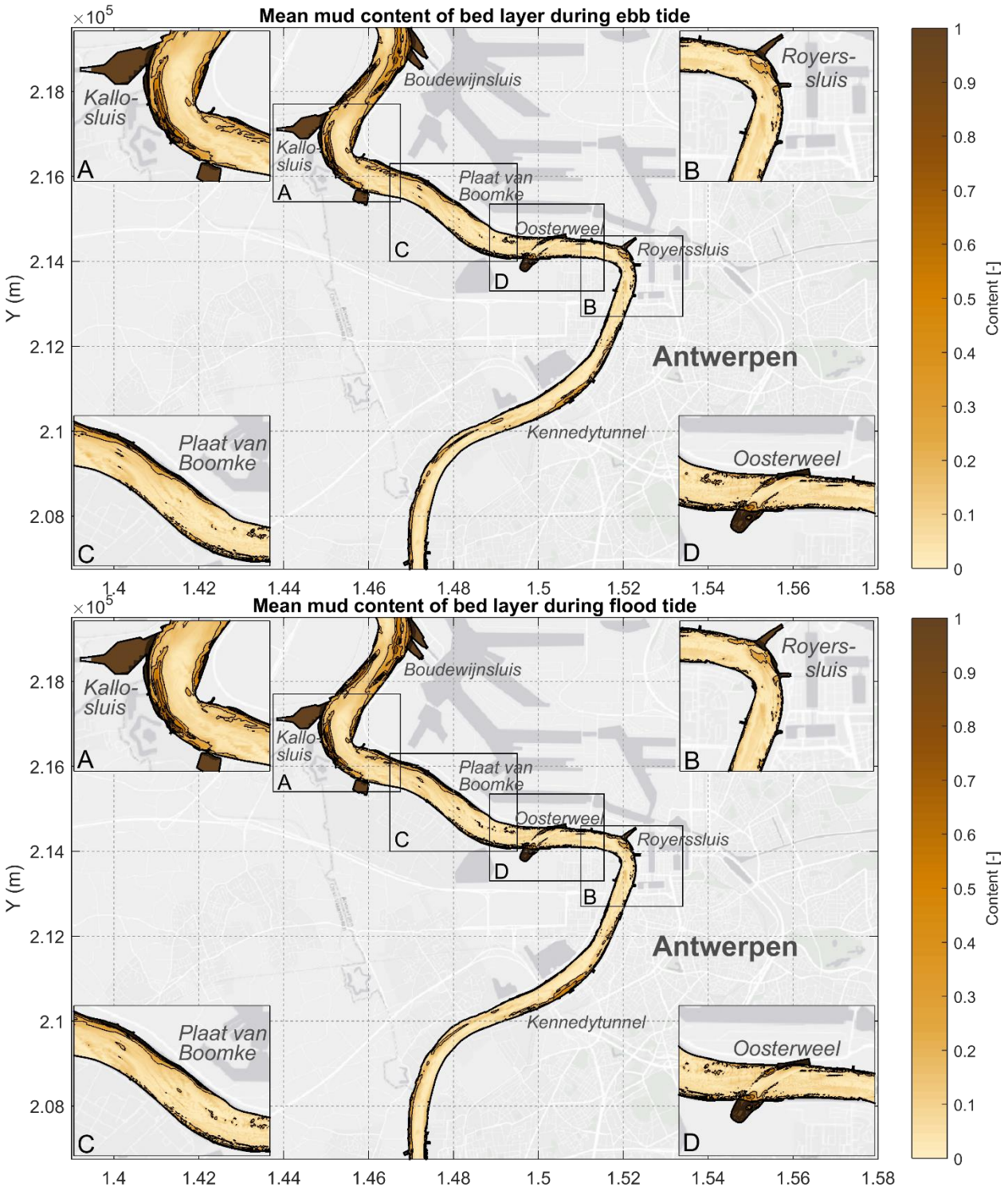
Mean mud content of bed layer during ebb tide
Mean mud content of bed layer during flood tide
×10^5
Y (m)
Content [-]
Kallo-sluis
Boudewijnsluis
Royers-sluis
Plaat van Boomke
Oosterweel
Royerssluis
Kennedytunnel
Antwerpen
A
B
C
D
2.18
2.16
2.14
2.12
2.1
2.08
1.4
1.42
1.44
1.46
1.48
1.5
1.52
1.54
1.56
1.58
0
0.1
0.2
0.3
0.4
0.5
0.6
0.7
0.8
0.9
1

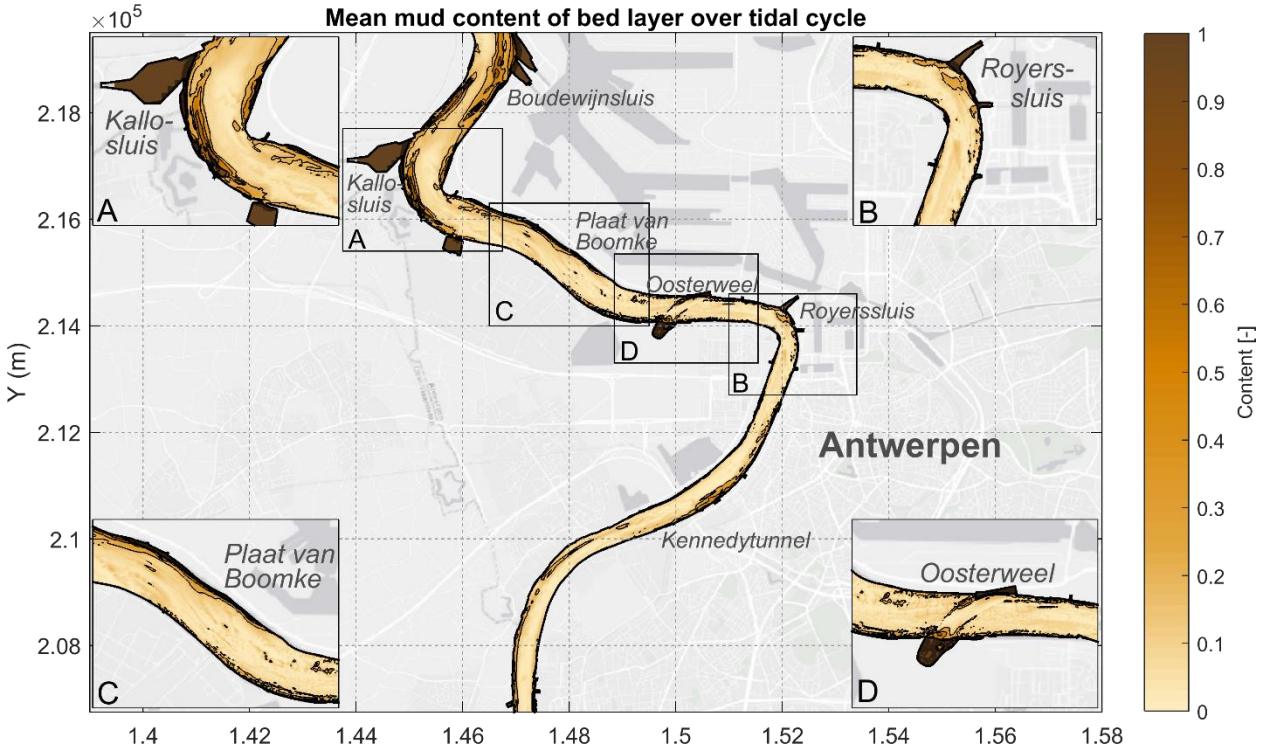
Mean mud content of bed layer over tidal cycle
×10^5
Y (m)
Content [-]
Kallo-sluis
Boudewijnsluis
Royers-sluis
Plaat van Boomke
Oosterweel
Royerssluis
Antwerpen
Kennedytunnel
A
B
C
D

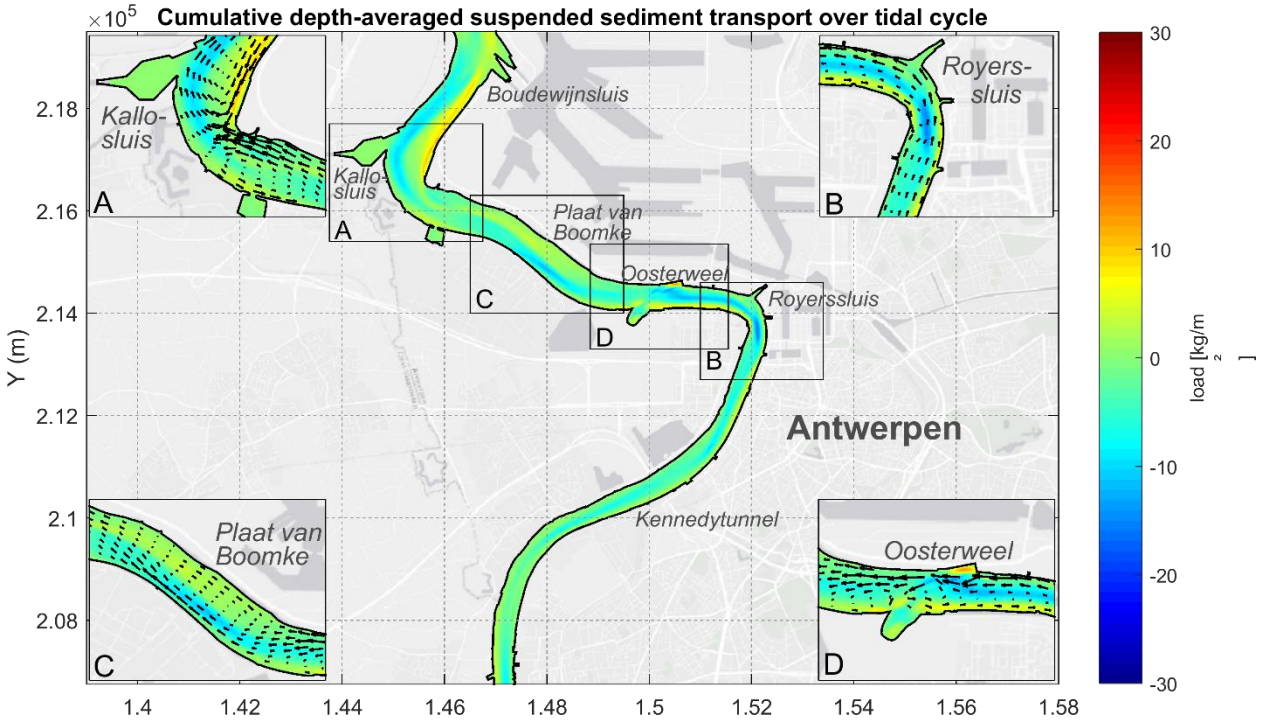
Cumulative depth-averaged suspended sediment transport over tidal cycle
×10^5
Y (m)
load [kg/m²]
Kallo-sluis
Boudewijnsluis
Royers-sluis
Plaat van Boomke
Oosterweel
Royerssluis
Antwerpen
Kennedytunnel
A
B
C
D

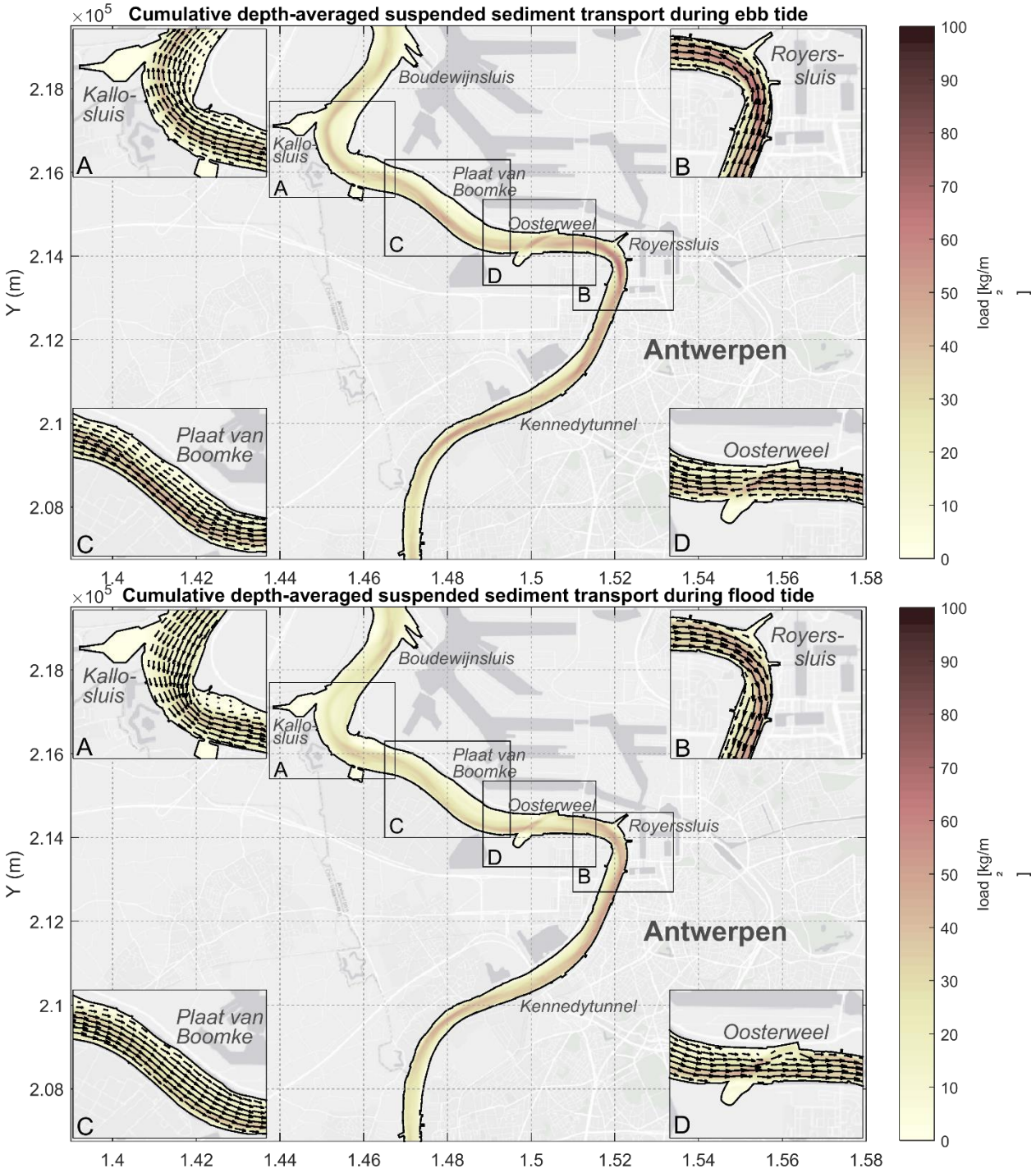
×10^5 Cumulative depth-averaged suspended sediment transport during ebb tide
Kallo-sluis
Boudewijnsluis
Royers-sluis
Plaat van Boomke
Oosterweel
Royerssluis
Antwerpen
Kennedytunnel
A
B
C
D
Y (m)
load [kg/m2]
×10^5 Cumulative depth-averaged suspended sediment transport during flood tide
Kallo-sluis
Boudewijnsluis
Royers-sluis
Plaat van Boomke
Oosterweel
Royerssluis
Antwerpen
Kennedytunnel
A
B
C
D
Y (m)
load [kg/m2]

G.2 Thalweg

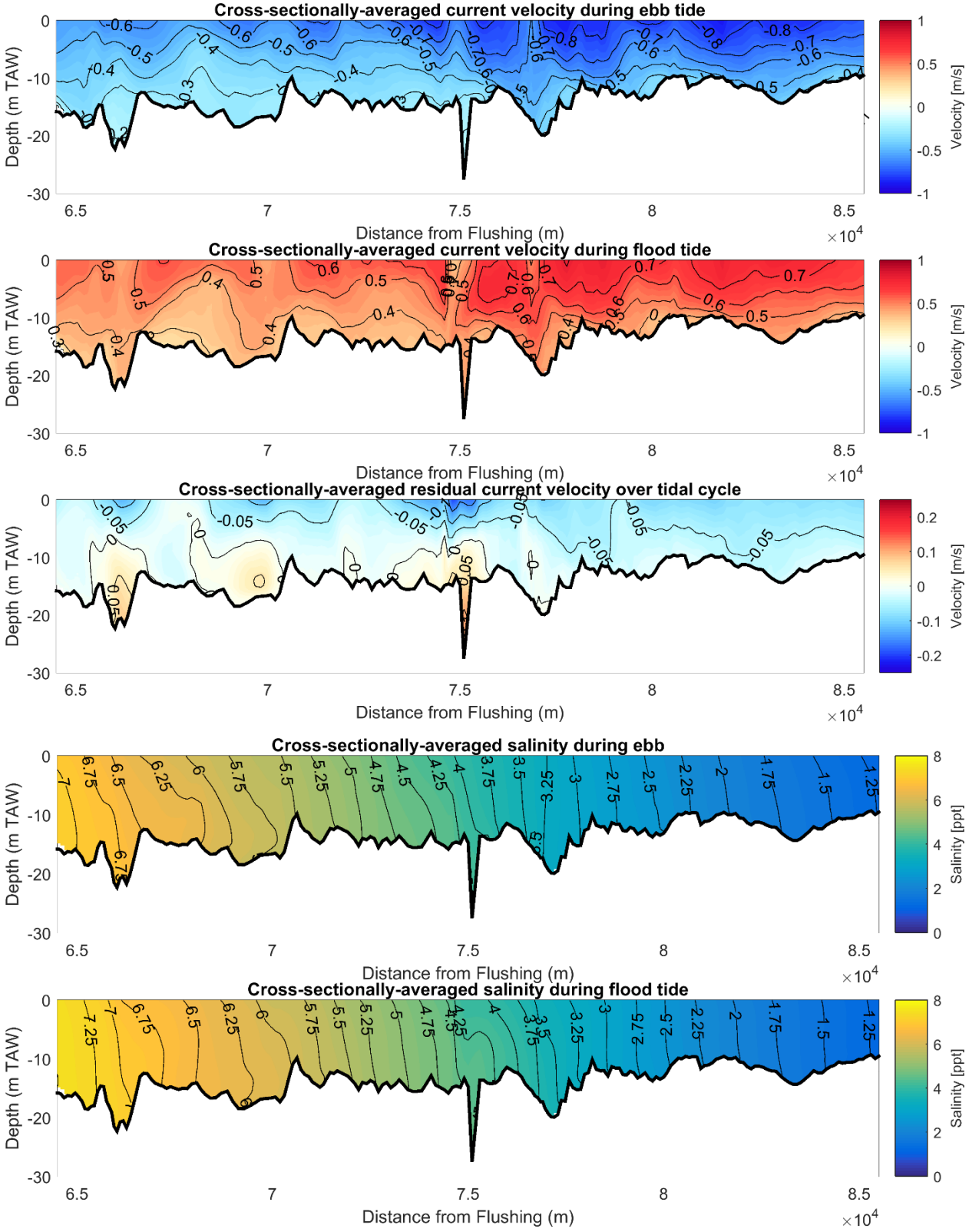
Cross-sectionally-averaged current velocity during ebb tide
Depth (m TAW)
Distance from Flushing (m)
×10^4
Velocity [m/s]
Cross-sectionally-averaged current velocity during flood tide
Depth (m TAW)
Distance from Flushing (m)
×10^4
Velocity [m/s]
Cross-sectionally-averaged residual current velocity over tidal cycle
Depth (m TAW)
Distance from Flushing (m)
×10^4
Velocity [m/s]
Cross-sectionally-averaged salinity during ebb
Depth (m TAW)
Distance from Flushing (m)
×10^4
Salinity [ppt]
Cross-sectionally-averaged salinity during flood tide
Depth (m TAW)
Distance from Flushing (m)
×10^4
Salinity [ppt]

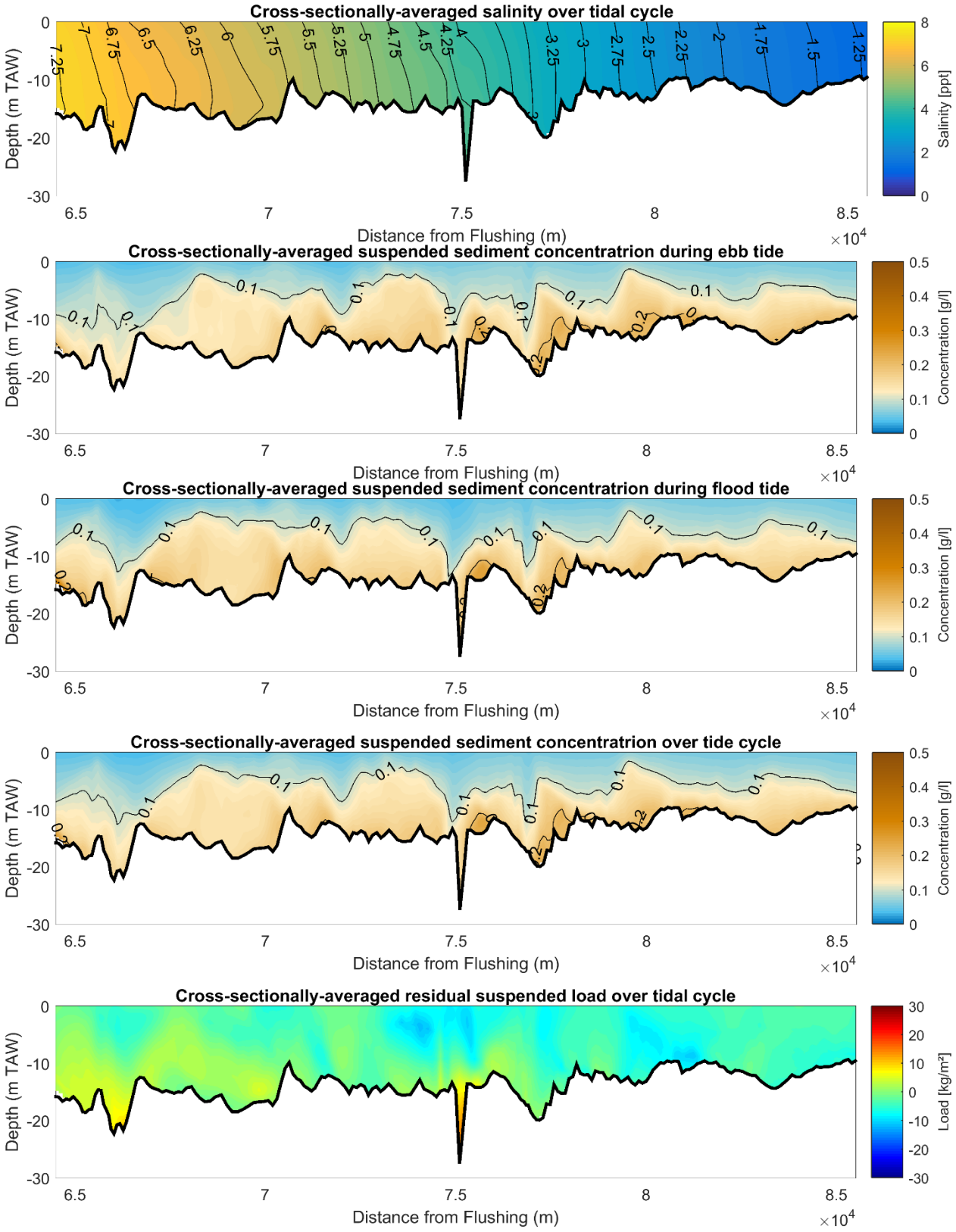
Cross-sectionally-averaged salinity over tidal cycle
Depth (m TAW)
Distance from Flushing (m)
×10^4
Salinity [ppt]
Cross-sectionally-averaged suspended sediment concentratrion during ebb tide
Concentration [g/l]
Cross-sectionally-averaged suspended sediment concentratrion during flood tide
Cross-sectionally-averaged suspended sediment concentratrion over tide cycle
Cross-sectionally-averaged residual suspended load over tidal cycle
Load [kg/m²]

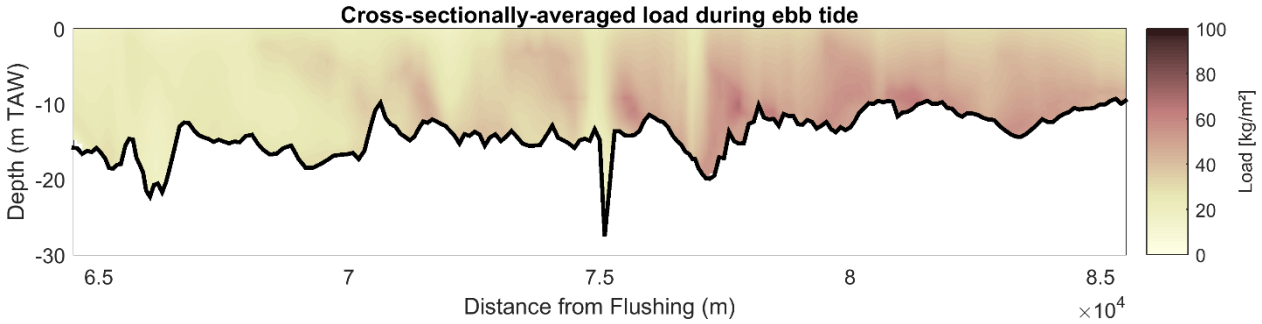

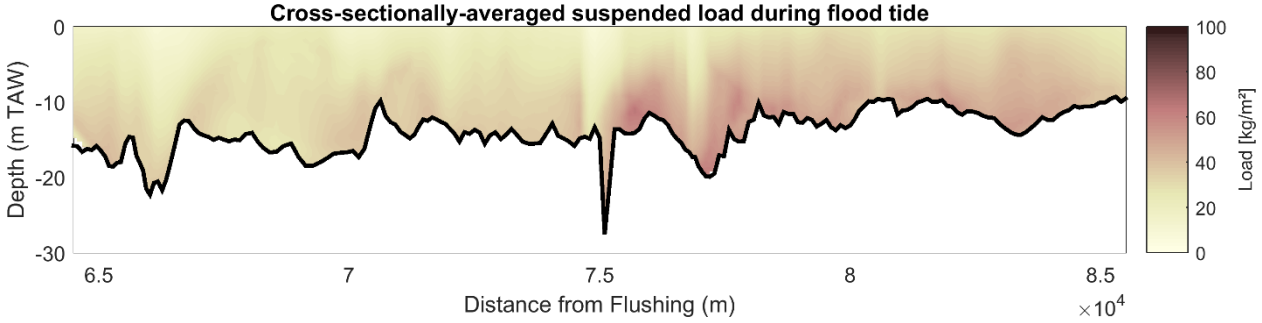

G.3 Transects

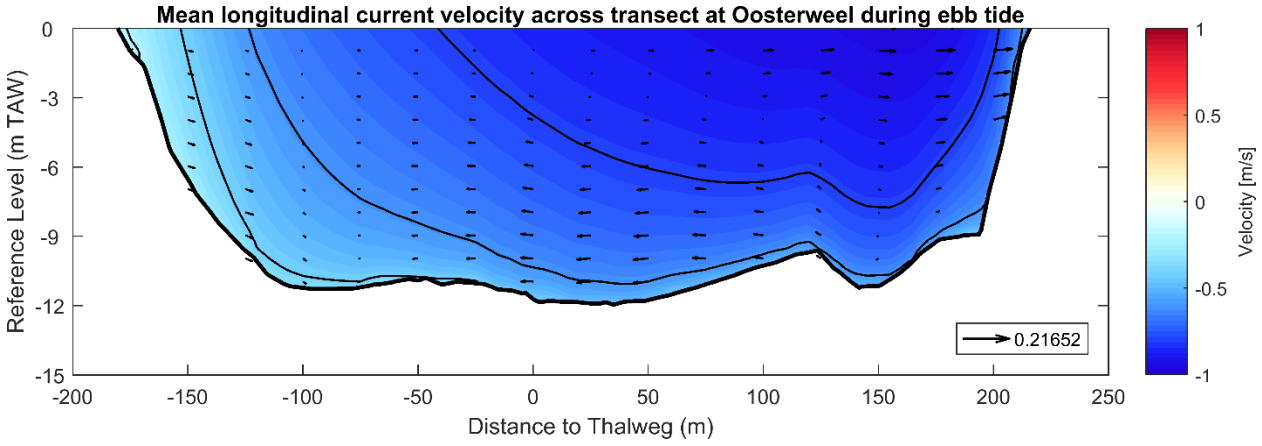

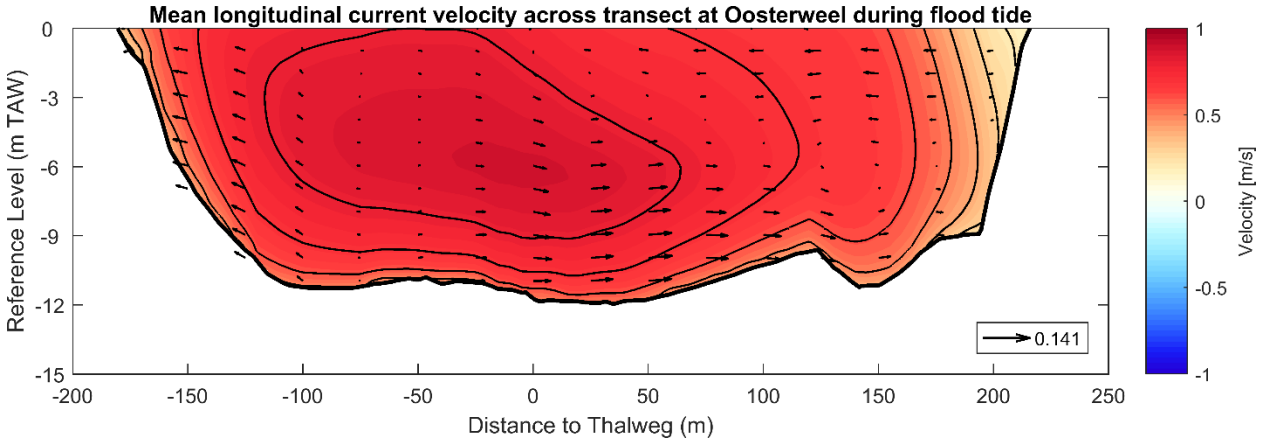

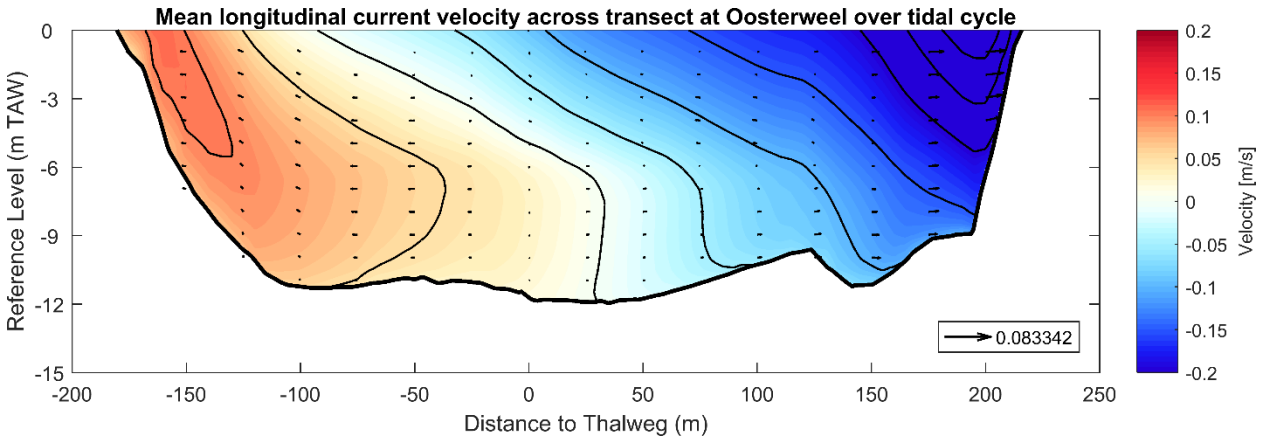
Mean longitudinal current velocity across transect at Oosterweel over tidal cycle
Reference Level (m TAW)
Distance to Thalweg (m)
Velocity [m/s]
0.083342

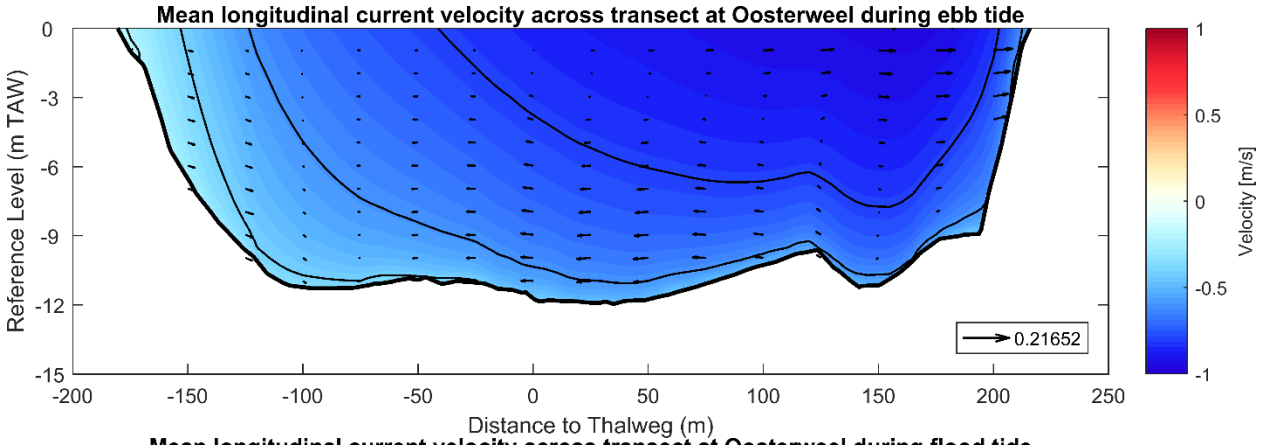
Mean longitudinal current velocity across transect at Oosterweel during ebb tide
Reference Level (m TAW)
Distance to Thalweg (m)
Velocity [m/s]
0.21652

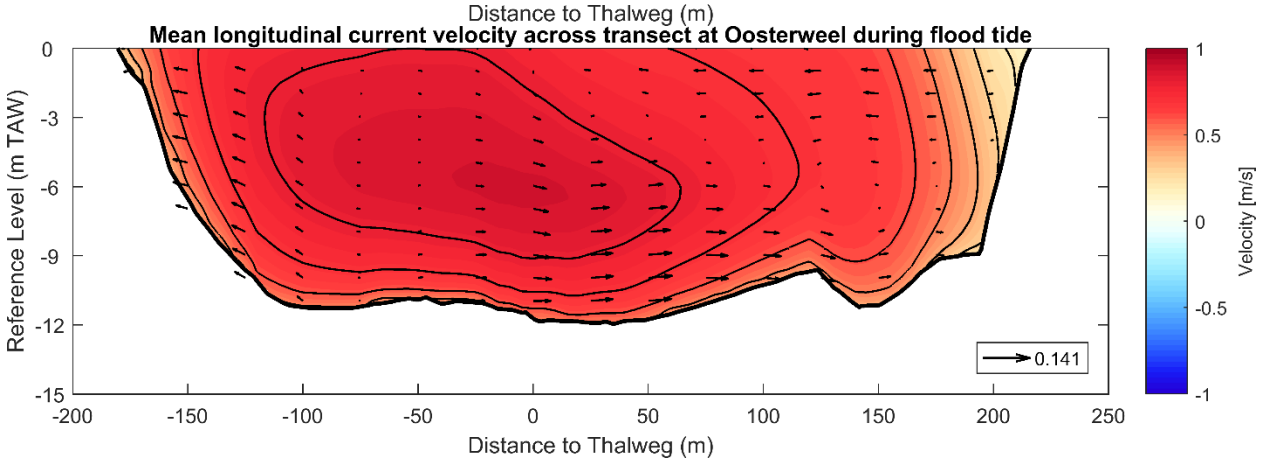
Mean longitudinal current velocity across transect at Oosterweel during flood tide
Reference Level (m TAW)
Distance to Thalweg (m)
Velocity [m/s]
0.141

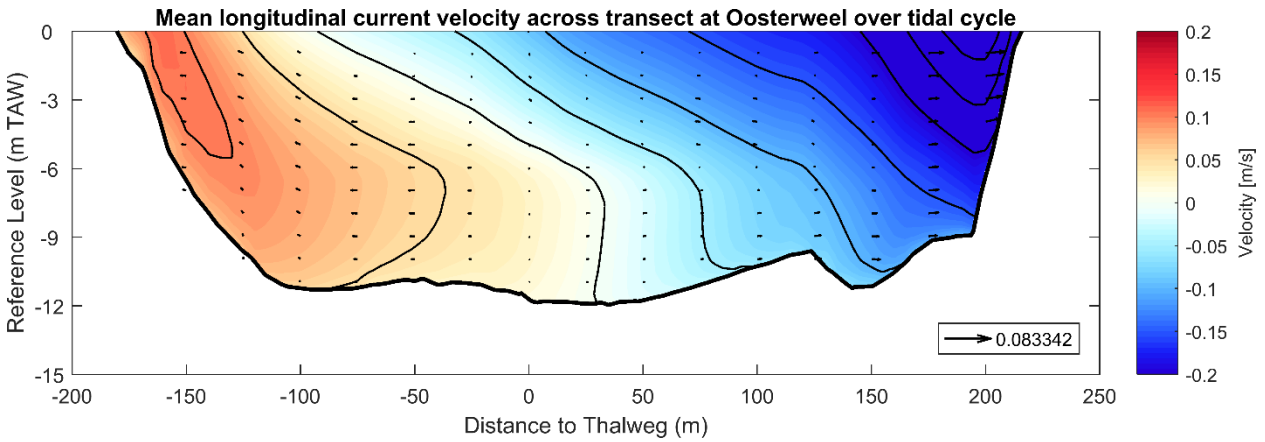
Mean longitudinal current velocity across transect at Oosterweel over tidal cycle
Reference Level (m TAW)
Distance to Thalweg (m)
Velocity [m/s]
0.083342

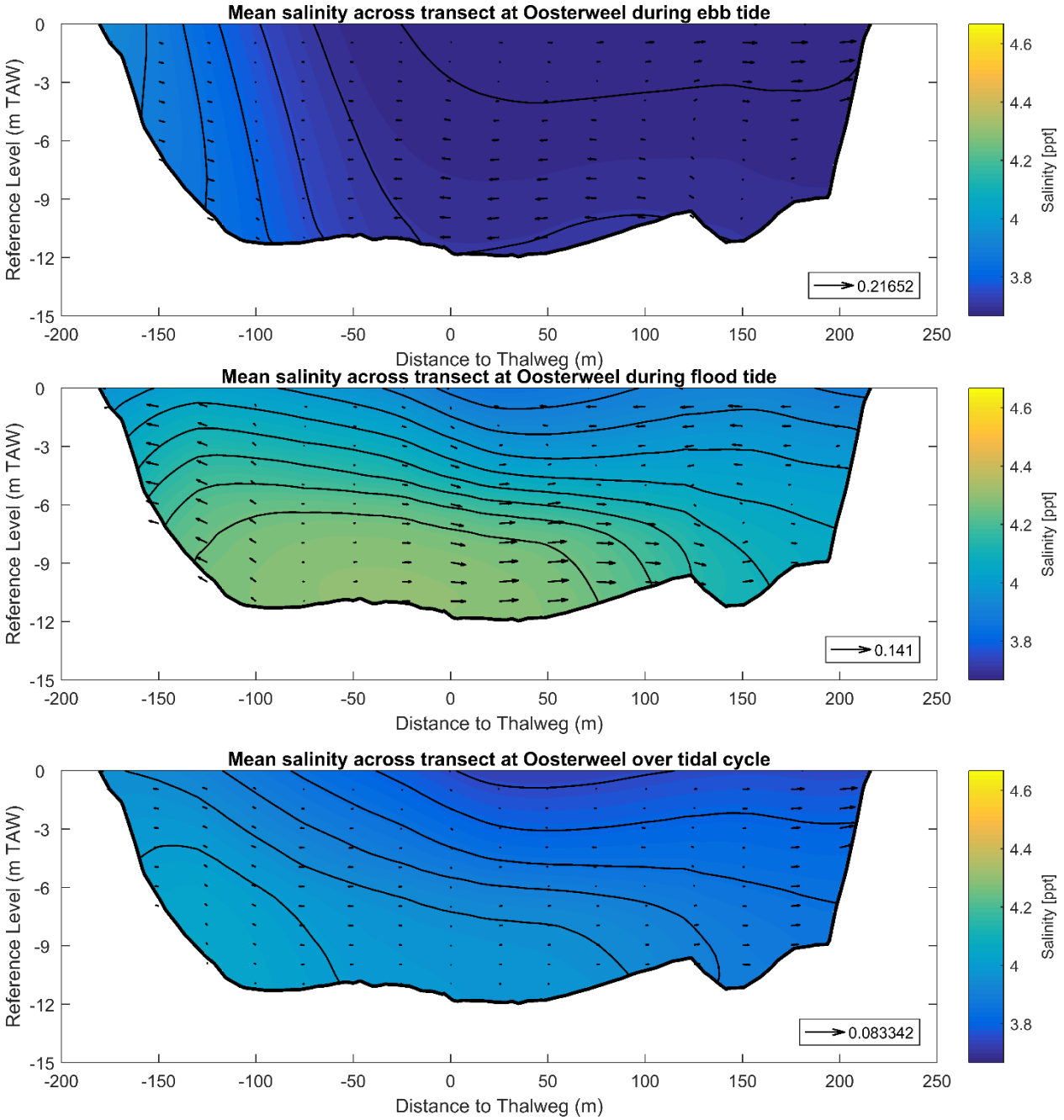
Mean salinity across transect at Oosterweel during ebb tide
Reference Level (m TAW)
0
-3
-6
-9
-12
-15
-200
-150
-100
-50
0
50
100
150
200
250
Distance to Thalweg (m)
0.21652
Salinity [ppt]
4.6
4.4
4.2
4
3.8
Mean salinity across transect at Oosterweel during flood tide
Reference Level (m TAW)
Distance to Thalweg (m)
0.141
Salinity [ppt]
Mean salinity across transect at Oosterweel over tidal cycle
Reference Level (m TAW)
Distance to Thalweg (m)
0.083342
Salinity [ppt]

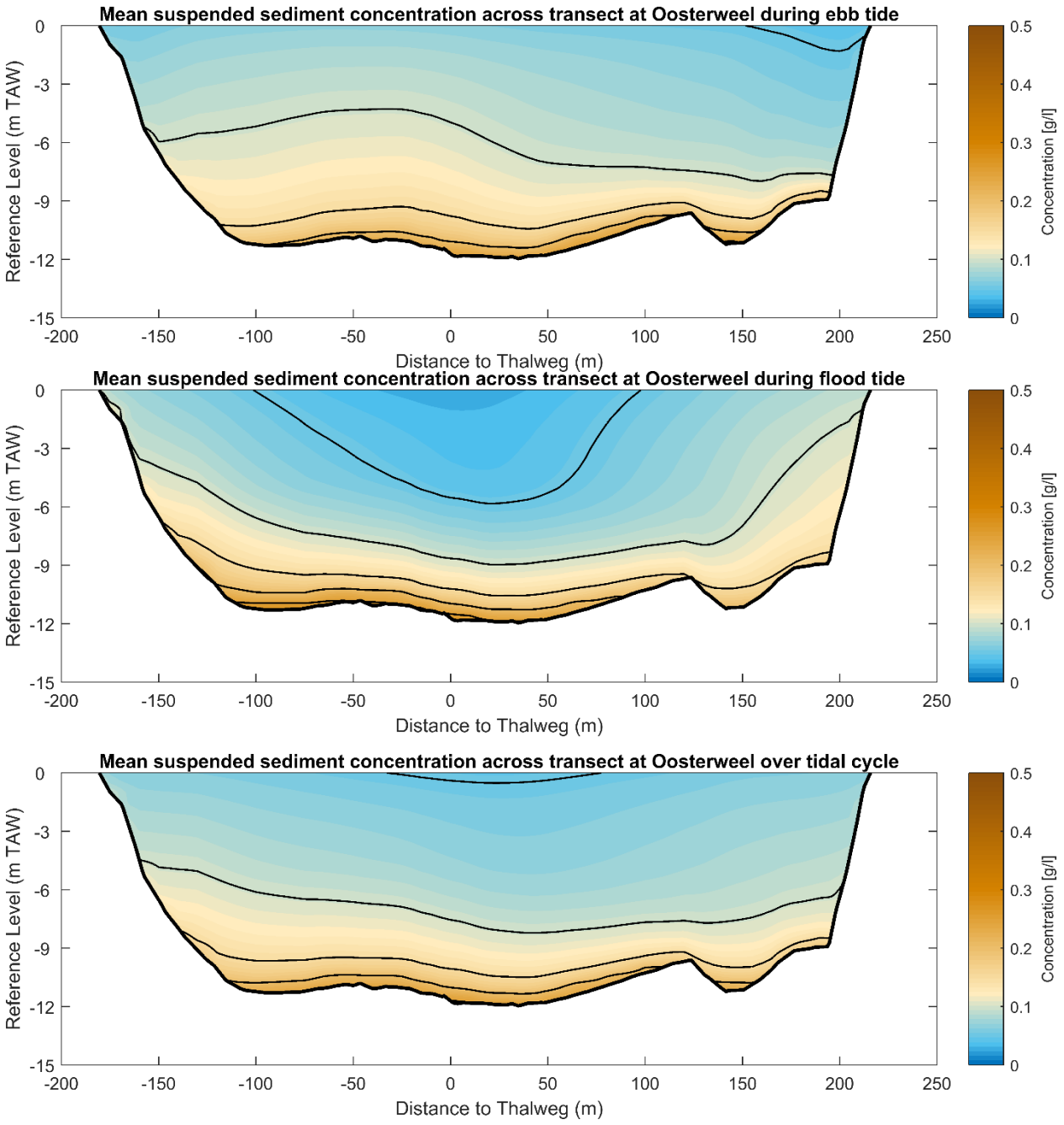
Mean suspended sediment concentration across transect at Oosterweel during ebb tide
Reference Level (m TAW)
0
-3
-6
-9
-12
-15
-200
-150
-100
-50
0
50
100
150
200
250
Distance to Thalweg (m)
Concentration [g/l]
0
0.1
0.2
0.3
0.4
0.5
Mean suspended sediment concentration across transect at Oosterweel during flood tide
Reference Level (m TAW)
Distance to Thalweg (m)
Concentration [g/l]
Mean suspended sediment concentration across transect at Oosterweel over tidal cycle
Reference Level (m TAW)
Distance to Thalweg (m)
Concentration [g/l]

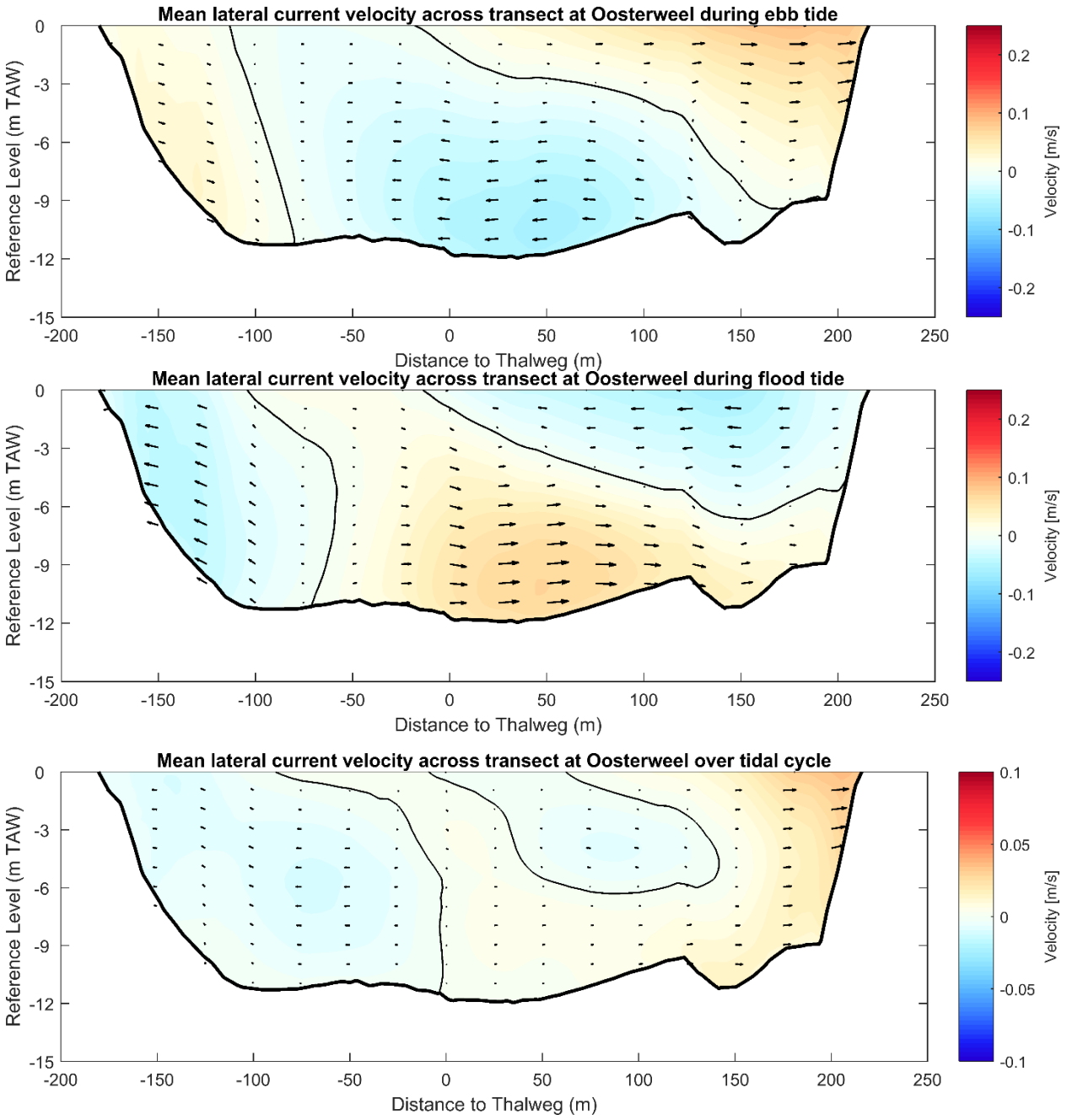
Mean lateral current velocity across transect at Oosterweel during ebb tide
Reference Level (m TAW)
Distance to Thalweg (m)
Velocity [m/s]
Mean lateral current velocity across transect at Oosterweel during flood tide
Reference Level (m TAW)
Distance to Thalweg (m)
Velocity [m/s]
Mean lateral current velocity across transect at Oosterweel over tidal cycle
Reference Level (m TAW)
Distance to Thalweg (m)
Velocity [m/s]

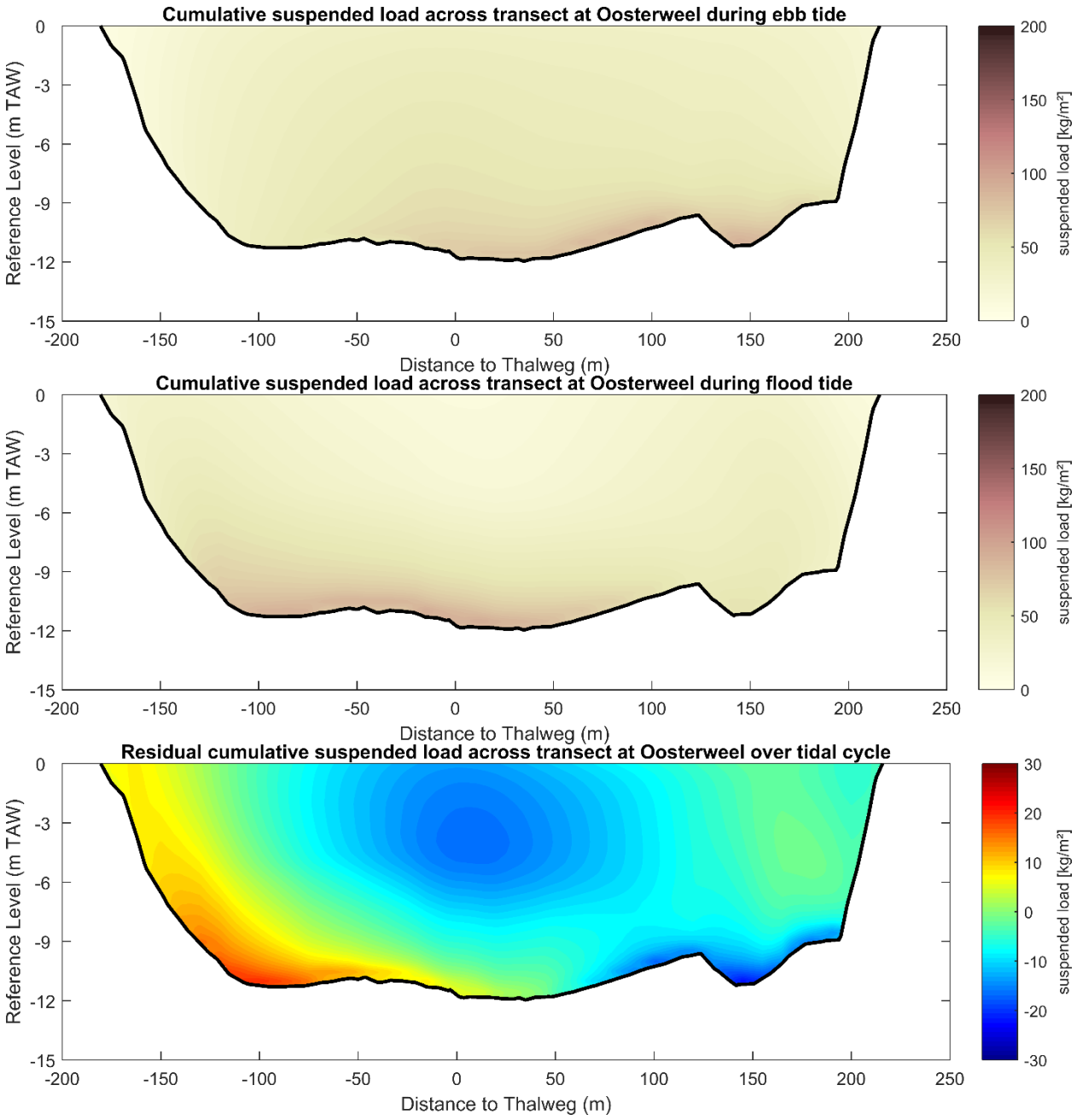
Cumulative suspended load across transect at Oosterweel during ebb tide
Reference Level (m TAW)
0
-3
-6
-9
-12
-15
-200
-150
-100
-50
0
50
100
150
200
250
Distance to Thalweg (m)
suspended load [kg/m²]
200
150
100
50
0
Cumulative suspended load across transect at Oosterweel during flood tide
Reference Level (m TAW)
Distance to Thalweg (m)
suspended load [kg/m²]
Residual cumulative suspended load across transect at Oosterweel over tidal cycle
Reference Level (m TAW)
Distance to Thalweg (m)
suspended load [kg/m²]
30
20
10
0
-10
-20
-30

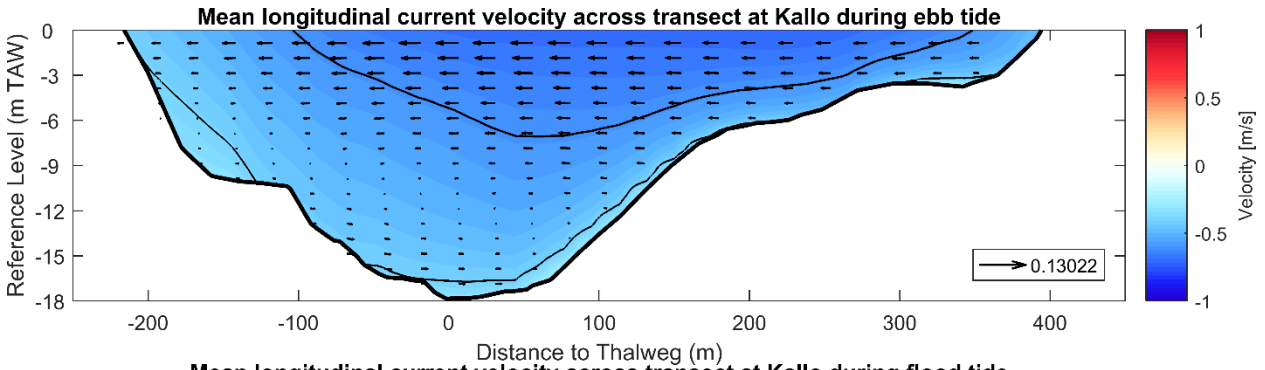
Mean longitudinal current velocity across transect at Kallo during ebb tide
Reference Level (m TAW)
Distance to Thalweg (m)
Velocity [m/s]
0.13022

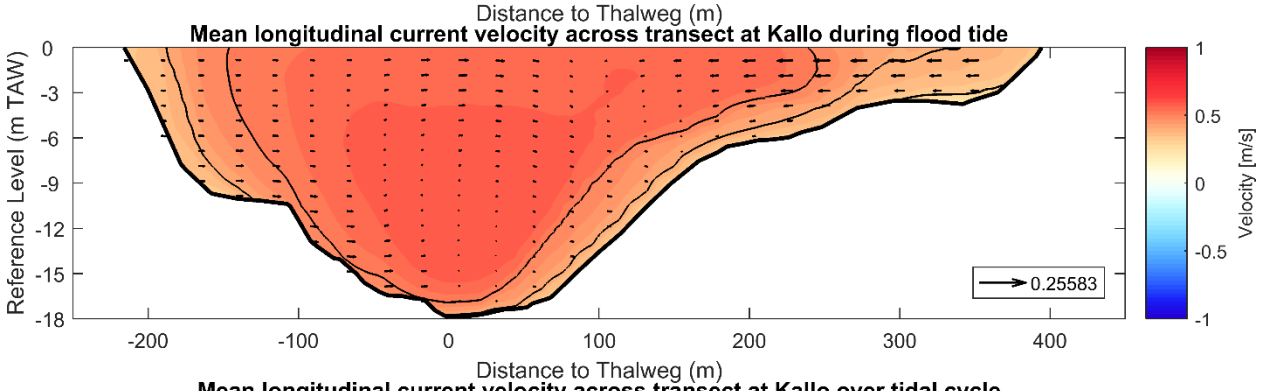
Mean longitudinal current velocity across transect at Kallo during flood tide
Reference Level (m TAW)
Distance to Thalweg (m)
Velocity [m/s]
0.25583

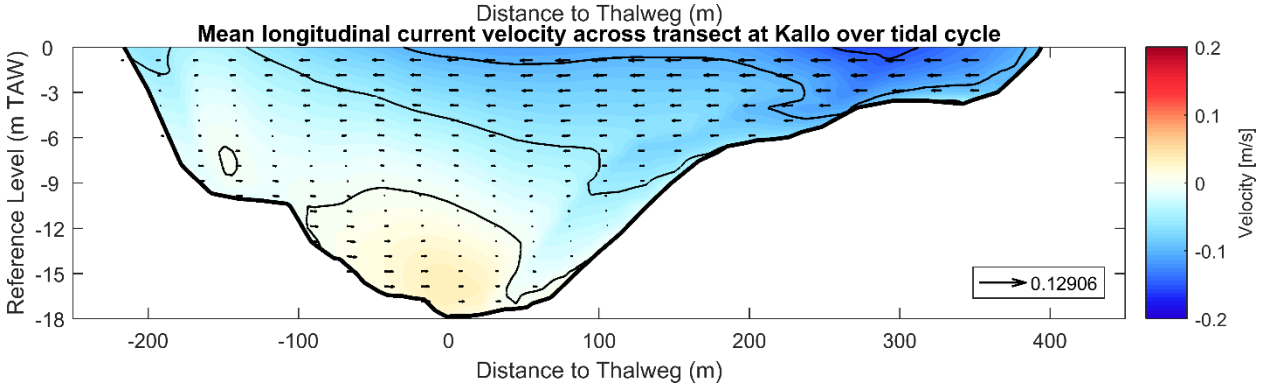
Mean longitudinal current velocity across transect at Kallo over tidal cycle
Reference Level (m TAW)
Distance to Thalweg (m)
Velocity [m/s]
0.12906

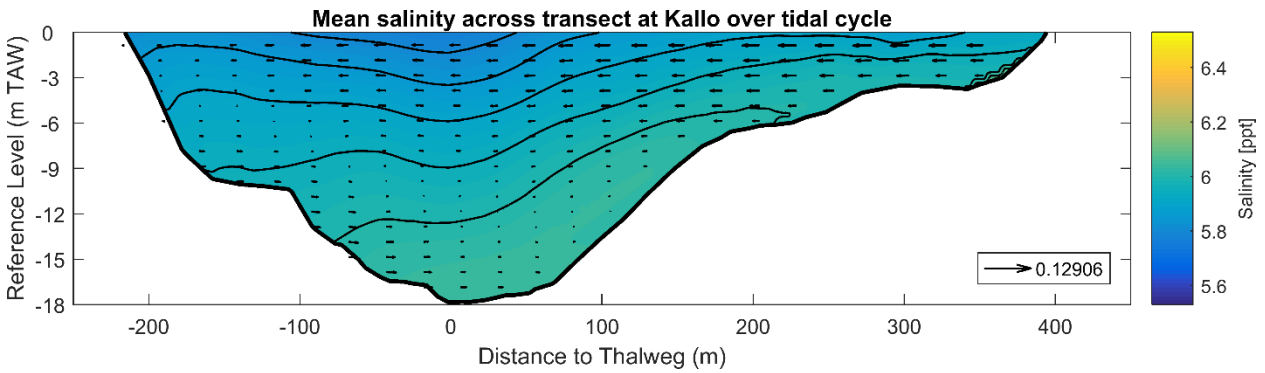
Mean salinity across transect at Kallo over tidal cycle
Reference Level (m TAW)
Distance to Thalweg (m)
Salinity [ppt]
0.12906

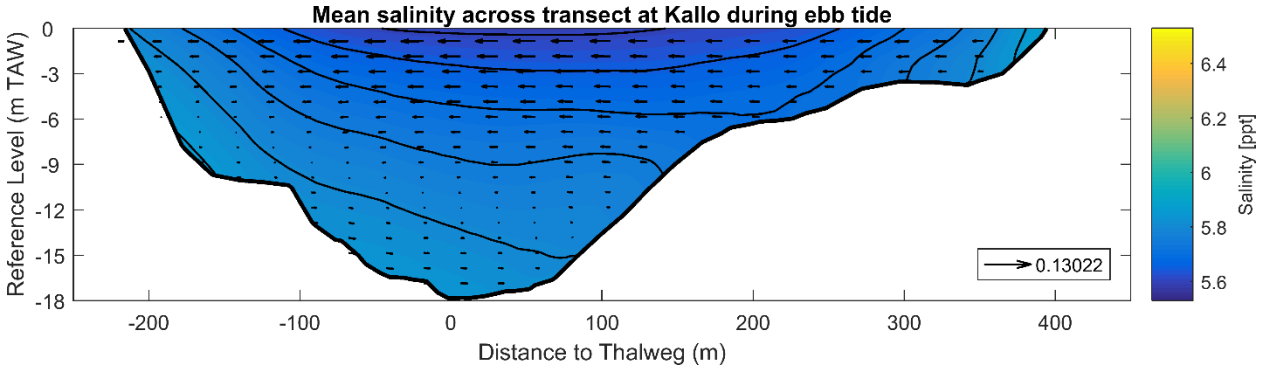
Mean salinity across transect at Kallo during ebb tide
Reference Level (m TAW)
Distance to Thalweg (m)
Salinity [ppt]
0.13022

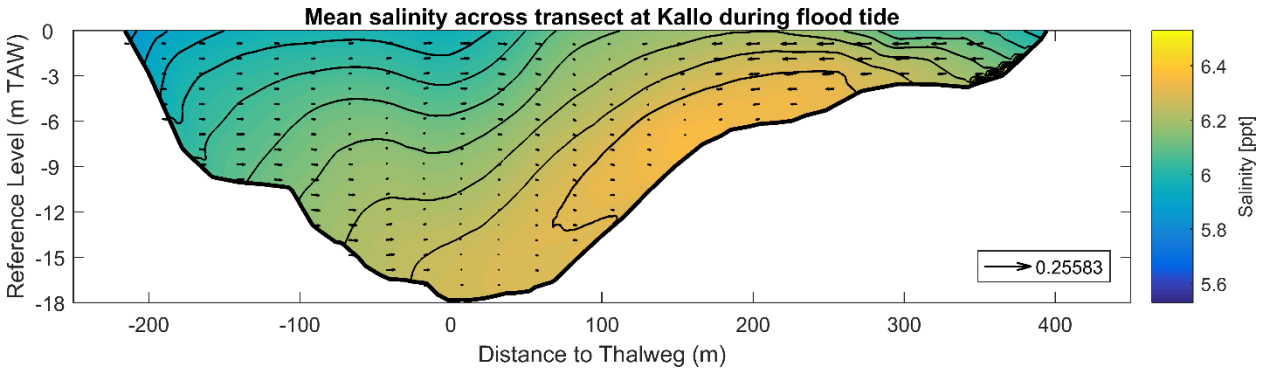
Mean salinity across transect at Kallo during flood tide
Reference Level (m TAW)
0
-3
-6
-9
-12
-15
-18
-200
-100
0
100
200
300
400
Distance to Thalweg (m)
0.25583
6.4
6.2
6
5.8
5.6
Salinity [ppt]

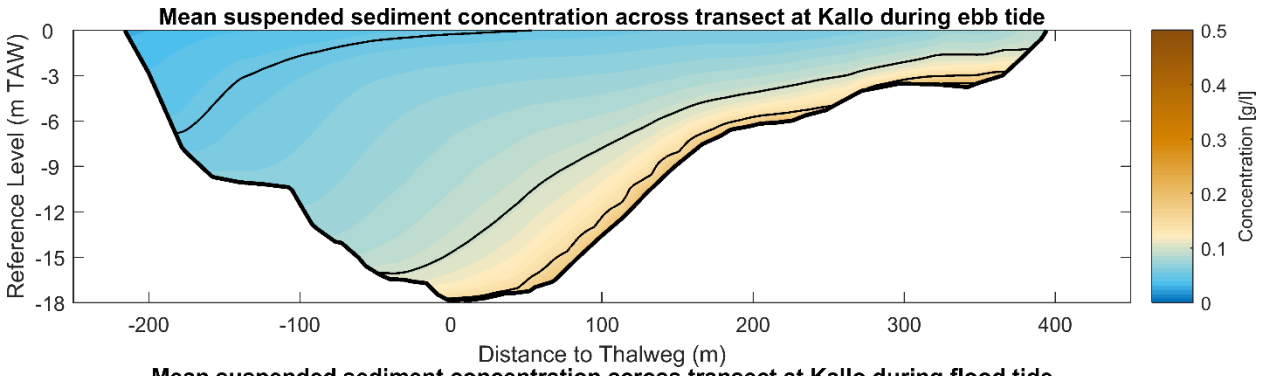
Mean suspended sediment concentration across transect at Kallo during ebb tide
Reference Level (m TAW)
0
-3
-6
-9
-12
-15
-18
-200
-100
0
100
200
300
400
Distance to Thalweg (m)
0.5
0.4
0.3
0.2
0.1
0
Concentration [g/l]

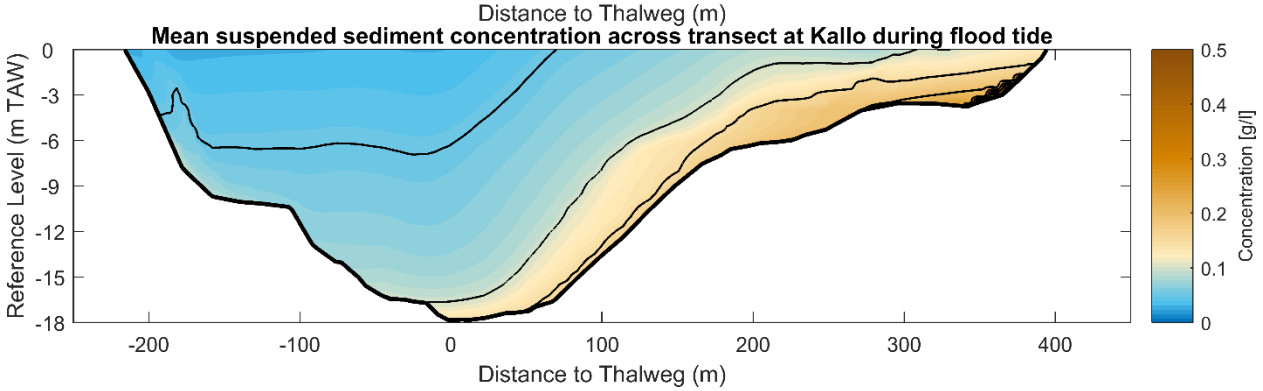
Mean suspended sediment concentration across transect at Kallo during flood tide
Reference Level (m TAW)
0
-3
-6
-9
-12
-15
-18
-200
-100
0
100
200
300
400
Distance to Thalweg (m)
0.5
0.4
0.3
0.2
0.1
0
Concentration [g/l]

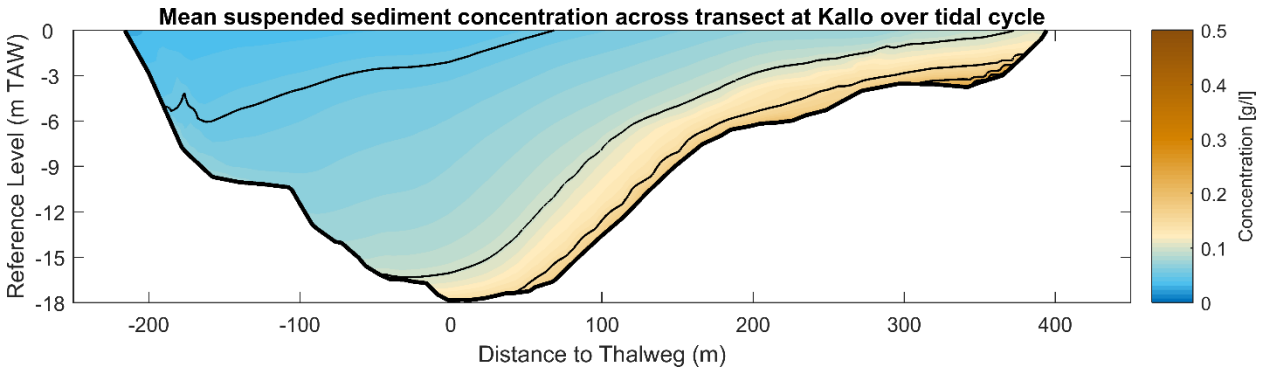
Mean suspended sediment concentration across transect at Kallo over tidal cycle
Reference Level (m TAW)
0
-3
-6
-9
-12
-15
-18
-200
-100
0
100
200
300
400
Distance to Thalweg (m)
0.5
0.4
0.3
0.2
0.1
0
Concentration [g/l]

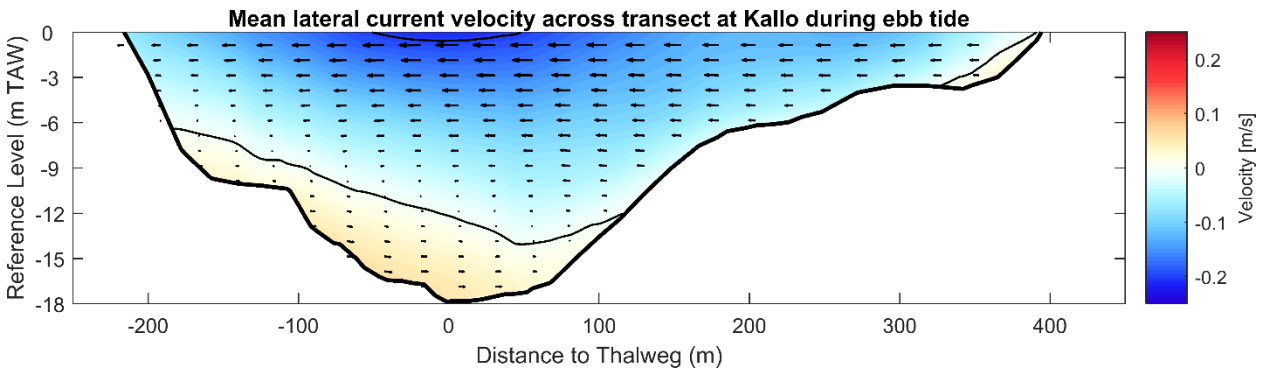
Mean lateral current velocity across transect at Kallo during ebb tide
Reference Level (m TAW)
0
-3
-6
-9
-12
-15
-18
-200
-100
0
100
200
300
400
Distance to Thalweg (m)
0.2
0.1
0
-0.1
-0.2
Velocity [m/s]

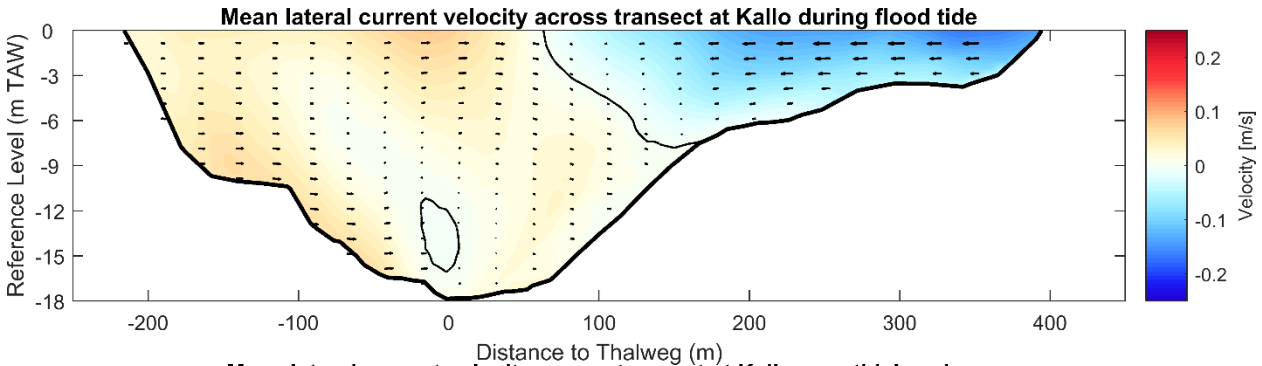
Mean lateral current velocity across transect at Kallo during flood tide
Reference Level (m TAW)
0
-3
-6
-9
-12
-15
-18
-200
-100
0
100
200
300
400
Distance to Thalweg (m)
0.2
0.1
0
-0.1
-0.2
Velocity [m/s]

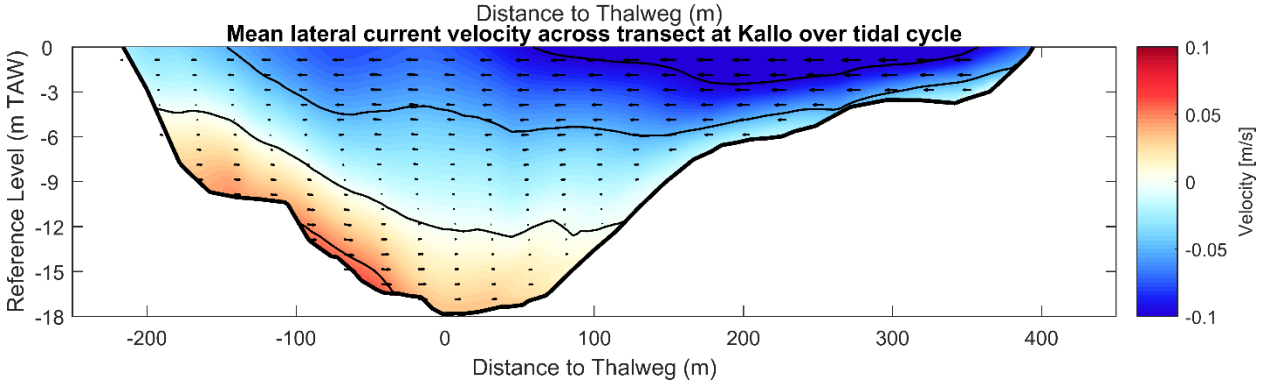
Mean lateral current velocity across transect at Kallo over tidal cycle
Reference Level (m TAW)
0
-3
-6
-9
-12
-15
-18
-200
-100
0
100
200
300
400
Distance to Thalweg (m)
0.1
0.05
0
-0.05
-0.1
Velocity [m/s]

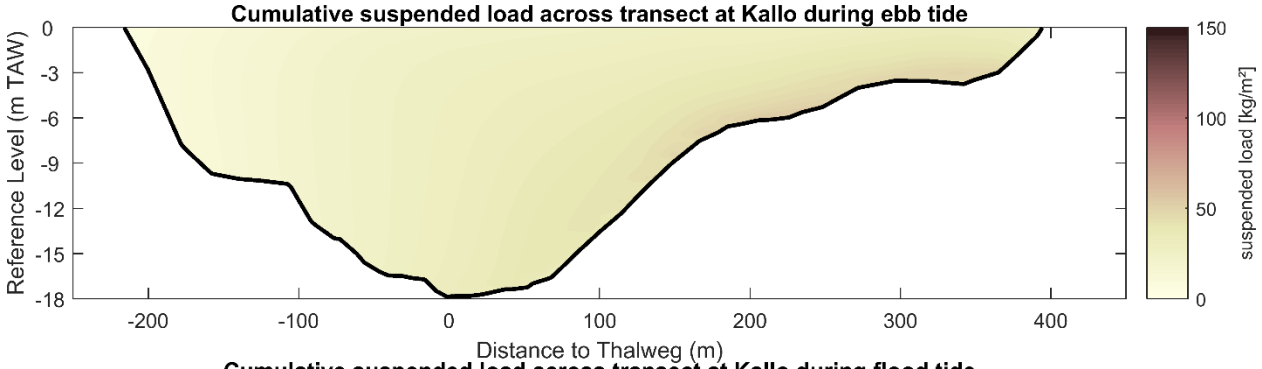
Cumulative suspended load across transect at Kallo during ebb tide
Reference Level (m TAW)
0
-3
-6
-9
-12
-15
-18
-200
-100
0
100
200
300
400
Distance to Thalweg (m)
150
100
50
0
suspended load [kg/m²]

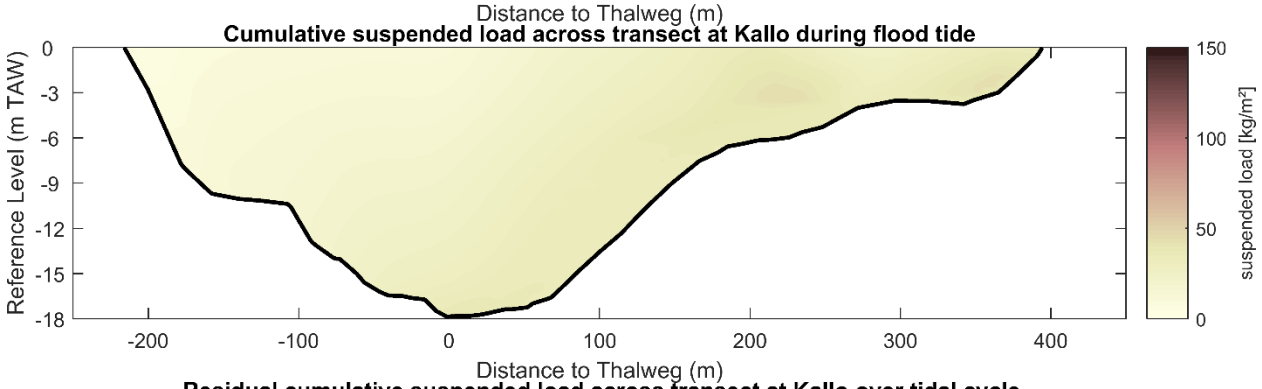
Cumulative suspended load across transect at Kallo during flood tide
Reference Level (m TAW)
0
-3
-6
-9
-12
-15
-18
-200
-100
0
100
200
300
400
Distance to Thalweg (m)
150
100
50
0
suspended load [kg/m²]

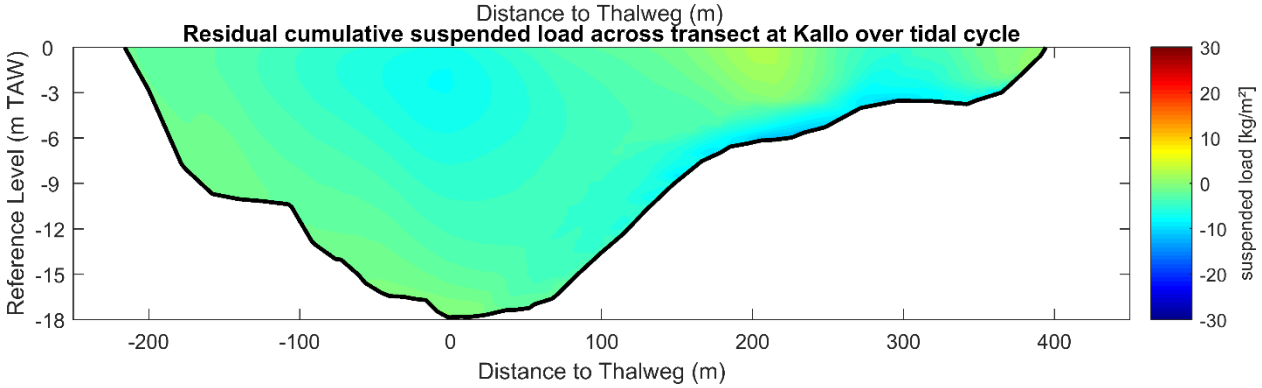
Residual cumulative suspended load across transect at Kallo over tidal cycle
Reference Level (m TAW)
0
-3
-6
-9
-12
-15
-18
-200
-100
0
100
200
300
400
Distance to Thalweg (m)
30
20
10
0
-10
-20
-30
suspended load [kg/m²]

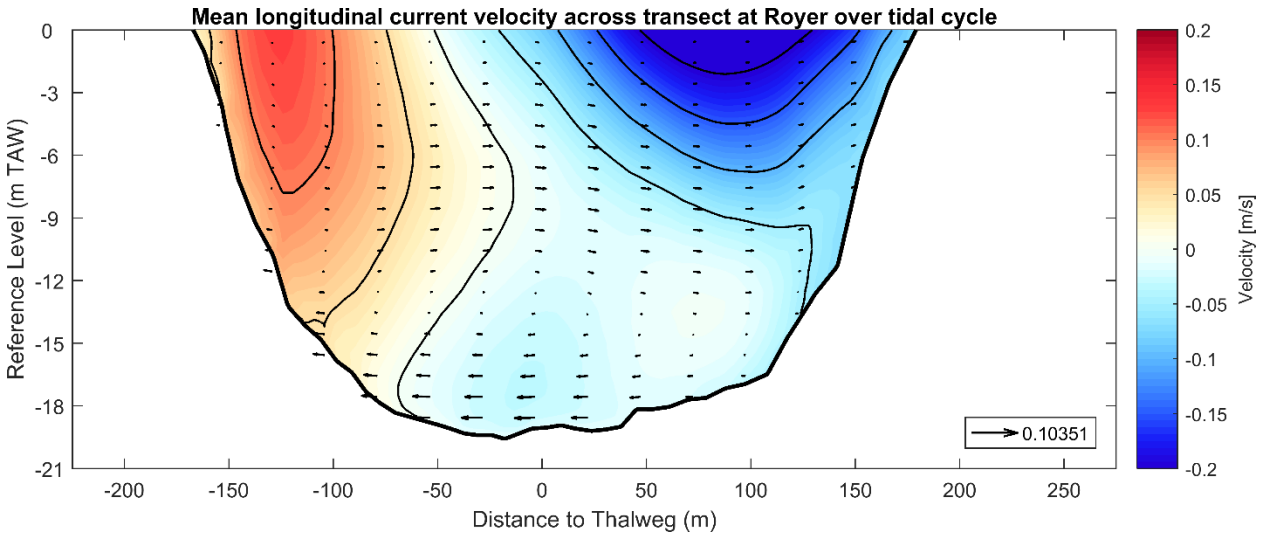
Mean longitudinal current velocity across transect at Royer over tidal cycle
Reference Level (m TAW)
Distance to Thalweg (m)
Velocity [m/s]
0.10351

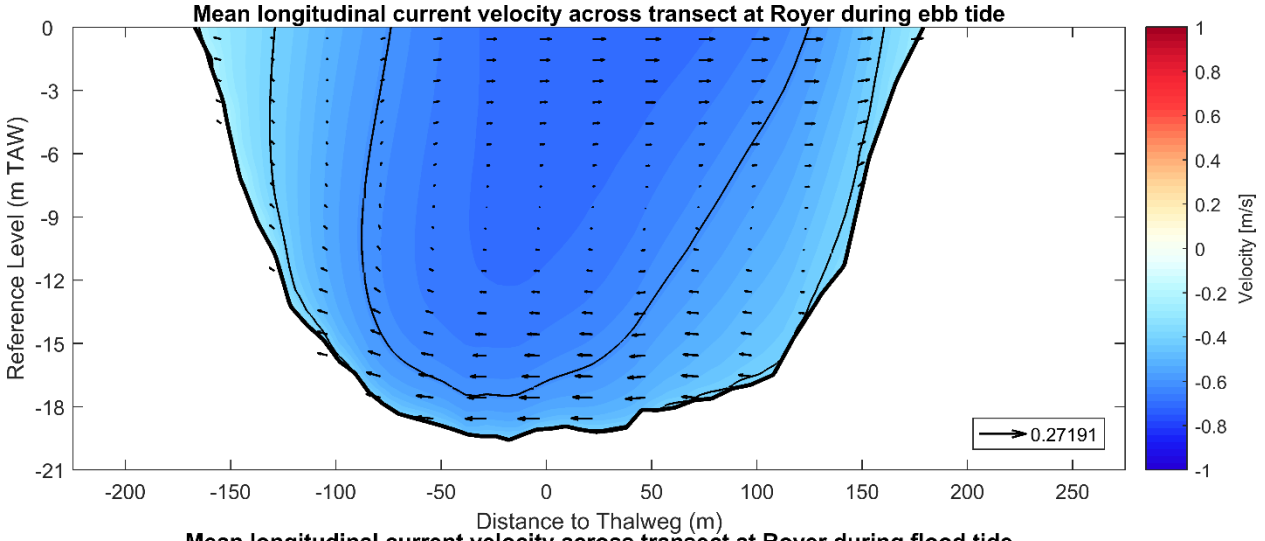
Mean longitudinal current velocity across transect at Royer during ebb tide
Reference Level (m TAW)
Distance to Thalweg (m)
Velocity [m/s]
0.27191

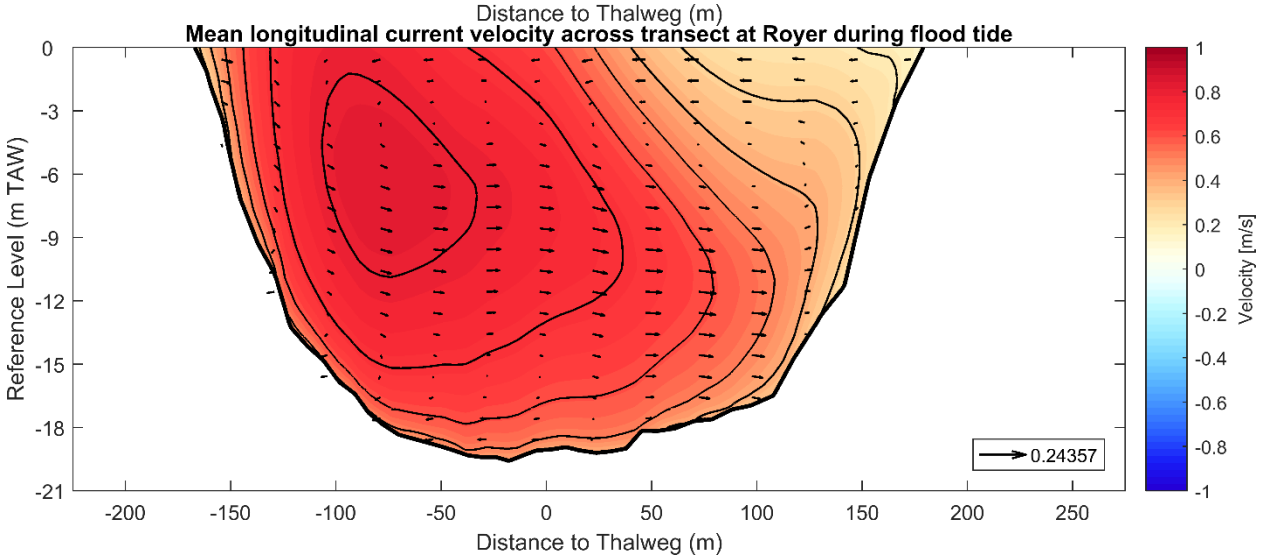
Mean longitudinal current velocity across transect at Royer during flood tide
Reference Level (m TAW)
Distance to Thalweg (m)
Velocity [m/s]
0.24357

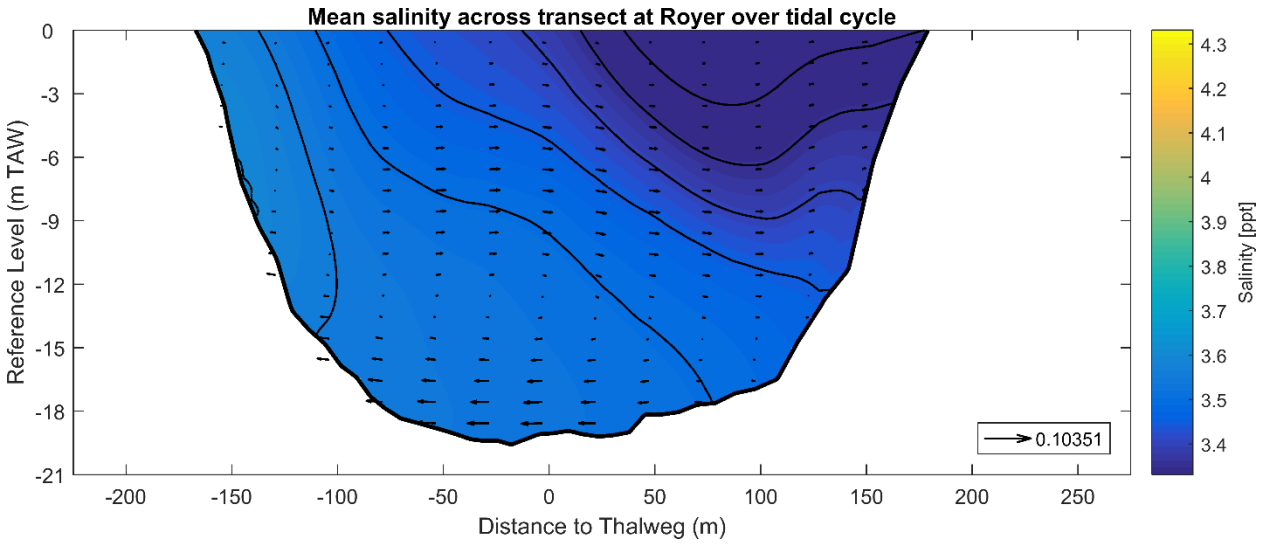
Mean salinity across transect at Royer over tidal cycle
Reference Level (m TAW)
0
-3
-6
-9
-12
-15
-18
-21
-200
-150
-100
-50
0
50
100
150
200
250
Distance to Thalweg (m)
0.10351
Salinity [ppt]
4.3
4.2
4.1
4
3.9
3.8
3.7
3.6
3.5
3.4

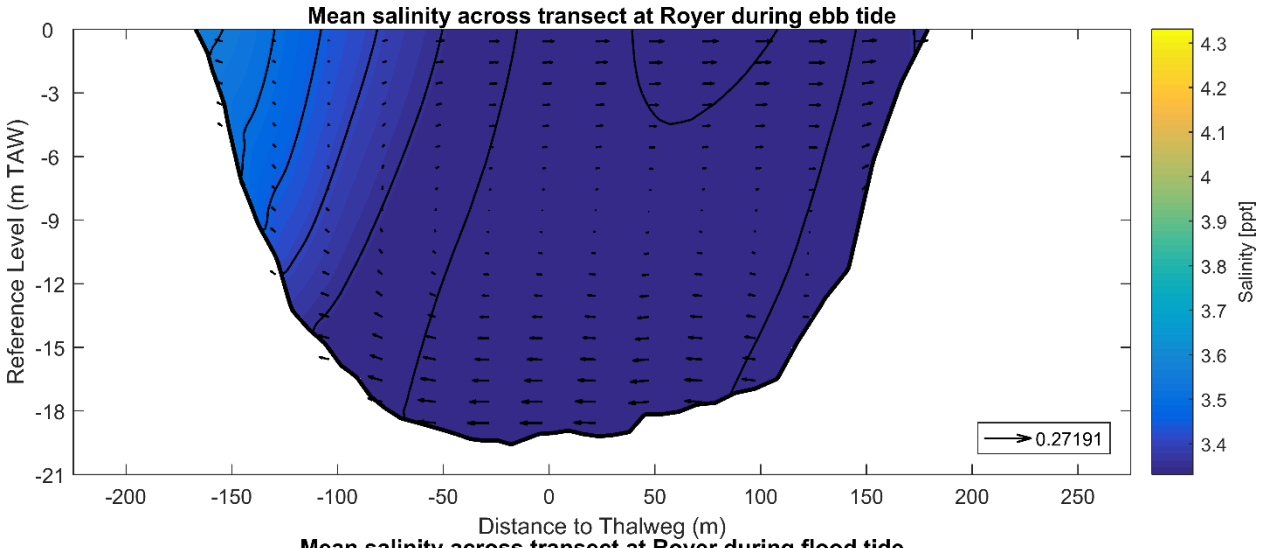
Mean salinity across transect at Royer during ebb tide
Reference Level (m TAW)
0
-3
-6
-9
-12
-15
-18
-21
-200
-150
-100
-50
0
50
100
150
200
250
Distance to Thalweg (m)
0.27191
Salinity [ppt]
4.3
4.2
4.1
4
3.9
3.8
3.7
3.6
3.5
3.4

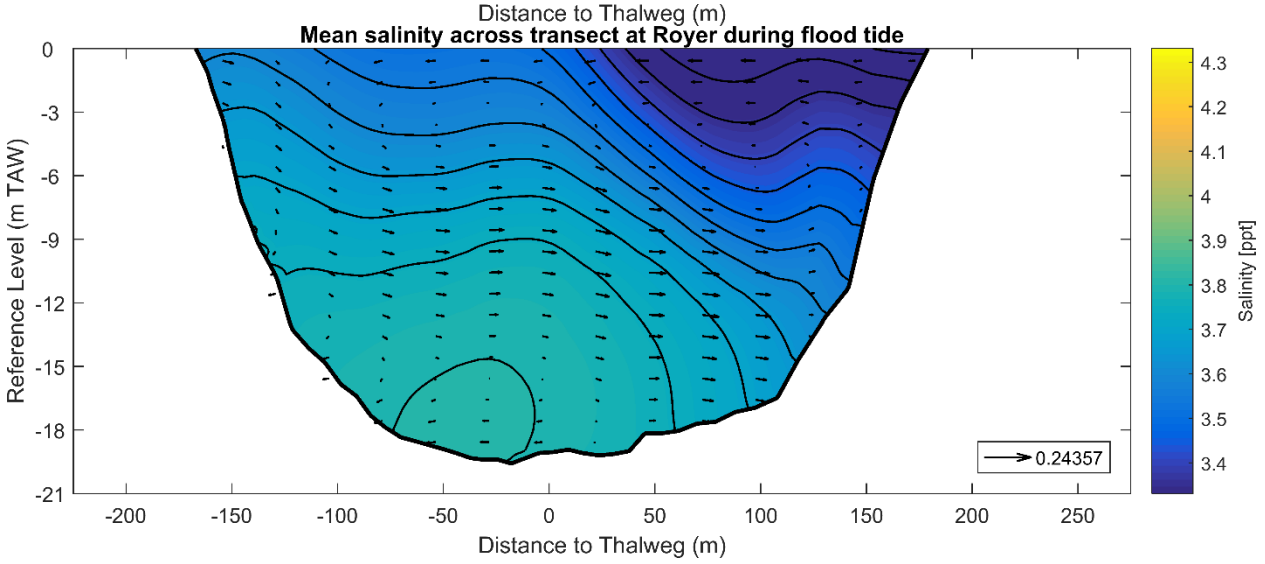
Mean salinity across transect at Royer during flood tide
Reference Level (m TAW)
0
-3
-6
-9
-12
-15
-18
-21
-200
-150
-100
-50
0
50
100
150
200
250
Distance to Thalweg (m)
0.24357
Salinity [ppt]
4.3
4.2
4.1
4
3.9
3.8
3.7
3.6
3.5
3.4

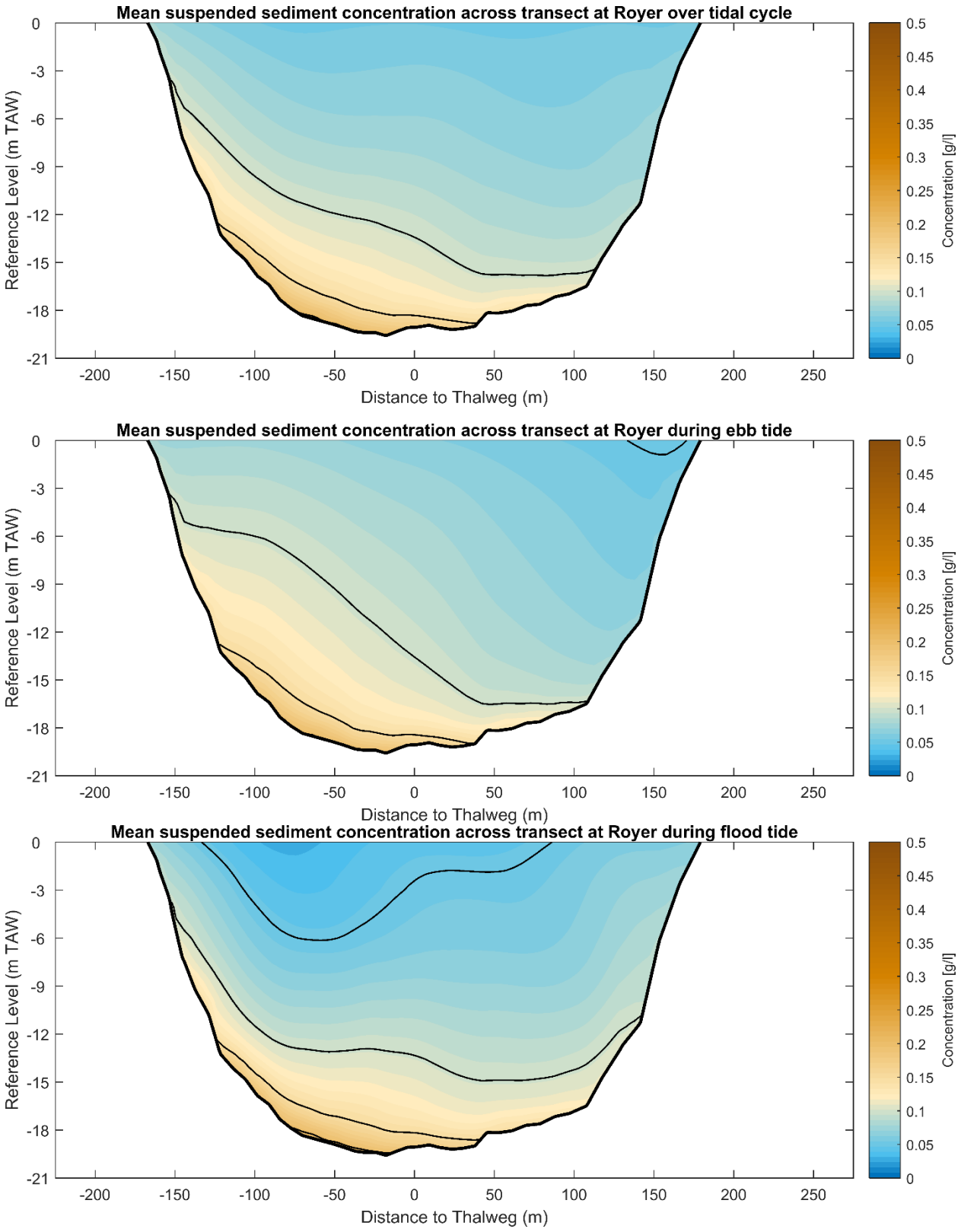
Mean suspended sediment concentration across transect at Royer over tidal cycle
Reference Level (m TAW)
0
-3
-6
-9
-12
-15
-18
-21
-200
-150
-100
-50
0
50
100
150
200
250
Distance to Thalweg (m)
Concentration [g/l]
0.5
0.45
0.4
0.35
0.3
0.25
0.2
0.15
0.1
0.05
0
Mean suspended sediment concentration across transect at Royer during ebb tide
Reference Level (m TAW)
Distance to Thalweg (m)
Concentration [g/l]
Mean suspended sediment concentration across transect at Royer during flood tide
Reference Level (m TAW)
Distance to Thalweg (m)
Concentration [g/l]

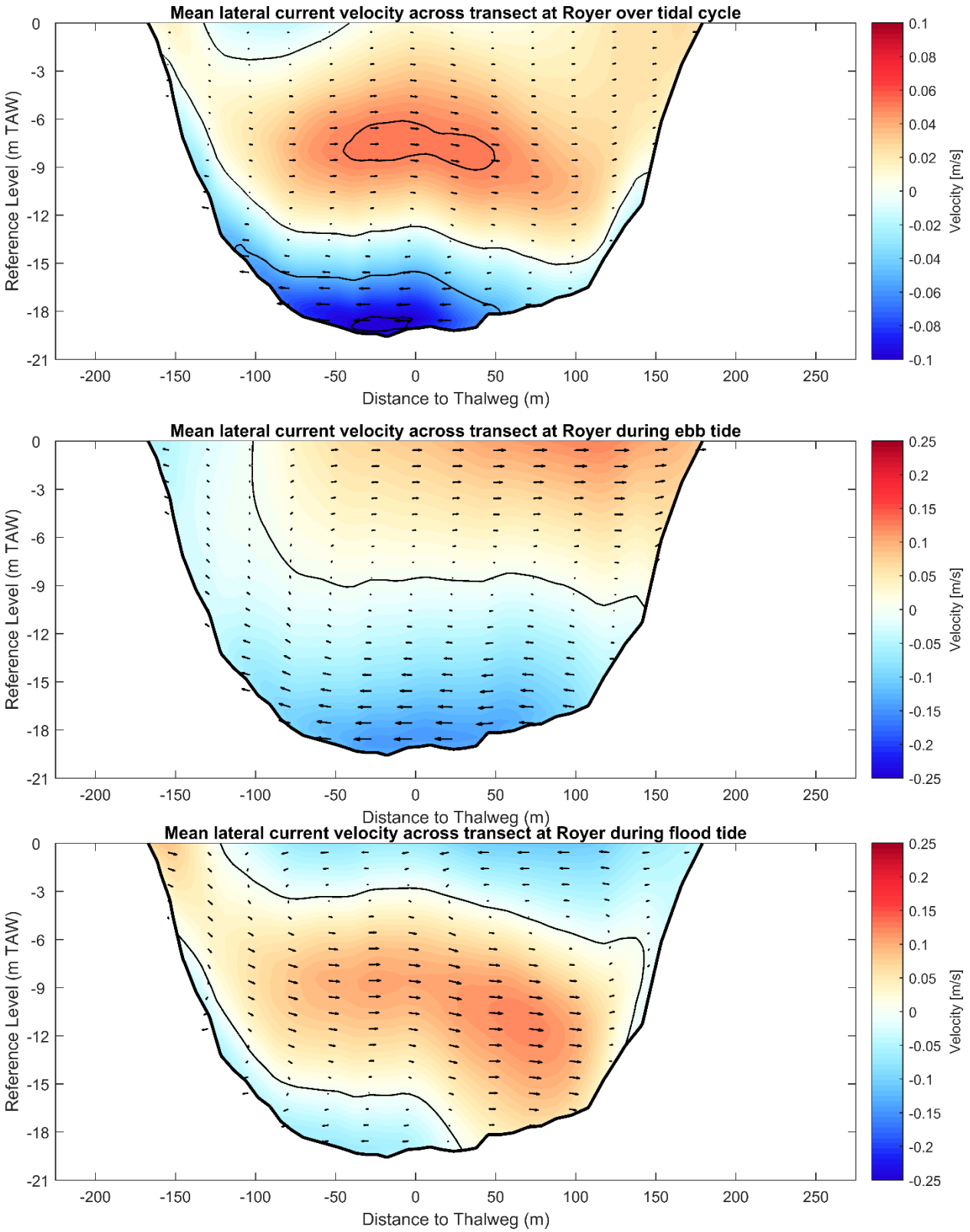
Mean lateral current velocity across transect at Royer over tidal cycle
Reference Level (m TAW)
Distance to Thalweg (m)
Velocity [m/s]
Mean lateral current velocity across transect at Royer during ebb tide
Reference Level (m TAW)
Distance to Thalweg (m)
Velocity [m/s]
Mean lateral current velocity across transect at Royer during flood tide
Reference Level (m TAW)
Distance to Thalweg (m)
Velocity [m/s]

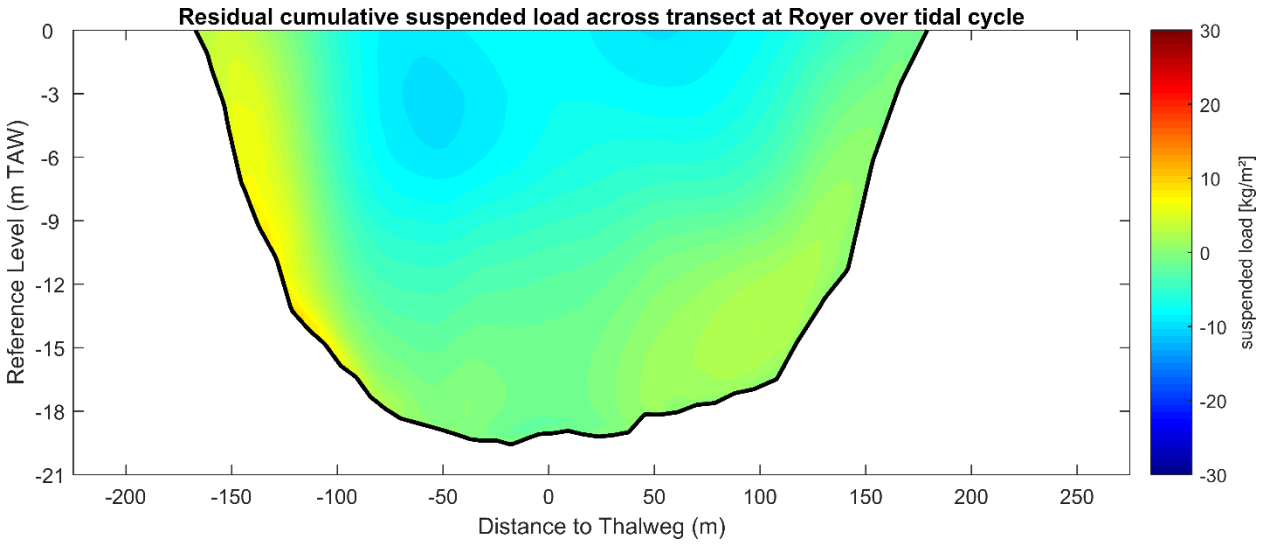
Residual cumulative suspended load across transect at Royer over tidal cycle
Reference Level (m TAW)
0
-3
-6
-9
-12
-15
-18
-21
-200
-150
-100
-50
0
50
100
150
200
250
Distance to Thalweg (m)
30
20
10
0
-10
-20
-30
suspended load [kg/m²]

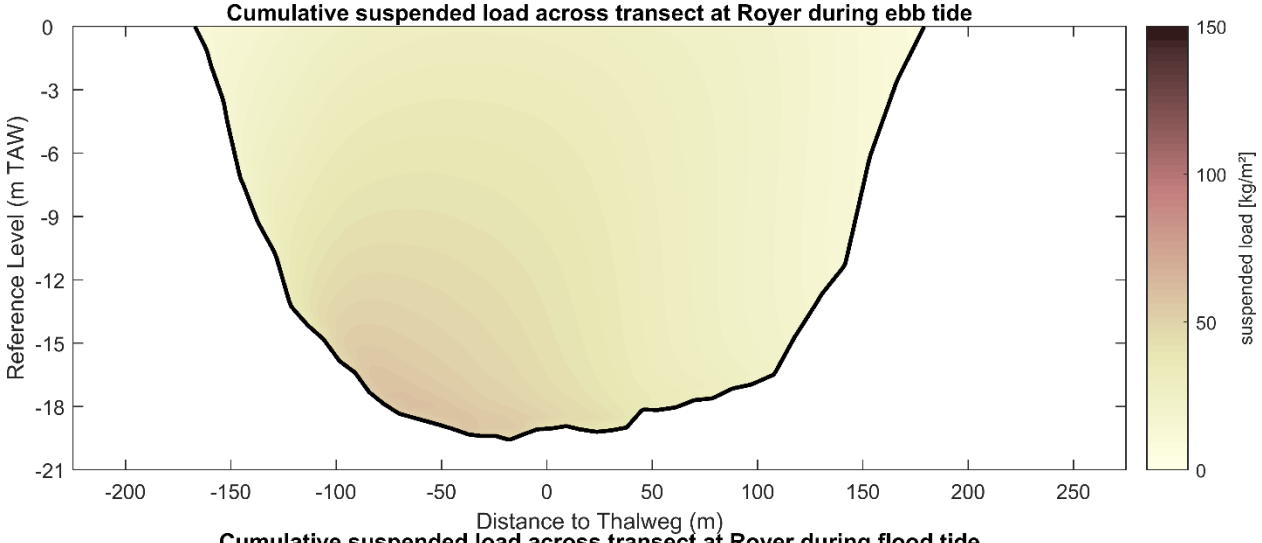
Cumulative suspended load across transect at Royer during ebb tide
Reference Level (m TAW)
0
-3
-6
-9
-12
-15
-18
-21
-200
-150
-100
-50
0
50
100
150
200
250
Distance to Thalweg (m)
150
100
50
0
suspended load [kg/m²]

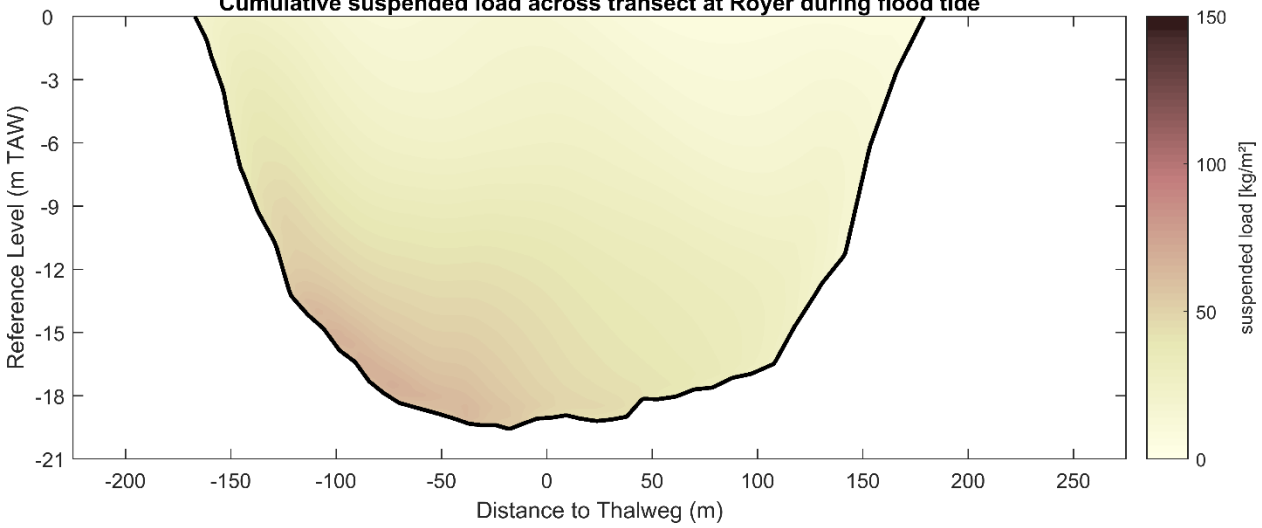
Cumulative suspended load across transect at Royer during flood tide
Reference Level (m TAW)
0
-3
-6
-9
-12
-15
-18
-21
-200
-150
-100
-50
0
50
100
150
200
250
Distance to Thalweg (m)
150
100
50
0
suspended load [kg/m²]

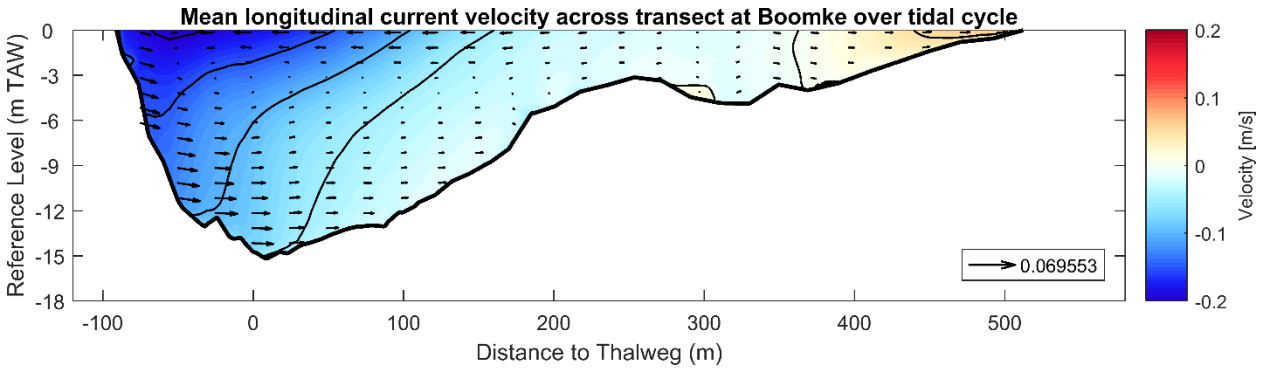
Mean longitudinal current velocity across transect at Boomke over tidal cycle
Reference Level (m TAW)
0
-3
-6
-9
-12
-15
-18
-100
0
100
200
300
400
500
Distance to Thalweg (m)
0.069553
0.2
0.1
0
-0.1
-0.2
Velocity [m/s]

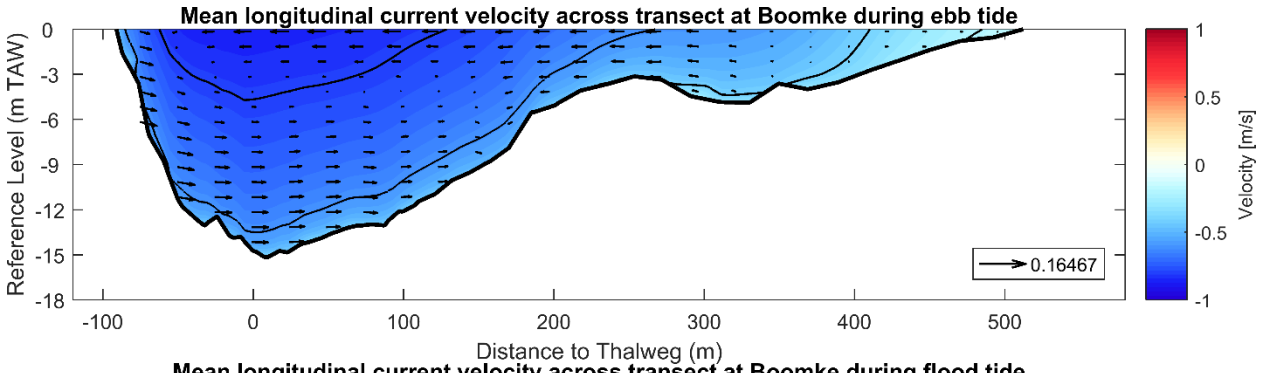
Mean longitudinal current velocity across transect at Boomke during ebb tide
Reference Level (m TAW)
0
-3
-6
-9
-12
-15
-18
-100
0
100
200
300
400
500
Distance to Thalweg (m)
0.16467
1
0.5
0
-0.5
-1
Velocity [m/s]

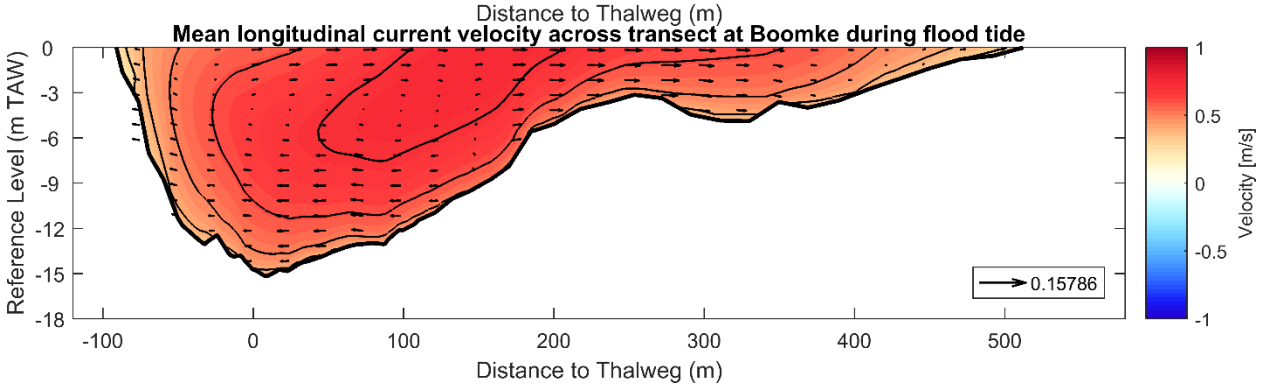
Mean longitudinal current velocity across transect at Boomke during flood tide
Reference Level (m TAW)
0
-3
-6
-9
-12
-15
-18
-100
0
100
200
300
400
500
Distance to Thalweg (m)
0.15786
1
0.5
0
-0.5
-1
Velocity [m/s]

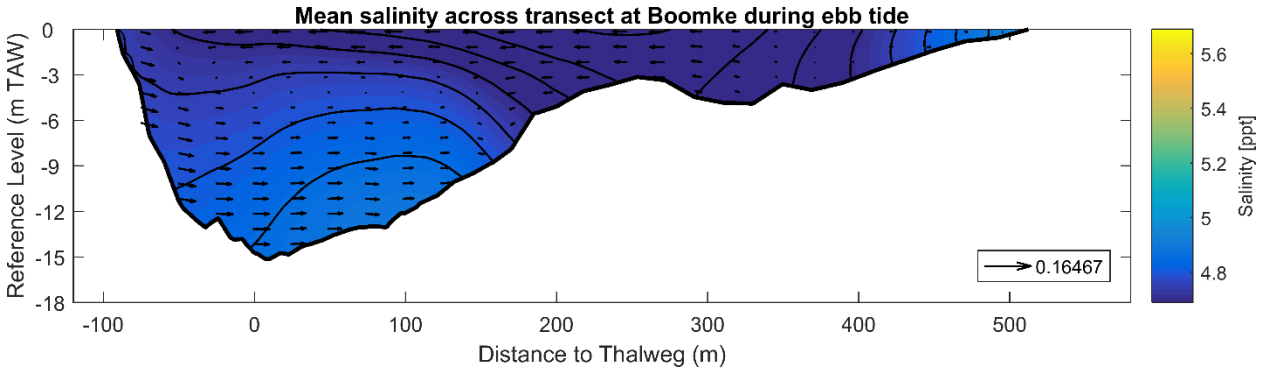
Mean salinity across transect at Boomke during ebb tide
Reference Level (m TAW)
0
-3
-6
-9
-12
-15
-18
-100
0
100
200
300
400
500
Distance to Thalweg (m)
0.16467
5.6
5.4
5.2
5
4.8
Salinity [ppt]

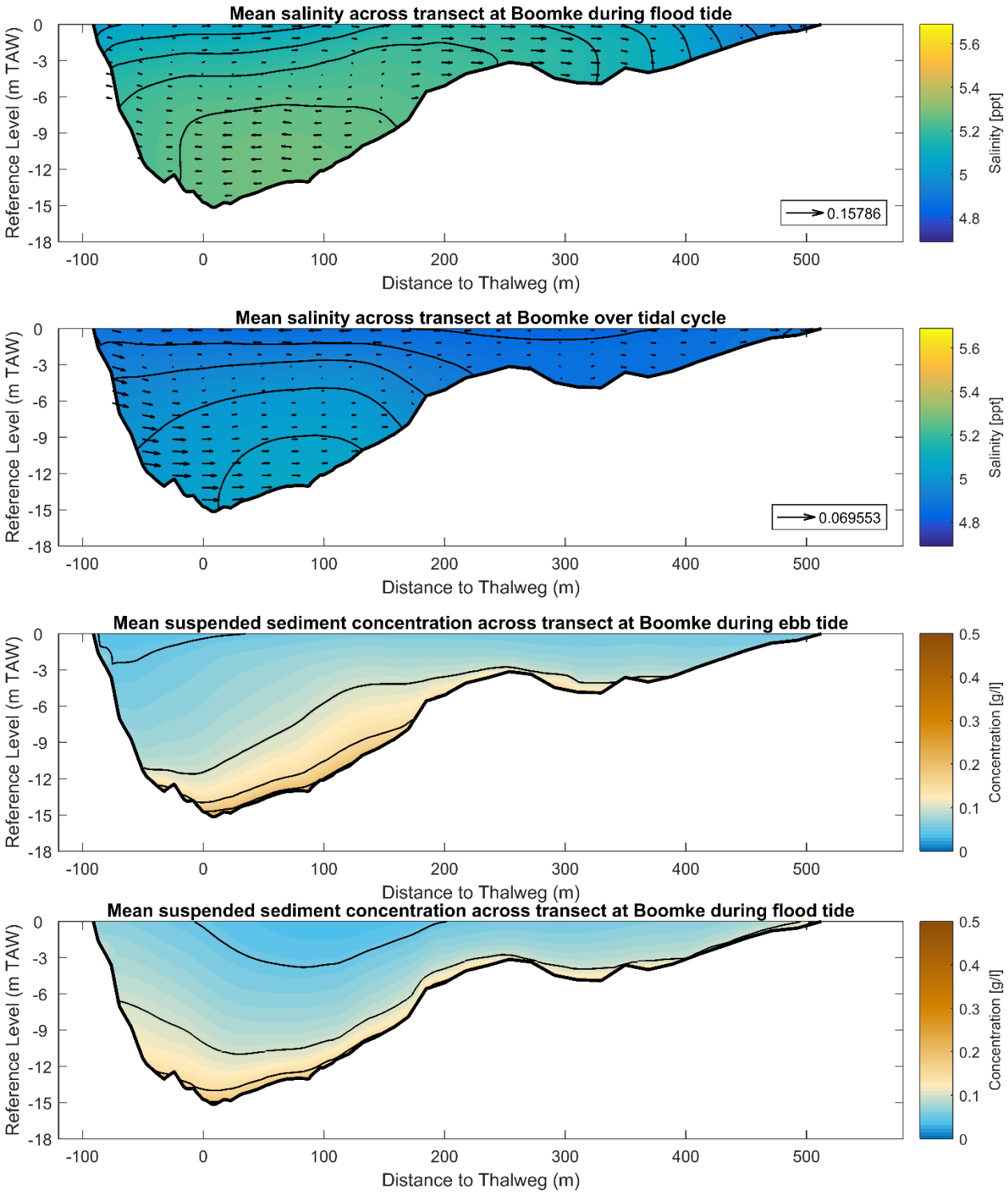
Mean salinity across transect at Boomke during flood tide
Reference Level (m TAW)
0
-3
-6
-9
-12
-15
-18
-100
0
100
200
300
400
500
Distance to Thalweg (m)
0.15786
Salinity [ppt]
5.6
5.4
5.2
5
4.8
Mean salinity across transect at Boomke over tidal cycle
Reference Level (m TAW)
Distance to Thalweg (m)
0.069553
Salinity [ppt]
Mean suspended sediment concentration across transect at Boomke during ebb tide
Reference Level (m TAW)
Distance to Thalweg (m)
Concentration [g/l]
0.5
0.4
0.3
0.2
0.1
0
Mean suspended sediment concentration across transect at Boomke during flood tide
Reference Level (m TAW)
Distance to Thalweg (m)
Concentration [g/l]

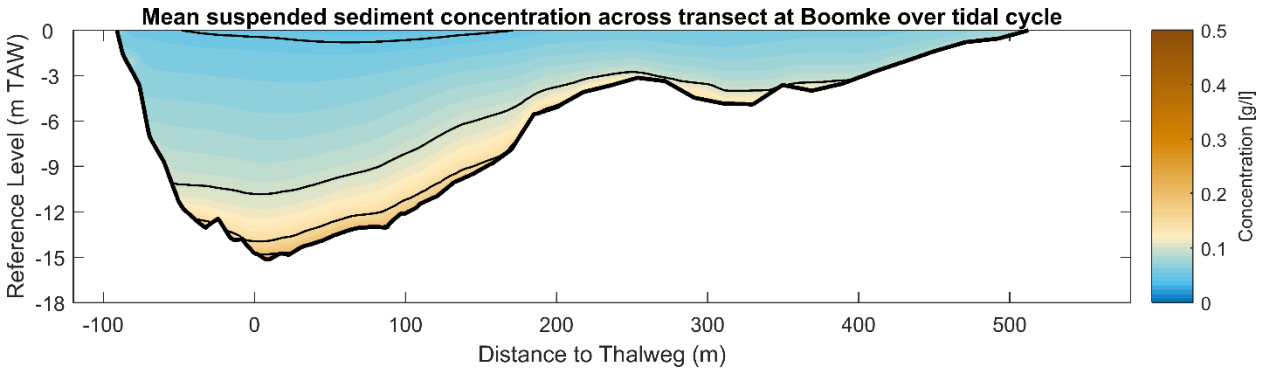
Mean suspended sediment concentration across transect at Boomke over tidal cycle
Reference Level (m TAW)
0
-3
-6
-9
-12
-15
-18
-100
0
100
200
300
400
500
Distance to Thalweg (m)
0.5
0.4
0.3
0.2
0.1
0
Concentration [g/l]

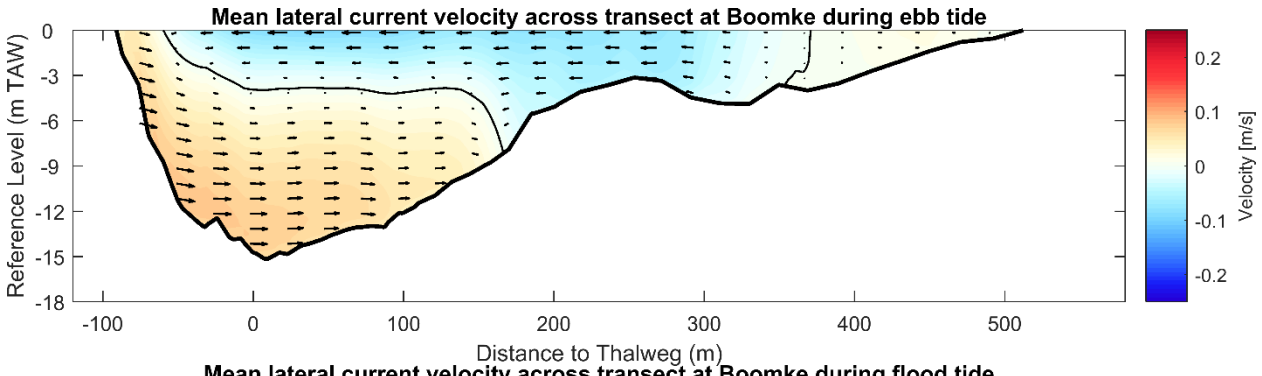
Mean lateral current velocity across transect at Boomke during ebb tide
Reference Level (m TAW)
0
-3
-6
-9
-12
-15
-18
-100
0
100
200
300
400
500
Distance to Thalweg (m)
0.2
0.1
0
-0.1
-0.2
Velocity [m/s]

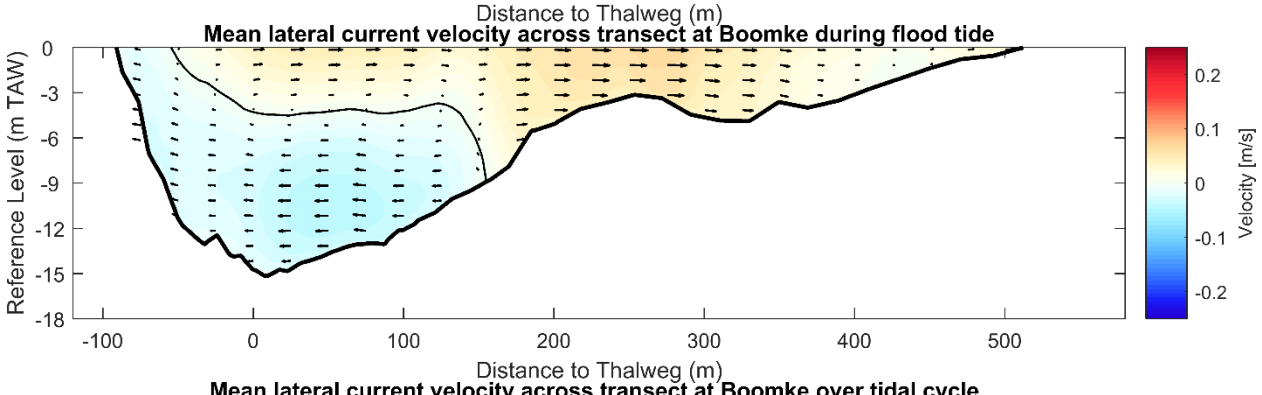
Mean lateral current velocity across transect at Boomke during flood tide
Reference Level (m TAW)
0
-3
-6
-9
-12
-15
-18
-100
0
100
200
300
400
500
Distance to Thalweg (m)
0.2
0.1
0
-0.1
-0.2
Velocity [m/s]

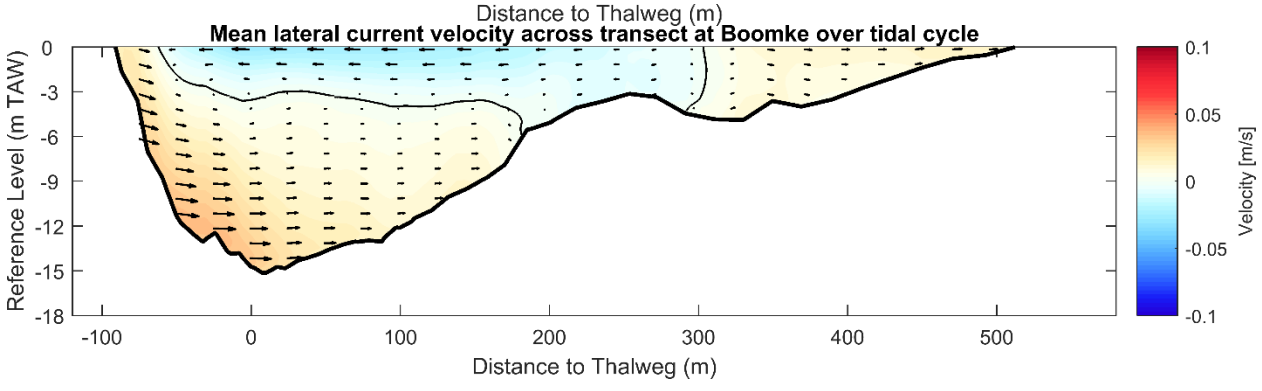
Mean lateral current velocity across transect at Boomke over tidal cycle
Reference Level (m TAW)
0
-3
-6
-9
-12
-15
-18
-100
0
100
200
300
400
500
Distance to Thalweg (m)
0.1
0.05
0
-0.05
-0.1
Velocity [m/s]

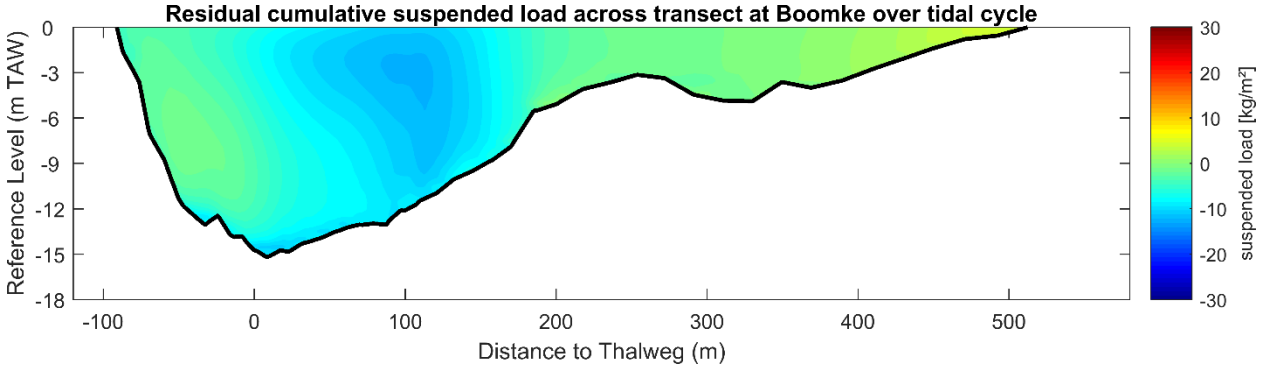
Residual cumulative suspended load across transect at Boomke over tidal cycle
Reference Level (m TAW)
0
-3
-6
-9
-12
-15
-18
-100
0
100
200
300
400
500
Distance to Thalweg (m)
30
20
10
0
-10
-20
-30
suspended load [kg/m²]

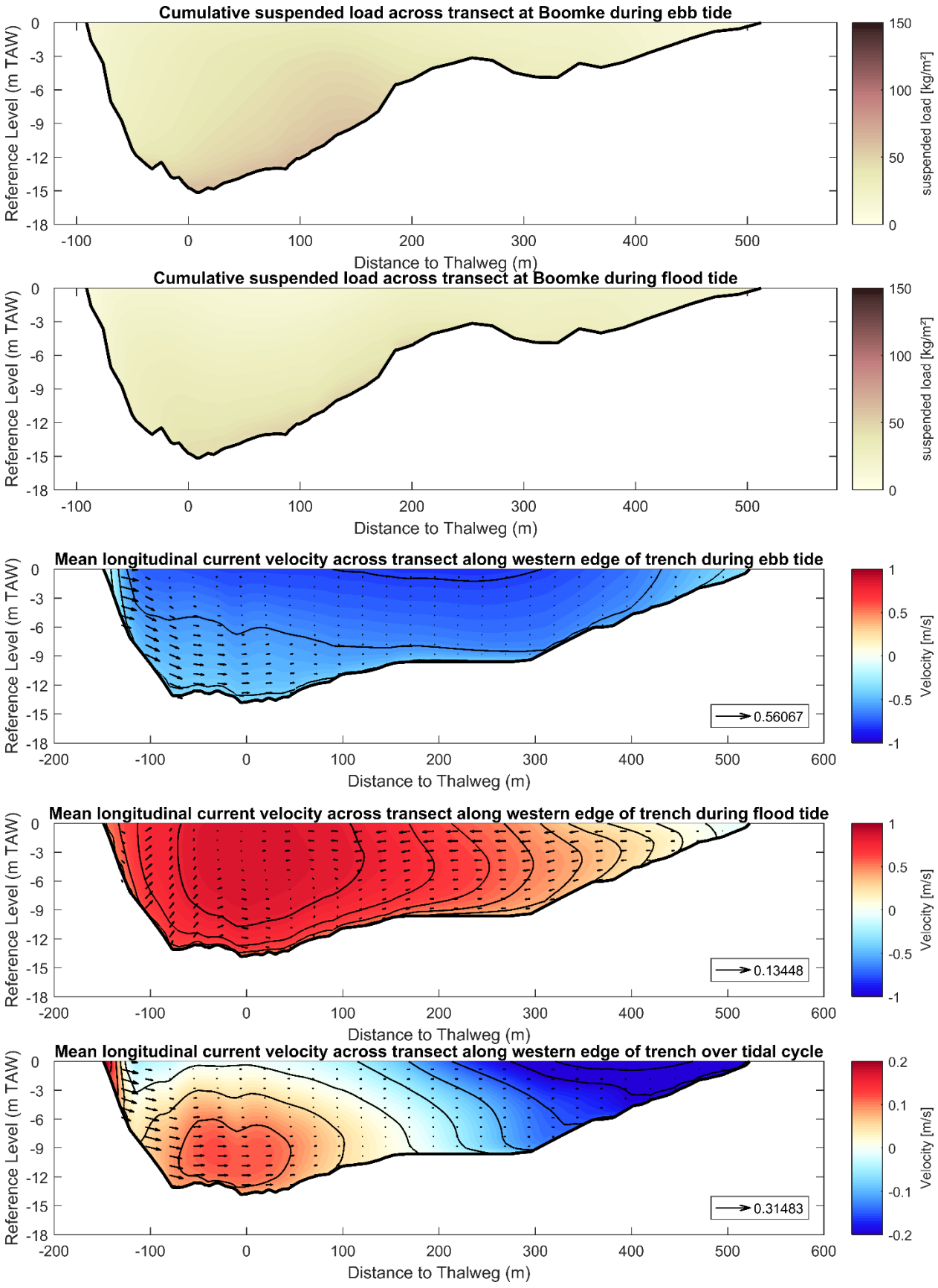
Cumulative suspended load across transect at Boomke during ebb tide
Reference Level (m TAW)
Distance to Thalweg (m)
suspended load [kg/m²]
Cumulative suspended load across transect at Boomke during flood tide
Reference Level (m TAW)
Distance to Thalweg (m)
suspended load [kg/m²]
Mean longitudinal current velocity across transect along western edge of trench during ebb tide
0.56067
Reference Level (m TAW)
Distance to Thalweg (m)
Velocity [m/s]
Mean longitudinal current velocity across transect along western edge of trench during flood tide
0.13448
Reference Level (m TAW)
Distance to Thalweg (m)
Velocity [m/s]
Mean longitudinal current velocity across transect along western edge of trench over tidal cycle
0.31483
Reference Level (m TAW)
Distance to Thalweg (m)
Velocity [m/s]

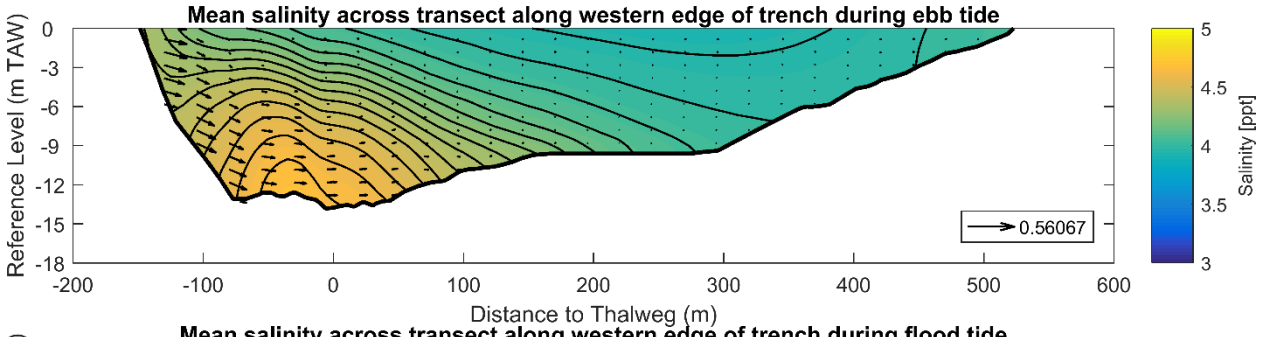
Mean salinity across transect along western edge of trench during ebb tide
Reference Level (m TAW)
Distance to Thalweg (m)
Salinity [ppt]
0.56067

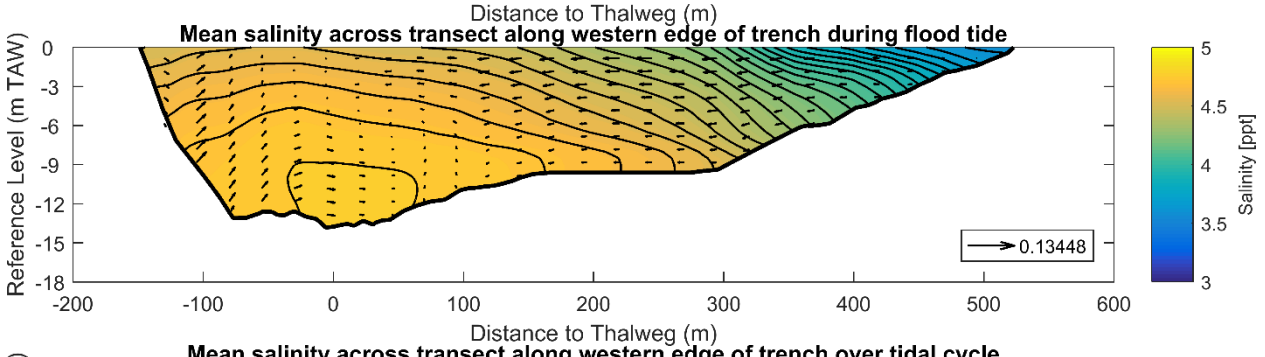
Mean salinity across transect along western edge of trench during flood tide
Reference Level (m TAW)
Distance to Thalweg (m)
Salinity [ppt]
0.13448

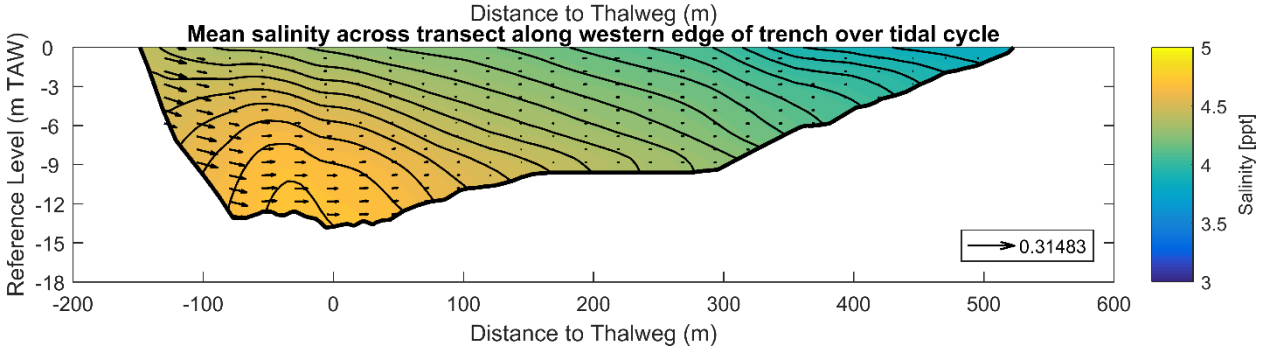
Mean salinity across transect along western edge of trench over tidal cycle
Reference Level (m TAW)
Distance to Thalweg (m)
Salinity [ppt]
0.31483

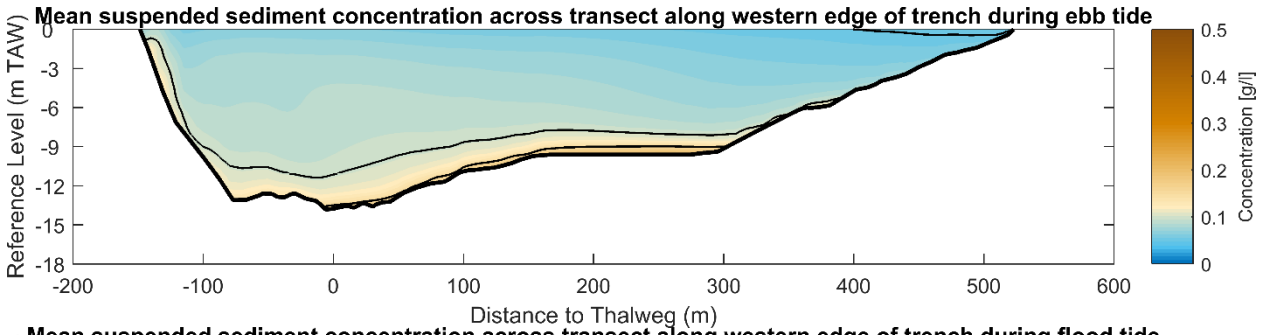
Mean suspended sediment concentration across transect along western edge of trench during ebb tide
Reference Level (m TAW)
Distance to Thalweg (m)
Concentration [g/l]

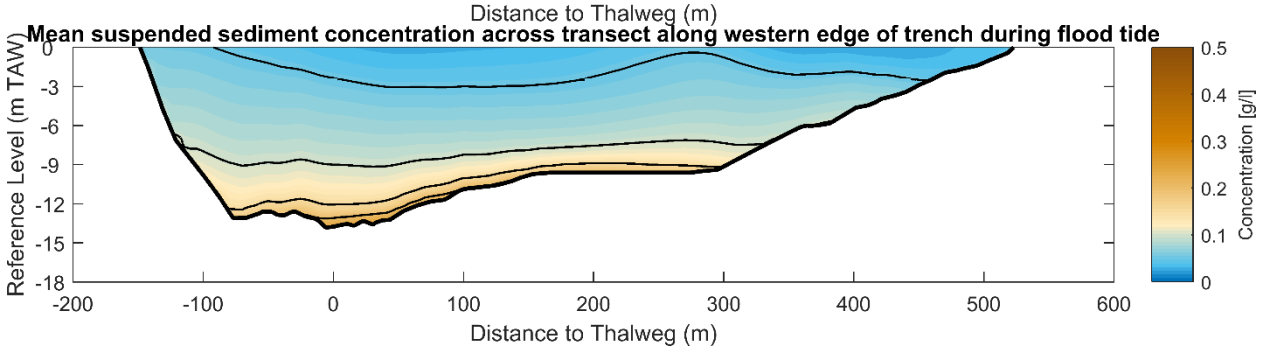
Mean suspended sediment concentration across transect along western edge of trench during flood tide
Reference Level (m TAW)
Distance to Thalweg (m)
Concentration [g/l]

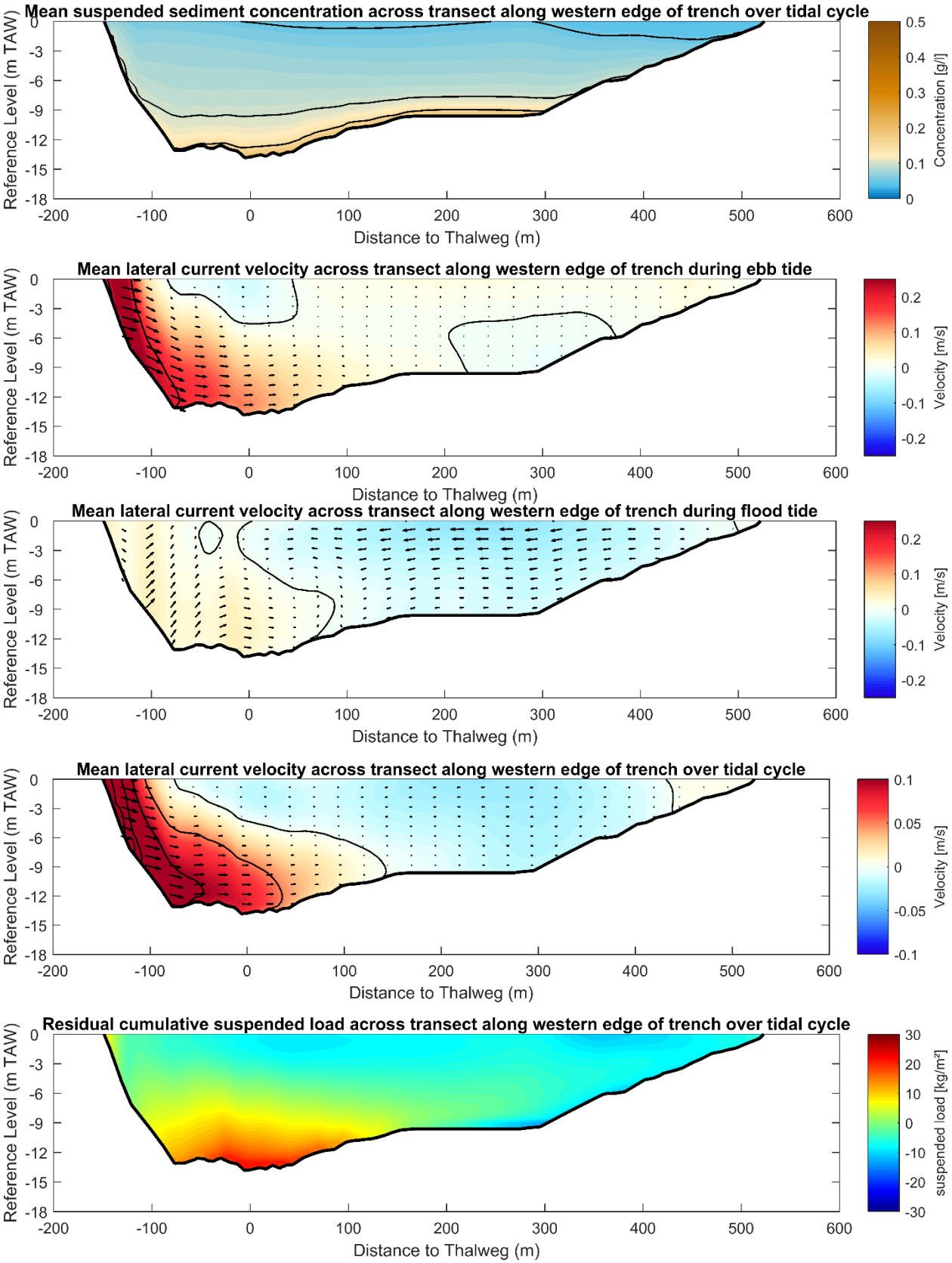
Mean suspended sediment concentration across transect along western edge of trench over tidal cycle
Reference Level (m TAW)
Distance to Thalweg (m)
Concentration [g/l]
Mean lateral current velocity across transect along western edge of trench during ebb tide
Velocity [m/s]
Mean lateral current velocity across transect along western edge of trench during flood tide
Mean lateral current velocity across transect along western edge of trench over tidal cycle
Residual cumulative suspended load across transect along western edge of trench over tidal cycle
suspended load [kg/m²]

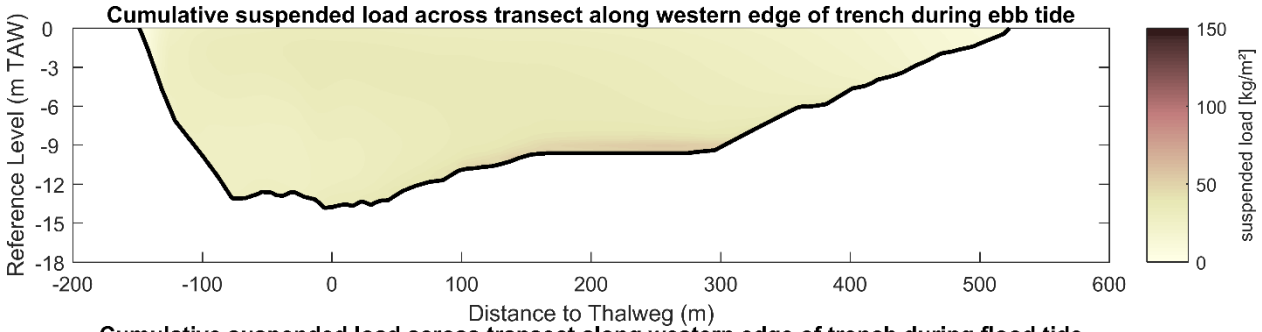
Cumulative suspended load across transect along western edge of trench during ebb tide
Reference Level (m TAW)
Distance to Thalweg (m)
suspended load [kg/m²]

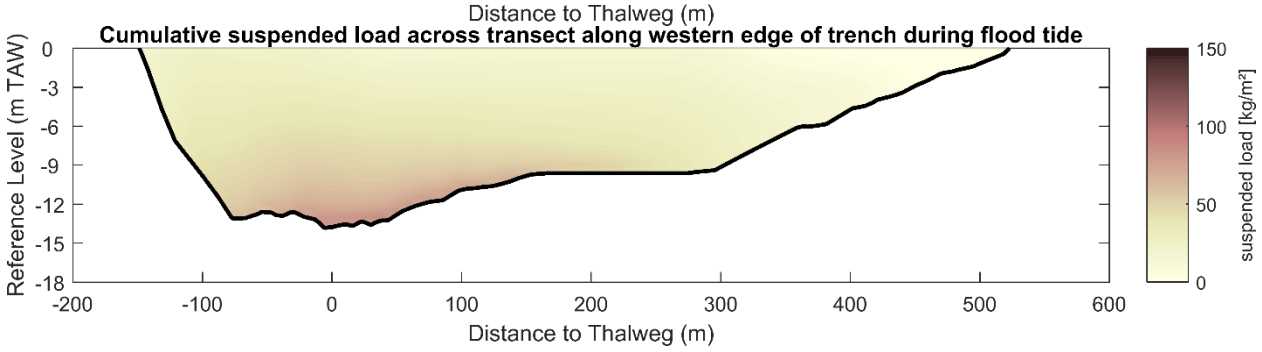
Cumulative suspended load across transect along western edge of trench during flood tide
Reference Level (m TAW)
Distance to Thalweg (m)
suspended load [kg/m²]

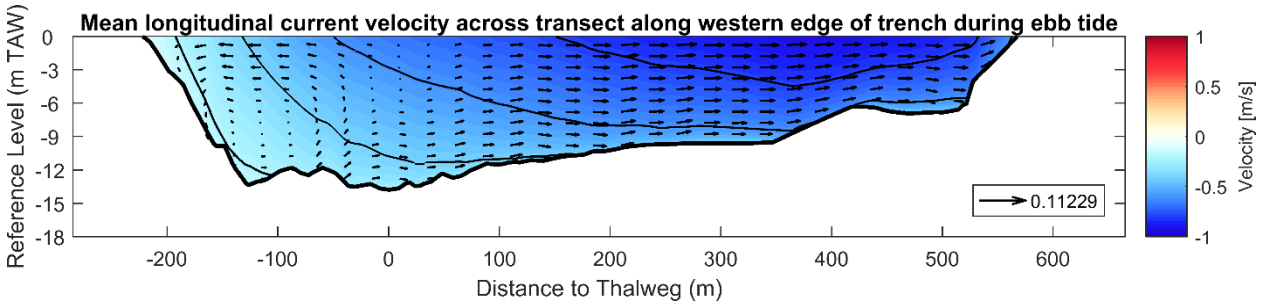
Mean longitudinal current velocity across transect along western edge of trench during ebb tide
0.11229
Reference Level (m TAW)
Distance to Thalweg (m)
Velocity [m/s]

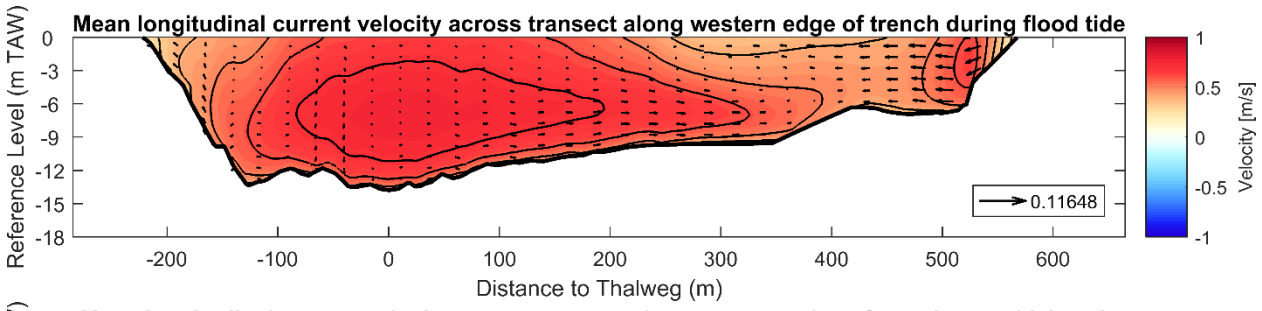
Mean longitudinal current velocity across transect along western edge of trench during flood tide
0.11648
Reference Level (m TAW)
Distance to Thalweg (m)
Velocity [m/s]

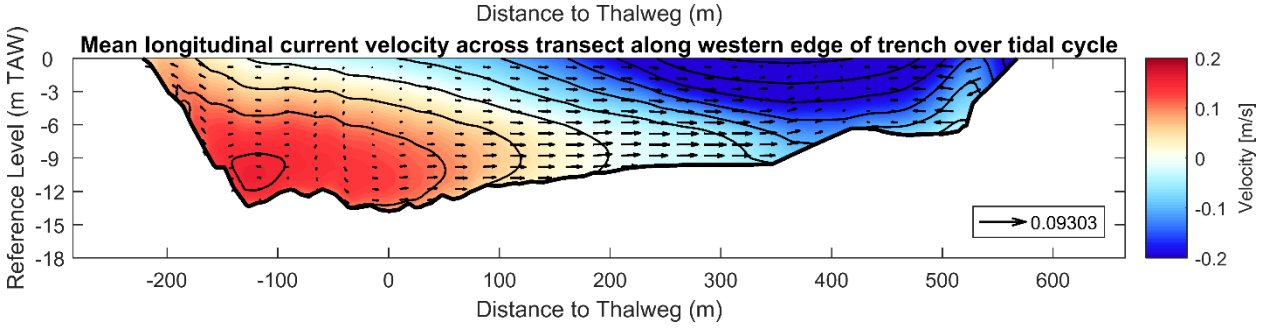
Mean longitudinal current velocity across transect along western edge of trench over tidal cycle
0.09303
Reference Level (m TAW)
Distance to Thalweg (m)
Velocity [m/s]

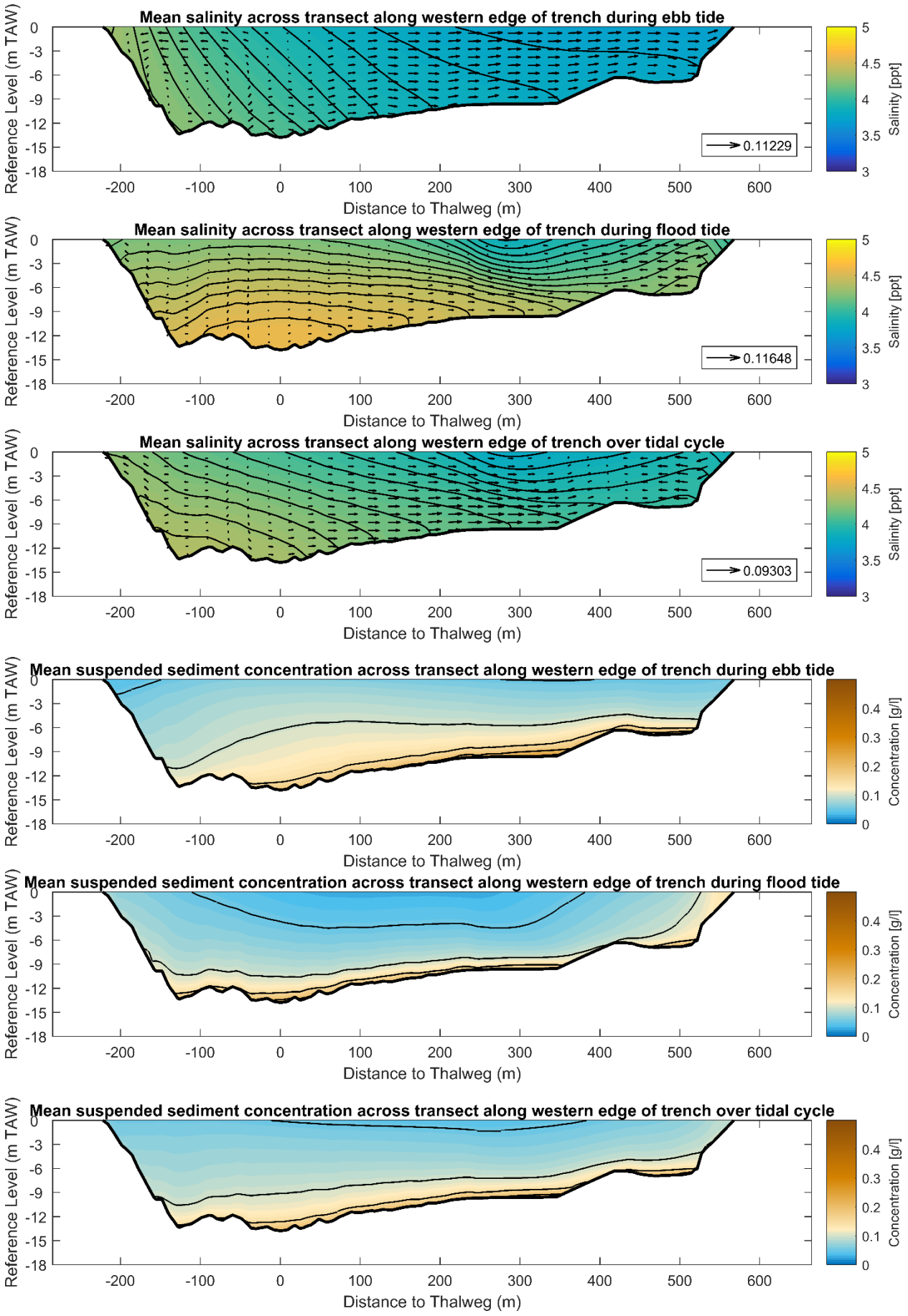
Mean salinity across transect along western edge of trench during ebb tide
Reference Level (m TAW)
Distance to Thalweg (m)
Salinity [ppt]
0.11229
Mean salinity across transect along western edge of trench during flood tide
0.11648
Mean salinity across transect along western edge of trench over tidal cycle
0.09303
Mean suspended sediment concentration across transect along western edge of trench during ebb tide
Concentration [g/l]
Mean suspended sediment concentration across transect along western edge of trench during flood tide
Mean suspended sediment concentration across transect along western edge of trench over tidal cycle

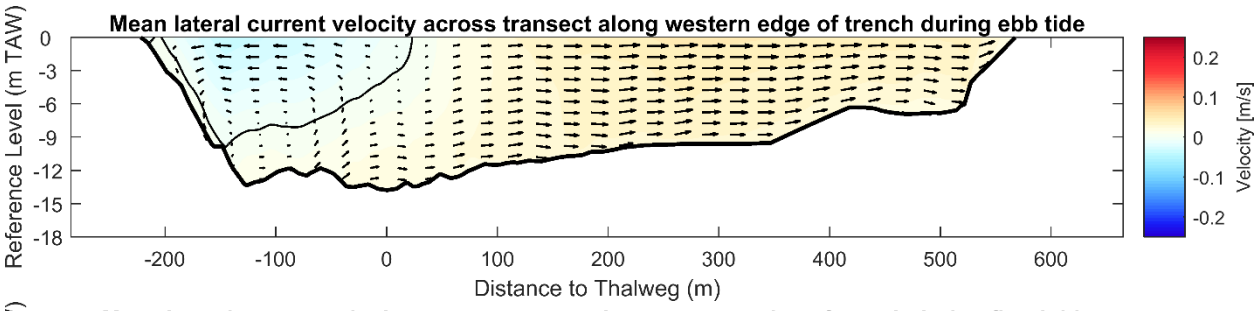
Mean lateral current velocity across transect along western edge of trench during ebb tide
Reference Level (m TAW)
0
-3
-6
-9
-12
-15
-18
-200
-100
0
100
200
300
400
500
600
Distance to Thalweg (m)
0.2
0.1
0
-0.1
-0.2
Velocity [m/s]

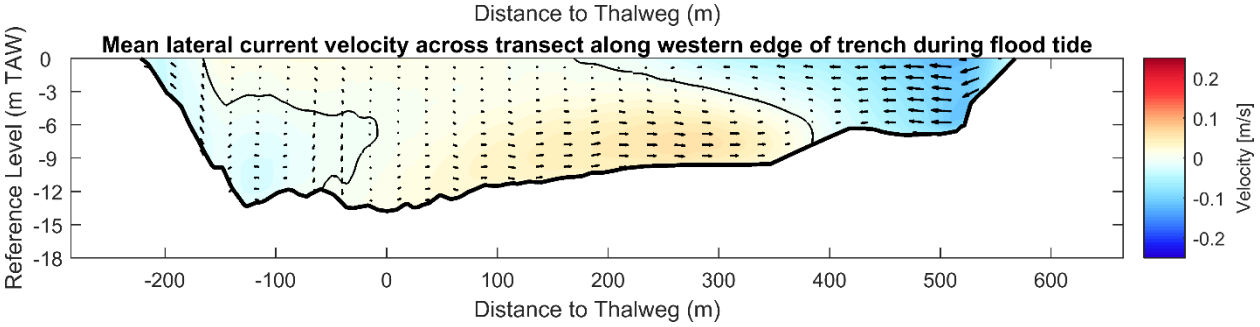
Mean lateral current velocity across transect along western edge of trench during flood tide
Reference Level (m TAW)
0
-3
-6
-9
-12
-15
-18
-200
-100
0
100
200
300
400
500
600
Distance to Thalweg (m)
0.2
0.1
0
-0.1
-0.2
Velocity [m/s]

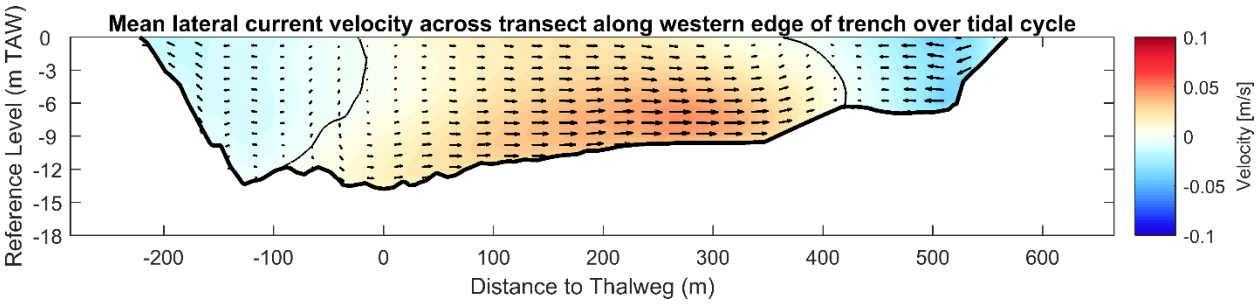
Mean lateral current velocity across transect along western edge of trench over tidal cycle
Reference Level (m TAW)
0
-3
-6
-9
-12
-15
-18
-200
-100
0
100
200
300
400
500
600
Distance to Thalweg (m)
0.1
0.05
0
-0.05
-0.1
Velocity [m/s]

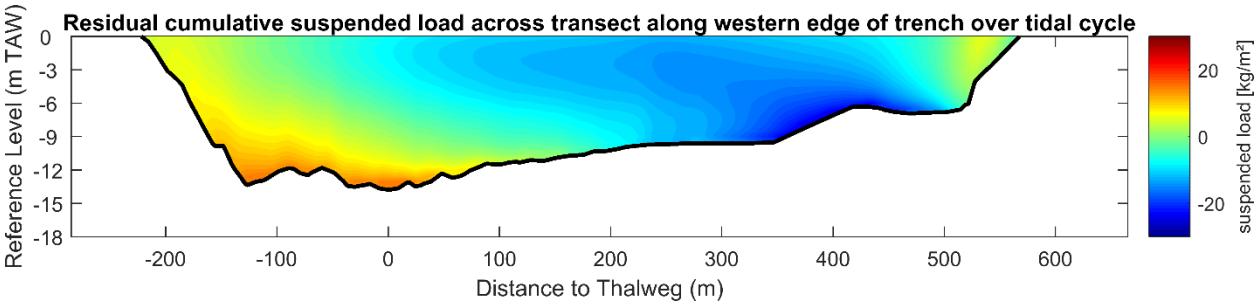
Residual cumulative suspended load across transect along western edge of trench over tidal cycle
Reference Level (m TAW)
0
-3
-6
-9
-12
-15
-18
-200
-100
0
100
200
300
400
500
600
Distance to Thalweg (m)
20
0
-20
suspended load [kg/m²]

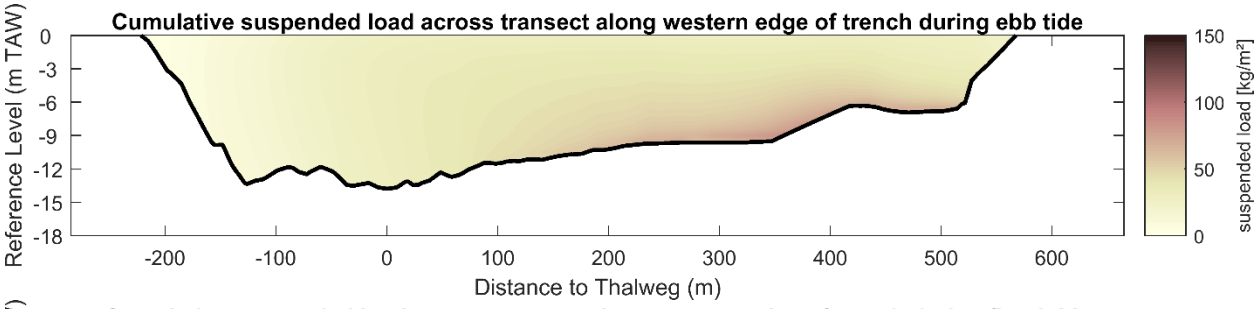
Cumulative suspended load across transect along western edge of trench during ebb tide
Reference Level (m TAW)
0
-3
-6
-9
-12
-15
-18
-200
-100
0
100
200
300
400
500
600
Distance to Thalweg (m)
150
100
50
0
suspended load [kg/m²]

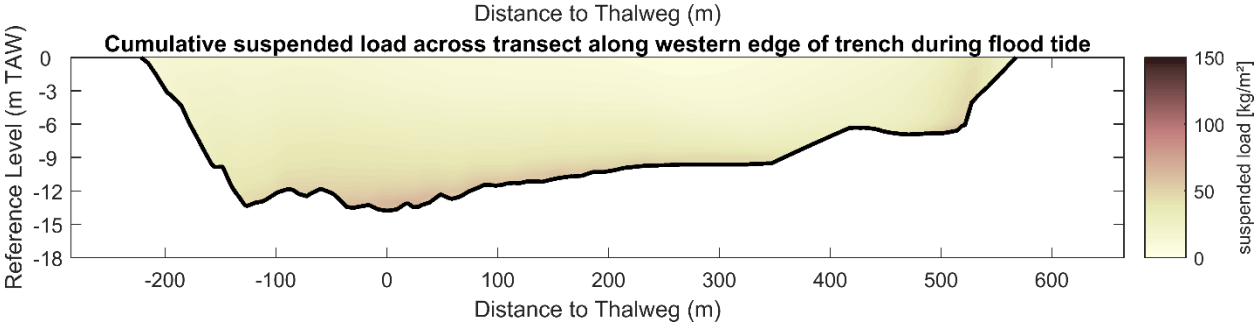
Cumulative suspended load across transect along western edge of trench during flood tide
Reference Level (m TAW)
0
-3
-6
-9
-12
-15
-18
-200
-100
0
100
200
300
400
500
600
Distance to Thalweg (m)
150
100
50
0
suspended load [kg/m²]

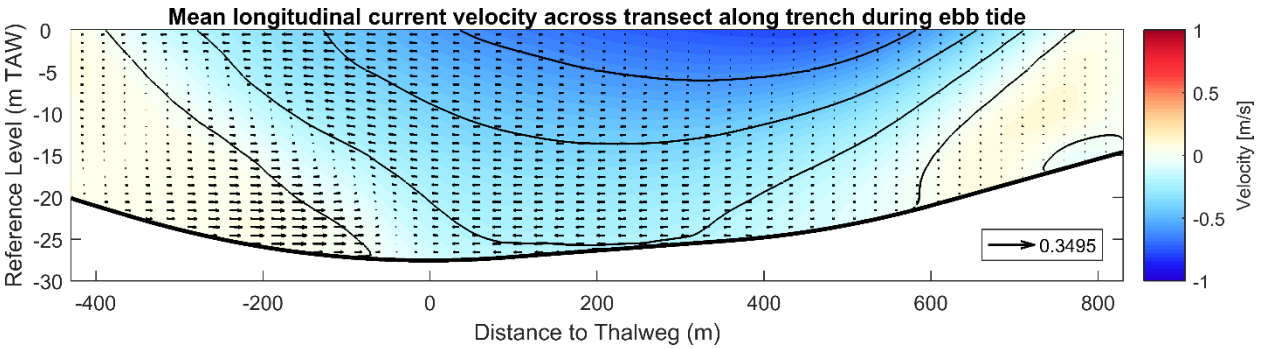
Mean longitudinal current velocity across transect along trench during ebb tide
Reference Level (m TAW)
Distance to Thalweg (m)
Velocity [m/s]
0.3495

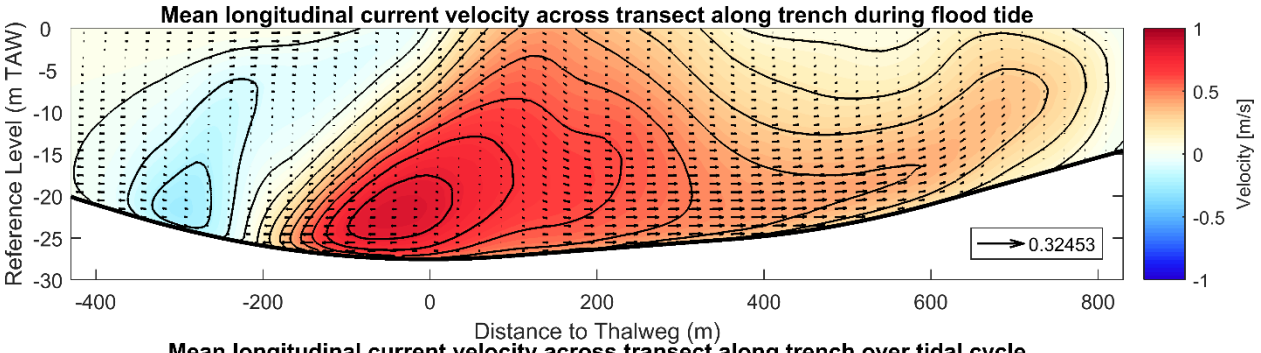
Mean longitudinal current velocity across transect along trench during flood tide
Reference Level (m TAW)
Distance to Thalweg (m)
Velocity [m/s]
0.32453

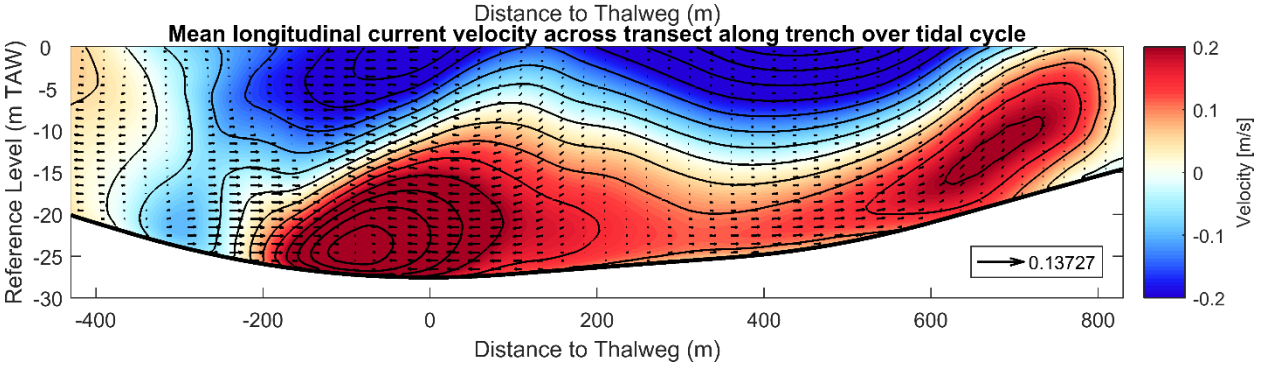
Mean longitudinal current velocity across transect along trench over tidal cycle
Reference Level (m TAW)
Distance to Thalweg (m)
Velocity [m/s]
0.13727

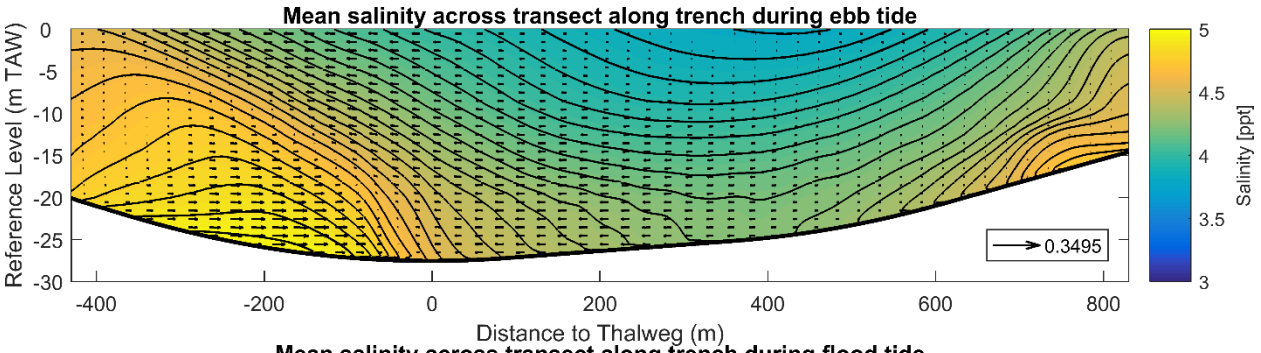
Mean salinity across transect along trench during ebb tide
Reference Level (m TAW)
Distance to Thalweg (m)
Salinity [ppt]
0.3495

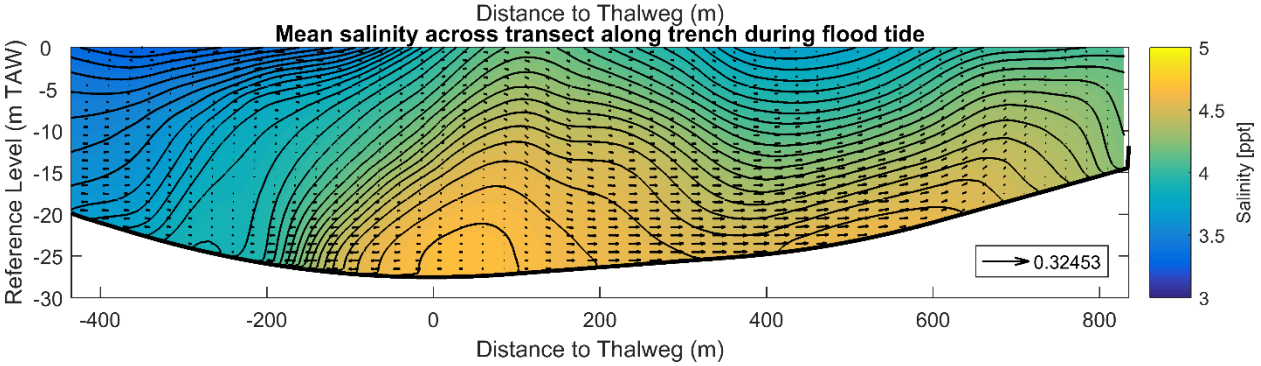
Mean salinity across transect along trench during flood tide
Reference Level (m TAW)
Distance to Thalweg (m)
Salinity [ppt]
0.32453

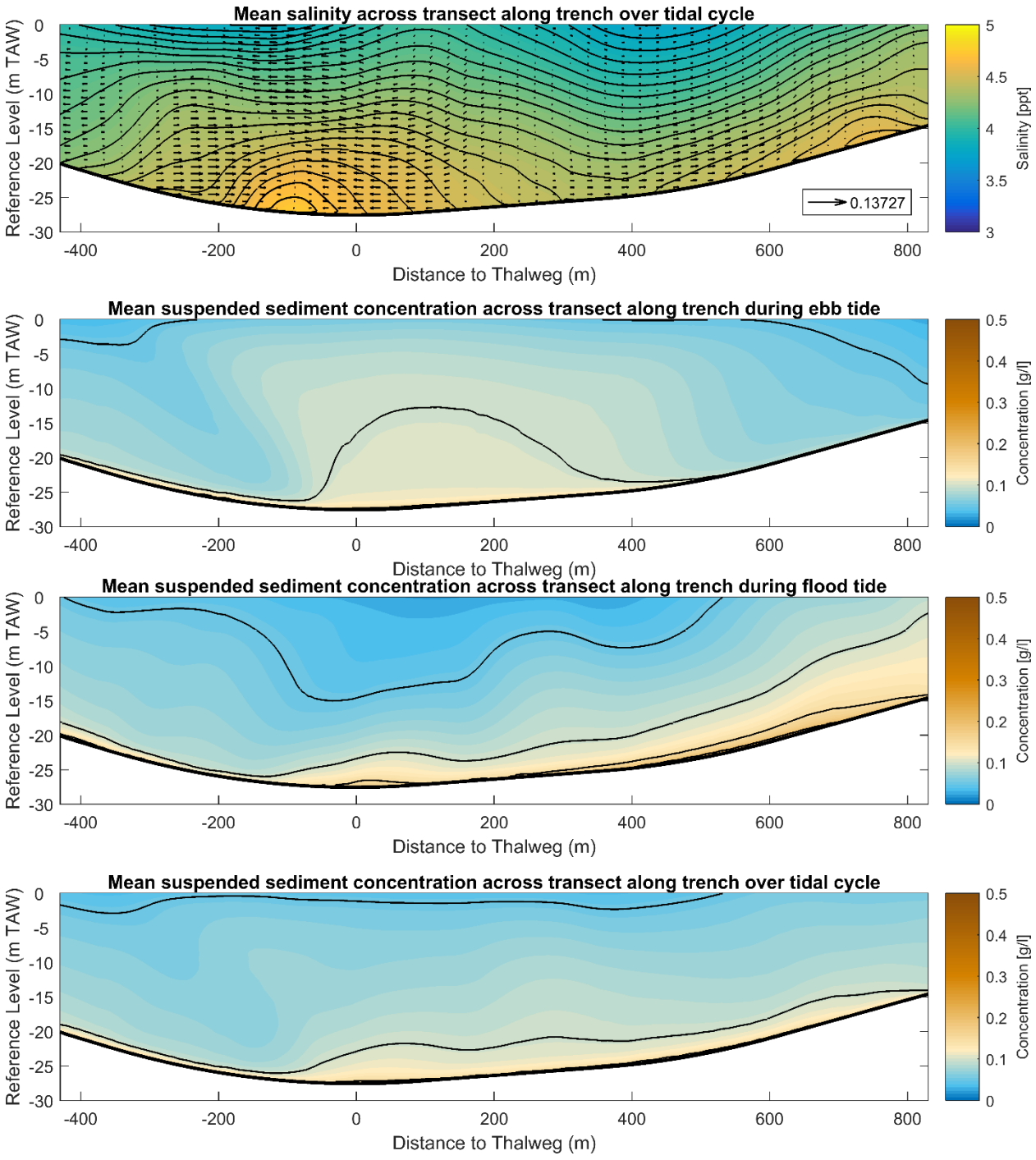
Mean salinity across transect along trench over tidal cycle
Reference Level (m TAW)
0
-5
-10
-15
-20
-25
-30
-400
-200
0
200
400
600
800
Distance to Thalweg (m)
0.13727
5
4.5
4
3.5
3
Salinity [ppt]
Mean suspended sediment concentration across transect along trench during ebb tide
Reference Level (m TAW)
Distance to Thalweg (m)
0.5
0.4
0.3
0.2
0.1
0
Concentration [g/l]
Mean suspended sediment concentration across transect along trench during flood tide
Reference Level (m TAW)
Distance to Thalweg (m)
Concentration [g/l]
Mean suspended sediment concentration across transect along trench over tidal cycle
Reference Level (m TAW)
Distance to Thalweg (m)
Concentration [g/l]

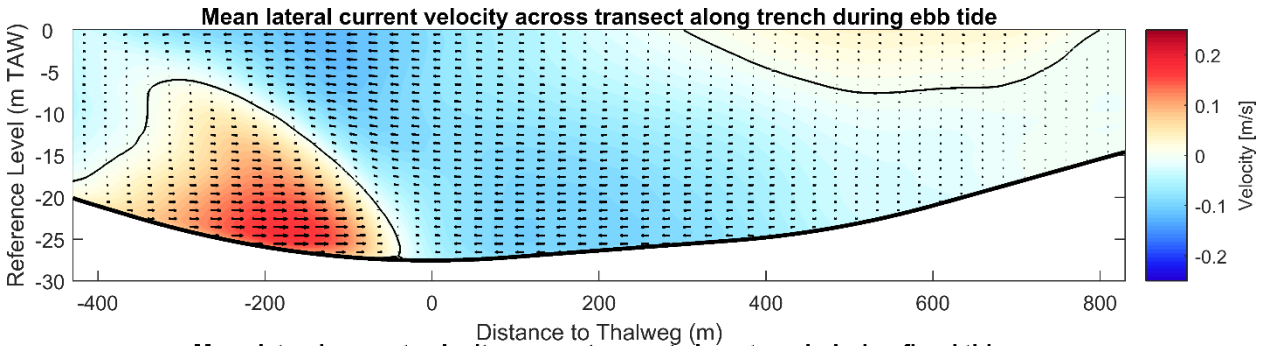
Mean lateral current velocity across transect along trench during ebb tide
Reference Level (m TAW)
0
-5
-10
-15
-20
-25
-30
-400
-200
0
200
400
600
800
Distance to Thalweg (m)
0.2
0.1
0
-0.1
-0.2
Velocity [m/s]

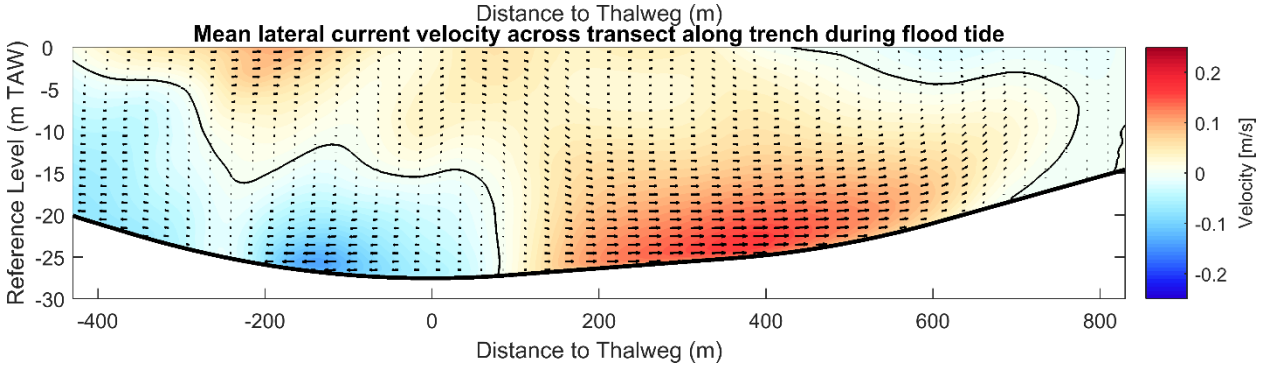
Mean lateral current velocity across transect along trench during flood tide
Reference Level (m TAW)
0
-5
-10
-15
-20
-25
-30
-400
-200
0
200
400
600
800
Distance to Thalweg (m)
0.2
0.1
0
-0.1
-0.2
Velocity [m/s]

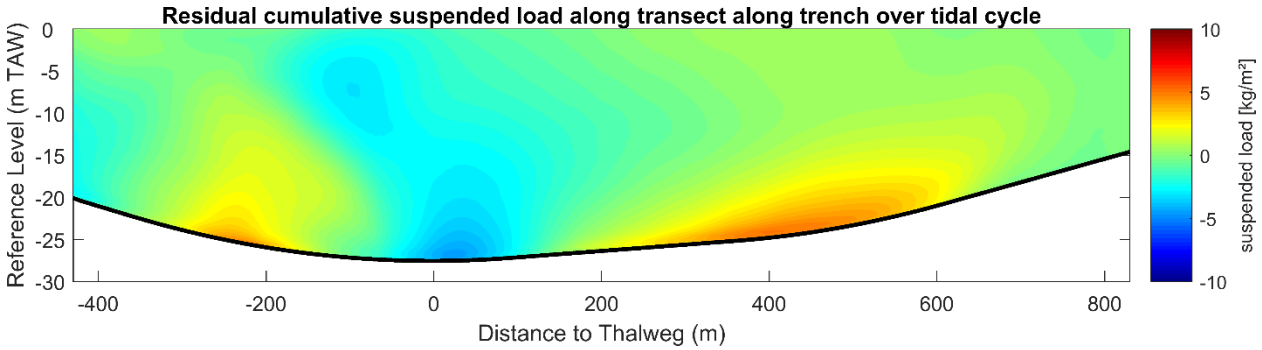
Residual cumulative suspended load along transect along trench over tidal cycle
Reference Level (m TAW)
0
-5
-10
-15
-20
-25
-30
-400
-200
0
200
400
600
800
Distance to Thalweg (m)
10
5
0
-5
-10
suspended load [kg/m²]

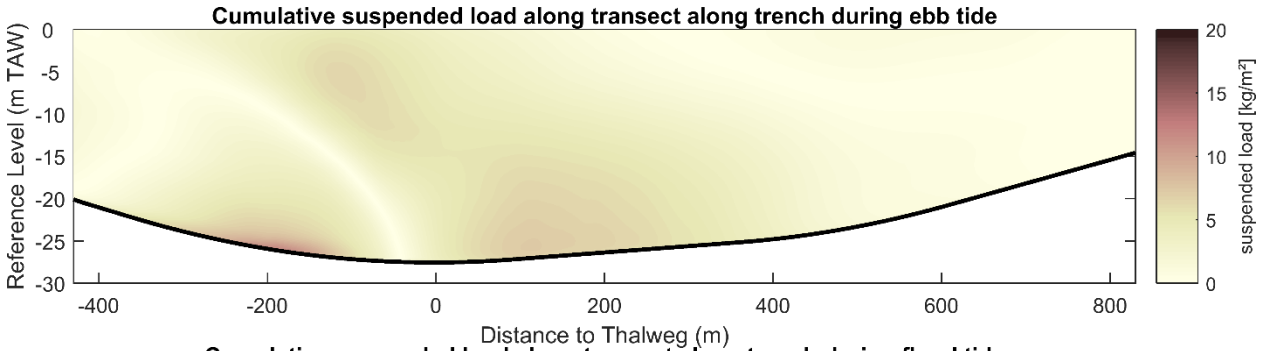
Cumulative suspended load along transect along trench during ebb tide
Reference Level (m TAW)
0
-5
-10
-15
-20
-25
-30
-400
-200
0
200
400
600
800
Distance to Thalweg (m)
20
15
10
5
0
suspended load [kg/m²]

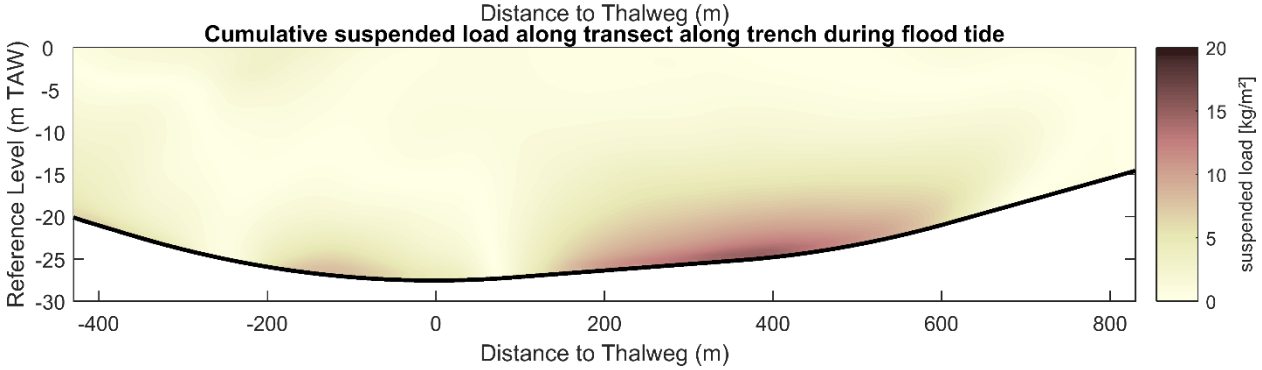
Cumulative suspended load along transect along trench during flood tide
Reference Level (m TAW)
0
-5
-10
-15
-20
-25
-30
-400
-200
0
200
400
600
800
Distance to Thalweg (m)
20
15
10
5
0
suspended load [kg/m²]

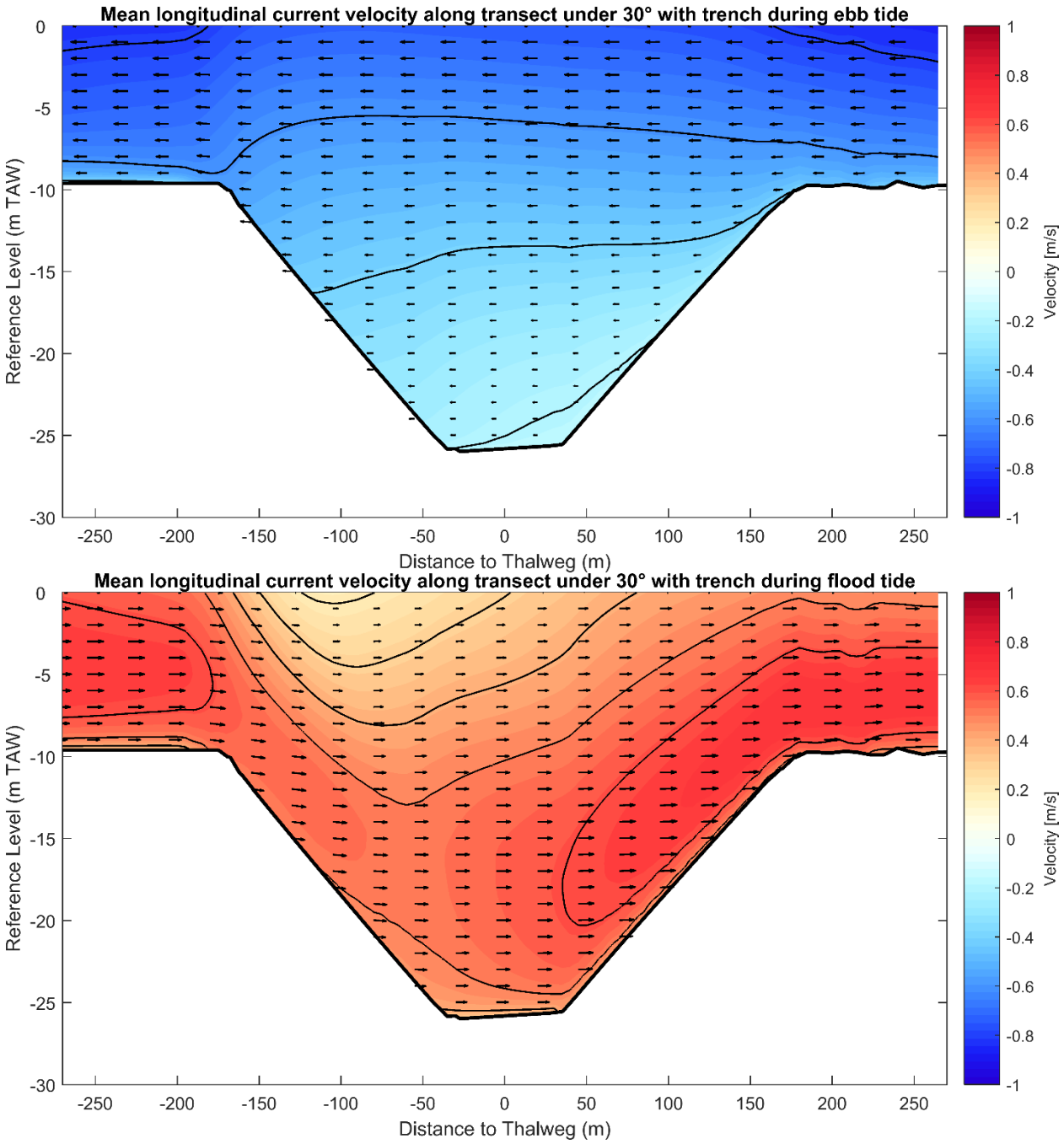
Mean longitudinal current velocity along transect under 30° with trench during ebb tide
Reference Level (m TAW)
Distance to Thalweg (m)
Velocity [m/s]
Mean longitudinal current velocity along transect under 30° with trench during flood tide
Reference Level (m TAW)
Distance to Thalweg (m)
Velocity [m/s]

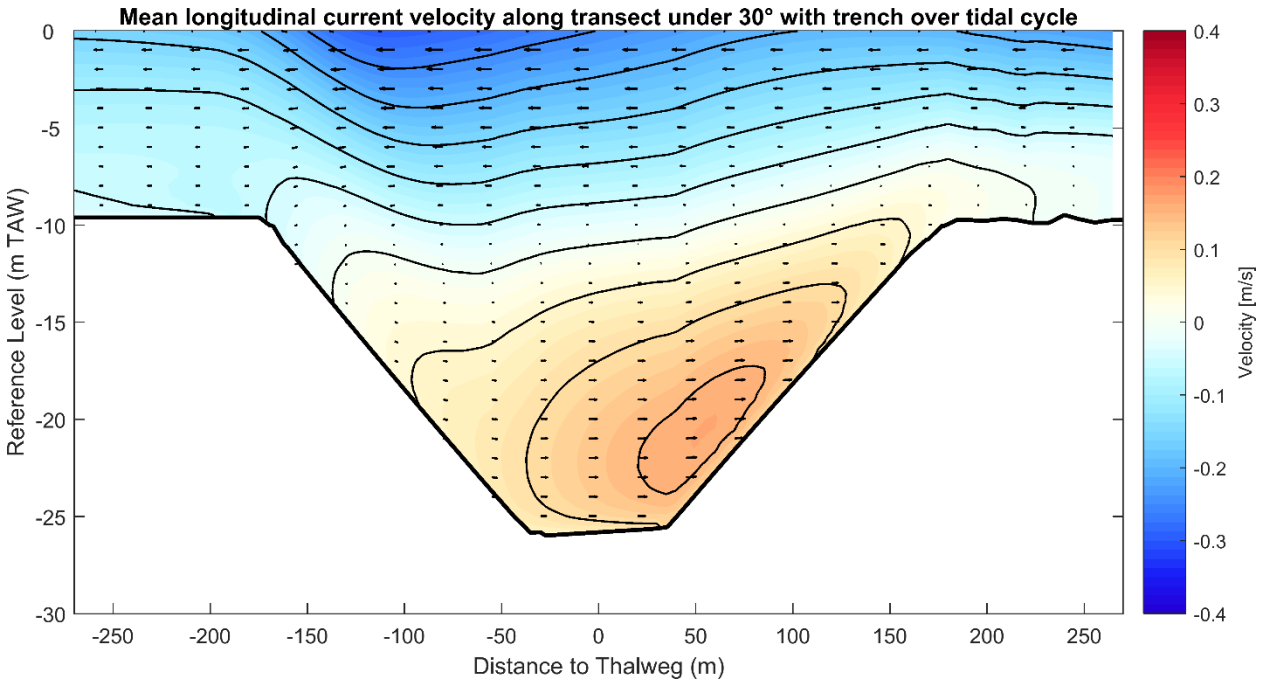
Mean longitudinal current velocity along transect under 30° with trench over tidal cycle
Reference Level (m TAW)
Distance to Thalweg (m)
Velocity [m/s]
0
-5
-10
-15
-20
-25
-30
-250
-200
-150
-100
-50
0
50
100
150
200
250
0.4
0.3
0.2
0.1
0
-0.1
-0.2
-0.3
-0.4

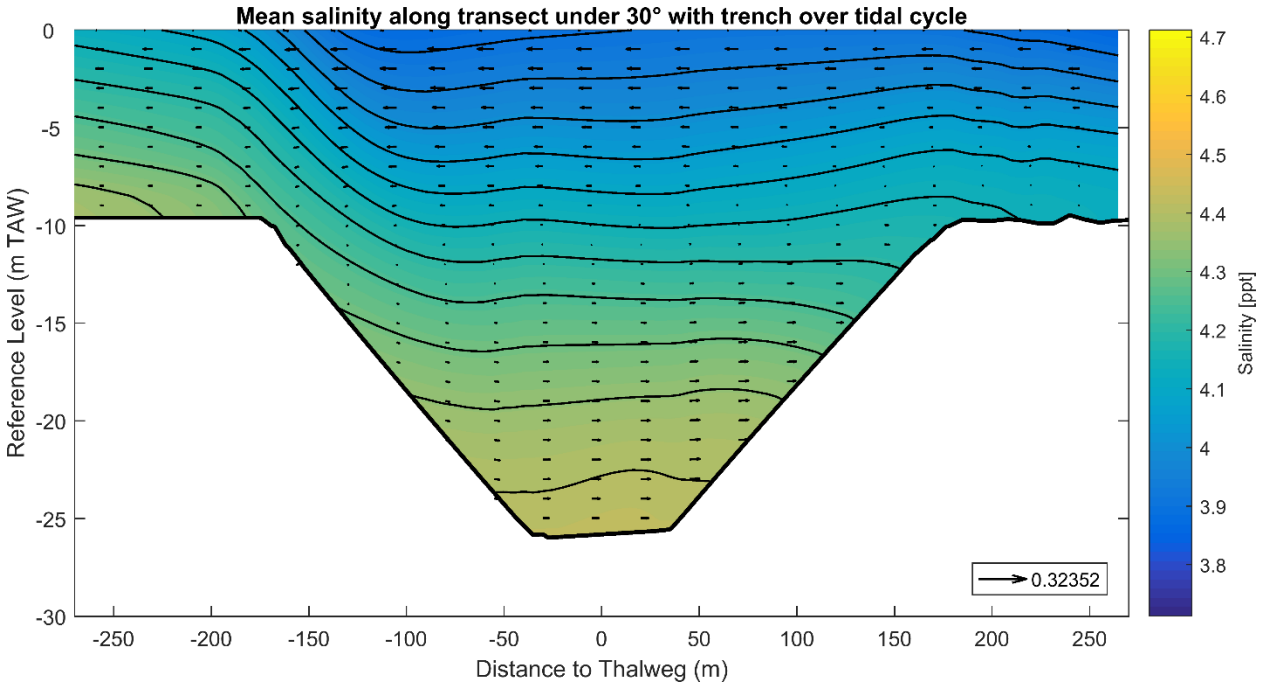
Mean salinity along transect under 30° with trench over tidal cycle
Reference Level (m TAW)
Distance to Thalweg (m)
Salinity [ppt]
0.32352
0
-5
-10
-15
-20
-25
-30
-250
-200
-150
-100
-50
0
50
100
150
200
250
4.7
4.6
4.5
4.4
4.3
4.2
4.1
4
3.9
3.8

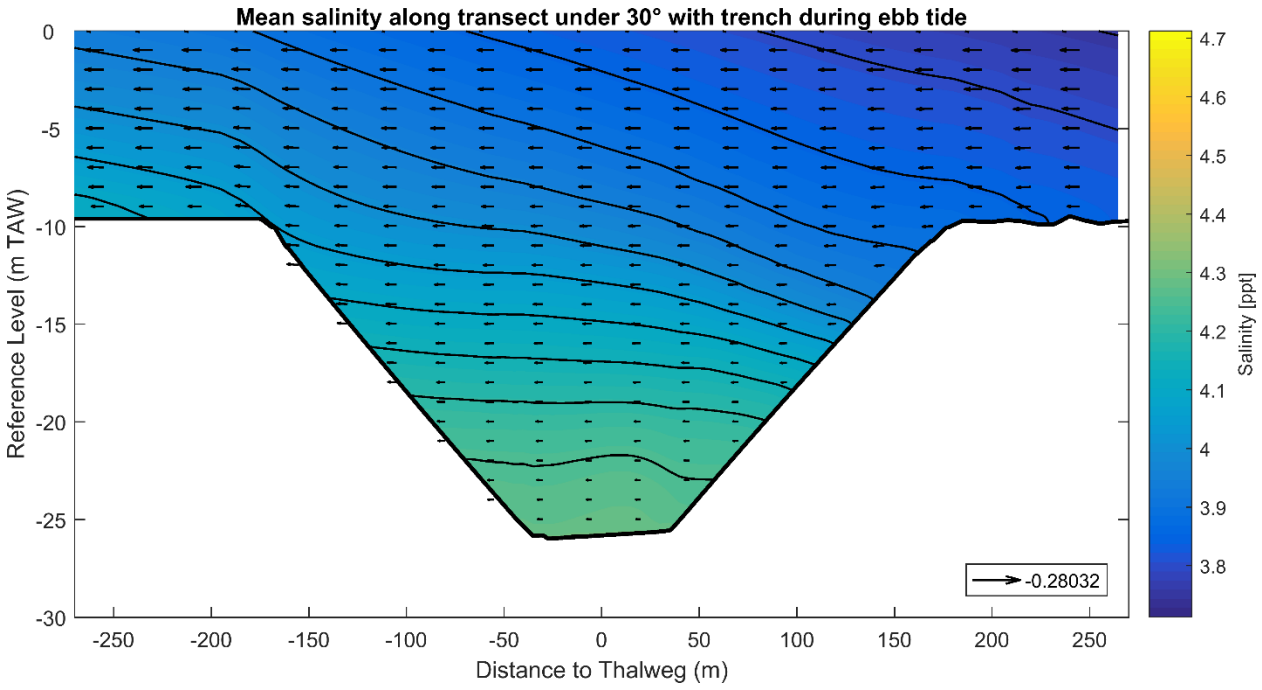
Mean salinity along transect under 30° with trench during ebb tide
Reference Level (m TAW)
0
-5
-10
-15
-20
-25
-30
-250
-200
-150
-100
-50
0
50
100
150
200
250
Distance to Thalweg (m)
-0.28032
Salinity [ppt]
4.7
4.6
4.5
4.4
4.3
4.2
4.1
4
3.9
3.8

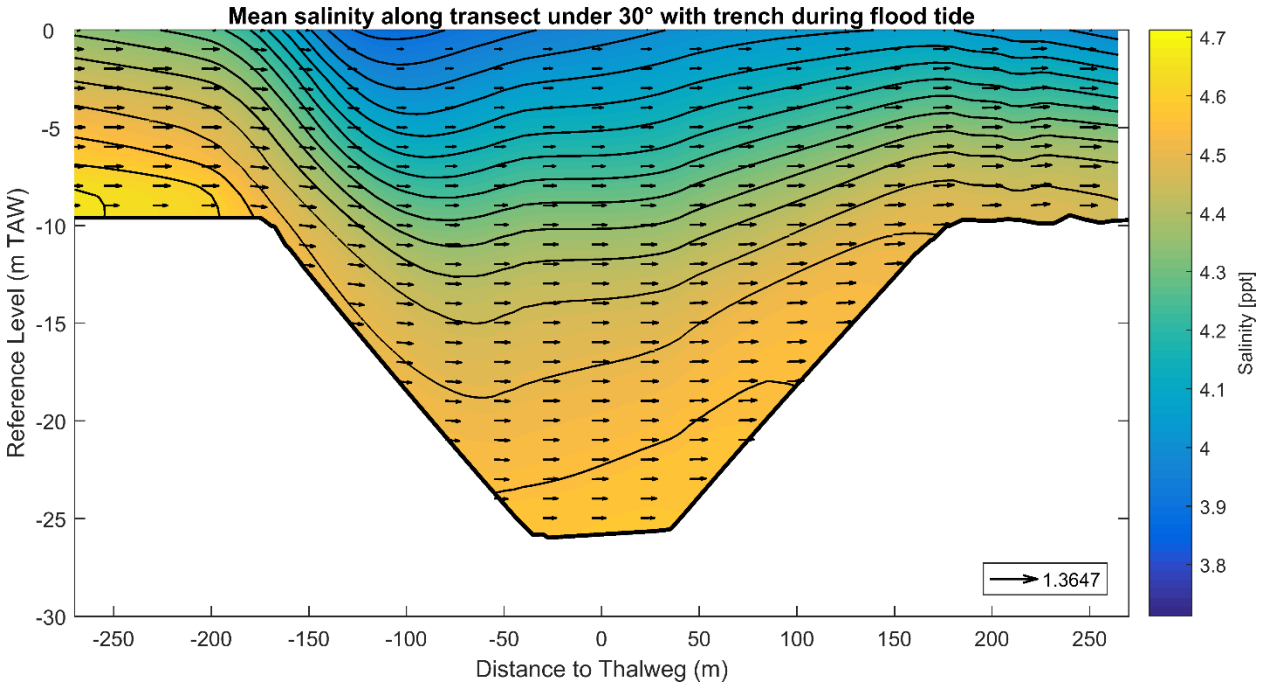
Mean salinity along transect under 30° with trench during flood tide
Reference Level (m TAW)
0
-5
-10
-15
-20
-25
-30
-250
-200
-150
-100
-50
0
50
100
150
200
250
Distance to Thalweg (m)
1.3647
Salinity [ppt]
4.7
4.6
4.5
4.4
4.3
4.2
4.1
4
3.9
3.8

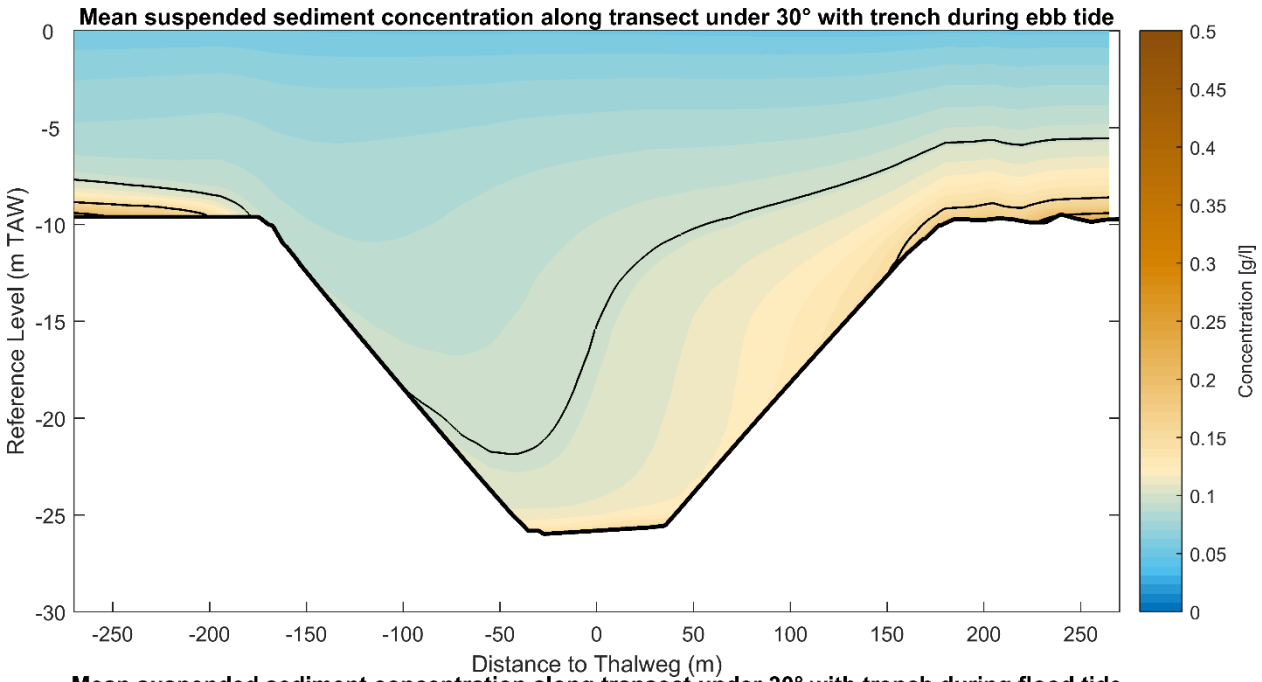
Mean suspended sediment concentration along transect under 30° with trench during ebb tide
Reference Level (m TAW)
0
-5
-10
-15
-20
-25
-30
-250
-200
-150
-100
-50
0
50
100
150
200
250
Distance to Thalweg (m)
Concentration [g/l]
0.5
0.45
0.4
0.35
0.3
0.25
0.2
0.15
0.1
0.05
0

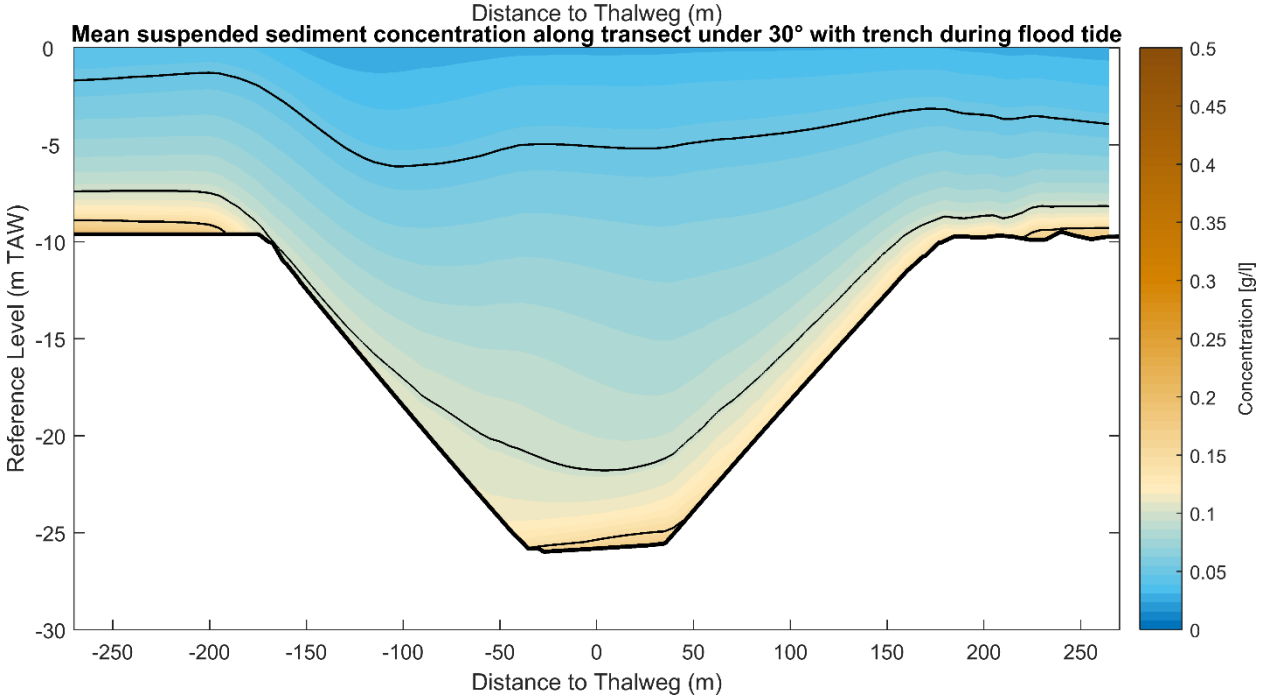
Mean suspended sediment concentration along transect under 30° with trench during flood tide
Reference Level (m TAW)
0
-5
-10
-15
-20
-25
-30
-250
-200
-150
-100
-50
0
50
100
150
200
250
Distance to Thalweg (m)
Concentration [g/l]
0.5
0.45
0.4
0.35
0.3
0.25
0.2
0.15
0.1
0.05
0

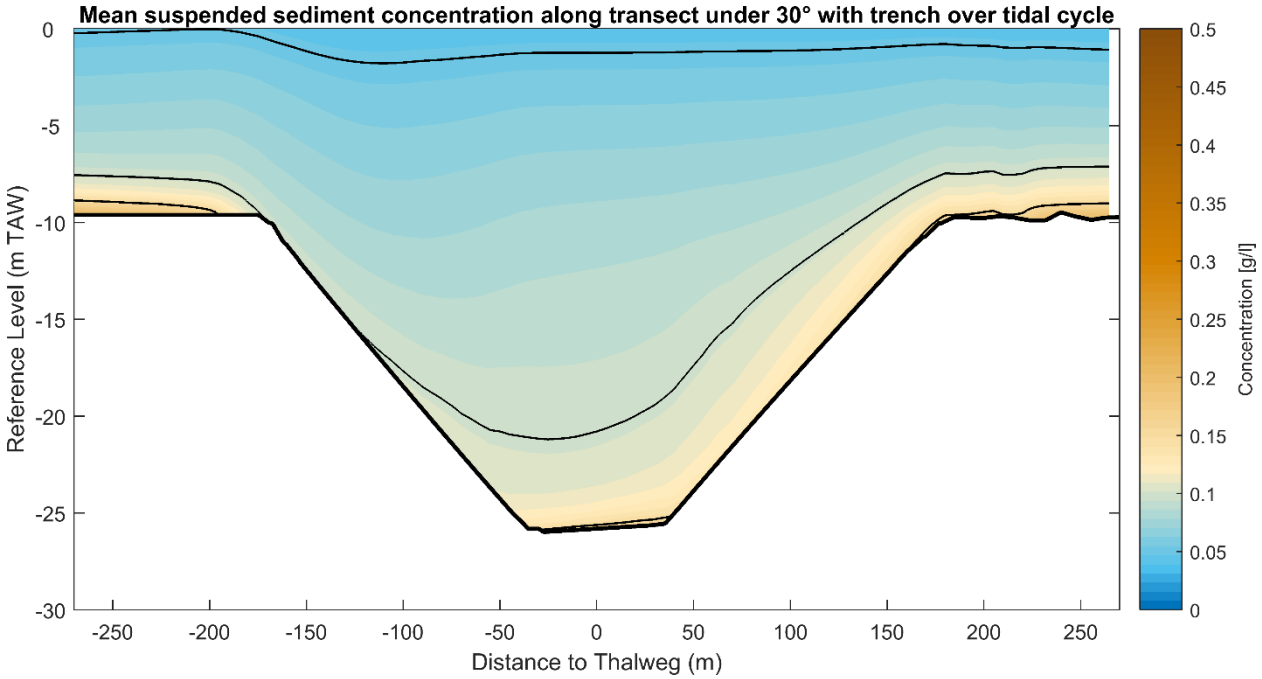
Mean suspended sediment concentration along transect under 30° with trench over tidal cycle
Reference Level (m TAW)
Distance to Thalweg (m)
Concentration [g/l]
0
-5
-10
-15
-20
-25
-30
-250
-200
-150
-100
-50
0
50
100
150
200
250
0.5
0.45
0.4
0.35
0.3
0.25
0.2
0.15
0.1
0.05
0

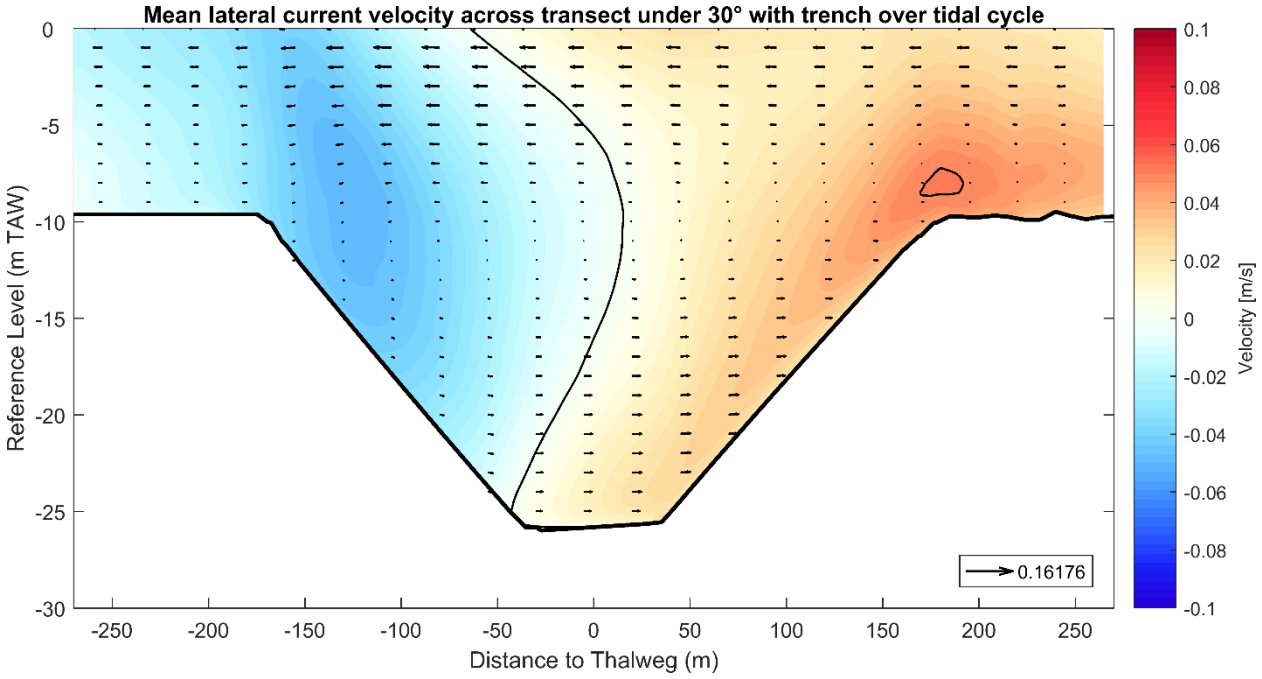
Mean lateral current velocity across transect under 30° with trench over tidal cycle
Reference Level (m TAW)
Distance to Thalweg (m)
Velocity [m/s]
0.16176
0
-5
-10
-15
-20
-25
-30
-250
-200
-150
-100
-50
0
50
100
150
200
250
0.1
0.08
0.06
0.04
0.02
0
-0.02
-0.04
-0.06
-0.08
-0.1

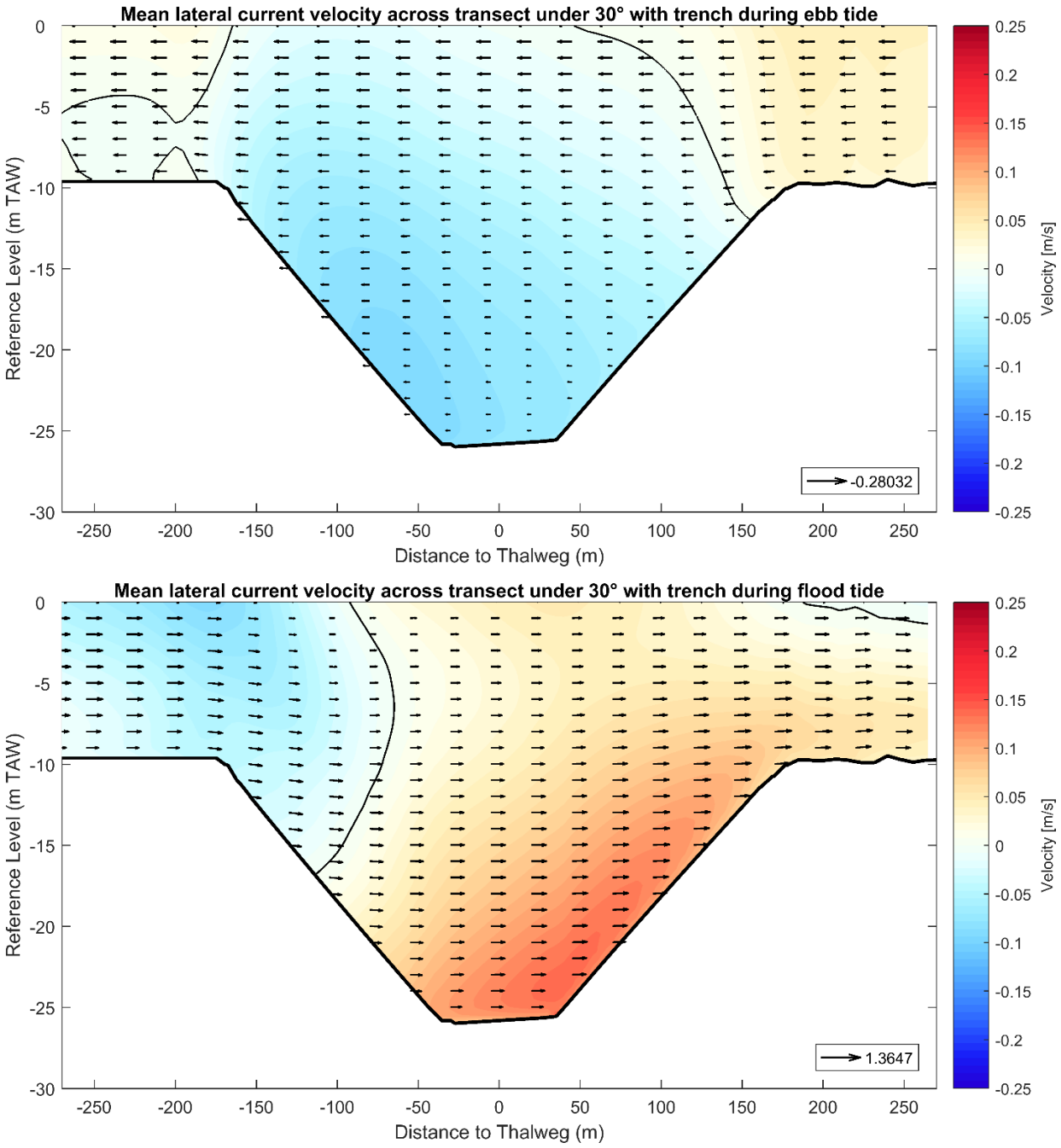
Mean lateral current velocity across transect under 30° with trench during ebb tide
Reference Level (m TAW)
Distance to Thalweg (m)
Velocity [m/s]
-0.28032
Mean lateral current velocity across transect under 30° with trench during flood tide
Reference Level (m TAW)
Distance to Thalweg (m)
Velocity [m/s]
1.3647

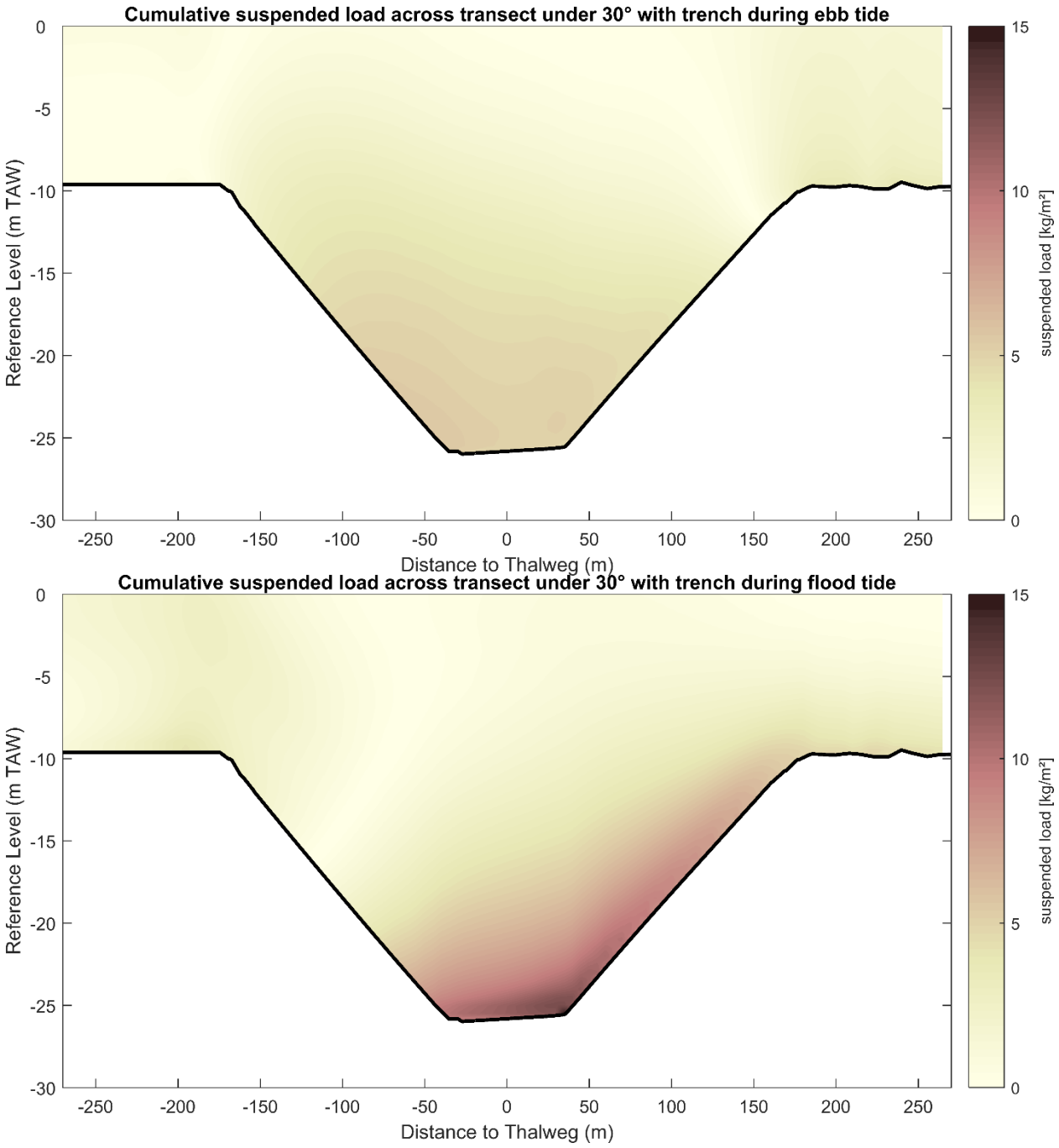
Cumulative suspended load across transect under 30° with trench during ebb tide
Reference Level (m TAW)
0
-5
-10
-15
-20
-25
-30
-250
-200
-150
-100
-50
0
50
100
150
200
250
Distance to Thalweg (m)
suspended load [kg/m²]
15
10
5
0
Cumulative suspended load across transect under 30° with trench during flood tide
Reference Level (m TAW)
Distance to Thalweg (m)
suspended load [kg/m²]

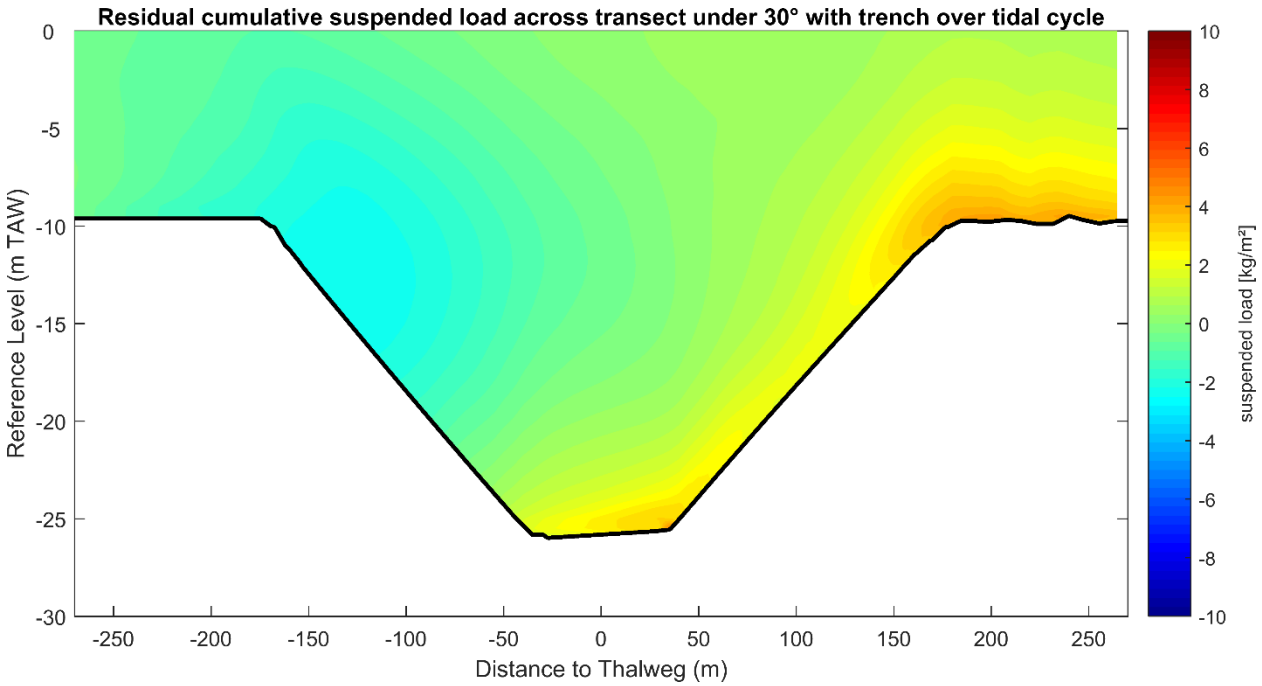
Residual cumulative suspended load across transect under 30° with trench over tidal cycle
Reference Level (m TAW)
Distance to Thalweg (m)
suspended load [kg/m²]
0
-5
-10
-15
-20
-25
-30
-250
-200
-150
-100
-50
0
50
100
150
200
250
10
8
6
4
2
0
-2
-4
-6
-8
-10

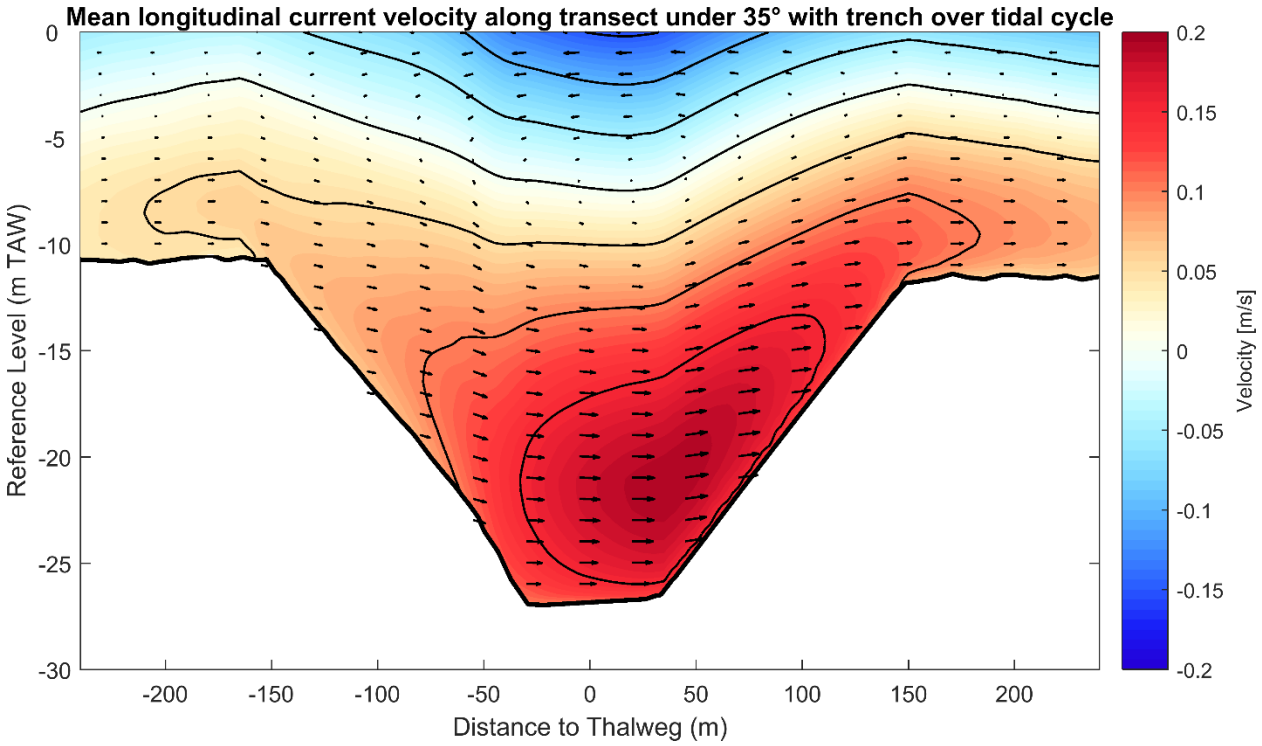
Mean longitudinal current velocity along transect under 35° with trench over tidal cycle
Reference Level (m TAW)
Distance to Thalweg (m)
Velocity [m/s]
0
-5
-10
-15
-20
-25
-30
-200
-150
-100
-50
0
50
100
150
200
0.2
0.15
0.1
0.05
0
-0.05
-0.1
-0.15
-0.2

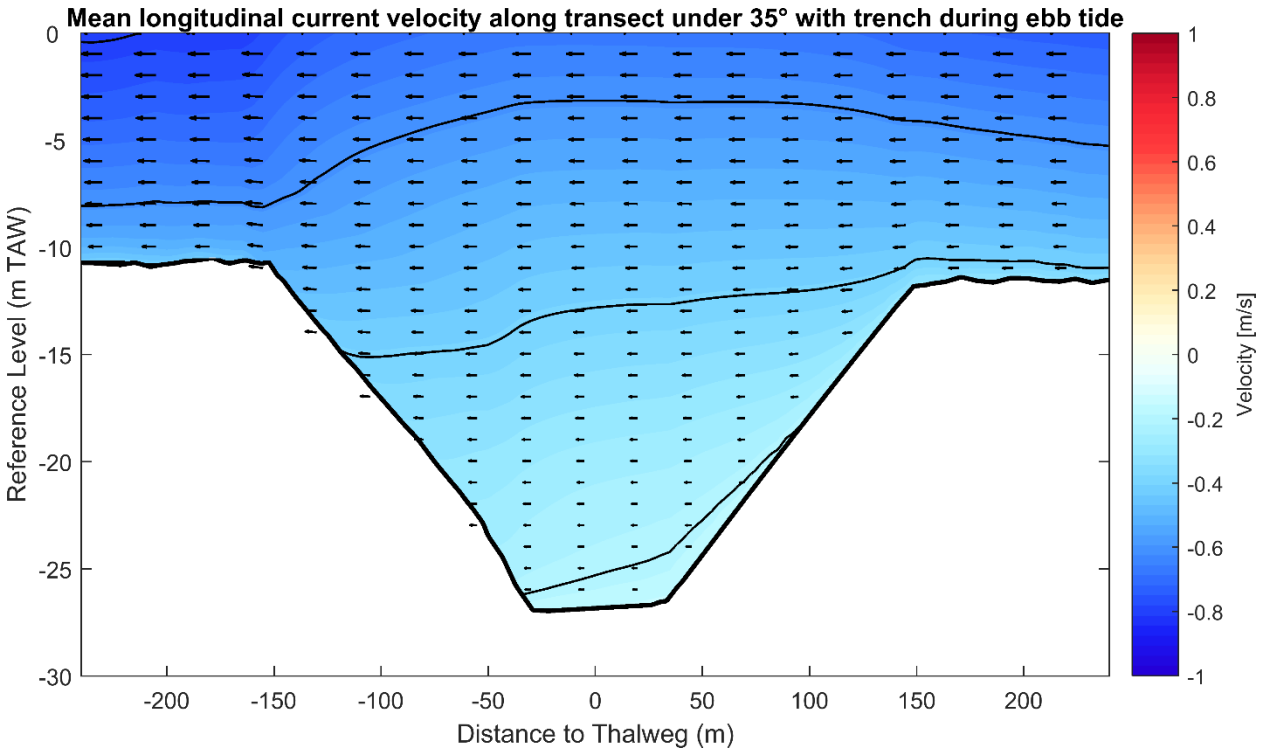
Mean longitudinal current velocity along transect under 35° with trench during ebb tide
Reference Level (m TAW)
0
-5
-10
-15
-20
-25
-30
-200
-150
-100
-50
0
50
100
150
200
Distance to Thalweg (m)
Velocity [m/s]
1
0.8
0.6
0.4
0.2
0
-0.2
-0.4
-0.6
-0.8
-1

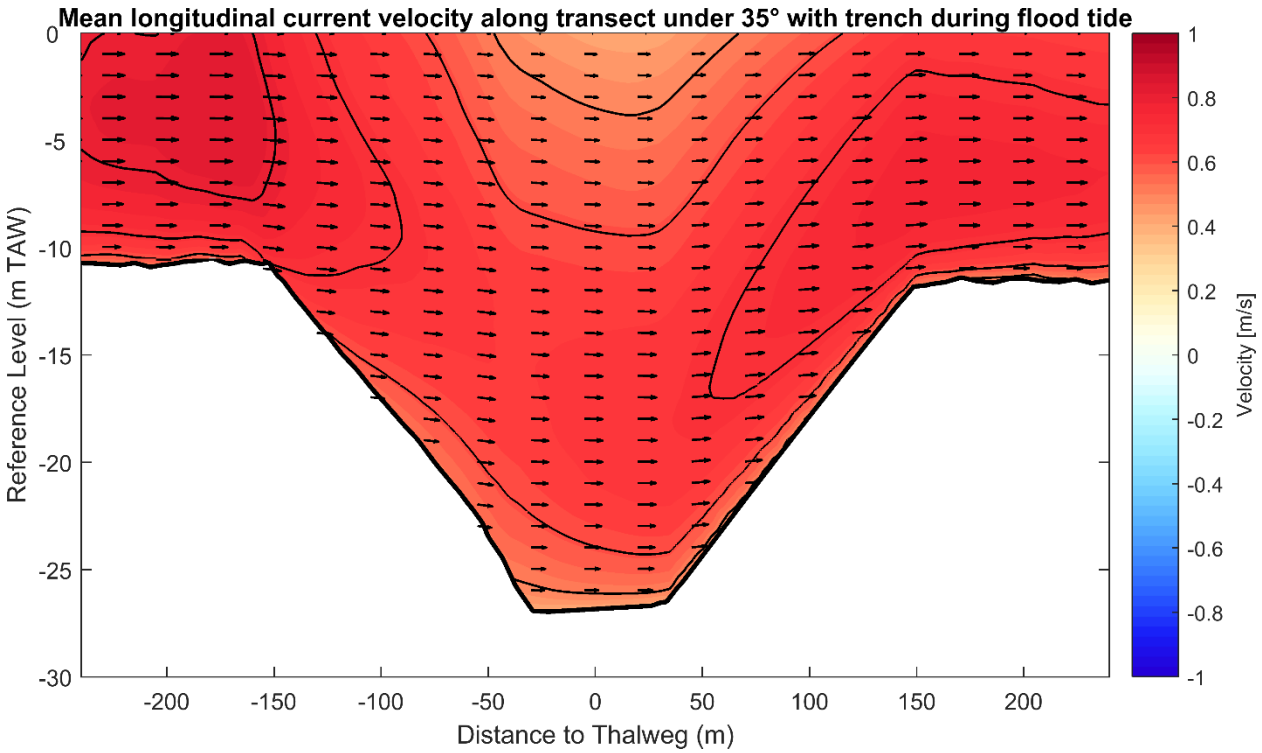
Mean longitudinal current velocity along transect under 35° with trench during flood tide
Reference Level (m TAW)
0
-5
-10
-15
-20
-25
-30
-200
-150
-100
-50
0
50
100
150
200
Distance to Thalweg (m)
Velocity [m/s]
1
0.8
0.6
0.4
0.2
0
-0.2
-0.4
-0.6
-0.8
-1

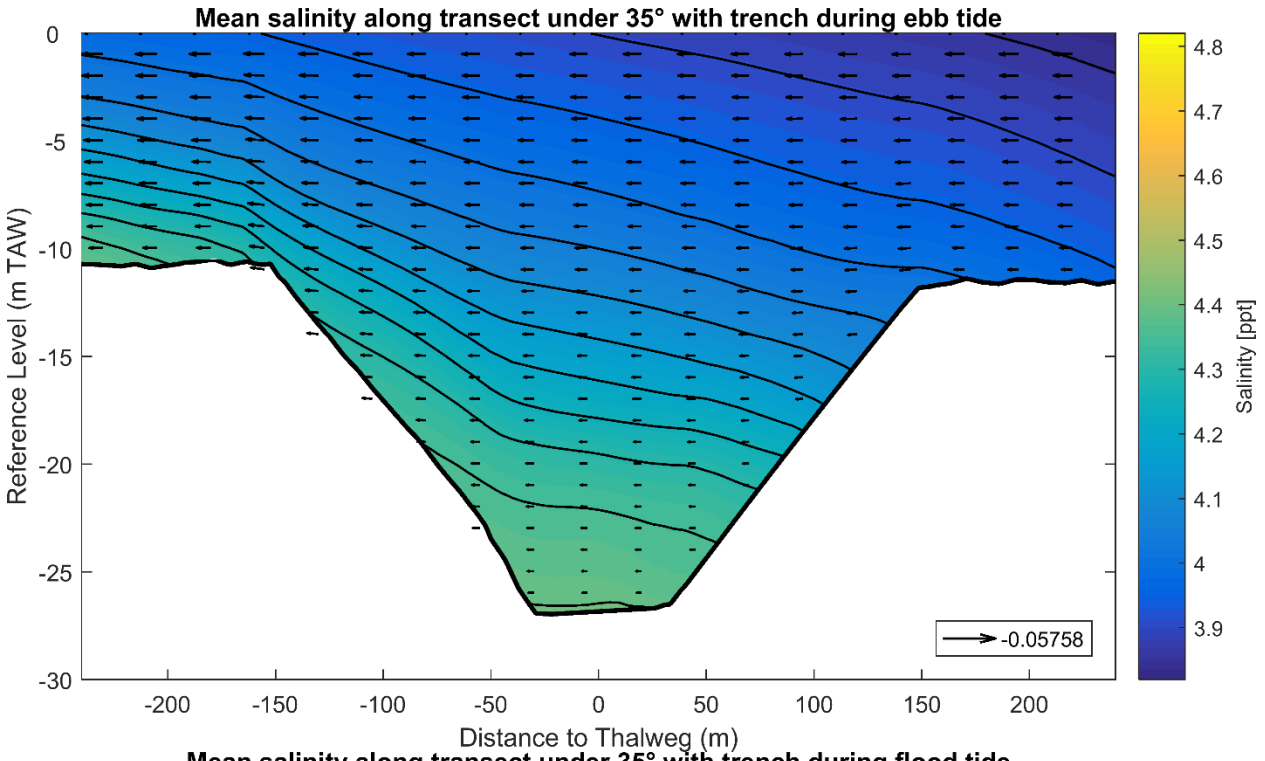
Mean salinity along transect under 35° with trench during ebb tide
Reference Level (m TAW)
0
-5
-10
-15
-20
-25
-30
-200
-150
-100
-50
0
50
100
150
200
Distance to Thalweg (m)
-0.05758
Salinity [ppt]
4.8
4.7
4.6
4.5
4.4
4.3
4.2
4.1
4
3.9

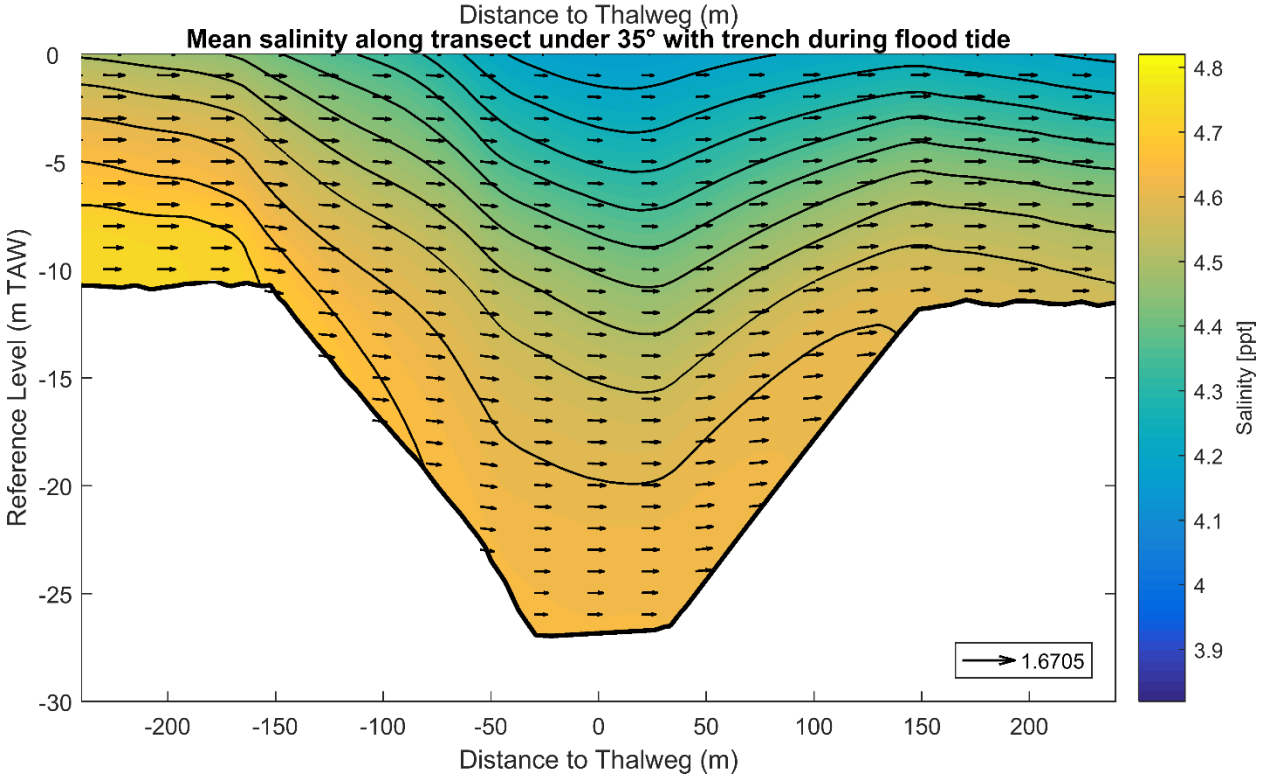
Mean salinity along transect under 35° with trench during flood tide
Reference Level (m TAW)
0
-5
-10
-15
-20
-25
-30
-200
-150
-100
-50
0
50
100
150
200
Distance to Thalweg (m)
1.6705
Salinity [ppt]
4.8
4.7
4.6
4.5
4.4
4.3
4.2
4.1
4
3.9

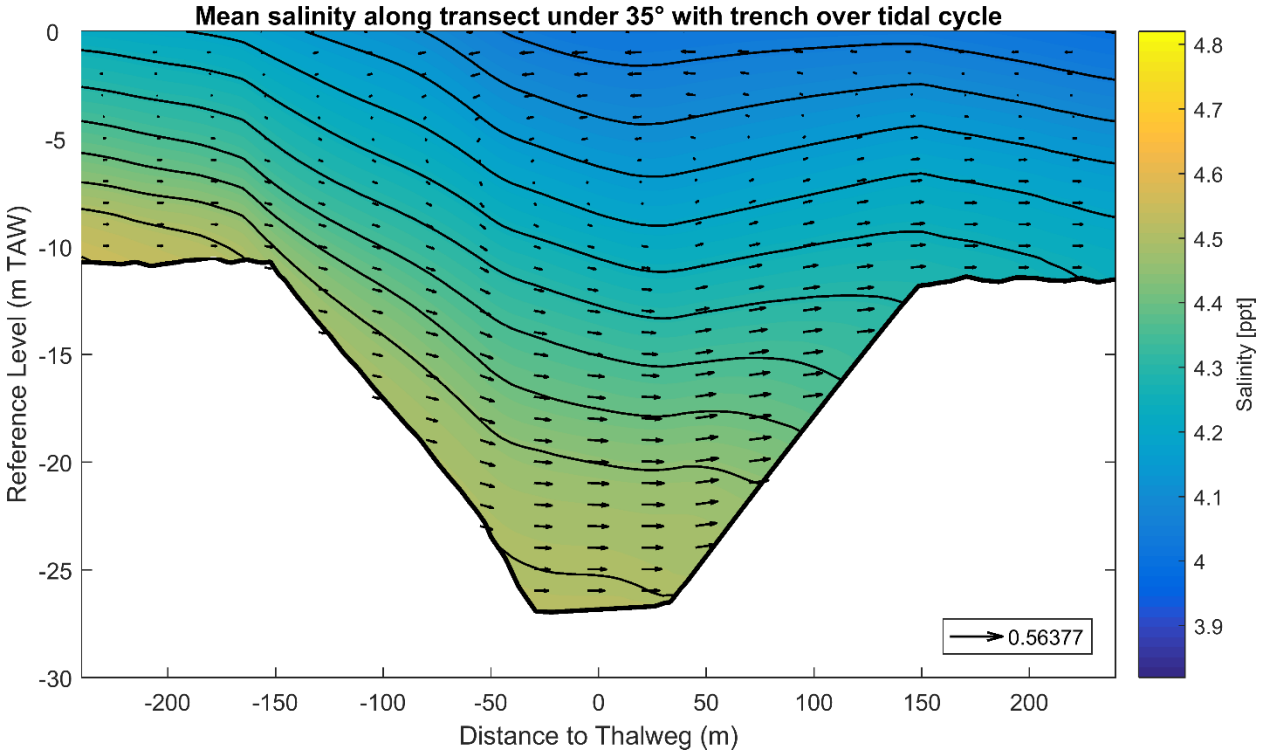
Mean salinity along transect under 35° with trench over tidal cycle
Reference Level (m TAW)
0
-5
-10
-15
-20
-25
-30
-200
-150
-100
-50
0
50
100
150
200
Distance to Thalweg (m)
0.56377
Salinity [ppt]
4.8
4.7
4.6
4.5
4.4
4.3
4.2
4.1
4
3.9

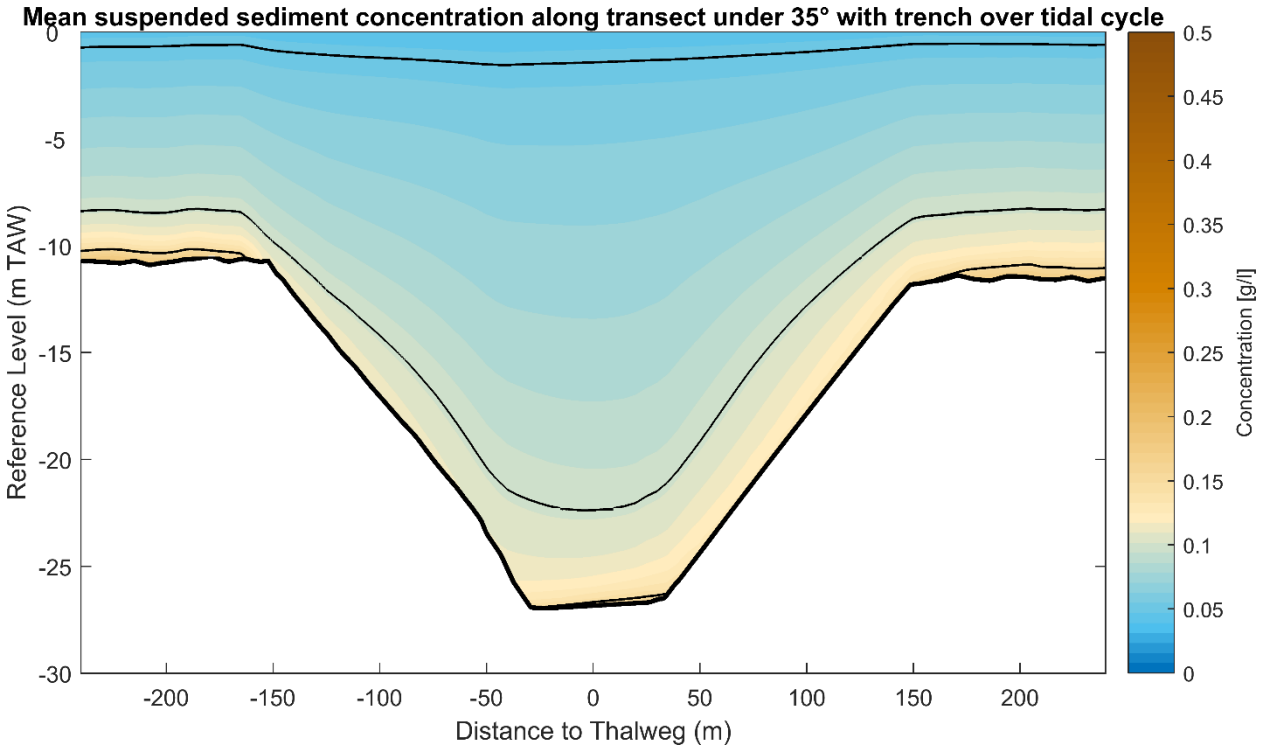
Mean suspended sediment concentration along transect under 35° with trench over tidal cycle
Reference Level (m TAW)
0
-5
-10
-15
-20
-25
-30
-200
-150
-100
-50
0
50
100
150
200
Distance to Thalweg (m)
Concentration [g/l]
0.5
0.45
0.4
0.35
0.3
0.25
0.2
0.15
0.1
0.05
0

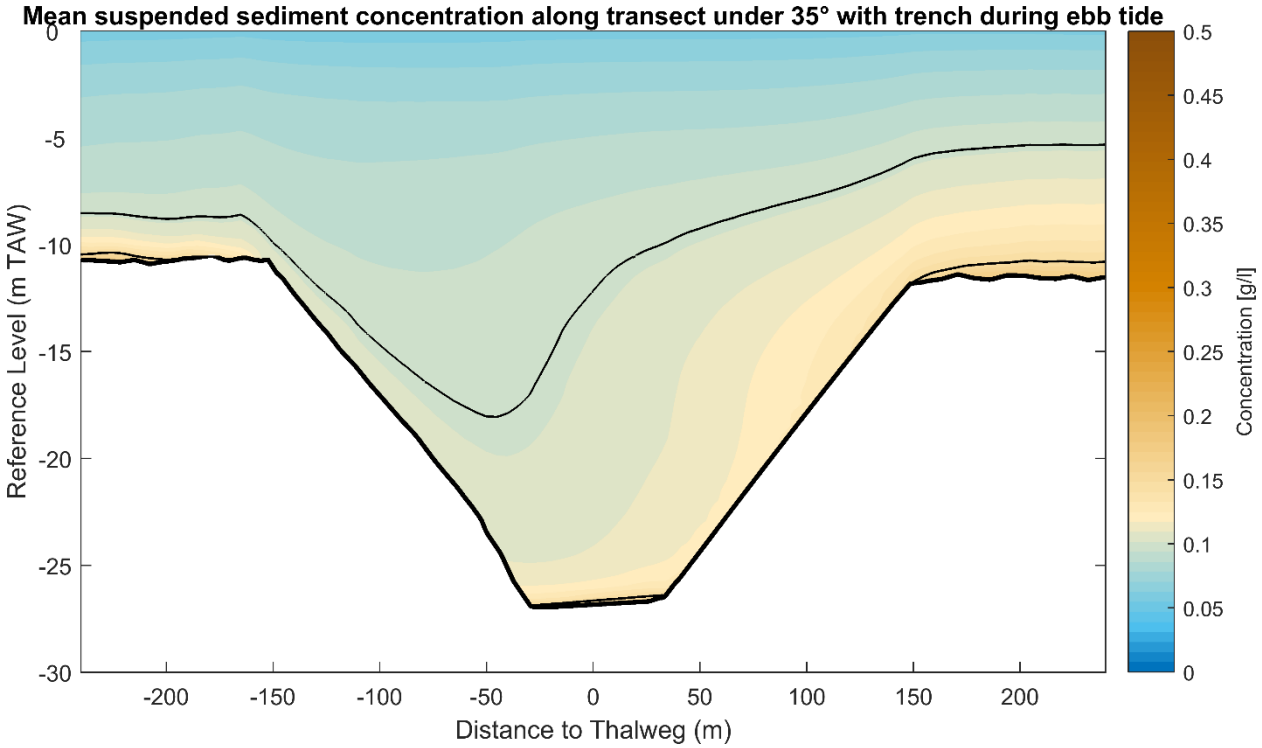
Mean suspended sediment concentration along transect under 35° with trench during ebb tide
Reference Level (m TAW)
0
-5
-10
-15
-20
-25
-30
-200
-150
-100
-50
0
50
100
150
200
Distance to Thalweg (m)
Concentration [g/l]
0.5
0.45
0.4
0.35
0.3
0.25
0.2
0.15
0.1
0.05
0

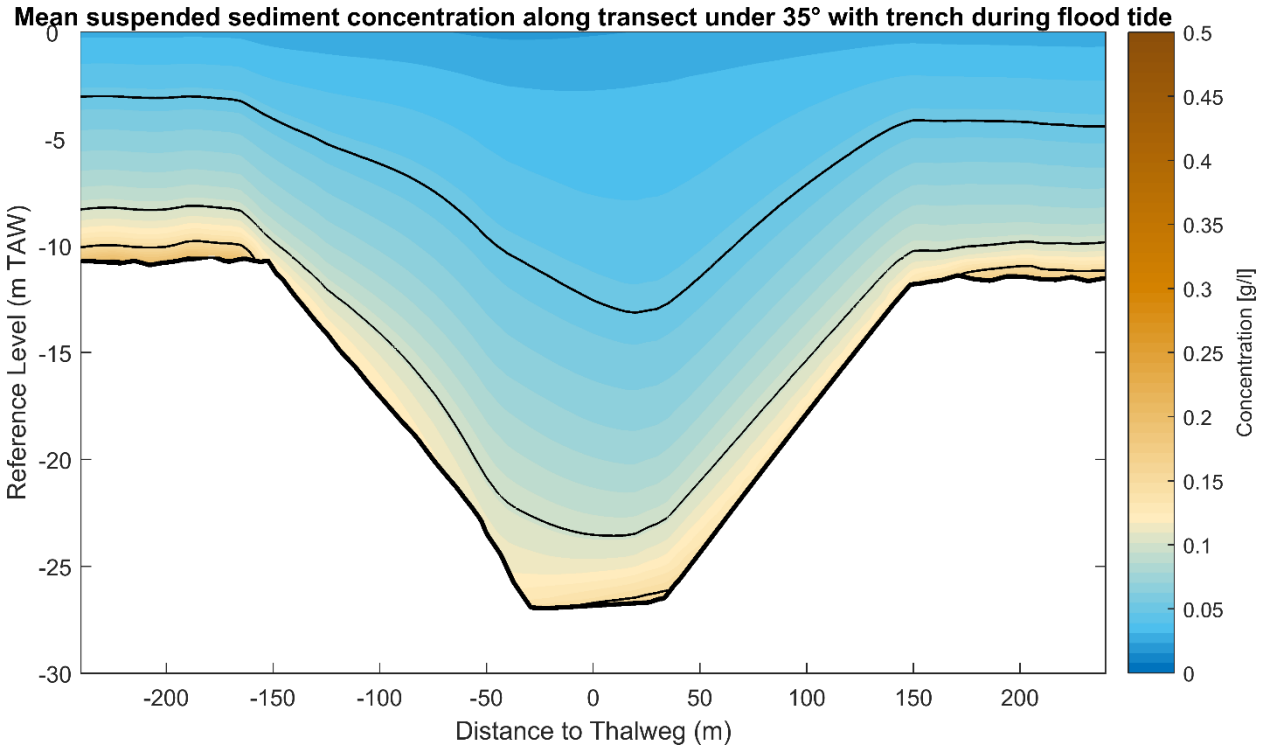
Mean suspended sediment concentration along transect under 35° with trench during flood tide
Reference Level (m TAW)
0
-5
-10
-15
-20
-25
-30
-200
-150
-100
-50
0
50
100
150
200
Distance to Thalweg (m)
Concentration [g/l]
0.5
0.45
0.4
0.35
0.3
0.25
0.2
0.15
0.1
0.05
0

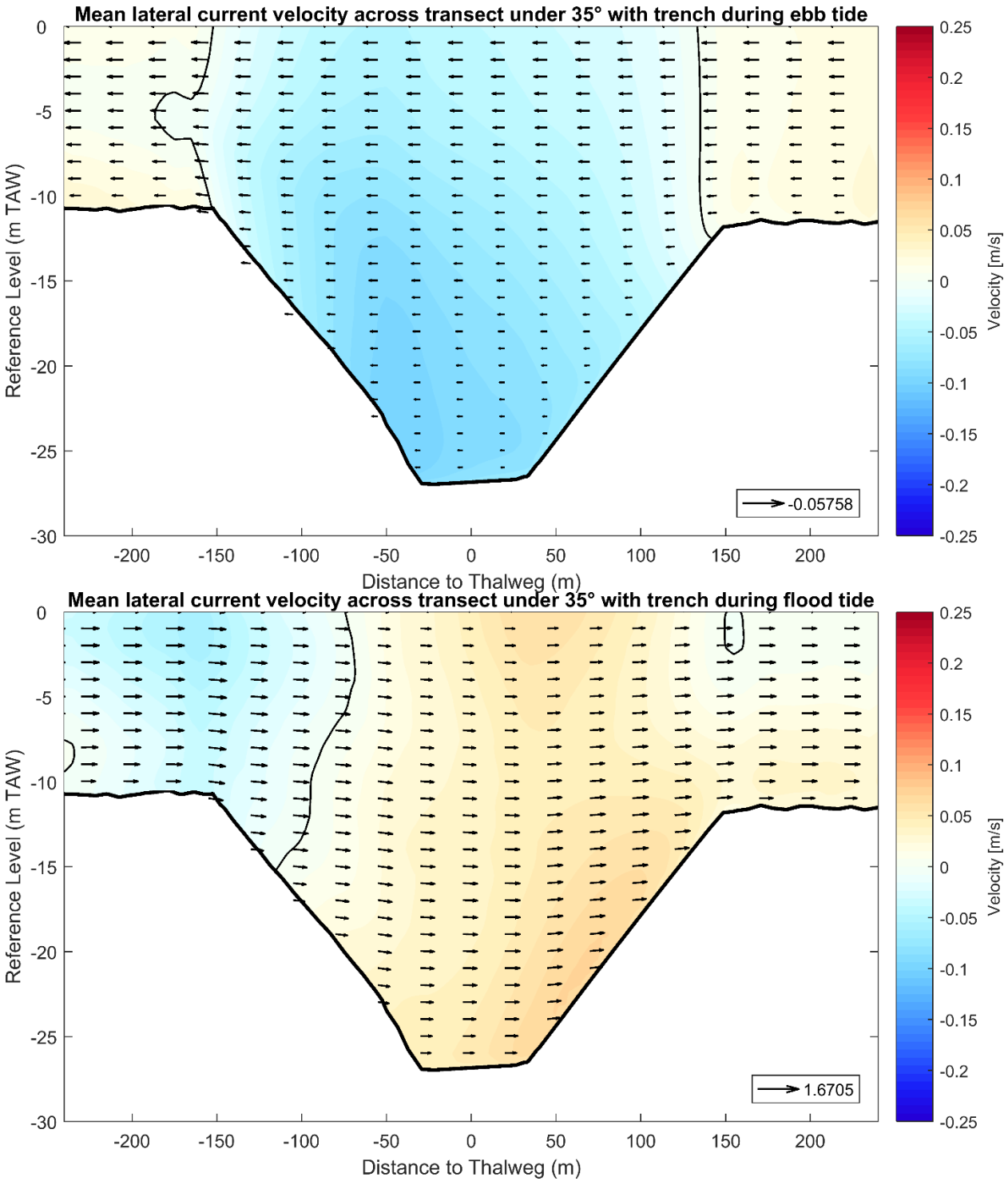
Mean lateral current velocity across transect under 35° with trench during ebb tide
Reference Level (m TAW)
Distance to Thalweg (m)
Velocity [m/s]
-0.05758
Mean lateral current velocity across transect under 35° with trench during flood tide
Reference Level (m TAW)
Distance to Thalweg (m)
Velocity [m/s]
1.6705

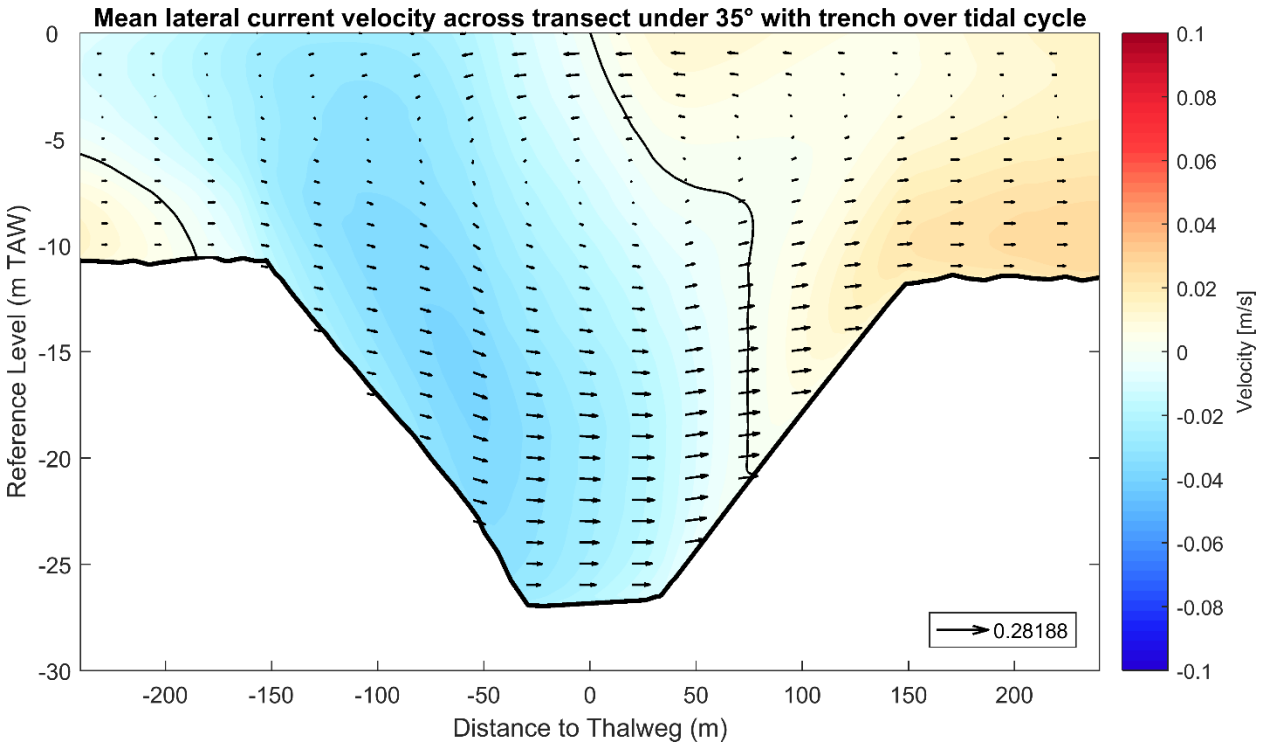
Mean lateral current velocity across transect under 35° with trench over tidal cycle
Reference Level (m TAW)
Distance to Thalweg (m)
Velocity [m/s]
0.28188

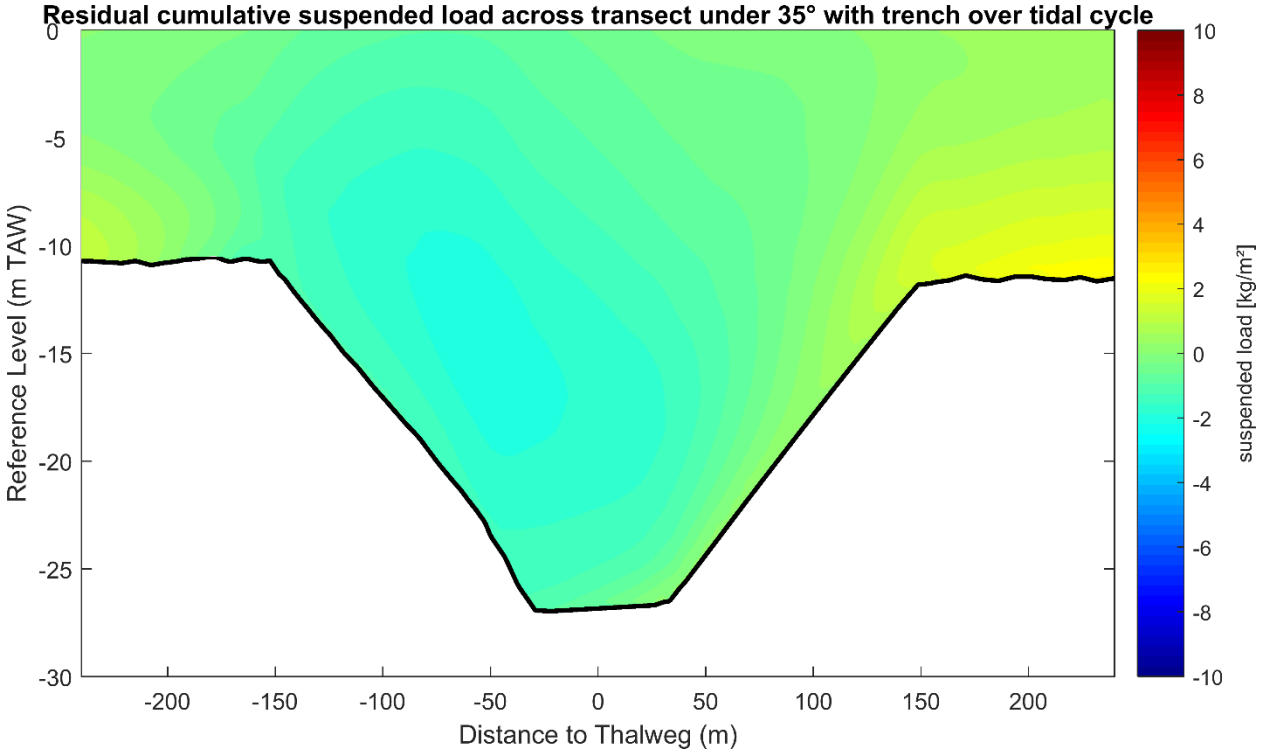
Residual cumulative suspended load across transect under 35° with trench over tidal cycle
Reference Level (m TAW)
Distance to Thalweg (m)
suspended load [kg/m²]

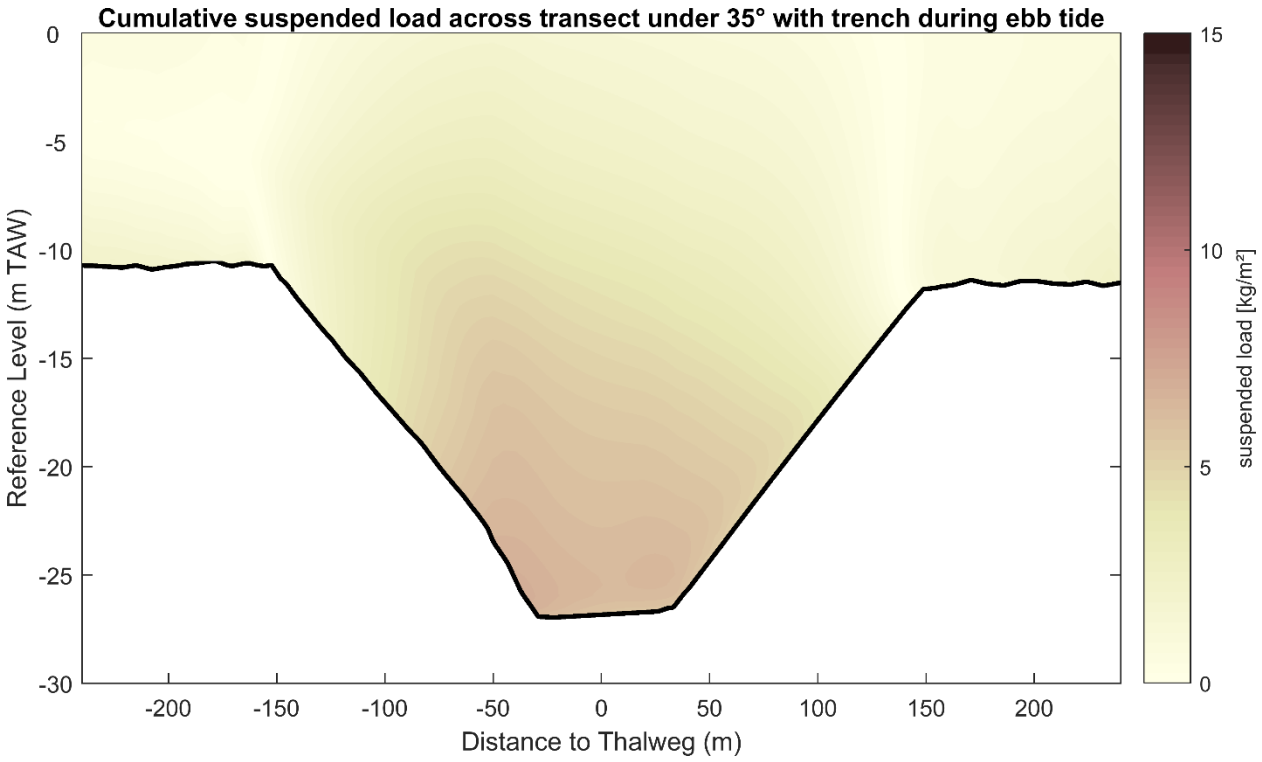
Cumulative suspended load across transect under 35° with trench during ebb tide
Reference Level (m TAW)
0
-5
-10
-15
-20
-25
-30
-200
-150
-100
-50
0
50
100
150
200
Distance to Thalweg (m)
15
10
5
0
suspended load [kg/m²]

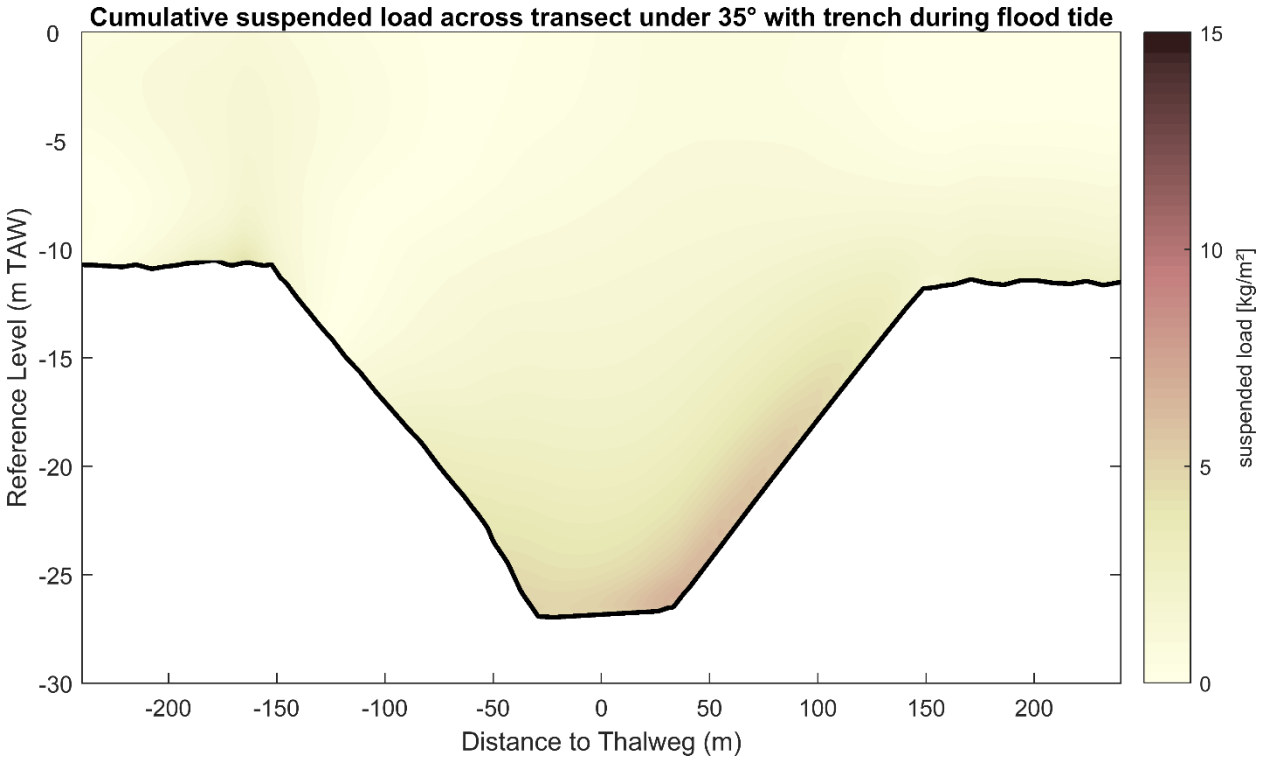
Cumulative suspended load across transect under 35° with trench during flood tide
Reference Level (m TAW)
0
-5
-10
-15
-20
-25
-30
-200
-150
-100
-50
0
50
100
150
200
Distance to Thalweg (m)
15
10
5
0
suspended load [kg/m²]

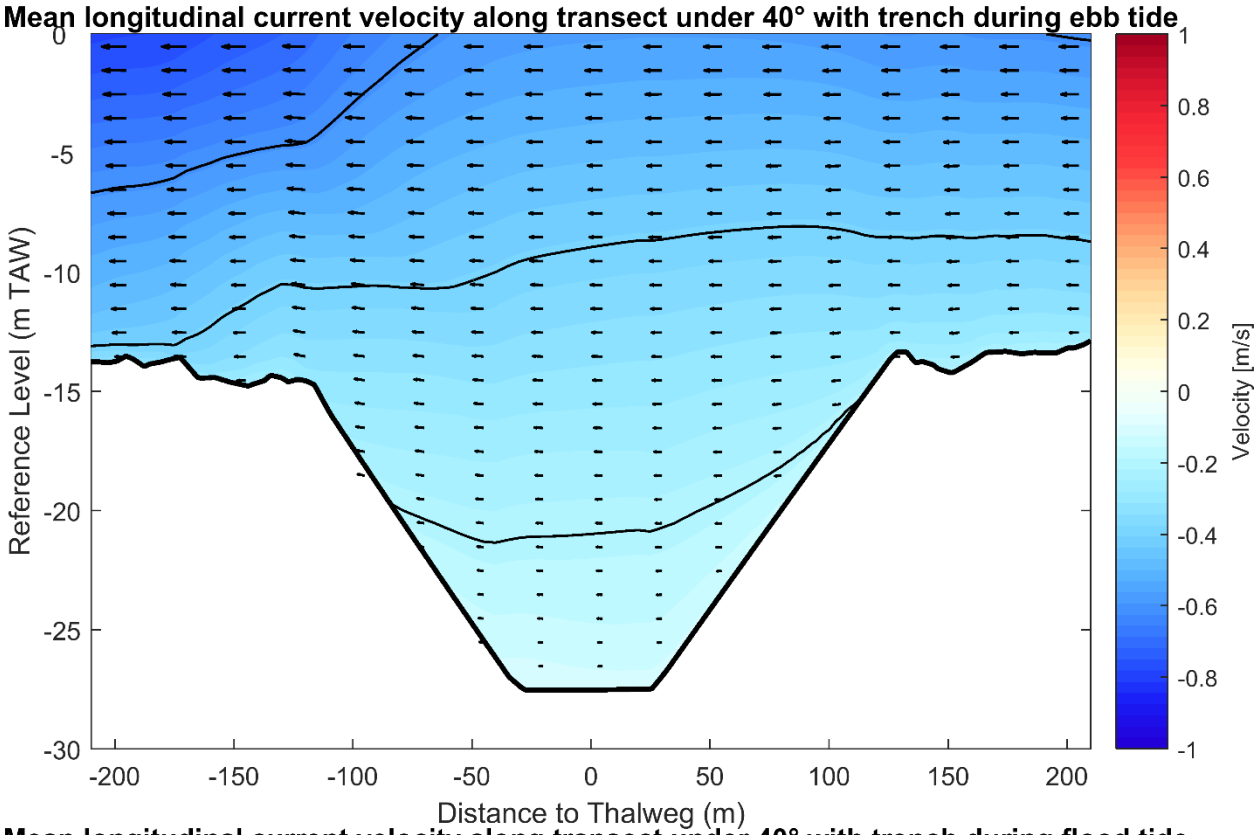
Mean longitudinal current velocity along transect under 40° with trench during ebb tide
Reference Level (m TAW)
0
-5
-10
-15
-20
-25
-30
-200
-150
-100
-50
0
50
100
150
200
Distance to Thalweg (m)
Velocity [m/s]
1
0.8
0.6
0.4
0.2
0
-0.2
-0.4
-0.6
-0.8
-1

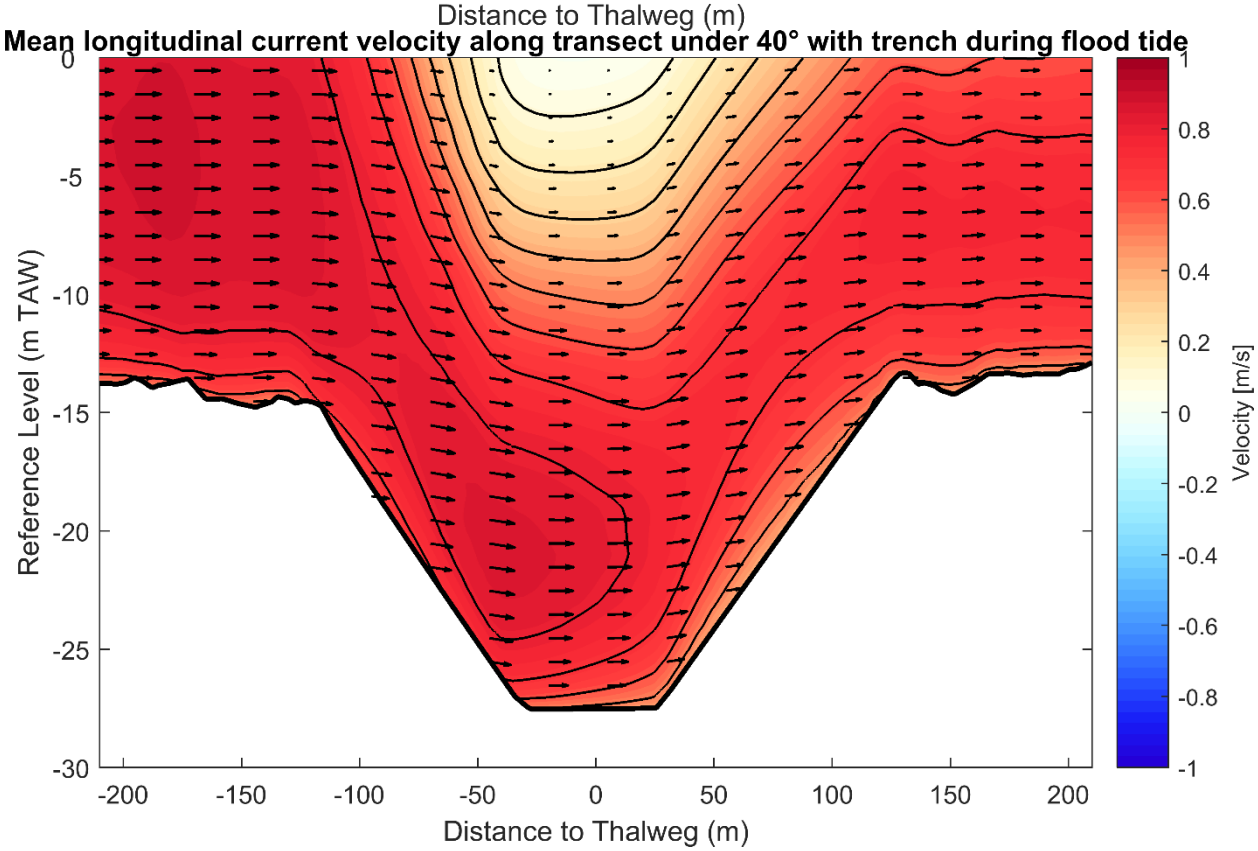
Mean longitudinal current velocity along transect under 40° with trench during flood tide
Reference Level (m TAW)
0
-5
-10
-15
-20
-25
-30
-200
-150
-100
-50
0
50
100
150
200
Distance to Thalweg (m)
Velocity [m/s]
1
0.8
0.6
0.4
0.2
0
-0.2
-0.4
-0.6
-0.8
-1

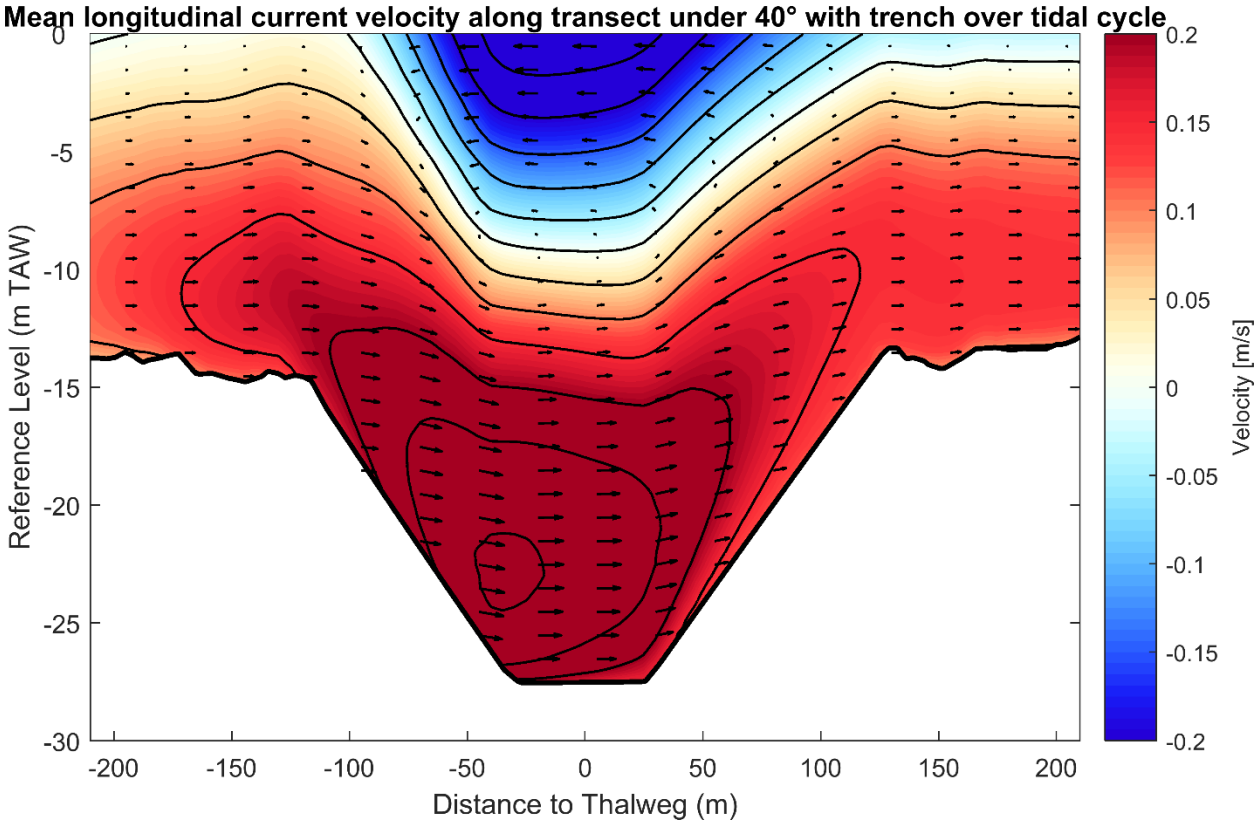
Mean longitudinal current velocity along transect under 40° with trench over tidal cycle
Reference Level (m TAW)
Distance to Thalweg (m)
Velocity [m/s]
0
-5
-10
-15
-20
-25
-30
-200
-150
-100
-50
0
50
100
150
200
0.2
0.15
0.1
0.05
0
-0.05
-0.1
-0.15
-0.2

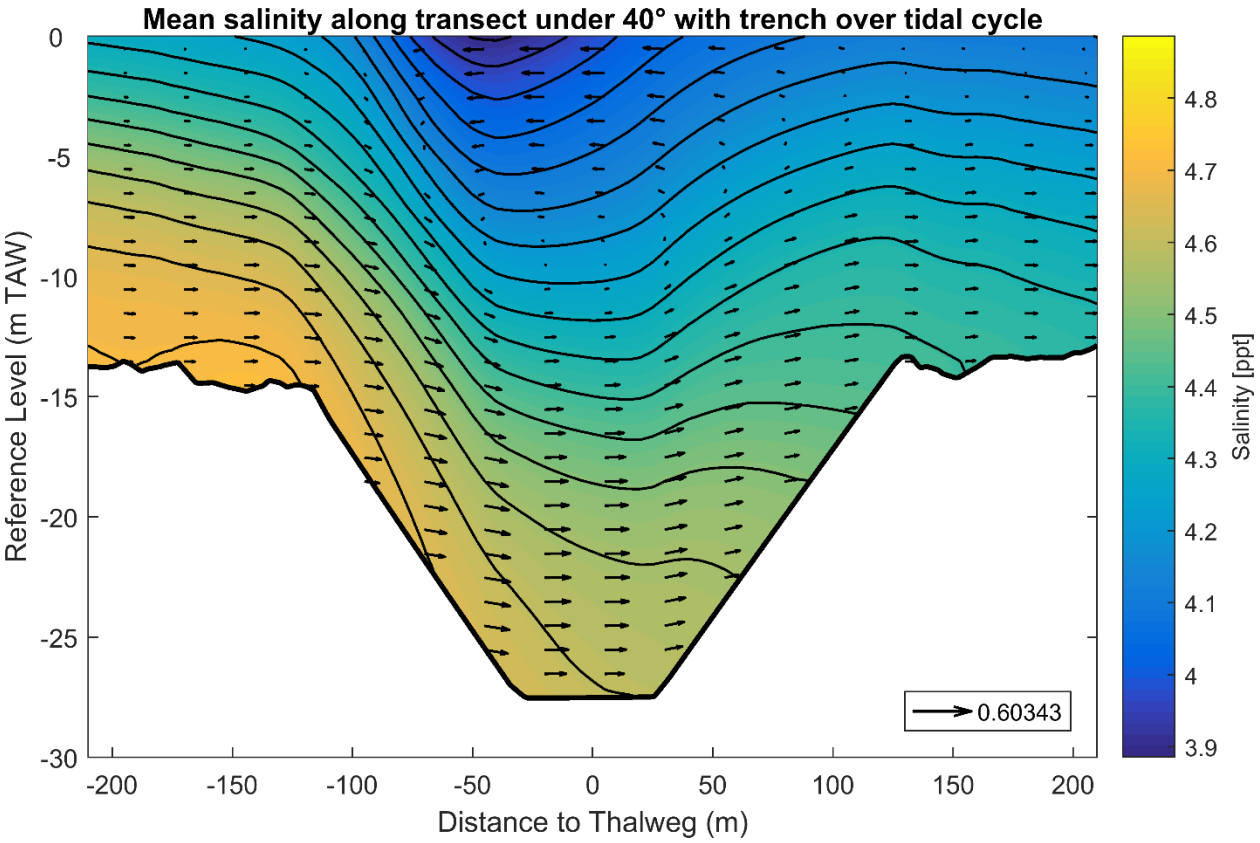
Mean salinity along transect under 40° with trench over tidal cycle
Reference Level (m TAW)
Distance to Thalweg (m)
Salinity [ppt]
0.60343
0
-5
-10
-15
-20
-25
-30
-200
-150
-100
-50
0
50
100
150
200
4.8
4.7
4.6
4.5
4.4
4.3
4.2
4.1
4
3.9

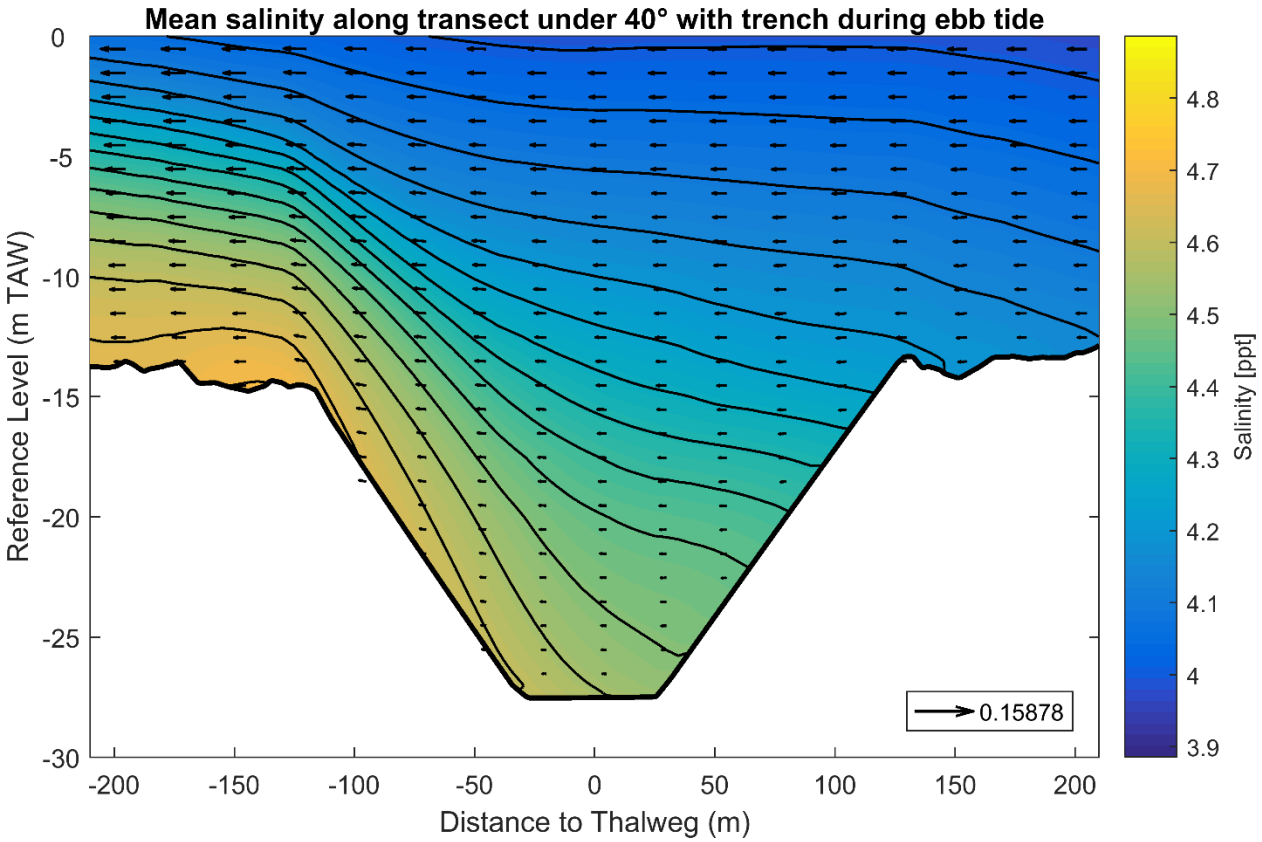
Mean salinity along transect under 40° with trench during ebb tide
Reference Level (m TAW)
0
-5
-10
-15
-20
-25
-30
-200
-150
-100
-50
0
50
100
150
200
Distance to Thalweg (m)
0.15878
Salinity [ppt]
4.8
4.7
4.6
4.5
4.4
4.3
4.2
4.1
4
3.9

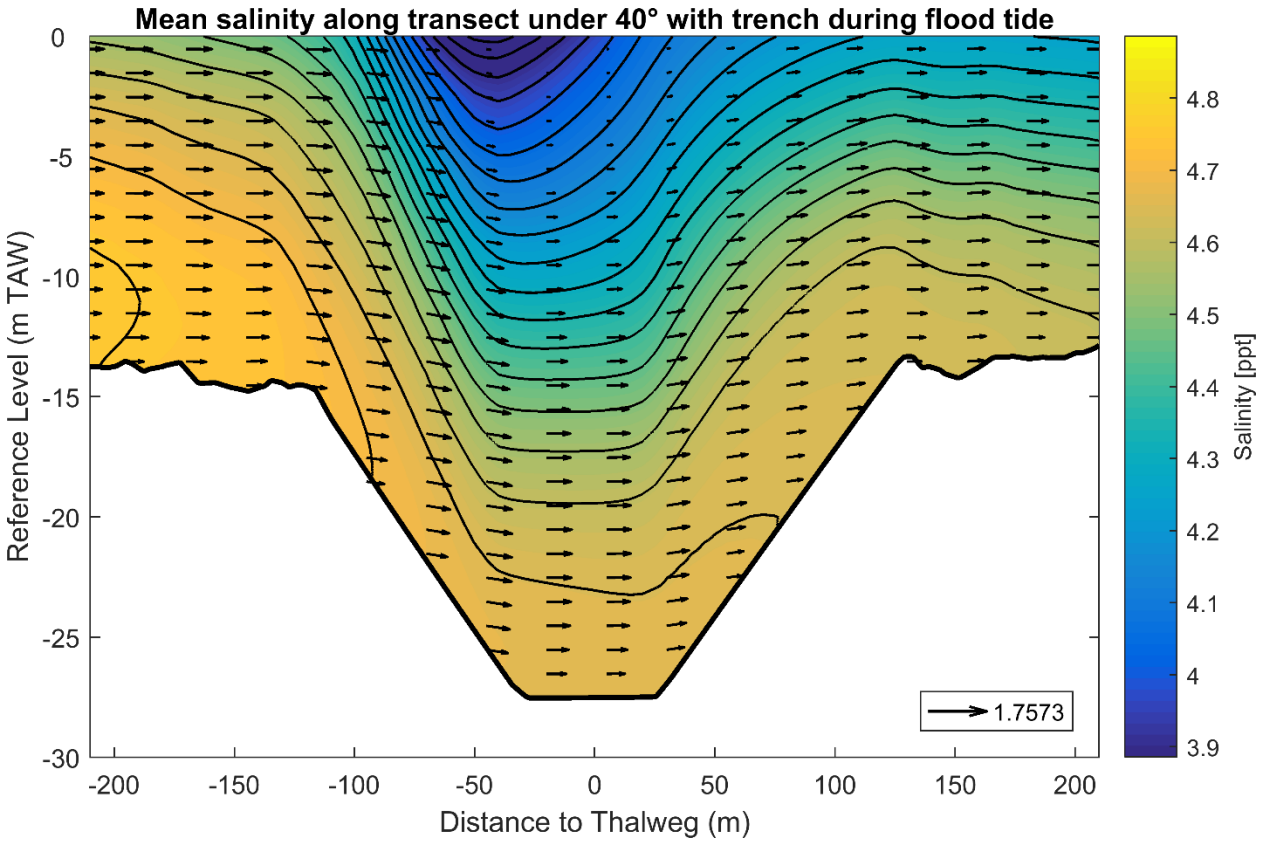
Mean salinity along transect under 40° with trench during flood tide
Reference Level (m TAW)
0
-5
-10
-15
-20
-25
-30
-200
-150
-100
-50
0
50
100
150
200
Distance to Thalweg (m)
1.7573
Salinity [ppt]
4.8
4.7
4.6
4.5
4.4
4.3
4.2
4.1
4
3.9

Mean suspended sediment concentration along transect under 40° with trench during ebb tide

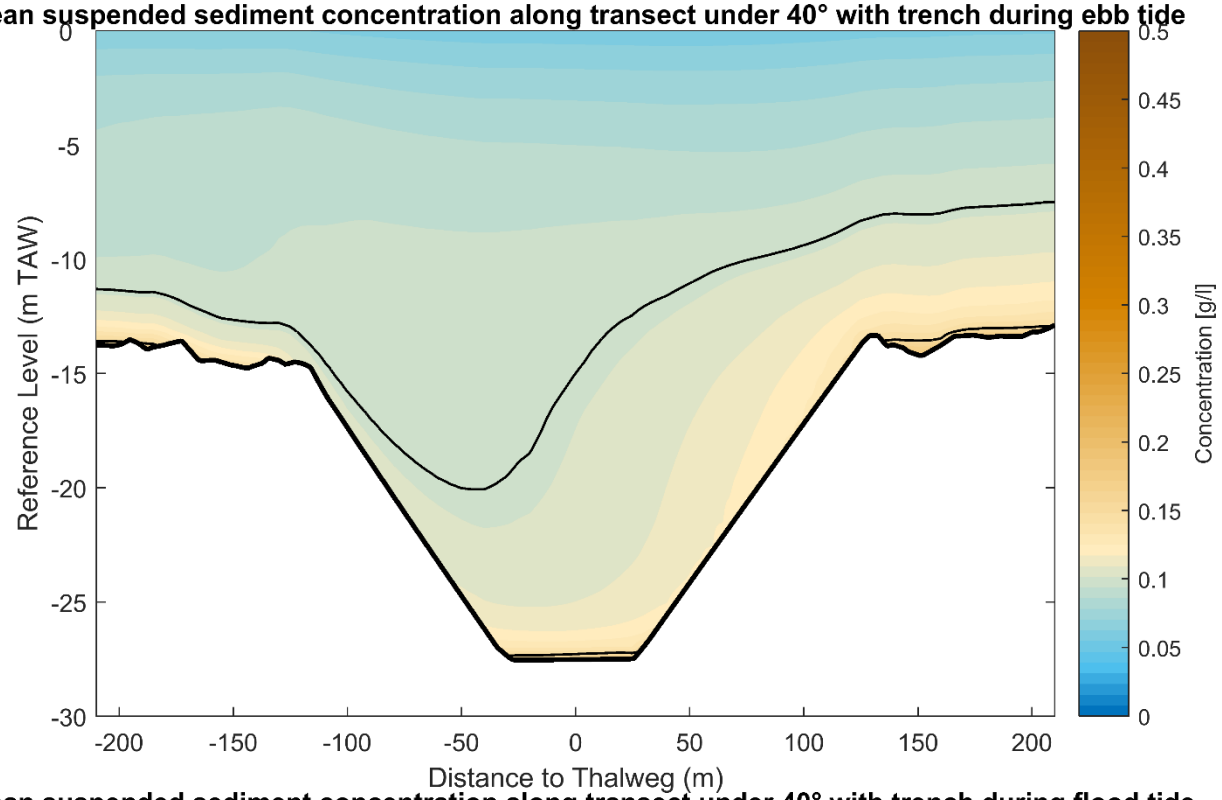

Mean suspended sediment concentration along transect under 40° with trench during flood tide

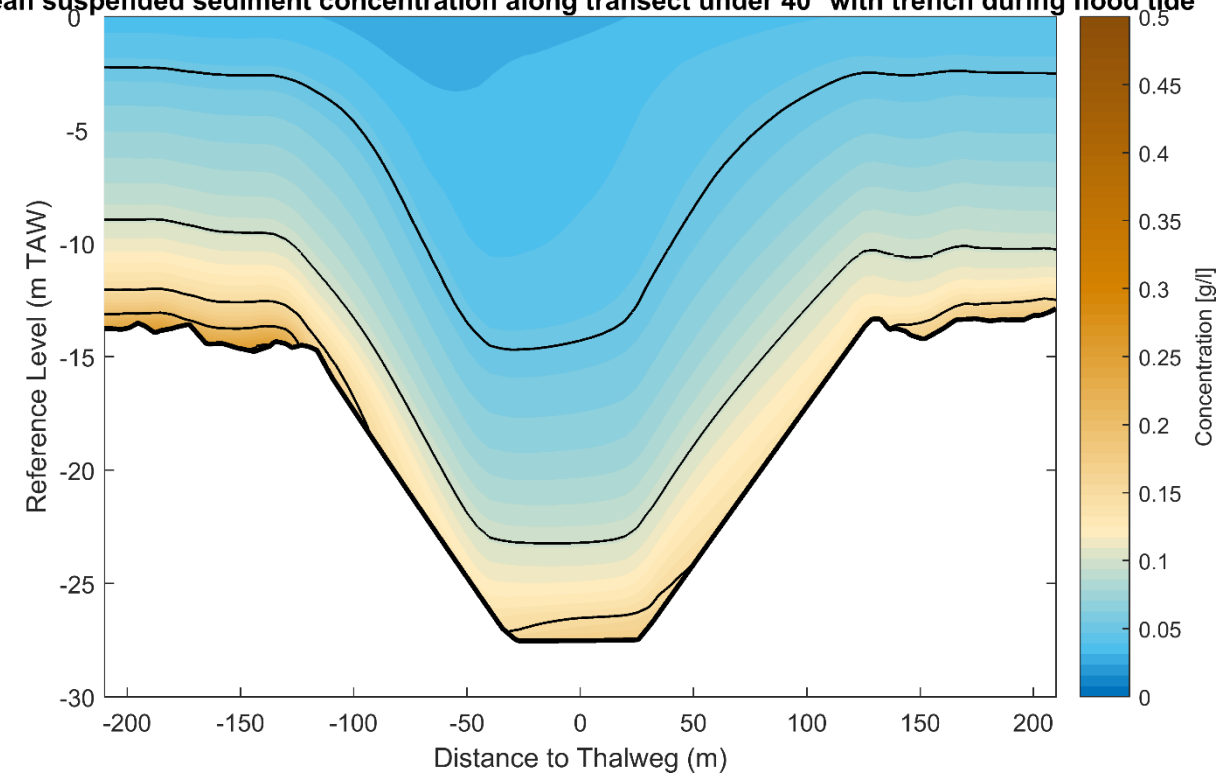

Mean suspended sediment concentration along transect under 40° with trench over tidal cycle

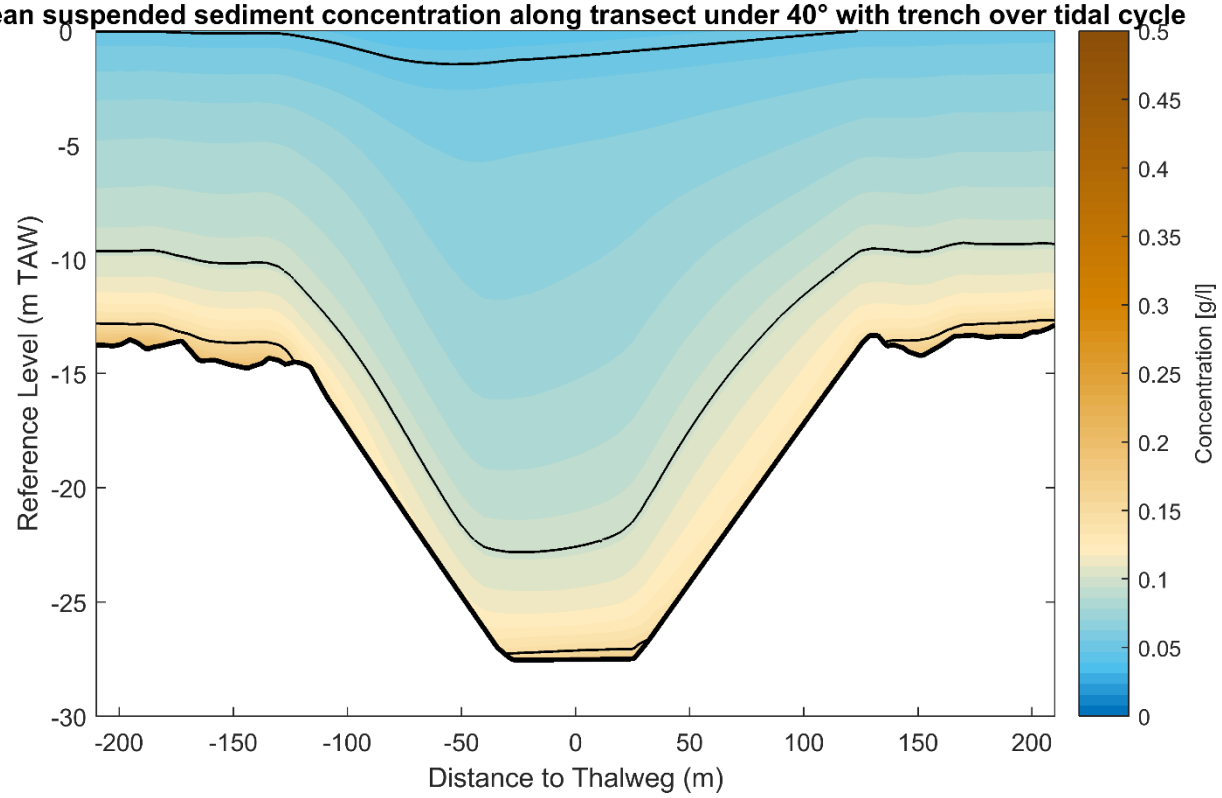

Mean lateral current velocity across transect under 40° with trench over tidal cycle

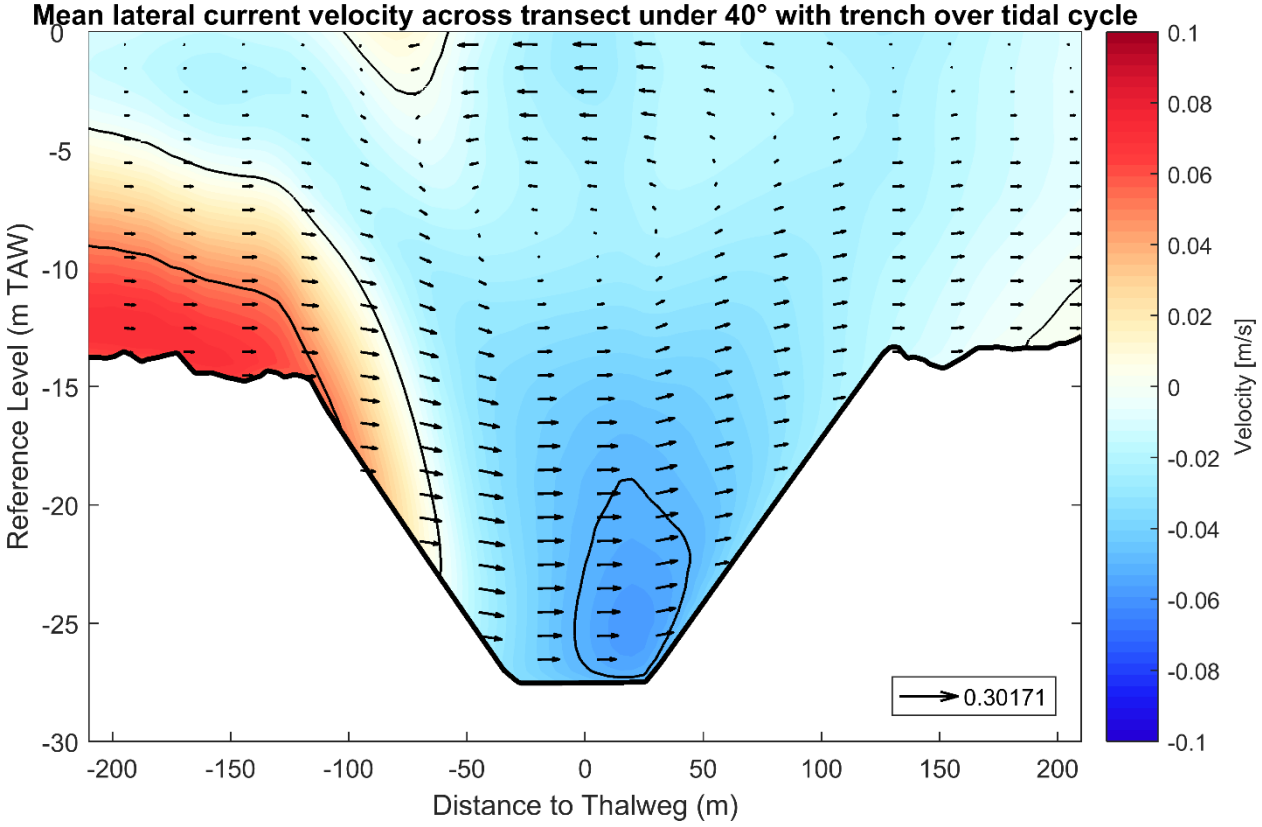

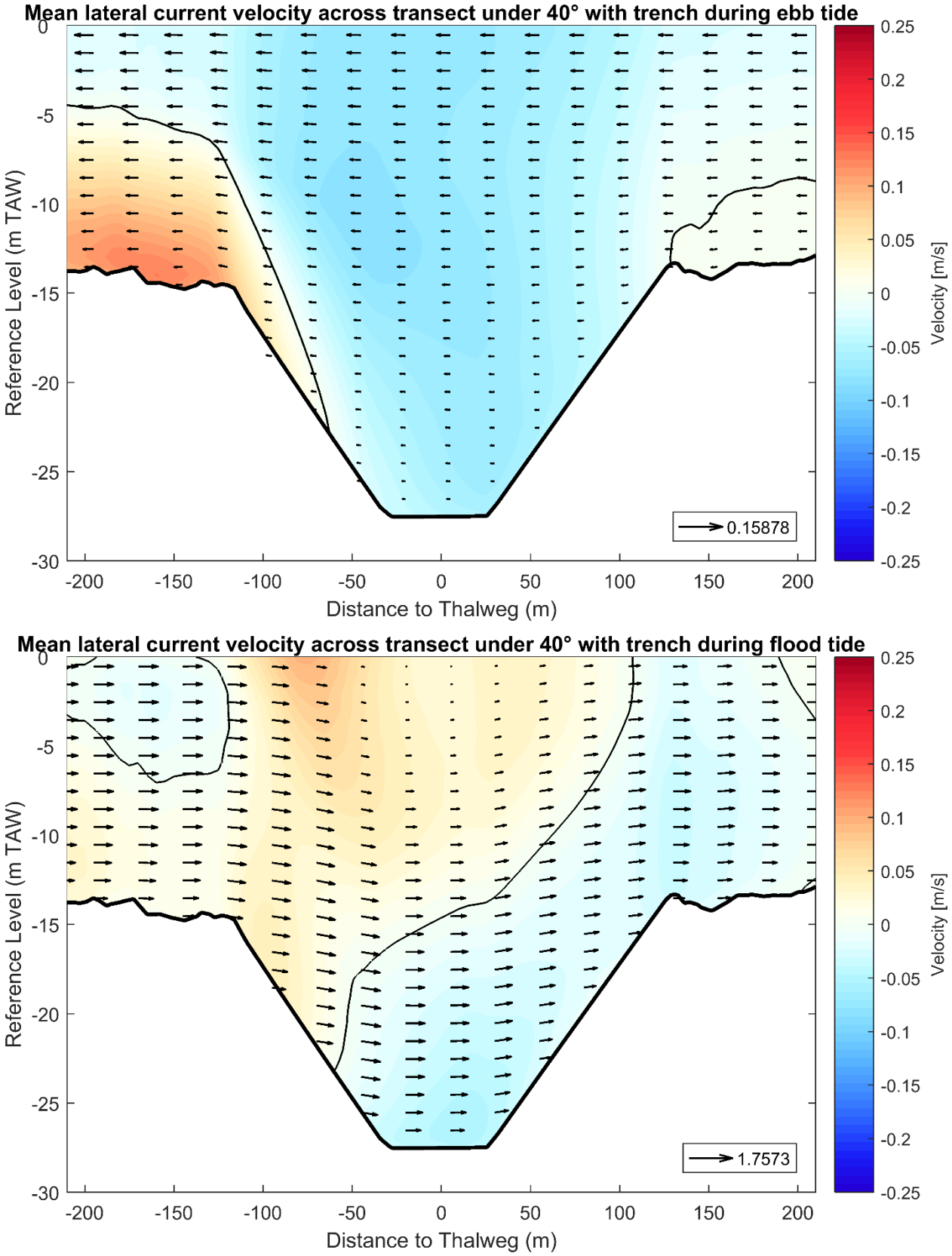
Mean lateral current velocity across transect under 40° with trench during ebb tide
Reference Level (m TAW)
Distance to Thalweg (m)
Velocity [m/s]
0.15878
Mean lateral current velocity across transect under 40° with trench during flood tide
Reference Level (m TAW)
Distance to Thalweg (m)
Velocity [m/s]
1.7573

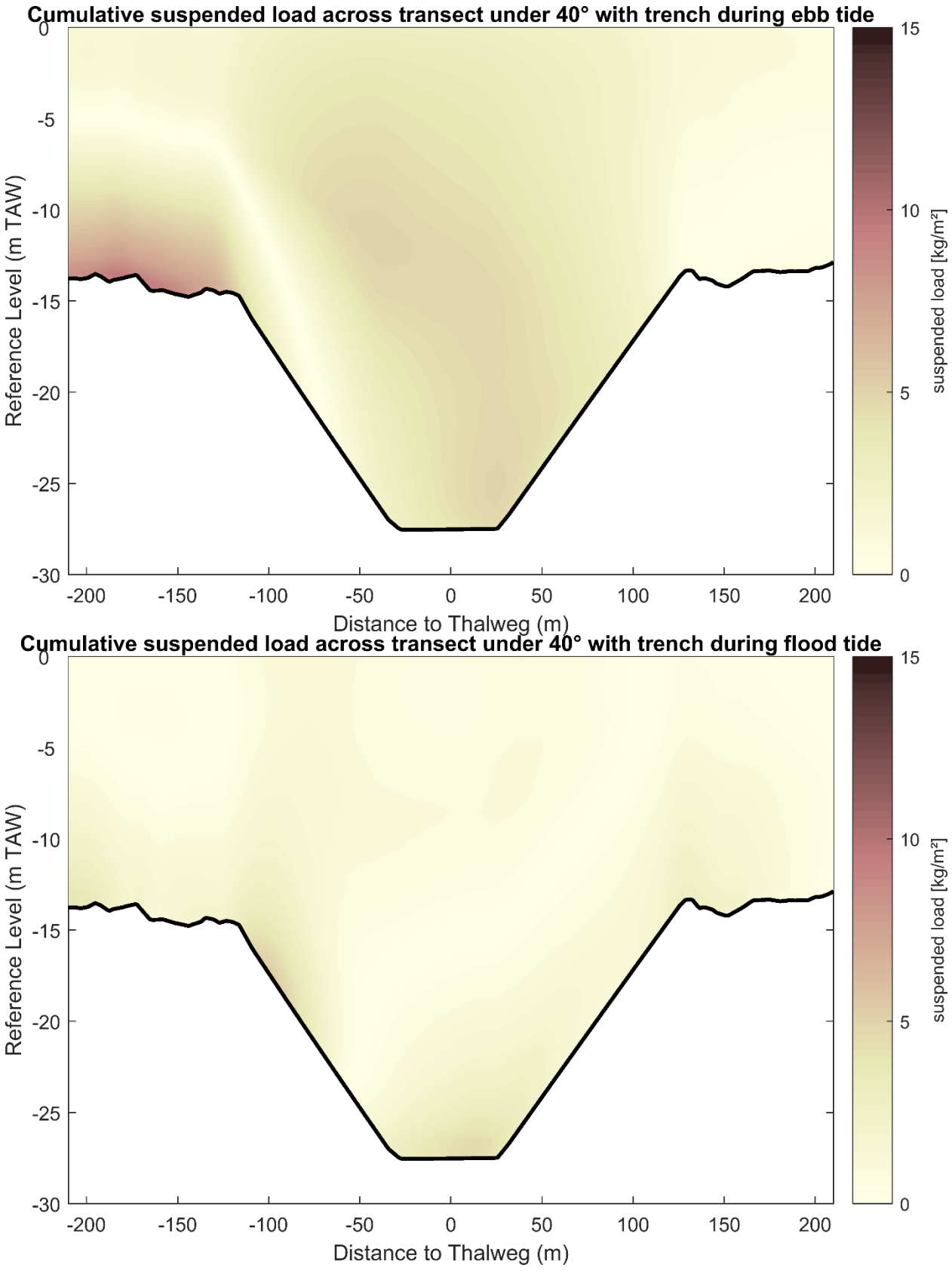
Cumulative suspended load across transect under 40° with trench during ebb tide
Reference Level (m TAW)
0
-5
-10
-15
-20
-25
-30
-200
-150
-100
-50
0
50
100
150
200
Distance to Thalweg (m)
suspended load [kg/m²]
15
10
5
0
Cumulative suspended load across transect under 40° with trench during flood tide
Reference Level (m TAW)
Distance to Thalweg (m)
suspended load [kg/m²]

Residual cumulative suspended load across transect under 40° with trench over tidal cycle

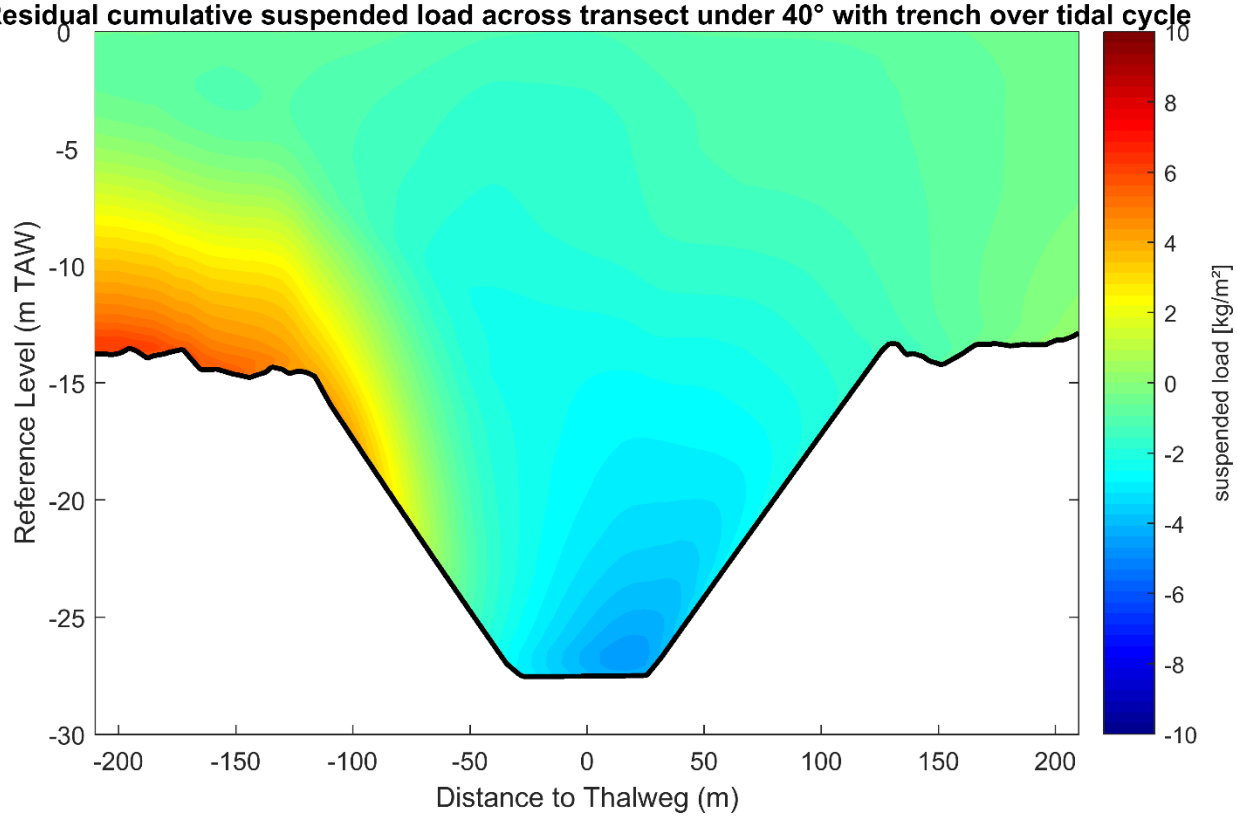

Mean longitudinal current velocity along transect under 45° with trench over tidal cycle

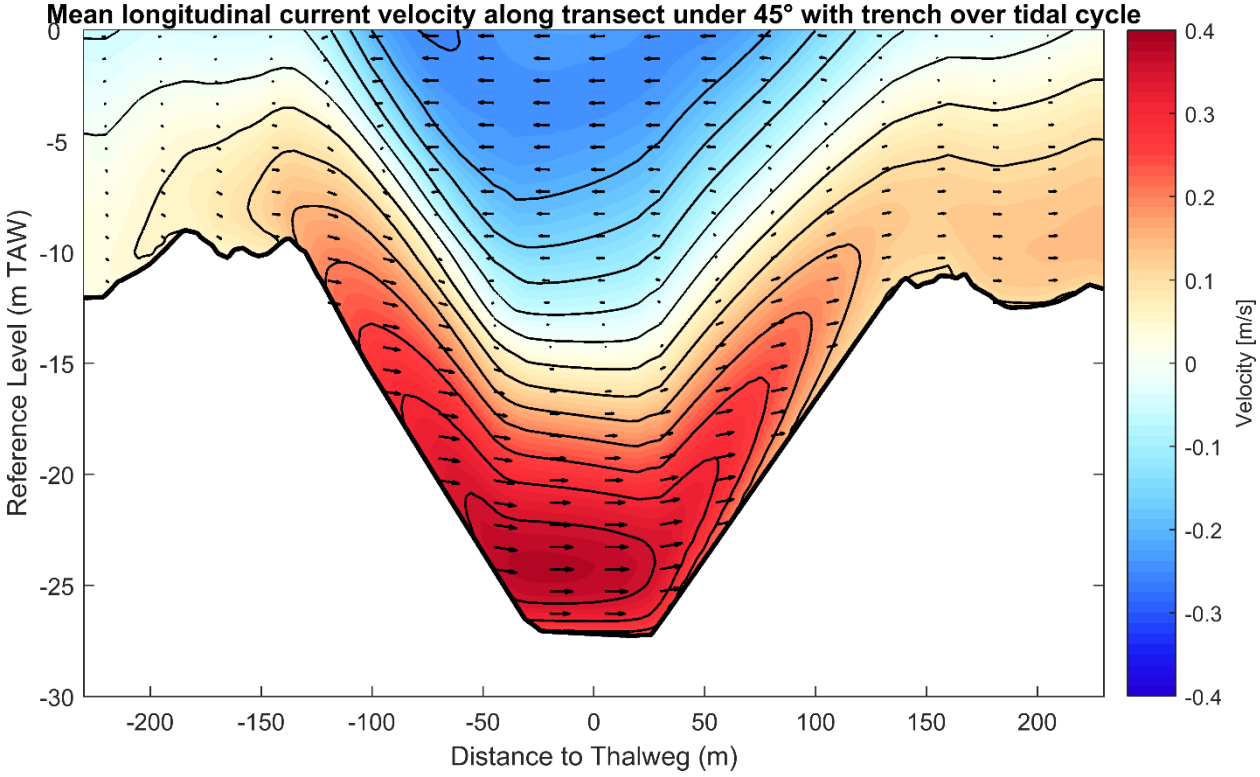

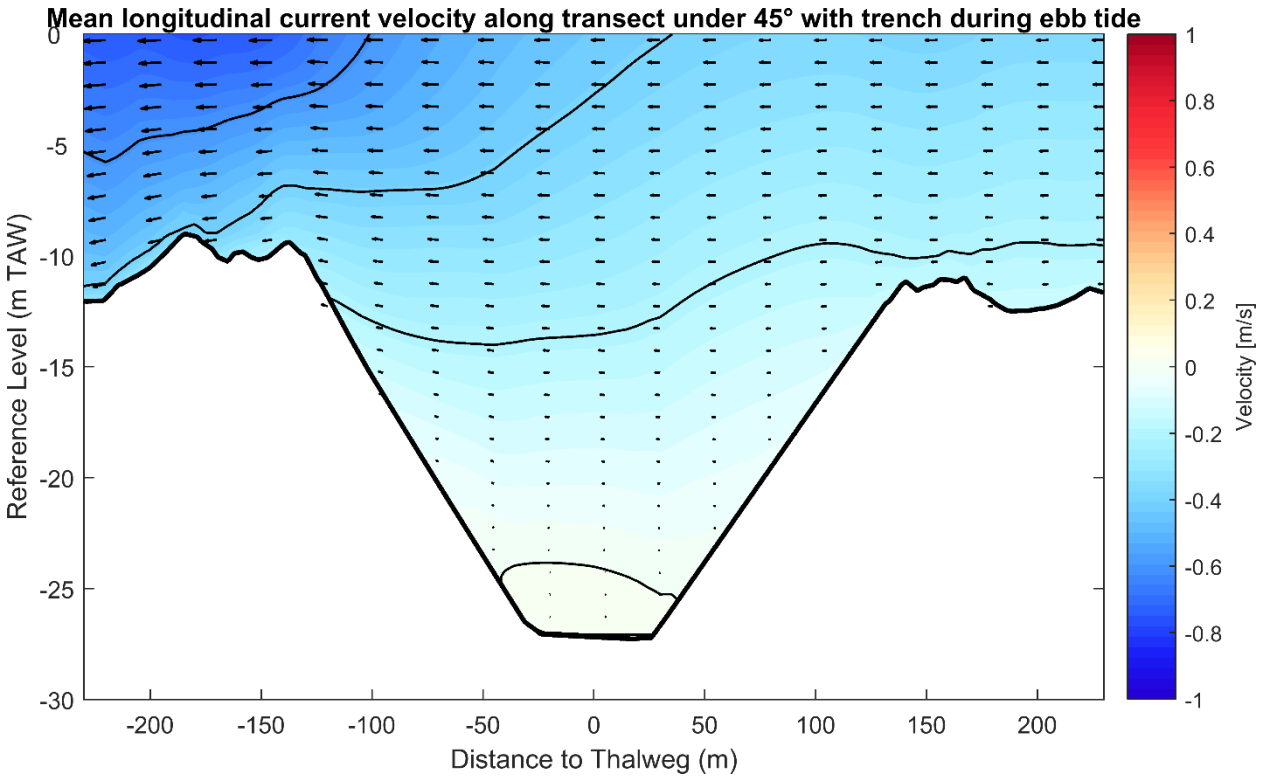
Mean longitudinal current velocity along transect under 45° with trench during ebb tide
Reference Level (m TAW)
0
-5
-10
-15
-20
-25
-30
-200
-150
-100
-50
0
50
100
150
200
Distance to Thalweg (m)
Velocity [m/s]
1
0.8
0.6
0.4
0.2
0
-0.2
-0.4
-0.6
-0.8
-1

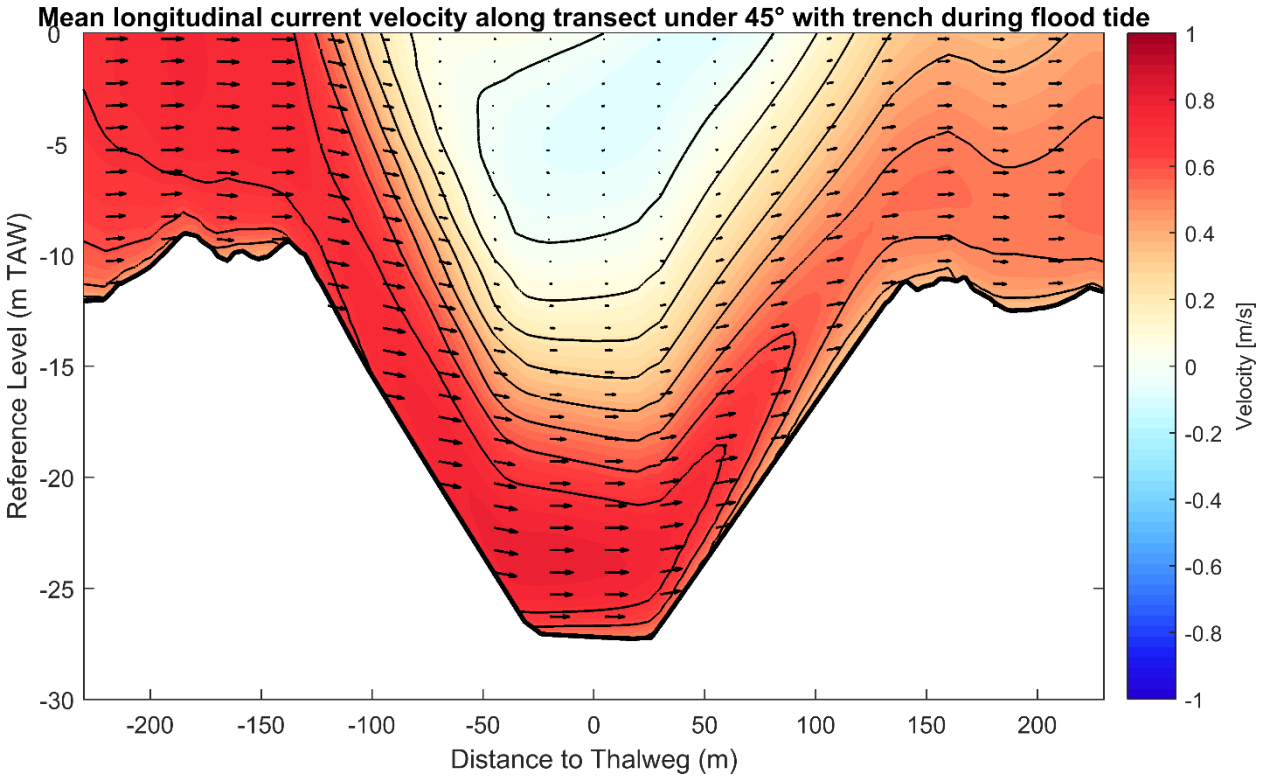
Mean longitudinal current velocity along transect under 45° with trench during flood tide
Reference Level (m TAW)
0
-5
-10
-15
-20
-25
-30
-200
-150
-100
-50
0
50
100
150
200
Distance to Thalweg (m)
Velocity [m/s]
1
0.8
0.6
0.4
0.2
0
-0.2
-0.4
-0.6
-0.8
-1

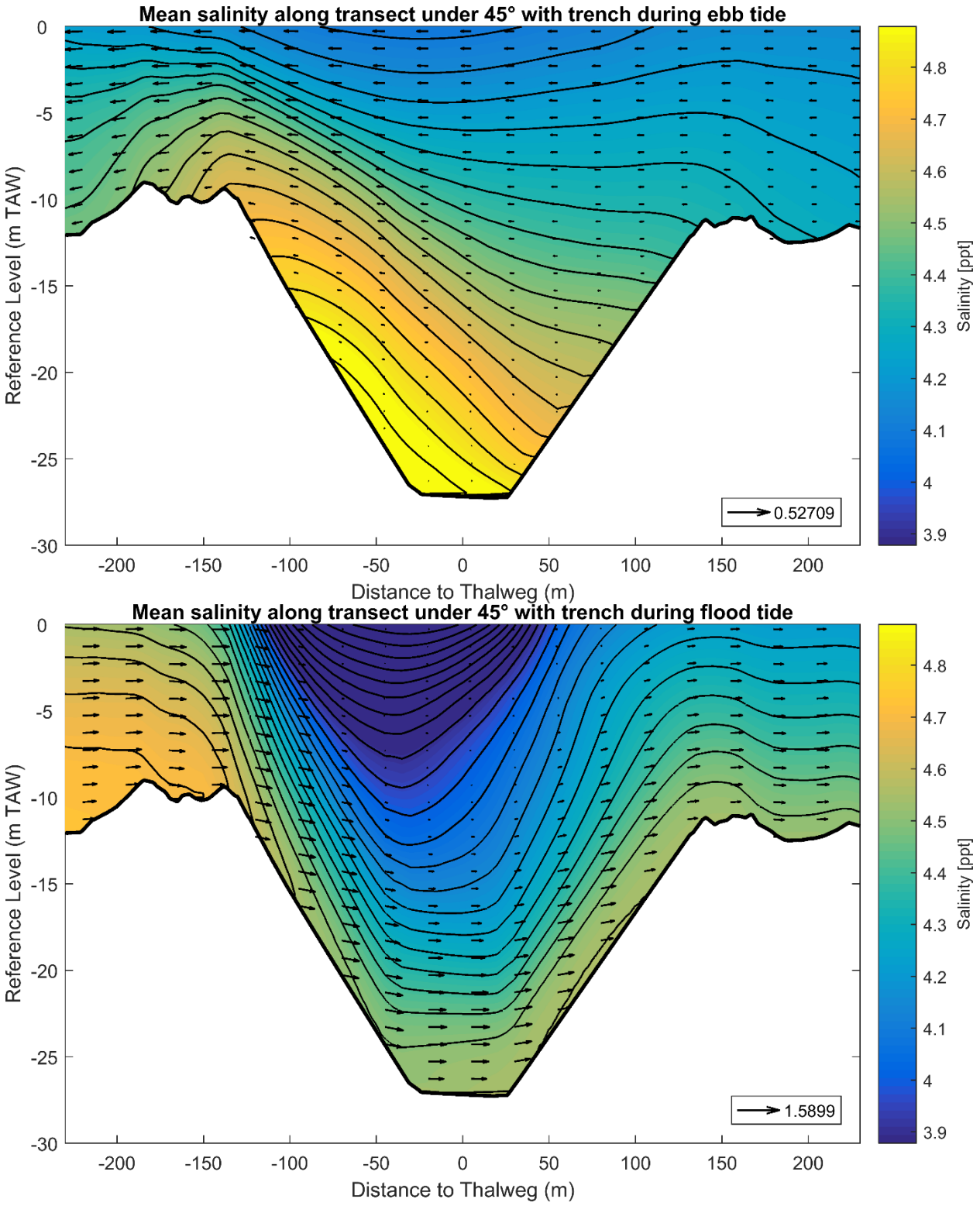
Mean salinity along transect under 45° with trench during ebb tide
Reference Level (m TAW)
0
-5
-10
-15
-20
-25
-30
-200
-150
-100
-50
0
50
100
150
200
Distance to Thalweg (m)
0.52709
Salinity [ppt]
4.8
4.7
4.6
4.5
4.4
4.3
4.2
4.1
4
3.9
Mean salinity along transect under 45° with trench during flood tide
Reference Level (m TAW)
Distance to Thalweg (m)
1.5899
Salinity [ppt]

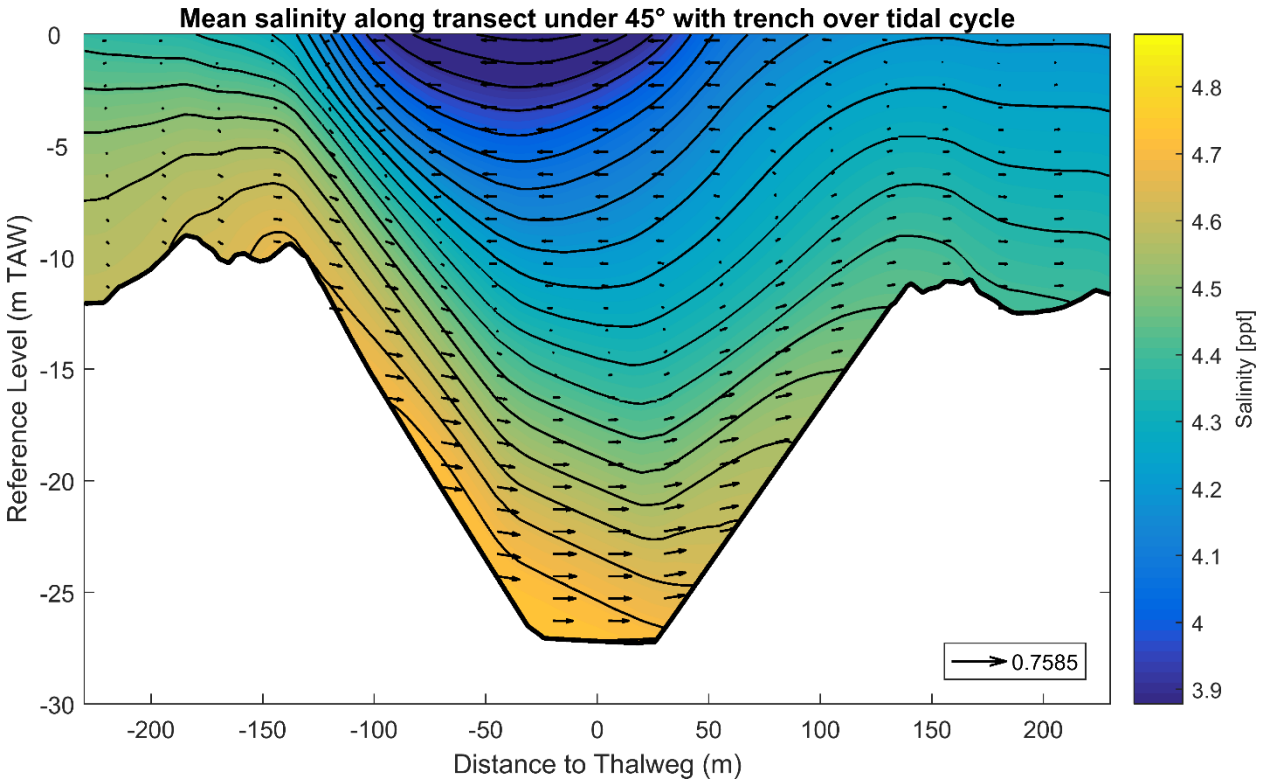
Mean salinity along transect under 45° with trench over tidal cycle
Reference Level (m TAW)
Distance to Thalweg (m)
Salinity [ppt]
0.7585

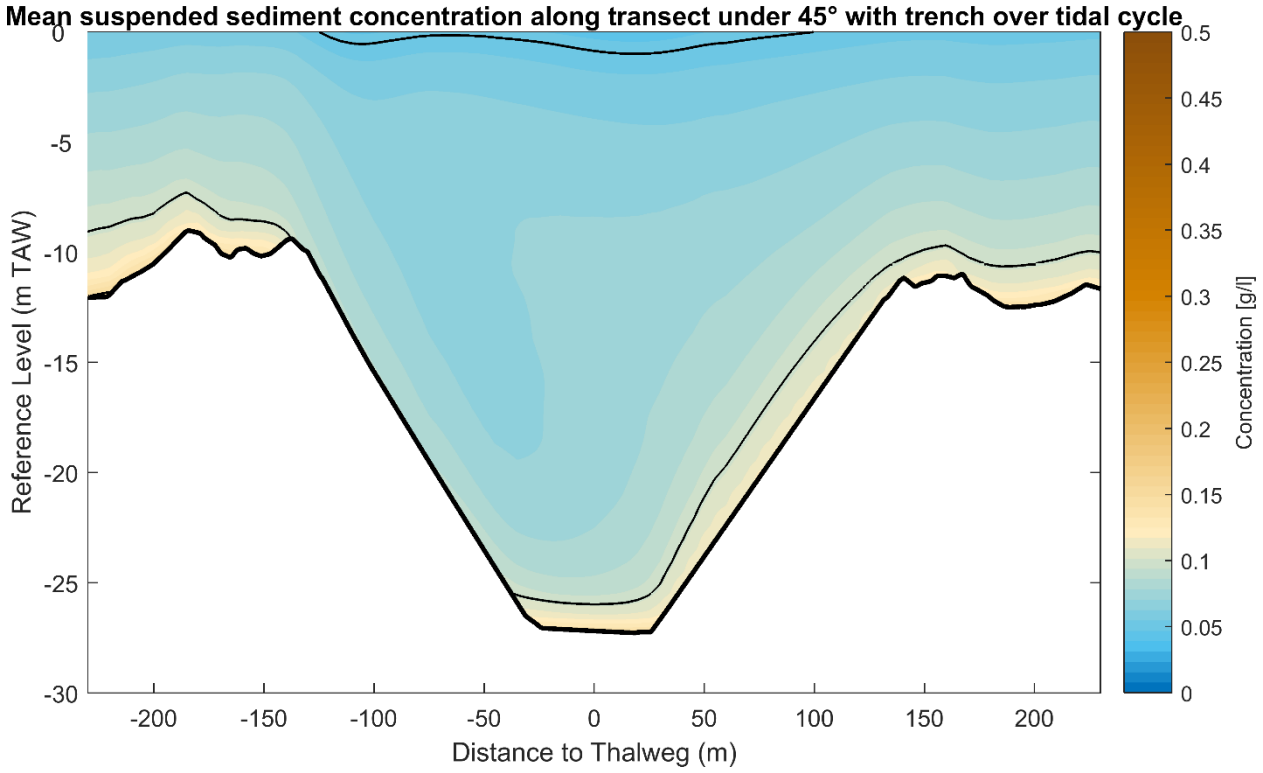
Mean suspended sediment concentration along transect under 45° with trench over tidal cycle
Reference Level (m TAW)
Distance to Thalweg (m)
Concentration [g/l]

Mean suspended sediment concentration along transect under 45° with trench during ebb tide

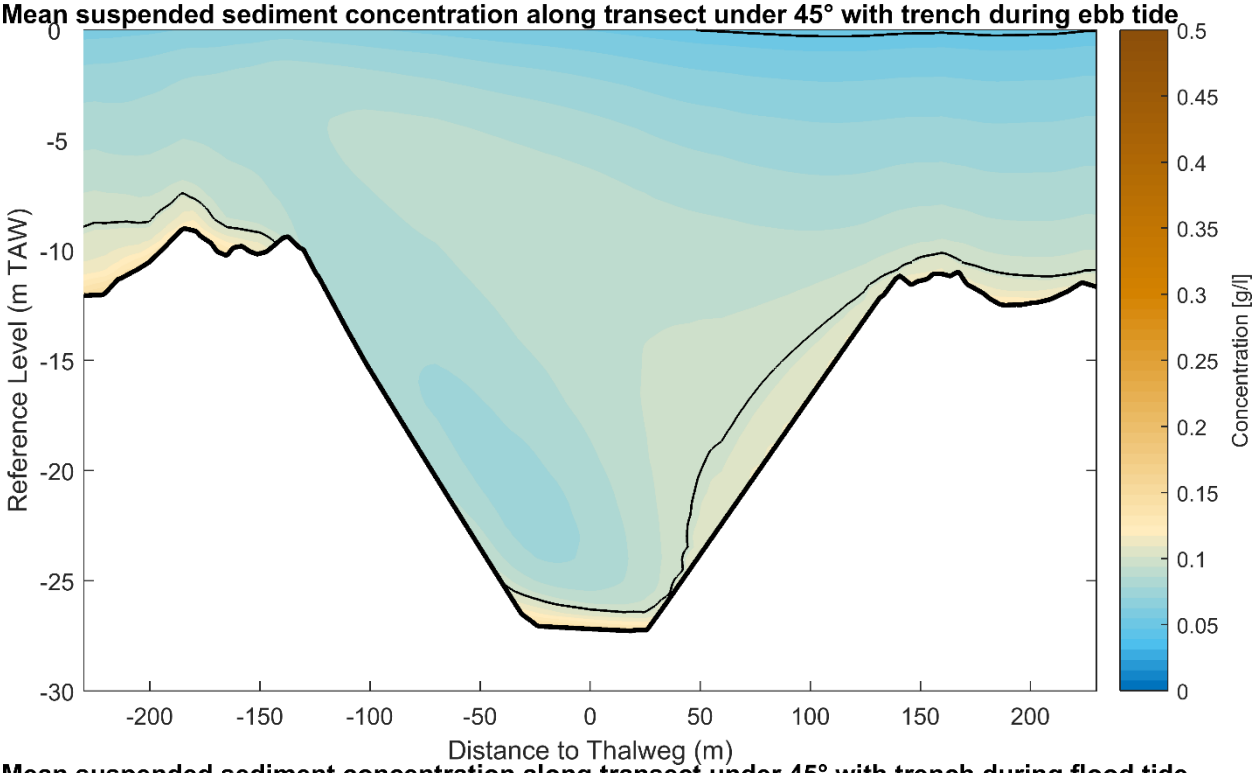

Mean suspended sediment concentration along transect under 45° with trench during flood tide

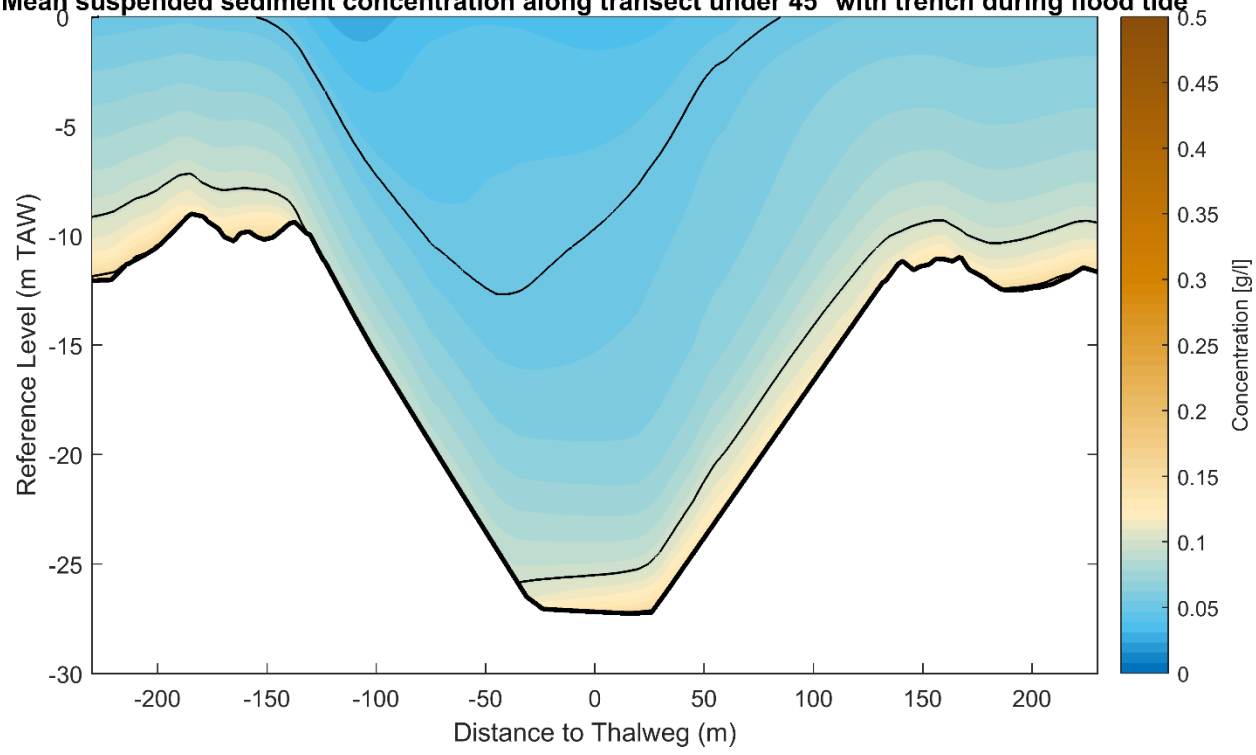

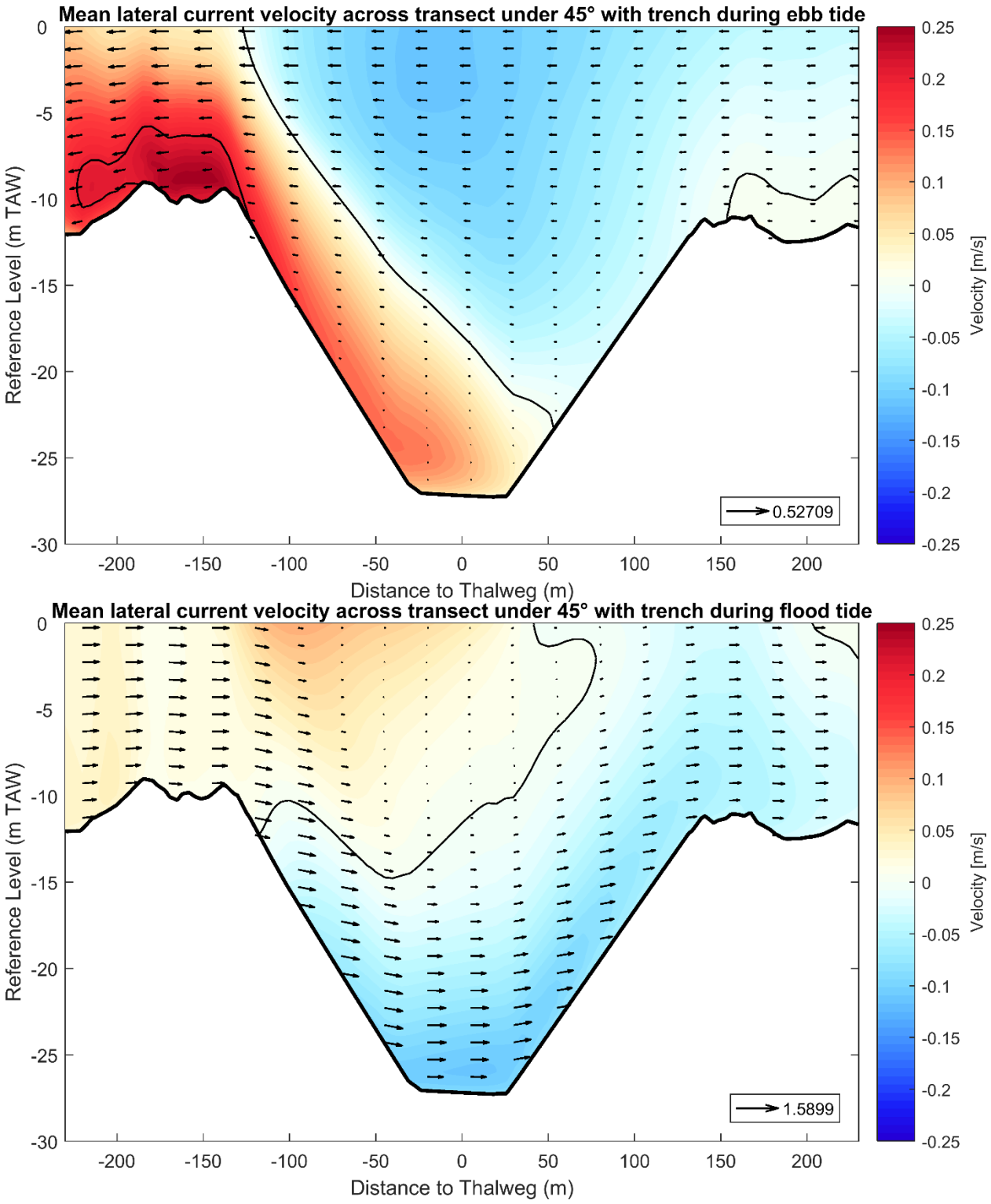
Mean lateral current velocity across transect under 45° with trench during ebb tide
Reference Level (m TAW)
Distance to Thalweg (m)
Velocity [m/s]
0.52709
Mean lateral current velocity across transect under 45° with trench during flood tide
Reference Level (m TAW)
Distance to Thalweg (m)
Velocity [m/s]
1.5899

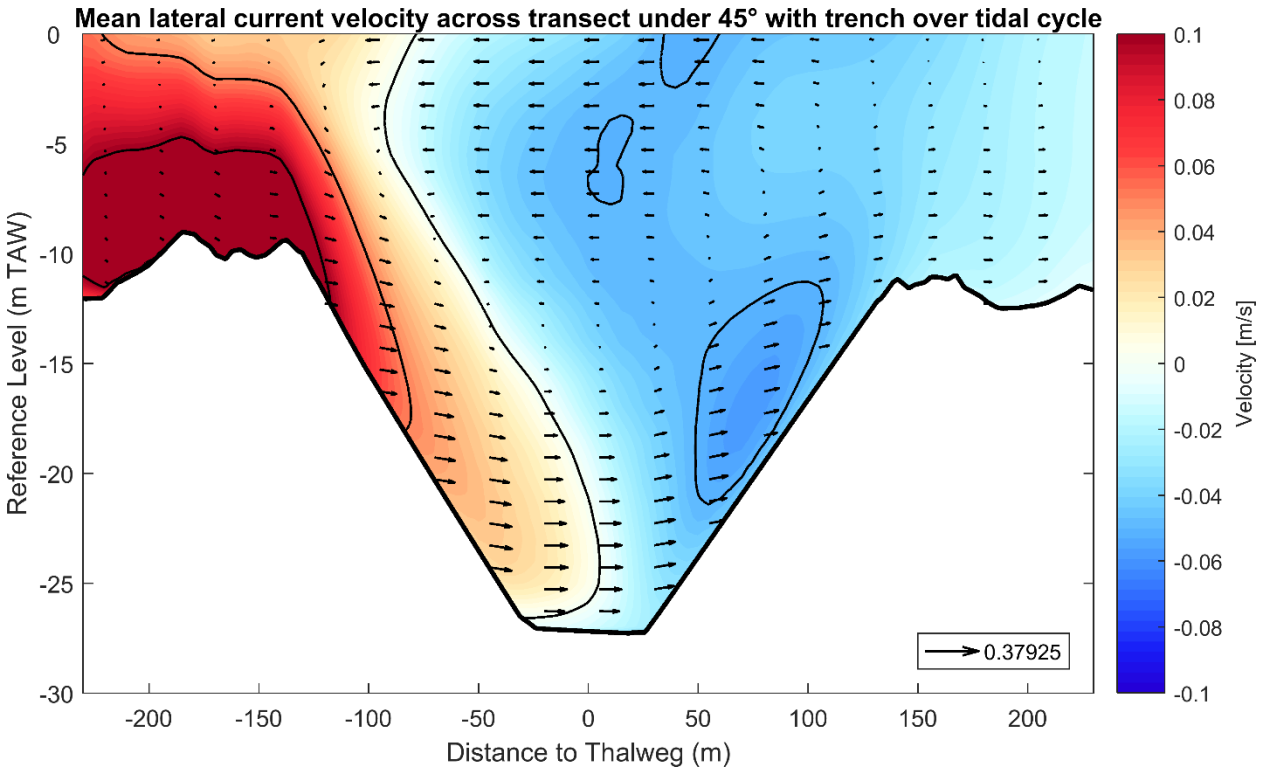
Mean lateral current velocity across transect under 45° with trench over tidal cycle
Reference Level (m TAW)
Distance to Thalweg (m)
Velocity [m/s]
0.37925

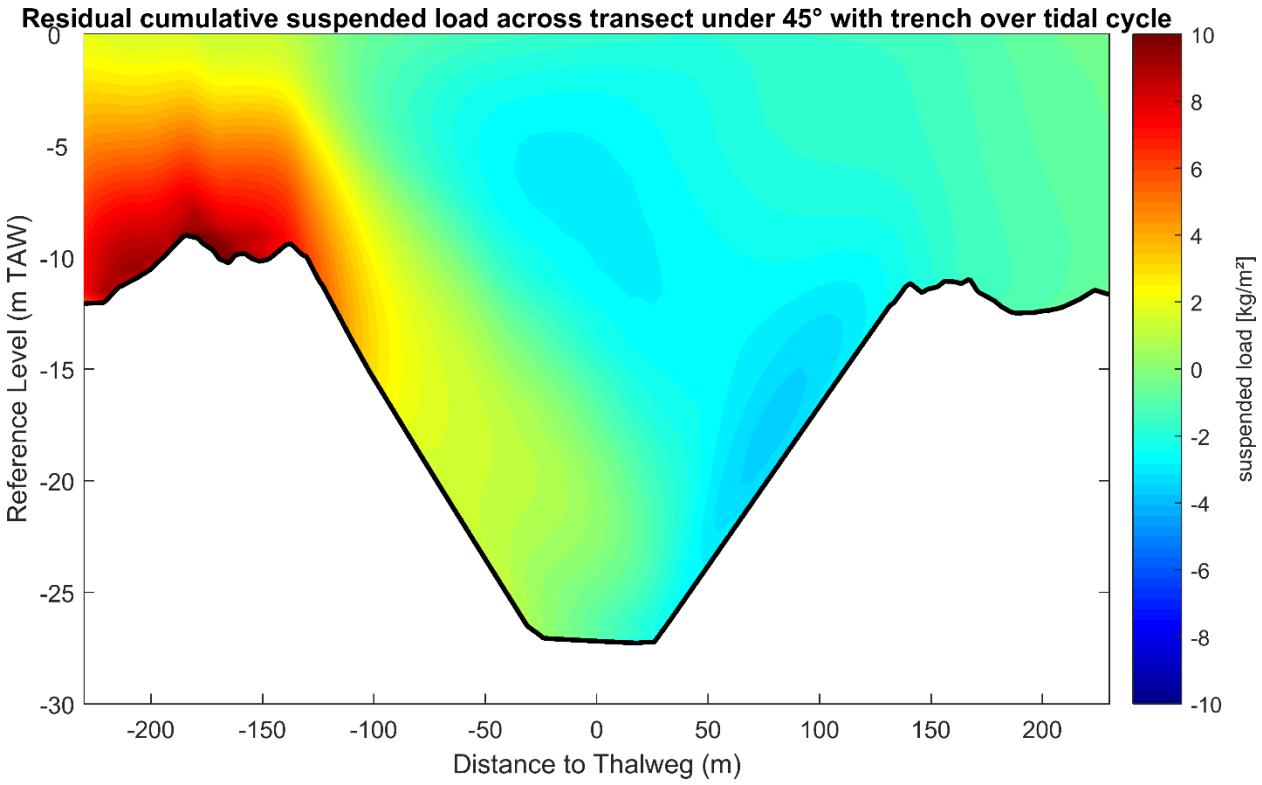
Residual cumulative suspended load across transect under 45° with trench over tidal cycle
Reference Level (m TAW)
Distance to Thalweg (m)
suspended load [kg/m²]

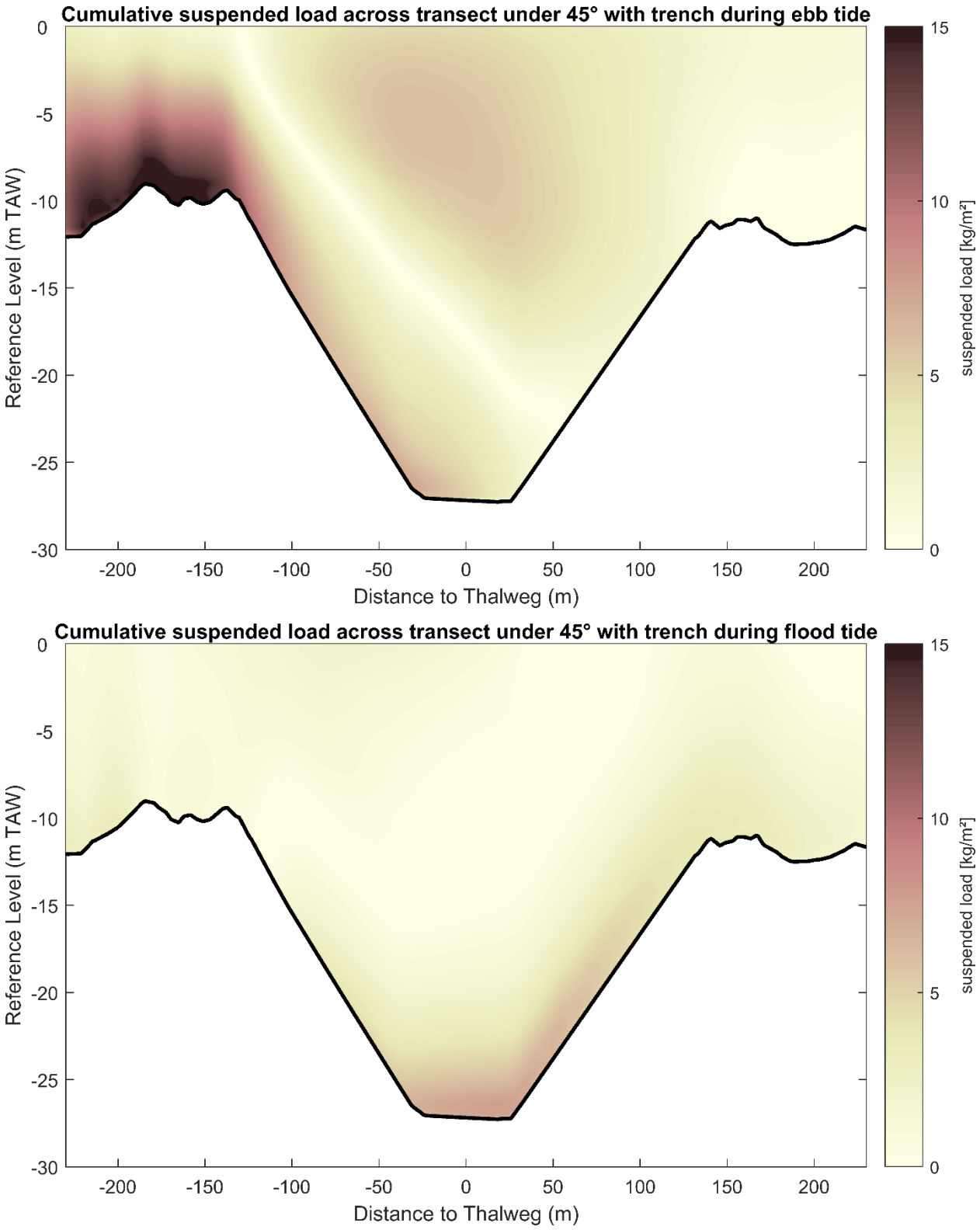
Cumulative suspended load across transect under 45° with trench during ebb tide
Reference Level (m TAW)
0
-5
-10
-15
-20
-25
-30
-200
-150
-100
-50
0
50
100
150
200
Distance to Thalweg (m)
15
10
5
0
suspended load [kg/m²]
Cumulative suspended load across transect under 45° with trench during flood tide
Reference Level (m TAW)
Distance to Thalweg (m)
suspended load [kg/m²]

G.4 Trench

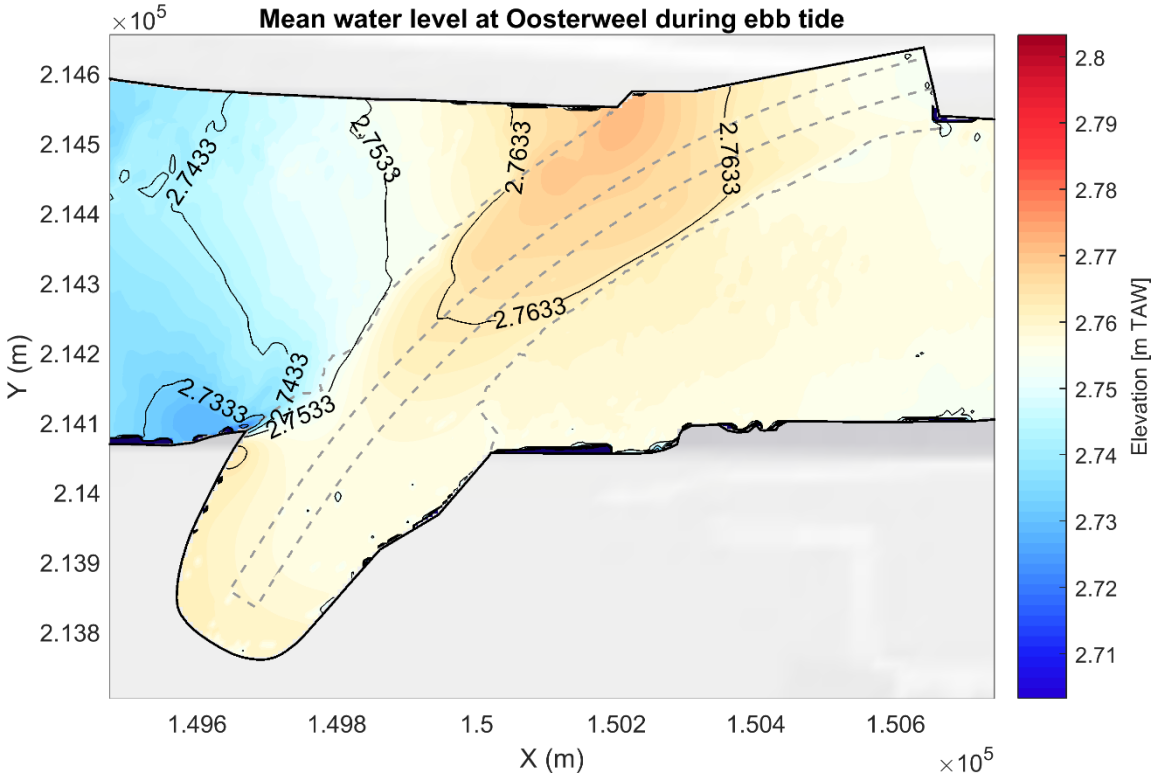
Mean water level at Oosterweel during ebb tide
×10^5
2.146
2.145
2.144
2.143
2.142
2.141
2.14
2.139
2.138
Y (m)
2.7433
2.7533
2.7633
2.7633
2.7633
2.7333
2.7433
2.7533
1.496
1.498
1.5
1.502
1.504
1.506
X (m)
×10^5
2.8
2.79
2.78
2.77
2.76
2.75
2.74
2.73
2.72
2.71
Elevation [m TAW]

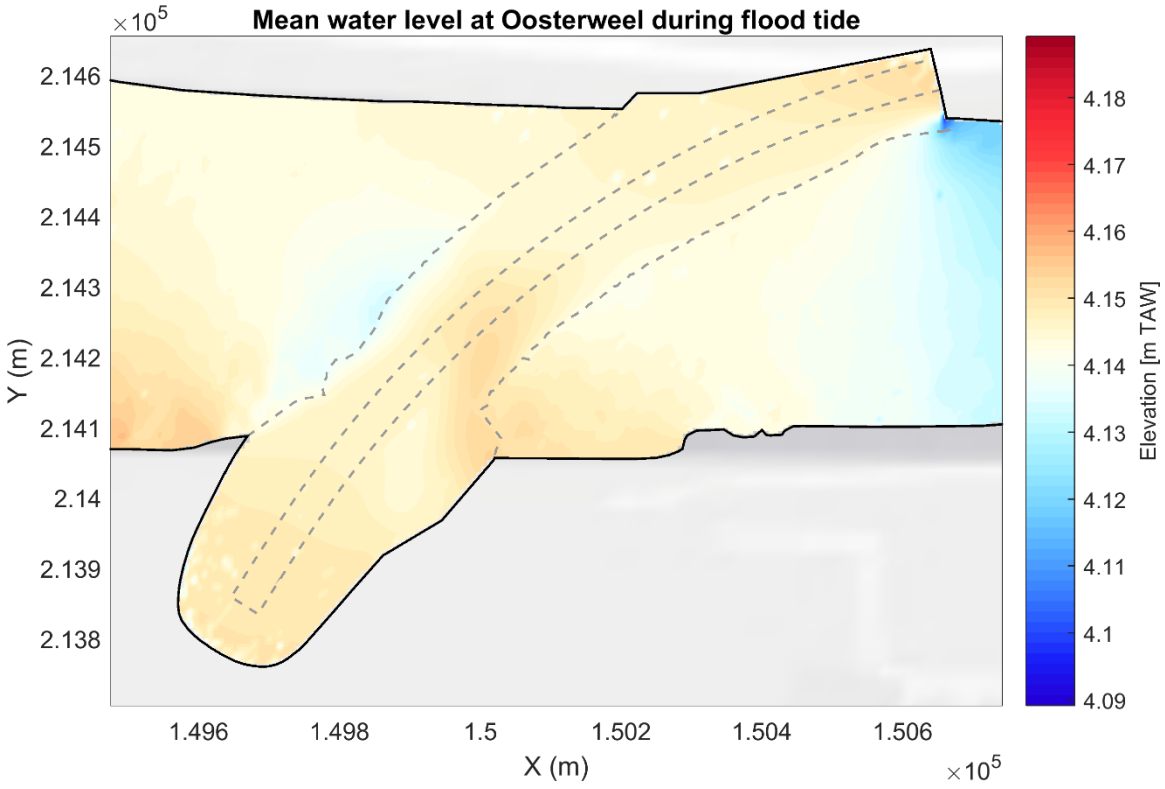
Mean water level at Oosterweel during flood tide
×10^5
2.146
2.145
2.144
2.143
2.142
2.141
2.14
2.139
2.138
Y (m)
1.496
1.498
1.5
1.502
1.504
1.506
X (m)
×10^5
4.18
4.17
4.16
4.15
4.14
4.13
4.12
4.11
4.1
4.09
Elevation [m TAW]

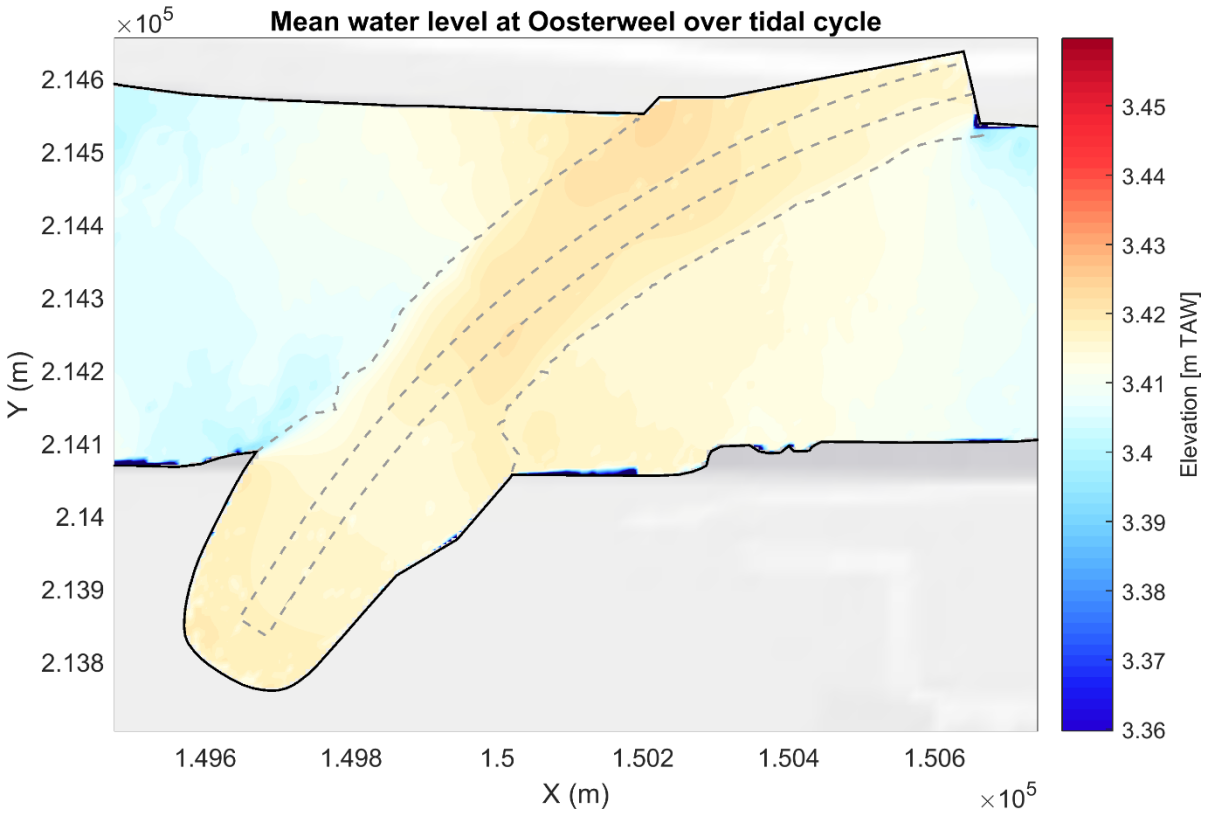
Mean water level at Oosterweel over tidal cycle
×10^5
2.146
2.145
2.144
2.143
2.142
2.141
2.14
2.139
2.138
Y (m)
1.496
1.498
1.5
1.502
1.504
1.506
X (m)
×10^5
3.45
3.44
3.43
3.42
3.41
3.4
3.39
3.38
3.37
3.36
Elevation [m TAW]

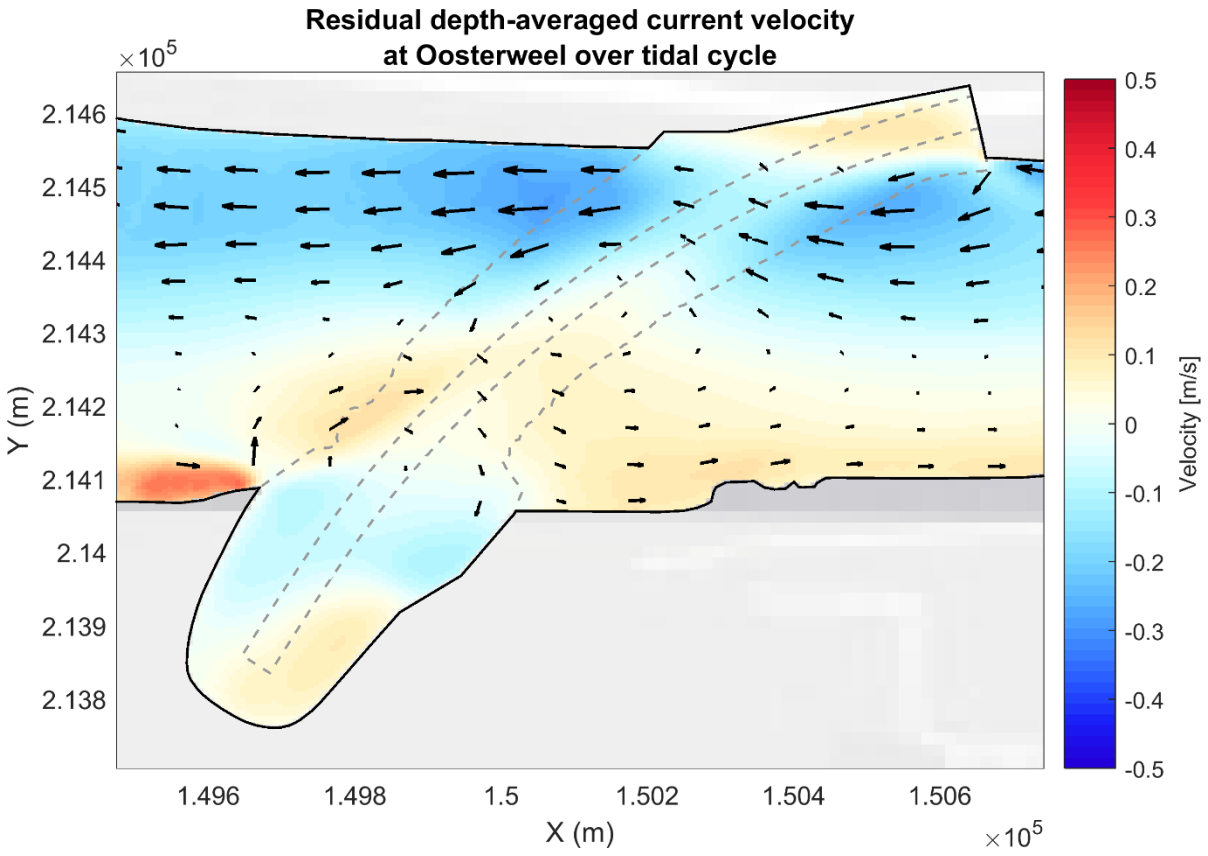
Residual depth-averaged current velocity
at Oosterweel over tidal cycle
×10^5
2.146
2.145
2.144
2.143
2.142
2.141
2.14
2.139
2.138
Y (m)
1.496
1.498
1.5
1.502
1.504
1.506
X (m)
×10^5
0.5
0.4
0.3
0.2
0.1
0
-0.1
-0.2
-0.3
-0.4
-0.5
Velocity [m/s]

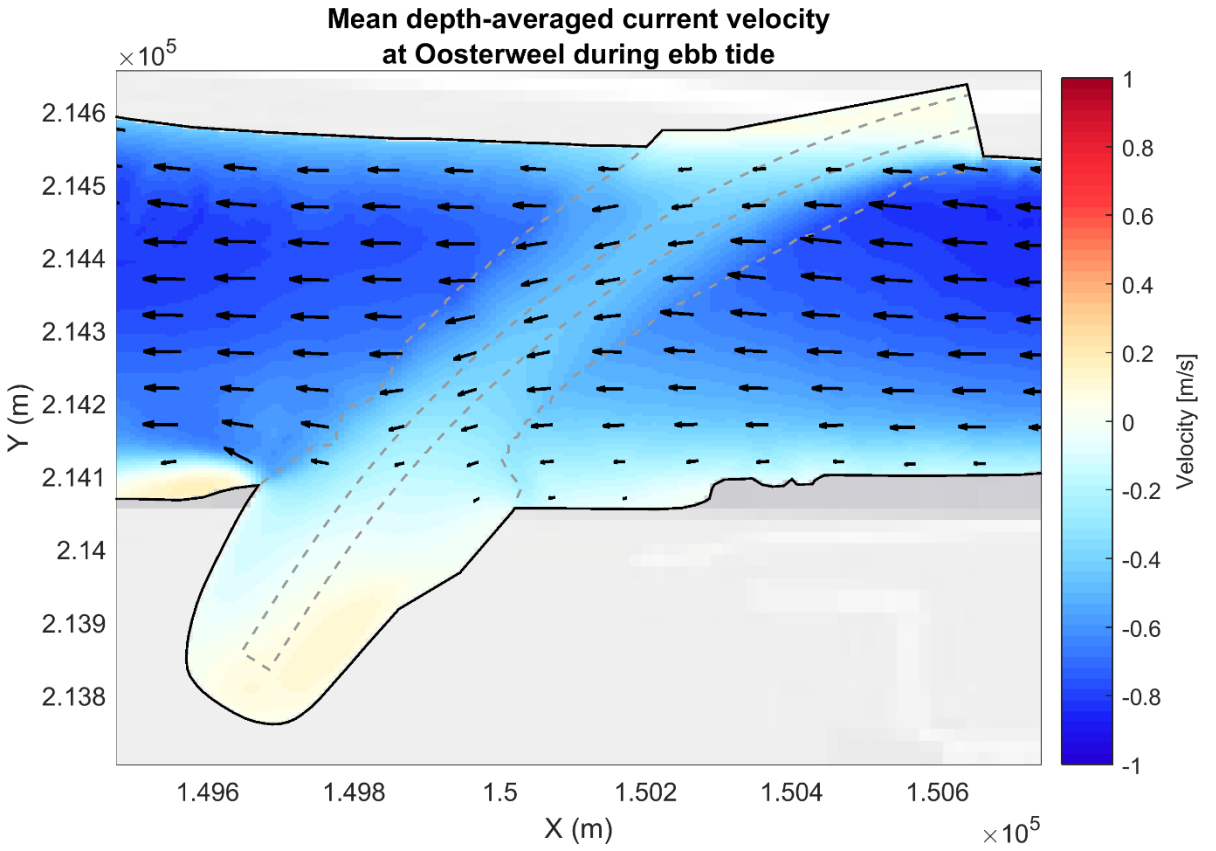
Mean depth-averaged current velocity
at Oosterweel during ebb tide
×10^5
2.146
2.145
2.144
2.143
2.142
2.141
2.14
2.139
2.138
Y (m)
1.496
1.498
1.5
1.502
1.504
1.506
X (m)
×10^5
1
0.8
0.6
0.4
0.2
0
-0.2
-0.4
-0.6
-0.8
-1
Velocity [m/s]

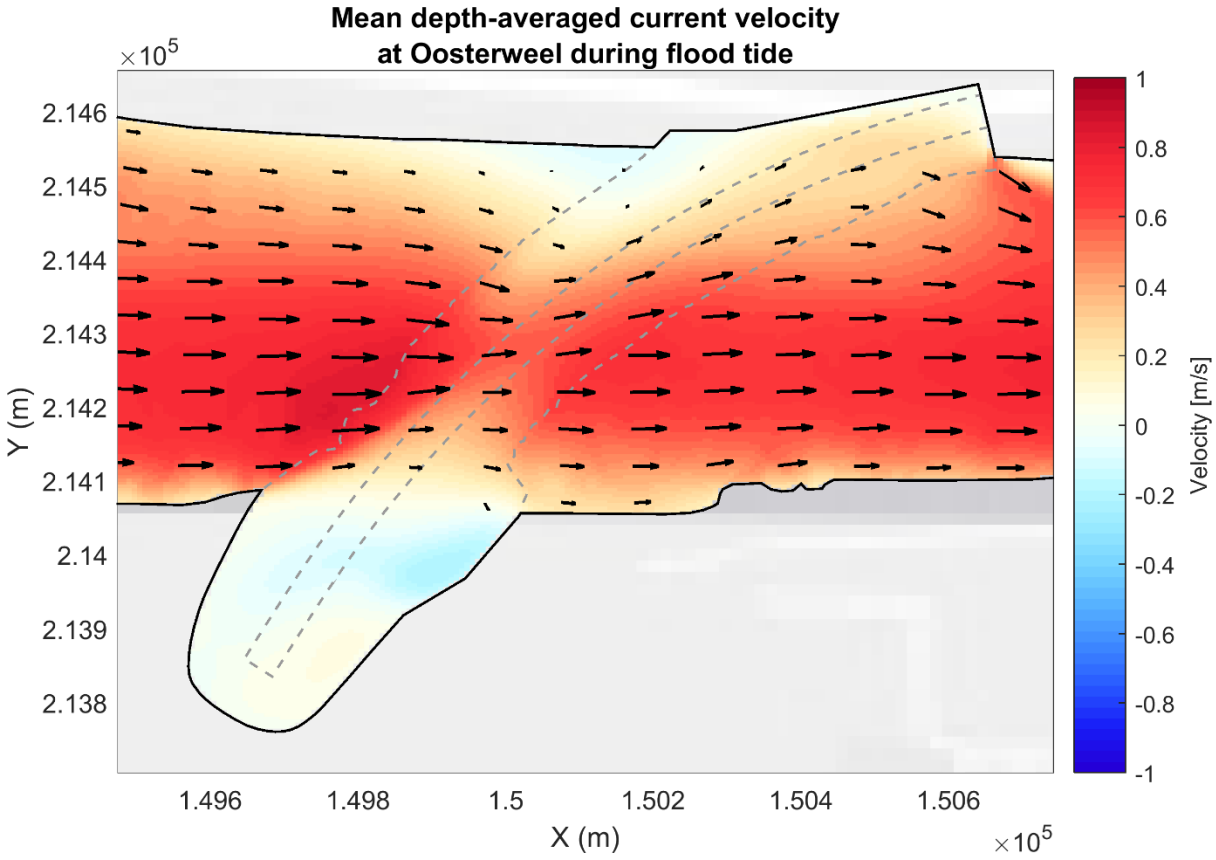
Mean depth-averaged current velocity
at Oosterweel during flood tide
×10^5
2.146
2.145
2.144
2.143
2.142
2.141
2.14
2.139
2.138
Y (m)
1.496
1.498
1.5
1.502
1.504
1.506
X (m)
×10^5
1
0.8
0.6
0.4
0.2
0
-0.2
-0.4
-0.6
-0.8
-1
Velocity [m/s]

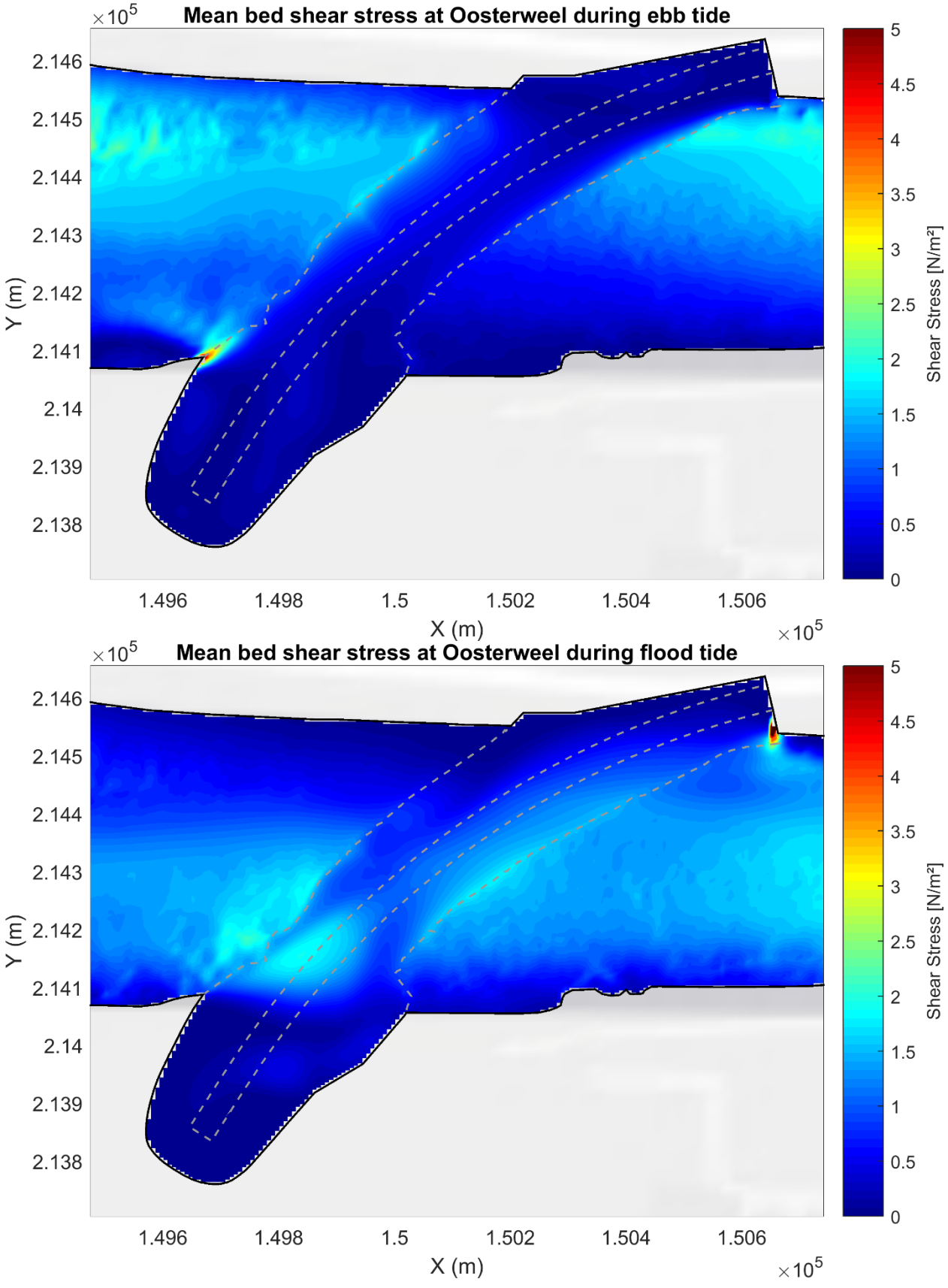
Mean bed shear stress at Oosterweel during ebb tide
×10^5
2.146
2.145
2.144
2.143
2.142
2.141
2.14
2.139
2.138
Y (m)
1.496
1.498
1.5
1.502
1.504
1.506
X (m)
×10^5
Shear Stress [N/m²]
5
4.5
4
3.5
3
2.5
2
1.5
1
0.5
0
Mean bed shear stress at Oosterweel during flood tide
×10^5
2.146
2.145
2.144
2.143
2.142
2.141
2.14
2.139
2.138
Y (m)
1.496
1.498
1.5
1.502
1.504
1.506
X (m)
×10^5
Shear Stress [N/m²]
5
4.5
4
3.5
3
2.5
2
1.5
1
0.5
0

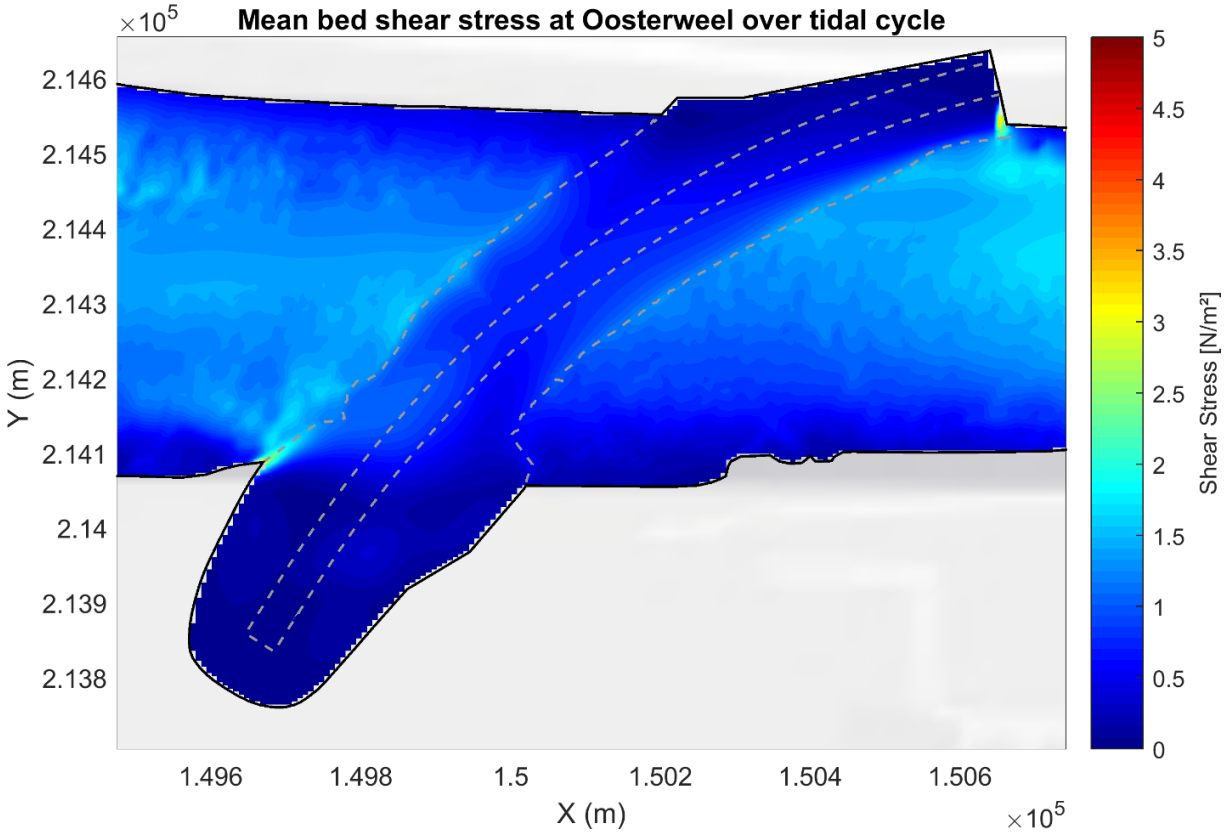
Mean bed shear stress at Oosterweel over tidal cycle
×10^5
2.146
2.145
2.144
2.143
2.142
2.141
2.14
2.139
2.138
Y (m)
1.496
1.498
1.5
1.502
1.504
1.506
X (m)
×10^5
5
4.5
4
3.5
3
2.5
2
1.5
1
0.5
0
Shear Stress [N/m²]

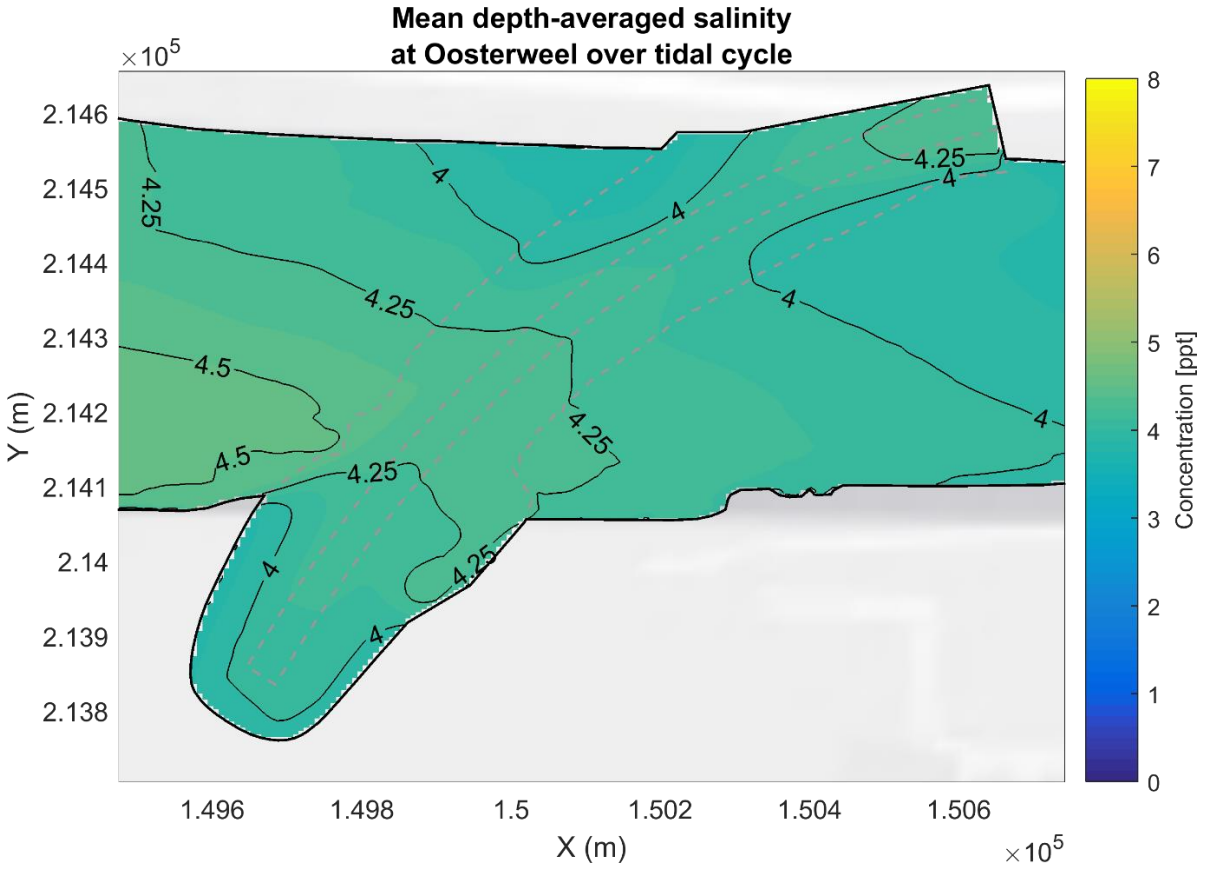
Mean depth-averaged salinity
at Oosterweel over tidal cycle
×10^5
2.146
2.145
2.144
2.143
2.142
2.141
2.14
2.139
2.138
Y (m)
4.25
4
4.5
1.496
1.498
1.5
1.502
1.504
1.506
X (m)
×10^5
8
7
6
5
4
3
2
1
0
Concentration [ppt]

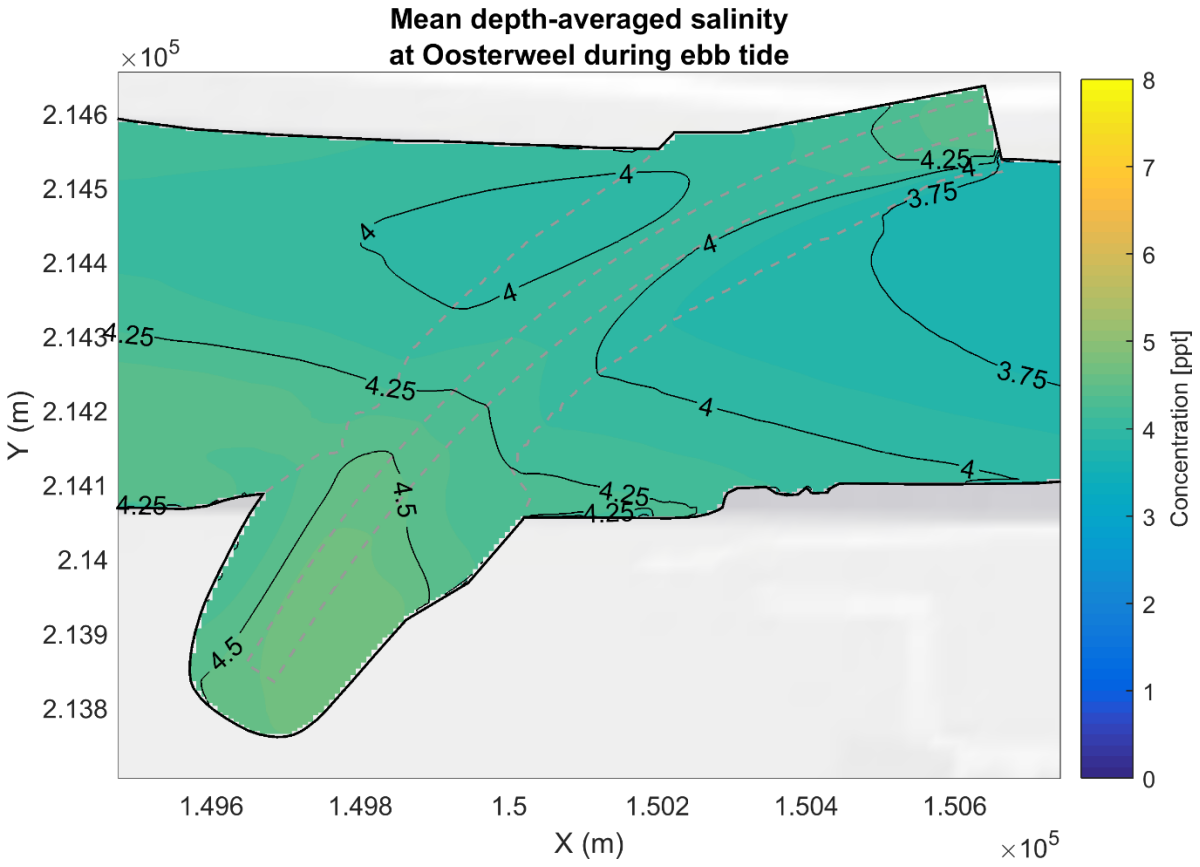
Mean depth-averaged salinity
at Oosterweel during ebb tide
×10^5
2.146
2.145
2.144
2.143
2.142
2.141
2.14
2.139
2.138
Y (m)
1.496
1.498
1.5
1.502
1.504
1.506
X (m)
×10^5
Concentration [ppt]
0
1
2
3
4
5
6
7
8

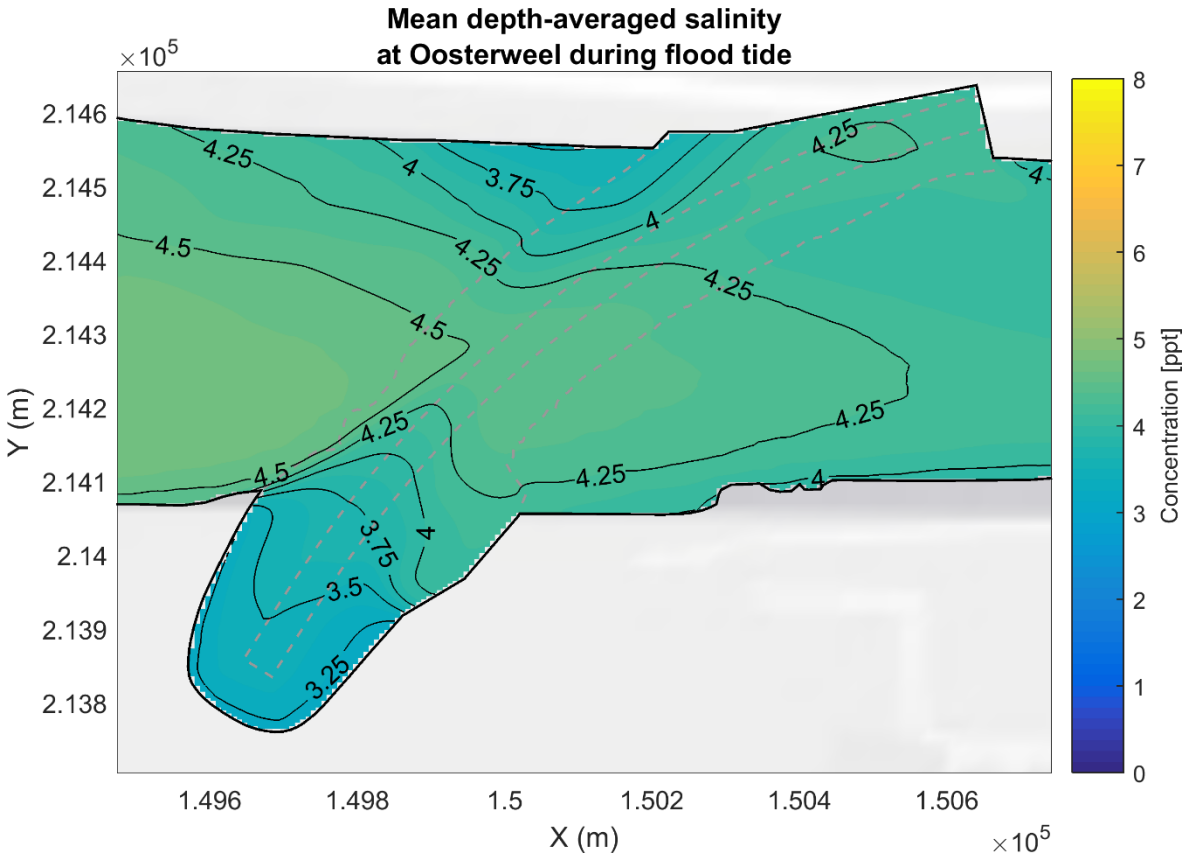
Mean depth-averaged salinity
at Oosterweel during flood tide
×10^5
2.146
2.145
2.144
2.143
2.142
2.141
2.14
2.139
2.138
Y (m)
1.496
1.498
1.5
1.502
1.504
1.506
X (m)
×10^5
Concentration [ppt]
0
1
2
3
4
5
6
7
8

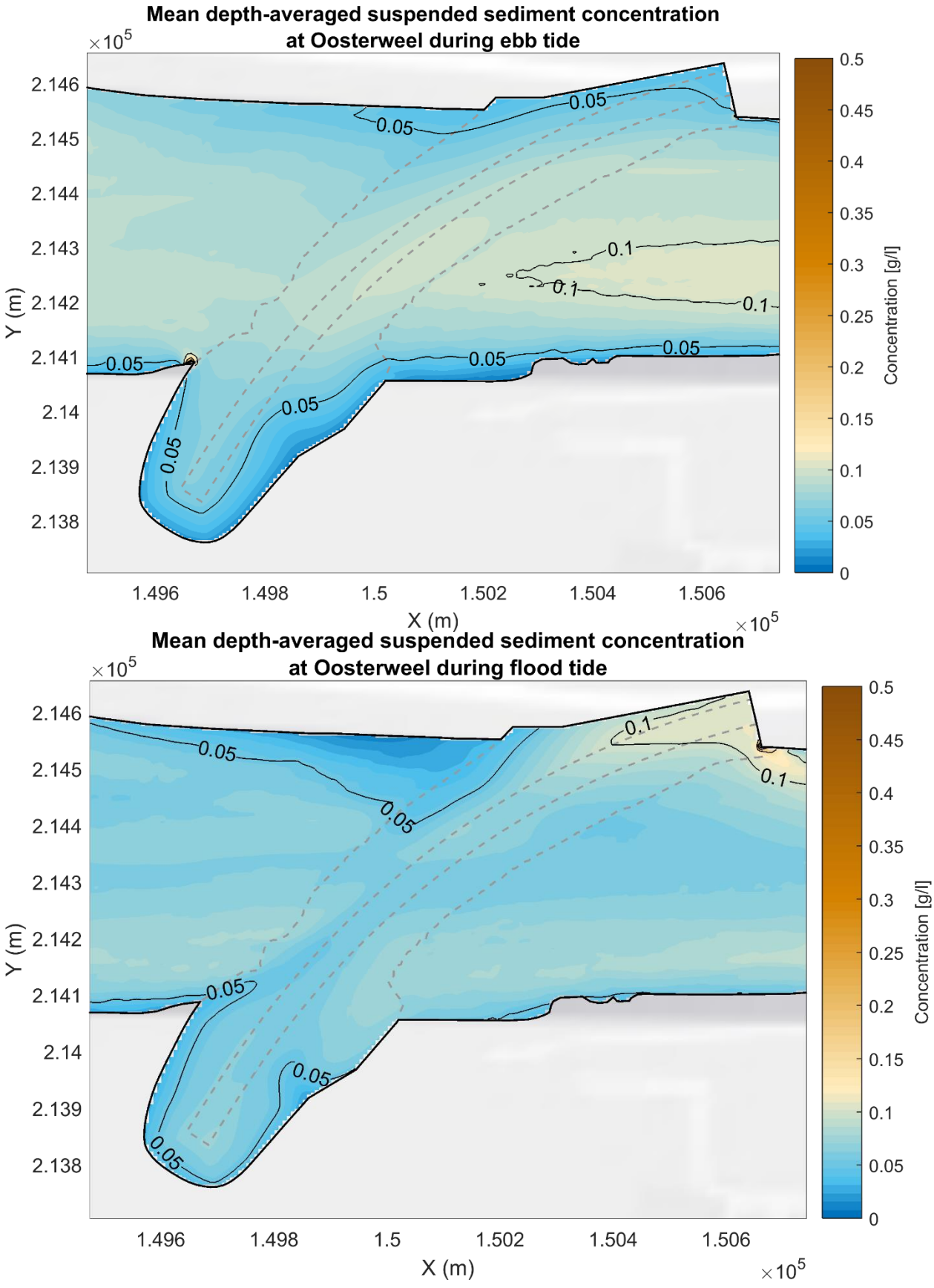
Mean depth-averaged suspended sediment concentration
at Oosterweel during ebb tide
×10^5
2.146
2.145
2.144
2.143
2.142
2.141
2.14
2.139
2.138
Y (m)
0.05
0.1
1.496
1.498
1.5
1.502
1.504
1.506
X (m)
×10^5
0.5
0.45
0.4
0.35
0.3
0.25
0.2
0.15
0.1
0.05
0
Concentration [g/l]
Mean depth-averaged suspended sediment concentration
at Oosterweel during flood tide
×10^5
2.146
2.145
2.144
2.143
2.142
2.141
2.14
2.139
2.138
Y (m)
0.05
0.1
1.496
1.498
1.5
1.502
1.504
1.506
X (m)
×10^5
0.5
0.45
0.4
0.35
0.3
0.25
0.2
0.15
0.1
0.05
0
Concentration [g/l]

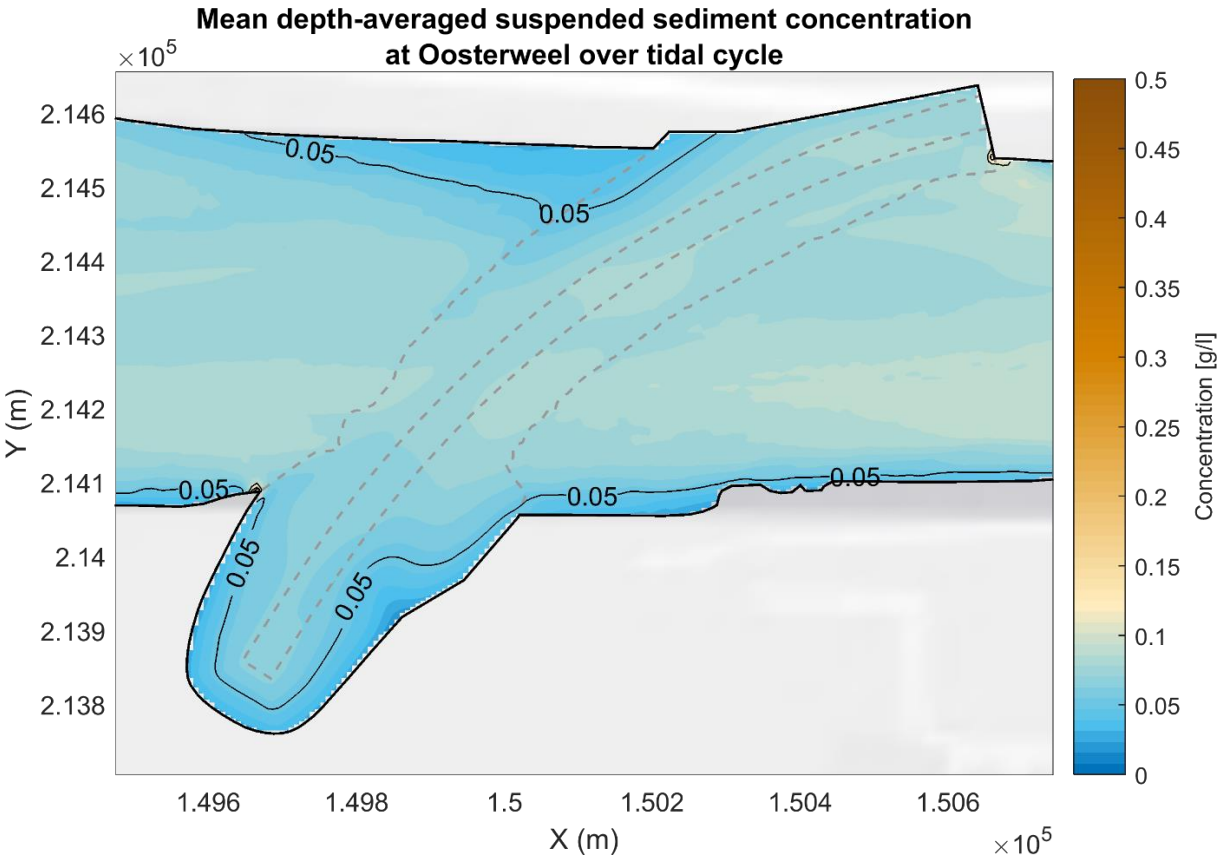
Mean depth-averaged suspended sediment concentration
at Oosterweel over tidal cycle
×10^5
2.146
2.145
2.144
2.143
2.142
2.141
2.14
2.139
2.138
Y (m)
0.05
0.05
0.05
0.05
0.05
0.05
1.496
1.498
1.5
1.502
1.504
1.506
X (m)
×10^5
0.5
0.45
0.4
0.35
0.3
0.25
0.2
0.15
0.1
0.05
0
Concentration [g/l]

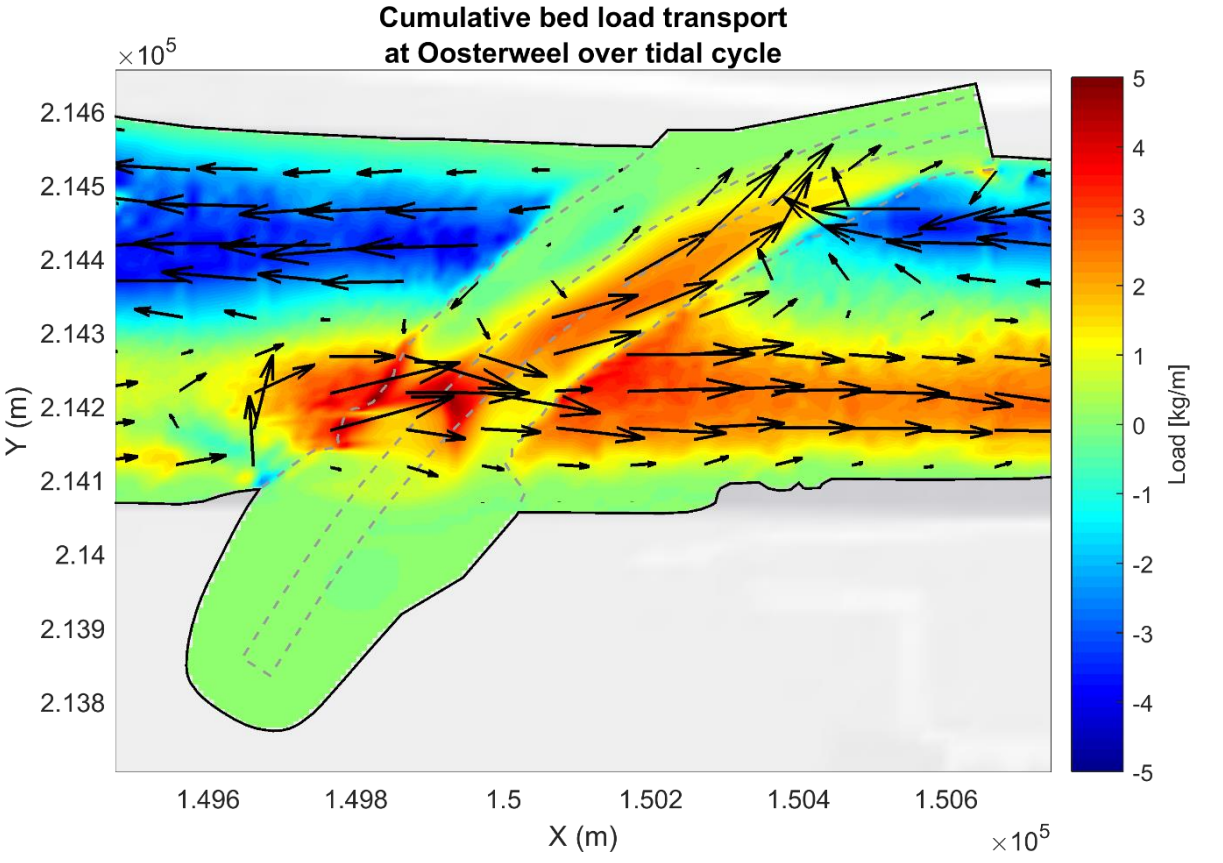
Cumulative bed load transport
at Oosterweel over tidal cycle
×10^5
2.146
2.145
2.144
2.143
2.142
2.141
2.14
2.139
2.138
Y (m)
1.496
1.498
1.5
1.502
1.504
1.506
X (m)
×10^5
5
4
3
2
1
0
-1
-2
-3
-4
-5
Load [kg/m]

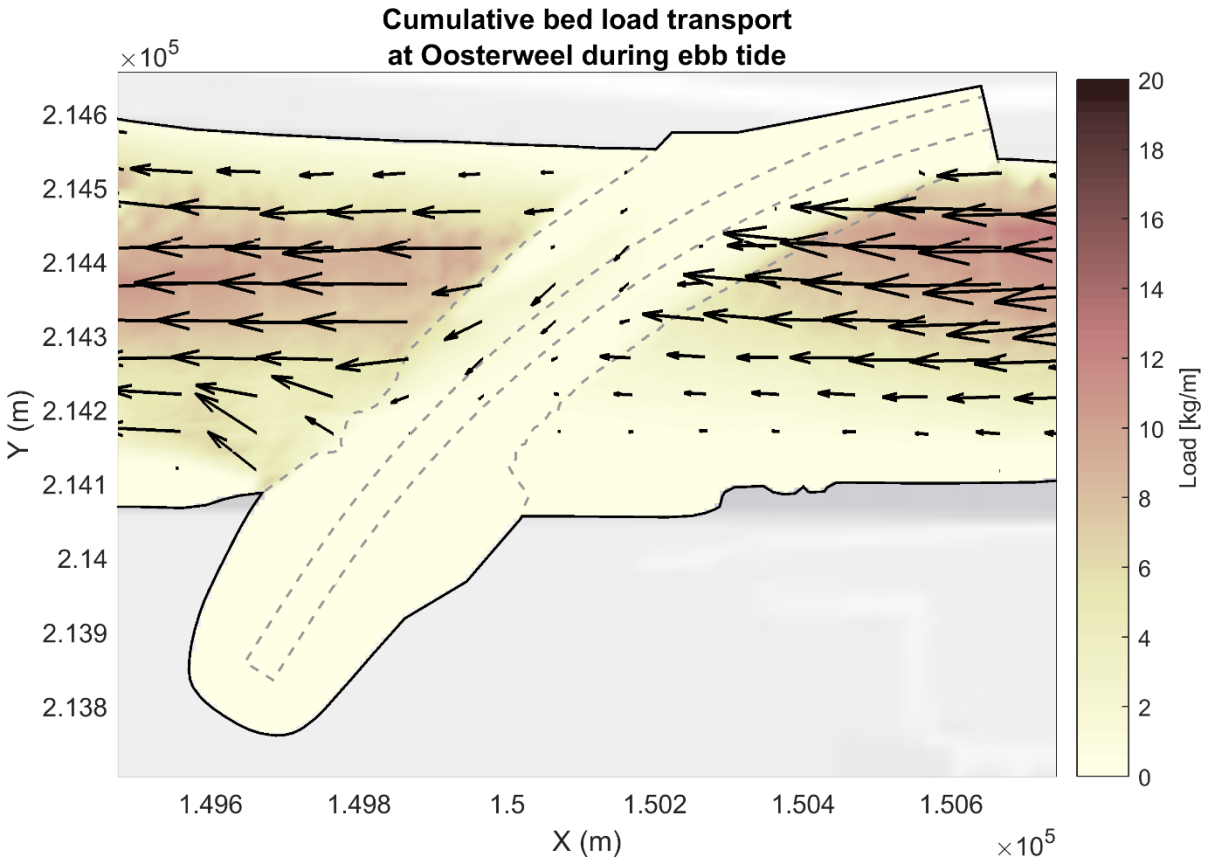
Cumulative bed load transport
at Oosterweel during ebb tide
×10^5
2.146
2.145
2.144
2.143
2.142
2.141
2.14
2.139
2.138
Y (m)
1.496
1.498
1.5
1.502
1.504
1.506
X (m)
×10^5
20
18
16
14
12
10
8
6
4
2
0
Load [kg/m]

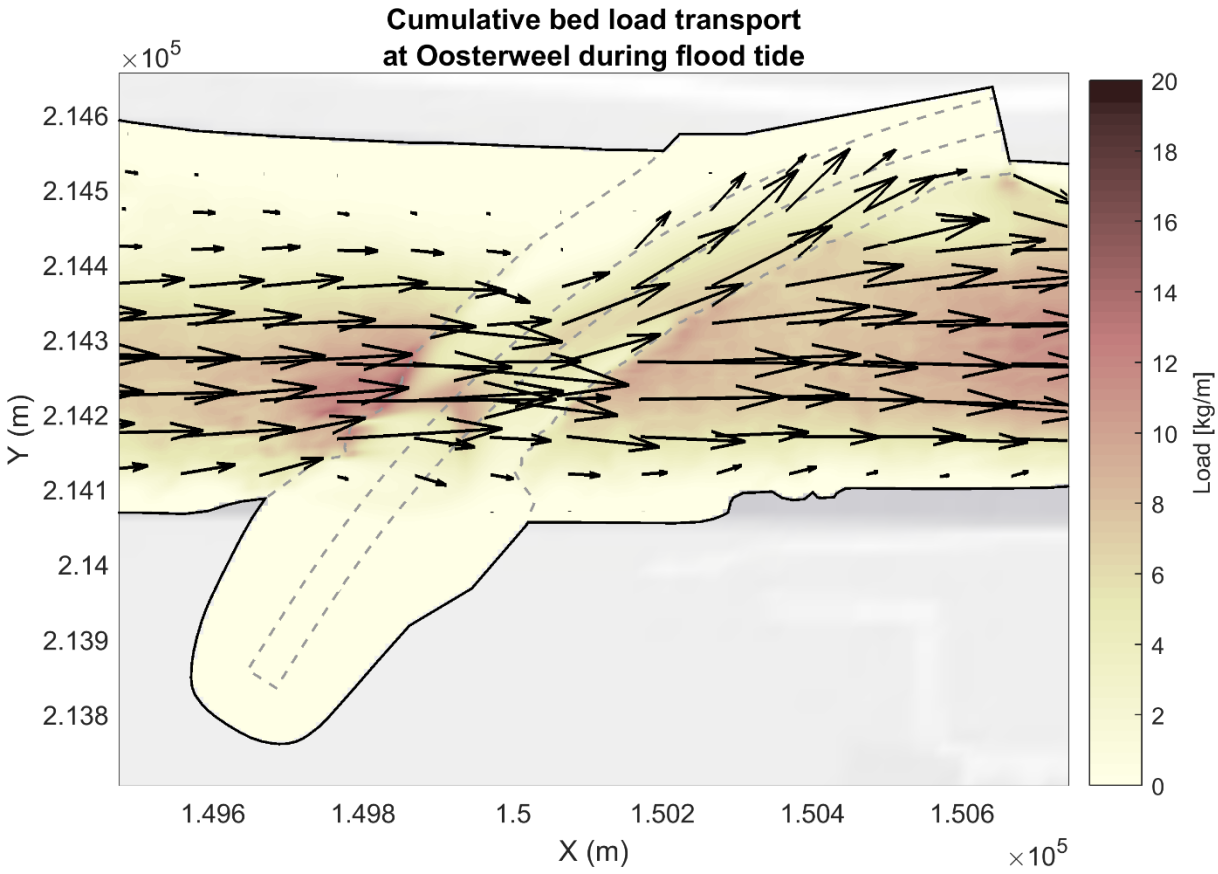
Cumulative bed load transport
at Oosterweel during flood tide
×10^5
2.146
2.145
2.144
2.143
2.142
2.141
2.14
2.139
2.138
Y (m)
1.496
1.498
1.5
1.502
1.504
1.506
X (m)
×10^5
20
18
16
14
12
10
8
6
4
2
0
Load [kg/m]

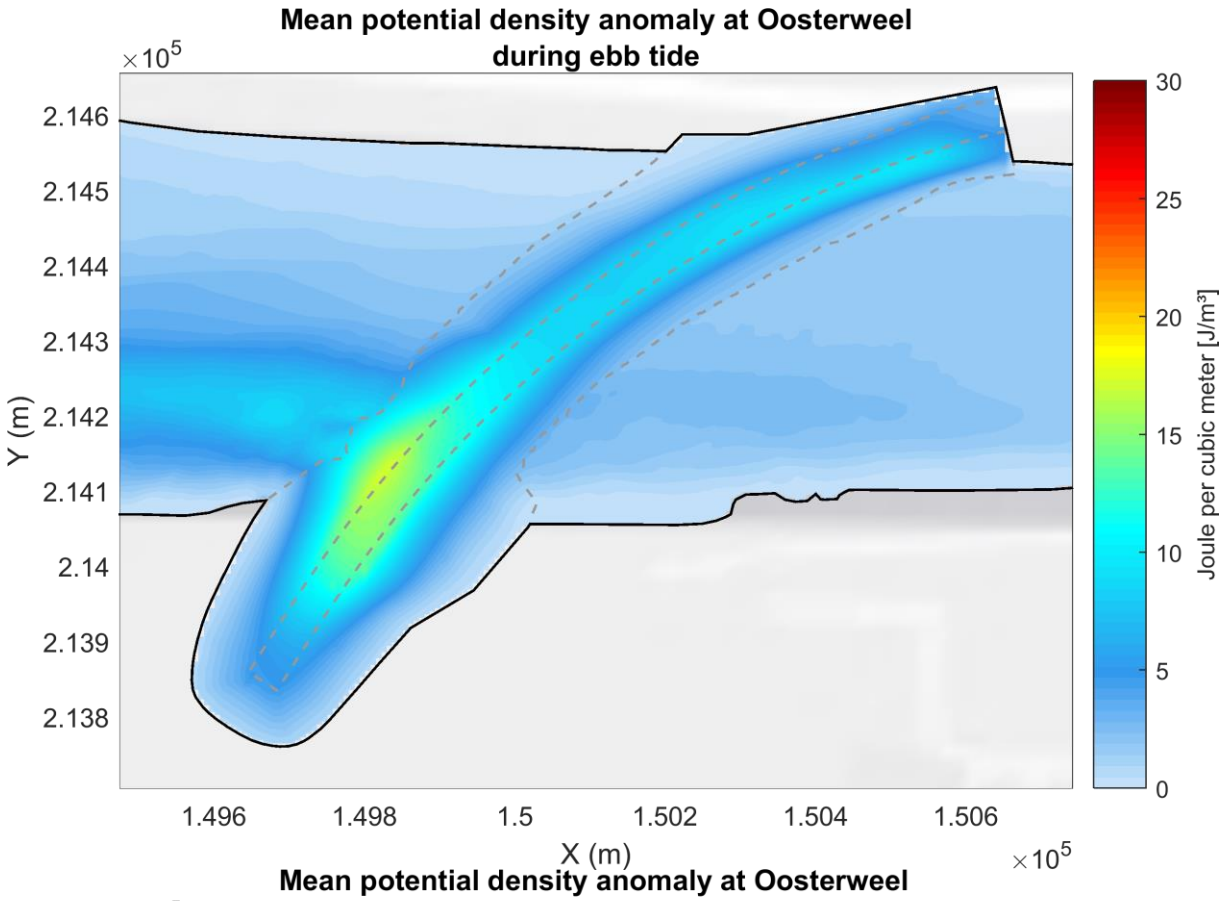
Mean potential density anomaly at Oosterweel
during ebb tide
×10^5
2.146
2.145
2.144
2.143
2.142
2.141
2.14
2.139
2.138
Y (m)
1.496
1.498
1.5
1.502
1.504
1.506
X (m)
×10^5
30
25
20
15
10
5
0
Joule per cubic meter [J/m³]

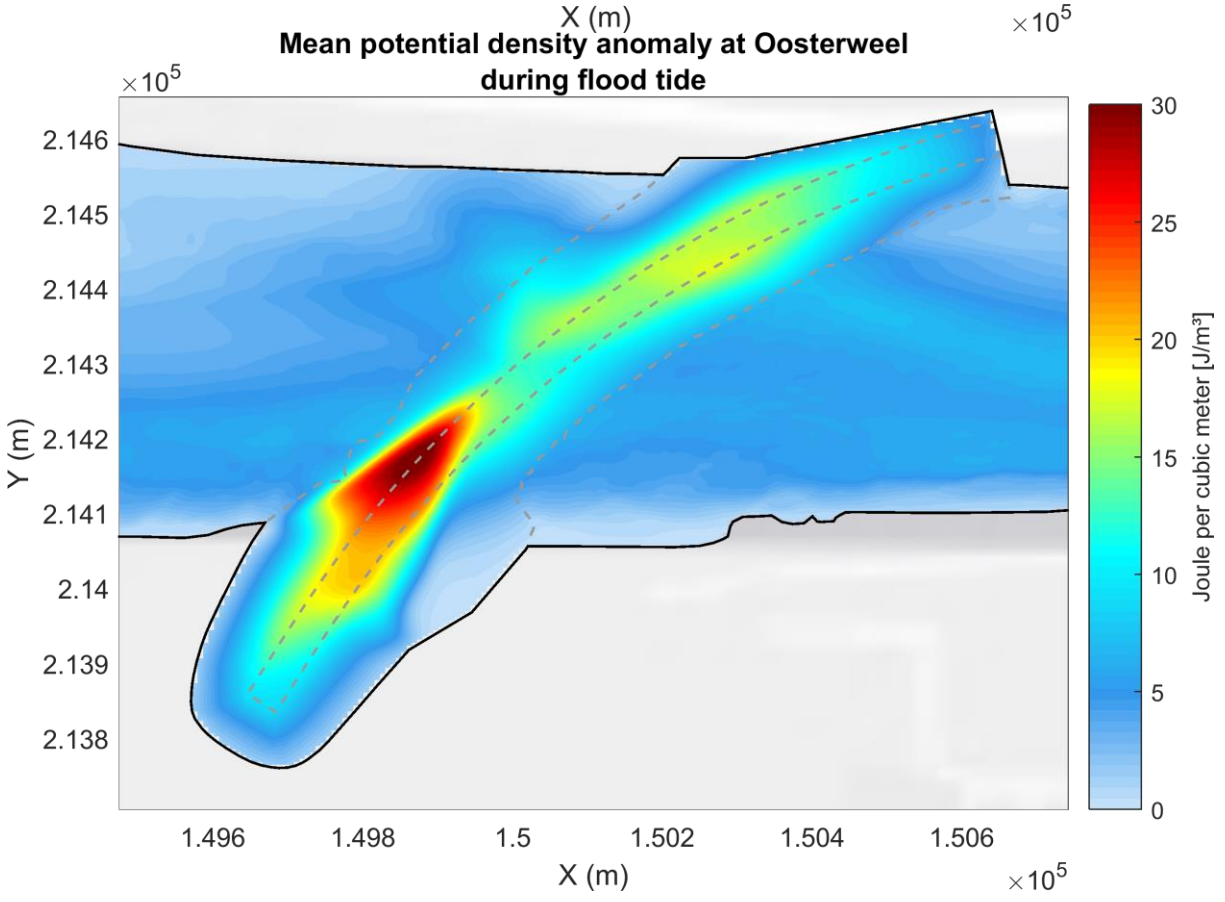
Mean potential density anomaly at Oosterweel
during flood tide
×10^5
2.146
2.145
2.144
2.143
2.142
2.141
2.14
2.139
2.138
Y (m)
1.496
1.498
1.5
1.502
1.504
1.506
X (m)
×10^5
30
25
20
15
10
5
0
Joule per cubic meter [J/m³]

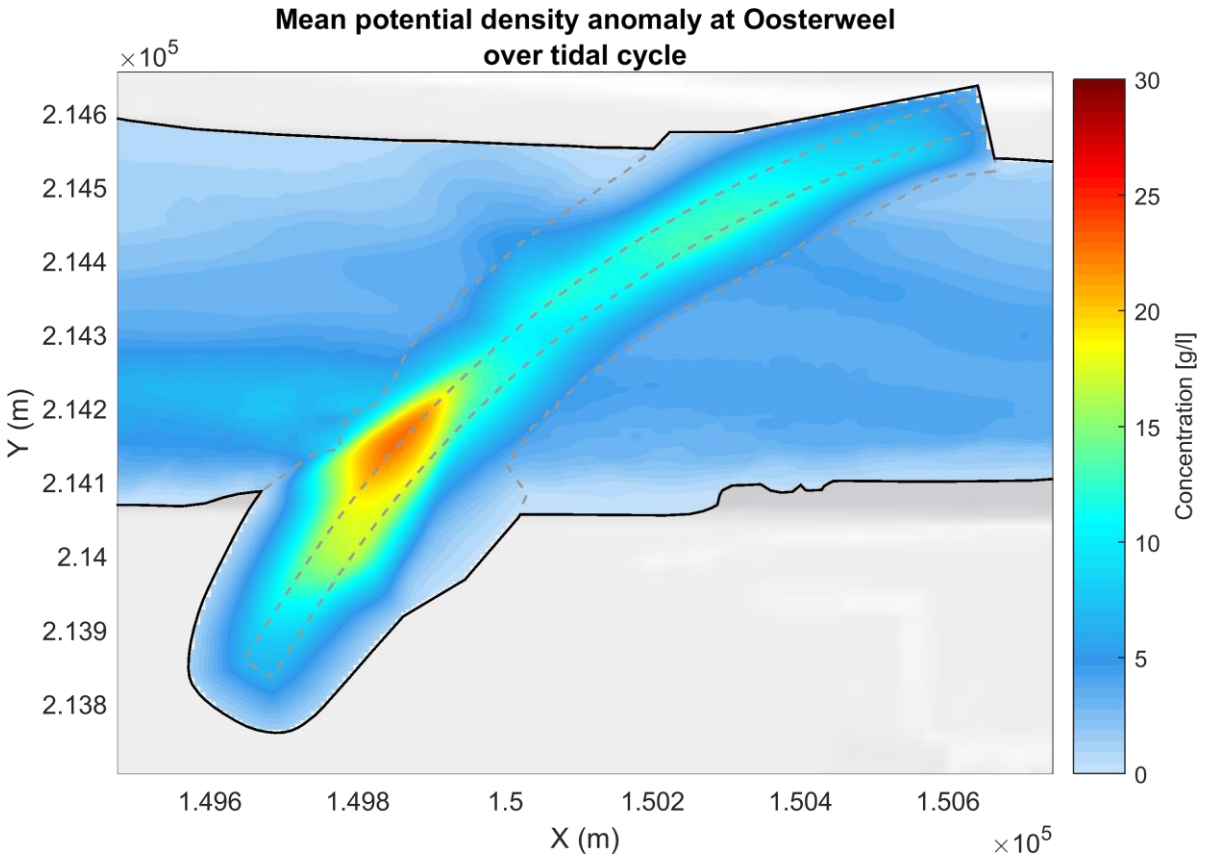
Mean potential density anomaly at Oosterweel over tidal cycle
×10^5
2.146
2.145
2.144
2.143
2.142
2.141
2.14
2.139
2.138
Y (m)
1.496
1.498
1.5
1.502
1.504
1.506
X (m)
×10^5
30
25
20
15
10
5
0
Concentration [g/l]

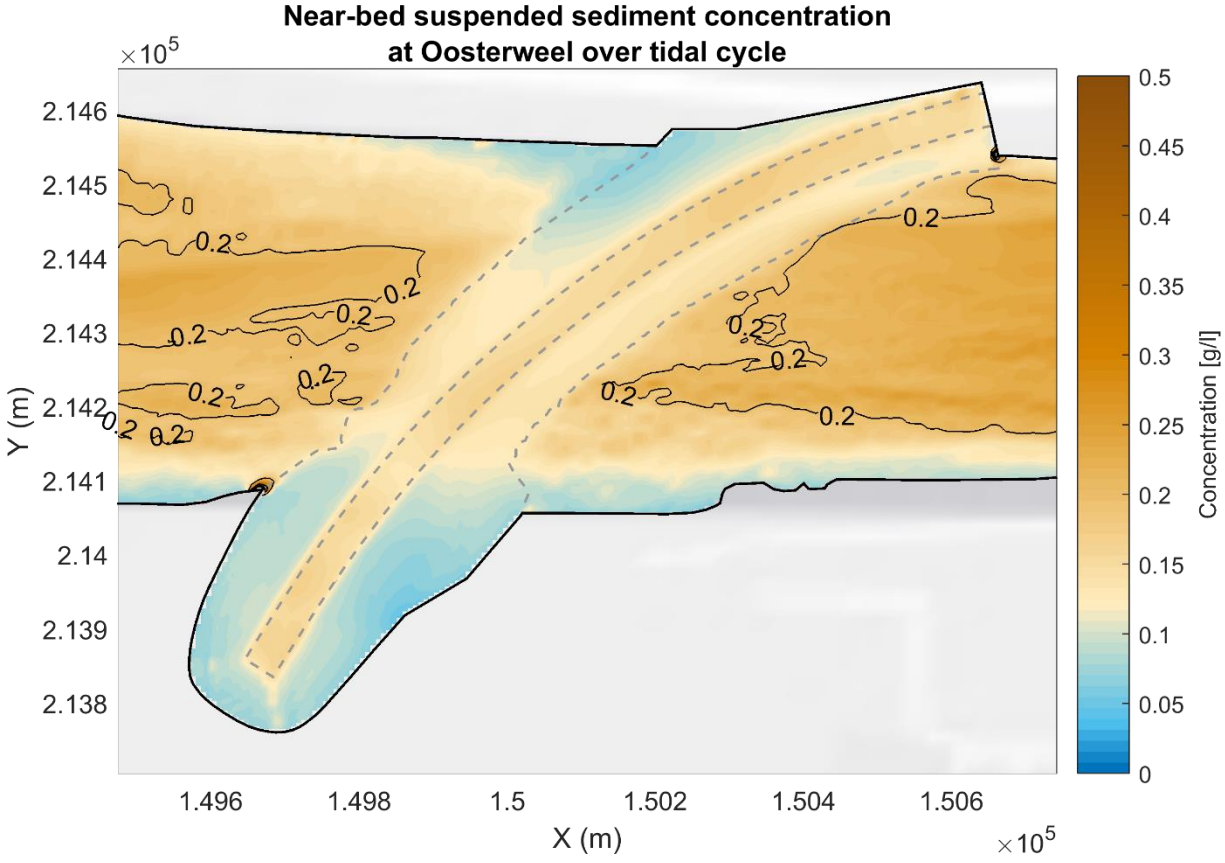
Near-bed suspended sediment concentration at Oosterweel over tidal cycle
×10^5
2.146
2.145
2.144
2.143
2.142
2.141
2.14
2.139
2.138
Y (m)
0.2
1.496
1.498
1.5
1.502
1.504
1.506
X (m)
×10^5
0.5
0.45
0.4
0.35
0.3
0.25
0.2
0.15
0.1
0.05
0
Concentration [g/l]

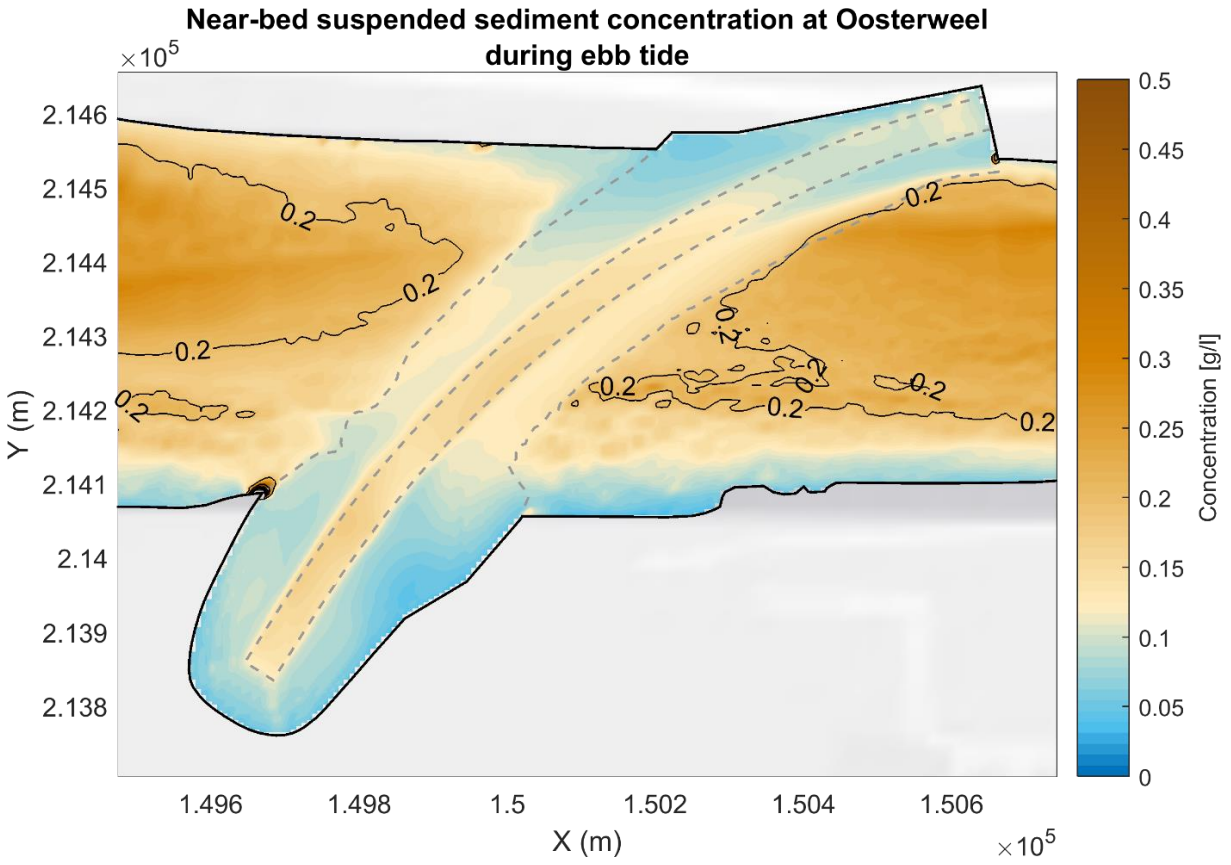
Near-bed suspended sediment concentration at Oosterweel during ebb tide
×10^5
2.146
2.145
2.144
2.143
2.142
2.141
2.14
2.139
2.138
Y (m)
1.496
1.498
1.5
1.502
1.504
1.506
X (m)
×10^5
0.2
0.5
0.45
0.4
0.35
0.3
0.25
0.2
0.15
0.1
0.05
0
Concentration [g/l]

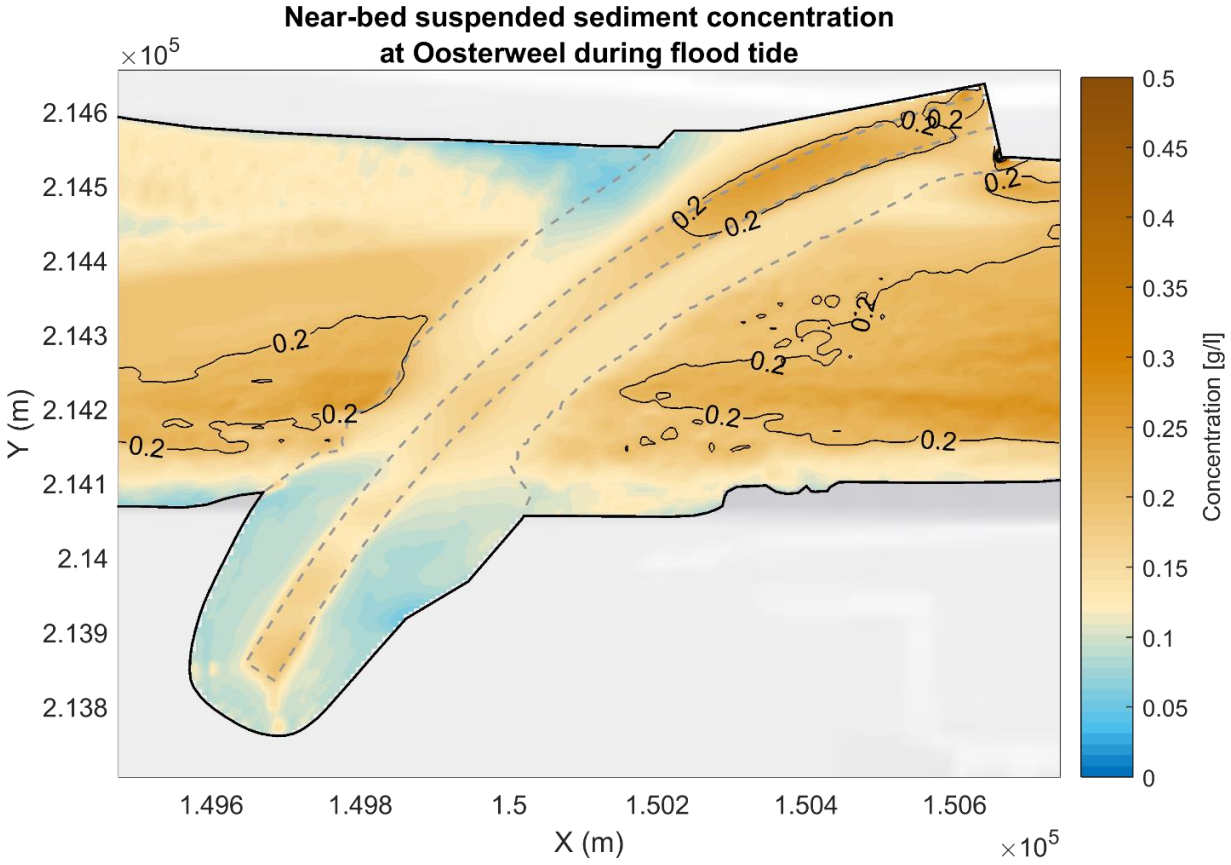
Near-bed suspended sediment concentration at Oosterweel during flood tide
×10^5
2.146
2.145
2.144
2.143
2.142
2.141
2.14
2.139
2.138
Y (m)
1.496
1.498
1.5
1.502
1.504
1.506
X (m)
×10^5
0.2
0.5
0.45
0.4
0.35
0.3
0.25
0.2
0.15
0.1
0.05
0
Concentration [g/l]

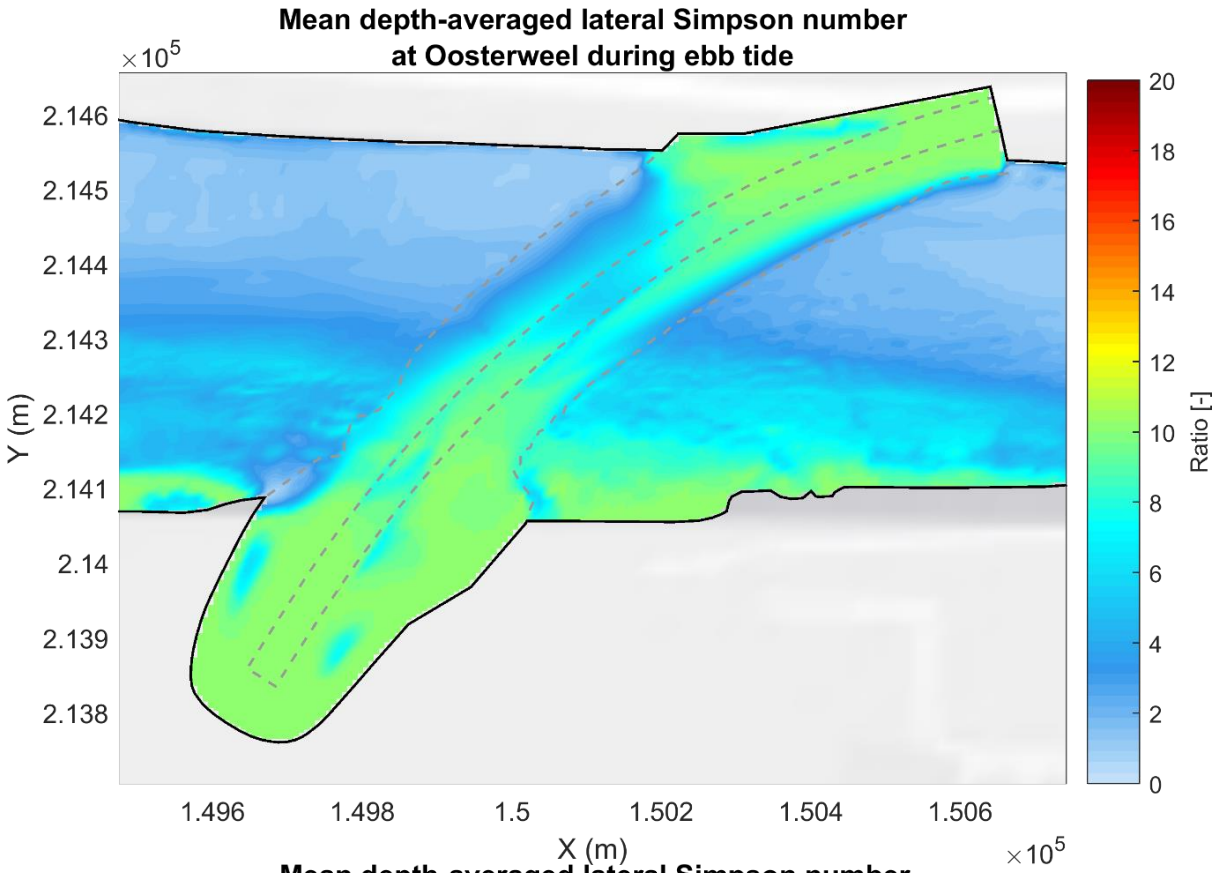
Mean depth-averaged lateral Simpson number
at Oosterweel during ebb tide
×10^5
2.146
2.145
2.144
2.143
2.142
2.141
2.14
2.139
2.138
Y (m)
1.496
1.498
1.5
1.502
1.504
1.506
X (m)
×10^5
20
18
16
14
12
10
8
6
4
2
0
Ratio [-]

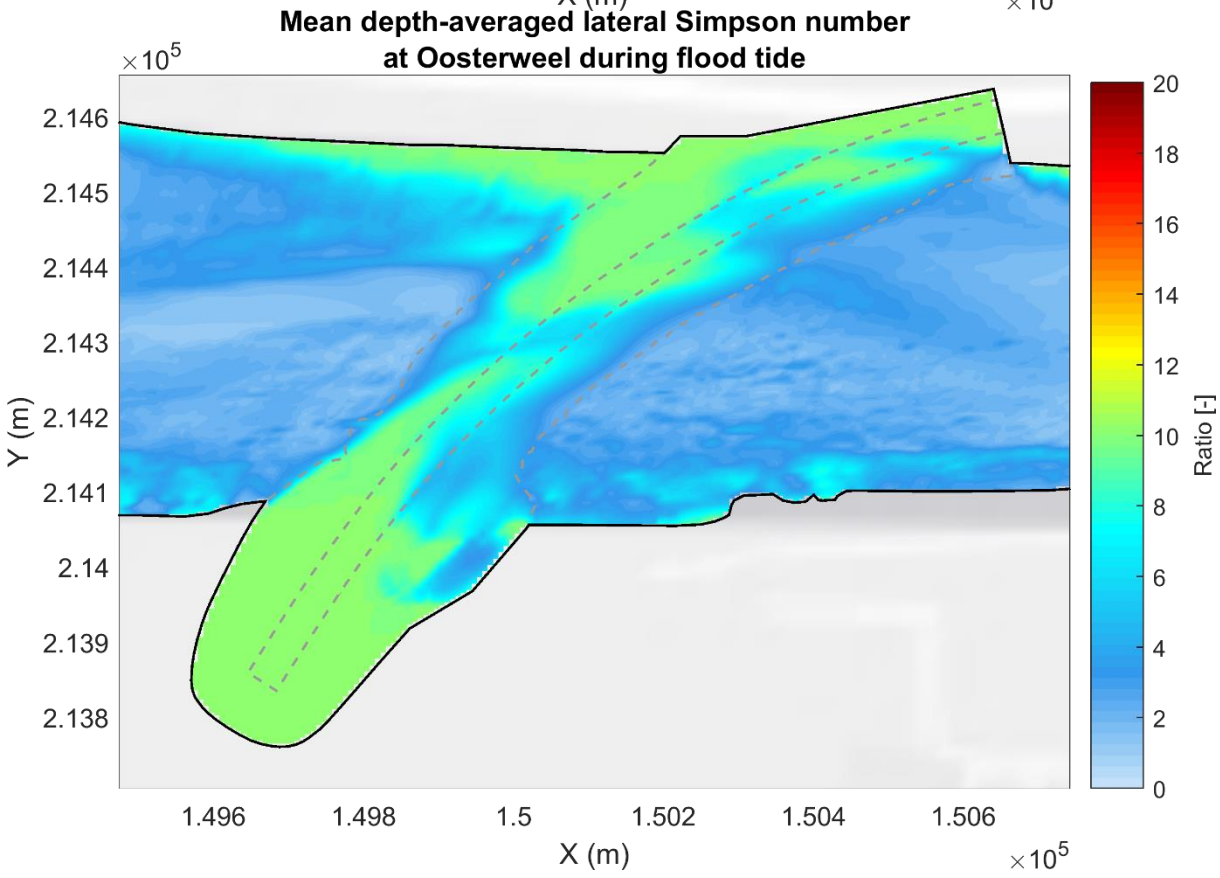
Mean depth-averaged lateral Simpson number
at Oosterweel during flood tide
×10^5
2.146
2.145
2.144
2.143
2.142
2.141
2.14
2.139
2.138
Y (m)
1.496
1.498
1.5
1.502
1.504
1.506
X (m)
×10^5
20
18
16
14
12
10
8
6
4
2
0
Ratio [-]

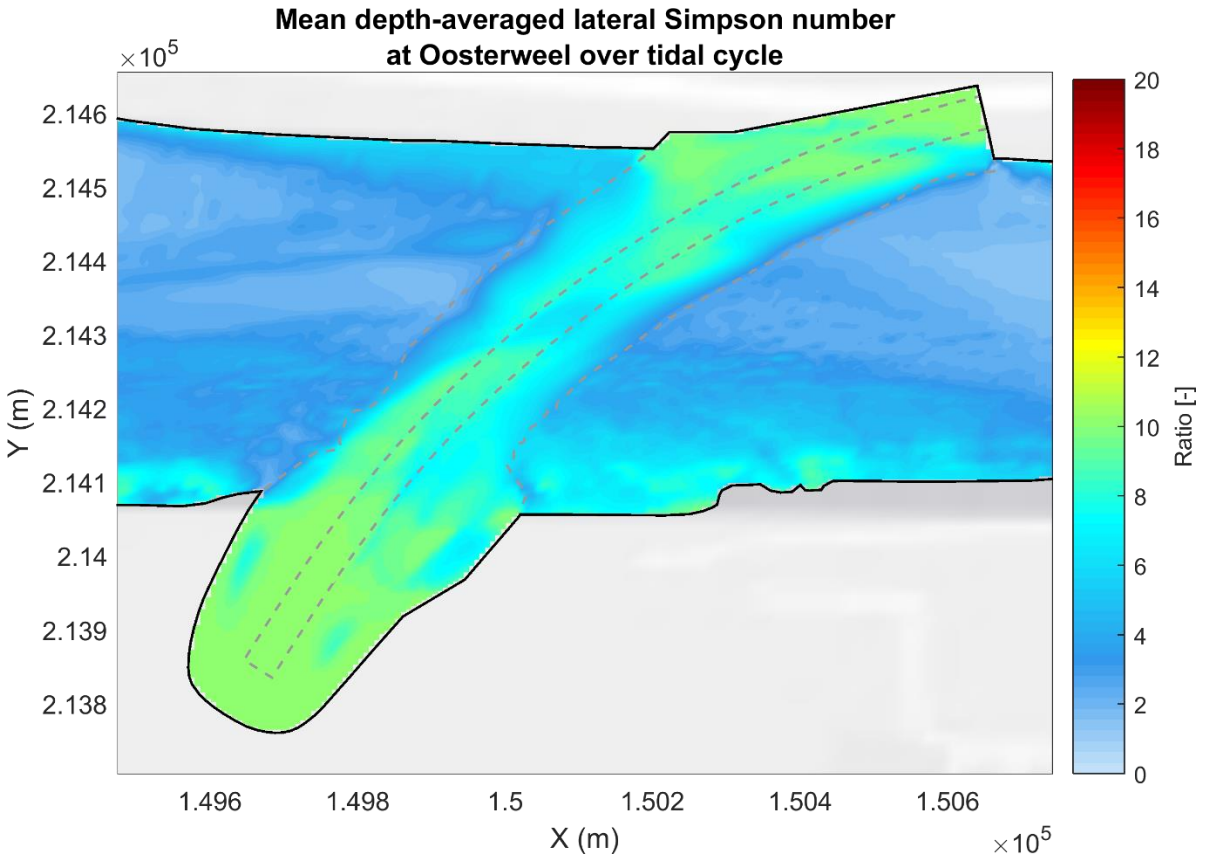
Mean depth-averaged lateral Simpson number
at Oosterweel over tidal cycle
×10^5
2.146
2.145
2.144
2.143
2.142
2.141
2.14
2.139
2.138
Y (m)
1.496
1.498
1.5
1.502
1.504
1.506
X (m)
×10^5
20
18
16
14
12
10
8
6
4
2
0
Ratio [-]

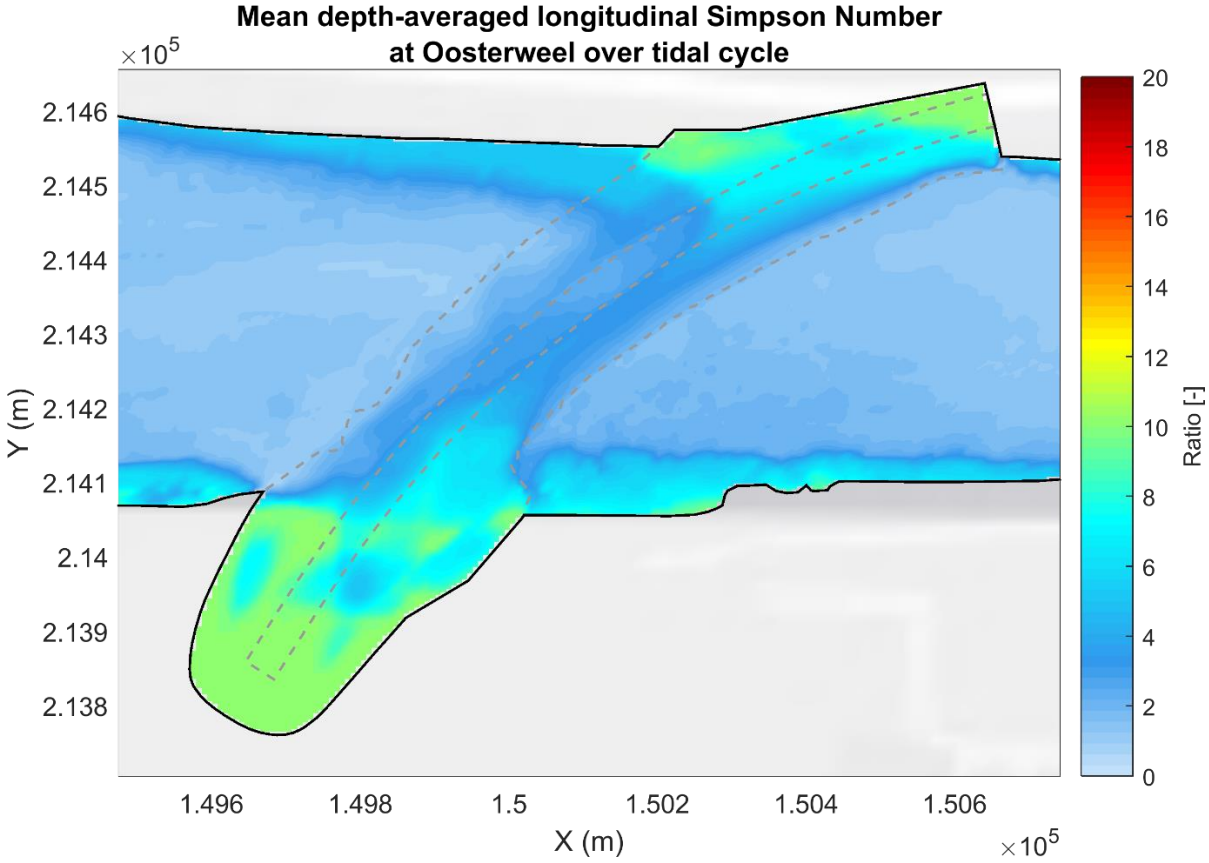
Mean depth-averaged longitudinal Simpson Number
at Oosterweel over tidal cycle
×10^5
2.146
2.145
2.144
2.143
2.142
2.141
2.14
2.139
2.138
Y (m)
1.496
1.498
1.5
1.502
1.504
1.506
X (m)
×10^5
20
18
16
14
12
10
8
6
4
2
0
Ratio [-]

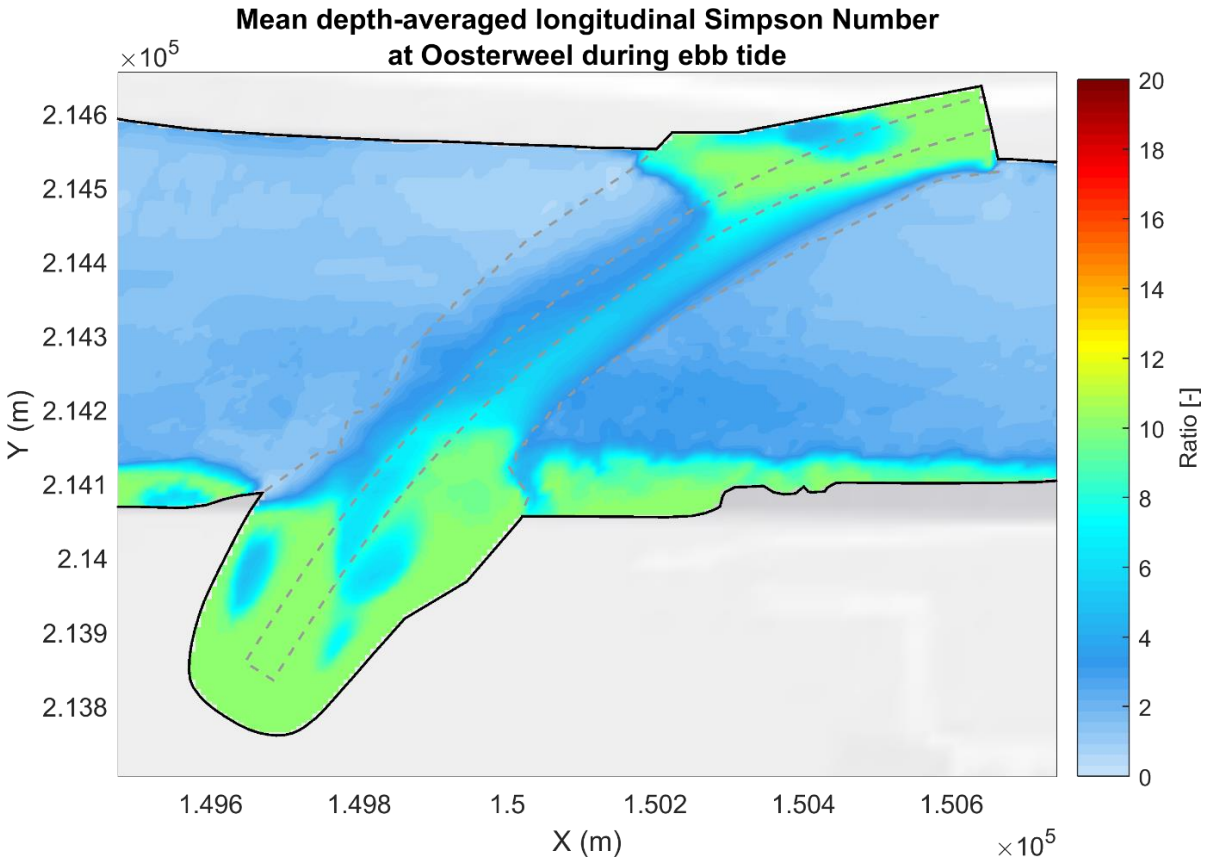
Mean depth-averaged longitudinal Simpson Number
at Oosterweel during ebb tide
×10^5
2.146
2.145
2.144
2.143
2.142
2.141
2.14
2.139
2.138
Y (m)
1.496
1.498
1.5
1.502
1.504
1.506
X (m)
×10^5
20
18
16
14
12
10
8
6
4
2
0
Ratio [-]

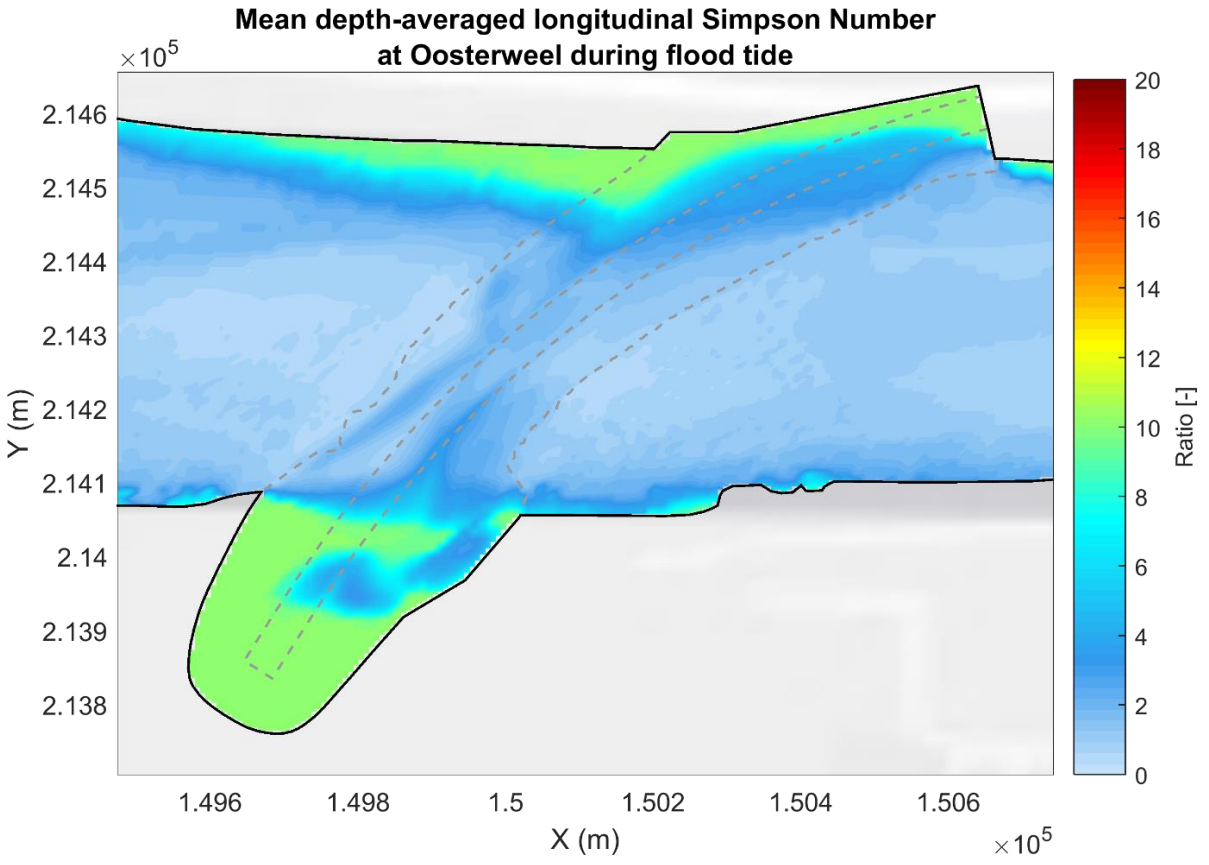
Mean depth-averaged longitudinal Simpson Number
at Oosterweel during flood tide
×10^5
2.146
2.145
2.144
2.143
2.142
2.141
2.14
2.139
2.138
Y (m)
1.496
1.498
1.5
1.502
1.504
1.506
X (m)
×10^5
20
18
16
14
12
10
8
6
4
2
0
Ratio [-]

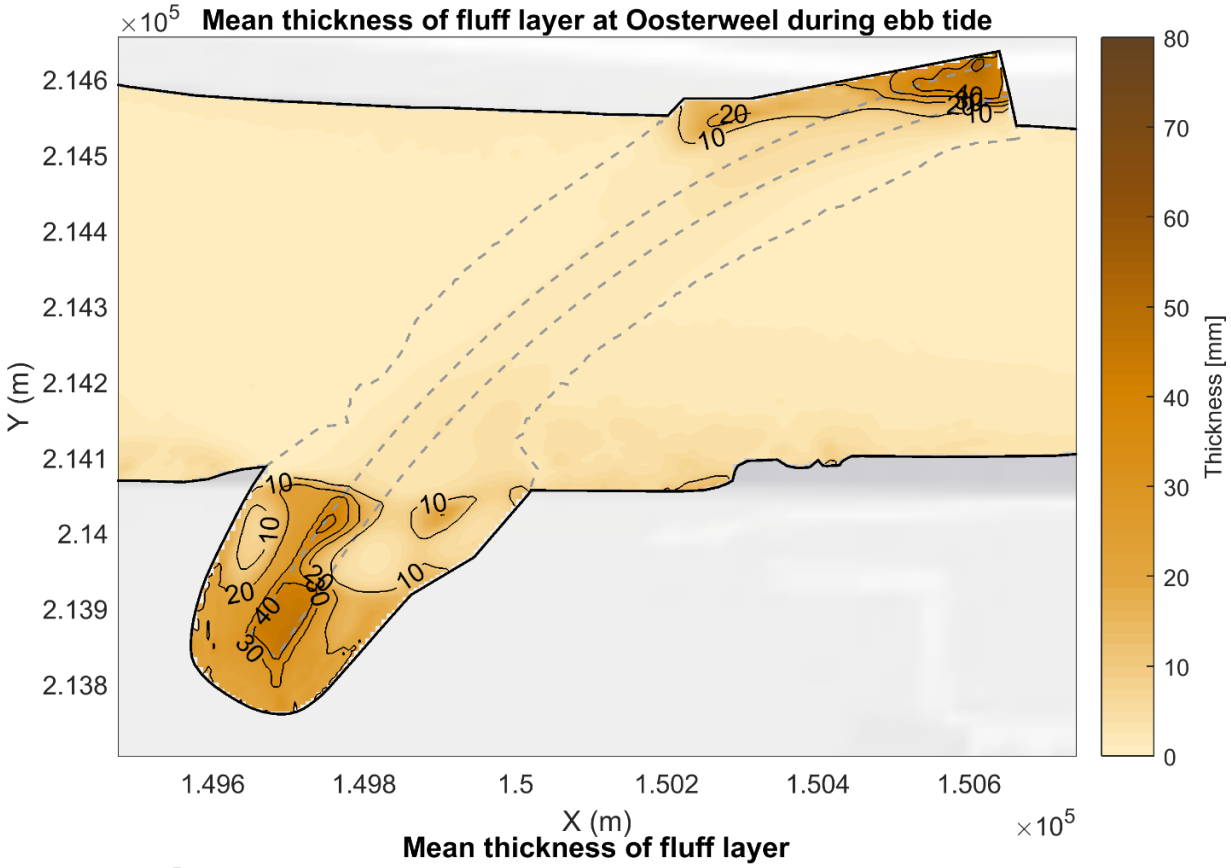
Mean thickness of fluff layer at Oosterweel during ebb tide
×10^5
2.146
2.145
2.144
2.143
2.142
2.141
2.14
2.139
2.138
Y (m)
1.496
1.498
1.5
1.502
1.504
1.506
X (m)
×10^5
Thickness [mm]
0
10
20
30
40
50
60
70
80

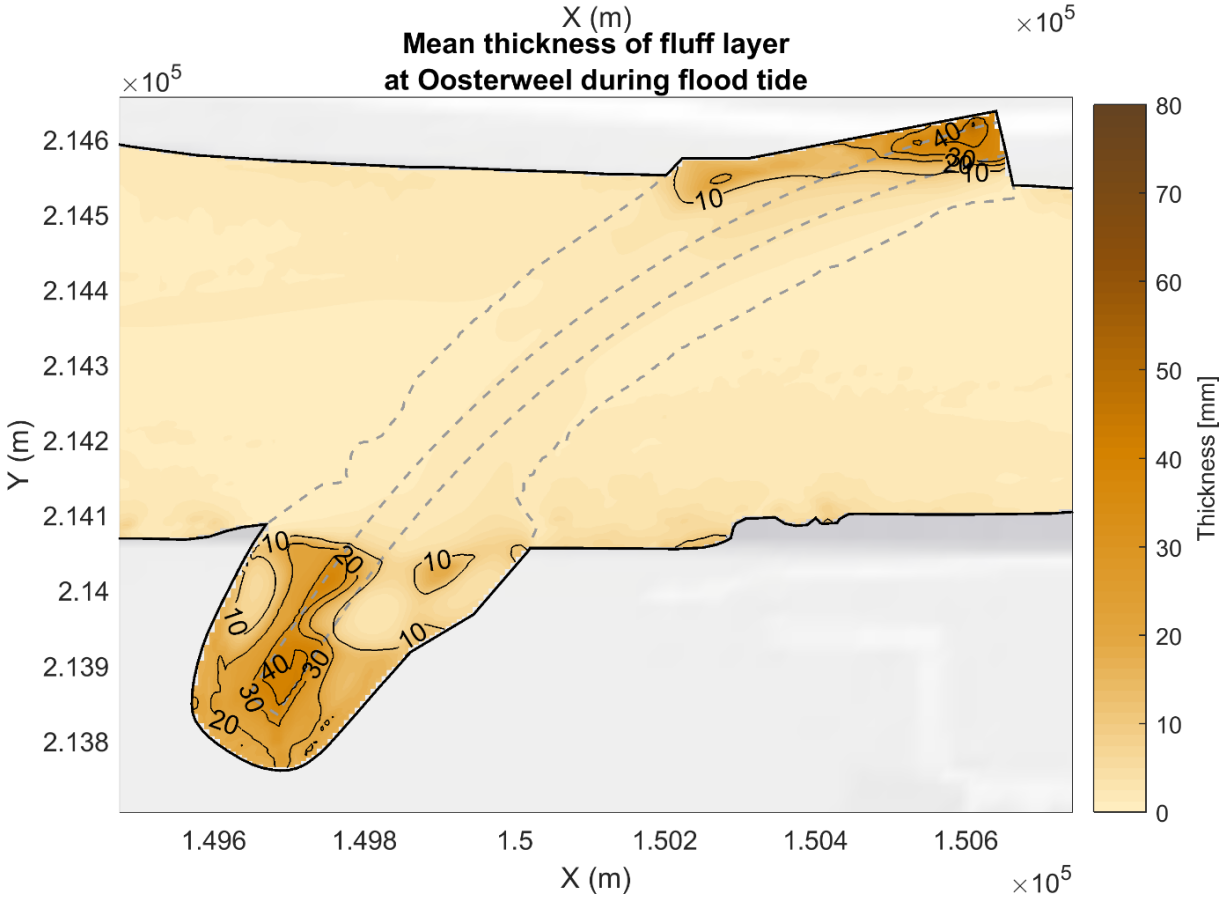
Mean thickness of fluff layer
at Oosterweel during flood tide
×10^5
2.146
2.145
2.144
2.143
2.142
2.141
2.14
2.139
2.138
Y (m)
1.496
1.498
1.5
1.502
1.504
1.506
X (m)
×10^5
Thickness [mm]
0
10
20
30
40
50
60
70
80

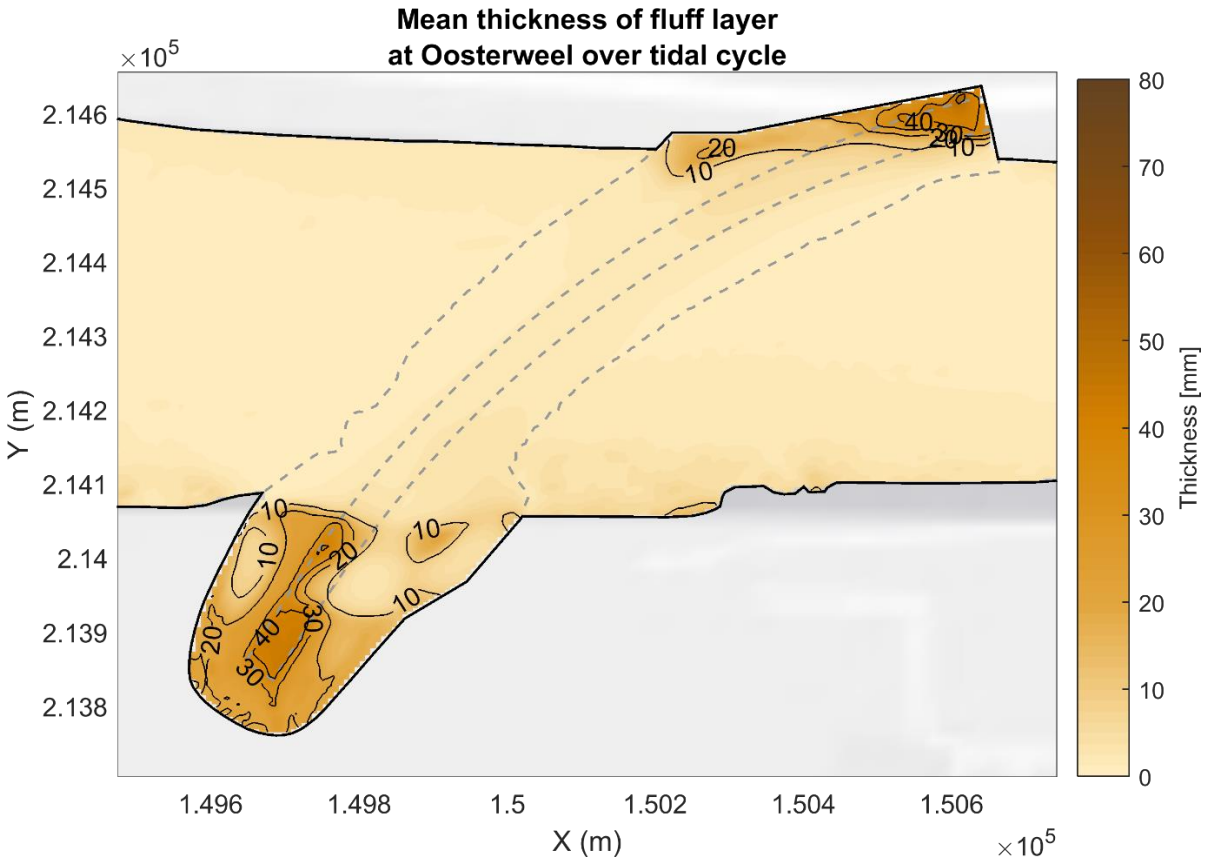
Mean thickness of fluff layer
at Oosterweel over tidal cycle
×10^5
Y (m)
X (m)
×10^5
Thickness [mm]

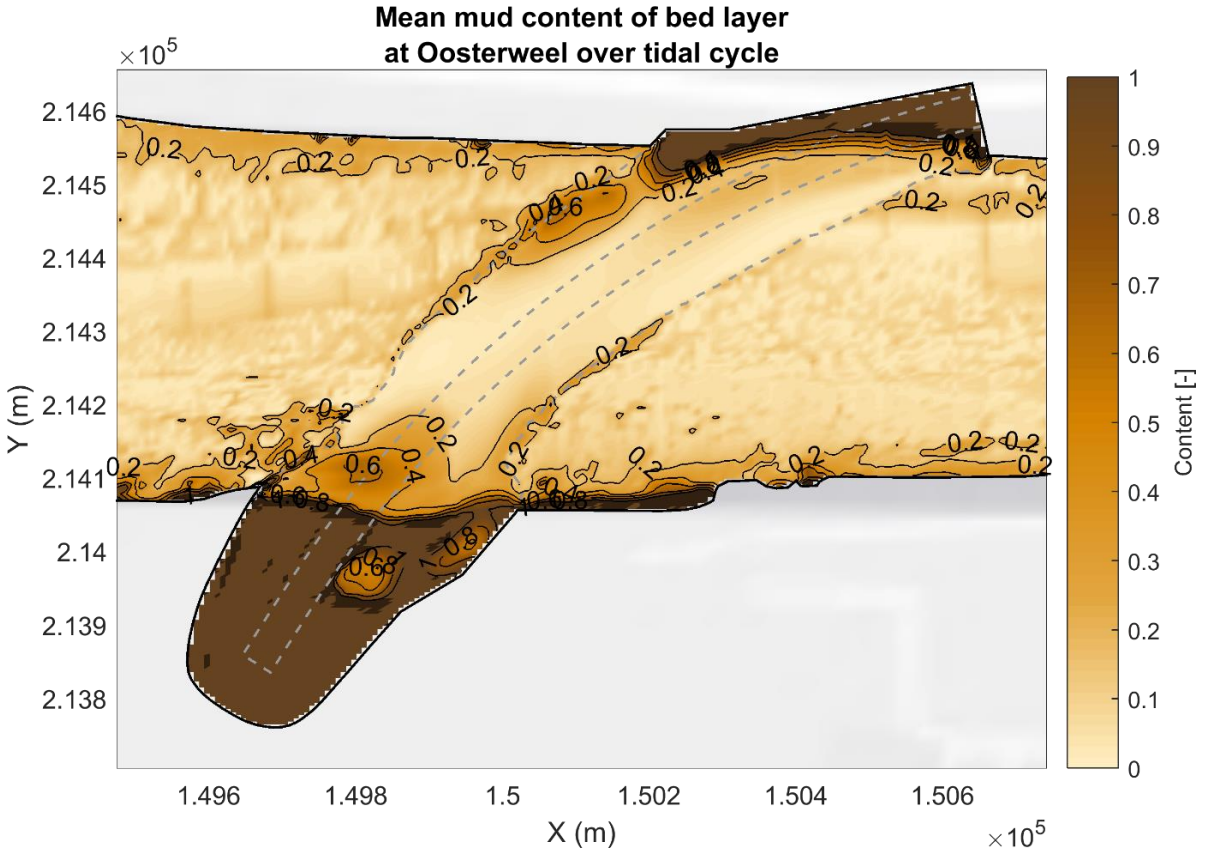
Mean mud content of bed layer
at Oosterweel over tidal cycle
×10^5
Y (m)
X (m)
×10^5
Content [-]

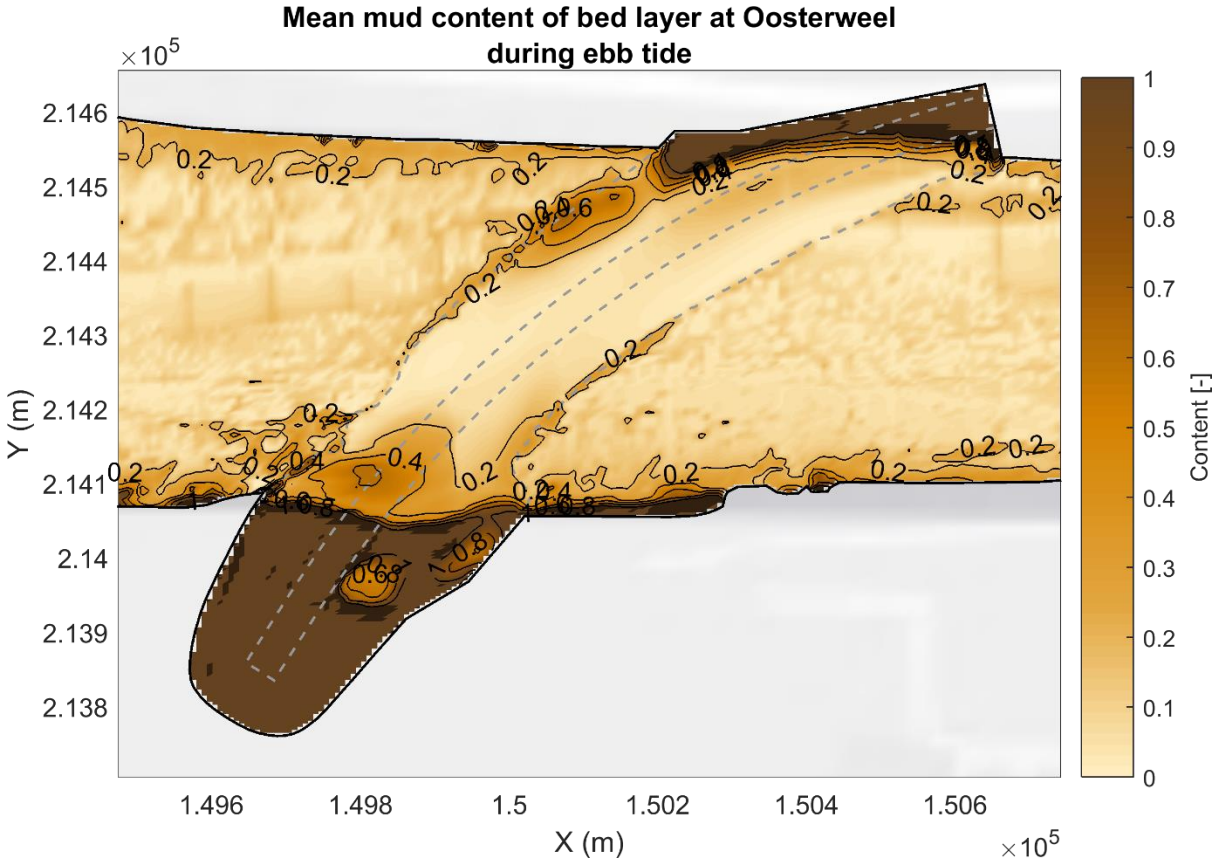
Mean mud content of bed layer at Oosterweel during ebb tide
×10^5
2.146
2.145
2.144
2.143
2.142
2.141
2.14
2.139
2.138
Y (m)
1.496
1.498
1.5
1.502
1.504
1.506
X (m)
×10^5
Content [-]
1
0.9
0.8
0.7
0.6
0.5
0.4
0.3
0.2
0.1
0

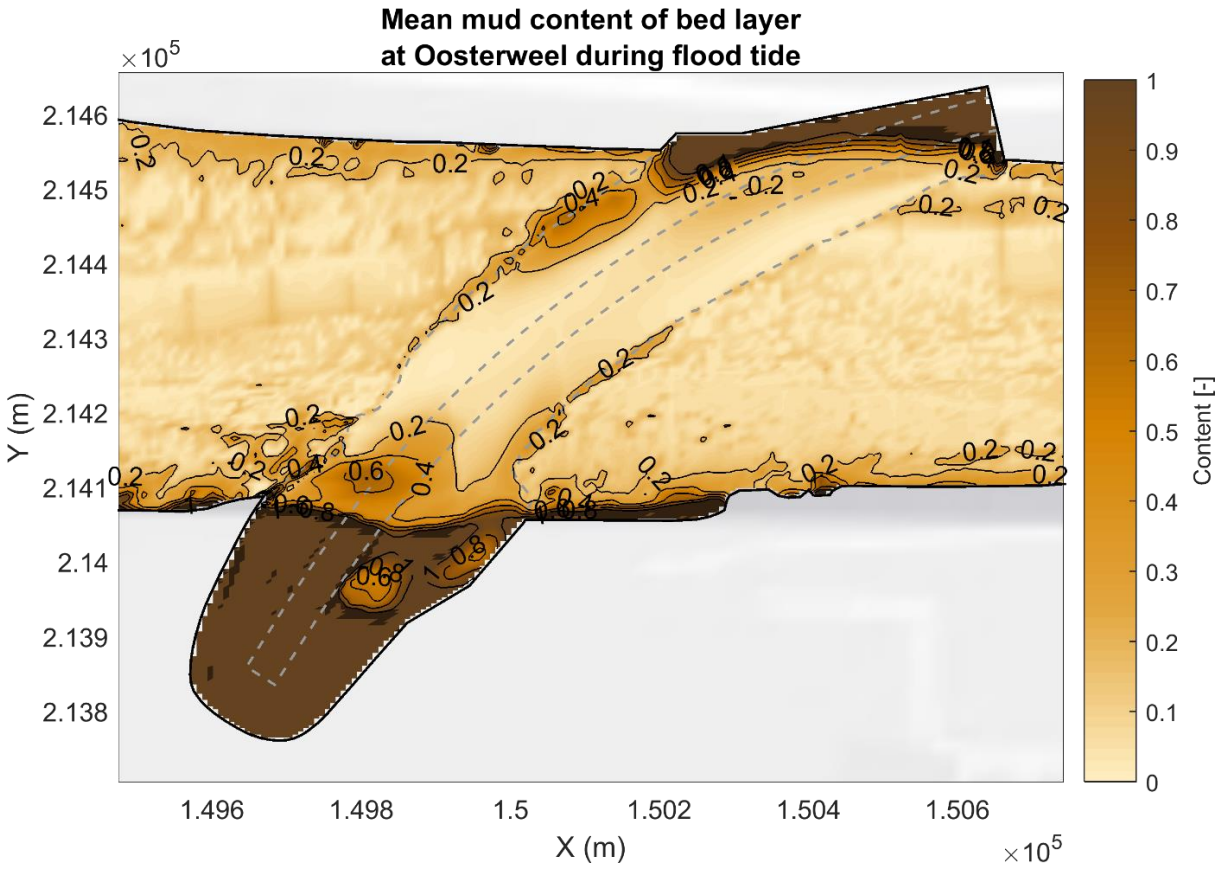
Mean mud content of bed layer at Oosterweel during flood tide
×10^5
2.146
2.145
2.144
2.143
2.142
2.141
2.14
2.139
2.138
Y (m)
1.496
1.498
1.5
1.502
1.504
1.506
X (m)
×10^5
Content [-]
1
0.9
0.8
0.7
0.6
0.5
0.4
0.3
0.2
0.1
0

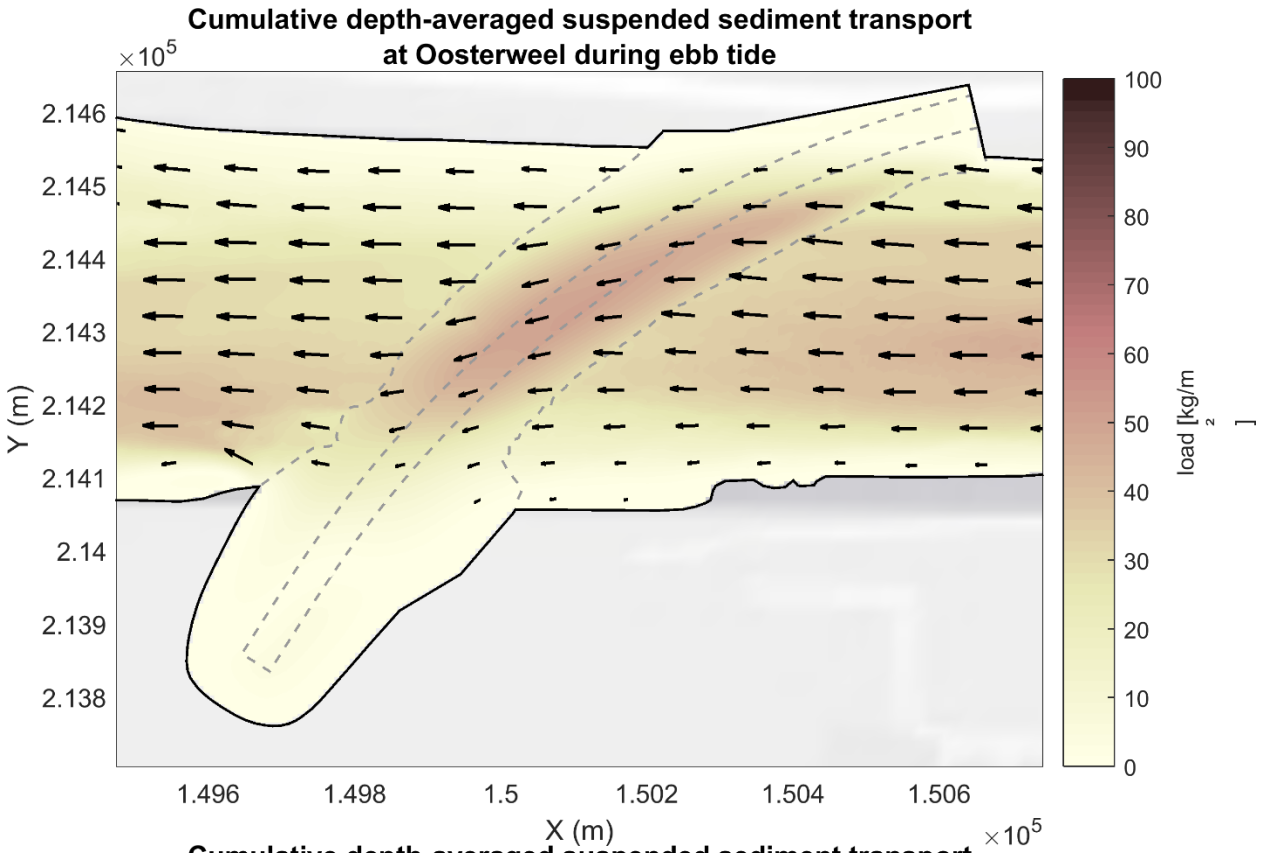
Cumulative depth-averaged suspended sediment transport
at Oosterweel during ebb tide
×10^5
2.146
2.145
2.144
2.143
2.142
2.141
2.14
2.139
2.138
Y (m)
1.496
1.498
1.5
1.502
1.504
1.506
X (m)
×10^5
100
90
80
70
60
50
40
30
20
10
0
load [kg/m2]

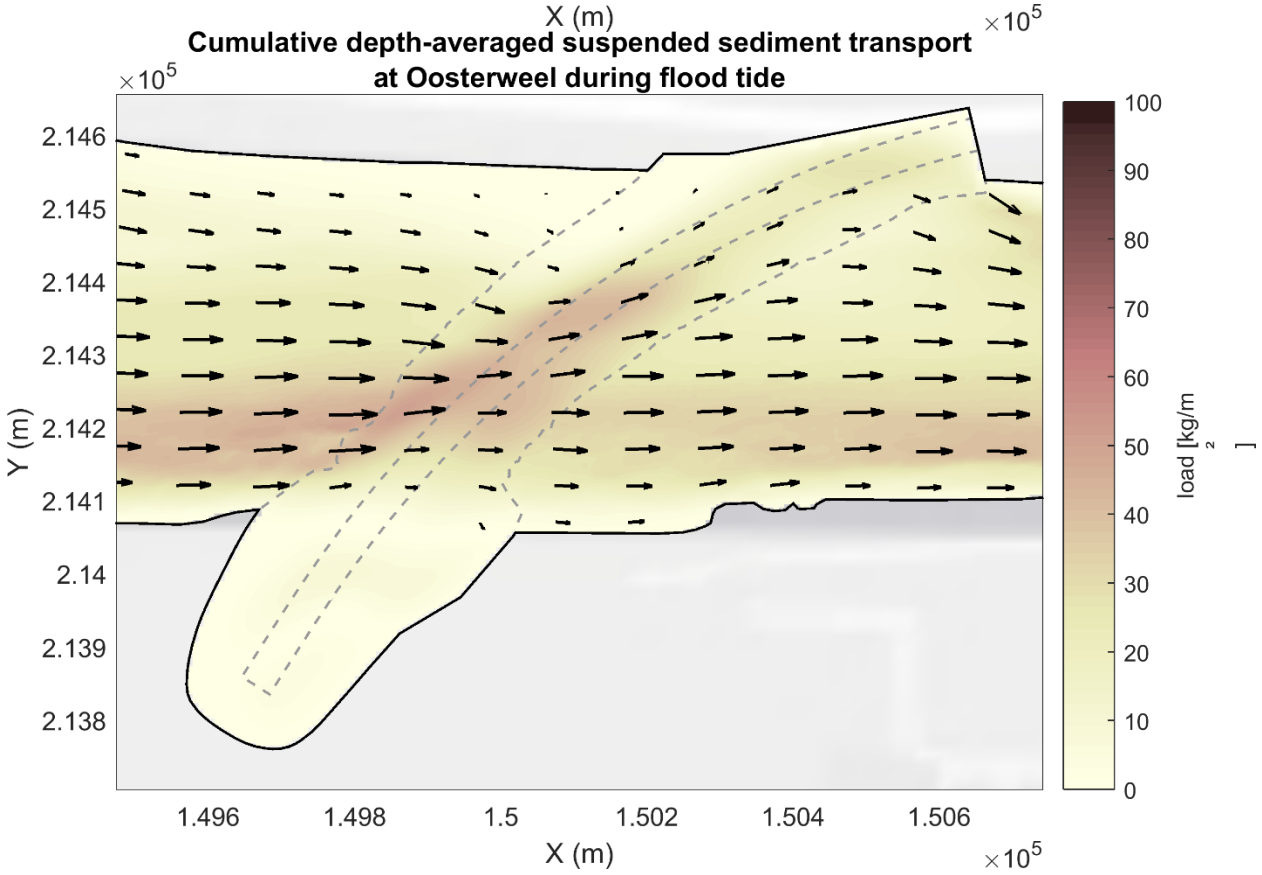
Cumulative depth-averaged suspended sediment transport
at Oosterweel during flood tide
×10^5
2.146
2.145
2.144
2.143
2.142
2.141
2.14
2.139
2.138
Y (m)
1.496
1.498
1.5
1.502
1.504
1.506
X (m)
×10^5
100
90
80
70
60
50
40
30
20
10
0
load [kg/m2]

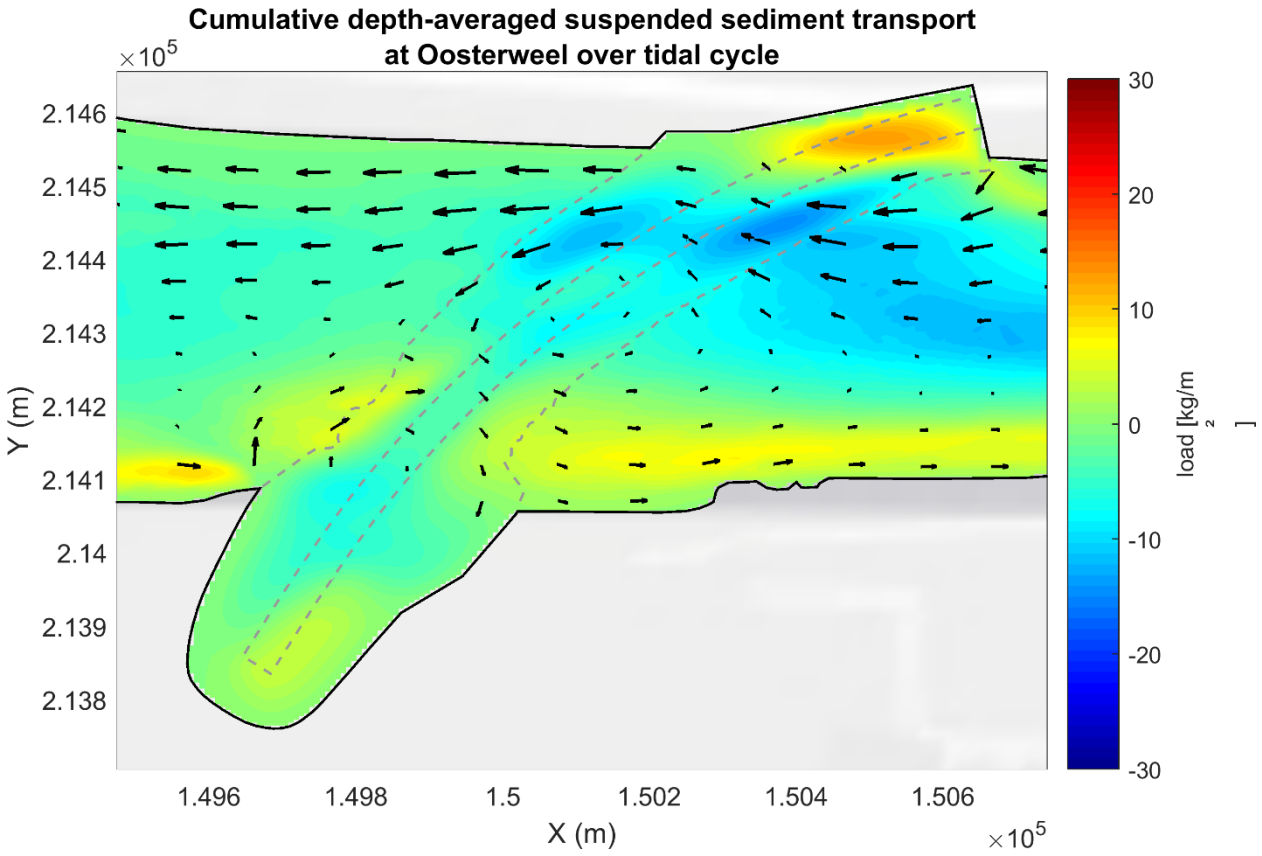
Cumulative depth-averaged suspended sediment transport
at Oosterweel over tidal cycle
×10^5
2.146
2.145
2.144
2.143
2.142
2.141
2.14
2.139
2.138
Y (m)
1.496
1.498
1.5
1.502
1.504
1.506
X (m)
×10^5
30
20
10
0
-10
-20
-30
load [kg/m^2]

Appendix H. Identified governing sediment transport and trapping mechanisms

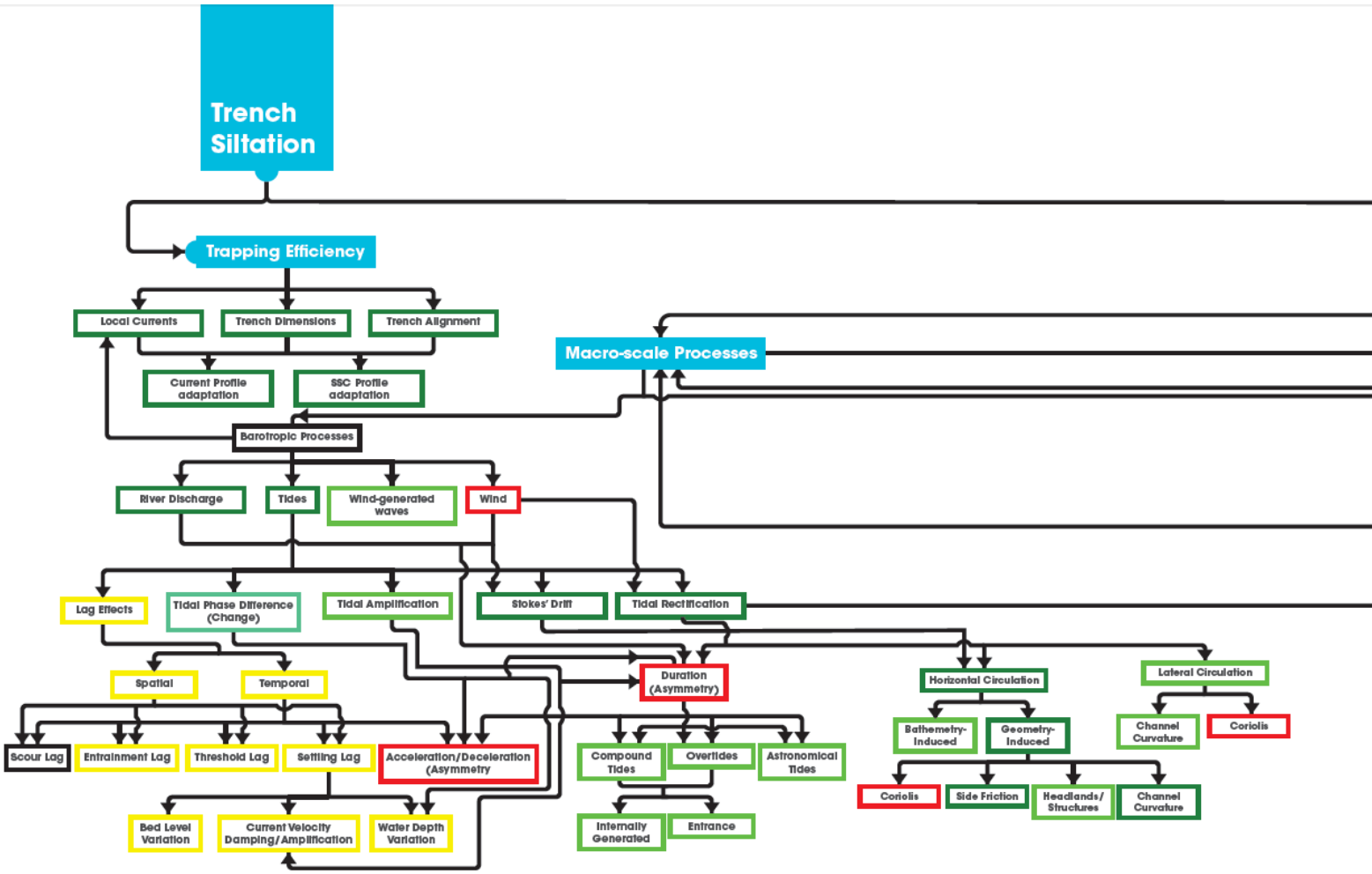
Trench Siltation
Trapping Efficiency
Local Currents
Trench Dimensions
Trench Alignment
Current Profile adaptation
SSC Profile adaptation
Macro-scale Processes
Barotropic Processes
River Discharge
Tides
Wind-generated waves
Wind
Lag Effects
Tidal Phase Difference (Change)
Tidal Amplification
Stokes' Drift
Tidal Rectification
Spatial
Temporal
Duration (Asymmetry)
Horizontal Circulation
Lateral Circulation
Scour Lag
Entrainment Lag
Threshold Lag
Settling Lag
Acceleration/Deceleration (Asymmetry
Compound Tides
Overtides
Astronomical Tides
Bathemetry-Induced
Geometry-Induced
Channel Curvature
Coriolis
Coriolis
Side Friction
Headlands/ Structures
Channel Curvature
Bed Level Variation
Current Velocity Damping/Amplification
Water Depth Variation
Internally Generated
Entrance

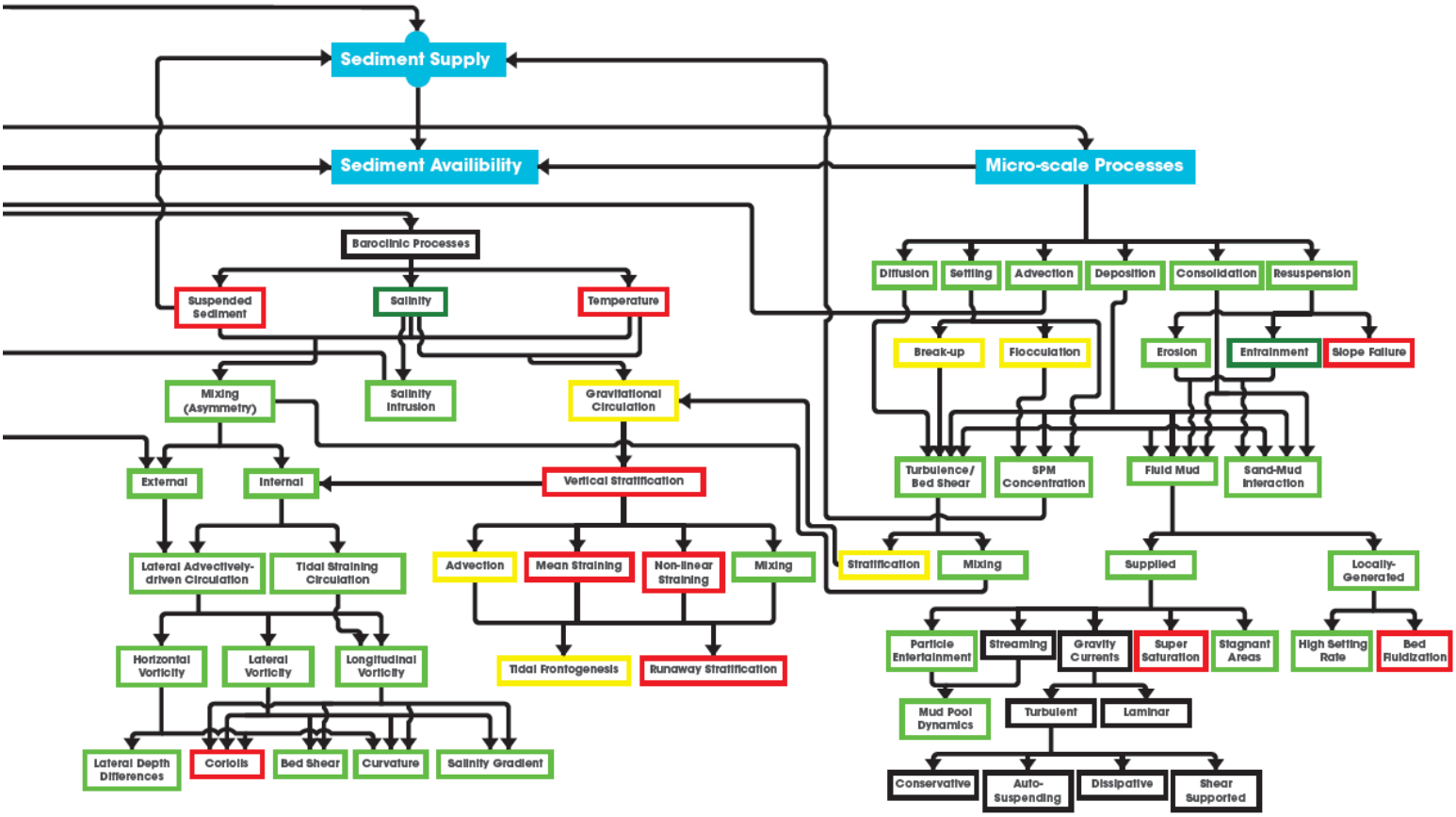
Sediment Supply
Sediment Availibility
Micro-scale Processes
Barocinic Processes
Suspended Sediment
Salinity
Temperature
Mixing (Asymmetry)
Salinity Intrusion
Gravitational Circulation
External
Internal
Vertical Stratification
Lateral Advectively-driven Circulation
Tidal Straining Circulation
Advection
Mean Straining
Non-linear Straining
Mixing
Horizontal Vorticity
Lateral Vorticity
Longitudinal Vorticity
Tidal Frontogenesis
Runaway Stratification
Lateral Depth Differences
Coriolis
Bed Shear
Curvature
Salinity Gradient
Diffusion
Setting
Advection
Deposition
Consolidation
Resuspension
Break-up
Flocculation
Erosion
Entrainment
Slope Failure
Turbulence/ Bed Shear
SPM Concentration
Fluid Mud
Sand-Mud Interaction
Stratification
Mixing
Supplied
Locally-Generated
Particle Entertainment
Streaming
Gravity Currents
Super Saturation
Stagnant Areas
High Setting Rate
Bed Fluidization
Mud Pool Dynamics
Turbulent
Laminar
Conservative
Auto-Suspending
Dissipative
Shear Supported